NSEL Report Series
Report No. NSEL-042
August 2015

Innovations and Advances in Structural Engineering

Honoring the Career of Yozo Fujino

(includes photos with students, friends, and colleagues)

Billie F. Spencer, Jr.
and
Paolo Gardoni
(Editors)

NSEL
NEWMARK STRUCTURAL ENGINEERING LABORATORY

Department of Civil and Environmental Engineering
University of Illinois at Urbana-Champaign

UILU-ENG-2015-1808

ISSN: 1940-9826

The Newmark Structural Engineering Laboratory (NSEL) of the Department of Civil and Environmental Engineering at the University of Illinois at Urbana-Champaign has a long history of excellence in research and education that has contributed greatly to the state-of-the-art in civil engineering. Completed in 1967 and extended in 1971, the structural testing area of the laboratory has a versatile strong-floor/wall and a three-story clear height that can be used to carry out a wide range of tests of building materials, models, and structural systems. The laboratory is named for Dr. Nathan M. Newmark, an internationally known educator and engineer, who was the Head of the Department of Civil Engineering at the University of Illinois [1956-73] and the Chair of the Digital Computing Laboratory [1947-57]. He developed simple, yet powerful and widely used, methods for analyzing complex structures and assemblages subjected to a variety of static, dynamic, blast, and earthquake loadings. Dr. Newmark received numerous honors and awards for his achievements, including the prestigious National Medal of Science awarded in 1968 by President Lyndon B. Johnson. He was also one of the founding members of the National Academy of Engineering.

Contact:
Prof. B.F. Spencer, Jr.
Director, Newmark Structural Engineering Laboratory
2213 NCEL, MC-250
205 North Mathews Ave.
Urbana, IL 61801
Telephone (217) 333-8630
E-mail: bfs@illinois.edu

This technical report is a reprint of the articles that appeared in the March 2015 issue of the Journal of Smart Structures and Systems that was edited by Billie F. Spencer, Jr. and Paolo Gardoni in honoring the career of Dr. Yozo Fujino. To promote wider distribution of this timely collection of papers, the Editor-in-Chief of the Journal, Prof. Chang-Koon Choi, has generously allowed its publication in the Newmark Structural Engineering Laboratory Report Series. In addition, an appendix has been added with photos of the students, friends, and colleagues with Dr. Fujino.

The cover photographs are used with permission. The Trans-Alaska Pipeline photograph was provided by Terra Galleria Photography (http://www.terragalleria.com/).

Smart Structures and Systems

An International Journal of Mechatronics, Sensors, Monitoring, Control, Diagnosis, & Life Cycle Eng.

Volume 15, Number 3, March 2015

CONTENTS

- Continued -

- See inside -

- Continued -

The Journal is accessible via the Internet at the following address:
http://technopress.kaist.ac.kr

Science Citation Index Expanded ; ISI Alerting Services ; Current Contents /Engineering, Computing and Technology ; Shock and Vibration Digest

Preface

Honoring the Career of Yozo Fujino

This special issue of Smart Structures and Systems (SSS) is dedicated to Dr. Yozo Fujino to celebrate his outstanding and innovative contributions to structural engineering during his career. The papers in this issue present a wide range of recent results on bridge dynamics, wind and earthquake effects on structures, health monitoring, and passive/active control technology. This collection of papers also provides a glimpse into the broad nature of Dr. Fujino's interests.

Prof. Fujino is an internationally recognized leader who has been an inspiration to industrial and academic scientists and engineers for over 30 years. During his brilliant academic career, Prof. Fujino has made and continues to make fundamental contributions to dynamics, control and monitoring of bridges considering both wind actions and earthquakes loading. He made significant academic contributions in modeling the nonlinear vibration of cable-stayed bridges and their active/passive control in the 1990s. He is the first person who identified the lateral vibration of cable-stayed bridges due to the synchronization of human walking in 1990, long before the well-known vibration problems of London's Millennium Bridge occurred. His studies on multiple tuned mass dampers (MTMD) and tuned liquid damper (TLD) are well known and frequently cited. In the past decade, he did ground breaking work on vibration-based monitoring, successfully extracting aerodynamic self-excited forces from ambient vibration of a suspension bridge and recognizing vibration modes that were not considered in design from seismic response data. The outcomes of his research are summarized in more than 300 papers in peer-reviewed international journals and more than 700 papers in international conference proceedings. In addition, he has consulted on over 30 signature bridge projects including Akashi Kaikyo Bridge in Japan, Millennium Bridge (vibration control) in UK and Stonecutters Bridge in Hong Kong, demonstrating his recognition not only for his research achievements, but also for his practical knowledge and experience in bridge engineering.

In addition to his numerous contributions to science and engineering, Dr. Fujino is a dedicated and passionate teacher and professor, inspiring young scientists and engineers to advance their knowledge and experiences. His exceptional guidance and mentorship has resulted in the graduation of over 150 M.E. and Ph.D. students, with many of these talented individuals contributing to and shaping the current industrial and academic civil engineering fields. Indeed, we are both personally indebted to Dr. Fujino for his mentorship and friendship, as are so many in the structural engineering community.

The list of national and international awards and honors is long and impressive, including the ASCE Scanlan Medal, the IABMAS T.Y. Lin Medal, and the Medal with Purple Ribbon from the Emperor of Japan. We are sure that there will be more to come.

Dr. Fujino's remarkable talents are not confined to the realm of engineering and science, as he also an accomplished painter, focusing mainly on water-color paintings of bridges. His painting is widely known in his professional community. He uses some paintings to explain his research

results at his technical conference presentations, providing a unique and warm flavor in his presentations, as well as to send New Year's Greetings to his friends and colleagues. For his demonstrated commitment to the social and artistic side of the profession, he recently received the ASCE Winter Award.

Dr. Fujino is currently a Distinguished Professor of Advanced Sciences at Yokohama National University (YNU) in Japan. He is also jointly appointed as a Program Director (Policy Adviser) for the Council for Science, Technology and Innovation, Cabinet Office, Japanese Government. Prior to joining YNU, he served for more than 30 years as a Professor of Civil Engineering and the head of the Bridge and Structures Laboratory at The University of Tokyo.

On behalf of all the contributors to this special issue, we would like to sincerely congratulate Dr. Yozo Fujino on a truly amazing career and wish him good health, happiness, and many more contributions to structural engineering in the years to come.

Billie F. Spencer, Jr.
Paolo Gardoni
University of Illinois at Urbana-Champaign

March 2015

Smart Structures and Systems, *Vol. 15, No. 3 (2015) 505-522*
DOI: http://dx.doi.org/10.12989/sss.2015.15.3.505

Mechanisms of thermally induced deflection of a long-span cable-stayed bridge

Yi Zhou[1a], Limin Sun[*1] and Zhijian Peng[2b]

[1]*State Key Lab for Disaster Reduction in Civil Engineering, Tongji University, Shanghai, 200092, P.R. China*
[2]*Shanghai Highway Investment Construction & Development Co., Ltd., Shanghai, 200335, P.R. China*

(Received October 27, 2014, Revised January 15, 2015, Accepted January 22, 2015)

Abstract. Variation of temperature is a primary environmental factor that affects the behavior of structures. Therefore, understanding the mechanisms of normal temperature-induced variations of structural behavior would help in distinguishing them from anomalies. In this study, we used the structural health monitoring data of the Shanghai Yangtze River Bridge, a steel girder cable-stayed bridge, to investigate the mechanisms of thermally induced vertical deflection (D_T) at mid-span of such bridges. The D_T results from a multisource combination of thermal expansion effects of the cable temperature (T_{Cab}), girder temperature (T_{Gir}), girder differential temperature (T_{Dif}), and tower temperature (T_{Tow}). It could be approximated by multiple linear superpositions under operational conditions. The sensitivities of D_T of the Shanghai Yangtze River Bridge to the above temperatures were in the following order: $T_{Cab} > T_{Gir} > T_{Tow} > T_{Dif}$. However, the direction of the effect of T_{Cab} was observed to be opposite to that of the other three temperatures, and the magnitudes of the effects of T_{Cab} and T_{Gir} were found to be almost one order greater than those of T_{Dif} and T_{Tow}. The mechanisms of the thermally induced vertical deflection variation at mid-span of a cable-stayed bridge as well as the analytical methodology adopted in this study could be applicable for other long-span cable-stayed bridges.

Keywords: cable-stayed bridge; temperature effect; mid-span deflection; mechanisms; structural health monitoring

1. Introduction

Bridges constitute a key role in a modern transportation system and their operational conditions have always been of great concern to bridge owners, users, and engineers. Structural health monitoring (SHM) technology enables long-term, continuous, and on-site measurement of the impact of environmental and loading conditions on a bridge. Consequently, a large number of SHM systems have emerged over the last two decades, almost all of which utilize features or indices extracted from measurements in detecting damages or anomalies (Boller *et al*. 2009). However, it is widely recognized that most structural condition indices vary with environmental factors, especially the temperature conditions. Hence, for more reliable structural evaluation, it is necessary to study thermal effects and how to cancel them out (Catbas *et al.* 2008, Deng *et al*.

*Corresponding author, Professor, E-mail: lmsun@tongji.edu.cn
[a] Ph.D. student, E-mail: zhouyi8659@126.com
[b] Chief Engineer, E-mail: pengzhijian@shgltz.com

http://www.techno-press.org/?journal=sss&subpage=8 ISSN: 1738-1584 (Print), 1738-1991 (Online)

2010, Gentile and Saisi 2013, Li *et al*. 2010, Magalhães *et al*. 2012, Moorty and Roeder 1992, Ni *et al*. 2011, Reynders *et al*. 2013, Sohn 2007, Wang 2009, Wenzel 2009). In this study, the authors investigated the relationship between the temperature and mid-span deflection of a long-span cable-stayed bridge, which is a basic performance indicator of the global rigidity and mechanical state of such a bridge.

During design phase of a bridge structure, the thermally induced vertical deflection at mid-span of bridge girder, denoted as D_T, is considered under the limit states, which do not represent structural behavior under normal operation. Field measurements are therefore undoubtedly the best method for investigating actual structures in the real-world. Barr *et al*. (2000), Burdet (2010), and Ghali *et al*. (2000) undertook long-term observations of the mid-span deflection of short and medium span girder bridges and considered the temperature gradient over the girder depth to be the main reason for variations in the deflection. Figueiras *et al*. (2005) also observed that the crown of a centenary arch bridge in Portugal curved upward with increasing temperature.

Thermal effects are not only due to temperature variations, but also to structural constraints. Owing to the complex system of a cable-supported bridge, its thermal effects are of particular interest. Studies on the famous Tsing Ma Suspension Bridge conducted by Xu *et al*. (2010) and Xia *et al*. (2013) revealed that the thermally induced vertical deflection at mid-span decreased with increasing temperature, and that the seasonal variation of D_T was much wider than that during a summer day. Xu *et al*. (2010) concluded that the D_T of the 1377-m-span suspension bridge was partially dominated by the deformation of the main cables. Another often cited SHM campaign on the Tamar Suspension Bridge in the UK, which was transformed into a hybrid cable-stayed and suspension bridge after its upgrade, revealed that a temperature increase caused a downward movement of the mid-span (Brownjohn *et al*. 2009, Koo *et al*. 2013). Based on a multiple linear regression analysis and subsequent comparison of regression coefficients, Westgate (2012) posited that the D_T of the 335-m-span Tamar Bridge was mainly affected by the elongation of the suspension cables. There have also been reports of the D_T of suspension bridges such as the Akashi Kaikyo Bridge (Katsuchi *et al*. 2008), the Yangluo Yangtze River Bridge (Li *et al*. 2011), and the Yeongjong Bridge (Kim *et al*. 2005), which have central spans of 1991, 1280, and 300 m, respectively. As with the two earlier mentioned bridges, the thermally induced vertical deflections at mid-span of these three bridges occur downward with increasing temperature.

Cable-stayed bridges with multi-cable systems are highly statically indeterminate and their inter-constraints are stronger than those of suspension bridges, resulting in more complex thermal effects. Cao *et al*. (2011) analyzed the D_T of the Zhanjiang Bay Bridge, a cable-stayed bridge with a 480-m central steel box girder span, over a period of five summer days. Unlike most other observations, the central span of the girder curved upward under high afternoon temperatures. This was attributed to the uniform temperature increase of the entire structure and/or the localized temperature increase of the top plate of the girder. However, the variation of the D_T over the seasonal cycle was not covered. Moreover, no temperature sensors were placed on the external surface of the towers. Thus the tower temperature used for the finite element (FE) model was highly uncertain. Li (2012) explored the thermally induced vertical deflection at mid-span of the Donghai Bridge, a cable-stayed bridge spanning 420 m and with a steel-concrete composite section girder, and obtained the data range between March and September 2007. The mid-span of the bridge exhibited a slight downward deflection with increasing effective temperature of the girder. The time lags between the deflection and the temperature were also observed. Although an ARX model for predicting the D_T was developed, the physical explanation of such a model was

not considered in the modeling process. Zhu *et al*. (2006) and Chen *et al*. (2006) respectively presented and modeled the same nine-day winter measurements on the Dafosi Yangtze River Bridge, a 450-m-span concrete cable-stayed bridge. It was observed that an increase in the temperature was accompanied by a downward movement at mid-span. An artificial neural network was used to reproduce the winter D_T measurements, but the model was not verified for summer measurements.

From the extensive previous works mentioned so far, it appears that all suspension bridges display similar characteristics, namely a downward thermally induced vertical deflection at mid-span with increasing temperature. However, the direction of the D_T of a cable-stayed bridge depends on the specific bridge; some bridges curve upward mid-span with increasing temperature, whereas others curve downward. Generally, the D_T of a cable-stayed bridge is much more complex and the underlining mechanism is not yet explicitly understood. Moreover, a preliminary study of the field measured D_T of the Shanghai Yangtze River Bridge found that it was difficult to simultaneously explain the seasonal and daily variations of the thermally induced vertical deflection at mid-span based on the air temperature or the temperature of a certain structural component. Hence, it is desirable to determine the mechanisms of variation of D_T using the field SHM data.

The rest of this paper consists of five parts. Section 2 presents the field measurements of the temperature and mid-span deflection of the Shanghai Yangtze River Bridge in February and July 2012. In Section 3, the possible reasons for the D_T variation are discussed qualitatively; and followed by an FE analysis in Section 4 to quantify the effects of the cable temperature (T_{Cab}), girder temperature (T_{Gir}), girder differential temperature (T_{Dif}), tower temperature (T_{Tow}), and temperature-dependent elastic moduli on the thermally induced vertical deflection at mid-span. Section 5 explains the monitoring results and compares the thermal effects of different mechanisms. The findings of this study do not only advance an understanding of the thermal effects on cable-stayed bridges, but also provide theoretic and measured bases for the design and evaluation of such bridges.

2. Monitoring results

2.1 Shanghai Yangtze River Bridge and its SHM system

The Shanghai Yangtze River Bridge is located on the outskirt of Shanghai City, China, at the southern fringe of the north subtropical zone. It is a five-span cable-stayed bridge with dual towers, dual cable planes, and a separated double-box steel girder. It has a span arrangement of 92 m + 258 m + 730 m + 258 m + 92 m = 1430 m and was opened to traffic on October 31, 2009 (Shao 2010). The SHM system of the bridge includes 227 sensors, which are used for real-time monitoring of the environmental and loading conditions as well as the static and dynamic responses of the bridge (Sun *et al*. 2010). The structural temperature and the mid-span deflection are respectively measured by Fiber Bragg Grating (FBG) temperature sensors and GPS technology, with sampling intervals of 1 min and 0.1 s, respectively. In this paper, the D_T is the vertical position or level at the middle of the central span, and the reference is assumed to be the elevation at the time of installing the sensor. A positive value indicates upward movement of the girder. The Shanghai Yangtze River Bridge forms a floating system along its longitudinal axis; it does not

have vertical bearings at the intersections of the girder and the tower. Unlike a monolithic girder-pier system, the thermal effects of the side piers and the subsidiary piers of the Shanghai Yangtze River Bridge, on which no temperature sensors were installed, have little effect on the superstructure. Hence, the temperature changes on those piers as well as the settlement at all the bases are neglected.

2.2 Characteristics of temperature field

The thermally induced vertical deflection at mid-span is a consequence of structural temperature distribution. In this paper, the measured temperatures are introduced into the FE model directly. This is done instead of a transient heat transfer analysis, which is highly uncertain with respect to the unmeasured heat boundary conditions, e.g., the intensity of solar radiation. Hence, it is necessary to first explore the temperature distribution. The ambient air temperature has two dominant cycles, a seasonal and a daily one. To take both cycles into consideration, measurements obtained in February and July, respectively the coldest and warmest months in 2012, were analyzed. The data for the individual months reflected the daily variations of the temperature and D_T, whereas comparison of the data for winter and summer reflected the seasonal variations. The relationships between the ambient temperature and the structural temperature for different structural components and during winter and summer are quite different. Only the distribution of the structural temperature is discussed below, using the data for February 19 and July 24 as examples. The hourly averaged temperature is used because of its slow variation.

2.2.1 Longitudinal temperature distribution of the girder

The temperatures at different sections of the top and bottom decks along the main girder vary at almost the same rate towards their peaks and troughs. Fig. 1 shows the longitudinal temperature distributions of the top and bottom decks of the steel box girder at the time of the peak temperature of the top plate on July 24 and the time of the trough temperature on February 19. It should be noted that the longitudinal temperature field is almost uniform along the girder, with the exception of the temperatures at both tower-girder intersections, which are a little lower than those of the other three sections. This is due to shading of the towers during the daytime. Without consider the difference of the baseline, the temperature distribution at the time of peak temperature on February 19 would be similar to that on July 24, and both would have a positive vertical temperature difference. Likewise, the temperature distributions at the trough temperature times on February 19 and July 24 are similar, although there is a negative temperature difference and its magnitude is much smaller than the positive difference for the peak temperature times. Hence, the following FE analysis considers the vertical temperature gradient but ignores the longitudinal gradient.

2.2.2 Temperature distribution in mid-span section of the girder

The structural temperature distribution at the mid-span section (Fig. 2) shows that the lateral thermal gradient is diminutive at both the peak and trough temperature times. The two outermost temperature sensors on the top plate were located just beneath the safety barriers on the deck, which might account for their readings being lower than those of the other four sensors on the top plate. Consequently, the average of the four sensors is used as the representative temperature of the top plate for the FE analysis, in which the lateral thermal gradient is also ignored.

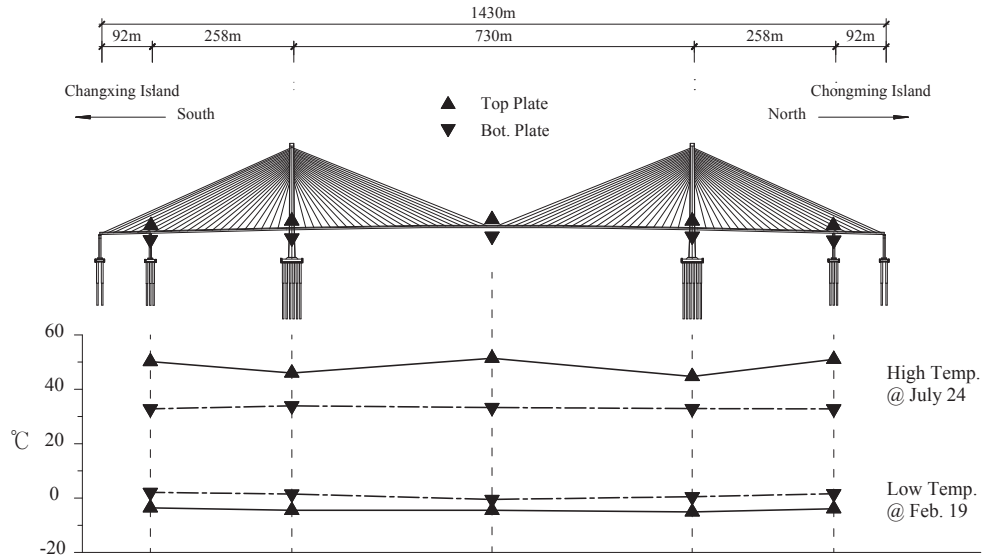

Fig. 1 Bridge's Elevation view and measured longitudinal temperature distribution of girder

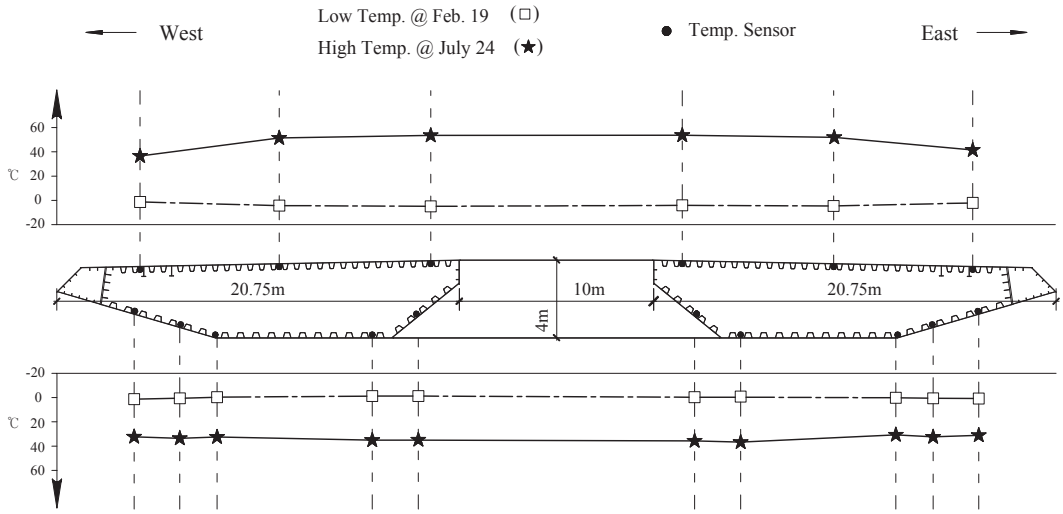

Fig. 2 Measured temperature distribution at mid-span section of girder

2.2.3 Tower temperature

The temperature of each concrete tower was monitored in one section at about midway along its height. The temperature evolutions of both towers were much similar and the interior temperatures were very stable with almost no daily variation. However, their external surface

temperature gradients were not negligible due to the effect of direct sunlight (Figs. 3 and 4). Based on the measurements, it is reasonable to assume in the FE model that both towers have identical temperature fields, which are uniform along their height. The thermal difference between the external north and south faces should be considered, whereas the internal temperatures can be neglected.

2.2.4 Cable temperature

All mearsured cables of the Shanghai Yangtze River Bridge have similar temperature variation trends. Fig. 5 shows the temperatures of the four longest cables of the center span, the mean of which is used to represent the temperature of all the stay-cables in the FE model, neglecting the temperature gradient along the cable length. It is necessary to note that the temperature sensors were installed on the cable surface rather than inside them. Hence, the measurements might differ from the actual temperatures of the steel wires.

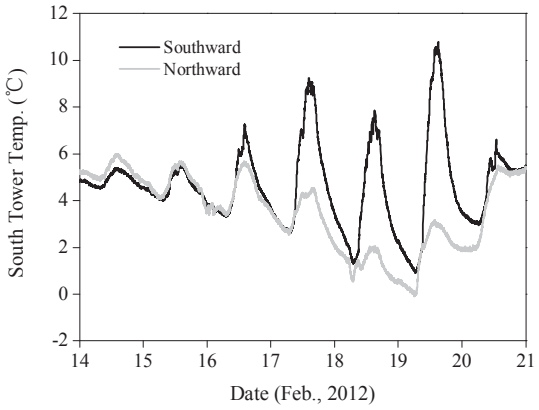

Fig. 3 Temperature of outer surfaces of south tower

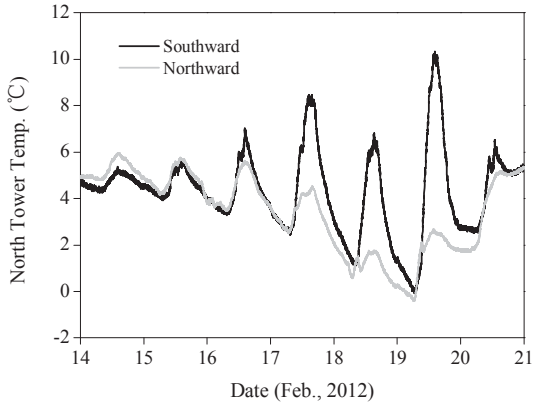

Fig. 4 Temperature of outer surfaces of north tower

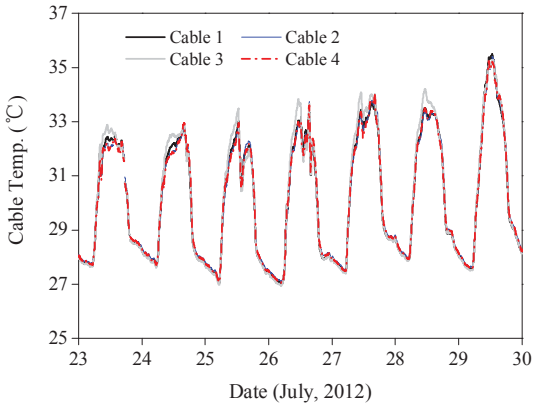

Fig. 5 Temperatures of four longest cables in center span

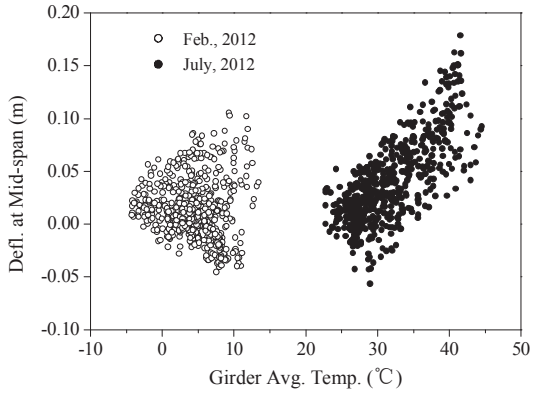

Fig. 6 D_T vs. T_{Gir}

2.3 Measured D_T

Compared to the effect of traffic, the thermally induced vertical deflection variation at mid-span is rather slow and can be represented by the hourly average of the measured deflections. Fig. 6 is a scatter plot of D_T versus T_{Gir} for two months. In July, an upward movement at the mid-span occurred with increasing girder temperature T_{Gir}. This is in agreement with the observation of Cao *et al*. (2011), but in conflict with those of Zhu *et al*. (2006) and Li (2012). However, in February, the D_T did not correlate well with the T_{Gir}. Moreover, the positions of the girder in February and July were almost the same. Hence, on an annual scale, the observation of an upward D_T with increasing temperature is very vague compared to that in July. Fig. 6 suggests that the girder temperature may not be the only factor that affects the D_T. In the next two sections, the authors discuss five mechanisms of D_T variation.

3. Mechanisms of D_T variation

Here we discuss five possible mechanisms of the thermally induced vertical deflection variation at mid-span, which correspond to the effects of the cable temperature T_{Cab}, girder temperature T_{Gir}, girder differential temperature T_{Dif}, tower temperature T_{Tow}, and variation of the material elastic modulus E. Considering a temperature increase as an example, Fig. 7 illustrates the five mechanisms. For simplicity, the vertical constraints on the sides of the bridge and the subsidiary piers are not shown.

3.1 Mechanism 1: cable temperature

The elongation of the cable due to increase in temperature lowers the girder mid-span (Fig. 7(a)).

3.2 Mechanism 2: girder temperature

The T_{Gir} indirectly affects the D_T. As the temperature increases, the girder expands at both ends, and then both towers move apart due to the cable constraints; this eventually raises the mid-span of the girder (Fig. 7(b)).

3.3 Mechanism 3: girder differential temperature

The T_{Dif} of the Shanghai Yangtze River Bridge's girder could exceed 20°C due to sunlight, resulting in curvature of the girder in the vertical plane. A cable-stayed bridge is analogous to an elastically supported continuous beam; hence, the magnitude and direction of the D_T depend on the number of spans. A question mark is therefore used to indicate the uncertainty of D_T direction in Fig. 7(c).

3.4 Mechanism 4: tower temperature

The tower height varies with the T_{Tow}, resulting in a change in the D_T (Fig. 7(d)). Moreover, the temperature difference between the north and south surfaces of the towers causes asymmetric deformation and therefore has little effect on the D_T of the girder. This is why the temperature difference of tower is not considered here.

3.5 Mechanism 5: change in elastic moduli

According to Xia *et al*. (2012), the temperature-dependent elastic moduli are the dominant cause of change in structural frequency with temperature. For unit temperature increase, the elastic moduli of steel and concrete decrease by 0.036% and 0.30%, respectively. Consequently, decreases in the elastic moduli of steel and concrete with increasing temperature also reduce the structural stiffness, thereby reducing the D_T (Fig. 7(e)).

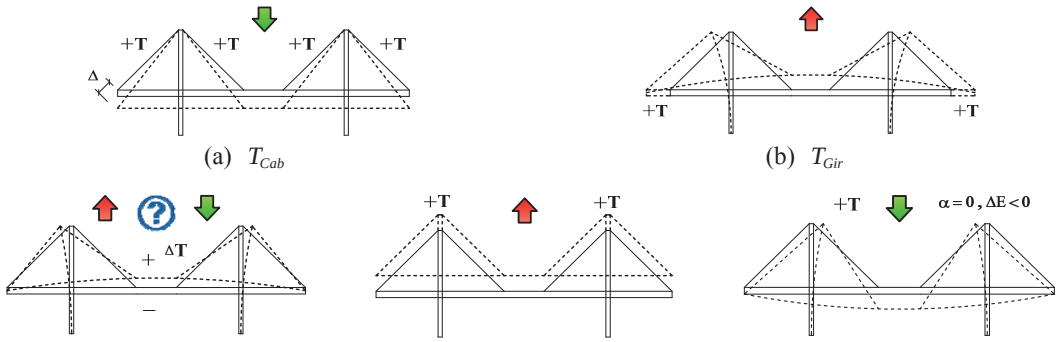

(a) T_{Cab} (b) T_{Gir}

(c) T_{Dif} (d) T_{Tow} (e) E variation

Fig. 7 Schematic diagrams of five D_T variation mechanisms

4. FE analysis

In this section, we develop an FE model for quantifying the sensitivities of the five mechanisms of the thermally induced vertical deflection variation at mid-span discussed in Section 3.

4.1 FE model and assumptions

The Shanghai Yangtze River Bridge is idealized as a 3D beam-element model with double girders, comprising 1673 elements and 1805 nodes (Fig. 8). Each cable is simulated by one element, the elastic modulus of which is modified by the Ernst formula (Eq. (1)) with the consideration of the sag effect.

$$E_{eq} = \frac{E_0}{1 + \frac{A_0 \cdot q^2 \cdot l^2}{12 \cdot F^3} E_0} \tag{1}$$

where E_{eq} is the equivalent elastic modulus of cables, E_0 is the initial modulus of cables, A_0 is the section area of cables, q is the self-weight of cables per unit length, l is cables' horizontal projection length, and F is the tension force in cables, which is set to the design tension. The variations of E_{eq} which result from the changing tension F and from the changing initial modulus E_0 are proven to be in the same order of magnitude. Because the thermally induced vertical deflection at mid-span is insensitive to the change of E_0 (see Section 4.3), thus we ignore the change of cables' equivalent elastic moduli with the changing tension.

4.1.1 Temperature loading

Based on the discussion in Subsection 2.2, five structural temperatures are taken into consideration, namely the top and bottom plate temperatures of the girder, the external north and south surface temperatures of the tower, and the cable temperature (see Table 1). The temperature gradient along the depth of both the girder and the tower was assumed to be linear.

Table 1 Temperature load in FE model

°C	Feb. 19 Trough Temp.	Feb. 19 Peak Temp.	July 24 Trough Temp.	July 24 Peak Temp.
Girder Top	-4.5	20.0	26.7	51.6
Girder Bottom	-0.6	5.4	27.8	32.5
Tower South	0.5	10.4	27.4	30.4
Tower North	-0.1	2.7	27.8	29.5
Cable	-1.3	7.2	28.0	32.5

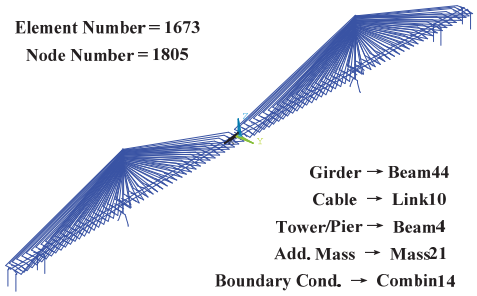

Fig. 8 Information on FE model

4.1.2 Thermal expansion/contraction effect

The effect of the thermal expansion/contraction on the D_T was simulated by introducing the linear thermal expansion coefficients $\alpha_s = 1.2e-5/°C$ and $\alpha_c = 1.0e-5/°C$ for steel and concrete, respectively.

4.1.3 Temperature-dependent elastic moduli

We assumed that the elastic moduli of steel and concrete, respectively denoted by E_S and E_C, vary linearly with temperature at the rates of $\alpha_{Es} = -0.00036/°C$ and $\alpha_{Ec} = -0.00300/°C$, respectively (Xia *et al*. 2012).

4.1.4 Calculation assumption

Due to the unavailability of the initial status of the temperature field and structural responses, the absolute thermal effects for a particular temperature field could not be obtained. Hence, we assumed that the structural thermal responses are a function of the temperature field and independent of the process of heating and cooling. The calculated thermal effects for a particular temperature field could therefore be defined as the difference between the response of the temperature field and that of a reference state. The applied reference state was a virtual condition in which the entire structure had a uniform temperature of 27°C, which is the air temperature at the girder closure. Actually, the reference state has no effect on the calculating response difference between two measured temperature fields.

4.2 Comparison with measurements

A total of four temperature fields (Table 1) at the peak and trough temperature times on February 19 and July 24 were inputted to the FE model to calculate the seasonal and daily variations of the structural responses and verify the applicability of the FE model. The calculation or measurements for the peak temperature on July 24 minus the counterparts for the trough temperature on February 19 represent the thermal effects on an annual scale, whereas the difference between the responses for the peak and trough temperatures on February 19 or July 24 could reflect the thermal effects on a daily scale for winter and summer, respectively.

In general, good agreement was observed between the calculated and measured thermally induced vertical deflections at mid-span (row A in Table 2). On both the annual and daily scales, the variation trend of the calculated D_T values are the same as that of the measured values (their signs are identical). Quantitatively, the differences between the calculations and measurements are about 9% for the annual change and 6% for the daily change on July 24, both of which are acceptable. The difference for February 19 exceeds 132%, which might be related to the fact that the actual variation of the D_T is small (about 0.05 m).

In addition to the D_T, the variations of the girder length, tower distance, total/elastic strain at both the top and bottom plates at mid-span, and the averaged tension of the four longest cables in the center span were also compared. From Table 2, consistency can be observed in the trends of the variation between the analytical and measurement results, which indicates that the developed FE model could identify the basic trends of the thermally induced responses on both the annual and daily scales. The quantitative deviation of the calculations from the measurements in Table 2 may be due to measurement errors, inaccuracy of the FE model, and approximations of the temperature field.

Table 2 Comparison of thermally induced quantities

			Feb. 19 $\Delta=Day_{High}-Day_{Low}$			July 24 $\Delta=Day_{High}-Day_{Low}$			July 24–Feb. 19 $\Delta=Year_{High}-Year_{Low}$		
			Measured	Analytical	RD* (%)	Measured	Analytical	RD (%)	Measured	Analytical	RD (%)
			(1)	(2)	(3)	(4)	(5)	(6)	(7)	(8)	(9)
A	D_T (m)		0.046	0.107	132.5	0.166	0.176	6.0	0.131	0.119	-8.9
B	Girder Length (m)		0.24	0.24	2.5	0.19	0.23	21.2	0.68	0.73	6.7
C	Tower Distance (m)		0.17	0.11	-38.5	0.18	0.12	-33.1	0.45	0.35	-21.9
D	Total Strain (με)	Top	188.41	179.29	-4.8	177.60	174.03	-2.0	551.87	528.28	-4.3
E		Bot.	162.65	180.58	11.0	135.07	174.82	29.4	486.39	529.55	8.9
F	Elastic Strain (με)	Top	-115.19	-114.71	-0.4	-114.00	-124.77	9.4	-109.33	-144.92	32.6
G		Bot.	109.85	108.58	-1.2	100.27	118.42	18.1	127.29	132.35	4.0
H	Cable Force (kN)		46.83	47.75	2.0	70.00	64.30	-8.1	96.65	74.40	-23.0

*Relative Difference (RD) = (Analytical - Measured)/Measured × 100%

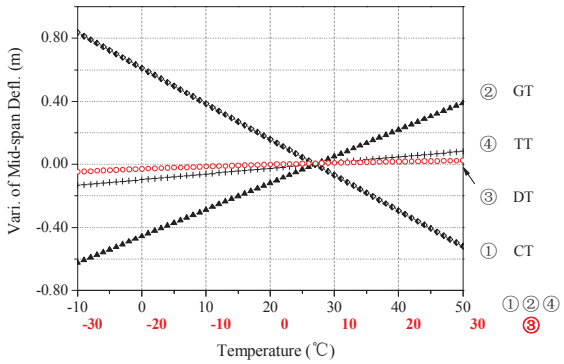

Fig. 9 Calculated D_T for four mechanisms

The total strain ε_M in Table 2 comprises the local deformation of the two parts; i.e., the thermally induced stress-free strain $\varepsilon_T = \alpha_S \cdot \Delta T$ and the elastic strain ε_E: $\varepsilon_M = \varepsilon_T + \varepsilon_E$. In the FE simulation, the temperature change ΔT was obtained as the average of the four sensors on the top or bottom plates (Fig. 2), whereas the measured elastic strain was determined using the value of ΔT of only one temperature sensor. This temperature difference is the reason why the analytical and measured values of the total strain minus the elastic strain in Table 2, which should be equal to $\alpha_s \cdot \Delta T$, are a little different.

After the verification of the FE model, the sensitivities of the five mechanisms of the thermally induced vertical deflection variation mentioned in Section 3 were quantitatively compared by parametric analysis to obtain further insight into the thermal effects.

4.3 Comparison of D_T sensitivities

Using the temperature-dependent elastic moduli of concrete and steel, we calculated the variation of D_T for exclusive changes in each of the mechanisms in Sections 3.1–3.4. Considering real-life possible ranges, the temperature variations for the four mechanisms were separately set as follows: (1) -10–50°C for cable temperature, (2) -10–50°C for girder temperature, (3) -30–30°C for girder differential temperature, and (4) -10–50 °C for tower temperature. Each temperature was varied in steps of 1°C. Particularly for T_{Dif}, the top plate temperature was increased from -15 to 15°C, whereas the bottom plate was decreased from 15 to -15°C, both in steps of 0.5°C. Sixty cases of each mechanism were considered and the corresponding calculated values of the D_T were used to draw the curve in Fig. 9, where the intersection point of all the four separate curves corresponds to the reference temperature 27°C. The relationship of the D_T with each of the four temperatures is almost linear over the normal temperature ranges. The slopes of the four curves represent the sensitivity of the thermally induced vertical deflection at mid-span to the respective temperatures, namely the variation of the D_T per unit temperature rise, which is referred to as the effect coefficient (β) in Table 3. It can be seen from column 2 of Table 3 that the sensitivities of the D_T to the four mechanisms are in the following order: T_{Cab} > T_{Gir} > T_{Tow} > T_{Dif}. Moreover, the level at mid-span decreases with increasing T_{Cab}, but increases with

increasing T_{Gir}, T_{Dif}, and T_{Tow}. Except the T_{Dif}, the directions of the other three temperatures' effects are in agreement with the qualitative judgments in Section 3.

Two calculation procedures were separately considered for the three main components of a cable-stayed bridge for mechanism 5. In Procedure 1, the thermal expansion effect was considered, whereas the elastic moduli changes with temperature were ignored. In Procedure 2, the elastic moduli changes with temperature were considered, whereas the thermal expansion effects were ignored ($\alpha_s = 0$ or $\alpha_c = 0$). The effect coefficients for the two calculation procedures are listed in columns 3 and 4 of Table 3, which indicates that the D_T sensitivity to changes in the elastic moduli is about one or two orders of magnitude less than that for the thermal expansion effect.

Worthy of note is also the fact that the effect coefficients in column 2 of Table 3 are equal to the sum of those in columns 3 and 4. The effects of the thermal expansion coefficient α and the elastic modulus E on the D_T can therefore be approximated by a linear superposition formula within the temperature range of -10–50°C.

The above discussions reveal that the D_T of a cable-stayed bridge is the resultant effect of the thermal expansion/contraction of multiple structural components. However, because of the different temperature ranges experienced by the T_{Cab}, T_{Gir}, T_{Dif}, and T_{Tow} in reality, their effect coefficients cannot be used to account for their actual respective effects on the D_T. These effects will be compared in the next section by considering the actual temperature variation ranges.

5. Discussions

Columns 3, 7, and 11 of Table 4 give the actual variations of the T_{Cab}, T_{Gir}, T_{Dif}, and T_{Tow} based on the measured temperatures at the peak and trough temperature times on February 19 and July 24 (i.e., ΔT_i, i=1 – 4). Columns 4, 8, and 12 present the product of the effect coefficients and the actual variations: $I_i = \beta_i \times \Delta T_i$, where the sign of I_i indicates the direction of the effect of the i^{th} mechanism on the D_T, and the absolute value $|I_i|$ is the actual effect. For easy comparison, the effects of the four mechanisms on the D_T were normalized by the effect of the T_{Gir}, I_2. The results are given in columns 5, 9, and 13. Furthermore, the contribution of each mechanism to the overall D_T can be estimated using

Table 3 Summary of effect coefficients (β) Unit: m/°C

	Mechanism	Expan./Contr. + E Change	Expan./Contr. only	E Change only
	(1)	(2)	(3)	(4)
A	1: T_{Cab}	**-0.0226**	**-0.0208**	**-0.0018**
B	2: T_{Gir}	**0.0169**	**0.0171**	**-0.0002**
C	3: T_{Dif}	**0.0012**	-	-
D	4: T_{Tow}	**0.0036**	**0.0041**	**-0.0005**

Table 4 Calculated D_T for each mechanism

	Mechanism (i)	β_i (m/°C)	Feb. 19 $\Delta=Day_{High}-Day_{Low}$				July 24 $\Delta=Day_{High}-Day_{Low}$				July 24–Feb. 19 $\Delta=Year_{High}-Year_{Low}$			
			ΔT_i (°C)	I_i (m)	$\lvert I_i\rvert/I_2$ (%)	C_i (%)	ΔT_i (°C)	I_i (m)	$\lvert I_i\rvert/I_2$ (%)	C_i (%)	ΔT_i (°C)	I_i (m)	$\lvert I_i\rvert/I_2$ (%)	C_i (%)
	(1)	(2)	(3)	(4) (2)×(3)	(5)	(6) (4)/Σ_1	(7)	(8) (2)×(7)	(9)	(10) (8)/Σ_2	(11)	(12) (2)×(11)	(13)	(14) (12)/Σ_3
A	1: T_{Cab}	**-0.0226**	8.5	-0.192	74.4	-172.3	4.5	-0.103	41.2	-56.9	33.9	-0.765	101.5	-619.8
B	2: T_{Gir}	**0.0169**	15.3	0.258	100.0	231.7	14.8	0.250	100.0	138.7	44.6	0.754	100.0	610.6
C	3: T_{Dif}	**0.0012**	18.6	0.022	8.5	20.1	20.2	0.024	9.6	13.4	23.0	0.028	3.7	22.4
D	4: T_{Tow}	**0.0036**	6.3	0.023	8.9	20.5	2.4	0.009	3.6	4.8	29.8	0.107	14.2	86.7
E	ΣI_i		Σ_1 = **0.111**			100	Σ_2 = **0.180**			100	Σ_3 = **0.123**			100

5.1 Verification of linear superposition

The summations Σ_1–Σ_3 in row E of Table 4 are very close to the calculated values of D_T in Table 2, the difference being about 3%. In other words, the superposition of the individual thermally induced vertical deflections at mid-span due to the T_{Cab}, T_{Gir}, T_{Dif}, and T_{Tow} is almost equal to the total D_T produced by the four mechanisms together, which indicates that the effects of the four mechanisms on the D_T can be approximated by the linear superposition. This observation is surprising for such a long-span cable-stayed bridge. Additionally, the fact that $\Sigma_3 < \Sigma_2$ in row E shows that it is possible for the seasonal variation of the D_T for a cable-stayed bridge to be less than the daily variation.

5.2 Comparison of effects of four mechanisms

In this subsection, we compare the effects of the T_{Cab}, T_{Gir}, T_{Dif}, and T_{Tow}, taking the actual temperature variation range into consideration. From column 13 in Table 4, the magnitudes of the effects of the T_{Cab} and T_{Gir} are one order larger than the effects of the T_{Dif} and T_{Tow} on the annual scale. However, the effects of these two dominant mechanisms on the D_T are opposite, which makes the contribution of the weakest mechanism, T_{Dif}, to account for 22.4% of the overall D_T variation after offsetting the effects of the T_{Cab} and T_{Gir}. Consequently, none of the four mechanisms can be omitted if a linear superposition model is used to predict the D_T.

From columns 5 and 9 of Table 4, it can be seen that, on the daily scale, the magnitudes of the effects of T_{Cab} and T_{Gir} are one order larger than those of T_{Dif} and T_{Tow}. It is worthy of note that the effect of T_{Gir} is not always greater than that of T_{Cab}, and that the relative importance of T_{Dif} and T_{Tow} is also uncertain. Although the temperature range of different structural

components depends on the weather conditions and the observation times due to the thermal lags, it is hardly possible for the T_{Cab} and T_{Gir} to have less effect than the T_{Dif} and T_{Tow}, which is because their effect coefficients are one order of magnitude larger than those of the latter two mechanisms (see Table 3).

5.3 Explanation of the monitoring results

The effect coefficients in Table 3 were used as the coefficients of a multiple linear formula for simulating the thermally induced vertical deflection at mid-span in accordance with the temperatures measured in February and July as shown in Eq. (3)

$$D_T^a = -0.0226 \cdot T_{Cab} + 0.0169 \cdot T_{Gir} + 0.0012 \cdot T_{Dif} + 0.0036 \cdot T_{Tow} + D_0 \tag{3}$$

where the D_T^a denotes the calculated D_T, and D_0 is a constant related to the initial state. To ensure the same baseline as the measured D_T, the offset D_0 can be estimated using

$$D_0 = Avg\left(D_T\right) - Avg\left(-0.0226 \cdot T_{Cab} + 0.0169 \cdot T_{Gir} + 0.0012 \cdot T_{Dif} + 0.0036 \cdot T_{Tow}\right) \tag{4}$$

where $Avg(\cdot)$ denotes the average operation and D_T is measured in February and July. The scatter plot of D_T^a versus T_{Gir} is shown in Fig. 10, with the original Fig. 6 overlaid. In terms of the distribution pattern of the points, the measured D_T and the simulated D_T^a are similar. The multiple linear formula presented as Eq. (3) can be used to properly explain the variation of the D_T. Furthermore, using the same D_0, Eq. (3) is also applicable to cases in January and August. Generally speaking, this physics-based model can be used to explain the annual and daily variations of the thermally induced vertical deflection at mid-span. Considering that it disregards the time lags and auto-regression of D_T, it can be easily applied in practice.

There was some discrepancy between the measured D_T and the calculated one; e.g., the relationship between the two appeared to be skewed in Fig. 12. It should be noted that the effect coefficients of the T_{Cab}, T_{Gir}, T_{Dif}, and T_{Tow} in Eq. (3) were obtained by an FE model that had not been calibrated using recorded data, which made the errors in the effect coefficients inevitable. Measurement errors and uncertainty of the temperature distribution are also possible reasons for the discrepancy and further studies are required to investigate these issues for more accurate evaluation of the structural conditions.

6. Conclusions

The mid-span deflection of a cable-stayed bridge girder is an informative indicator of structural conditions and its normal variation induced by the environment factors must be first ascertained in order to achieve more reliable structural evaluation. In this study, we used the SHM data of the Shanghai Yangtze River Bridge to investigate the mechanisms of the thermally induced vertical deflection at mid-span (D_T) by FE analysis. The findings of the study include: (1) Under normal operational conditions, the D_T variation of a cable-stayed bridge is the resultant of a multisource combination of thermal expansion effects mainly related to the cable temperature (T_{Cab}), girder

temperature (T_{Gir}), girder differential temperature (T_{Dif}), and tower temperature (T_{Tow}); and the relationships can be well approximated by a multiple linear superposition. There is no general monotonic trend between the D_T variation and the ambient temperature or the temperature of a particular structural component. (2) The thermal sensitivities of the D_T variation of the Shanghai Yangtze River Bridge to the contributory temperatures are in the following order: $T_{Cab} > T_{Gir} > T_{Tow} > T_{Dif}$. The D_T occurs downward with increasing T_{Cab}, but upward with increasing T_{Gir}, T_{Dif}, and T_{Tow}. Taking the actual temperature range into consideration, the magnitudes of the effects of the T_{Cab} and T_{Gir} are almost one order greater than those of the T_{Dif} and T_{Tow}. This mechanism can be used to explain the seasonal and daily variations of the D_T. (3) The structural temperature distribution, rather than the ambient temperature, should always be monitored along with the deformation so that the structural responses during operation can be normalized to the same temperature field to obtain a more reliable structural condition assessment.

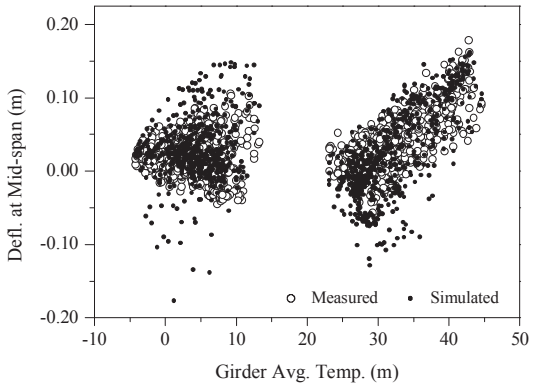

Fig. 10 D_T^a / D_T vs. T_{Gir} (February and July)

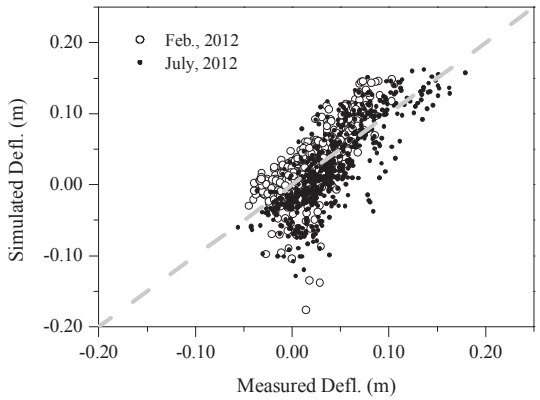

Fig. 11 D_T^a vs. D_T (February and July)

Strictly speaking, the conclusions here only aim at Shanghai Yangtze River Bridge. Further studies of the thermal effects are required for more cable-stayed bridges with different structural layouts and climatic conditions. However, the mechanisms of the thermally induced vertical deflection variation at mid-span of a cable-stayed bridge as well as the analytical methodology adopted in this study could be applicable; and the results herein provide valuable information on structural behavior interpretation.

Acknowledgments

The authors express their profound appreciation of the financial support of the National Basic Research Program of China (973 Program): Basic research on life-cycle disaster control and performance-based design of super long-span bridges (Grant No.: 2013CB036305), as well as the assistance of Shanghai Yangtze River Bridge Management Co., Ltd. and Shanghai Just One Technology Development Co., Ltd.

References

Barr, P., Eberhard, M., Stanton, J., Khaleghi, B. and Hsieh, J. C. (2000), *High performance concrete in Washington State SR18/SR516 overcrossing: final report on girder monitoring*, Washington State Transportation Center.

Boller, C., Chang, F.K. and Fujino, Y. (2009), *Encyclopedia of Structural Health Monitoring*, John Wiley & Sons, Ltd., Chichester, United Kingdom.

Brownjohn, J.M.W., Worden, K., Cross, E., List, D., Cole, R. and Wood, T. (2009), "Thermal effects on performance on Tamar Bridge", *Proceedings of the 4th International Conference on Structural Health Monitoring of Intelligent Infrastructure (SHMII-4)*, Zurich, Switzerland, July.

Burdet, O.L. (2010), *Thermal effects in the long-term monitoring of bridges*, IABSE Symposium Report, Venice, Italy, September.

Cao, Y., Yim, J., Zhao, Y. and Wang, M.L. (2011), "Temperature effects on cable stayed bridge using health monitoring system: a case study", *Struct. Health Monit.*, **10**(5), 523-537.

Catbas, F.N., Susoy, M. and Frangopol, D.M. (2008), "Structural health monitoring and reliability estimation: long span truss bridge application with environmental monitoring data", *Eng. Struct.*, **30**(9), 2347-2359.

Chen, D., Jing, G. and Huang, Z. (2006), "Prediction of bridge structural performance under temperature by artificial neural network", *Struct. Engineers*, **22**(4), 24-28. (In Chinese)

Deng, Y., Ding, Y. and Li, A. (2010), "Structural condition assessment of long-span suspension bridges using long-term monitoring data", *Earthq. Eng. Eng. Vib.*, **9**(1), 123-131.

Figueiras, J., Félix, C. and Afonso Costa, B. (2005), "Testing and monitoring of a centenary arch bridge", *Struct. Infrastruct. E.*, **1**(1), 63-73.

Gentile, C. and Saisi, A. (2013), "Long-term Dynamic Monitoring of the historic "San Michele" Iron Bridge (1889)", *Proceedings of the IABSE Spring Conference 2013*, Rotterdam, Netherlands, May.

Ghali, A., Elbadry, M. and Megally, S. (2000), "Two-year deflections of the Confederation Bridge", *Can. J. Civil Eng.*, **27**(6), 1139-1149.

Katsuchi, H., Yamada, H. and Kusuhara, S. (2008), "Structural monitoring and design verification of Akashi Kaikyo Bridge", *Proceedings of the Earth & Space 2008*, Long Beach, California, United States, March.

Kim, S., Kim, C. and Lee, J. (2005), *Monitoring results of a self-anchored suspension bridge*, Sensing Issues in Civil Structural Health Monitoring, (Ed. Ansari, F.), 475-484.

Koo, K.Y., Brownjohn, J.M.W., List, D.I. and Cole, R. (2013), "Structural health monitoring of the Tamar

Suspension Bridge", *Struct. Control Health Monit*., **20**(4), 609-625.
Li, H., Li, S., Ou, J. and Li, H. (2010), "Modal identification of bridges under varying environmental conditions: temperature and wind effects", *Struct. Control Health Monit.*, **17**(5), 495-512.
Li, X. (2012), *Static behavior analysis of cable-stayed bridge based on long-term monitoring data*, Master Thesis, Tongji University, Shanghai.
Li, X., Ren, W. and Zhong, J. (2011), "Making good use of suspension bridge health monitoring system", *Proceedings of the 1st International Conference on Civil Engineering, Architecture and Building Materials (CEABM 2011)*, Haikou, P. R. China, June.
Magalhães, F., Cunha, A. and Caetano, E. (2012), "Vibration based structural health monitoring of an arch bridge: From automated OMA to damage detection", *Mech. Syst. Signal Pr.*, **28**, 212-228.
Moorty, S. and Roeder, C. (1992), "Temperature-dependent bridge movements", *J. Struct. Eng. - ASCE* , **118**(4), 1090-1105.
Ni, Y., Xia, H., Wong, K. and Ko, J. (2011), "In-Service condition assessment of bridge deck using long-term monitoring data of strain response", *J. Bridge Eng.*, **17**(6), 876-885.
Reynders, E., Wursten, G. and De Roeck, G. (2014), "Output-only structural health monitoring in changing environmental conditions by means of nonlinear system identification", *Struct. Health Monit.*, **13**(1), 82-93.
Shao, C. (2010), "Shanghai Yangtze River Bridge—the longest Road-cum-Rail bridge in china", *J. Struct. Eng. - ASCE*, **20**(3), 291-295.
Sohn, H. (2007), "Effects of environmental and operational variability on structural health monitoring", *Philos. T. R. Soc. A*, **365**(1851), 539-560.
Sun, Z., Wu, H.S., Wang, Q.M., Lu, Y.C. and Zhou, Z.F. (2010), "Reliability assessment oriented monitoring system design for Shanghai Yangtze River Bridge", *Proceedings of the 5th International Conference on Bridge Maintenance, Safety and Management (IABMAS)*, Philadelphia, United States, July.
Wang, M.L. (2009), *Loads and temperature effects on a bridge*, Encyclopedia of Structural Health Monitoring, (Eds., Boller, C., Chang, F. and Fujino, Y.), John Wiley & Sons, Ltd.
Wenzel, H. (2009), *The influence of environmental factors*, Encyclopedia of Structural Health Monitoring, (Eds., Boller, C., Chang, F. and Fujino, Y.), John Wiley & Sons, Ltd.
Westgate, R.J. (2012), *Environmental effects on a suspension bridges performance*, Ph.D. Dissertation, The University of Sheffield, Sheffield.
Xia, Y., Chen, B., Weng, S., Ni, Y. and Xu, Y. (2012), "Temperature effect on vibration properties of civil structures: a literature review and case studies", *J. Civil Struct. Health Monit.*, **2**(1), 29-46.
Xia, Y., Chen, B., Zhou, X. and Xu, Y. (2013), "Field monitoring and numerical analysis of Tsing Ma Suspension Bridge temperature behavior", *Struct. Control Health Monit.*, **20**(4), 560-575.
Xu, Y.L., Chen, B., Ng, C.L., Wong, K.Y. and Chan, W.Y. (2010), "Monitoring temperature effect on a long suspension bridge", *Struct. Control Health Monit.*, **17**(6), 632-653.
Zhu, Y., Fu, Y., Chen, W. and Huang, S. (2006), "Online deflection monitoring system for Dafosi Cable-stayed Bridge", *J. Intel. Mat. Syst. Str.*, **17**(8-9), 701-707.

Smart Structures and Systems, *Vol. 15, No. 3 (2015) 523-541*
DOI: http://dx.doi.org/10.12989/sss.2015.15.3.523

Effects of local structural damage in a steel truss bridge on internal dynamic coupling and modal damping

Hiroki Yamaguchi[1], Yasunao Matsumoto[*1] and Tsutomu Yoshioka[2]

[1]*Department of Civil and Environmental Engineering, Saitama University*
255 Shimo-Ohkubo, Sakura, Saitama 338-8570, Japan
[2]*Nippon Engineering Consultants Co., Ltd, 3-23-1, Komagome, Toshima, Tokyo 170-0003, Japan*

(Received November 15, 2014, Revised February 15, 2015, Accepted February 18, 2015)

Abstract. Structural health monitoring of steel truss bridge based on changes in modal properties was investigated in this study. Vibration measurements with five sensors were conducted at an existing Warren truss bridge with partial fractures in diagonal members before and after an emergency repair work. Modal properties identified by the Eigensystem Realization Algorithm showed evidences of increases in modal damping due to the damage in diagonal member. In order to understand the dynamic behavior of the bridge and possible mechanism of those increases in modal damping, theoretical modal analysis was conducted with three dimensional frame models. It was found that vibrations of the main truss could be coupled internally with local vibrations of diagonal members and the degree of coupling could change with structural changes in diagonal members. Additional vibration measurements with fifteen sensors were then conducted so as to understand the consistency of those theoretical findings with the actual dynamic behavior. Modal properties experimentally identified showed that the damping change caused by the damage in diagonal member described above could have occurred in a diagonal-coupled mode. The results in this study imply that damages in diagonal members could be detected from changes in modal damping of diagonal-coupled modes.

Keywords: structural health monitoring; truss bridge; vibration measurement; ERA; diagonal member-coupled vibration; modal damping; damage detection

1. Introduction

A number of bridges constructed during the rapid economic growth period from 1950's are having aging problem in Japan. There were serious incidents due to deterioration or damage for steel truss bridges found in rigorous inspections conducted after the tragic bridge collapse in Minneapolis, USA (Fujino and Siringoringo 2008). In the current standard bridge management strategy in Japan, primary periodic inspections rely on visual inspection, although various nondestructive test methods have been used in second step detailed inspections (National guideline 2014). For visual inspection, decreases in the number of skilled engineers and the reliability in subjective method are current and future concerns. Recent accidents found in steel truss bridges imply some limitations of visual inspection. Diagnosis of bridges based on physical behaviors

*Corresponding author, Professor, E-mail: ymatsu@mail.saitama-u.ac.jp

http://www.techno-press.org/?journal=sss&subpage=8 ISSN: 1738-1584 (Print), 1738-1991 (Online)

through measurements of deformations, stresses, vibrations, and so on, is required.

Vibration-based structural health monitoring, SHM, has been considered as a complementary method to visual inspection and studied worldwide (Doebling *et al*. 1996, Balageas *et al*. 2006, Boller *et al*. 2009). Practical applications of vibration monitoring to existing bridges have been made mainly to specific long span bridges (e.g., Ko and Ni 2005, Fujino and Siringoringo 2008). There have been studies that investigate the relationship between the dynamic characteristics and artificial damages in existing bridges (e.g., Kim and Stubbs (2003), Maeck and de Roeck (2003)).

For the application of vibration-based SHM to steel truss bridge to detect local damages, such as fatigue cracks, corrosion, and bolt loosening, a number of sensors may be required, which leads to trade-off between monitoring cost and ability of damage detection. It would be, therefore, worth to develop a method to detect damage or evaluate structural state with less number of sensors. For SHM with less number of sensors, complimentary theoretical consideration is necessary. Previous studies of the dynamic characteristics of truss bridges can be referred to understand the global dynamic characteristics of truss bridges (e.g., Shama *et al*. 2001, Spyrakos *et al*. 2004), although there have not been studies of local vibration for damage detection in a local member to the authors' knowledge. In truss bridges, internal dynamic coupling between local vibration modes, such as bending of a member, and global vibration of the main truss can occur when their natural frequencies are close together. Similar coupling mechanism and its effect on modal damping have been reported for cable coupling vibration in a cable-stayed bridge (Yamaguchi *et al*. 2004).

The present study investigated SHM of steel truss bridges based on changes in modal properties, in particular, modal damping with internal dynamic coupling. Experimental and theoretical modal analyses were conducted for an existing truss bridge with partial fractures in diagonal members. Differences in natural frequency and modal damping identified before and after an emergency repair for diagonal members are discussed for possible application to SHM in this paper.

2. Effect of fracture in diagonal member on modal properties of truss bridge

2.1 Bridge studied

The bridge investigated was a bridge over a river for road traffic in-service from 1965. The bridge consisted of five separated spans, each of which was a simply supported Warren truss with a span length of 70.77 m and a width of 6.0 m (Fig. 1). The tension diagonal members had an H-section and the compression diagonal members had a box section, as shown in Figs. 1(c) and 1(d). There were eight or nine oval openings in the web of each tension diagonal members, except those at the ends of each span, for the reduction of the weight of steel (Fig. 2(a)).

During a visual inspection in July 2007 after 42-year service, partial fractures were found near the edge of gusset plate at either top or bottom end of longest tension diagonal members (D5 in Fig. 1), among which one in the fourth span resulted in loss of the half of its H-shaped cross section (Fig. 2(a)). In August 2007, as an emergency measure, additional steel plates with the same thickness as the member (i.e., 8 mm) were fixed by high strength bolts to cover both sides of the flanges and web for a length of about 1.5 m from the end of the members (Fig. 2(b)).

2.2 Vibration measurement

Vibration measurements were made at the fourth span in which the loss of half cross section

was found in D5. The measurements were conducted before and after the emergency repair in August 2007. Vibrations induced by a dump truck of 196 kN weight with three axles running over the bridge were recorded while there was no other traffic on the bridge. The dump truck ran in the traffic lane at the upstream side at a speed of 20, 30 or 40 km/h with three repetitions.

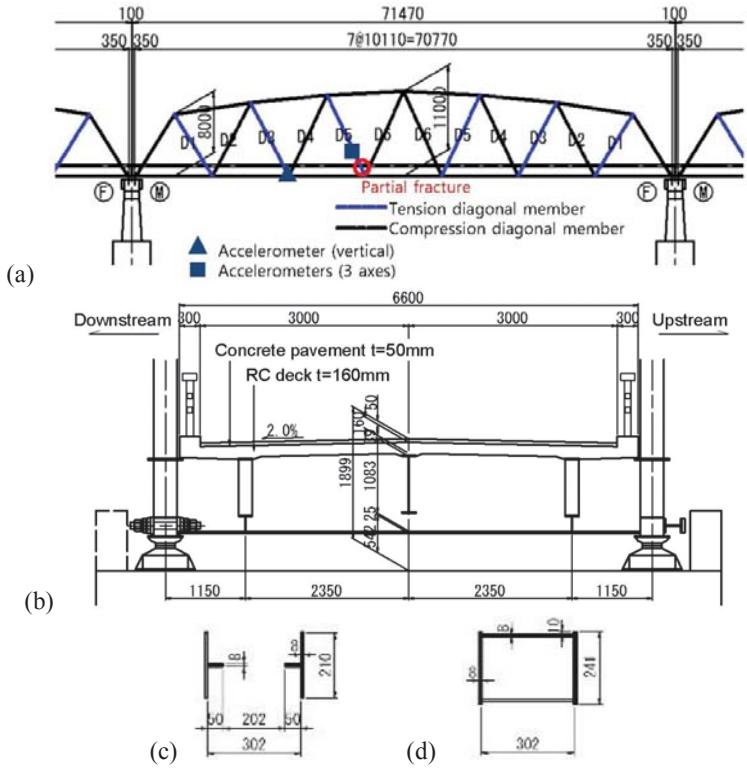

Fig. 1 Steel truss bridge investigated: (a) side view of single span (fourth span), (b) cross section of bridge, (c) cross section of tension diagonal member, (d) cross section of compression diagonal member. Unit [mm].

Fig. 2 (a) Partial fracture in D5 in fourth span and (b) repair with additional plates

Table 1 Comparison of modal properties of selected vibration modes between before and after repair

	Natural frequency [Hz]			Modal damping ratio		
	Before	After	Ratio	Before	After	Ratio
D5 in-plane only	7.146	9.847	-27%	0.0055 (0.0008)	0.0039 (0.0017)	41%
Lower chords	7.130	7.250	-2%	0.0106 (0.0005)	0.0059 (0.0003)	80%

There was limited time available for the measurement during the period of emergency repair work. Therefore, only five sensors were used in this measurement set. Accelerometers, ARF-10A or ARF-20A, Tokyo Sokki Kenkyujo, were attached to the diagonal member D5 at the upstream side at the quarter point of its length and to the lower chord members at both upstream and downstream sides at the quarter span. The measurement was made in the vertical, in-plane and out-of-plane directions at the diagonal member, and in the vertical direction only at the lower chord member. Signals from the accelerometers corresponding to vibrations including free vibration induced by the dump truck running were recorded in a laptop PC at 200 samples per second. The measurement duration was determined to cover free vibration lasting for about 30 seconds.

2.3 Experimental modal analysis

Modal properties of the bridge were identified from the field recorded data by the Eigensystem Realization Algorithm, ERA (Juang and Pappa 1985). Hankel matrices required at the first step in ERA were constructed from free vibration records extracted from the measured vibrations. The size of Hankel matrices was 1000 by 500, which was determined based on the stability of results in preliminary analyses. Raw results of the ERA analysis consisted of real modal properties and spurious modal properties due to measurement noise and other causes. In the present study, the screening criteria to extract realistic modes were the Modal Amplitude Coherence, MAC (Juang and Pappa 1985) calculated with all degrees of freedom used in the analysis, of 0.995 or greater and the damping ratio between 0 and 0.05. Stable poles in the stabilization diagram consisting of those satisfying the screening criteria were then extracted as real poles of the system.

2.4 Modal properties before and after repair in diagonal member

Fig. 3 shows examples of Fourier spectra of accelerations measured for a speed of 40 km/h with highest signal to noise ratio. The Fourier spectra were calculated with 8192 point FFT which resulted in the frequency resolution of 0.0244 Hz. As observed in Figs. 3(a) and (b), the dominant frequencies in the in-plane vibration of D5 were different before and after the repair. On the other hand, there were no clear changes in the vertical vibration of the lower chord (Figs. 3(c) and 3(d)).

Table 1 shows the results of the ERA analysis that were the averages and standard deviations determined from three repetitions of the dump truck running at 40 km/h. In the table, a set of modal properties identified from the ERA analysis with the data at D5 in-plane only, and another set identified with the data at two locations in the lower chords are presented. The details of those selected modes are discussed further with theoretical analysis in a later section of this paper.

For the modal properties obtained with D5 in-plane vibration only, the natural frequency decreased by 27% and the modal damping ratio increased by 41% with the partial fracture with respect to the structural condition after the repair on the assumption that the structural condition after the repair was close to its healthy condition (Table 1). For the modal properties identified from the vertical vibrations at the lower chords, the difference in natural frequency before and after the repair was not significant while the difference in modal damping ratio was 80%. The standard deviation of modal damping ratio shown in Table 1 was not large so that the average values identified could be considered reliable.

As observed in the table, the natural frequencies for the two modes before the repair were close together. It can be hypothesized that internal dynamic coupling between vibration of the main truss and vibration of the local diagonal member with the partial fracture could have occurred and caused the increases in the modal damping of the vibration mode identified from the records at the lower chord members. In order to discuss this possible mechanism of damping increase, more detailed modal analyses were conducted theoretically and experimentally.

3. Theoretical modal analysis of the truss bridge

3.1 Finite element models of the bridge

Three types of finite element, FE, models were developed with general-purpose FE software, FEMAP with NX Nastran V9.3 (Fig. 4). In order to understand the dynamic characteristics of the bridge, additional vibration measurements with fifteen sensors were conducted, as discussed later. The measurements were made at the first span of the bridge due to the limitation of measurement arrangement. The models were, therefore, developed based on the condition of the first span. In the first span, a partial fracture was found at the top of D5 diagonal member at downstream side, referred to as D5l, and additional plates were attached for repair (Fig. 4(b)).

Some details of the basic model in Fig. 4(a) are described below.

1) Any damages in the bridge, such as the corrosions in steel members and the deteriorations in the RC slab observed in the visual inspection, were not considered.

2) Each upper and lower chord member was modeled by a single beam element and each diagonal member was modeled by a single rod element with axial stiffness only.

3) The oval openings in the web of diagonal D3 and D5, shown in Fig. 2(a), were modeled by equivalent reduction in the cross sectional area distributed over the whole length of the member.

Table 2 Properties of cross section of D5 member with additional plates

	Cross sectional area	Moment of inertia of area	
	A [cm^2]	In-plane I_y [cm^4]	Out-of-plane I_z [cm^4]
Healthy	41.6	123.5	9359
With additional plates	214.2	5402	39707
Ratio	5.1	4.4	4.2

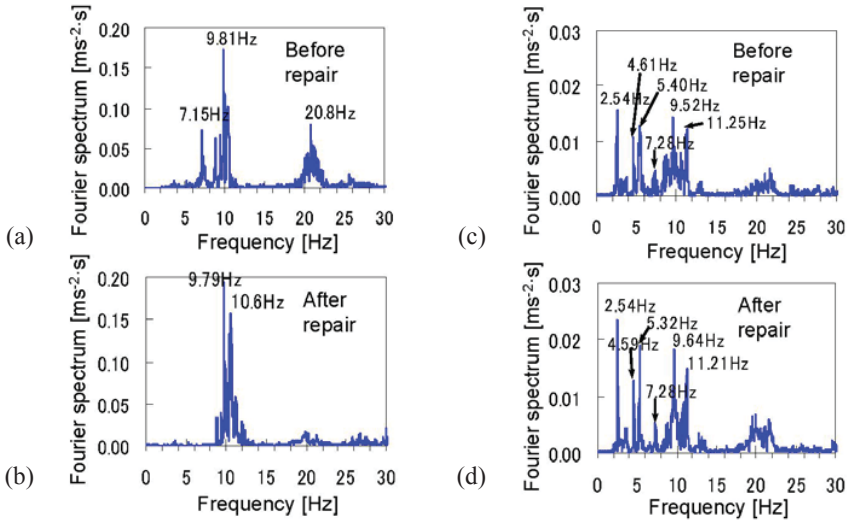

Fig. 3 Fourier spectra of measured acceleration. With dump truck running at 40 km/h. (a) D5, in plane, before repair, (b) D5, in-plane, after repair, (c) lower chord at quarter span, vertical, before repair, (d) lower chord at quarter span, vertical, after repair

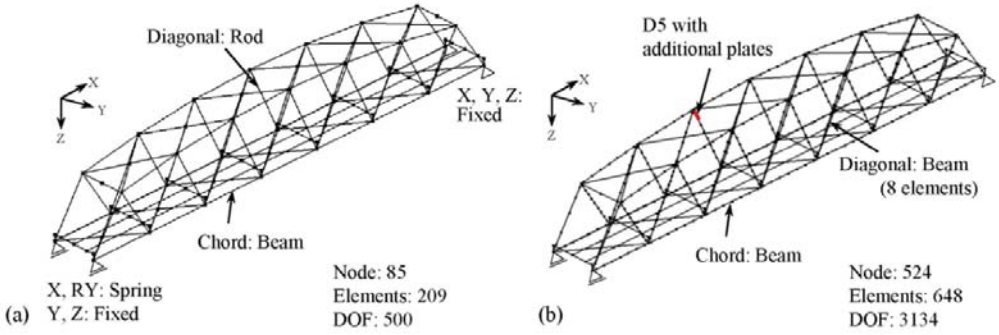

Fig. 4 (a) Basic model and (b) model with diagonal vibration and with additional plates

4) The contribution of the floor system and RC slab to the bending stiffness of the bridge was modeled by beam elements placed at the positions of stringers having stiffness equivalent to the stringers and the RC slab with Young's modulus ratio of 7. The cross beams, lateral bracings and portal bracings were modeled by beam elements.

5) For each beam element, the mass per unit length was assigned. The gusset plates attached to the diagonals and cross beams were modeled by lumped masses and assigned to the closest joint.

6) The Young's modulus and Poisson's ratio of steel were 2.0×10^8 kN/m^2 and 0.3, respectively.

7) It was reported that, in general, the horizontal displacements at roller supports and the rotational displacements at pin and roller supports are little in operational conditions and frictional forces act at those supports (Yoneda 1994). Therefore, the frictional resistance in the longitudinal translation at the roller supports and the rotation at the pin and roller supports were modeled by

spring elements. The spring constant for the longitudinal translation was determined as 1.0×10^4 kN/m that corresponded to the vertical reaction force of 1000 kN for self-weight, the dynamic friction coefficient of 0.01 and the longitudinal displacement of 1 mm. The spring constant for the rotation used in the analysis were 5.0×10^5 kNm/rad. These parameters were determined by trial and error based on the comparison with field vibration records, which is discussed in 4.3.2.

8) The piers and foundations were not modeled on the assumption that their effects on the operational vibrations of the superstructure were negligible.

The basic model described above neglected the vibration of diagonal members. In the model with diagonal vibration, the upper and lower chord and diagonal members were modeled by beam elements (Fig. 4(b)). The ends of diagonal members were modeled as rigid connections with the range of gusset plates in consideration, although the actual conditions could be elastic. In analyses with this model, the effect of self-weight was considered by conducting initial nonlinear static analysis and eigenvalue analyses were then conducted in consideration of the geometric stiffness. The effect of geometric stiffness appeared to be negligible for modal properties for global vibration modes of the bridge but increase the natural frequencies of local vibration modes dominated by vibration of tension diagonal member by about 10% (Yoshioka *et al.* 2009).

In addition, another model in consideration of additional steel plates at D5l for repair described above was developed. The effect of local structural change on the modal properties of the bridge could be understood theoretically from this model. Table 2 compares the properties of cross section of D5 in healthy and repaired conditions. These properties were assigned to the top element in D5l to model the increases in stiffness and mass by the additional plates (Fig. 4(b)).

3.2 Modal properties of the bridge

3.2.1 Classification of vibration mode

Table 3 shows the natural frequencies identified from the three models. In order to select vibration modes from different models for comparison, the Modal Assurance Criterion, referred to as MAC* in this paper, that indicated the similarity between different mode shapes were used.

$$MAC^* = \left|\phi \cdot \varphi\right|^2 \Big/ \left|\phi\right|^2 \left|\varphi\right|^2 \tag{1}$$

where ϕ and φ are modal vectors to be compared. A pair of vibration modes that yielded the maximum MAC* was selected for comparison in Table 3. The components in modal vectors for the degrees of freedom common in all models were used in the calculation of MAC*.

Fig. 5 shows principal vertical global modes identified in the model with diagonal vibration. In this paper, the vibration modes dominated by vibrations of the upper and lower chord members are called truss modes. There were vibration modes dominated by vibrations of diagonal members with no significant vibrations of the chord members, which are referred to as diagonal-dominant modes (Fig. 6). In the bridge studied, there were four diagonal members with common dimensions in a span, which resulted in four diagonal-dominant modes induced by those four diagonal members, such as those in Fig. 6 for D5. These four diagonal modes were different in the phases between the four diagonal members. Additionally, there were vibration modes in which vibrations of the main truss were coupled internally with local vibrations of diagonal members, as observed in Fig. 5. These vibration modes are referred to as diagonal-coupled modes in this paper. In such diagonal-coupled modes, deformations of the upper and lower chord members appeared to be relatively small due to significant deformations of diagonal members.

Table 3 Comparison of natural frequencies and MAC*

	Mode shape	Basic		With diagonal vibration				With additional plates			
		Order	Freq. [Hz]	Order	Freq. [Hz]	(MAC*)	Ratio	Order	Freq. [Hz]	(MAC*)	Ratio
Truss mode	1st horizontal symmetric	1	1.907	1	2.000	(0.90)	1.05	1	1.998	(0.91)	1.05
	1st vertical symmetric	3	2.446	2	2.567	(1.00)	1.05	2	2.567	(1.00)	1.05
	1st torsional symmetric	4	4.240	4	4.621	(0.85)	1.09	4	4.619	(0.83)	1.09
	1st vertical asymmetric	6	5.228	6	5.364	(1.00)	1.03	6	5.371	(1.00)	1.03
	1st horizontal asymmetric	7	5.333	7	5.600	(0.70)	1.05	7	5.599	(0.71)	1.05
	longitudinal rigid body	8	6.521	8	6.611	(1.00)	1.01	8	6.620	(1.00)	1.02
	2nd vertical symmetric	9	7.670	9	7.656	(0.83)	1.00	9	7.676	(0.83)	1.00
	1st torsional asymmetric	11	8.674	10	8.714	(0.97)	1.00	10	8.729	(0.97)	1.01
Coupled	2nd horizontal symmetric	12	8.879	11	8.956	(0.62)	1.01	11	8.958	(0.62)	1.01
Diagonal dominant mode (D5 in-plane)	1st (4 members in phase)		---	12	9.074	---	---	12	9.092	(0.73)	1.00
	1st (up & downstream members out of phase)		---	13	9.135	---	---	13	9.186	(0.47)	1.01
	1st (same side out of phase)		---	15	9.248	---	---	15	9.264	(0.48)	1.00
	1st (4 members out of phase)		---	16	9.281	---	---		---	---	---
	1st of D5 with additional plates		---		---	---	---	19	9.870	---	---
Coupled mode	2nd vertical asymmetric	14	9.982	17	9.325	(0.91)	0.93	16	9.325	(0.90)	0.93
Truss mode	3rd vertical symmetric	15	11.272	21	9.990	(0.90)	0.89	21	9.992	(0.90)	0.89
	2nd torsional symmetric	16	12.345	33	11.556	(0.80)	0.94	33	11.563	(0.81)	0.94

(The ratios and MAC* for truss and coupled modes were calculated with respect to the basic model.)
(The ratios and MAC* for diagonal modes were calculated with respect to the mode with diagonal vibration.)
(The 12th and 14th modes for the basic model were truss modes but, for comparison with other models, tabulated as coupled modes.)

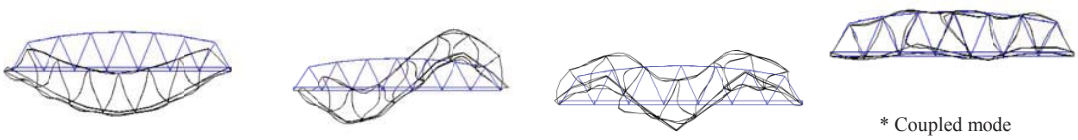

* Coupled mode

(2nd, 1st symmetic, 2.567 Hz) (6th, 1st asymmetic, 5.364 Hz) (9th, 2nd symmetic, 7.656 Hz) (17th, 2nd asymmetic, 9.325 Hz)

Fig. 5 Vertical truss modes (modal order, mode shape type, natural frequency)

(12th, 9.074 Hz) (13th, 9.135 Hz) (15th, 9.248 Hz) (16th, 9.281 Hz)

Fig. 6 Diagonal-dominant mode (modal order, natural frequency)

As discussed above, there were mainly three types of vibration modes, i.e., the truss, diagonal-dominant, and diagonal-coupled modes: the vibration modes identified from the models are classified into those three types in Table 3. It was, however, difficult to define general criteria to classify different types of vibration modes. In this study, therefore, those criteria were defined based on the ratio of the maximum component in modal vector for diagonal members to that of lower chord members for descriptive purposes: 0.6 or less for the truss mode, between 1.9 and 9.0 for the diagonal-coupled mode, and 12 or greater for the diagonal-dominant mode.

3.2.2 Distribution of natural frequencies and diagonal-coupled mode

Fig. 7 shows the distribution of natural frequencies, including those presented in Table 3, against modal order for the basic model and the model with diagonal vibration. For the basic model, there were truss modes only, as described above. As indicated in Fig 7, there were four diagonal-dominant modes at about 9 Hz for D5 members with the maximum slenderness ratio and, in addition, diagonal-coupled modes were observed also in that frequency range. This implies that dynamic coupling between a truss mode and a diagonal-dominant mode, resulting in a diagonal-coupled mode, could be induced when the natural frequencies of those modes were close together.

For the truss and diagonal-coupled modes at orders higher than the 2nd vertical asymmetric bending modes, the natural frequencies tended to decrease for the model with diagonal vibration, compared to the basic model, as observed in Table 3. These decreases in natural frequencies may be caused by increases in effective mass due to coupling of truss mode with diagonal-dominant mode. Additionally, the similarity of modal shapes between the basic model and the model with diagonal vibration tended to decrease by dynamic coupling between the main truss and the diagonal members, as observed in the decreases in the MAC* in Table 3.

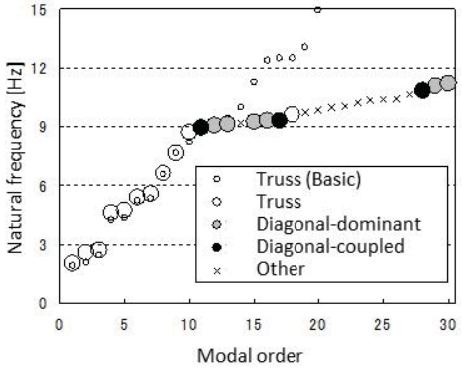

Fig. 7 Distribution of natural frequencies for basic model and model with diagonal vibration

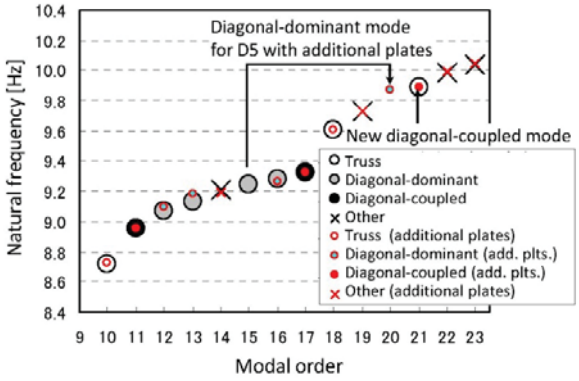

Fig. 8 Effect of additional plates on natural frequencies for 10th to 23rd modes

Effects of local structural change on modal properties are discussed by comparing results between the model with diagonal vibration and the model with additional plates. The natural frequency of the D5 dominant mode increased to 9.87 Hz for the mode with additional plates, although there were no other clear differences in natural frequencies between the two models (Table 3). This implies that the effects of additional plates on the natural frequencies of truss and diagonal-coupled modes were not significant. Fig. 8 compares the distribution of natural frequencies between the model with diagonal vibration and the model with additional plates for the 10th to 23th modes. A diagonal-coupled mode appeared at a frequency close to the natural frequency of diagonal mode of D5 with additional plates at 9.87 Hz.

4. Experimental identification of modal properties of the bridge

4.1 Vibration measurement

The modal properties identified theoretically in the previous section were compared with these obtained from a set of vibration measurement in the real bridge. The measurements were made at the first span where measurements with a wired system were possible. Fifteen vibration sensors consisting of 6 servo velocity-meters, VSE-15D, Tokyo Sokushin, and 9 piezoelectric accelerometers, PV-87, Rion, were located in two different arrangements (Fig. 9). Differences in the performance of two different sensors did not have any effects on the results in the frequency range between 2 and 20 Hz discussed in this paper. The velocity-meters used in the measurement had a capability of generating a signal proportional to acceleration. Accelerations of the bridge in service from all sensors were recorded at 100 samples per second for about 10 minutes.

The measurement locations in Case 1 shown in Fig. 9(a) were determined for the identification of global vibration modes of the main truss. Vertical vibrations were measured at locations on the road surface close to each node in the lower chord members except for both ends of the span where no measureable vertical vibration was expected. Additionally, vibrations were measured at the quarter point from the bottom of D5 at the upstream side, referred to as D5u. Two accelerometers located at the edges of the web measured in-plane vibration and an accelerometer

located at the center of the flange measured out-of-plane vibration as shown in Fig. 9(a).

In Case 2, accelerometers were placed at the quarter point of diagonal members, D5u, D5u', D5l, D5l' and D3l (Fig. 9(b)). Vertical vibrations at nodes in the lower chord members were also measured at the locations shown in Fig. 9(b). Additionally, vibrations in the horizontal direction perpendicular to the bridge axis were measured at the nodes U2 and U5 at the quarter span.

4.2 Experimental modal analysis

As in the preceding section, ERA was applied to free vibration records extracted from the measured vibration. Five and two free vibrations induced by a single vehicle passing, referred to as Vehicles 1 to 7, were selected from Cases 1 and 2, respectively, based on the vibration amplitude and video recording. The number of rows of Hankel matrices was 1500 times the number of sensors and the number of columns was 500, which were determined from preliminary analyses. In the analysis, the following screening criteria were used to extract realistic modal properties: the Modal Amplitude Coherence, MAC, of 0.9 or greater, the damping ratio between 0 and 0.05, the difference in the natural frequencies identified at two consecutive system orders of 0.02 Hz or less, and the Modal Assurance Criterion, MAC* defined in Eq. (1), of 0.9 or greater. In Eq. (1), ϕ and φ are the corresponding modal vectors identified at two consecutive system orders.

The measurement of in-plane motion of diagonal members included the effect of vertical and rotational motion of the main truss, which should be extracted so as to estimate the deformation of diagonal member only. The vertical and rotational rigid body displacements were calculated from the measurements at two adjacent joints in the lower chord and used to extract the effect of rigid body components from the in-plane measurement at diagonal members. In this adjustment, the horizontal displacement in the bridge axis was neglected, which could be justified by the fact that the horizontal displacement at roller support was little.

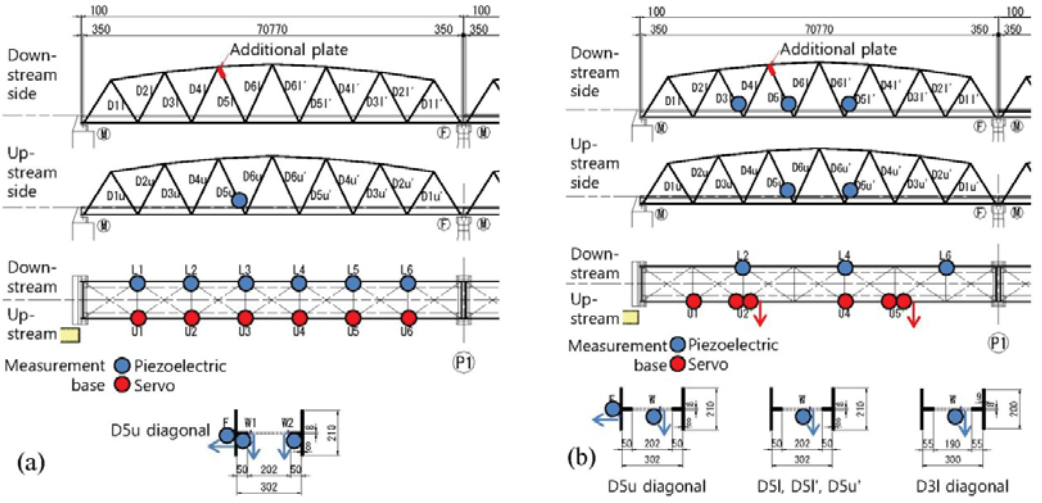

Fig. 9 Locations of vibration sensors. (a) Case 1, (b) Case 2

4.3 Modal properties identified experimentally

4.3.1 Modal properties identified from experiments

Fig. 10 shows a stabilization diagram obtained from the ERA analysis with 14 locations from Case 1. Fourteen channels out of 15 were used in the analysis because, in Case 1, the measurement at the joint U3 was not properly recorded. In Fig. 10, the Fourier spectra of the accelerations at U1 are also shown. In the frequency range below 8 Hz, the natural frequencies identified stably by ERA agreed with the peak frequencies in the Fourier spectra. On the other hand, there were many natural frequencies identified by ERA at frequencies around 9 Hz, although one peak only was observed in the acceleration spectra at U1, which implies that there were many diagonal dominant modes in this frequency range. Additionally, the natural frequencies identified from the model with additional plates in the FE analysis are presented at the top of Fig. 10. Although there was a difference between the natural frequency of 7.676 Hz in the analysis for the 2nd vertical symmetric mode and the corresponding experimental value, the analytical and experimental values agreed well for lower order modes than that mode.

4.3.2 Discussion of experimentally identified modal properties

Table 4 compares the natural frequencies identified from the experiments and the FE model. The variations in the natural frequencies with different vehicles were not significant although the variations for the 1st vertical symmetric, 2nd vertical asymmetric, and 2nd torsional symmetric modes were relatively greater than the other modes. In Table 4, the values in brackets are the MAC* calculated with the components in modal vectors for the joints in the lower chords normalized by the maximum vertical component for the lower chords.

For lower order modes from the 1st vertical symmetric to the 1st vertical asymmetric modes, the differences in natural frequencies between experiment and analysis were less than 1% and the MAC* ranged between 0.99 and 1. It should be noted that the theoretical results were obtained with support conditions that modeled support friction by spring constants determined by trial and error within a range physically reasonable. If the frictions at the supports were neglected, the natural frequency of the 1st vertical symmetric mode differed from the experimental identification by -6%. The effect of support friction was clear in the 1st vertical symmetric and 1st vertical asymmetric modes only.

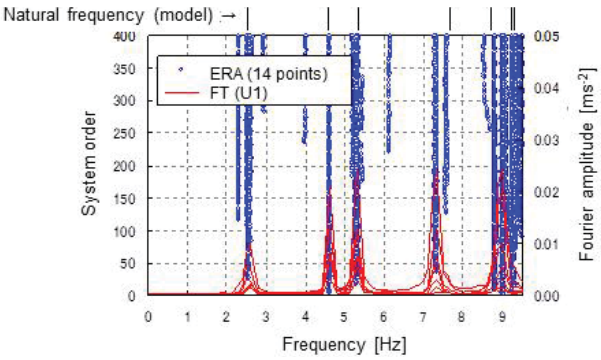

Fig. 10 Natural frequencies from experiment (ERA and FT) and FE model (Vehicles 1 to 7)

Table 4 Comparison of natural frequencies (in [Hz]) between experiment and theoretical analysis

	Mode shape	Experiment									Analysis		Ratio
		Case 1					Case 2		Average				
		Veh. 1 (Dump)	Veh. 2 (1 box)	Veh. 3 (Coupe)	Veh. 4 (Truck)	Veh. 5 (Truck)	Veh. 6 (Coupe)	Veh. 7 (Coupe)		(MAC*)	Ord.	Frq.	Ex/An
Truss	1st horizontal symmetric	---	---	---	---	---	---	---	---	(---)	1	1.998	---
	1st vertical symmetric	2.570	2.531	2.541	2.552	2.544	2.587	2.587	2.559	(1.00)	2	2.567	1.00
	1st torsional symmetric	4.605	4.609	4.606	4.617	4.603	4.610	4.608	4.608	(1.00)	4	4.619	1.00
	1st vertical asymmetric	5.293	5.302	5.324	5.239	5.302	5.305	5.302	5.295	(0.99)	6	5.371	1.01
	longitudinal rigid body	---	---	6.133	---	---	---	---	6.133	(0.73)	8	6.620	1.08
	2nd vertical symmetric	7.300	7.316	7.309	7.305	7.306	---	7.308	7.307	(0.98)	9	7.676	1.05
	1st torsional asymmetric	---	8.810	8.815	8.816	---	8.822	---	8.816	(0.80)	10	8.729	0.99
Diagonal (D5 in-plane)	4 members in phase	9.006	9.008	9.007	9.005	9.008	9.021	9.025	9.011	(---)	12	9.092	1.01
	Opposite side out of phase	9.052	9.325	9.243	9.339	9.243	9.090	---	9.215	(---)	13	9.186	1.00
	Same side out of phase	9.241	---	9.358	---	---	9.101	---	9.233	(---)	15	9.264	1.00
	1st with additional plates	---	---	---	---	---	9.762	9.932	9.847	(---)	19	9.870	1.00
Coupled	2nd vertical asymmetric	9.240	---	---	---	9.320	9.338	9.290	9.297	(0.74)	16	9.325	1.00
Truss	3rd vertical symmetric	10.169	10.076	---	10.123	10.099	10.121	10.132	10.120	(0.88)	21	9.992	0.99
	2nd torsional symmetric	11.548	11.674	11.240	11.356	11.792	11.390	11.388	11.484	(0.91)	33	11.563	1.01

(For the calculation of MAC*, components in modal vector for diagonal members were not used.)
(For diagonal-dominant modes, the modal shapes could not be identified due to limited number of sensors.)

The difference in natural frequency for the longitudinal rigid body mode between experiment and analysis was 8% with the MAC* of 0.73. These differences in natural frequency and mode shape may be because the spring constants determined to reduce differences between experiment and analysis mainly for lower order modes were not appropriate for the longitudinal rigid body mode. The longitudinal rigid body mode identified with Vehicle 3 only may be difficult to be induced by vehicle passing and cannot be judged as an effective mode for health monitoring. Therefore, the spring constants for the support were not updated to represent this mode.

For the 2nd vertical symmetric mode, the MAC* was relatively high at 0.98 but the differences in natural frequency was 5%. This difference in natural frequency might be caused by possible error in the spring constants representing support friction. The MAC* was relatively high possibly because the horizontal components in modal vectors were not used.

For higher order modes than the 1st torsional asymmetric mode with complex mode shapes, the MAC* was not high but the natural frequencies identified from experiment and theoretical analysis agreed well with a difference of about 1%.

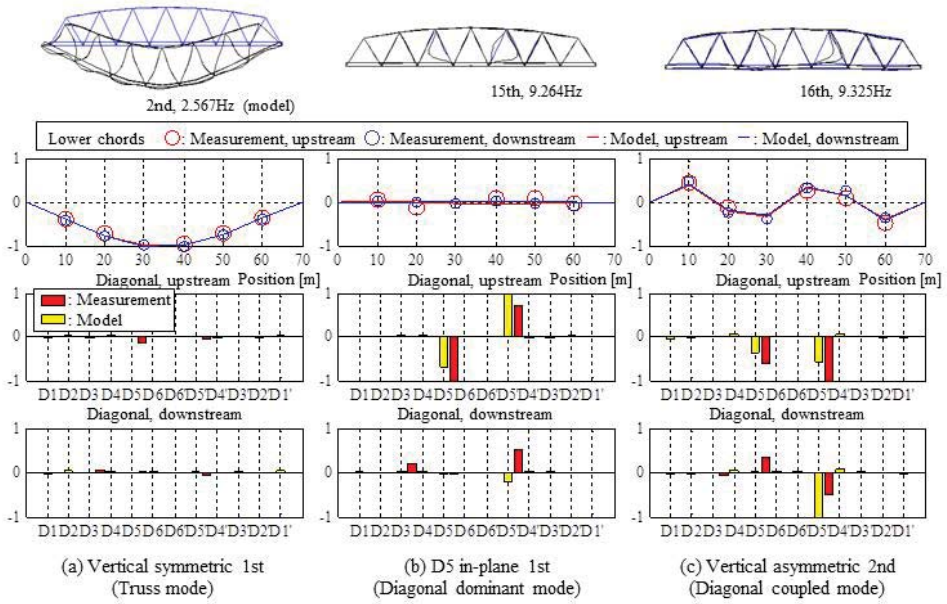

Fig. 11 Comparison of mode shapes identified from experiment and model

The D5 diagonal dominant modes in the experiment appeared to correspond to those identified theoretically, although the modal shapes were not identified clearly. For the Case 1, the four vibration modes dominated by D5 motion were identified at frequencies around 9 Hz but their mode shapes could not be distinguished with the measurement at a single D5 member only. For the Case 2, the measurement was made at four D5 diagonals but the corresponding measurements at the joints in the lower chords could not made so that the adjustment to estimate the amplitude of diagonal members only was not possible.

4.3.3 Dynamic coupling of diagonal members

In order to investigate the internal dynamic coupling between the main truss and diagonal members, the normalized modal vectors identified from Cases 1 and 2 were combined. The modal vectors identified from Vehicle 1 in Case 1 were combined with those from Vehicle 6 in Case 2 based on the closeness of natural frequencies. The components in modal vectors common in the two measurement cases were averaged in the combination.

Examples of the mode shapes are compared with the corresponding mode shapes obtained with the model with additional plates in Fig. 11. The top figures are the mode shapes in the FE analysis, the figures in the second row are the mode shapes for the lower chord members in the experiment and the FE analysis, and the figures at bottom two rows show the components in modal vectors for diagonal members after the adjustment described above by bar plot. The components of modal vectors shown in Fig. 11 were normalized by the maximum component in modal vector among all measurement locations. As observed in Figs. 11(a) and 11(b), the truss and diagonal-dominant

modes obtained theoretically were identified in the experiment, although there were some discrepancies in components in modal vectors. The modal component of D5 at downstream side appeared to be small in the experiment and analysis. The 2nd vertical asymmetric mode appeared to be coupled with vibration of D5 with similar trends in modal vector in the experiment and analysis (Fig. 11(c)).

Fig. 12 shows the degree of coupling of vibration of D5u diagonal member with vibration of the main truss represented by the ratio of the component in modal vector for D5u to the maximum component in modal vector for the lower chords. Although there appeared to be discrepancies between the experiment and theoretical analysis, increases in the degree of coupling were observed in the frequency range 9 to 11 Hz for the experiment and analysis. Possible reasons for discrepancies in the degree of coupling between experiment and analysis may include the fixed ends of diagonal members in the model that might not represent possible loosening of rivets. Particularly, if this coupling was interpreted as internal resonance, the effect of damping at connections on resonance responses would be significant. There were diagonal-dominant modes induced by Vehicles 1 and 2 observed at about 10.7 Hz that were not identified in the theoretical analysis. An additional FE analysis showed that these diagonal dominant modes could be torsional modes of diagonal member, although the details of analysis are not presented in this paper.

4.3.4 Dependence of modal damping on amplitude

Fig. 13 shows the relation between modal damping ratios and natural frequencies identified by ERA with Vehicles 1 to 7. As observed in Fig. 13, there were variations in the modal damping ratios identified after the screening described in the preceding section. The modal damping ratios for the 1st vertical symmetric and 1st vertical asymmetric modes varied with different vehicles. For other modes, the variations in modal damping ratios appeared to be small, although those modes were identified from less number of records.

A possible source of the variation in modal damping ratios for the lower order modes might include the dependence of modal damping on vibration amplitude. Fig. 14 shows the relation between modal damping ratios and the maximum initial modal amplitude in the lower chords for Vehicles 1 to 7. The initial modal amplitude was determined by dividing the initial modal acceleration amplitude identified by ERA by the square of natural circular frequency. All modal damping ratios identified stably at different system orders were shown in the figure.

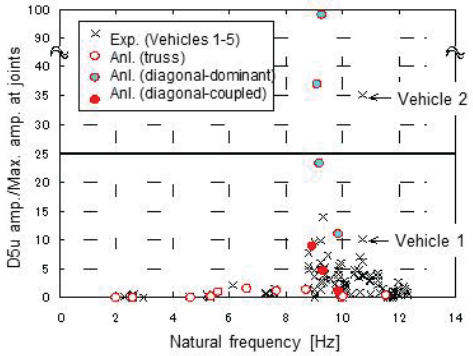

Fig. 12 Degree of coupling of D5u diagonal member with main truss

The modal damping ratios for the lower order modes in Fig. 14(a), in particular the 1st vertical symmetric mode, showed amplitude dependence in which the modal damping ratio tended to increase with increases in the initial modal amplitude. In a separate study, theoretical complex modal analysis was conducted with frictional damping at the movable supports and material damping in members, and the results showed that the contribution of the frictional damping to modal damping appeared to be significant in those lower order modes (Yoshioka *et al*. 2009). According to those results, the amplitude dependence of modal damping for the lower order modes may be caused by amplitude dependence of frictional damping at the supports.

For other higher order vertical modes including the 2nd vertical asymmetric mode, which was a diagonal-coupled mode, there were no clear signs of amplitude dependence in modal damping ratio, although these modes were identified in a range of small amplitude only. This may imply that, for higher order vertical modes that can be coupled with local vibration of diagonal members, the modal damping ratio can be identified stably and, therefore, those modes could be used to detect possible changes in damping due to damages in diagonal members.

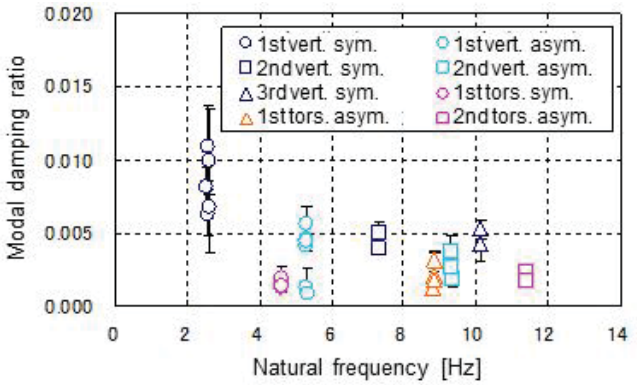

Fig. 13 Relation between modal damping ratios and natural frequencies identified experimentally

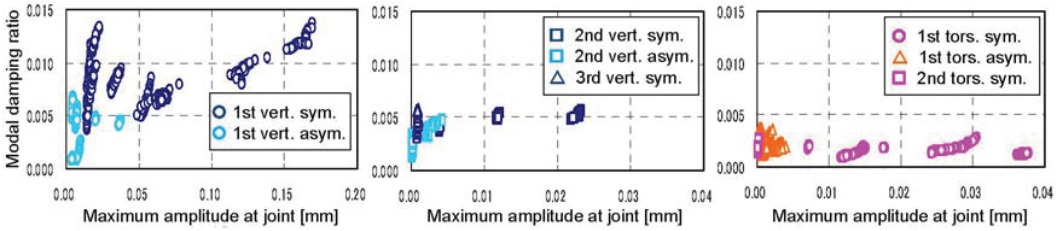

(a) Lower order vertical modes (b) Higer order vertical modes (c) Torsional modes

Fig. 14 Amplitude dependence of modal damping ratios. sym: symmetric; asym.: asymmetric

5. Detection of damages in diagonal members based on changes in modal damping

As discussed in 2.4, changes in modal properties were observed before and after the repair in the diagonal member. There were significant changes in modal damping ratio for the vibration modes shown in Table 1. Comparisons between the Fourier spectra shown in Fig. 3 and the results of theoretical and experimental modal analysis could conclude that the mode with D5 in-plane only was the 1st in-plane symmetric bending mode of the diagonal member, and the mode with the lower chords was the 2nd vertical symmetric mode that was coupled with vibration of D5 members (Table 1). This implies that diagonal-coupled modes that can be identified with small number of sensors at joints in lower chords could be used to detect damages in diagonal members.

In order to understand coupling between the 2nd vertical symmetric mode and diagonal-dominant mode for D5 with the partial fracture, an additional ERA analysis was conducted with data measured with one sensor at D5 and two at the lower chords. Fig. 15 shows the relation between natural frequency and modal damping ratio for the diagonal-dominant mode and the 2nd vertical symmetric mode, and the relation between natural frequency and degree of dynamic coupling of D5 with the main truss. The degree of dynamic coupling was defined by dividing the component in modal vector for D5 by that at the lower chord. For the 2nd vertical asymmetric mode, although no significant coupling of D5 with the main truss was observed after the repair, D5 diagonal before the repair was coupled clearly due to decrease in natural frequency of diagonal-dominant mode. The coupling of D5 with the main truss caused an increase in modal damping of the 2nd vertical symmetric mode possibly due to damping increase in the damaged diagonal.

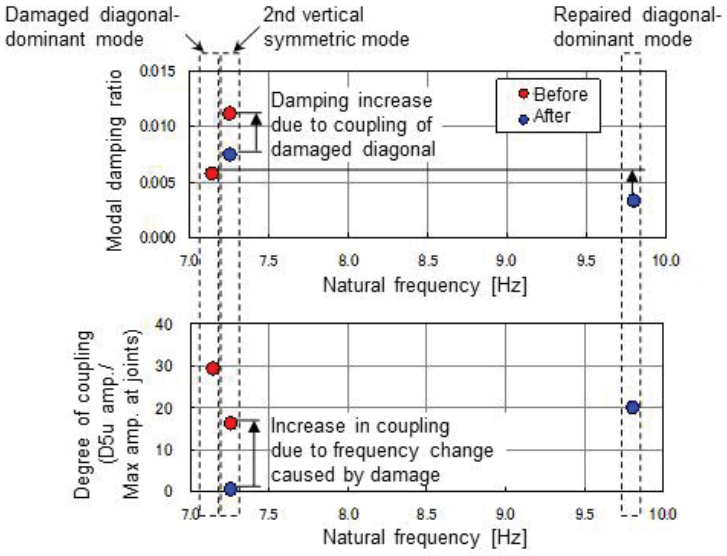

Fig. 15 Changes in modal properties of 2nd vertical symmetric mode before and after repair

The discussion above implies that modal damping ratios of diagonal-coupled modes could be used to identify damages in diagonal members: damages in diagonal members could be detected without direct measurement of vibrations of diagonal members, which could lead to an effective SHM based on vibration measurement. For bowstring type truss bridges, such as the bridge investigated in this study, the natural frequencies of diagonal-dominant modes are different depending on the length of diagonal members so that it could be possible to identify members with damage by the method discussed here.

It should be noted that damages discussed in this paper were cracks that could induce significant increase in frictional damping. Further investigations are required to identify types of damages which could be detected by the method discussed in this study.

6. Conclusions

Conclusions derived from this study are listed below.

- Vibration modes of truss bridges include truss modes that are vibration of the main truss with vibration of the upper and lower chord members dominant, diagonal-dominant modes that are local vibration mode, and diagonal-coupled modes in which truss mode and diagonal-dominant mode are coupled together.
- A local structural change, i.e., the repair of damaged diagonal member with additional steel plates in this study, did not have significant effect on the natural frequency of diagonal-coupled mode, but caused relatively clear changes in the degree of coupling between diagonal member and main truss. Although quantitative evaluation of the degree of coupling was difficult, there was qualitative consistency between the experiment and theoretical analysis.
- The modal damping ratios identified experimentally showed clear variations. Amplitude dependence of modal damping was observed for the 1st vertical symmetric mode and 1st vertical asymmetric mode with significant effect of frictional damping at the supports. However, for higher order vibration modes that could be coupled with local diagonal vibration, the modal damping ratios could be identified stably and their dependence on amplitude was not significant. These can be advantages in evaluating the condition of diagonal members based on damping changes in diagonal-coupled modes.
- The experimental modal analysis with vibration records measured in the bridge before and after the repair of damaged diagonal member showed little changes in natural frequencies but clear increases in modal damping ratio possibly due to coupling of damaged diagonal member. This implies that damages in diagonal members could be detected by monitoring damping of diagonal-coupled modes with a small number of sensors.

References

Balageas, D., Fritzen, C.P. and Guemes, A. (2006), *Structural Health Monitoring*, Wiley-ISTE

Boller, C., Chang, F.K. and Fujino, Y. (2009), *Encyclopedia of Structural Health Monitoring*. Wiley.

Doebling, S.W., Farrar, C.R., Prime, M.B. and Shevitz, D.W. (1996), *Damage identification and health monitoring of structural and mechanical systems from changes in their vibration characteristics, A Literature Review*, Los Alamos National Laboratory Report La-13070-MS.

Fujino, Y. and Siringoringo, D.M. (2008), "Structural health monitoring of bridges in Japan: an overview of the current trend", Proceedings of the *4th International Conference on FRP Composites in Civil Engineering*, Zurich.

Juang, J.N. and Pappa, R.S. (1985), "An eigensystem realization algorithm for modal parameter identification and modal reduction", *J. Guid. Control. Dynam.*, **8**(5), 620-627.

Kim, J. and Stubbs, N. (2003), "Nondestructive crack detection algorithm for full-scale bridges", *J. Struct. Eng.- ASCE*, **129**(10), 1358-1366.

Ko, J.M. and Ni Y.Q. (2005), "Technology developments in structural health monitoring of large-scale bridges", *Eng. Struct.*, **27**, 1715-1725.

Maeck J. and de Roeck, G. (2003), "Damage assessment using vibration analysis on the Z24-bridge", *Mech. Syst. Signal. Pr.*, **17**(1), 133-142.

National Guideline (2014), *Guideline for periodic inspection of bridges*, Ministry of Land, Infrastructure, Transport and Tourism, Japan. (in Japanese)

Shama, A.A., Mander, J.B., Chen, S.S. and Aref, A.J. (2001), "Ambient vibration and seismic evaluation of cantilever truss bridge", *Eng. Struct.*, **23**, 1281-1292.

Spyrakos, C.C., Raftoyiannis, I.G. and Ermopoulos, J.C. (2004), "Condition assessment and retrofit of a historic steel-truss railway bridge", *J. Constr. Steel Res.*, **60**, 1213-1225.

Yamaguchi, H., Fujiwara, T., Yamaguchi, K., Matsumoto, Y. and Tsutsumi, K. (2004), "Coupling of cable vibration and its damping effect in long span cable-stayed bridge: the Tatara Bridge", *J. Struct. Mech. Earth. Eng. - JSCE*, **766**(68), 309-323. (in Japanese)

Yoneda, M. (1994), "Some considerations on damping characteristics of bridge structures due to Coulomb friction force at movable support", *J. Struct. Mech. Earth. Eng. - JSCE*, **492**/I-23, 137-145. (in Japanese).

Yoshioka, T., Yamaguchi, H., Itou, S. and Harada, M. (2009), "Identification vibration characteristics of the steel truss bridge and influence of diagonal member damage on damping", *Kozo Kogaku Ronbunshu, A (J. Struct. Eng., A)*, **60**A, 295-305. (in Japanese)

Smart Structures and Systems, *Vol. 15, No. 3 (2015) 543-553*
DOI: http://dx.doi.org/10.12989/sss.2015.15.3.543

Joints: the weak link in bridge structures and lifecycles

Bojidar Yanev*

Executive Director, Bridge Inspection & Management, Department of Transportation, New York City
55 Water St., NY 10041, USA

(Received September 24, 2014, Revised January 9, 2015, Accepted February 15, 2015)

Abstract. The condition of the vehicular bridge network in New York City, as represented by ratings obtained during biennial inspections is reviewed over a period of three decades. Concurrently, the bridges comprising the network are considered as networks of structural elements whose condition defines the overall bridge condition according to New York State assumptions. A knowledge-based matrix of assessments is used in order to determine each element's vulnerability and impact within the network of an individual structure and the network of City bridges. In both networks expansion deck joints emerge as the weak link. Typical joint failures are illustrated. Bridge management options for maintenance, preservation, rehabilitation and replacement are examined in the context of joint performance.

Keywords: bridge; design; deterioration; joint; life-cycle; maintenance; management; rehabilitation

1. Introduction

Processes and products commonly fail at discontinuities. Engineering structures most frequently fail at joints. This is particularly true of bridges where joints function under dynamic conditions in aggressive environments. Hence, the statement that "the only good joint is no joint" is claimed by numerous contributing authors. That thinking is pursued in two directions. On bridges of up to several relatively shorter spans numerous publications, including Burke (2009) and Azizinamini *et al*. (2013) recommend jointless bridges and integral abutments. The large cyclic displacements of long-span bridges are accommodated by special expansion devices, such as the modular joints, designed and manufactured to detailed specifications including installation, maintenance and replacement. Between these two extremes, both options co-exist in the vast population of multi-span bridges serving vehicular traffic for many decades. The joints of such bridges can be limited to fewer locations and designed for larger movement, or located at every second span and built for smaller displacements and greater impact.

The performance of expansion joints has been assessed quantitatively on project levels and qualitatively on network levels. Syntheses, such as Burke (1989) and Purvis (2003) have identified typical modes of failure and expected lifecycles of specific joint types. Element- and span-specific biennial inspections reports generate qualitative condition ratings allowing for comparisons between bridge elements, structures and entire networks. Attempts to correlate the findings point to deck joints as a particularly vulnerable link in both the product of design and in the process of

*Corresponding author, Dr., E-mail: byanev@dot.nyc.gov

http://www.techno-press.org/?journal=sss&subpage=8 ISSN: 1738-1584 (Print), 1738-1991 (Online)

management. Consequently, their deficiencies must be addressed on all stages and levels of the bridge life-cycles. On a network level, the American Association of State Highway and Transportation Officials (AASHTO) Load and Resistance Factor Design (LRFD) Bridge Specifications amplify the design live load for joints by an impact factor of 75%. On project levels, joint malfunctions persist in construction, maintenance and operation. In order to fully address the problem therefore, the product of bridge design must be examined as a network of structural elements, whereas the process of network management must be reviewed as a product of the most pressing needs for urgent action.

2. The vehicular bridge network

In 2013 New York City is responsible for 789 vehicular and pedestrian bridges with approximately 5,000 spans and a total deck area of 1.5 million m^2. Among them are the Brooklyn (1883), Williamsburg (1903), Manhattan (1909) and Queensborough – Ed Koch (1909) and 25 moveable bridges (swing, lift, bascule and retractile), as well as many multi-span viaducts. The bridges are inspected at least biennially according to New York State standards. The condition of all elements in all spans is rated from 7 (new) to 1 (failed). The overall bridge condition rating R is calculated according to the formula of Eq. (1). It is a weighted average of the lowest ratings of 13 structural elements. The elements i and their respective weights w_i are shown in Table 1.

$$R = \sum_{i=1}^{13} w_i R_i \tag{1}$$

where:

R_i - lowest condition rating of element i observed on the bridge during a regular inspection (not necessarily in the same span)

w_i - weight assigned to element i.

The condition ratings obtained by Eq. (1) represent mostly deterministic and qualitative visual assessments. After more than 30 years of accrual, they appear suitable for statistical analysis. Such analysis however treats the data as homogenous, thus overlooking the following significant information. The work invested in each structure varies widely depending on its age, size, and function. Condition ratings $R > 4.5$ at bridges older than 50 years invariably imply substantial investments in rehabilitation. To illustrate the point, the condition ratings of the New York City bridges for 1990 and 2012 are plotted with respect to their "year built" in Figs. 1(a) and 1(b). Based on similar data, Yanev and Chen (1993) found the bridge condition ratings to be normally distributed, with a mean of roughly 4.5. An average deterioration rate obtained from either set of data points in Fig. 1 would never drop below the rating of 3 (not functioning as designed). Moreover, a cluster of bridges aged between 80 and 100 years are in very good condition. In contrast, the data points representing the lowest rated bridges for any age (denoted by the respective Bridge Identification Numbers in Fig. 1) have risen significantly over the examined period. This is easily understood when taking into account that approximately $US 4 billion have been spent over the last 30 years at the four East River crossings alone, even though they remain "built" in 1883, 1903, 1909, and 1909, respectively. New York City DOT has spent roughly $US 500 million annually on captial bridge projects for over a decade. Thus Figs. 1(a) and 1(b) illustrate the bridge network improvement as a result of capital reconstruction.

Table 1 Elements and weights in the bridge condition formula, NYS DOT

i	1	2	3	4	5	6	7	8	9	10	11	12	13	∑
Element	Bearings, anchor bolts, pads	Backwalls	Abutments	Wingwalls	Seats	Primary member	Secondary member	Curb	Sidewalk	Deck	Wearing surface	Pier	Joints	
w_i	6	5	8	5	6	10	5	1	2	8	4	8	4	72

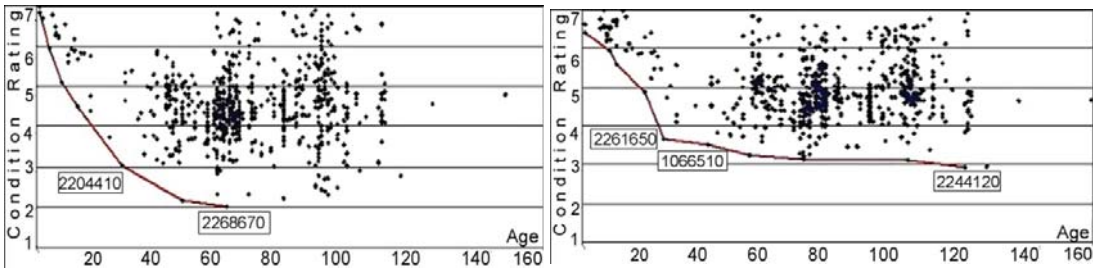

(a) 1990 (b) 2012

Fig. 1 Condition rating versus age for the New York City bridges in 1990 and 2012

During the 1990s the annual expenditures for capital reconstruction & component rehabilitation peaked at $US 600 million. Yanev (2007) demonstrated that the condition rating improvements resulting from these expenditures are in equilibrium with the fastest, rather than the average rate of deterioration. The steepest line of decline consistently approaches the rating of 3 in 30 years. Over the period illustrated in Figs. 1(a) and 1(b) the average overall bridge condition did not change very significantly. In contrast, the lowest condition ratings no longer fall below 3 in 2012.

The network level equilibrium between serviceable bridge conditions and related expenditures is currently maintained at an annual cost of about $US 400/m^2. Having eliminated the rigid constraint of service failures presented by poor bridges through reconstruction / rehabilitation, management can further optimize direct and user life-cycle costs by maintenance / preservation.

3. The bridge element network

According to Section 2, the annual reconstruction / rehabilitation costs of a large network are governed by the bridges rated below the acceptable condition level. Similarly, if individual structures are modeled as networks of elements, their annual maintenance / preservation costs under budget constraints should depend on the elements with the fastest rate of deterioration and the greatest impact. With condition ratings for all bridge elements in all spans, the New York State bridge database supports such modeling.

Agrawal and Kawaguchi (2009) obtained element deterioration rates for New York State bridges by Markov and Weibull models, ultimately recommending the latter. The resulting life-cycles are consistently around 75 years. As for bridges, so for their elements, the deterioration rates obtained from large databanks by statistical methods systematically obscure the worst and hence, most important cases. For the vehicular bridges in California, rated by the AASHTO Guide for Commonly Recognized Structural Elements, Thompson and Johnson (2005) concluded that the Markovian model alone is "inadequate … to estimate transition probabilities from a historical inspections data set alone. Important information is clearly missing. The authors believe that this missing information is maintenance activity."

Fig. 2 shows the condition ratings of certain structural elements included in Eq. (1) with respect to their age for the New York City vehicular bridges in 2012. Once again, rather than deriving averages, lines are drawn through the worst condition ratings obtained at any age. It can be observed that the elimination of the worst bridge conditions, shown in Fig. 1(b) is not matched by a corresponding improvement in the worst element conditions in Fig. 2 for that year. Consequently, whereas Figs. 1(a) and 1(b) illustrate overall bridge condition improvements obtained by reconstruction / rehabilitation, Figs. 2(a) - 2(f) do not show element condition improvement that might result from maintenance / preservation. Whether spontaneous or deliberate, such a management choice merits examination.

Yanev, Testa and Garvin (2003) and Yanev and Richards (2011) optimized network lifecycle expenditures by correlating the levels of maintenance task performance and the corresponding element life extensions. The 15 maintenance tasks, recommended by Bieniek *et al*. (1989, 1999) were assumed to influence the condition ratings of the 13 structural elements of Eq. (1) according to deterministically selected importance factors. The shortest known lifecycles of the bridge elements, such as those in Figs. 2(a)- 2(f) are assumed to occur at no maintenance.

The described method treats structural elements as independent. Bridge design similarly considers bridge structures as sets of discrete elements, to be dimensioned for prescribed loads. This potential discontinuity in the design process must be deliberately eliminated before it translates into a discontinuity of the final product. The design of details transferring loads between elements came under intense scrutiny in 2007 after the gusset plate failures at the deck truss bridge carrying Rte. I-35 over the Mississippi River.

An alternative view is proposed in order to better reveal structural vulnerabilities that might be suitable targets for bridge maintenance / preservation, before reconstruction / rehabilitation become inevitable. In the absence of qualitative / quantitative data, bridge managers have to rely on the engineering knowledge gained from inspection, maintenance, and particularly from the evidence of structural element failures. The set of values in Table 2 are one example. They are assembled as follows. The bridge structure is considered as a network comprised of the 13 elements in Table 1 and Eq. (1). The impact of each element on the others is rated from 0 to 1 by increments of 0.1 along the rows. As a result, the sum of each row in column 14 represents the estimated impact of the respective element within the structural network. Once the matrix is completed in this manner, the sums of each column shown in row 14 would conversely represent the estimated vulnerability of each element to the rest. Alternatively, one could estimate vulnerabilities along the columns, and the impact would obtain along the rows. Elements are assigned impact / vulnerability of 1 with respect to themselves, accounting for the values of 1 along the main diagonal of the matrix. The values are deterministic, as were the weights w_i in Table 1, and reflect knowledge of structural behavior and the worst case trends exhibited in Figs. 1 and 2.

The "impact" and "vulnerability" indexes in Table 2, column and row 14, respectively, are comparable to the values of w_i in Table 1, with some significant differences. The most vulnerable elements of Table 2 are primary members, bearings, anchor bolts & pads, and decks. Leading in impact are joints, decks and wearing surface. Primary members, joints, and decks, followed by bearings obtain highest cumulative scores, suggesting most critical combinations of impact and vulnerabiliy. Of these elements, joints have by far the shortest useful life, as shown in Fig. 2(f). Thus they can be regarded as the weak link in the bridge structural chain, best suited for early maintenance / preserevation actions. That distinction is shared by scuppers and paint, which are not included in Eq. (1). Their inclusion in the equation and in Table 2 would improve the model of the structural vulnerability to early deterioration.

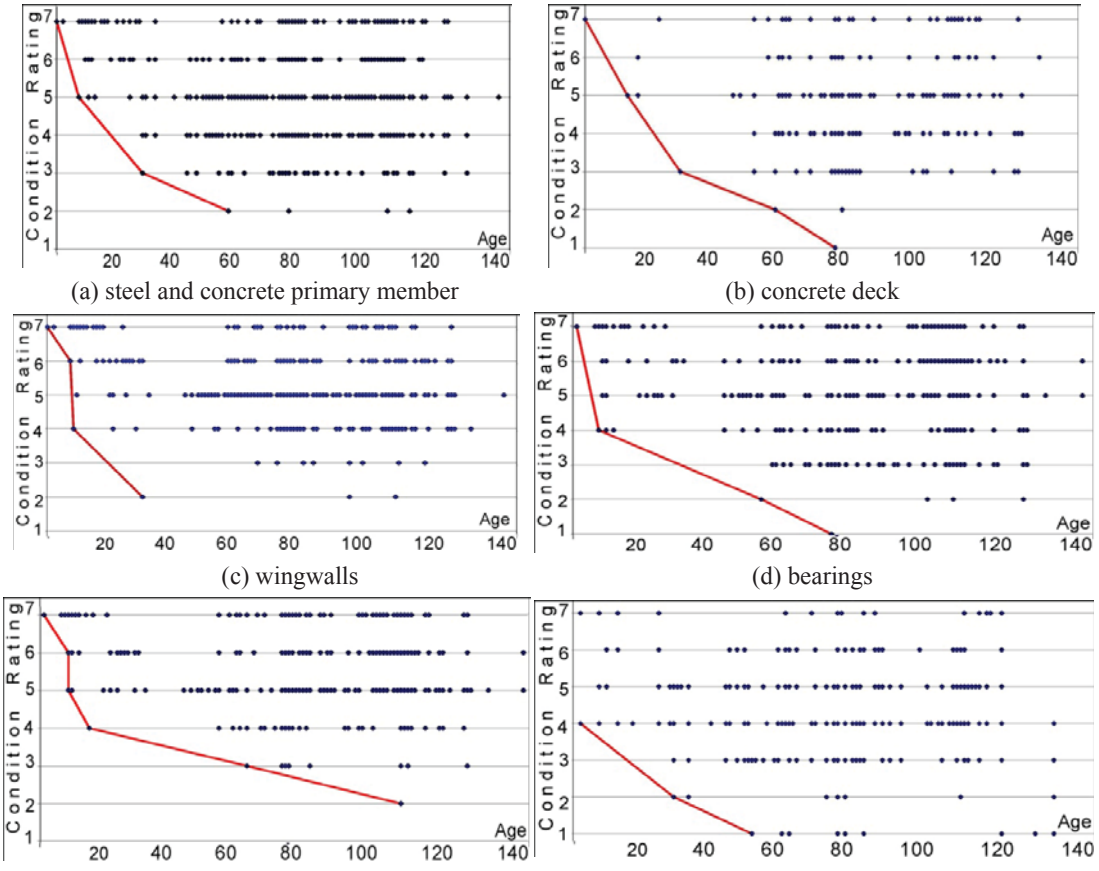

(a) steel and concrete primary member (b) concrete deck

(c) wingwalls (d) bearings

(e) backwalls (f) joints

Fig. 2 Condition ratings versus age for critical bridge elements in 2012

(a) armor joint, concrete (b) monodeck, torn angle (c) protruding seal

(d) missing seal (e) concrete header (f) butt joint, elastomeric header

(g) poured in place seal (h) cushion joint (i) plug joint

Fig. 3 Typical malfunctions of deck joints

Table 2 A sample "correlation" between the conditions of the critical bridge elements

i		1	2	3	4	5	6	7	8	9	10	11	12	13	14
	Element	Bearings, anchor bolts, pads	Backwalls	Abutments	Wingwalls	Seats	Primary members	Secondary members	Curb	Sidewalk	Deck	Wearing surface	Piers	Joints	∑ (Impact)
1	Bearings	1	0.5	0.5	0.2	1	1	0.3	0	0	0.3	0.1	1	0.8	6.7
2	Backwall	0.7	1	0.3	0.3	0.4	0.4	0	0	0	0	0	0	0	3.1
3	Abutments	0.7	1	1	1	0.8	0.4	0.2	0	0.4	0.1	0.2	0	0.2	6
4	Wingwall	0	0	1	1	0	0	0	0	0.3	0	0	0	0	2.3
5	Seats	1	0.3	0.4	0.1	1	1	0.2	0	0	0.3	0	1	1	6.3
6	Primary members	1	0.5	0.5	0	1	1	1	0	0	0.9	0	0.8	0.8	7.5
7	Secondary members	0.2	0	0	0	0.2	0.8	1	0	0	0	0	0.2	0	2.4
8	Curbs	0	0	0	0	0	0.2	0	1	1	0.8	0.9	0	0.2	4.1
9	Sidewalks	0	0	0	0	0	0.2	0.1	1	1	0.8	0.5	0.2	0.1	3.9
10	Deck	0.8	0.2	0.2	0	0.3	0.9	0.5	1	1	1	1	0.7	1	8.6
11	Wearing surface	0.7	0.2	0.4	0	0.7	0.8	0.4	1	0.4	1	1	0	1	7.6
12	Piers	1	0	0	0	1	1	0	0	0	1	0	1	0.7	5.7
13	Joints	1	0.5	0.5	0	0.8	1	1	0.6	0	1	1	0.7	1	9.1
14	∑ Vulnerability	8.1	4.2	4.8	2.6	7.2	8.7	4.7	4.6	4.1	7.2	4.7	5.6	6.8	73.3
15	∑ Vuln. + ∑ Impact	14.8	7.3	10.8	4.9	13.5	16.2	7.1	8.7	8.0	15.8	12.3	11.3	15.9	

4. The weak link: deck joints

In 2013, 677 of the 789 bridges on the New York City inventory were vehicular, with approximately 4,000 spans. The total number of joints exceeded 3,000, of which 1409 were expansion ones. Figs. 3(a)-3(i) illustrate typical joints and their malfunctions. Prevalent are the steel armored joints with rubber seals shown in Figs. 3(a)-3(e). Rarer are the "cushion" joints, as in Fig. 3(h). The butt joints with or without steel edges, shown in Figs. 3(f)-3(g) are used in decks with minimal thermal movements. Elastomeric concrete headers, as in Fig. 3(f) are replacing the regular concrete ones. Polymer poured-in-place sealants are used in decks without armor, as in Fig. 3(g). Proprietary inflatable seals are used for joints accommodating slightly larger displacements than the butt joints. The extreme traffic hazards of failing armor and cushion joints are temporarily mitigated by plug joints, as in Fig. 3(i), by paving over with asphalt or, ultimately by steel plates, as in Fig. 4(a). The practices, malfunctions and failures reported by Purvis (2003) pertain in all of the represented cases.

Typical malfunctions observed by NYC DOT Bridge Inspections include the following:
Compression seals: debris accumulation, ruptured, protruding, missing.

Poured-in-place seals (butt joints): drying out, debonding;
Steel armor: loose, broken, protruding;
Cushion joint: broken bolts, loose, missing plates;
Concrete header: cracked, sagging, broken, exposed re-bars;
Elastomeric header: poor adhesion of sealant;
Concrete decks: broken corners;
Asphalt pavement: cracked, sinking;
Plug joints: cracked, eroded strip, bulging, sinking;

Modular & finger joints are not included herein due to their special functions and properties. They are particularly vulnerable to misalignment, impact and debris accumulation. Their impact on the serviceability of large bridges is critical.

The impact of joint failures on the vulnerable structural elements is irreversible. Figs. 4(a)-4(d) show damage to decks, bearings, pedestals, fascia and entire piers under expansion joints. The rest of the bridge shown in Fig. 4(d) appears in good condition.

(a) steel plate replacing a failed joint (b) spalling fascia

(c) bearings, pedestals under expansion joint (d) pier rehabilitation at expansion joint

Fig. 4 Structural consequences of expansion joint malfunctions

5. Conclusions

Products and processes fail at discontinuities arising between their components and their stages, respectively. The life-cycle performance of expansion joints identifies them as discontinuities both in the designed product and in the management process. Designed and built for an unrealistic type of service and maintenance, they are managed with unrealistic performance expectations. Their replacement is often the only available remedy, amounting to rehabilitation, because of its complexity. As each stage of the process relies on the next one to improve the performance of the product, the useful life of joints is effectively minimized. Thus steps towards improving the performance of the product must be taken at all stages of the process.

- Design

Fu *et al*. (2003, p. 15) conclude that decks are primarily designed and reinforced for flexure, but fail in "shear fatigue". Fatigue design is well advanced for steel, but not for the other involved materials, including concrete, elastomeric concrete, polymer sealants, and so on. AASHTO LRFD has emphasized the vulnerability of joints to fatigue and fracture by increasing their live load impact factor from 33% to 75%. The increase however, reflects primarily the performance of modular joints and is likely to be used in their design. The higher impact factor does not extend to decks. There is abundant evidence that if the steel armor does not fail, it destroys the concrete header and if the header holds, it breaks away from the deck. The following questions arise:

What are the appropriate dynamic loads acting on joints?

What materials and dimensions can resist these loads over an acceptable number of cycles?

While these questions remain unresolved, most expansion joints are not designed for a specific performance, but adopted from a "state-of-the-art" inventory of available supplies.

- Construction / Rehabilitation

The steel and concrete joint elements and compression seals are usually installed according to design specifications for the product, which is typically limited to the joint itself. Minor structural misalignments can impose unsustainable loads on joints. The poured in place seals are sensitive to ambient conditions and material preparation. As a result, their performance is highly uneven. Adhesion to elastomeric and regular concrete headers is poor. There are no warrantees covering their expected useful life under AASHTO traffic loads.

- Maintenance / Preservation

Compression and poured in place seals are not regularly cleaned and replaced. Loose steel angles are not bolted until they break or break the concrete header. Bearings, pedestals and troughs under expansion joints are not cleaned. Plug joints can be installed as emergency replacement of cushion joints with an expected life of 2 - 4 years, depending on the traffic volume and the demand for structural movement.

All joint-related maintenance tasks, including the inspections require extensive traffic closures and incur high direct and user costs. Traffic and water under the bridge further constrain remedial work. As a result, lapses in joint maintenance typically accelerate reconstruction, as illustrated in Figs. 4(a)-4(d).

Carol (2013) has investigated the dynamic performance of polymer concrete as a partial repair for failed joint headers. The findings underscore the importance of taking into account dynamic loads and avoiding material discontinuities, such as the ones arising between steel and concrete in armor joints.

The elements comprising the bridge condition formula in Eq. (1) and enumerated in Tables 1

and 2 have been chosen more than 35 years ago in order to prioritize rehabilitation / reconstruction. The expansion joint deficiencies described thus far and the potential countermeasures remain below the scope of reconstruction, but exceed "routine" maintenance. The Bridge Preservation Guide (FHWA, 2008) addresses that gap in the management options. It contains a set of activities designed to arrest at relatively low cost the deterioration of elements with high impact before the critically important decks, primary members and piers are affected. Condition rating trends, such as the ones shown in Figs. 2 suggest that scuppers would be a suitable target for bridge preservation, along with expansion joins. Painting is already treated as rehabilitation.

- Condition Assessment

The present conclusions are drawn from qualitative visual assessments of structural conditions and loosely related expenditures quantified in money. Since there is no uniquely defined correlation between the two, the costs of maintenance / preservation activities are known, but their benefits in terms of life extension are at best assumed. Over the period reflected in Fig. 1, structural condition assessments emphasized the elimination of imminent hazards, ultimately achieved by reconstruction / rehabilitation. As the needs & benefits related to maintenance / preservation gain in importance, so does the demand for their quantification. That demand has yet to be met, with the help of the newly developed capabilities for non-destructive testing and evaluation (NDT&E). Current long-term bridge health monitoring initiatives have concentrated on the performance of bridge decks. There are also advances in the monitoring of seismic performance and scour. The performance of expansion joints under traffic is another monitoring target which would advance bridge design.

So far, joint malfunctions are fully addressed when their consequences, such as the failure of decks, bearings and pedestals become manifest. In the meanwhile, vehicular traffic is growing in volume and gaining in weight. Joints and their "headers" regularly break under cyclic or unique impact. The "impact" and "vulnerability" estimates in Table 2 represent an assumed structural response to assumed traffic loads. Without quantifiable measurements, it would be hard to base important management decisions on the result. Fu *et al*. (2013, p. 21) state "Taking the advantage of more WIM (Weigh-in-motion) data accumulated over the past decade, developing a new load requirement has become simpler and more quantitative." WIM systems are typically deployed at long-span bridges, but appear appropriate for multi-span structures on high volume traffic corridors as well. Armored joints would lend themselves well to instrumenting for monitoring of the live load impact.

Recent heavy snowfalls in the New York City area, as well as over the entire East Coast have revealed the extreme vulnerability of armored expansion joints to plowing equipment, as illustrated in Fig. 3(b). A joint strong enough to sustain regular direct impact of a plow may not be cost-effective. Therefore a performance-based design should incorporate details avoiding such impact.

- Management

Joint failures are ultimately management failures. In a robust operation, no stage of the process or element of the product should inherit or transmit deficiencies to the others. The safe and cost-effective lifecycle of structures and networks requires redundancy, which in turn depends on continuity. In a typical bridge network, where 35% of the spans have expansion joints, the benefits of addressing these discontinuities before the need arises to address the entire structures are considerable.

Note: The material presented herein expresses the views of the author and not those of any organization.

References

Agrawal, A. K. and A. Kawaguchi. (2009), *Bridge Element Deterioration Rates*, Project C-01-51, Transportation Infrastructure Research Consortium, NYS DOT, NY, USA.

Azizinamini, A. *et al*. (2013), *Bridges for Service Life Beyond 100 Years: Innovative Systems, Subsystems and Components,* SHRP2 – Project R19A, Florida International University, University of Nebraska, Lincoln, USA.

Bieniek, M. *et al*. (1989, 1999), *Preventive Maintenance Management System for the New York City Bridges*, Consortium of Civil Engineering Departments of New York City Colleges and Universities, the Center of Infrastructure Studies, Columbia University, New York, USA.

Burke, M.P. (2009), *Integral and Semi-Integral Bridges*, John Wiley & Sons, Hoboken, New Jersey, USA.

Burke, M.P. (1989), *Bridge Deck Joints*, National Cooperative Highway Research Council Synthesis of Highway Practice #141, Transportation Research Board, National Research Council, Washington, D.C., USA.

Carol, C. (2013), Preliminary Analysis of Polymer Concrete Used for Bridge Deck Joint Repairs, Louisiana Transportation Research Center Project No. 12-4TIRE, Baton Rouge, La. USA.

FHWA (2008), Bridge Preservation Guide, Office of the Infrastructure, Federal Highway Administration, U.S. Department of Transportation, Washington, D.C., USA.

Fu, G. *et al*. (2003), *Effect of Truck Weight on Bridge Network Costs*, Report 495, National Cooperative Highway Research Council, Transportation Research Board, National Research Council, Washington, D.C.

Purvis, R. (2003), *Bridge Deck Joint Performance*, Synthesis 319, National Cooperative Highway Research Council, Transportation Research Board, National Research Council, Washington, D.C., USA.

Thompson, P.D. and Johnson, M.B. (2005), "Markovian bridge deterioration: developing models from historical data", *Struct. Infrastruct. E.*, **1**(1), 85- 91.

Yanev, B.S. and Chen, X. (1993), "Life-Cycle Performance of New York City Bridges", *Transportation Research Record* No. 1389, National Research Council, Washington, D.C., USA.

Yanev, B.S. (1997) "Life-Cycle Performance of Bridge Components in New York City", *Recent Advances in Bridge Engineering*, EMPA, Zurich, Switzerland.

Yanev, B.S. (2007), *Bridge Management*, John Wiley, Hoboken, New Jersey, USA.

Yanev, B., Testa, R.B. and Garvin, M. (2003), "Maintenance Strategy to Minimize Bridge Life-Cycle Costs", *Transportation Research Circular No. E-C049*, April 2003.

Yanev. B. and Richards, G.C. (2011), "Bridge Maintenance in New York City", Transportation Research Record No. 2220, Transportation Research Board, Washington, D.C., USA, pp. 28-37.

Smart Structures and Systems, *Vol. 15, No. 3 (2015) 555-576*
DOI: http://dx.doi.org/10.12989/sss.2015.15.3.555

Research and practice of health monitoring for long-span bridges in the mainland of China

Hui Li*[1,2], Jinping Ou[1,2], Xigang Zhang[3], Minshan Pei[3] and Na Li[3]

[1]*Key Lab of Structures Dynamic Behavior and Control (Harbin Institute of Technology), The Ministry of Education, China*
[2]*School of Civil Engineering, Harbin Institute of Technology, Harbin, 150090, China*
[3] *CCCC Highway Consultants CO., Ltd., Beijing, China*

(Received November 27, 2014, Revised January 18, 2015, Accepted January 25, 2015)

Abstract. The large number of long-span bridges constructed in China motivates the applications of structural health monitoring (SHM) technology. Many bridges have been equipped with sophisticated SHM systems in the mainland of China and in Hong Kong of China. Recently, SHM technology has been extended to field test systems. In this view, SHM can serve as a tool to develop the methods of life-cycle performance design, evaluation, maintenance and management of bridges; to develop new structural analysis methods through validation and feedback from SHM results; and to understand the behavior of bridges under natural and man-made disasters, rapidly assess the damage and loss of structures over large regions after disasters, e.g., earthquake, typhoon, flood, etc. It is hoped that combining analytical methods, numerical simulation, small-scale tests and accelerated durability tests with SHM could become the main engine driving the development of bridge engineering. This paper demonstrates the above viewpoint.

Keywords: structural health monitoring; bridge; life-cycle performance evaluation; data

1. Introduction

A number of long-span bridges have been constructed or will be constructed in the mainland of China. The total number of the highway bridges and railway bridges in the mainland of China has ranked number 1 in the world. However, the long-span bridges suffer from the long-term actions of loads and environment, natural disasters, man-made disasters and performance deterioration (fatigue, durability, etc). Therefore, a highly efficient management technology is needed for so many bridges in the mainland of China. SHM technique can aid to understand the performance evolution rules through monitoring, and then provide early alarm and decisions for maintenance.

SHM is considered to originate from smart sensor technology in the early 1990s. A SHM system includes modules for sensing, data acquisition and transmission, data management, data processing, data analysis, modeling, safety evaluation and decision-making. Ou and Li (2010) reviewed the SHM techniques in the mainland of China.

Various smart sensors have been developed over the past three decades. However, optical fiber sensors and wireless sensor networks have the most promising prospects (Ansari 2008, Bao *et al*.

*Corresponding author, Professor, E-mail: lihui@hit.edu.cn

http://www.techno-press.org/?journal=sss&subpage=8 ISSN: 1738-1584 (Print), 1738-1991 (Online)

1993, Zhou and Ou 2009, Dong *et al*. 2013, Lynch and Loh 2005, Spencer *et al*. 2004, Yu *et al*. 2009). Recent years, the compressive sampling-based data packet loss recovery methods have been proposed as an improvement of the reliability of data transmission of wireless sensors.

Many vibration-based damage detection and model updating approaches have been extensively proposed (Doebling *et al*. 1996, Sohn *et al*. 2003, Li *et al*. 2008, Li *et al*. 2011, Bao *et al*. 2012). However, the accuracy of the vibration-based damage detection and model updating cannot meet the practical requirement due to uncertainties of environment and structures, too few sensors and minor local damage of bridges.

This paper presents an overview of applications of structural health monitoring systems for long-span bridges in the mainland of China. Representative sophisticated SHM systems for long-span bridges are introduced. Based on practical experience, the variables to be monitored, the placement of sensors, the type of sensors, and the sampling rate and scheme of data are described. The methods of data analysis and modeling, and the safety evaluation based on the SHM technique are presented.

2. Applications of SHM systems for long-span bridges in the mainland of China

2.1 Overview of applications of SHM systems for long-span bridges in the mainland of China

A number of SHM systems have been designed and implemented in long-span bridges in the mainland of China. Some of them are listed in Table 1. The table shows that the sophisticated SHM systems are very complex, consisting of hundreds of sensors, complex data acquisition and data transmission systems, database for management and safety evaluation. The systems are operated and remotely controlled online. The data analysis and condition assessment are conducted in both online and offline schemes. The evaluation results are presented in visualization. The data analysis and safety evaluation reports can be automatically generated and sent to the managers.

The variables to be monitored can be categorized into three groups, i.e., loads and environmental actions, local response and global response. The load and environmental measurements record vehicular weight (by weigh-in-motion system and digital camera), the temperature and humidity (by thermal couples, FBG temperature sensors and humidity sensors), the wind (by ultrasonic anemoscope for fluctuating wind and propeller anemometer for static wind), earthquake ground motion (by triaxial accelerometer), the vessel collision(by accelerometer), and rain fall. Local response includes the strain in key elements (by strain gauges, vibrating wire sensors and FBG strain gauges), the cable tension (by accelerometers, load cells, FBG strain sensors and electromagnetic sensors) and damage (by acoustic emission, ultrasonic detection), the corrosion (by electrochemical-based sensors, optical fiber sensors), the reaction force of supports/anchorages (by load cells and displacement transducers), and the scour (by radar, ultrasonic systems, optical fiber sensors, vibrating sensors). The global response includes the acceleration and displacement (by accelerometers, global positioning systems (GPS), displacement transducer, inclination sensors).

2.2 Representative SHM systems for two cable-supported long-span bridges

Two SHM systems are introduced here, one for a suspension bridge and the other for a

cable-stayed bridge. Figs. 1 and 2 show the layout of the sensors in these two representative SHM systems for a long-span suspension bridge and a cable-stayed bridge, respectively.

Table 1 Overview of bridges implemented SHM systems in the mainland of China

Name of bridge	Information of bridge (type, span length, total length, tower height, completion year)	Sensors and number	Data used for condition assessment
Xihoumen Bridge*	Suspension bridge,1650m+578m 5.452km, 211.286m 2009	Anemometer (6+2), Temperature & Humidity sensor (7) , Temperature sensor (46+73),Strain gauge (96), Grating-ruler sensor(3), Displacement transducer (4), Cable tension sensor(49), Unaxial accelerometer (22), Triaxial accelerometer (2) , Inclination sensor (16), GPS(15), **Total sensors: 341**	Wind, traffic load, deflection, displacement, vibration, strain, cable force
Jintang Bridge*	Cable-stayed bridge 77 m+218m+620 m+218m+77m 26.54km 204m 2009	Anemometer (2+2), Temperature & Humidity sensor (7) , Temperature sensor (9+166),Strain gauge (144), Grating-ruler sensor(6), Unaxial accelerometer (8+15), Triaxial accelerometer (2) , Inclination sensor (10), Inter connecting pipe (46),Cable tension sensor(72), Load cell(12), , GPS(4), **Total sensors: 505**	Wind, traffic load, deflection, displacement, vibration, strain, cable force
Hong Kong-Shenzhen Western Corridor*	Cable-stayed bridge 180m+90m+75m 5545m 139m 2007	Anemometer (4+1), Rain falling gauge(1), Temperature & Humidity sensor (1) , Temperature sensor (27), Strain gauge (284), Displacement transducer(4), Unaxial accelerometer (30), Triaxial accelerometer (1) , Inclination sensor (6), Inter connecting pipe (15),Cable tension sensor(17), Load cell(6), Weight-in-Motion sensor (2) Digital Camera(2) **Total sensors: 401**	Wind, traffic load, deflection, displacement, vibration, strain, cable force
Qinlinwan Bridge*	Cable-stayed bridge 2×50m+180m+2×50m 1069m 128.485m 2010	Anemometer (1), Temperature & Humidity sensor (3) , Temperature sensor (32),Strain gauge(52), Displacement transducer(4), Unaxial accelerometer (24+29), Triaxial accelerometer (2) , Inclination sensor (8), Inter connecting pipe (24),GPS(2), Vehicle Speedometer(1), Digital Camera(2) **Total sensors: 184**	Wind, traffic load, deflection, displacement, vibration, strain, cable force
Waitan Bridge*	Cable-stayed bridge 225m+90m 1393m 85.243m 2010	Anemometer (2), Temperature & Humidity sensor (3) , Temperature sensor (26),Strain gauge (37),Displacement transducer(4), Unaxial accelerometer (26+14), Triaxial accelerometer (1) , Inclination sensor (6), Inter connecting pipe (20),GPS(1), Vehicle Speedometer(1), Digital Camera(2) **Total sensors: 142**	Wind, traffic load, deflection, displacement, vibration, strain, cable force
Wantou Bridge*	Arch bridge 48m+180m+48m 833m — 2009	Anemometer(1), Temperature & Humidity sensor(2), Temperature sensor(19), Strain gauge(21), Unaxial accelerometer (15), Displacement transducer(4), GPS(1), electromagnetic sensor(10), Digital Camera(2), Vehicle speedometer (1) **Total sensors: 76**	Wind, traffic load, deflection, displacement, vibration, strain, cable force
Mingzhou Bridge*	Arch bridge 100m+450m+100m 1250m	Anemometer(1), Temperature & Humidity sensor(1), Temperature sensor(40), Strain gauge(54), Unaxial accelerometer (15),	Wind, Traffic load, deflection, displacement, Vibration, Strain, cable force

	— 2011	Triaxial accelerometer (2) , Displacement transducer(4), GPS(3), electromagnetic sensor(22), Digital Camera(2), Vehicle speedometer (1) **Total sensors: 145**	
Caofeidian 1# Bridge*	Cable-stayed bridge 138m+138m 2.35km 120m 2010	Anemometer (2), Temperature & Humidity sensor (2) ,FBG temperature sensor (34),FBG strain gauge (34), Weight-in-Motion(1), Unaxial accelerometer (38), Triaxial accelerometer (1) , Bi-Inclination sensor (4), Inter connecting pipe (14),Digital Camera(2) **Total sensors: 132**	Wind, Traffic load, deflection, displacement, Vibration, Strain, cable force
TonglinYangtze River Bridge*	Cable-stayed bridge 80+90+190+432+190+90+80m 2592m 153.65m 1995	Anemometer (1), Temperature & Humidity sensor (1) ,FBG temperature sensor (32),FBG strain gauge (32), FBG displacement transducer(4),Vehicle speedometer (1), Inter connecting pipe (22),GPS(10) **Total sensors: 103**	Wind, Traffic load, deflection, displacement, Vibration, Strain, cable force
Hangzhou Bay Bridge*	Cable-stayed bridge 70+160+448+160+70m (South Channel Bridge) 100+160+318m (North Channel Bridge) 36km 178.8m(North Channel Bridge) 194.3m(South Channel Bridge) 2008	North Bridge: Anemometer (2+2), Temperature & Humidity sensor (6), Weight-in-Motion sensor (2), FBG temperature sensor (24),FBG strain gauge (58), Unaxial accelerometer (28+49), Triaxial accelerometer (2) Displacement transducer (10),Inter connecting pipe (36), GPS (4), Digital Camera (2) **Total sensors: 225** South Bridge: Anemometer (2+1), Temperature & Humidity sensor (5), FBG temperature sensor (20),FBG strain gauge (46), Unaxial accelerometer (22+25), Triaxial accelerometer (2) Displacement transducer (9), Inter connecting pipe (18),GPS (4) **Total sensors:154**	Wind, Traffic load, deflection, displacement, Vibration, Strain, cable force
Nanjing Fourth Yangtze River bridge*	Suspension bridge 410.2 + 1418 + 363.4m 28.996km 230.9m 2012	Anemometer (4+2), Temperature & Humidity sensor (14), Weight-in-Motion sensor (2), Temperature sensor (6+15),Strain gauge (36), Unaxial accelerometer (39), Bi-accelerometer (16),Triaxial accelerometer (4) Displacement transducer (12),Inclination sensor (17), GPS (19), GPS basestation (2) **Total sensors: 188**	Wind, Traffic load, deflection, displacement, Vibration, Strain, cable force
Jiaxing-Shaoxing Bridge*	Cable-stayed bridge 70+200+5×428+200+70m 10.137km 169.964~173.174 m 2013	Anemometer (4+1), Rain falling gauge (1), Temperature & Humidity sensor (11),Scour sensor (7), Corrosion sensor (12), Weight-in-Motion sensor (1), Temperature sensor (45),Strain gauge (182), Unaxial accelerometer (156+38), Triaxial accelerometer (2) Displacement transducer (54),Inter connecting pipe (48), Inclination sensor (18), GPS (5), GPS basestation (1),Digital Camera (48) **Total sensors: 634**	Wind, Traffic load, deflection, displacement, Vibration, Strain, cable force
Taizhou Yangtze River Highway Bridge	Suspension bridge Main span 1080 m, 2940 m 191.5 m 2012	Anemometer (1),Temperature and Humidity sensor (1), Static GPS (11), Uniaxial accelerometer (39), Triaxial accelerometer (12), Strain gauge (168),Temperature sensor (42)	Environment information: wind speed; atmospheric temperature; humidity; internal temperature of the bridge. Displacement of the bridge; displacement of bridge support; acceleration; strain and stress

Donghai Bridge	cable-stayed bridge 420 m 32.5 km 195 m 2006.	Temperature sensor 70, Strain monitoring point64, Static GPS 9, Anemometer 3, Accelerometer56, Fatigue meter 48, Extensometer 8, Water Pressure Sensor 76, Cable tension sensor 16, Corrosion sensor 36	Environment information: wind speed; atmospheric temperature; humidity; internal temperature of the bridge. Structural response: overall displacement of the bridge; displacement of bridge support; acceleration; strain and stress
Su-Tong Yangtze River Bridge	Cable-stayed bridge 1088 m 2088 m 300.4 m 2008	Displacement meter: 12, Hygrometer: 9, Accelerometer: 38, Magnetic dynamometer: 16, Inclination sensor: 6, Strain gauge: 333, Fiber optic sensor: 16, Anemometer: 11, GPS base station: 12; Corrosion sensor: 12; Non Stress Meter: 2.	Environment information: wind speed; atmospheric temperature; humidity; internal temperature of the bridge. Structural response: overall displacement of the bridge; displacement of bridge support; acceleration; strain and stress.
Jiangyin Yangtze River Highway Bridge	Suspension bridge 1385m 2008m 193m 1999	Fiber optic strain sensor: 1680, Accelerometer: 35, Fiber optic temperature sensor: 36, GPS base station: 9, Hygrometer: 2, Temperature sensor: 2, Triaxial ultrasonic anemometer: 2, Displacement meter: 4, Barometer: 2, electromagnetic sensor: 14.	Displacement and vibration of main girder and bridge tower; tension force of suspension cable; temperature field; humidity; wind speed.
Nanjing Second Yangtze River Bridge	Cable-stayed bridge 628m 2938m 195.41m 2001	Total station 22 prisms on the main girder, 16 displacement measurement points for each tower), vibrating wire strain gauge, electromagnetic sensor, anemometer, temperature sensor, hygrometer	Alignment and strain of main girder; tension force of stay cables; displacement of bridge tower; temperature field of main girder; vibration of main girder and bridge tower; traffic load; wind speed.
Nanjing Third Yangtze River Bridge	Cable-stayed bridge 648m 1288m 215m 2006	Accelerometer: 43, Strain gauge: 488+244, Temperature and humidity sensor: 6, Anemometer: 2, cable tension sensor: 168, displacement sensor: 72, Deflection sensor: 42, Bearing force sensor: 12	Alignment and strain of main girder; tension force of stay cables; displacement of bridge tower; temperature field of main girder; vibration of main girder and bridge tower; traffic load; wind speed and humidity; Bearing force.
Zhenjiang-Yangzhou Yangtze River Highway Bridge (Cable-stayed bridge)	Cable-stayed bridge 406m 756.8m 146.9m 2005	Accelerometer: 80, Strain sensor: 60, Anemometer: 1, Temperature sensor: 24, GPS base station: 8	Alignment and strain of main girder; tension force of stay cables; vibration of tower, steel box girder, main cable and stay cables; temperature field of main girder
Zhenjiang-Yangzhou Yangtze River Highway Bridge (suspension bridge)	Suspension bridge 1490m 2430m 209.9m 2005.	Accelerometer: 93, Strain sensor: 72, Anemometer: 1, Temperature sensor: 40, GPS base station: 8.	Alignment and strain of main girder; tension force of stay cables; vibration of tower, steel box girder, main cable and stay cables; temperature field of main girder
Chonghai Yangtze River Bridge	Six-span continuous beam steel bridge102m+4×185m+102m 2011	Anemometer: 2, Temperature and humidity sensor: 8, Structural temperature sensor: 72, Expansion joint displacement sensor: 8, Deflection sensor: 9, Strain sensor: 72, Vibrometer: 26, Collision sensor: 21, External tendon force sensor: 16.	Load：Wind speed; atmospheric temperature; humidity; structure temperature; pavement temperature; traffic load; Structural response: acceleration(vibration of main structure, earthquake, collision), structure deflection; strain and stress; displacement of support and

			expansion joints; external tendon force.
Shanghai Yangpu Bridge	Cable-stayed bridge 602m 1172m 208m 1993	Strain sensor: 40, Piezoelectric sensor: 5	Acceleration; traffic load; tension force; strain; deformation; overall displacement, etc.
The Xiabaishi Bridge	Prestressed concrete continuous rigid frame bridge 145m+2×260m+145 m 810m 2003	Accelerometer: 153(49 measurement points plus 2 reference points for vertical, longitudinal and horizontal directions each).	Vibration of the bridge
Qingzhoucable-stayed bridge	Cable-stayed bridge 605m 1185m 175m 2002	Accelerometer: 348(180 for bridge deck and 168 for each stay cable), Level gauge, Total station, Deflection sensor.	Vibration of bridge deck and stay cables; deflection of bridge deck; displacement of tower, tension force of stay cables.
Wulongjiang Bridg	Prestressed concrete T-frame bridge 58m+3×144m+58m 548m 1971 (retrofitted in 2007, SHM system was implemented in 2007).	Anemometer, Temperature and humidity sensor, GPS base station, Vibrating wire strain gauge, Fiber optic strain sensor, Accelerometer.	Temperature field of bridge structure, humidity, wind direction, bridge displacement and acceleration, strain of concrete.

Fig. 1 shows that eight anemoscopes are installed on the deck and towers to measure the inflow of wind. Temperature and humidity sensors are installed on the bridges. It is noted that there is no sensor for vehicular weight in Fig. 1. In fact, weigh-in-motion systems have been embedded into each lane at one cross section of girders, which are included in traffic management system, rather than in structural health monitoring system. The accelerometers are installed on the free field near the bridge piers to measure seismic input and to investigate the travelling wave effects. Strain gauges are installed on the girders to investigate strain and fatigue damage. Since fatigue damage has been extensively observed in the "U" reinforced rib on the top of steel box-girders, strain gauges are attached to the upper plates of the box-girders. Load cells are installed at the anchorages of the main cables to measure the cable tension. Load cells and accelerometers are attached on the cables/hangers to measure the tension force and the vibration of the cables/hangers. For suspension bridges, the longest hangers near the tower are likeliest to be excited into oscillations and equipped with accelerometers. For the global response, the acceleration of cables, girders and towers are measured by accelerometers. The displacement of the main cables, towers and girders is measured by both GPS and inclinometers. The relative displacement between the tower and the girder is measured by displacement transducers.

At the six-tower cable-stayed Jiashao Bridge, similar with the suspension bridge above, anemoscopes are installed on girders and top of towers to record wind; humidity and temperature are measured by humidity and temperature sensors; weigh-in-motion systems have been embedded in one end of bridge to measure vehicular weight, speed and volume; and rainfall sensor is also used for monitoring rainfall intensity. The turbulence in the river is dramatic, scour is severe and should be closely monitored by SHM. Scour sensors and corrosion sensors are installed on the pier. Pressure transmitter is densely installed on the girder to measure the displacement. The displacement of the towers is measured by inclinometers and GPS, and the vibration of girders and towers is recorded by accelerometers. Accelerometers also measure the cable tension force and oscillation. Strain sensors have been attached on girders and piers. Displacement transducers have

been installed at the connections of girders and piers and joint mentioned below. Considering such long bridge, stressed induced by temperature variations must be released. To that end, a joint is installed in the middle of the structure. The joint has very complex configuration and it requires particular attention during the design of the SHM system. Many sensors have been installed on this joint, as shown in Fig. 2 (in the middle of entire bridge span).

2.3 Lessons from the practice of SHM technique

The lessons from the practice of sophisticated SHM systems are summarized as follows:

The maximum vehicular loads, seasonal wind and typhoons, and temperature have been obtained and compared with those in design codes and with the design parameters. The SHM systems have observed overweight vehicles.

The measured strain and cable tension forces are much smaller than the design values under normal operating conditions. As a consequence, fatigue damage of the steel box girders and cables is also small. Normally, fatigue life of bridge structures is much longer than that specified in design codes.

The displacement of the main cables in suspension bridge is very small at normal operating conditions.

Bridge acceleration is induced mainly by wind and heavy trucks. For suspension bridges, the girder and the hangers close to the towers are readily excited to dramatic oscillations, as shown in Fig. 3. For cable-stayed bridges, stay cables, particular the longer ones, may oscillate under wind. Vortex-induced-vibration has been observed at the girder of the suspension bridge, as shown in Fig. 4.

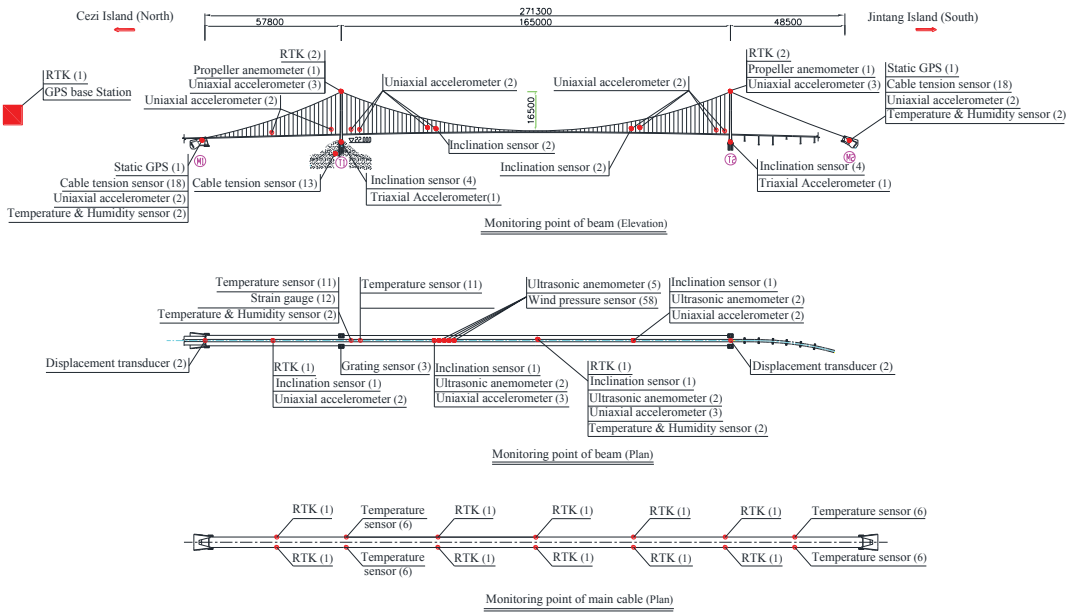

Fig. 1 Layout of sensors in a suspension bridge in China

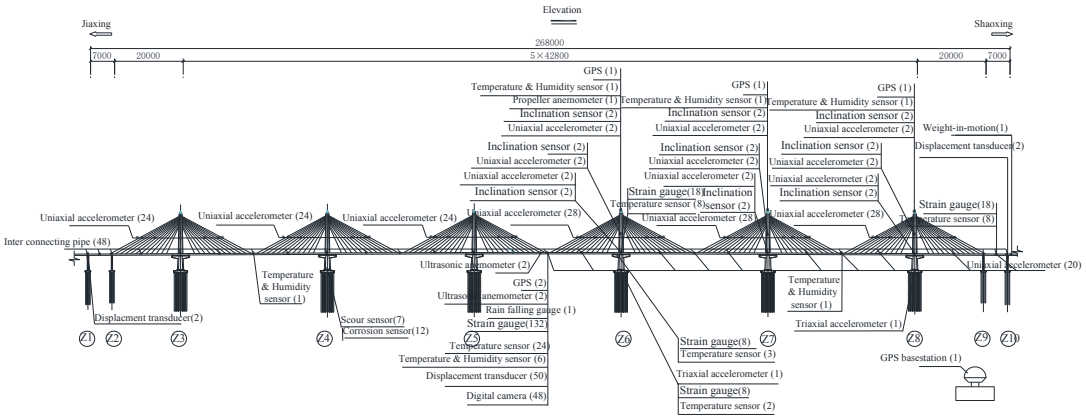

Fig. 2 Layout of sensors for a six-tower cable-stayed bridge in China

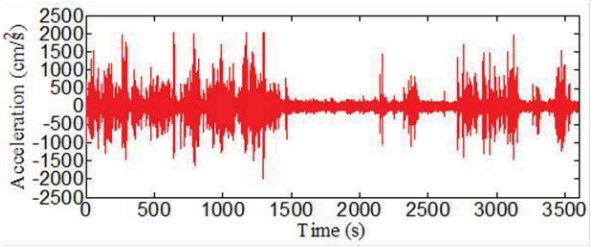

Fig. 3 Wind-induced-vibration of hanger

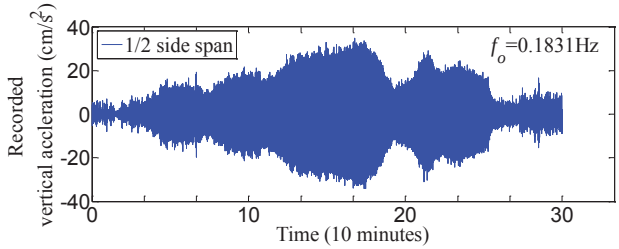

Fig. 4 Vortex-induced-vibration of girder

The natural frequencies, damping ratios and mode shapes are obtained based on the monitored acceleration by using the stochastic subspace identification method (SSI). The natural frequencies may vary with temperature. Damping ratios are more scatter than the frequencies and vary with the wind-induced vibrations due to aerodynamic effects. This has also been observed by Jo *et al*. (2009) and Koh *et al*. (2009) in the suspension bridges in Hong Kong and Korea, respectively.

The sensor life-spans are much shorter than the life-span of bridges. The maintenance of the

SHM system can extend the life-span of the whole SHM system. Furthermore, the long-term performance and stability of sensors cannot be completely ensured. Durable, replaceable and maintainable sensors are needed

Some variables are still very hard to monitor, such as wind load, fatigue damage, cracks inside concrete, corrosion inside concrete structures, cables and anchorages. The wave-propagation methods may be a potential solution for minor local damage detection.

The data sampling scheme and data store schemes require special attention in order to avoid accrual of mega-data. Compressive sensing technology may be used in SHM in the future (Bao *et al*. 2011). Cloud technology provides an efficient and convenient tool for SHM data management.

The data quality provided by SHM systems is not entirely satisfactory. Some data are contaminated by strong noise, even incorrect, e.g. ultrasonic anemoscope cannot work properly under rain conditions. Methods for automatic data processing, and data quality confirmation, and correction must be developed.

Deterioration in structural performance is hard to obtain by the monitored data at this stage. More efficient sensors for local minor damage monitoring should be developed in the future.

Methods for data driven-based diagnosis at macro-scale view and model-based diagnosis at fine scale will become a hot topic in this field. The relationship between the output and input is not unique. One individual output may be a multiple-coupled effects of loads and environmental factors. This is not clear in field SHM, which is quite different from laboratory tests. It is particularly hard to investigate the behavior of bridges under an individual loads and environmental factors. Decomposition methods obtaining unique projections between single individual output and single individual input should be particularly investigated. Big data may be a tool to solve this issue.

3. Data analysis, modeling and safety evaluation based on SHM technology

3.1 Analysis and modeling of loads

Vehicular, wind and temperature are the main loads for long-span bridges. Here, we focus on vehicular load, which causes the ultimate state-based failure of the structure and fatigue cumulative damage. The weigh-in-motion device is widely employed to measure the vehicular loads. Using the monitored data, the extreme value and fatigue spectrum of the vehicular load can be established.

Zhang (2013) systematically investigates the vehicle load based on SHM system. The extreme value model of vehicle includes inter-arrival times between vehicles and weight probabilistic model. The analysis of the monitored vehicle load datasets indicates that the inter-arrival times of vehicles at normal conditions can be simulated by a Gamma process; while at dense conditions, the analysis of the monitored vehicle load datasets shows that the inter-arrival time follows a Weibull distribution. Considering the tail distribution is much important to the extreme value model, a truncated distribution of vehicle weights that incorporates empirical and generalized Pareto distribution(semi-parametric distribution) is proposed (Zhang 2013, Gu *et al*. 2014) and the approach for determining the threshold of the above semi-parametric distribution is presented. The extreme value distribution estimation of vehicle loads at the Nanjing 3rd Yangtze River Bridge is calculated by using the proposed semi-parametric model and the monitored vehicle loads. The results are shown in Fig. 5.

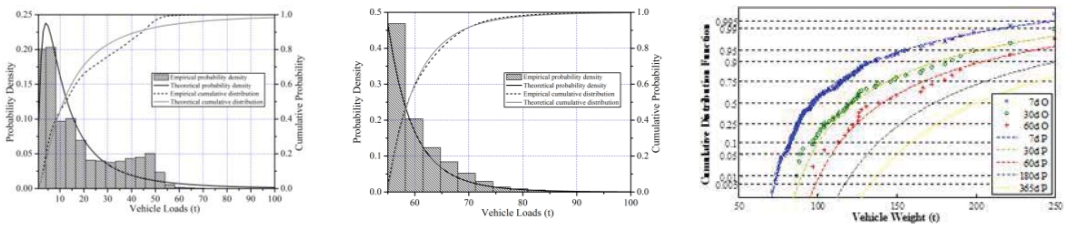

Fig. 5 Extreme value model of vehicles

Lan *et al*. (2011) establishes a fatigue spectrum model for the vehicle load based on the Miner model of the fatigue effect. The volume of the traffic over the life-span of a bridge is predicted by a Logistic model. This model can be updated with the monitored data.

The vehicular loads are distributed over a bridge. The identification and modeling of vehicular loads taking account of vehicle spatial distribution, especially for the heavy trucks, proposed by Bao *et al*. (2013) by use the compressive sampling method. Chen *et al*. (2014) use the combination of weigh-in-motion systems and cameras (computer vision technique) to identify temporal-spatial distribution of heavy trucks.

3.2 Vortex-induced vibration of long-span bridges

Long-span suspension bridges are wind-sensitive structures. Vortex-induced vibration of bridges with twin-box girders have been observed in several bridges. Fig. 6 shows representative records of vortex-induced vibrations of a suspension bridge. The wind conditions which induce this kind of vibration have been identified and analyzed as shown in Fig. 6. It can be seen that the vortex-induced vibration of the girder occurs at wind speed within 4-14 m/s with a direction of perpendicular to the bridge and with slight turbulence. Wind along the bridge span may be non-uniform, which can decrease the vortex-induced vibration amplitude (Li *et al*. 2011, Li *et al*. 2014, Laima *et al*. 2013)

3.3 Vibration monitoring, tension force identification and fatigue damage assessment of cables/hangers

Cables and hangers are among the most important elements for long-span bridges. These elements suffer from wind-induced vibrations, parametric excited vibration, corrosion and fatigue or their coupled effects and may even break during accidents, or may cause driver discomfort. The vibration monitoring and tension force identification of cables and hangers are very critical to ensure structural and public safety.

(1) Vibration of cables and hangers

The vibration of cables and hangers has been monitored. One representative vibration of the hanger in a suspension bridge is shown in Fig. 7. It can be seen that the two monitored accelerations are quite different. The former is with larger amplitude and many high frequency components, while the latter is with small amplitude and low frequency components, implying collisions between neighbor hangers in the former case.

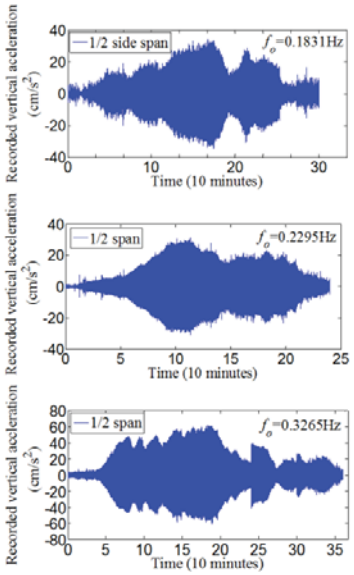

(a) Vortex-induced vibration of girder with various modes under different wind conditions

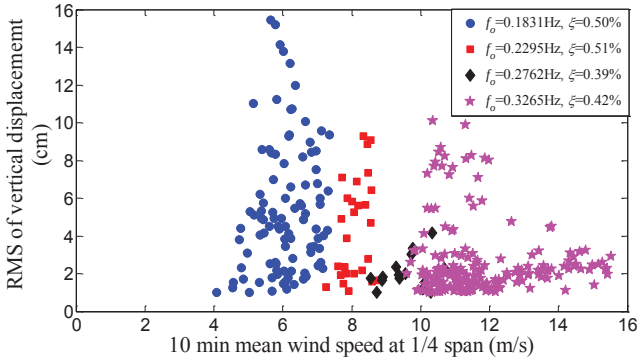

(b) Wind speed

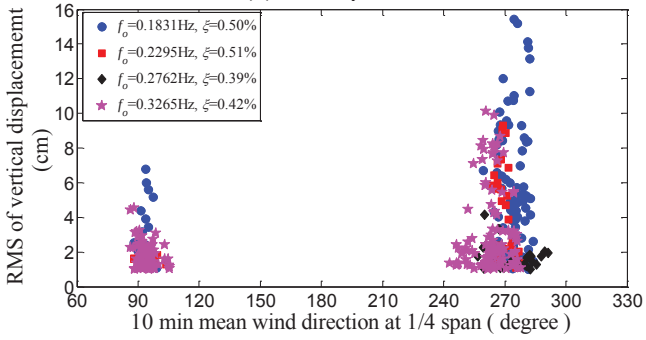

(c) Wind direction

Continued-

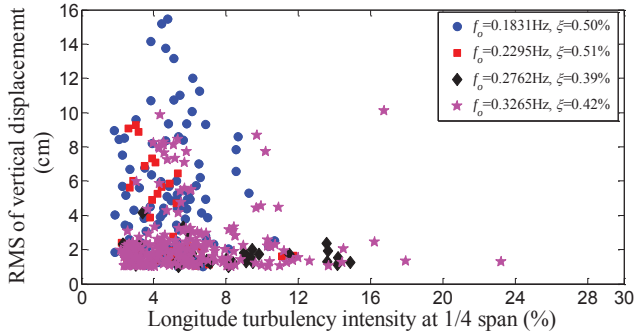

(d) Wind turbulence

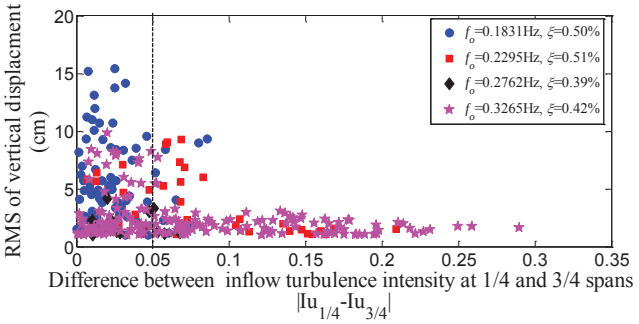

(e) Discrepancy in longitudinal turbulence intensity

Fig. 6 Time histories of representative recorded wind-induced vibrations and corresponding wind conditions

Dramatic vibrations of cables are also observed in a cable-stayed bridge, as shown in Fig. 8. It can be seen from Fig. 8 that the acceleration is very large, while the displacement is very small, implying that the cable vibration contains high frequency components and modes. This demonstrates the cable vibration is the vortex-induced with high multiple modes (Chen *et al.* 2013).

2) Identification of cable tension force

Self-sensing smart cables have been developed (Li *et al.* 2009, Ou and Li, 2010), with embedded glass fiber reinforced polymer (GFRP) bars. They contain FBG sensors and are anchored at the two ends of the cable together with the steel wires. However, the sensors in the smart cable are hard to replace.

Vibration-based cable tension identification is the most widely applied method because the equipment is easily replaced and with a low cost. This method obtains the cable tension force by using the relationship between cable tension force and natural frequency of the cable. However, this method can only identify the average cable tension over a time period, while the time-varying cable tension force in real time is needed for fatigue damage assessment. Li et al (2014) proposed a time-variant cable tension force identification method by using the extended Kalman filter (EKF) and the observed acceleration of the cable. The time variant cable tension force is regarded as a

state variable of the cable dynamic system, and can be identified by using the EKF. The identified accuracy and robustness of the proposed method is validated through numerical study and a small-scale test. The results are shown in Fig. 9. Furthermore, Yang *et al*. (2015) proposed a data-driven identification algorithm for time varying cable tension force using blind source separation.

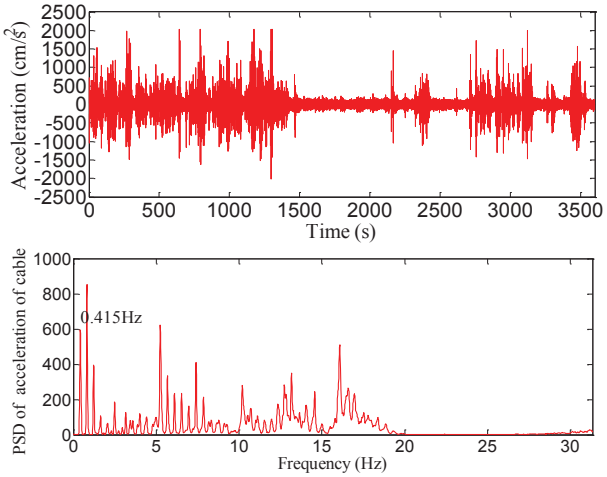

(a) Monitored acceleration with large amplitude and the frequency response

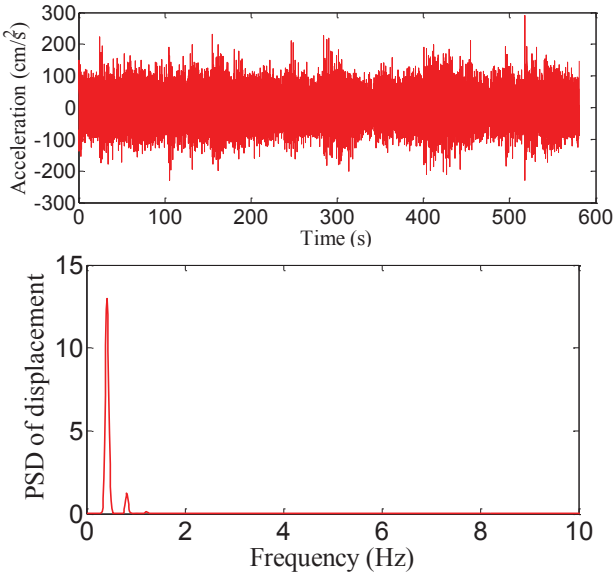

(b)Monitored acceleration with small amplitude and frequency response

Fig. 7 Monitored acceleration of a hanger with different vibration patterns

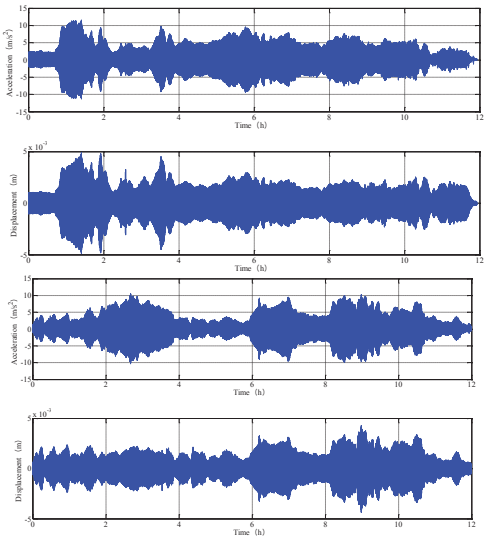

Fig. 8 Vortex-induced vibration of a stay-cable in a cable-stayed bridge

(a) under single vehicle with and without noise

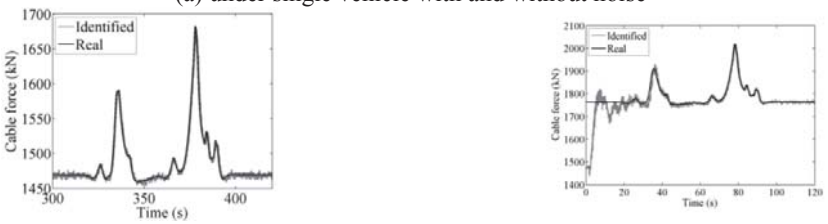

(b) under multiple-vehicles with noise and initial errors

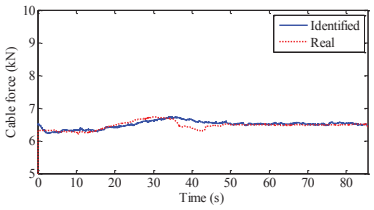

(c) test result

Fig. 9 Time-variant cable tension identification method using EKF

(3) Fatigue damage assessment

Once the stress time history of the cable is obtained by the monitoring or identification results, the fatigue damage of the stay cable can be calculated by the rain flow method and the Miner fatigue model. Each wire can be modeled as a series of elements, while the whole parallel wire cable can be simulated as a parallel model. Li *et al.* (2012) analyze the fatigue life of cables and discussed the failure criteria of the cable by using the approach proposed by Faber *et al*. (2003). Li *et al.* (2009) assess the fatigue damage for stay cables in a cable-stayed bridge in Tianjin, China, based on the monitored stress of self-sensing smart cables. The results are shown in Fig. 10. It can be seen from Figs. 10(a) and 10(b) that the vehicular effect on the short cables is larger than that on the long cables; moreover, the cable force is almost independent of the temperature. It can be concluded from Fig. 10(c) that the fatigue damage is very slight, which is inconsistent with the observations on actual bridges.

(4) Corrosion effects on fatigue damage of steel wires and stay cables

Li *et al*. (2012) investigate the fatigue life of corroded steel wires and stay cables that have been in use for 18 years in a coastal city and replaced during the repair of the bridge. The test results indicate that pitting corrosion dramatically shortens the fatigue life of the steel wires in stay cable and makes the fatigue life more random, as shown in Fig. 11. Pitting corrosion supplies the initial defects in the cable, which accelerate the fatigue damage process.

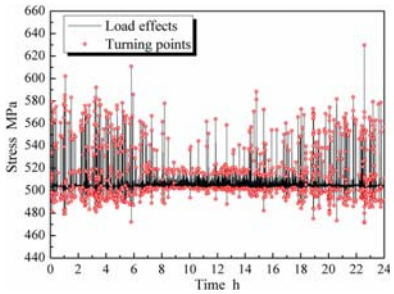

(a) Stress in stay cable C1 (short cable)

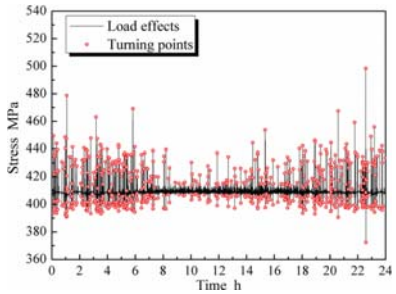

(b) Stress in stay cable C10 (long cable)

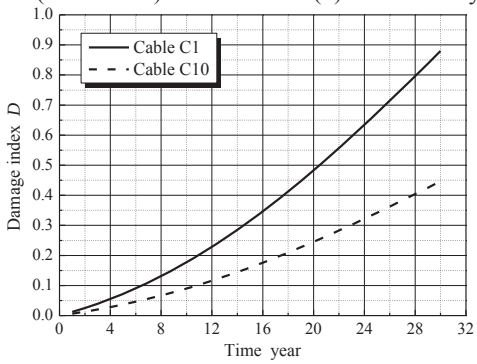

(c) Fatigue damage of C1 and C10

Fig. 10 Fatigue damage assessment for stay cables

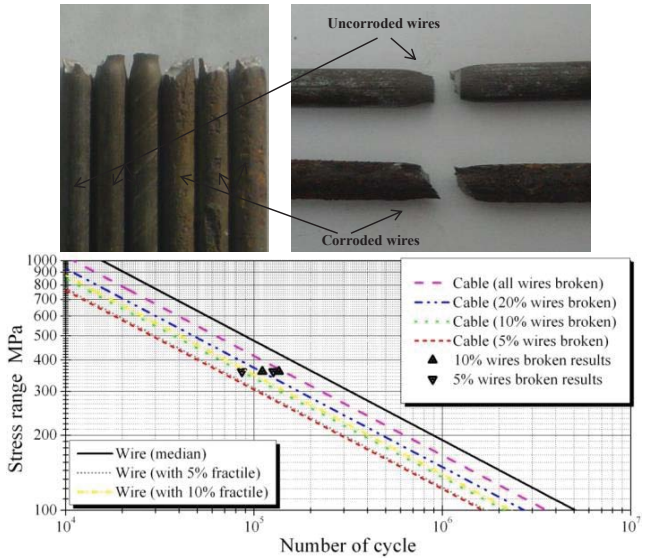

Fig. 11 Fatigue failure of individual steel wires and fatigue life of cables with corrosion

4. Brieft introduction to the design code of SHM systems for large highway bridges authorized by the Ministry of Transportation of China

The Ministry of Transportation of China has authorized a Design Code of SHM Systems for Large Highway Bridges to be issued in June, 2015. The design code includes the sensors, as well as the data acquisition, data analysis, alarms, and safety evaluation. The design code contains 8 chapters, listed in Table 2 as follows

Table 2 Content list of the design code of SHM systems for large highway bridges

Chapter 1	General requirement
Chapter 2	Terminology and symbols
Chapter 3	General Technical Specifications for SHM System
Chapter 4	Monitored Variables and Sensor Locations Selection
Chapter 5	Sensors
Chapter 6	Data Acquisition, Transmission and Management
Chapter 7	Data Analysis, Structural Safety Evaluation and Alarm
Chapter 8	Integrated SHM Systems and Software Packages

4.1 Mandatory regulations in bridges implemented with SHM systems

Bridges must be equipped with SHM systems if they have at least one of the following features: RC beam bridges with a span ≥ 150 m; arches with a span ≥ 200 m; cable-stayed with a span ≥ 300 m; suspension with a span ≥ 500 m; and other complex and important bridges.

4.2 Variables to be monitored and sensor locations

The monitored variables are categorized into three groups, i.e., loading and environmental variables, global response (vibration acceleration and deformation) and local response of a structure.

Loading and environmental variables include vehicle weight, wind velocity, earthquake ground motion and harsh environmental conditions (temperature, humidity, chloride, etc.).

Global responses of bridges include acceleration and displacement of structures.

Local responses of structures include strain, crack, fatigue, scour, corrosion, broken of structural members, displacement and reactions at bearings, supports and joints.

The locations of sensors for load and environmental monitoring should be determined by practical experience.

For global structural response, accelerometer locations can be determined by optimization methods; and displacement transducers locations can be determined by structural analysis.

The locations of sensors for local structural responses are determined based on structural and vulnerability analysis, e.g., the points of elements or cross section of highest stresses and importance, whose failure would cause structural failure.

4.3 Regulations of sensors

Because the sensor life-span is much shorter than that of the bridge, the sensors must be durable, maintainable and replaceable. The sensors in SHM systems for large bridges are divided into two types, inside the structure and on the surface of the structure. The durability of embedded sensors should not be shorter than 20 years. The life-span of sensors attached to the surface of a structure should be longer than 3-5 years and they should be maintainable and replaceable.

4.4 Regulation of data acquisition

Data should be collected in the following categories: data collected only above a pre-set threshold; data collected at a fixed time, e.g., every 4 or 6 hours; and event-driven data collection, e.g., the event of a vessel collision with a bridge pier. Data explosion and data management confusion should be avoided.

4.5 Alarm, data analysis and structural safety evaluation

An alarm can be given based directly on the data. Data analysis should be conducted and a report should be automatically generated and sent to the manager.

The structural safety evaluation is divided into three levels as follows:

Level 1 is performed based on the monitored data analysis and the comparison between monitored values and designed ones.

Level 2 can be performed following an extreme event or an accident, e.g., earthquake, typhoon, overload, vessel collision, etc. For instance, the amplitude, duration, dominant frequency, response spectrum of acceleration of ground motion, the structural response amplitude and residual deformation, the natural frequency and damping ratio are analyzed. If the amplitude of the earthquake ground motion is larger than the design value, or the structural response excesses the design value or material strength, or residual deformation is observed, the frequency decreases or damping ratio increases to compare with the healthy status, the structural safety should be conducted as specified in level 3.

Level 3 includes model-based ultimate state and fatigue evaluation. The structural model should be updated based on the monitoring of global response and local response, e.g., the element can be updated based on crack monitoring; the resistance of a bridge is then obtained based on the updated model; the monitored loads and environmental actions or the design loads and environmental actions are applied on the updated model and increase step by step up to collapse of the bridges. The maximum loads and environmental actions are in terms of ultimate loads and environmental actions. The ratio of the ultimate loads and environmental actions with respect to the monitored loads and environmental actions are the safety level. The evaluation criteria have been suggested in the design code based on level 3 results.

4.6 Integrated SHM systems and software packages

The SHM systems should integrate all software packages and hardware. The software includes a platform for the entire system operation, data acquisition software, data transmission protocol, database, data processing and analysis, automatic safety evaluation, and result visualization.

5. Future trends and challenges

SHM technology has been researched and developed extensively for three decades. The goals, the benefits and the gap between the goals and current technologies of SHM technology should be recognized.

The WiFi-based wireless sensor technology and mobile wireless sensor technology (Bao *et al*. 2012, Bao *et al*. 2013) may be a future trend.

The most challenge are obtaining exact models of damaged structures (the damage may be caused by a disaster or long-term performance deterioration), exact loads and environmental actions, and safety evaluation and service lifetime prediction. The possible solution for exact structural models may be combining the monitoring and inspection information, by structural analysis and damage detection, modeling of damaged bridges and model updating techniques. Based on the exact structural model, the performance deterioration of structural even element resistance can be obtained. The exact loads and environmental actions may be obtained by more monitoring devices and identification algorithms. Based on the updated damaged structure model and the exact loads and environmental actions, the safety evaluation and lifetime prediction can be well performed, which is the main goal of structural health monitoring.

SHM is an *in-situ* field test technology covering various research topics in multiple disciplines, as shown in Fig. 12. It can serve for structural engineering, wind engineering, earthquake engineering, and so on, as shown in Fig. 13. In-situ field tests become the 4th important structural research tool, along with analytical methods, numerical simulations, and small scale model tests,

as shown in Fig. 14. SHM acts as an engine promoting the development of engineering as a discipline.

Big data technology not only provides a powerful tool for research of structural health monitoring, but also may provide an opportunity to find new phenomena and develop new research areas based on structural health monitoring. Cloud technology will help us to more efficiently and conveniently manage and utilize data.

The further development of SHM technology may be a precursor towards to a smart society, including the sensing of every variable everywhere, powerful signal processing capability, automatic signal transmission, convenient mobile receivers everywhere, and remote control. This trend will raise many challenges.

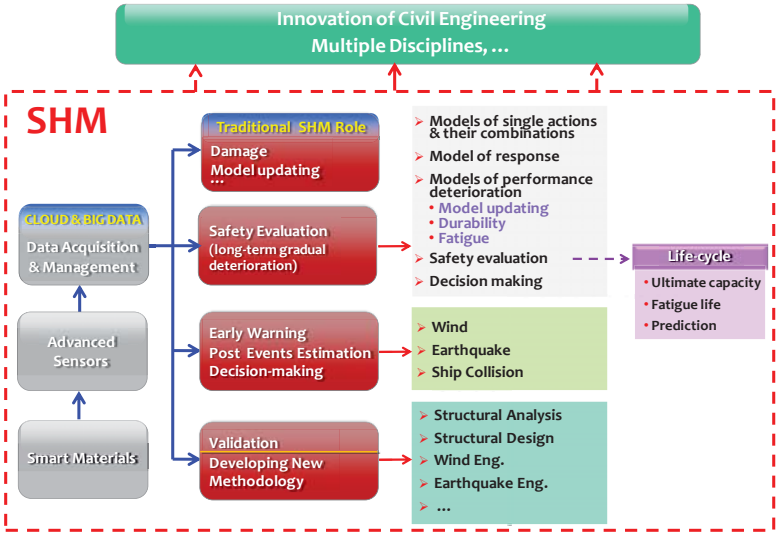

Fig. 12 Research issues for SHM technology

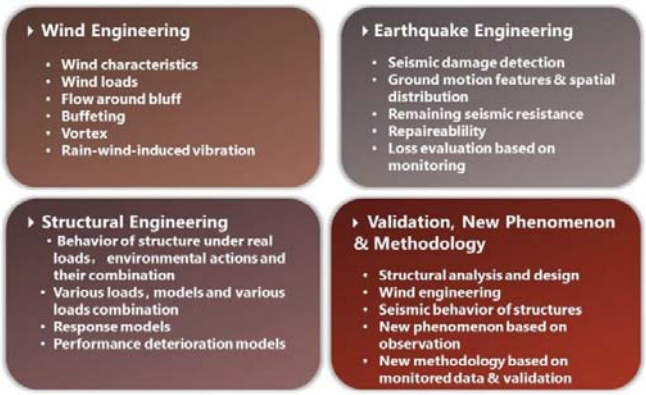

Fig. 13 The future trends of SHM technique in structural engineering

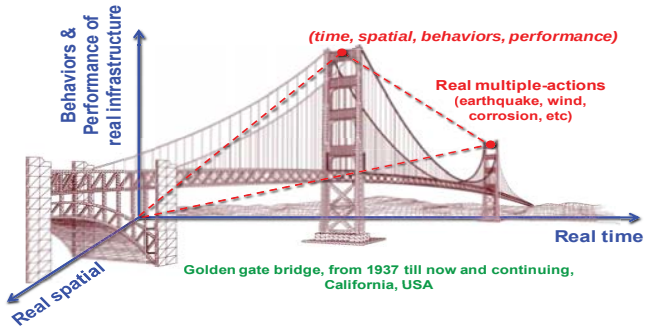

(a) The positive role of SHM technique in structural engineering

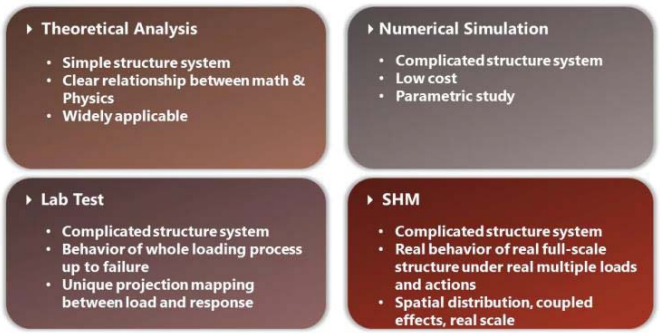

(b) Four scientific research tools

Fig. 14 Positive roles of four research tools as the main engine driving development of engineering disciplinary

Acknowledgments

The authors gratefully acknowledge the financial support provided by the Natural Science Foundation of China (Project No:51161120359, 9121530), the Ministry of Science and Technology (Project No. 2011BAK02B01 and 2011BAK02B02), the National Basic Research Program of China (Project No. 2013CB036305) and the Sino-US collaboration project (No. S2015GR1198).

References

Ansari, F. (2008), "Practical implementation of optical fiber sensors in civil structural health monitoring", *J. Intel. Mat. Syst. Str.*, **19**(10), 1163-1172.

Bao, X., Webb, D.J. and Jackson, D.A. (1993), "32-km distributed temperature sensor based on Brillouin loss in an optical fiber", *Opt. Lett.*, **18**(18), 1561-1563.

Bao, Y., Beck, J.L. and Li, H. (2011), "Compressive sampling for accelerometer signals in structural health

monitoring", *Struct. Health Monit.*, **10**(3), 235-246.
Bao, Y., Li, H., An, Y. and Ou, J. (2012), "Dempster-Shafer evidence theory approach to structural damage detection", *Struct. Health Monit.*, **11**(1), 13-26.
Bao, Y., Wu, F., Zhu, X., Zhang, X. and Li, H. (2012), "A mobile wireless sensor-based structural health monitoring technique", Workshop on Civil Structural Health Monitoring (CSHM-4), Berlin, Germany.
Bao, Y., Li, H., Sun, X., Yan, Y. and Ou, J.P. (2013), "Compressive sampling–based data loss recovery for wireless sensor networks used in civil structural health monitoring", *Struct. Health Monit.*, **12**(1), 78-95.
Bao, Y., Li, H., Zhang, F. and Ou, J. (2013), "Compressive sampling based approach for identification of moving loads distribution on cable-stayed bridges", *Proceedings of the SPIE Smart Structures/NDE*, 11-15 March, San Diego, California USA.
Chen, W.L., Li, H., Ou, J.P and Li, F.C. (2013), "Numerical simulation of vortex-induced vibrations of inclined cables under different wind profiles", *J. Bridge Eng. - ASCE*, **18**(1), 42-53.
Chen, Z.C., Li, H. and Bao, Y. (2014), "Computer vision based approach for identification of moving loads distribution on long-span bridges", *Proceedings of the 5th Asia-Pacific Workshop on Structural Health Monitoring*, Shenzhen, China, December 4-5, 2014 (CD-ROM).
Doebling, S.W., Farrar, C.R., Prime, M.B. and Shevitz, D.W. (1996), *Damage identification and health monitoring of structural and mechanical systems from changes in their vibration characteristics: A literature review*, LA--13070-MS, Los Alamos National Laboratory, New Mexico, USA.
Dong, Y.K., Ba, D.X., Jiang, T.F., Zhou, D.W., Zhang, H.Y., Zhu, C.Y., Lu, Z.W, Li, H., Chen, L. and Bao, X.Y. (2013), "High-spatial-resolution fast BOTDA for dynamic strain measurement based on differential double-pulse and second-order sideband of Modulation", *IEEE Photonics J.*, **5**(3), 2600407.
Faber, M.H., Engelund, S. and Rachwits, R. (2003), "Aspects of parallel wire cable reliability", *Struct. Saf.*, **25**(2), 201-225.
Gu, Y.M., Li, S.L, Li, H. and Guo, Z.M. (2014), "A novel Bayesian extreme value distribution model of vehicle loads incorporating de-correlated tail fitting: Theory and application to the Nanjing 3rd Yangtze River Bridge", *Eng. Struct.*, **59**, 386-392.
Ko, J.M., Ni, Y.Q., Zhou, H.F. *et al*. (2009), "Investigation concerning structural health monitoring of an instrumented cable-stayed bridge", *Struct. Infrastruct. E.*, **5**(6), 497-513.
Koh, H.M., Lee, H.S., Kim, S.K. and Choo, J.F. (2009), Monitoring of bridges in Korea, Chapter 124 in Encyclopedia of Structural Health Monitoring, (Eds., C. Boller, F.K. Chang and Y. Fujino), John Wiley & Sons, Ltd.
Laima, S.J., Li, H., Chen, W.L and Li, F.C. (2013), "Investigation and control of vortex-induced vibration of twin box girders", *J. Fluid. Struct.*, **39**, 205-221.
Lan, C.M., Li, H. and Ou, J.P. (2011), "Traffic load modeling based on structural health monitoring data", *Struct. Infrastruct. E.*, **7**(5), 379-386.
Li, H., Bao, Y. and Ou, J. (2008), "Structural damage identification based on integration of information fusion and Shannon entropy", *Mech. Syst. Signal Pr.*, **22**, 1427-1440.
Li, H., Laima, S.J., Zhang, Q.Q., Li, N. and Liu, Z.Q. (2014), "Field monitoring and validation of vortex-induced vibrations of a long-span suspension bridge", *J. Wind Eng. Ind. Aerod.*, **124**, 54-67.
Li, H., Ou, J.P. and Zhou, Z. (2009). "Application of optical fibre Bragg gatings sensing technology-based smart stay cables", *Opt. Laser. Eng.*, **47**(10), 1077-1084.
Li, H., Huang, Y., Ou, J. and Bao, Y. (2011), "Fractal dimension-based damage detection method for beams with a uniform cross-section", *Comput. -.Aided Civil Infrastruct. Eng.*, **26**(3), 190-206.
Li, H., Laima, S.J., Ou, J., Zhao, X.F., Zhou, W.S., Yu, Y., Li, N. and Liu, Z.Q. (2011), "Investigation of vortex-induced vibration of a suspension bridge with two separated steelbox girders based on field measurements", *Eng. Struct.*, **33**(6),1894-1907.
Li, H., Lan, C.M., Ju, Y. and Li, D.S. (2012), "Experimental and numerical study of the fatigue properties of corroded parallel wire cables", *J. Bridge Eng. - ASCE*, **17**(2), 211-220.
Li, H., Zhang, F.J. and Jin, Y.Z. (2014), "Real-time identification of the time-varying tension of stay cables with monitored cable transversal acceleration", *Struct. Control Health Monit.*, **21**(7), 1100-1117.
Lynch, J. and Loh, K.J. (2005), "A summary review of wireless sensors and sensor networks for

structuralhealth monitoring", *Shock Vib. Digest*, **38**(2), 91-128.
Ou, J.P. and Li, H. (2010), "Structural health monitoring in mainland China: review and future trends", *Struct. Health Monit*., **9**(3), 219-231.
Sohn, H., Farrar, C.R., Hemez, F.M., Shunk, D.D., Stinemates, D.W. and Nadler, B.R. (2003), *A review of structural health monitoring literature: 1996-2001*, Laboratory Report, LA-13976-MS, Los Alamos National Laboratory, New Mexico, USA.
Spencer Jr., B.F., Ruiz-Sandoval, M. and Kurata, N. (2004), "Smart sensing technology: opportunities and challenges", *Struct. Control Health Monit.*, **11**, 349-368.
Yang. Y.C., Li, S.L., Nagarajaiah, S., Li, H. and Zhou, P. (2015), "Real-time output-only identification of time-varying cable tension via complexity pursuit", *J. Struct. Eng. – ASCE*, (accepted).
Yu, Y., Ou, J., Zhang, J, Zhang, C. and Li, L. (2009), "Development of wireless MEMS inclination sensor system for swing monitoring of large scale hook structures", IEEE *T. Ind. Electron*., **56**(4), 1072-1078.
Zhang, F.J. (2013), *Identification and modeling approaches of tension in stay cables and vehicles on cable-stayed bridges*, Ph.D. Thesis of Harbin Institute of Technology.
Zhou, Z. and Ou, J. (2009), "R&D of optical fiber based sensors and their applications", *Proceedings of the SEM 2009 Annual Conference*, Albuquerque, New Mexico, June 1 - 4, 2009, USA.

Smart Structures and Systems, *Vol. 15, No. 3 (2015) 577-592*
DOI: http://dx.doi.org/10.12989/sss.2015.15.3.577

Can we substitute the intuition of an experienced bridge inspector by monitoring?

Helmut Wenzel*[1], Hiroshi Tanaka[2a], Michaela Höllrigl-Binder[1] and Helga Allmer[1]

[1]*VCE Vienna Consulting Engineers ZT GmbH, Hadikgasse 60, 1140 Vienna, Austria*
[2]*University of Ottawa, 161, Louis Pasteur St., A115, Ottawa, Ontario, K1N 6N5, Canada*

(Received November 27, 2014, Revised January 18, 2015, Accepted January 20, 2015)

Abstract. Damage quantification is a major goal of the SHM community. Methodologies to introduce a quantity for actual condition of a structure into the assessment process are desired. The idea that the condition of a structure is represented in the character of its dynamic response is fully accepted by the SHM community. The VCLIFE methodology quantifies condition analyzing input from monitoring.

Keywords: SHM; Monitoring

1. Introduction

Experienced bridge inspectors are able to express a first condition assessment shortly after having visited a bridge which normally proves to be rather reliable. What we call intuition might be experience-driven human sensing of bridge performance. The human body is sensitive to vibration and classifies the excitation it is exposed to. On the other hand, we as humans, change our behavior when we feel pain indicating damage. The same happens to bridge structures. In case of damage the load paths modify. This is reflected in the response of the structures to ambient and forced vibrations. Model based observer monitoring concepts use this approach and actually measure what human intuition tells us. The approach and technology described below provide background information as well as examples of successful application.

Dedication to Yozo Fujino

I met Yozo Fujino more than 20 years ago at an IABSE event and was impressed by his knowledge of and approach to bridge assessment. He is one of those experienced engineers who are called when complicated and high profile cases arise. Since that first encounter we have discussed the subject of bridge assessment many times and both worked in damage detection. I am delighted to dedicate some of our later results, developed in the IRIS project, to Yozo Fujino and his achievements.

*Corresponding author, Professor, E-mail: wenzel@vce.at
[a] Ph.D.

http://www.techno-press.org/?journal=sss&subpage=8 ISSN: 1738-1584 (Print), 1738-1991 (Online)

2. Structural non-linearity and energy transfer

The concept described in this chapter has been developed within the large European research project IRIS and comprises only a portion of the methodology. The complete work is documented in (Wenze 2013) and available for download under www.vce.at/iris .

The findings described herein have been discussed within our research group including myself (concept and approach), Hiroshi Tanaka (fluid dynamics), Helga Allmer (physics and mechanics) and Michaela Höllrigl-Binder (mathematics). We were looking into the subject from the point of view of energy transfer in a changing system over time. Our approach was tested in many cases by destructive testing and published it in journals and conferences. We are glad to report that the idea has been taken up by many research groups and is frequently quoted in respective publications.

Cascading energy transfer in a dynamical system could be caused by the development of nonlinear characteristics of the structural response caused by various reasons.

Suppose a nonlinear mechanism develops in both the damping and stiffness of a structure, whose dynamic behavior is modeled by a Single Degree of Freedom (SDOF), as a result of progressive structural damage. Fig. 1 illustrates the progress of such damage.

It can be typically represented by the equation of motion by modifying both the damping and stiffness terms as follows

$$m\ddot{z} + c\left[1 + \varepsilon_2(z)\right]\dot{z} + k\left[1 - \varepsilon_1(z)\right]z = 0 \tag{1}$$

where ε_1 and ε_2 are the linear or nonlinear correction terms introduced corresponding to the development of structural damage and $z(t)$ represents the dynamic response of the structure in general. Note that it is unlikely to have any change in the inertia term. Eq. (1) can be rewritten as

$$m\ddot{z} + c\dot{z} + kz = k\varepsilon_1(z)z - c\varepsilon_2(z)\dot{z} = F(z,\dot{z}) \tag{2}$$

where $F(z,\dot{z})$ is generally a nonlinear function of z and/or $\dot{z}$, such as

$$F(z,\dot{z}) = C_1 z^2 + C_2 \dot{z}^3 \tag{3}$$

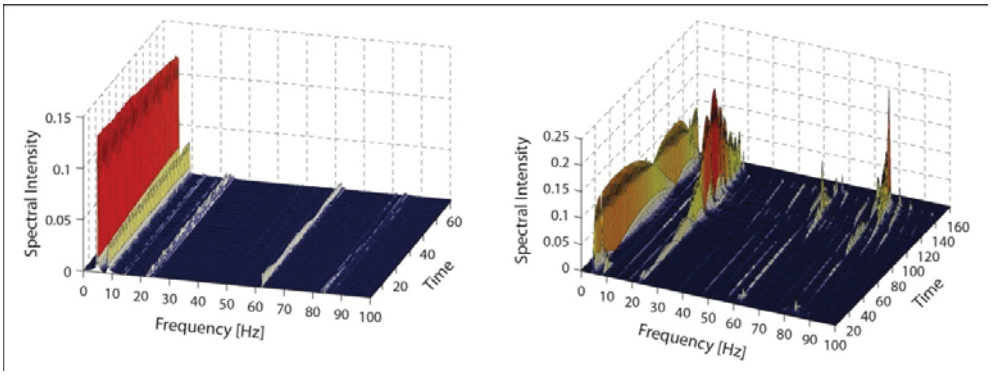

Fig. 1 Spectral development over time for a sound structure (left) and during a damage test at MPA Stuttgart (right)

Eq. (3) implies that if z is modeled as a vibration with frequency ω, then $F(z,\dot{z})$ is generally a function of fluctuations with the frequencies expressed by the multiples of ω. For example, substitution of $z = A\sin\omega t$ in Eq. (3) obtains Eq. (4).

$$F(z,\dot{z}) = \frac{C_1 A^2}{2}\left(1-\cos 2\omega t\right) + \frac{C_2 A^3 \omega^3}{4}\left(3\cos\omega t + \cos 3\omega t\right) \tag{4}$$

This in turn will result in a dynamic response represented by functions of twice, thrice higher frequencies than the original ones for this case. The same process will be repeated as time allows and, as a result, a part of the system's dynamic energy will be gradually distributed to an increasingly higher frequency range.

Where would this process end? For the case of damage-caused nonlinearity, the high frequency energy components dissipate as heat or noise and, if not, the destruction or rupture of the structure would play a role. Even if it does not reach the destruction point, the mechanism of structural response will change significantly when damage progresses that far.

3. The energy cascade in turbulence

Energy cascading, such as the one described in the preceding section, can be associated with various types of nonlinear physical phenomena. It is typically observed in dynamics of turbulent fluid flow. The process of energy cascading is one of the most central issues in the case of fully developed turbulence.

The English physicist L.F. Richardson (1881-1953) conceived of turbulence as an assembly of eddies of different sizes, where eddies could be hypothetically visualized as individual vortices of some measurable diameter. He had the idea that large eddies are prone to break into smaller eddies, which break up into even smaller eddies and so on as spelled out by the following famous parody:

"Big whirls have little whirls
That feed on their velocity,
And little whirls have lesser whirls
And so on to viscosity." - by L.F. Richardson (1922)-

In each break-up process, the larger eddy transfers its dynamic energy to the smaller ones without dissipating it, meaning that the energy transfer process in turbulence is inviscid. In such a process, the role of viscous forces is negligible in comparison to the inertia forces. However, energy has to be eventually dissipated somewhere, at much smaller wave lengths, or higher frequencies. This is a viscous process. Fluid viscosity has an important role only at those small scales.

This process can be modeled mathematically as follows: the Navier-Stokes equation is a non-linear equation because of an inherent non-linearity of fluid inertia as shown in Eq. (5)

$$\rho\left(\frac{\partial u_i}{\partial t} + u_j\frac{\partial u_i}{\partial x_j}\right) + \frac{\partial p}{\partial x_j} = \frac{\partial}{\partial x_j}\left(\mu\frac{\partial u_i}{\partial x_j}\right) \tag{5}$$

Out of the three terms involved in the equation, the pressure gradient can be ignored in the

present discussion. In the energy dissipation process described herein, the inertia term becomes less important in comparison to the viscous force in higher frequency range, and hence the whole equation becomes almost linear for this case, whereas at much larger length scales, or in the lower frequency range, the inertia term becomes predominant and hence the equation becomes highly non-linear. This is where cascading takes place. Note therefore that the non-linear characteristics of the equation, in particular of the inertia force for this case, are deeply associated with the energy cascading phenomena explained by Richardson.

4. Nonlinear damping

Relationship of energy cascading as a result of advancing nonlinearity in a dynamical system is therefore evident in two different phenomena. A very interesting aspect of this conclusion is that the detection of energy cascading could be potentially utilized as a tool for the structural health monitoring. The traditional idea of knowledge-based structural health monitoring focused on identifying the reduction of stiffness, which proved to be far less sensitive than desired for practical purposes. In contrast, by finding the transfer of dynamic energy to higher frequencies through spectral analysis of ambient vibrations, it may be possible to detect damage development in a structure at its earlier stages. Any extent of structural damage can of course change the local structural damping or energy dissipation and stiffness. As a consequence, the global dynamic properties of the structure, i.e., the eigenfrequencies, mode shapes and modal damping would be all somewhat influenced.

It must be kept in mind that structural nonlinearity is attributed, not only to developing damage. Field experience indicates that the magnitude of modal damping is often amplitude-dependent. Damping increases with amplitude due to energy consumption at friction bearings, bending action of piers, behavior of the bridge outfitting as well as the structure-vehicle interaction (Wenzel 2009).

Admittedly the present method would also detect the developing structural nonlinearity due to large motion. However, if there is a development of structural damage as its consequence, the nonlinear characteristics would be retained by the structure after the large amplitude motion disappeared and should be thus detected.

5. Data analysis

For identifying the energy cascading phenomena, the following data analysis can be applied.

5.1 Data preparation

Acceleration signals $a_i(t)$ are measured for a period of $t_i \le t \le t_i + T$, where $i = 1,2,...,n$, with the sampling frequency and measuring period of typically $f_S = 500\,\text{Hz}$ and $T = 5\,\text{min}$, respectively. n is the number of files.

5.2 Analysis

Calculation of the acceleration spectra $G_i(f)$ by a conventional FFT routine for the frequency range of $0 \le f \le f_M$ is required first. $f_M = f_S/2$ is the folding frequency. The *normalized spectral density functions* are then calculated as shown in Eq. (6).

$$F_i(f) = \frac{G_i(f)}{\sigma_i^2} \qquad \text{where } \sigma_i^2 = \sum_f G_i(f)\Delta f \tag{6}$$

Normalization of spectral density is justified since our interest is only in the change of energy distribution pattern and not in the actual magnitude of the spectral density, which depends on the total dynamic energy supplied by excitation and is always expected to change during the ambient vibration survey. It is also useful to calculate the fraction of dynamic energy corresponding to less than any particular frequency level f as shown in Eq. (7).

$$E_i(f) = \sum_{k=0}^{f} F_i(k)\Delta k \tag{7}$$

where $E_i(f)$ is the *spectral distribution function* which is expected to more clearly reveal the fraction of energy transferred to different frequency ranges, resulting in the change of its pattern.

5.3 Presentation

Visual presentation of $F_i(f)$ and $E_i(f)$ with respect to time (i) and frequency (f) would indicate the transfer of energy to higher frequencies by the change in spectral pattern, where $1 \le i \le n$ and $0 \le f \le 250$ Hz.

5.4 Reading of spectral patterns

When the distribution function $E_i(f)$ is examined, it should be noted that the energy cascading caused by structural nonlinearity discussed herein is only a partial transfer of energy through the free vibration process of the structure. As stated in Section 2 not all dynamic energy is transferable to high frequency range. Some of the energy should remain with the lower vibration modes.

Another important point is that during the vibration survey various dynamic excitations or disturbances from the external environment may act on the structure. As a result, new dynamic energy will be supplied to the system augmenting the energy fraction at corresponding frequencies. The characteristics of these excitations are often hard to identify. However, when there are any predominant excitation frequencies, there may be distinct spectral peaks observed at those particular frequencies. If the excitation resembles broad-band noise, a part of this energy will be absorbed at eigenfrequencies and corresponding spectral peaks will show up as additional spikes in the figures.

The change of pattern in $E_i(f)$ is, therefore, not expected to be monotonous. Hence, what needs to be observed is a general tendency of the energy shift, which, it is hoped, will be indicated by a gradual change of the colored pattern.

The shift of pattern can be quantified by locating the centroid of the area under the spectral

distribution $E_i(f)$ as shown in Eq. (8).

$$\bar{r} = \sum_f f E_i(f)\Delta f \Big/ \sum_f E_i(f)\Delta f \tag{8}$$

The shift of the centroid is unlikely to be monotonous. What should be observed is the general tendency of its change.

6. Example: Overpass S101, Reibersdorf (2008)

The following example is based on the measurement of dynamic bridge response carried out in December 2008 for the highway overpass S101 in Reibersdorf, Upper Austria. The structure was progressively damaged prior to its demolition, in order to observe the effects on the dynamic characteristics [1]. Sampling frequency of the acceleration record was 500 Hz.

Figs. 2 and 3 depict the progressive change of the normalized acceleration spectrum $F_i(f)$ and the distributed spectrum $E_i(f)$ for the frequency range of $0 \le f \le 25$ Hz from the measured results. There were a number of physical operations applied to the bridge during three days of measurement. Some of them are specified next to the figures. Some of these operations can be clearly identified from the patterns of the functions $F_i(f)$ and $E_i(f)$. When the concrete pier or slab is being cut, presumably the severing operation produced large extent of high frequency noise and, consequently, a large fraction of the total dynamic energy appears in a much higher frequency range as a substantial spike in $E_i(f)$. In the afternoon of the third day, for example, there was "a vibrating roller working next to the bridge, causing clearly noticeable vibrations on the bridge", according to the measurement report. This noise may be also contributing to the above mentioned spikes.

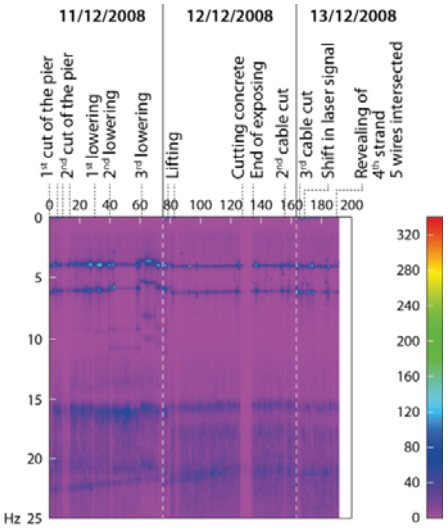

Fig. 2 Normalized acceleration spectra $F_i(f)$

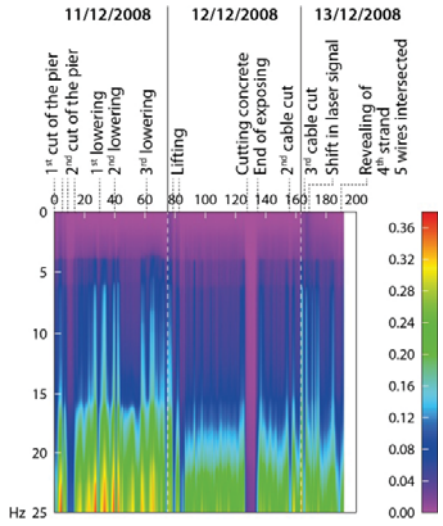

Fig. 3 Spectral distribution functions $E_i(f)$

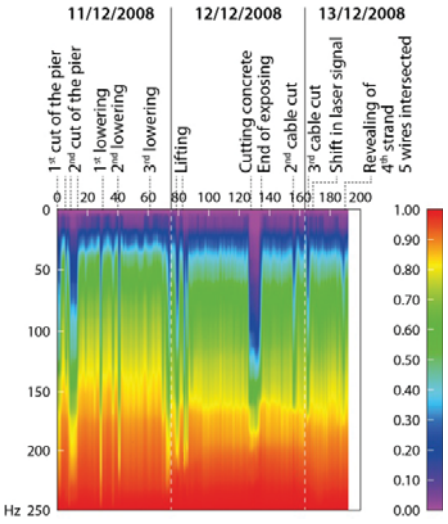

Fig. 4 Spectral distribution functions $E_i(f)$

It is clear by observing the $E_i(f)$ pattern that, with the progressive damage artificially induced in the bridge, an increasing fraction of dynamic energy was redistributed to the higher frequency range, as indicated by the shift of dark blue and yellow band towards right, meaning the higher percentage fraction is in the high frequency side of the figure. Fig. 4 is the same $E_i(f)$ function shown for much wider frequency range up to 250 Hz. It is clear that an almost stepwise energy shift took place after the lifting of the damaged pier in the beginning of the second day.

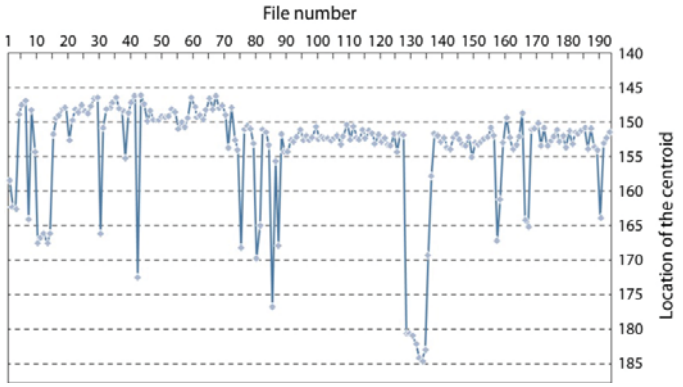

Fig. 5 Normalized acceleration spectra $F_i(f)$

The same tendency is demonstrated even more clearly by calculating the shift of the centroid $\bar{r}$ of the area under $E_i(f)$ as shown in Fig. 5. By disregarding the spikes due to various kinds of noise, the general trend is clearly one of shifting towards a higher frequency range with time.

6.1 Further discussion on the test results

Fig. 6 shows some changes in the 1st and 2nd eigenfrequencies during these three days, most likely caused by the change in bridge's physical conditions. What is shown as "Amplitude" indicates the ordinate of the normalized spectra at this particular frequency, namely the modal intensity of the dynamic energy. Artificial damage of the bridge pier was applied on the North-West column of the bridge and the measurements B and C were taken at the mid-span of the bridge on West and East side, respectively.

It is evident that there were two steps of frequency reduction, though the second one is less clear, corresponding to the cutting of the pier on the first day. This was the first damage induced in the bridge. Immediately following the second cut, the structure recovered its first mode frequency but not the second mode. Note that the column was still maintained at its original elevation by jacking. The measurement report (Wenzel *et al.* 2009) states that "no restoring forces observed" for the same period. A most conspicuous loss of stiffness, both in the first and second modes, took place during the lowering of the pier. During that period it was observed that a part of the dynamic energy started being clearly transferred to the higher frequency range. This corresponds to the reported development of cracks in the structure due to its settlement. The recovery of both frequencies on the second day corresponds to re-lifting of the column and the insertion of steel plates under it. Substantial transfer of energy is observed compared to the previous day. The plot of the modal energy (shown as "Amplitude"), also shows that only a small fraction of energy remains associated with the first and the second modes through this period. The gradual reduction of both frequencies through the day may have been caused by the change of ambient temperature or a gradual settling of the structure. The further cascading process seems to be associated with the cutting of concrete slab and steel tendons. It is interesting to observe that no change of the first and second eigenfrequencies was observed during this operation.

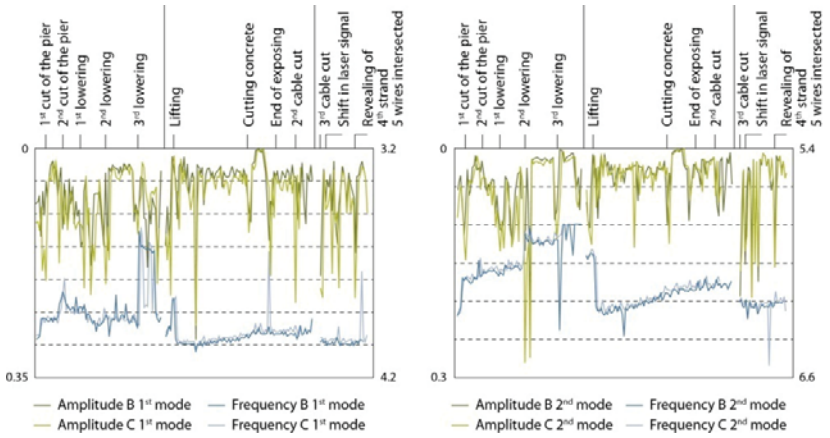

Fig. 6 Change of the 1st (left) and 2nd (right) frequency

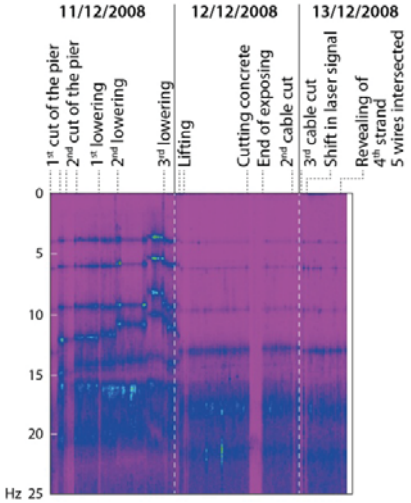

Fig. 7 Normalized acceleration spectra Fi(f) on the pier

The third tendon was severed on the third day and apparent re-settling of the structure was stated in the measurement report. Further transfer of dynamic energy is obvious in Fig. 3, though again this operation had no visible effects on lower eigenfrequencies.

Another set of spectral presentations, Figs. 8-10, results from the acceleration record obtained directly above the damaged pier. The general tendency of the reduction of eigenfrequencies and energy transfer towards high frequency range, is the same as seen in the preceding results, but it can be observed even more clearly with this set of data. What is clearly different from the other sets of data are the conspicuous spectral peaks in the frequency range of $8 \leq f \leq 13$ Hz. Explanation of these peaks is not immediately provided.

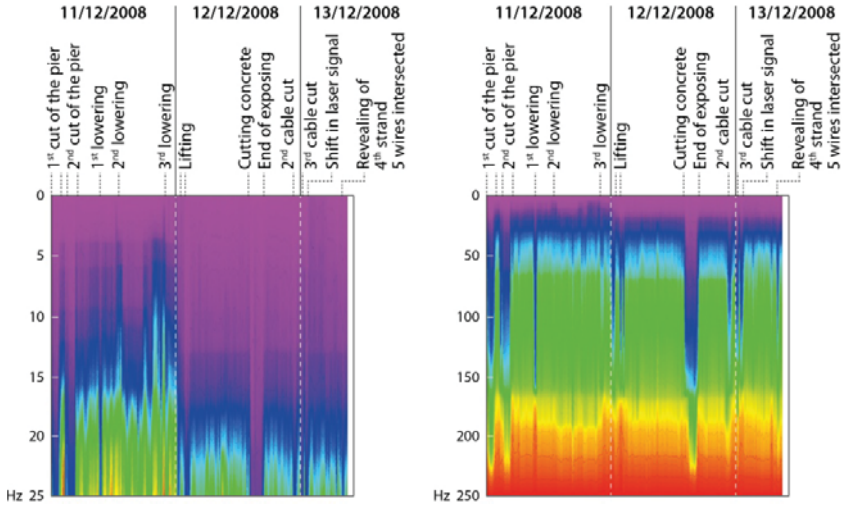

Fig. 8 Spectral distribution functions $E_i(f)$ on the pier

7. Other sample cases

The proposed spectral analysis method for damage identification seems to be successful at least in the case of the S101 overpass. Admittedly, however, the case was rather ideal. The scheduled damage was successively applied to the structure and the measurement was carried out in a controlled environment, without disturbances, such as on-going traffic. Nevertheless, after the encouragement of this initial success, the method has been further tried out on other bridges. A brief summary of sample cases follows.

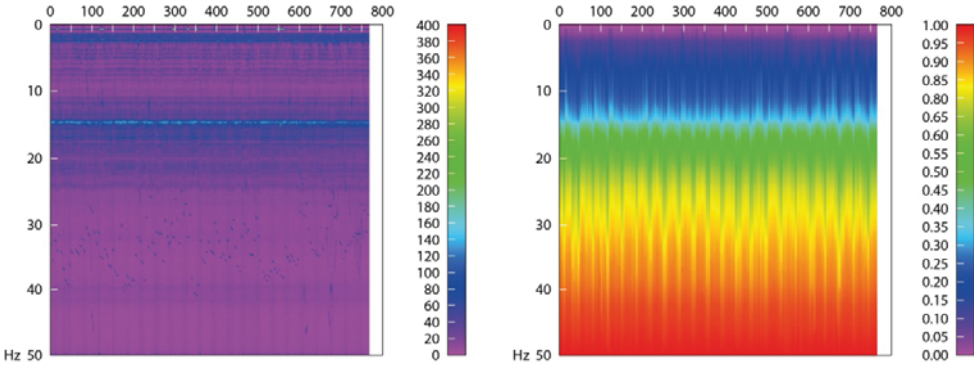

Fig. 9 Europabrücke: based on midday records

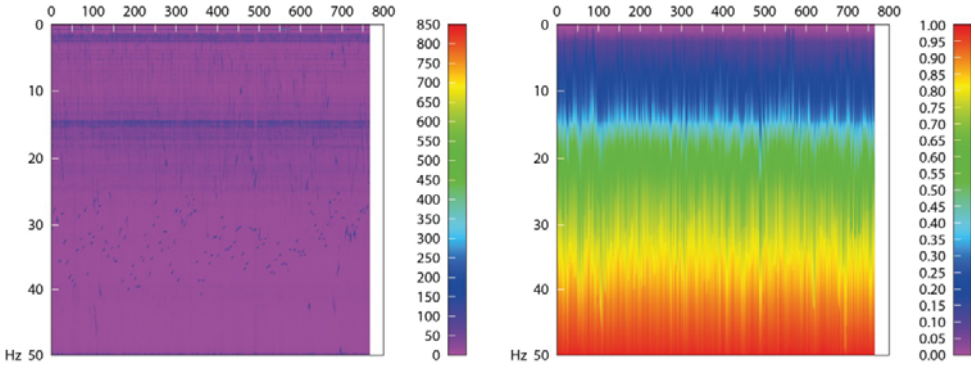

Fig. 10 Europabrücke: based on midnight records

7.1 Europabrücke (2005)

The Europabrücke, opened in 1963, is one of the main alpine north-south routes for urban and freight traffic. It currently carries over 30000 motor vehicles per day. The superstructure is a steel box girder of variable height along the span with an orthotropic deck. The bridge is 657 m long and consists of six spans of different length, carrying six lanes, three in each direction, with a total width of 25 m. In order to assess the prevailing vibration intensities with regard to possible fatigue damage, a permanent measuring system has been installed since 2003. Extensive records of vibration measurement exist. Figs. 9 and 10 represent the analyzed results of the records from May to October 2005, at middays and midnights, respectively. They show a basically healthy, stable condition of the structure, with no indication of serious structural non-linearity.

The statistical evaluation of the data reveals a significant change of the pattern for 80% of the energy after the 4th week of observation, but the whole plot shows a fluctuation that might be due to different traffic. Fig. 11 shows the boxplots of midday and midnight results.

It must be kept in mind, however, that the existence of structural non-linearity, in stiffness and/or damping, is not necessarily 100% equivalent to a state of structural damage. There may be a case where micro-cracks are developing, for example, but the overall structural behavior does not show any sign of nonlinearity.

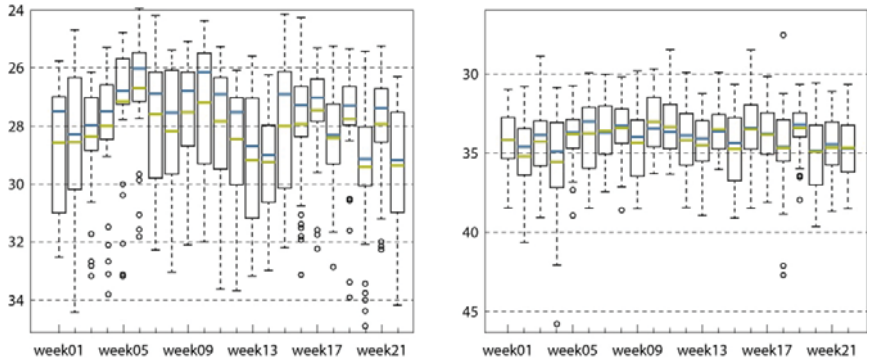

Fig. 11 Europabrücke: midday (left) and midnight (right) – boxplot of 80% of energy

7.2 Melk B3A (2000–2009)

This is an example of a structure deteriorating over a period of nine years. Disregarding some irregularities, the gradual change of the spectral pattern (Fig. 12) clearly indicates that more and more dynamic energy is transferred towards higher frequency ranges.

In looking at the change in spectral patterns, it is important to compare the cases of the same structure under similar physical conditions. For example, all measurements of this particular bridge were carried out under its service conditions, namely under traffic loads. Since traffic loads tend to enhance the bridge vibration in a certain limited range of frequency, the resulted spectral pattern is different from that obtained under more random ambient excitations such as micro-tremors or wind. Under such conditions, the spectra tend to shift towards a lower frequency range compared to conditions without traffic. In order to avoid this effect, an effort was made to extract some data obtained when the bridge was freely vibrating without traffic loads. The resulting spectral pattern without traffic excitation is shown in Fig. 13.

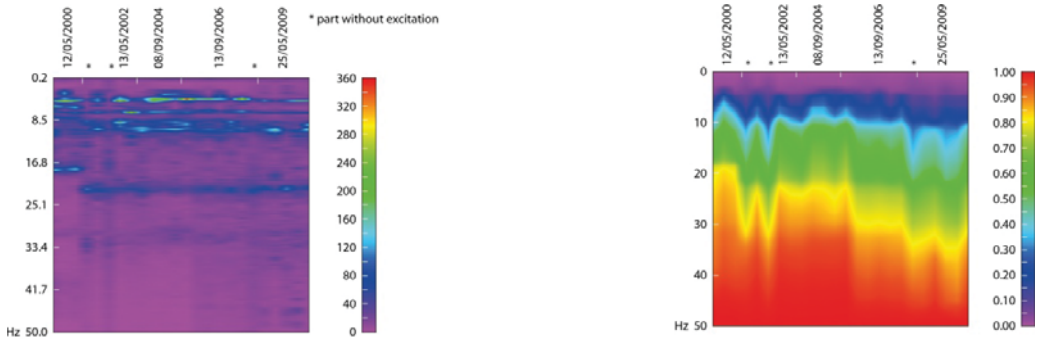

Fig. 12 Melk B3A

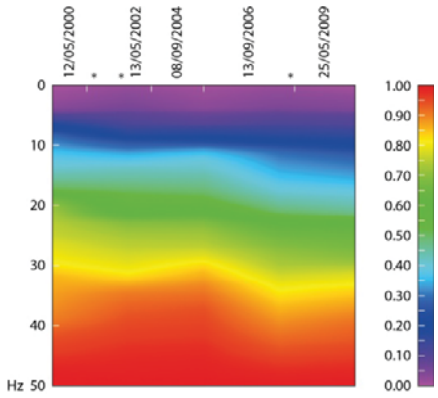

Fig. 13 Melk B3A: without traffic

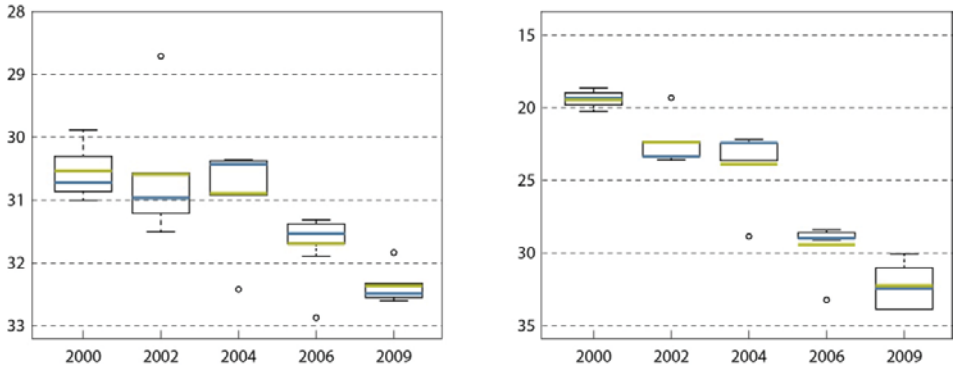

Fig. 14 Melk B3A: boxplot of the centroid (left) and boxplot of 80% of the energy (right)

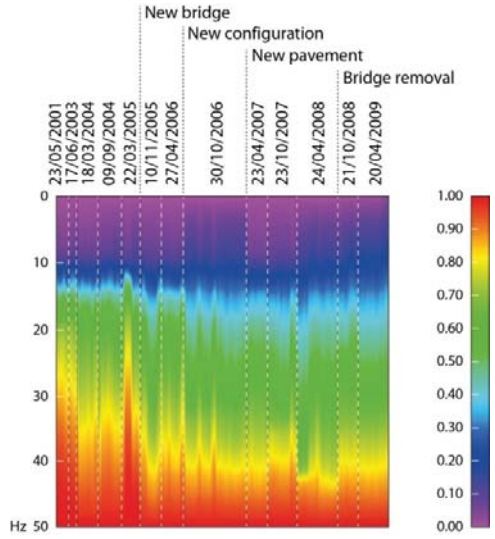

Fig. 15 Flughafen

Concerning the statistical evaluation of this bridge, it depends on which value is used. For this bridge the results of the location of the centroid of the energy distribution and the value of 80% of energy are presented to show that there can be a difference: significant changes for this structure can be observed with the analysis of variance (ANOVA) for the location of the centroid from the 5th observation period (that is the year 2006) and for the value for 80% of energy from the 4th observation period (that is the year 2004). Fig. 14 shows the boxplots of these results.

7.3 Flughafen Vorfahrt (2004–2009)

The access bridge in front of the terminal 2 of the Vienna International Airport was opened in 1956 and widened to 10.5 m in 1968. Measurements of the dynamic characteristics took place after a concern was expressed regarding its load carrying capacity. Available data are from eleven different groups of files accumulated over a period of five years, March 2004 through April 2009, while the construction work was progressing. There were a number of changes in structural configuration, therefore, over this period (Furtner 2009). Regardless of the history of various events occurring at the structure, there is clearly a general trend of dynamic energy shift towards higher frequency ranges throughout the period (Fig. 15).

The first 33 of the existing data files were sampled at a frequency of 100 Hz and the last 98 files at 500 Hz. When the sampling frequency was 100 Hz, any spectral information in high frequencies beyond 50 Hz would have been lost. An important question is whether any meaningful engineering judgment could be made based only on the information of less than the cut-off frequency. The effects of sampling rates on the depicted spectral patterns were examined, because of this reason, based on the data of this bridge only from the last 98 files, by comparing the following two cases:

// for $0 < f \leq 50$ Hz by re-sampling the data at 100 Hz, namely every fifth points and

// for $0 < f \leq 250$ Hz based on the data available at 500 Hz sampling.

Figs. 16 and 17, (A) and (B) compare the normalized spectra $F_i(f)$ and the cumulative distribution $E_i(f)$ of both cases. Transfer of energy to a higher frequency range that took place between various events is clearly better recognized by the results of (B). The high spectral peaks started appearing in the higher frequency range after milling of the ramp started in April 2007, indicating a significant change of spectral pattern. In terms of the cumulative spectral energy $E_i(f)$, it is more clearly recognized by case (B), rather than (A), since presumably more and more energy is transferred to the frequency range beyond 50 Hz. Note, however, that high frequency noise is also effectively cut off for the case of (A) due to low sampling frequency and it sometimes makes it easier to look at the color pattern since the spikes caused by operational noise are reduced.

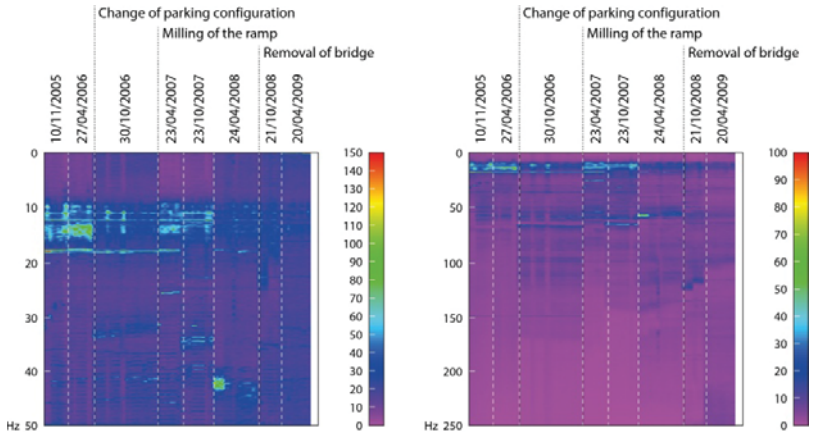

Fig. 16 Flughafen: $F_i(f)$ the last 98 files (A) and (B)

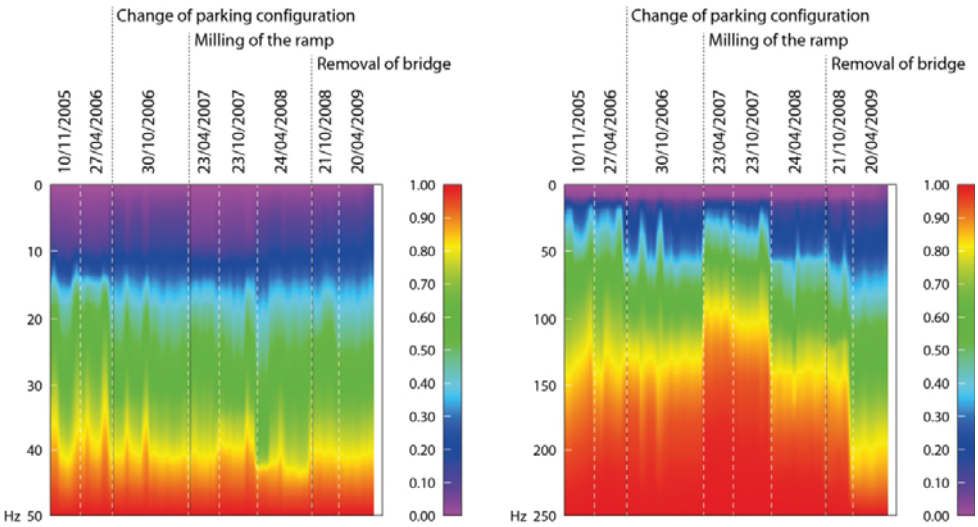

Fig. 17 Flughafen: $E_i(f)$ the last 98 files (A) and (B)

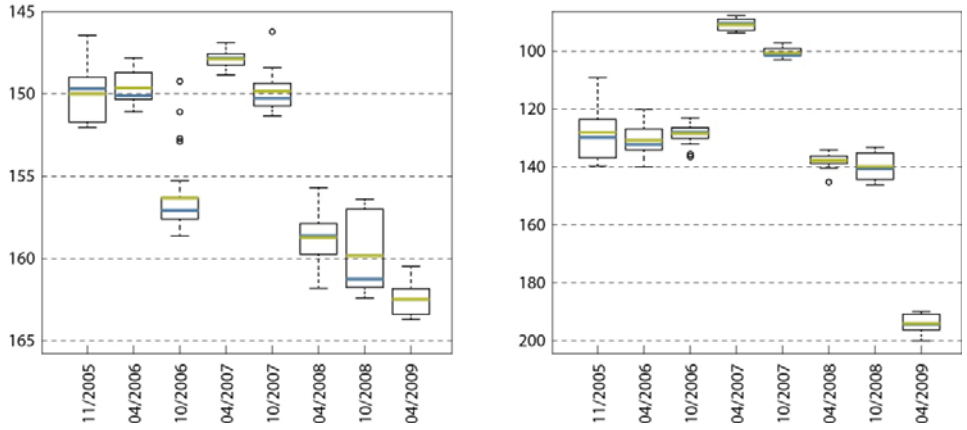

Fig. 18 Flughafen: boxplot of the centroid (left) boxplot of 80 % of the energy (right)

The statistical analysis obtains significant changes for this structure with the analysis of variance (ANOVA) for the location of the centroid from the 3rd observation period (that is the year 2006) and for the value for 80% of energy from the 4th observation period (that is the year 2004). Fig. 18 shows the boxplots of these results.

8. Conclusions

The proposed spectral method (VCLIFE) was applied to on-site measurement data at several different bridges. The results presented herein indicate a possibility of effectively detecting the development of structural damage by looking at the change of the spectral pattern due to the shift of dynamic energy towards a higher frequency range. It should be noted that the results are more informative when the sampling frequency is high enough, generally speaking.

The energy shift seems to be quite characteristic to the structures with developing damages. It is believed that a combination of the ambient vibration survey and the proposed spectral analysis can be an effective and simple structural health monitoring tool. To this end, it would be ideal if a criterion for the extent of structural damage corresponding to any indicator of the energy shift can be established. Locating the centroid of the area under $E_i(f)$ curves is one possibility but its validity would require further investigation.

A sampling frequency of 500 Hz is recommended for future measurements. For identifying the high frequency shift of dynamic energy, it is desirable to minimize the effects of extraneous disturbances, particularly those of traffic load. Ideally, if the spectrum of excitation force can be identified even approximately, its contribution towards the output spectra can be estimated, however, this is not the case most of the time. Minimization of noise effects could be achieved by taking a long enough record so that undesirable noise, including the traffic load, can be regarded more or less an evenly distributed excitation. Taking several consecutive files, each 330 seconds long, would suffice. Ideally, the free vibration record of the structure should be observed over a certain period of time. Importantly any measurements involving multiple locations on a structure should be made with respect to a fixed reference point throughout the project.

References

Furtner, P. (2009), Flughafen Wien Schwechat Vorfahrt Ost Terminal 2 – Objekt 102, Dynamische Charakteristik der Bauwerke, Periodische Nachmessung und Interpretation der Ergebnisse. Report 09/1042, April 2009.

Wenzel, H. (2009), *Health Monitoring of Bridges*, J. Wiley and Sons Ltd., Chichester – England, ISBN 9780470031735, 2009.

Wenzel, H. et al. (2013), *Industrial Safety and Life Cycle Engineering*, VCE Vienna Consulting Engineers ZT GmbH, Vienna, Austria, ISBN 9783200031791, 2013.

Wenzel, H. and Pichler D. (2005), *Ambient Vibration Monitoring*, J. Wiley and Sons Ltd., Chichester – England, ISBN 0470024305, 2005.

Wenzel, H., Veit-Egerer, R., Widmann, M. and Jaornik, P. (2009), WP3 Demonstration Report. Deliverable D11.1, October 2009.

Smart Structures and Systems, *Vol. 15, No. 3 (2015) 593-608*
DOI: http://dx.doi.org/10.12989/sss.2015.15.3.593

Approaching the assessment of ageing bridge infrastructure

Christian Boller*, Peter Starke, Gerd Dobmann, Chen-Ming Kuo and Chung-Hsin Kuo

Chair in Non-Destructive Testing and Quality Assurance (LZfPQ), Saarland University, 66123 Saarbrücken, Germany

(Received November 25, 2014, Revised February 5, 2015, Accepted February 7, 2015)

Abstract. In many of the industrialized countries an increasing amount of infrastructure is ageing. This has become specifically critical to bridges which are a major asset with respect to keeping an economy alive. Life of this infrastructure is scattering but often little quantifiable information is known with respect to its damage condition. This article describes how a damage tolerance approach used in aviation today may even be applied to civil infrastructure in the sense that operational life can be applied in the context of modern life cycle management. This can be applied for steel structures as a complete process where much of the damage accumulation behavior is known and may even be adopted to concrete structures in principle, where much of the missing knowledge in damage accumulation has to be substituted by enhanced inspection. This enhanced and continuous inspection can be achieved through robotic systems in a first approach as well as built in sensors in the sense of structural health monitoring (SHM).

Keywords: ageing infrastructure; structural health monitoring; fatigue; PHYBAL; steel; concrete; inspection robotics

1. Introduction

1.1 Ageing infrastructure life cycle management – a motivation

In many of the highly industrialized countries today a lot of infrastructure has been built when economy has been taking off. In Germany this has been specifically after WW II as it has been happening in a similar way in Japan too. Other countries such as France, the UK, Canada or the USA have accumulated also a large number of infrastructure over the last century or two, although the establishment of their infrastructure may have been spread more evenly over time. All of this infrastructure was built somehow for a vaguely specified period of time which could even be defined as 'forever', although when thoroughly checked the assumed life is said to be no more than 100 years. However, nobody truly has made this check or better, this infrastructure said to last for at least 100 years is most likely to last much longer. Much of this infrastructure is even listed which is a definition per se that life can be 'forever'. In many of the cases the degree of damage of this infrastructure is not sufficiently known because loads have not been clearly recorded and design documents have vanished. However, loads resulting from operation as well as the

*Corresponding author, Professor, E-mail: christian.boller@izfp.fraunhofer.de

http://www.techno-press.org/?journal=sss&subpage=8 ISSN: 1738-1584 (Print), 1738-1991 (Online)

environment may have changed significantly, specifically in the case of bridges, which do make a sufficiently realistic estimation of the damage condition of those structures even more difficult.

All of this ageing infrastructure needs to be managed with regard to its integrity and the question of the damage to be tolerated from a structural integrity as well as from an economic point of view arises. Life cycle management therefore becomes essential and the question is on how to take this approach. Structures being exposed to loads do damage specifically when they exceed a threshold value. Those loads can be mechanical as well as environmental where the two types of load interact in a way that the environmental loads will reduce the threshold of the mechanical loads leading damage to be initiated. Loads applied to structures can be measured in terms of traffic loads, wind, snow, temperature, humidity and possibly more. However, a key question arises what damage those loads cause and what damage is defined to be (crack, delamination, stiffness loss, material loss, etc.). A further question arises as to how damage accumulates as a function of loads over time and when a damage becomes critical. Such an assessment can only be done when:

1. A detectable damage can be defined from an inspection point of view,
2. A critical damage can be defined from a structural integrity point of view,
3. The time for the damage to grow between the detectable and the critical damage condition can be determined.

Such an approach is fairly possible with metallic materials at least to a significant extent. It starts from the fact that damage can be detected by means of nondestructive testing and a tolerable damage can be defined from a structural integrity point of view as well. In metals such as steel damage is widely defined as a crack and with the help of fracture mechanics the time can be predicted how long a damage/crack will take to progress from a detectable to a critical size. This time interval combined with the stochastic nature of damage progression will then determine when an inspection will have again to be made and where a non-critical damage may be found that then will have to be rectified. This is to what extent damage tolerant design is performed in aviation where the objective is lightweight design. However, when lightweight design is less of an issue such as in civil engineering, damage tolerant design can still be of an advantage in terms of extending a structure's safe operational life.

When it comes to non-metallic structures such as made from concrete the damage tolerance approach becomes more complicated since neither the detectability nor the criticality of damage as well as the way damage propagates as a function of applied loads is known. However, still the damage tolerance approach described for metallic structures can be applied in principle with the difference that many of the damaging phenomena including the damage accumulation process are less known. Damage assessment in concrete structures today is still fairly crude and is mainly based on visual inspection only where an experienced inspector will judge if a structure has to be classified as 'green', 'yellow', or 'red' equivalent to a traffic light system. Neither a quantifiable degree of damage nor a description of damage accumulation exists for concrete structures so far and it is such that only by visual inspection those structures can be assessed today with the additional effect that the experience and hence images gathered can serve as a database to study damage progression as a function of applied loads. Furthermore this procedure does possibly allow the respective mechanisms leading to damage progression in a fairly composite material such as reinforced concrete to be derived.

Civil infrastructures with bridges being a good example are large and hence difficult, risky and expensive to inspect. This prevents those structures to be inspected frequently by human inspectors. However when it comes to damage tolerance of those structures where damage mechanisms are

fairly unknown such as with concrete a frequent inspection at least of the locations being damage critical is a must. The solution to this problem can therefore currently only be seen through automation of the inspection process. Throughout the following options for a modern life cycle management of civil infrastructure is described, first for the more established process for steel structures and then for the emerging issue of ageing concrete structures. Principally the processes for the two material types are the same however the achievement for the two different types of material are different which allows gaps for future research initiatives to be identified.

2. Steel infrastructure assessment

Anyone dealing with fatigue knows that fatigue life scatters. This scatter can be a factor of two or even more in fatigue life when it comes to metallic structures where the fatigue behavior such as with the description of crack propagation is comparatively well known. As regards the age of bridges the average age of German railway steel bridges is close to 90 years now with the oldest being 175 years of age (Deutsche Bahn AG). Those bridges may easily last another 100 years in average but this requires more care in monitoring and maintenance and the consideration that a certain degree of damage might be tolerated. Many of those bridges have become landmarks and possibly listed, which has now the endurance of those structures mainly to be infinite. Nobody can therefore consider those structures to be free of damage and the question is: *How much damage can those structures sustain?*

Design concepts of such a nature being called *damage tolerant design* are well known within the context of aeronautics. Damage tolerant design defines a condition of a detectable damage and a tolerable damage respectively (Fig. 1) and allows for a damage progression period ΔN to be calculated for a specific operational load using damage accumulation rules such as elastic or elastic-plastic fracture mechanics in the case of metals. To provide for scatter in damage occurrence an inspection is performed after a period of $\Delta N/2$ and in case no obvious damage is found the process is repeated until damage is identified where the damage found then has to be repaired (Fig. 2).

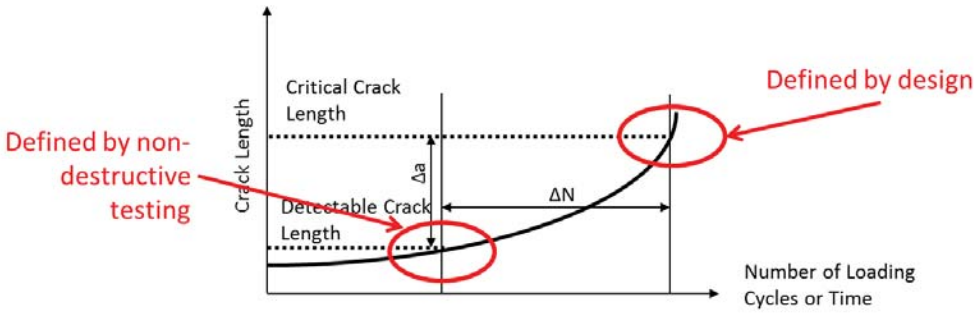

Fig. 1 Definition of damage tolerance limits in damage tolerant design

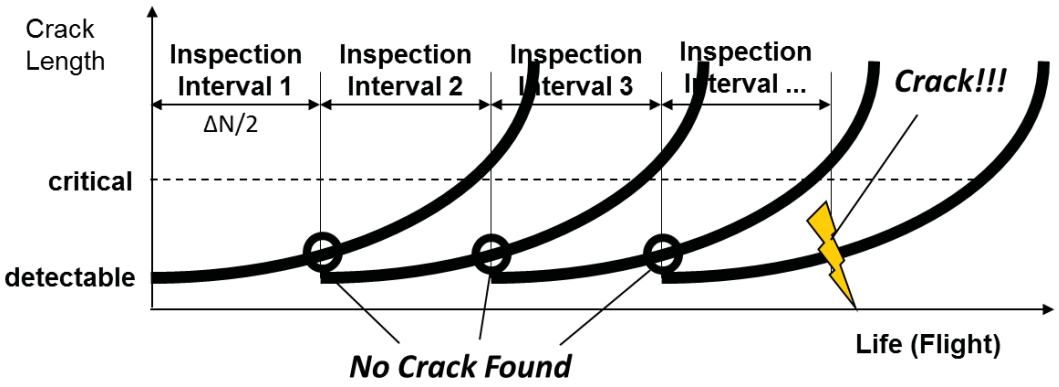

Fig. 2 The damage tolerance design principle

The reason aeronautics takes advantage of damage tolerant design is to design structures lighter weight what can be seen from the schematic fatigue life curve shown in Fig. 3. However, within civil engineering lightweight design may not be a design issue of paramount importance while the other parameter in the fatigue life curve being available to take advantage of is operational life, which is essential within the civil engineering environment. Hence applying damage tolerance to civil engineering structures can help the average operational life of the structures under consideration to be enhanced. The smaller (earlier) damage can be detected the larger the inspection interval can be defined. This is why inspection methods are considered which do detect damage even at a microscopic level, which occurs during a period when a structure is loaded under fatigue.

The fact that damage accumulation and hence damage progression is a non-linear process, specifically when loads applied to the structure are of an arbitrary nature too, and the maintenance processes can possibly be combined with fatigue life prognostic tools, the damage tolerance approach taken can have the advantage to predict the individual life of structures and with this to establish a maintenance scheduling plan in the end.

Assuming fatigue to be the critical damaging factor may lead to another issue with regard to the assessment, which is the availability of fatigue data. For many of the old infrastructure this data is either not or not sufficiently available and also the material is possibly difficult to be obtained. Furthermore the damage condition of the civil infrastructure to be assessed may not be sufficiently well known. Hence the most suitable way in assessing the structure's real damage condition would be to experimentally analyze material from the infrastructure to be considered. This however requires a method to be used that only requires a very limited amount of material to be taken from the infrastructure to be inspected.

A method that allows S-N curves and the respective material properties to be determined is PHYBAL (Starke 2007, Starke *et al*. 2010). PHYBAL is a short-time calculation of S–N and fatigue life curves of metallic materials. With PHYBAL the S-N and fatigue life curves for different metallic materials and material conditions can be determined on the basis of one load increase test and two constant amplitude tests only. A stepwise or continuous load increase test (LIT) is performed first to estimate the endurance limit and to select appropriate stress amplitudes

for constant amplitude tests (CAT) with one single specimen. Fig. 4(a) shows the experimental approach as a principle. The LIT starts at a stress amplitude of $\sigma_{a,start}$ which is chosen below 25% of the materials' yield strength being increased stepwise by $\Delta\sigma_a$ after a defined number of cycles ΔN or continuously until the specimen finally fails. Along this test different other parameters being relevant to damage can be measured such as plastic strain ε_{pl}, temperature ΔT, electrical resistance ΔR or even electromagnetic impedance Z (Fig. 4(b)). Within this procedure two relevant stress parameters are selected a) $\sigma_{a,LIT}$ being the stress level where one of the damage relevant parameters significantly changes from zero, which can be also used for the estimation of the endurance limit and b) $\sigma_{f,LIT}$ being the stress level at which the specimen fails. Two constant amplitude fatigue tests need to be further performed the one being slightly above $\sigma_{a,LIT}$ and the other slightly below $\sigma_{f,LIT}$ respectively.

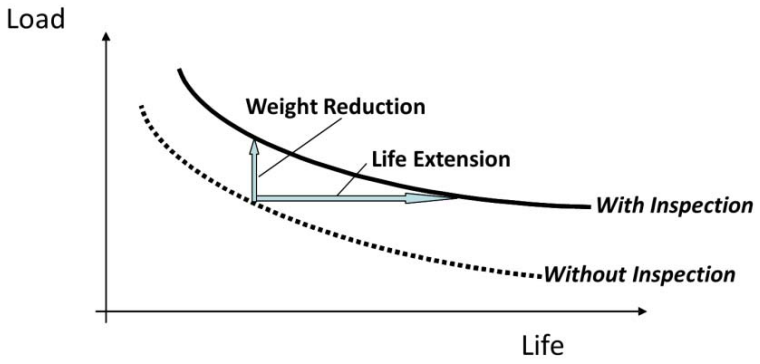

Fig. 3 Effect of damage tolerance principle on allowable fatigue life curve

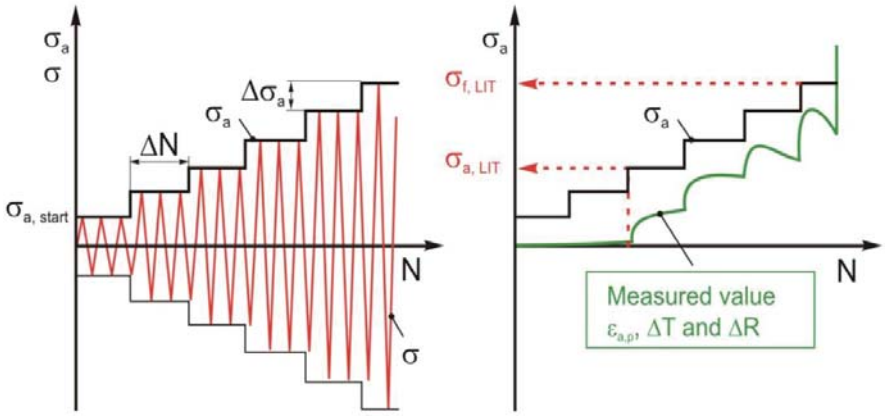

Fig. 4 A schematic view of stress amplitude σ_a (a) and measured values $\varepsilon_{a,p}$, ΔT and ΔR (b) in a stepwise load increase test

In the respective case for a quenched and tempered SAE 4140 steel shown in Fig. 5 where $\sigma_{a,LIT}$ has been 480 MPa and $\sigma_{f,LIT}$ has been 680 MPa respectively, the stress levels for these CAT have been chosen to be 500 MPa and 640 MPa respectively.

In Fig. 6 the stress amplitude is plotted versus the damage relevant parameters recorded in the LIT as well as the respective damage relevant value obtained at half of the fatigue life for the two CATs. To take the pre-damage of lower load levels of the LIT into account, the values of the two CATs are used as anchoring points for the transfer of the stress-damage parameter relation of the LIT to the one for constant amplitude loading by a linear interpolation function based on the stress amplitude ratios of CAT and LIT.

A power law proposed by Morrow (1964) is used to describe cyclic stress-strain (CSS) curves of the load increase test and the constant amplitude tests. This power law has been used in a generalized formulation with the cyclic hardening coefficient K'_M instead of K' and the cyclic hardening exponent n'_M instead of n' respectively, applying the different damage parameters M mentioned above such as plastic strain, temperature, electrical resistance or electromagnetic impedance, leading this power law to become

$$\sigma_\alpha = K' \cdot \left(\varepsilon_{a,p}\right)^{n'} \rightarrow \sigma_a = K'_M \cdot (M)^{n'_M} \tag{1}$$

A similar approach is made with regard to the S-N-curve where the Basqu in Eq. (5) is applied. Here the fatigue strength coefficient σ'_f is replaced by the $\sigma'_{f,M}$ and the fatigue strength exponent b by b_M respectively, leading to

$$\sigma_a = \sigma'_f \cdot \left(2N_f\right)^b \rightarrow \sigma_a = \sigma'_{f,M} \cdot \left(2N_f\right)^{bM} \tag{2}$$

According to Morrow the fatigue strength exponent b_M can be calculated on the basis of the cyclic hardening exponent n'_M

$$b = \frac{-n}{5n'+1} \rightarrow b_M \frac{-n_M}{5n'_m+1} \tag{3}$$

With the strain hardening exponent n'_M being known from the LIT the fatigue strength exponent b_M is determined and with the result of one of the CAT the fatigue strength coefficient $\sigma'_{f,M}$ can be determined from Eq. (2) too. This finally allows the S-N-curve to be described on the basis of b_M and $\sigma'_{f,M}$ only leading to

$$N_f = 0.5 \cdot \left(\frac{\sigma_a}{\sigma'_{f,M}}\right)^{1/b_M} \tag{4}$$

Fig. 6(a) shows results of proportionally downscaling CAT results from the LIT results and proving that a linear relationship can be drawn between the two CAT results obtained.

Fig. 6 shows on the right hand diagramme the S-N curve obtained with the PHYBAL approach and the good match with experimental data for the quenched and tempered SAE 4140. Compared to conventional fatigue testing and the way materials data have been presented in the past (Boller and Seeger 1987) PHYBAL is an approach that reduces the effort of generating materials data for

cyclic loading by a factor of ten. In other words: This much more efficient provision of fatigue data is first of all a great help because it allows materials fatigue data to be provided even for an aged structure in terms of the material's residual fatigue strength. Provision of testing material may be possible in case a component of the aged structure considered may be replaced and the respective samples for materials data generation can be manufactured. However, if sample material has been taken from a component replaced on the respective structure it is still not known which degree of damage the material tested has. With much of the ageing infrastructure considered, data of the pristine material is not available and it is such that a relative approach has to be taken to obtain a more tangible value of the stage the structure under consideration is damaged.

The approach on how to obtain those more tangible values is through the design of the structure being considered. For this the geometry, type of materials and loads have to be known. It is specifically the latter which might have been initially assumed and which need to be monitored to obtain an adequate figure. This is reasonably possible today, specifically within the context of structural health monitoring (SHM), making use of the various types of sensors being available such as electrical or optical fiber strain sensors as well as vibration sensors of different kinds. Options of such a type of sensors including the monitoring concepts have been described in reference books such as (Boller *et al*. 2009). The outcome of such a loads recording approach may not represent the complete life of the structure considered, however, it does at least represent the shape of the loading spectrum and with this a major portion under which the structure has been operated. This now allows a fatigue life estimation of the structure to be made in combination possibly with a FE analysis and to determine at which locations damage has accumulated more when compared to others. This principally relative damage profile can then be finally referenced to the degree of damage of the component replaced where the samples for materials' data experimental validation had been taken from.

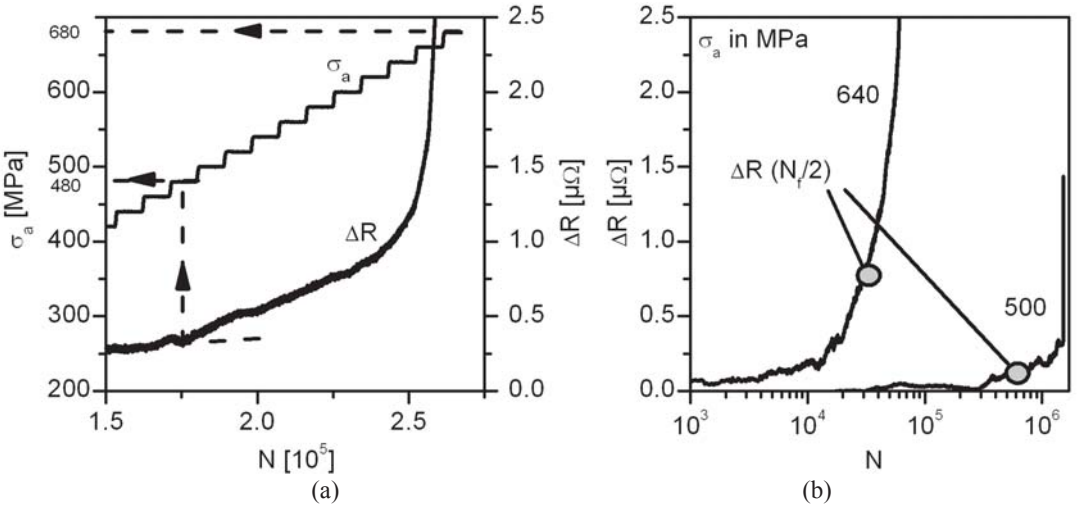

Fig. 5 Stepwise load increase test (LIT) for quenched and tempered SAE 4140 with stress amplitude a and change in electrical resistance ΔR related to fatigue cycles applied (a) and electrical resistance versus fatigue cycles applied at two stress levels of a constant amplitude test (b)

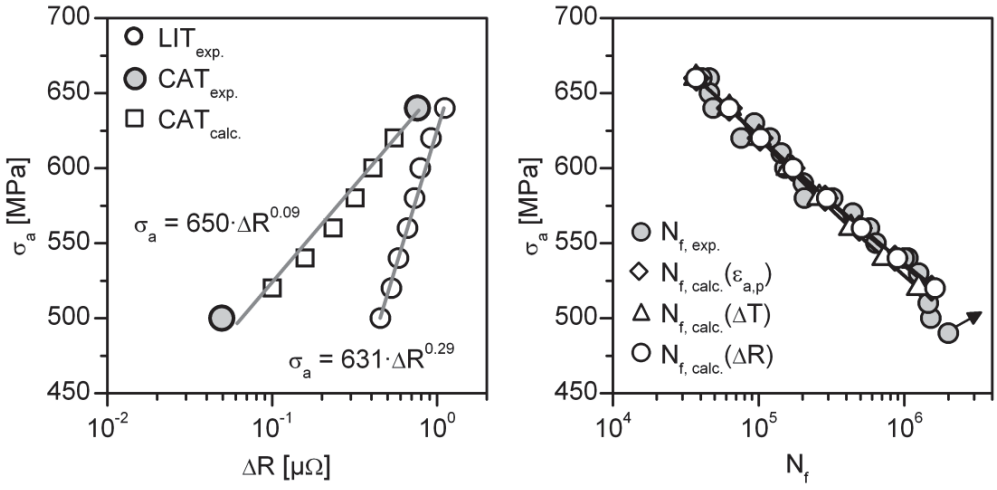

Fig. 6 Cyclic stress-resistance $\sigma_a - \Delta R$ curves for a load increase test (LIT_{exp}), ΔR values at $N = N_f/2$ for two constant amplitude tests (CAT_{exp}) and $\sigma_a - \Delta R$ curve calculated for constant amplitude loading (CAT_{calc}) (a) as well as comparison of experimental lifetimes ($N_{f,exp}$) and S-N curves calculated on the basis of $\varepsilon_{a,p}, \Delta T$ and ΔR for constant amplitude loading (b) for quenched and tempered SAE 4140

With this in mind and the PHYBAL approach described above it is now possible to locate the S-N curve within the range of different damage conditions including the pristine condition in a way it has been described by Haibach (2006) and possibly others and which is shown in Fig. 7 below.

The approach is based on an S-N curve to be described as a bi-linear function

$$N = N_E \cdot (S_a / S_E)^{-k} \qquad for\ S_a \geq S_E$$
$$N = \infty \qquad for\ S_a < S_E \tag{5}$$

where k, N, N_E, S_a and S_E represent the slope of the S-N curve, the number of cycles, the number of cycles at the endurance limit, the stress amplitude and the stress amplitude at the endurance limit respectively. This function can also be described for a material where the damage is $0 < D < 1$. In that case the S-N curve is shifted to the left when compared to the S-N curve for the pristine condition and the endurance limit is reduced along a locus shown in Fig. 7 which depends on a parameter q being a function of the way damage accumulates in the material considered. Knowing the relative degree of damage or better the damage distribution of the complete structure through a fatigue life calculation performed for the structure considered, now allows the degree of damage to be determined of the component that has served to determine the materials data in accordance to the PHYBAL approach. With this figure in mind and the material's data residual fatigue life determined from the PHYBAL approach the endurance limit and hence

the degree of damage can be determined. If a possibly second material sample taken from another structural component having a different degree of damage condition and allowing for replacement can be made available, then a second S-N curve in accordance to the PHYBAL approach is generated which can finally allow the complete spectrum of residual life S-N curves for different damage conditions to be determined. This will then allow the structure considered to be fully assessed in terms of its residual operational life.

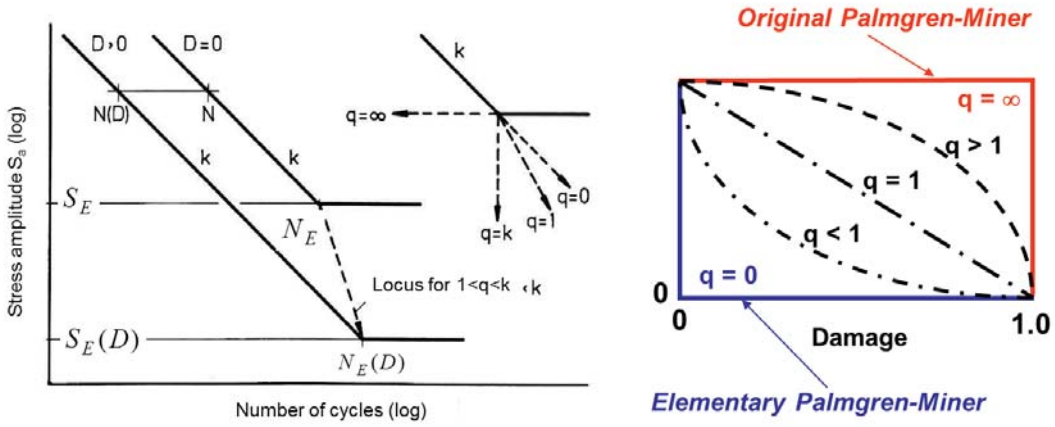

Fig. 7 Schematic of handling S-N curves for a material under different damage conditions

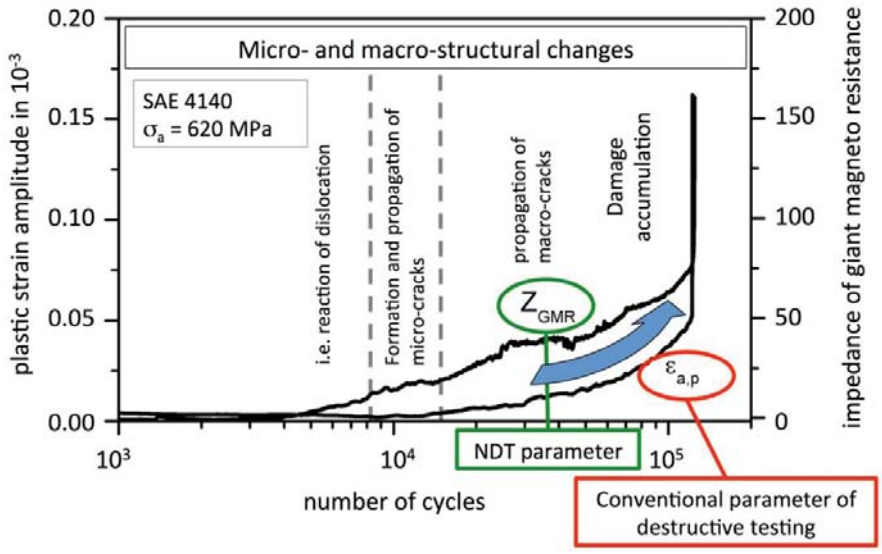

Fig. 8 Change of different physical parameters over fatigue life of a quenched and tempered SAE 4140 steel under constant amplitude loading with a stress amplitude of 620 MPa

The different damage parameters M considered such as plastic strain, temperature, electrical resistance or electromagnetic impedance are very much associated with physical parameters being used in nondestructive testing (NDT). Specifically electromagnetic techniques such as measuring eddy current impedance, permeability, higher harmonics or Barkhausen noise are techniques which have been used to characterize materials under different conditions including ageing at even sub-microscopic cracking conditions. An overview of the capabilities of those techniques with regard to describing mechanical conditions of materials has been provided in (Boller *et al*. 2011) and its capabilities in analyzing materials even at microscopic level has been described in (Sheikh Amiri *et al*. 2014) respectively. Fig. 8 shows the result obtained on a quenched and tempered SAE 4140 steel fatigue tested under constant amplitude loading with a stress amplitude of 620 MPa where the electromagnetic impedance has been measured using a giant magnetic resistor (GMR) (Starke *et al*. 2009). A sensitivity higher than measuring plastic strains has been determined which gives rise to the fact that damage and hence damage accumulation can be measured even below the stage where micro-cracking does emerge.

3. An Approach for lifecycle management of aged steel infrastructure

As to the methodology described above a lifecycle management concept for ageing steel infrastructure can now be established. It is based on the availability of the digital (FE) model of the structure considered including the load spectrum being applied to it. This model can be determined for even an old structure and can be continuously updated by monitoring strain sequences at well-selected locations. With this a fatigue life estimation becomes possible which allows damage accumulation to be determined at discrete locations of the structure considered where the locations become indicators for visible damage is to be expected first. Since crack initiation is a stochastic process a FE model may require an update with regard to the structural damage condition detected such that a more precise prediction can be achieved. This looks possible when NDT data such as with electromagnetic techniques can be sampled and correlated to the different damage conditions over a fatigue life. This may be performed along the LIT and CAT experiments in case the PHYBAL method is applied and will result in diagrams of the type shown in Fig. 6. This will describe the non-linearity of damage accumulation and may serve as the calibration source once it has been normalized such that the non-linearity in damage accumulation can be literally applied all along the S-N curve. It will significantly help to circumvent the errors made when applying linearized damage accumulation rules such as proposed by Palmgren and Miner. Performing electromagnetic sampling at various locations of interest along the structure considered on the other hand will allow a full profile of the electromagnetic parameters over the structure to be generated. This profile of electromagnetic parameters can be converted to a stress distribution profile based on the information provided in Fig. 6. Merging this with the damage parameter progression curve obtained for a CAT performed at a defined stress amplitude such as shown in Fig. 8 will principally allow a reference point with regard to the degree of damage and hence the number of cycles to be found, which will then allow the damage profile of the structure to be determined in even absolute terms. This profile can be matched and further updated with the fatigue life predictions made and will principally allow for a continuous model update gradually refining any damage assessment models such that the structure considered can be managed in terms of maintenance, repair and overhaul in the longer term. With sensing devices such as monitoring loads or damage being even placed stationary at damage critical locations will allow a

way of structural health monitoring to be performed on a wireless basis making management of a large number of steel infrastructure possible from a central location only.

4. Concrete infrastructure assessment

Concrete is a material much more difficult to understand with regard to its damaging behavior when compared to metals. It is a composite material at macro-scale of a mainly brittle nature, which can be pre-stressed and may possess cracks already at its onset. It is not exposed to mechanical loads only but also to environmental loads where moisture, corrosion and resulting carbonation can play a significant role. Concrete structures as they are designed today as well as in the past are said to be principally damage free. This is however far from reality as can be seen with an increasing number of concrete structures worldwide now deteriorating.

The approach on how to assess a concrete structure with respect to its life cycle management is principally similar to the one applied for steel. Damage could be tolerated provided the criticality of the damage is known and the way the damage progresses from a detectable to a critical stage. The way concrete structures are assessed today is mainly by visual inspection only. The structures are then categorized such as in accordance to a traffic light system, which must be considered as a rather subjective approach. Application of NDT in civil engineering can still be considered to be in its infancy. First publications in this field appeared in the mid 1980ies and there is still not much NDT technology being already available which possesses the maturity to be standardized. Overviews with regard to some latest developments of NDT in civil engineering can be found in (Kurz *et al*. 2011, Dobmann *et al*. 2010) as well as in the proceedings of some recent conferences (Wiggenhauser *et al*.).

If damage tolerance was to be applied to concrete structures then much inspection would have to be required since the period from when first cracking may be observed on a concrete structure up to a condition where concrete coverage falls off due to corrosion at and carbonation along the metallic rebars may be short or at least fairly impossible to predict. Frequent inspection calls for automation of the inspection process and this inspection can become risky, specifically when a structure becomes large such as in the case of a bridge. Automation of the process using a robot (or multiple robots) equipped with sensors such as digital cameras is therefore an option interesting to be explored since it can be used to replace the human inspector. The approach having been taken for inspection is based on a micro aerial vehicle (MAV), which is equipped with a digital camera underneath such as shown in the case of an octocopter in Fig. 9. The MAV is flown remotely and scans the building to be monitored. The camera is set in a continuous trigger mode with a frequency of 3Hz, which is also known as the time based method of image capturing. Even though the robot is fitted with a GPS receiver and can operate GPS based, the entire flight process is manually controlled. This is due to the lack of GPS signal when the vehicle flies close to the structure to be monitored. The autopilot together with some additional features such as a vector thrust propulsion system only provides auto-stabilization and altitude control. Flight stability of the robotic vehicle is important since it is directly correlated to the quality of the images taken.

To successfully run the photographic monitoring initially, a flight route well planned is most essential. For a camera with an image ratio of say 4:3, a horizontal flight route scanning will produce a series of pictures with lowest achievable distortion, which is the reason why a horizontal scanning is usually preferred. During the monitoring process a volume of several GB of images is easily accumulated. From those images only a fraction of the best can be taken for being stitched

together. To enhance that fraction of useful images different measures have been taken in terms of stabilizing the MAV's attitude control through a vector thrust system and optimizing the waypoint control through a fuzzy logic control algorithm built into the camera system (Kuo *et al*. 2014). To speed up the image stitching process automated image stitching tools have been used as well. However, manual corrections are still required when structures are photographically 'assembled' of the dimensions shown in Fig. 10. The resolutions to be obtained in the end are those shown in Fig. 11 where a cracking pattern is observed on the left. Such cracking patterns are typical in concrete resulting from carbonation and corrosion along rebars and are a precursor that concrete parts are due to come off. Tools for clearly identifying such cracking patterns along an automated process are therefore essential for which a resulting picture can be seen in the middle of Fig. 11. Once time passes by, concrete parts will come off as is shown for the same location on the right hand side of Fig. 11. This also shows one of the advantages of automated imaging using a MAV.

Fig. 9 Octocopter MAV system with digital camera

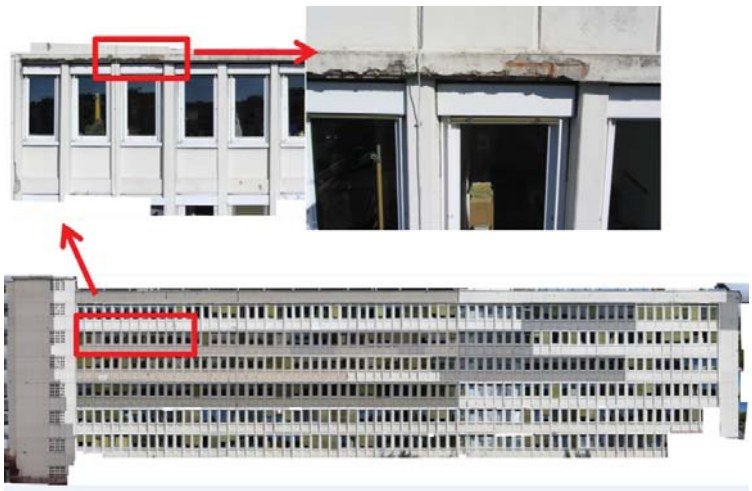

Fig. 10 Stitched images of a major building (bottom image) with resolutions to be zoomed in (top images). Note that different colors of images are due to images taken at different weather conditions

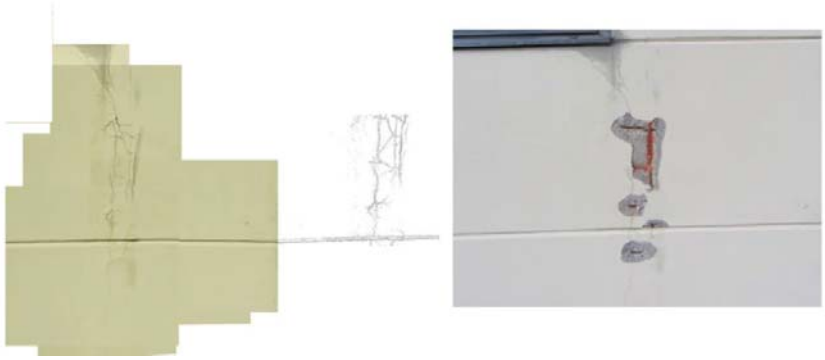

Fig. 11 Damage in a concrete wall (left), resulting crack pattern (middle) and damage 11 months later (right)

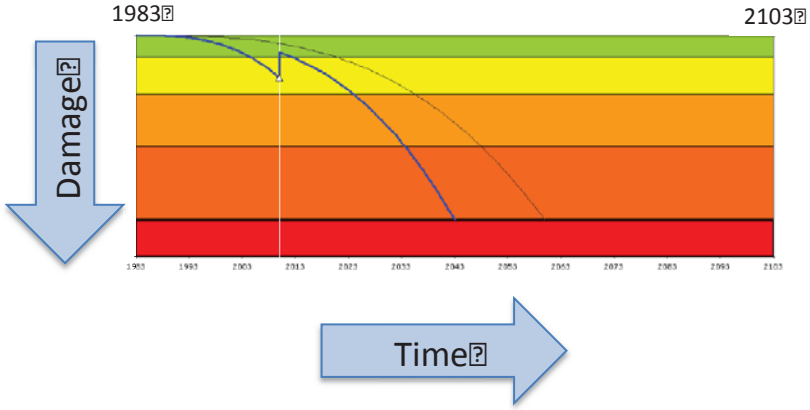

Fig. 12 Theoretical global life cycle curve for a bridge and resulting impact due to enhanced maintenance

Once an infrastructure such as a building has been fully recorded and possibly modeled in 3D, only the critical locations have to be recorded in later stages, making this method of infrastructure monitoring highly efficient when compared to the conventional methods where men have to climb along critical maneuvers to access the locations of interest. Taking images of those critical locations at close intervals will allow a sequence of the damage incubation and progression process to be constructed that may allow the still mainly unknown damage mechanisms in concrete to be assessed and better understood. With the ability to further allocate each pixel geometrically a means will be provided to generate a full map of damages present at least in 2D. With the inclusion of further NDT techniques such as radar or thermography further means will be provided that will allow the structure to be monitored sub surface. By merging those data with the visually obtained data through a data fusion process one will gradually obtain a 3D image of the damage that will further allow the damage mechanisms observed to be better understood.

4. Conclusions

Inspection of civil infrastructure such as bridges has been increasingly improved over the past decades. With FE modelling emerging as an established technique, stress, strain and temperature distributions in structures have become viably determinable. Similar observations regarding simulation can be made with regard to the dynamic behavior of structures. The consequences of loads applied to structures can therefore be simulated and with the emergence of a variety of sensors those loads can be monitored too. Hence a fairly realistic loading behavior can be simulated in structures which again can be correlated to the resulting damaging behavior of the structural material considered. Description of this damaging behavior is qualitatively different with respect to the type of material and the type of damage considered. With metals and fatigue the degree of damage modelling is comparatively advanced while with corrosion it is already less and becomes close to zero when moving to other types of materials such as concrete, wood or polymer based composites. This leaves visual observation and assessment as the only option and denominator in getting the condition related information retrieved and to be combined with the structural design methods applied.

Keeping this general state-of-the-art in structural assessment in mind life cycle assessments of metallic structures can be well performed and can even be expanded from a traditional safe life to a damage tolerant approach. Combined with destructive and nondestructive assessment techniques a structural material's damage condition can be characterized and merged with prognostic tools such as used for fatigue life evaluation. In that regard the PHYBAL approach provides a significant progress since it allows much more fatigue related material information to be retrieved from a material's fatigue test than this has been possible in the past. This opens a new quality and potential in structural assessment specifically also with the increasing amount of ageing infrastructure. Based on monitoring the operational load spectrum with specific sensors at dedicated locations the residual life of principally each structure can be determined in the case of metals allowing individual maintenance programs to be established in accordance to operational needs. With the additional introduction of a damage tolerance principle this can further help to postpone maintenance actions and alleviate pressure that might have been imposed when conventional safe life time-based approaches would have had to be performed.

When considering the case of concrete structures, visual inspection is the only approach accepted for structural assessment currently. Even if other more efficient non-destructive testing techniques might be accepted in the future, visual inspection will still build the basis as it has been with metallic structures too. Establishing a monitoring approach therefore on the basis of visual inspection is logic for whatever material a structure might be made of, specifically when the image is on a digital and hence pixel basis. This pixel-based digitized information builds a basis into which additional information can be hung and that can be fed back as an image just in the way information on a structure's condition should be communicated even to people not being experts with respect to damage analysis and SHM.

The approach being proposed here provides a variety of elements that as a combination meets the requirements and definitions set for SHM to be performed (Boller 2009) and it can be seen as an amendment to what has already been compiled in (Boller 2009) and possibly other pieces of reference. With such a diagnostic and prognostic approach a means is therefore provided that allows structures to be better assessed in terms of their degree of damage as well as their residual operational life. Generating such a type of such damage related information is important in at least two regards. First of all it allows to better differentiate the degrees of severity of the different

damaging condition of a structure which then allows respective maintenance actions to be planned in much more detail and more efficiently than this is done conventionally today. This is important from the point of view that maintenance actions do have to be optimized from a cost and organizational point of view and to which the approaches proposed here do contribute. Furthermore the digitally based approach resulting from the pixel based visual inspection provides an excellent data base onto which any further structural information retrieved from other NDT techniques can be added and built upon. This will allow true log files of structures to be established in the future and allow a structure's integrity history to be retrieved in much more detail than this has been done before.

The damage tolerance principle as a tool of life cycle management of civil infrastructure is therefore principally applicable to any type of structural material. However where the material's damaging behavior is better known such as with metals more of the prognostic capabilities can be taken to substitute the inspection effort while with other materials such as concrete a larger inspection effort is required until prognostic tools will become available one day. This larger inspection effort can currently be compensated through robotic inspection. That the damage tolerance principle is becoming viable in civil engineering has been proven with some life cycle analysis and management concept proposed in (Wenzel *et al*. 2013, Veit-Egerer *et al*. 2013) where deterioration of a civil infrastructure is determined as a scatter band as shown as an example in the diagram of Fig. 12 considering the variety of possible uncertainties involved. This diagram principally does not display anything else than an inversion of a crack propagation curve s shown in Fig. 1 before. However what Fig. 12 additionally shows is the criticality of the damage in terms of a traffic light system and what implications investments in maintenance would have, shown by the kinks in the lower bound degradation curve. With such a procedure the drawbacks of negligence in maintenance can be clearly visualized even to the non-engineering community and a first steps towards a more efficient life cycle assessment and resulting management of civil engineering structures can be made.

References

Basquin, O.H. (1910), Proceedings ASTM 10, 10, 625.

Boller, C., Altpeter, I., Dobmann, G., Rabung, M., Schreiber, J., Szielasko, K. and Tschuncky, R. (2011), "Electromagnetism as a means for understanding materials mechanics phenomena in magnetic materials", *Materialwissenschaft und Werkstofftechnik*, **42**(4), 269-278.

Boller, C., Chang, F.K. and Fujino, Y. (2009), Eds.: *Encyclopedia of Structural Health Monitoring*, John Wiley & Sons, Chichester,UK.

Boller, C. and Seeger, T. (1987), *Materials Data for Cyclic Loading*, Elsevier Science Publ.

Deutsche Bahn AG (private communication)

Dobmann, G., Kurz, H .J., Taffe, A. and Streicher, D. (2010), Development of Automated Non-Destructive Evaluation (NDE) Systems for Reinforced Concrete Structures and Other Applications; (Eds., Mairhofer, C., Reinhardt, H.W. and Dobmann, G.), *Non-Destructive Evaluation of Reinforced Concrete Structures;* Vol. 1: Deterioration Processes and Standard Test Methods; Woodhead Sc. Publ., Cambridge.

Haibach, E. (2006), Betriebsfestigkeit, 3rd Ed., Springer Verlag Heidelberg (in German).

Kuo, C.H., Kuo, C.M. and Boller, C. (2014), "Adaptive measures to control micro aerial vehicles for enhanced monitoring of civil infrastructure", *Proceedings of the 6th World Conf. on Struct. Control & Monitoring*, Barcelona, Spain.

Kurz, J.H., Boller, C. and Dobmann, G. (2011), "Condition assessment of civil infrastructure in europe – recent developments and what might be ahead", *J. Eng. Mech. - ASCE*, **139**(6), 702- 711.

Morrow, J.D. (1964), ASTM-Internal Friction, Damping and Cyclic Plasticity STP 378, 1964, 45.
Sheikh Amiri ,M., Thielen, M., Rabung, M., Marx, M., Szielasko, K. and Boller, C. (2014), "On the role of crystal and stress anisotropy in magnetic Barkhausen noise", *J. Magnetism Magnetic Mater*., **372**, 16- 22.
Starke, P. (2007), Lebensdauerberechnung bei ein- und mehrstufig beanspruchten Proben aus vergütetem 42 CrMo 4; Dr.-Ing. thesis, Lehrstuhl für Werkstoffkunde, Technische Universität Kaiserslautern (in German).
Starke, P., Walther, F. and Eifler, D. (2009), "New fatigue life calculation method for quenched and tempered steel SAE 4140", *Mat. Sci. Eng. A*., **523**(1-2), 246-252.
Starke, P., Walther, F. and Eifler, D. (2010), ''PHYBAL'' a short-time procedure for a reliable fatigue life calculation", *Adv. Eng. Mater*., **12**(4), 276- 282.
Wiggenhauser, H. *et al*., Bauwerksdiagnose, also available on www.ndt.net
Wenzel, H., Veit-Egerer, R. and Widmann, M. (2013), Life Cycle Analysis Applied to the New Jersey Case Study; (Ed., H. Wenzel), IRIS – Industrial Safety and Life Cycle Engineering; Vienna Consulting Engineers ZT GmbH.
Veit-Egerer, R., Wenzel, H. and Lima, R. (2013), *Ageing Behaviour of Structural Components for Integrated Lifetime Assessment & Asset Management*, ibid.

Smart Structures and Systems, *Vol. 15, No. 3 (2015) 609-625*
DOI: http://dx.doi.org/10.12989/sss.2015.15.3.609

Control system modeling of stock management for civil infrastructure

Masato Abé*

BMC Corporation, WGB Marive West 25th Floor, Nakase 2-6-1, Mihama-ku, Chiba 261-7125, Japan

(Received November 17, 2014, Revised February 12, 2015, Accepted February 17, 2015)

Abstract. Management of infrastructure stock is essential in sustainability of society, and its analysis and optimization are studied in the light of control system modeling in this paper. At the first part of the paper, cost of stock management is analyzed based on macroscopic statistics on infrastructure stock and economical growth. Stock management burden relative to economy is observed to become larger at low economic growth periods in developed economies. Then, control system modeling of stock management is introduced and by augmenting maintenance actions as control input, dynamic behavior of stock is simulated and compared with existing time history statistics. Assuming steady state conditions, applicability of the model to cross sectional data is also demonstrated. The proposed model is enhanced so that both preventive and corrective maintenance can be included as system inputs, i.e., feedforward and feedback control inputs. Optimal management strategy to achieve specified deteriorated stock level with minimal cost, expressed in terms of preventive and corrective maintenance actions, is derived based on estimated parameter values for corrosion of steel bridges. Relative cost effectiveness of preventive maintenance is shown when target deteriorated stock level is lower.

Keywords: stock management; control theory; system dynamics; preventive maintenance; optimization

1. Introduction

Management of infrastructure is essential for sustainability of society (Yanev 2007). Relationship between economic growth and public investment has been discussed from the view point of theory of economic growth (Aschauer 1990, Barro 1990, Gramlich 1994), and the effect of maintenance is also studied (Kalaitzidakis and Kalyvitis, 2004). Fig. 1 shows development of infrastructure stock and gross domestic product (GDP) of Japan, normalized by GDP deflator with respect to 2000 (Abé *et al*. 2007). Because scales of infrastructure stock and GDP are comparable, maintenance and replacement of infrastructure would cause considerable burden to national economy, while integrity of the stock is critical for economic activity. To reduce maintenance cost, effectiveness of maintenance actions at earlier stage of deterioration, i.e., preventive maintenance, has been emphasized (Yanev 2007, Abé *et al*. 2007).

The authors consider infrastructure management activity from three aspects, as shown in Fig. 2: i.e., i) risk management; ii) stock management; and iii) asset management (Abé and Fujino 2009a,

*Corresponding author, Chief Researcher, E-mail: masato@hashimori.jp

http://www.techno-press.org/?journal=sss&subpage=8 ISSN: 1738-1584 (Print), 1738-1991 (Online)

Fujino *et al*. 2009). Risk management focuses safety and vulnerability of infrastructure so that risk, particularly fatal risk, due to accidents or natural disasters, is minimized. Stock management is defined to improve durability and optimize environmental burden and life cycle cost. Asset management is to assure use and existence value, which reflects utility and functionality such as traffic volume in the case of highway bridges. In practice, these three aspects need to be integrated into a unified solution for each structure, with possibly different weights. For light use bridges, risk management would be the first and stock would be the second, but least attention would be required for asset consideration. In contrast, for heavy use structures, importance of risk management may be higher, but stock management consideration yield to asset management, since disruption to utility will not be tolerated.

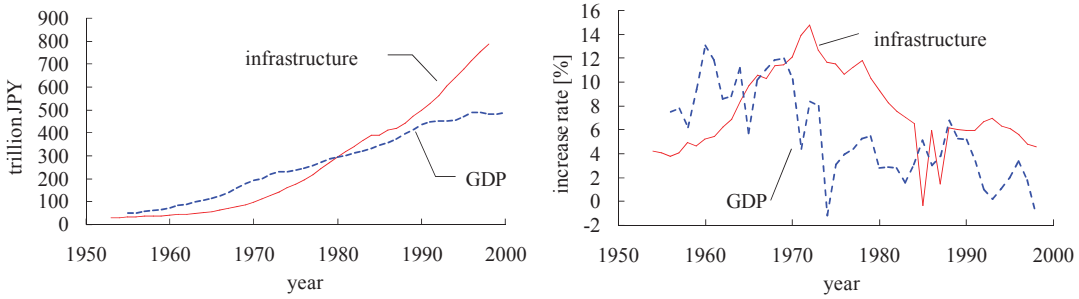

(a) Infrastructure stock and GDP (b) Stock to GDP ratio

Fig. 1 Development of infrastructure stock and GDP in Japan.

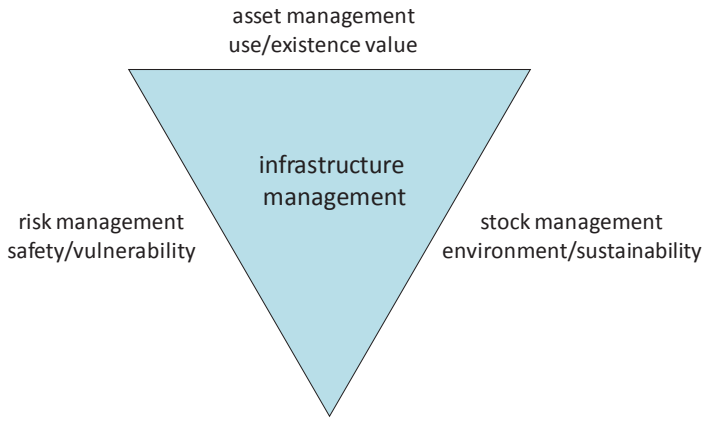

Fig. 2 Three aspects of infrastructure management

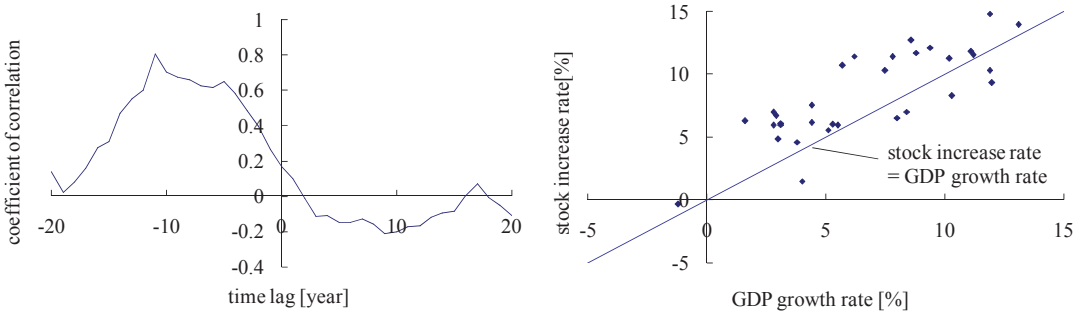

(a) Time lag between stock and GDP (b) Stock to GDP ratio with 11years of delay

Fig. 3 Effect of time delay between infrastructure stock and GDP growths

Among these three aspects, risk management of civil infrastructures for natural disasters and accidents has recently been reported by the authors in details (Fujino and Abé 2007, Abé and Shimamura 2014, Abé *et al*. 2014). In this paper, terms "asset" and "stock" are used to express different meanings as described above, although the term "asset" is commonly used to include both meanings in the existing literature (Uddin *et al*. 2013, Wenzel 2013, ISO 55000 2014). Here, the word "stock" is employed to emphasize that the formulation is focused on deterioration, and risk and functionality are not explicitly treated and considered secondary in the scope of the current paper.

In this study, a comprehensive framework for stock management is proposed based on control system theory, which generalizes statistical analyses of fragmented data sets on stock management collected in Japan and previously reported by the authors (Abé *et al*. 2007, Abé and Fujino 2007, Abé *et al*. 2008, Abé and Fujino 2009b, Abé *et al*. 2012), with further enhancement to national economic statistics.

First, national statistics are studied to provide macroscopic overview on dynamics of infrastructure stock and national economy. Then, control system theory is introduced to express system dynamics and maintenance action, and its optimization is investigated based on the proposed model. In the study of optimization, comparison of preventive and corrective maintenance is emphasized, because current practice is basically corrective, while advantages of preventive maintenance have long been discussed and stressed in engineering community (Yanev 2007, Abé *et al*. 2007).

2. Macroscopic analysis

In this section, macroscopic statistical relationship between infrastructure stock accumulation and growth of GDP is discussed with consideration to time delay effect. Then, life cycle cost is estimated by statistical regression.

2.1 Stock and GDP

Macroscopically, difficulty of stock management, especially, sustainability is expected to arise

when required cost for maintenance increases more than GDP, and takes larger portion of national economy. Because stock is essentially accumulation, while GDP is the annual flow, stock naturally tends to surpass GDP as economy grows. Time histories of corresponding growth rates of Japan are given in Fig. 1(b), which show that infrastructure growth follows economic growth.

Cross correlation between growth rates of GDP and stock shown in Fig. 3(a) reveals maximum correlation of 0.8 at time lag of 11 years. Regression between stock and GDP growths with 11 years delay is provided in Fig. 3(b). This delay causes considerable increase of stock when economic growth descends as shown in Fig. 4(a). Stock to GDP ratio was around 0.5 at the high economic growth in 1960s, and increased up to 1.6 at 2000. Increase of stock to GDP ratio ρ by time lag of ΔT can be calculated as

$$\rho = \frac{s_0}{I_0} e^{(\alpha - \alpha_{GDP})\Delta T} \tag{1}$$

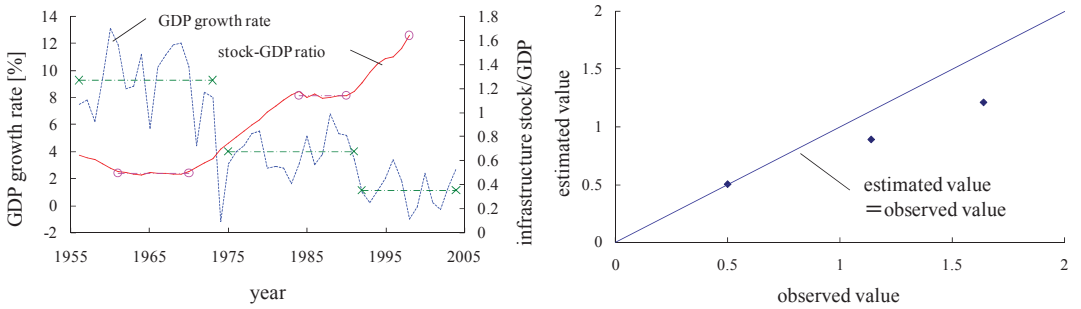

(a) GDP growth rate and stock-GDP ratio (b) Prediction of stock-GDP ratio

Fig. 4 Growth of infrastructure stock and GDP in Japan

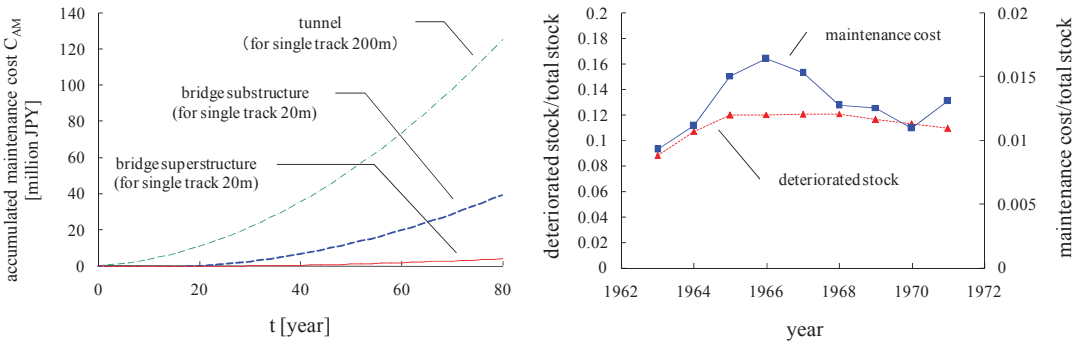

(a) Accumulated maintenance cost (b) Deteriorated stock and maintenance cost

Fig. 5 JNR statistics on stock management

where, s_0: initial stock; I_0: initial GDP; α: stock growth rate; and α_{GDP}: GDP growth rate. Fig. 3(b) indicates that values of α and α_{GDP} are almost equivalent with the time lag of 11 years. Fig. 4(b) shows comparison between the observed value of ρ and estimation by Eq. (1). Stock to GDP ratio is estimated by assuming ΔT =11 years lag, and piece-wise average values of GDP growth rate shown by chain line in Fig. 4(a) are substituted to both α and α_{GDP}. Delay in growth rates is observed to contribute rapid increase of stock, and subsequently relative increase of maintenance cost. This phenomenon would especially be observed at low economic growth conditions followed by high growth, which can be applied to many developed national economies. Delays between growth and socio-economic phenomena are commonly observed and have been pointed out to be one of the major causes of catastrophe in growth (Meadows *et al*. 1972).

2.2 Maintenance cost

Fig. 5(a) shows statistical regression of cumulative maintenance cost statistics collected from Japan National Railway (JNR) before privatization of 1986, normalized by passenger base fare to 1986 currency value. Details of the original data can be found in Abé *et al*. (2007), and Abé and Fujino(2009b). It can be observed that accumulated maintenance cost C_{AM} follows quadratic curve, i.e.

$$C_{AM} = c_m t^2 \tag{2}$$

Average annual life cycle cost which is summation of initial or replacement cost C_I and maintenance cost is given by

$$c = \frac{C_I + C_{AM}}{t} \tag{3}$$

Optimal life to minimize this average cost yields

$$t_{opt} = \sqrt{\frac{C_I}{c_m}} \tag{4}$$

by relationship between arithmetic and geometric means. Corresponding accumulated maintenance cost is calculated as

$$C_{AM} = c_m t_{opt}^2 = C_I \tag{5}$$

which equals replacement cost. Then, optimal annual average of maintenance and replacement cost becomes

$$c_{opt} = \frac{2C_I}{t_{opt}} \tag{6}$$

Therefore, annual maintenance and replacement cost to replacement cost would be $2/t_{opt}$. If structural lifetime is 100 years, annual maintenance and replacement cost would be 2% of the total stock. Because maintenance and replacement cost is expressed by constant ratio to stock, increase of stock to GDP ratio observed in the previous section would directly lead increase of maintenance and replacement cost.

JNR statistics on history of deteriorated stock and maintenance cost from 1963 to 1971 are shown in Fig. 5(b) (Abé and Fujino 2007). Approximately 10% of the stock is deteriorated and this state is maintained by annual spending of about 1 to 1.5% of total stock. Assuming this state is optimal, the expected life would be 130 to 200 years according to Eq. (6).

3. Fundamental feedback control system model

In this section, linear feedback control model of stock management is constructed and verified by the data of Fig. 5(b) as well as cross sectional data collected from local governments in Japan (Abé and Fujino 2009b).

3.1 Feedback control model

Linear feedback control system in matrix form can be expressed as

$$\dot{\mathbf{x}} = \mathbf{A}\mathbf{x} + \mathbf{B}\mathbf{u} \tag{7a}$$

$$\mathbf{u} = \mathbf{C}\mathbf{x} \tag{7b}$$

To match the existing statistics in Fig. 5(b), a single output two state model is employed, where entire stock s and deteriorated stock d are taken as state variables and maintenance cost u is selected as a control input, i.e.

$$\mathbf{x} = \begin{bmatrix} s \\ d \end{bmatrix}, \quad \mathbf{A} = \begin{bmatrix} \alpha & \varepsilon_1 \\ \beta & -\beta \end{bmatrix}, \quad \mathbf{B} = \begin{bmatrix} \varepsilon_2 \\ \delta \end{bmatrix}, \quad \mathbf{C} = \begin{bmatrix} c_s & c_d \end{bmatrix} \tag{7c,d,e,f}$$

Here, structures which need repair are categorized to be deteriorated, and others are defined to be sound. Although ratings of the structures are usually multiple and more than two, judgment for requirement for repair is paid higher attention and inspection specifications are well defined in details for this category in JNR. Therefore, these two states are employed owing to availability and reliability of data. This formulation can be extended to multiple condition ratings by expanding the number of states.

In infrastructure stock management, deteriorated stock would not be abandoned immediately, rather used continuously. Therefore entire stock, which includes deteriorated stock, is chosen as a state variable. Sound stock can be calculated simply by (s-d). Parameter α denotes infrastructure growth rate, β is annual deterioration rate representing ratio of generated deteriorated stock from sound stock for each year, δ stands for maintenance effectiveness to reduce deteriorated stock by $|\delta|$ with unit input of u. To be consistent with physical tendency, the following sign conventions are assumed: i.e., $\alpha > 0$; $\beta > 0$; and $\delta < 0$. Parameters ε_1 represents deteriorated stock influence on stock growth, and ε_2 is the interaction of maintenance cost and infrastructure stock growth. Both effects become prominent when restriction of public investment becomes stringent, and substitution between investment and maintenance is not negligible. In this paper, this interaction is neglected since the tendency is not clearly observed in existing statistics. However, in near future, this substitution could become substantial and would require attention. Feedback gain c_d expresses maintenance following detection of deteriorated stock which corresponds to corrective maintenance, while c_s is planned maintenance regardless of the results of inspection, i.e.,

preventive maintenance.

In this formulation, deterioration rate β does not change before and after the feedback maintenance action, and extension of life by repair is not explicitly modeled. Because maintenance actions cannot be separated in existing inspection records, this treatment of β is consistent with the available data. Change of deterioration rate can be implicitly included at the feedforward term or maintenance effectiveness terms, which will be explained in the next section.

Closed loop solution for the system with initial value of $\boldsymbol{x}_0=[s_0,d_0]^T$ is

$$s = s_0 e^{\alpha t} \tag{8a}$$

$$d = \frac{s_0(\beta+\delta c_s)}{\alpha+\beta-\delta c_d} e^{\alpha t} + \left[d_0 - \frac{s_0(\beta+\delta c_s)}{\alpha+\beta-\delta c_d} \right] e^{(-\beta+\delta c_d)t} \tag{8b}$$

Sign relationship of parameters yields $\alpha>0$, and $-\beta+\delta c_d<0$, and

$$d \to \frac{s_0(\beta+\delta c_s)}{\alpha+\beta-\delta c_d} e^{\alpha t} \tag{9}$$

as t goes to infinity. Representing steady state by subscript ∞, ratio of deteriorated stock to total stock at steady state can be expressed by

$$r_\infty = \frac{d_\infty}{s_\infty} \to \frac{\beta+\delta c_s}{\alpha+\beta-\delta c_d} \tag{10}$$

Deteriorated stock ratio r_∞ decreases with increase of absolute values of α and δ. When $\alpha = \delta = 0$, no new construction and maintenance exist, and r_∞ becomes 1 as expected. Note that even with no maintenance r_∞ does not become 1 when new construction exists as

$$r_\infty = \frac{\beta}{\alpha+\beta} \tag{11}$$

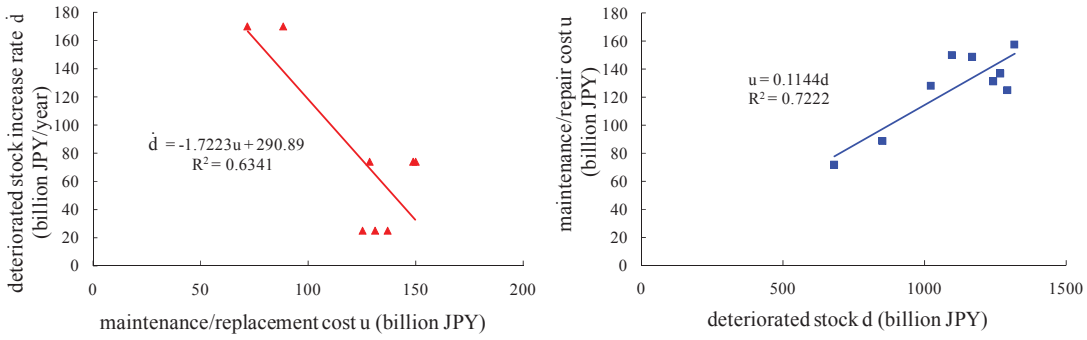

(a) Maintenance cost and deteriorated stock rate (b) Deteriorated stock and maintenance cost

Fig. 6 Regression relationship for parameter estimation

By Eq. (10), steady state value of deteriorated stock can easily be estimated for general conditions.

3.2 Time history analysis

JNR data, given in Fig. 5(b), are employed for time history analysis and verification.

3.2.1 Parameter estimation

Parameter values in the system model are estimated as follows. First, the value of α is estimated to be 0.057 (standard deviation of 0.014) using stock data of the entire period. Then, value of δ is estimated to -1.7 by regression of d by u as shown in Fig. 6(a). Because intercept of regression corresponds to the increase rate of deteriorated stock without maintenance input u, the value β is estimated to 0.034 by dividing intercept value by average sound stock of 8755 billion JPY (standard deviation 1323 billion JPY).

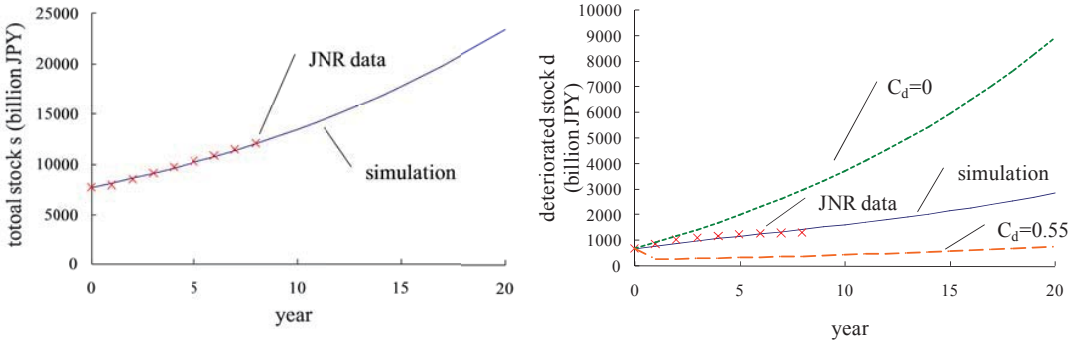

(a) Total stock (b) Deteriorated stock

Fig. 7 Simulation results on stock

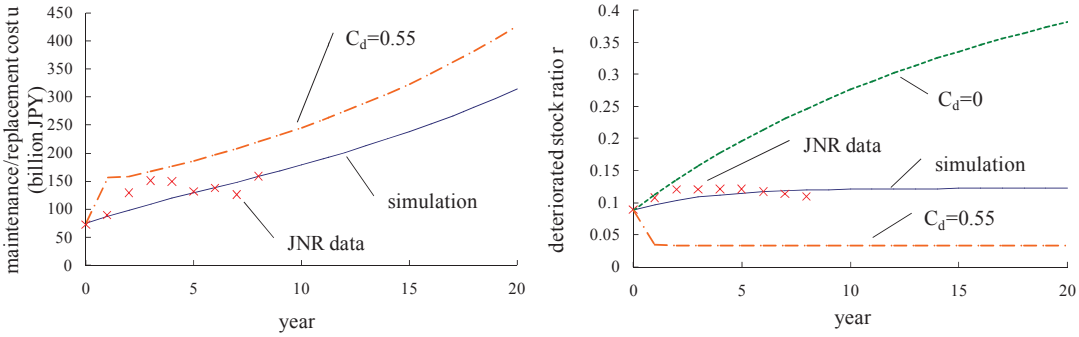

(a) Maintenance cost (b) Deteriorated stock ratio

Fig. 8 Simulation results on maintenance cost and deteriorated stock ratio

Because maintenance budget was calculated based on inspection results of deteriorated stock in management practice of the day, c_s is assumed to be 0, and c_d is estimated by regression of Fig. 6 (b) as 0.11 (coefficient of determination 0.72).

These parameter values are obtained through linear regression because of limitation of number of data points and may be affected by autocorrelation of error. Statistical reliability and accuracy of the parameter values needs to be investigated as larger sets of data become available.

3.2.2 Simulation

Employing above parameter values and applying 1963 values as the initial condition, JNR time history data is simulated. The results are shown in Figs. 7 and 8. Because of data restriction, same data set is used for both parameter estimation and simulation. Hence these results do not verify the model strictly, but it can be seen that average tendencies are reproduced and the model structure is capable of simulating fundamental properties of the system. Oscillating contents in Fig. 8 are not observed in simulation, which could be modeled by extending dimension of the model. Further data collection and improvement are needed for the extension.

In the same figures, parametric study results, where zero and five times of the actual maintenance, i.e., c_d=0 and c_d=0.55, are also plotted. Policy change can easily be simulated by the proposed model.

3.3 Cross sectional analysis

Model parameters can also be identified from cross sectional data, assuming steady state condition. Fig. 9 shows statistics of highway bridges owned by five local governments in 2006 (Abé and Fujino 2009b) arranged by system variables and parameters proposed in this study.

Parameters in the system are identified as follows. First, α is directly calculated from the ratio of new construction to stock for each local government. Then β is derived from Fig. 9. Vertical intercept of Fig. 9(a) corresponds to deteriorated stock ratio for no maintenance. Also, relationship between stock increase rate and deteriorated stock ratio is obtained from Fig. 9(b), hence the value of β is derived from Eq. (10) as 0.022 (standard deviation 0.021).

Finally, δ is obtained by the observation that intercept of Fig. 9(b) gives deteriorated stock ratio without new construction and assuming c_s=0 in Eq. (10), as -1.17 (standard deviation 1.18).
Both β and δ have relatively large standard deviation, which reflect variability of conditions of local governments.

Fig. 10 shows comparison of deteriorated stock ratios calculated using identified parameter values under the assumption of steady state condition and actual values. Correlation coefficient of Fig. 10(b) is 0.69.

Absolute values of parameters β and δ are observed to be smaller than the value identified by JNR statistics in the previous section. Although direct comparison is difficult because of difference of statistical basis, it may be interpreted as the changes of technological and social conditions. Technological development lowered the value of β by improvement of durability, while change of social conditions reduces δ effect by more complicated field work environment and higher quality requirement.

4. Preventive maintenance model

In the previous section, the maintenance action is assumed as feedback of the deteriorated stock found in inspection, which reflects corrective maintenance. In this section, effect of preventive maintenance, which is maintenance action applied to sound stock is studied by enhancing the proposed control system model

4.1 Enhancement of control system model

To model preventive maintenance, feedforward input is augmented and the system is extended to 2-input-2-state system

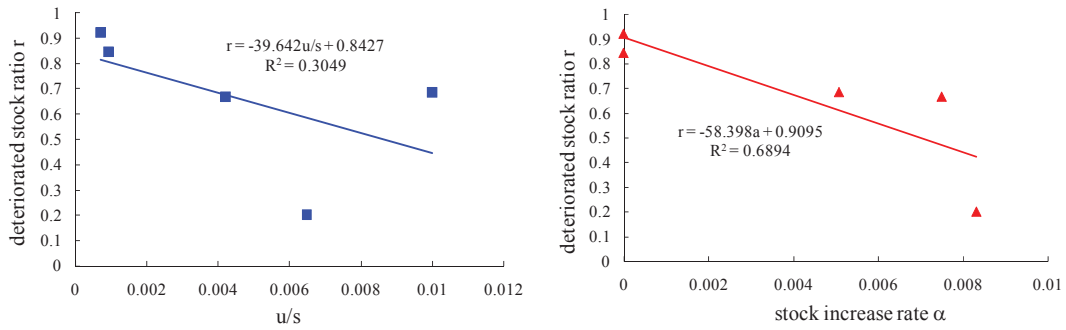

(a) Maintenance cost and deteriorated stock (b) Accuracy of estimation

Fig. 9 Statistics of local governments

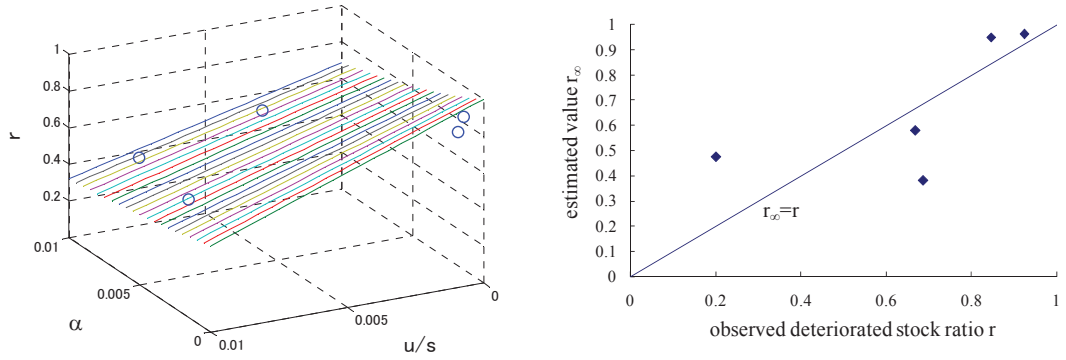

(a) Observation and estimation (b) Accuracy of estimation

Fig. 10 Estimation in cross section data

$$\mathbf{x} = \begin{bmatrix} s \\ d \end{bmatrix}, \quad \mathbf{u} = \begin{bmatrix} u_s \\ u_d \end{bmatrix} \tag{12a,b}$$

$$\mathbf{A} = \begin{bmatrix} \alpha & 0 \\ \beta & -\beta \end{bmatrix}, \mathbf{B} = \begin{bmatrix} 0 & 0 \\ \delta_s & \delta_d \end{bmatrix}, \mathbf{C} = \begin{bmatrix} c_s & -c_s \\ 0 & c_d \end{bmatrix} \tag{12c,d,e}$$

Here, u_s and u_d are inputs to express preventive and corrective maintenance actions. Parameters δ_s and δ_d stand for maintenance effectiveness for preventive and corrective maintenance respectively, and c_s and c_d are corresponding feedforward and feedback gains. Closed loop solution for d is

$$d = \frac{s_0(\beta + \delta_s c_s)}{\alpha + \beta + \delta_s c_s - \delta_d c_d} e^{\alpha t} + \left[d_0 - \frac{s_0(\beta + \delta_s c_s)}{\alpha + \beta + \delta_s c_s - \delta_d c_d} \right] e^{(-\beta + \delta_s c_s - \delta_d c_d)t} \tag{13}$$

Steady state solutions are

$$d_\infty = \frac{s_0(\beta + \delta_s c_s)}{\alpha + \beta + \delta_s c_s - \delta_d c_d} e^{\alpha t} \tag{14a}$$

$$r_\infty = \frac{d_\infty}{s_\infty} = \frac{\beta + \delta_s c_s}{\alpha + \beta + \delta_s c_s - \delta_d c_d} \tag{14b}$$

Maintenance inputs at steady state can be expressed by

$$\frac{u_{s\infty}}{s_\infty} = c_s(1 - r_\infty), \quad \frac{u_{d\infty}}{s_\infty} = c_d r_\infty \tag{15a,b}$$

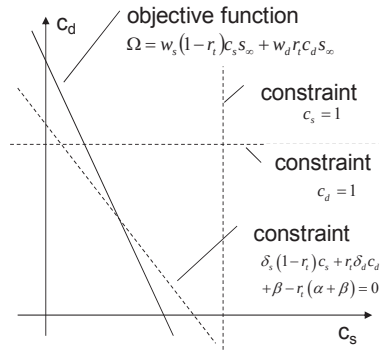

(a) Optimization by linear programming

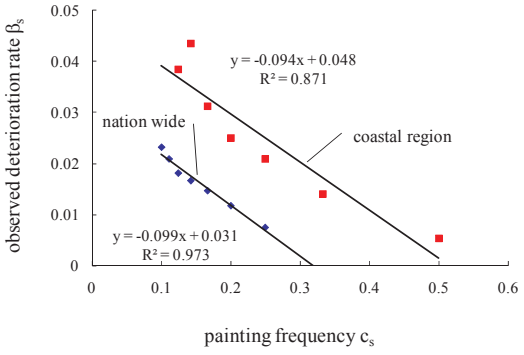

(b) Parameter estimation

Fig. 11 Optimization method and parameters

4.2 Optimization

Optimization of control law, i.e., optimization of preventive and corrective maintenance gains c_s and c_d, is investigated. The optimization problem for stock management can be described as; i) target deteriorated stock ratio by minimum cost; or 2) minimization of deteriorated stock ratio by given budget. Because, mathematically, both optimization objectives can be transformed to fundamentally the same linear programming problem, the first optimization problem is solved in this paper.

Objective function is expressed by weighted sum of preventive and corrective maintenance at steady state

$$\Omega = w_s u_{s\infty} + w_d u_{d\infty} \tag{16}$$

If w_s and w_d are selected as preventive and corrective maintenance costs for unit stock, the sum Ω becomes total maintenance cost. Corresponding constraint is to keep target deteriorated stock ratio as specified value r_t

$$r_t = r_\infty = \frac{\beta + \delta_s c_s}{\alpha + \beta + \delta_s c_s - \delta_d c_d} \tag{17}$$

This optimization problem can be rewritten in terms of management variables, c_s and c_d. The objective function is now

$$\Omega = w_s (1 - r_t) c_s s_\infty + w_d r_t c_d s_\infty \tag{18a}$$

with constraints,

$$\delta_s (1 - r_t) c_s + r_t \delta_d c_d + \beta - r_t (\alpha + \beta) = 0\,, \quad 0 \le c_s \le 1\,, \quad 0 \le c_d \le 1 \tag{18b,c,d}$$

This optimization problem is a typical linear programming problem, which is shown Fig. 11(a). The condition for existence of solution is that the constraint has domain within the first quadrant.

$$\beta - r_t (\alpha + \beta) \ge 0 \quad \text{or} \quad r_t \le \frac{\beta}{\alpha + \beta} \tag{19a,b}$$

If this condition is not satisfied, required r_t is achieved without any maintenance input.

In Fig. 11(a), inclination of the objective function is given by

$$\frac{w_s}{w_d}\left(1 - \frac{1}{r_t}\right) \tag{20a}$$

and inclination of constraint is

$$\frac{\delta_s}{\delta_d}\left(1 - \frac{1}{r_t}\right) \tag{20b}$$

If $w_s/w_d < \delta_s/\delta_d$, inclination of constraint is steeper than the objective function. Hence, optimal solution is to minimize the corrective maintenance, or equivalently, to maximize preventive maintenance, as

for $\dfrac{r_t(\alpha+\beta)-\beta}{\delta_s(1-r_t)}<1$

$$c_s=\frac{r_t(\alpha+\beta)-\beta}{\delta_s(1-r_t)},\quad c_d=0,\quad \Omega=\frac{w_s\left(r_t(\alpha+\beta)-\beta\right)}{\delta_s} \tag{21a,b,c}$$

for $\dfrac{r_t(\alpha+\beta)-\beta}{\delta_s(1-r_t)}\geq 1$

$$c_s=1,\quad c_d=\frac{r_t(\alpha+\beta)-\beta-\delta_s(1-r_t)}{r_t\delta_d} \tag{22a,b}$$

$$\Omega=w_s(1-r_t)+\frac{w_d\left(r_t(\alpha+\beta)-\beta-\delta_s(1-r_t)\right)}{\delta_d} \tag{22c}$$

On the other hand, if $w_s/w_d > \delta_s/\delta_d$,

for $\dfrac{r_t(\alpha+\beta)-\beta}{r_t\delta_d}<1$

$$c_s=0,\quad c_d=\frac{r_t(\alpha+\beta)-\beta}{r_t\delta_d},\quad \Omega=\frac{w_d\left(r_t(\alpha+\beta)-\beta\right)}{\delta_d} \tag{23a,b,c}$$

for $\dfrac{r_t(\alpha+\beta)-\beta}{r_t\delta_d}\geq 1$

$$c_s=\frac{r_t(\alpha+\beta)-\beta-r_t\delta_d}{\delta_s(1-r_t)},\quad c_d=1,\quad \Omega=\frac{w_s\left(r_t(\alpha+\beta)-\beta-r_t\delta_d\right)}{\delta_s}+w_d r_t \tag{24a,b,c}$$

The expression $w_s/w_d < \delta_s/\delta_d$ can be transformed to $|\delta_d/w_d|<|\delta_s/w_s|$, which indicates that the cost effectiveness of preventive maintenance is higher. Similarly, $w_s/w_d > \delta_s/\delta_d$ yields $|\delta_d/w_d|>|\delta_s/w_s|$, and shows relative advantage of corrective maintenance. In this way, the optimization solutions can also be interpreted intuitively.

5. Application to stock management

In this section, management application of the optimal solution is discussed followed by parameter estimation described in the first half. Among the parameters in the system model, α corresponds to new construction, which is assumed to be not directly related to maintenance and given exogenously. Parameters which need to be identified are: β, δ_s and δ_d.

Here, corrosion of steel bridges is taken as an example. Major preventive maintenance for corrosion is painting. Fig. 11(b) shows comparison of corrosion life and painting frequency reported by JNR (Abé *et al*. 2007, Abé *et al*. 2008). Note that expected life is the inverse of deterioration rate β, and c_s corresponds to frequency of maintenance per year. Apparent

deterioration rate β_s with preventive maintenance can be written as

$$\beta_s = \beta + \delta_s c_s \tag{25}$$

Hence, inclination of regression yields to preventive maintenance effect δ_s and vertical intercept equals to deterioration rate β. Deterioration rate at the coastal area is identified as 0.0487 and national average 0.0317. Preventive maintenance effect δ_s is -0.0946 for coastal area and -0.0995 for national average. Although deterioration rates are different, preventive maintenance effects are almost similar. In the following analysis, β =0.03, and δ_s =-0.1 are selected for simplicity.

One of the popular corrective maintenance measures for cross-section loss due to corrosion is cover plate attachment. Expected lives before and after corrective maintenance are considered to be different, and the ratio gives the corrective maintenance effect as

$$\delta_d = -\frac{\beta}{\beta_d} \tag{26}$$

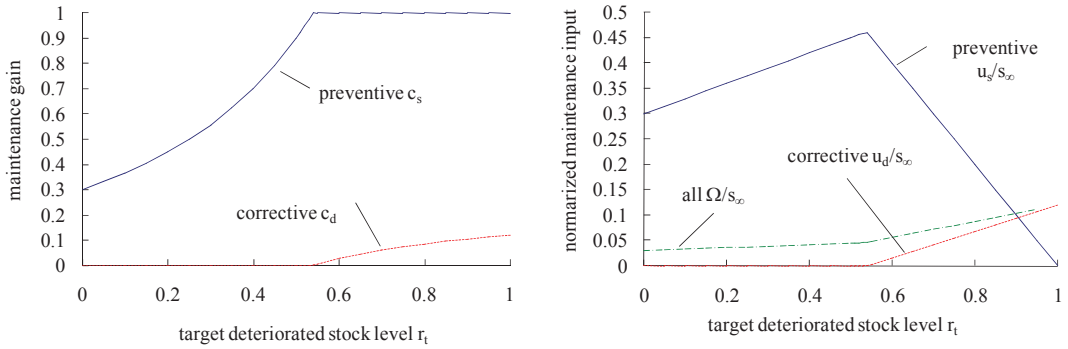

(a) Maintenance ratio (b) Normalized maintenance input

Fig. 12 Target deteriorated stock level and maintenance strategy (w_s=0.1, w_d=1)

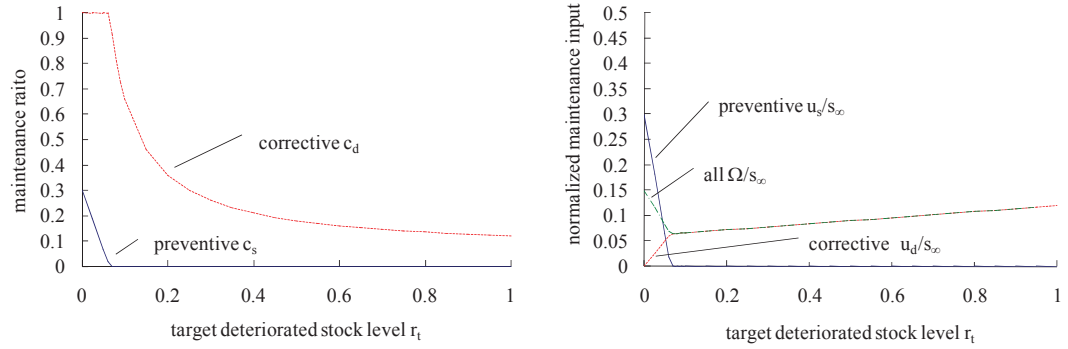

(a) Maintenance ratio (b) Normalized maintenance inpu

Fig. 13 Target deteriorated stock level and maintenance strategy (w_s=0.5, w_d=1)

In other words, repaired stock and sound stock are not distinguished in the proposed model, corrective maintenance effect is modified to keep the deteriorated stock equivalent. Because in plate welding repair, expected life was assumed to be an half of the original life in JNR practice (Abé *et al*. 2007), δ_d =-0.5 is selected in the following analysis.

Applying these parameters to the results in the previous section, preventive maintenance becomes superior in this example of corrosion when $w_s/w_d<\delta_s/\delta_d = (-0.1)/(-0.5) = 0.2$, which means preventive maintenance cost represented by w_s is cheaper than one fifth of the corrective maintenance cost w_d.

Fig. 12 shows target deteriorated stock level r_t and corresponding optimal c_s and c_d as well as maintenance quantity u_s, u_d, and Ω. In the analysis, growth rate α is taken 0 for simplicity. Similar tendency is observed for α around several percent. In this analysis, w_s is taken to be one-tenth of w_d, i.e., w_s =0.1 and w_d =1, which implies preventive maintenance is advantageous. When target deteriorated stock level r_t is small, only preventive maintenance is selected as seen Fig. 12(a). As target level increases, corrective maintenance are also included, because substantial deteriorated stock is allowed. To reduce maintenance quantity Ω, as shown in Fig. 12(b), lowering target level and increasing preventive maintenance is advantageous. Target level r_t zero is observed to give minimal maintenance theoretically. Note that, in reality, unexpected or unknown defects can appear, so corrective maintenance cannot be eliminated entirely.

Fig. 13 shows an example with w_s =0.5 and w_d =1, where corrective maintenance becomes relatively advantageous. Although corrective maintenance is superior in wider range, preventive maintenance should also be included to reduce deteriorated stock level r_t at lower values as shown in Fig. 13(a). Fig. 13(b) shows that total amount of maintenance is lowest at r_t =0.07. In order to reduce r_t below this value, increase of preventive maintenance is required, while preventive maintenance is relatively expensive in this case.

6. Conclusions

In this paper, dynamic modeling of infrastructure stock and its management are studied using statistics mainly collected by JNR before privatization of 1986. Major conclusions are as follows:

- Stock management cost is discussed based on macroscopic statistical analysis. Time history analysis of national economic statistics indicates stock management burden relative to economy tends to become larger at low economic growth followed by high growth, which is commonly observed in developed economies.
- Control system model for stock management is constructed and its validity is discussed based on estimated parameters from JNR statistics. By modeling maintenance actions as control input, dynamic behavior of stock is simulated and verified. Assuming steady state conditions, the model is also shown to be applicable to cross sectional data.
- The proposed model is enhanced so that both preventive and corrective maintenance can be included as system inputs. Optimal management strategy, which is combination of preventive and corrective maintenance, is derived based on estimated parameter values for corrosion of steel bridges. Relative advantage of preventive maintenance is shown when target deteriorated stock level is lower.

The proposed model is based on observed statistical dynamics of stock. For the project level or network level with small number of structures, where statistical treatment is not appropriate, further studies would be required to extend the concept to uncertainty of systems.

Acknowledgements

The research work in this paper is supported by CREST Advanced Integrated Sensing Technologies Program of Japan Science and Technology Agency, "Monitoring and Management of Disaster and Accident Risk for Urban Infrastructure (Principle Investigator: Prof. Yozo Fujino)."

References

Abé, M., Abe, M. and Fujino, Y. (2007), "Development and characteristics of infrastructure maintenance of Japan with emphasis on bridges", *J. Japan Soc. Civil Engineers, Series F*, **63**, 190-199 (in Japanese).

Abé, M. and Fujino. Y. (2007), "Reanalysis of life cycle costs in management of steel railway bridges", *Proceedings of the 2007 International Symposium on Integrated Life-Cycle Design and Management of Infrastructure*, Shanghai, China.

Abé, M., Fujino, Y. and Abe, M. (2008), "Evaluation of maintenance strategies by infinite horizon life-cycle costs", *J. Japan Soc. Civil Engineers, Series A*, **64**, 814-824 (in Japanese).

Abé, M. and Fujino, Y. (2009a), "Bridge Monitoring in Japan", *Encyclopedia of Structural Health Monitoring*, Chapter 125, 2131-2148, John Wiley & Sons Inc.

Abé, M. and Fujino, Y. (2009b), "Macroscopic analysis on stock management through control system theory", *J. Japan Soc. Civil Engineers, Series A*, **65**, 474-486 (in Japanese).

Abé, M., Fujino, Y. and Abe, M. (2012), "Application of linear system model for stock management to preventive maintenance", *J. Japan Soc. Civil Engineers, Series A1*, **68**(2), 325-330 (in Japanese).

Abé, M. and Shimamura, M. (2014), "Performance of railway bridges during 2011 Tohoku Earthquake", *J. Perform. Constr. Fac.*, **28**(1), 13-23.

Abé, M., Shimamura, M. and Fujino, Y. (2014), "Risk management and monitoring of Japanese railway bridges", *Proceedings of the ICE - Forensic Engineering*, **167**(2), 88-98.

Aschauer, D.A. (1990), *Public Investment and Private Sector Growth*, Economic Policy Institute.

Barro, R.J. (1990), "Government spending in a simple model of endogenous growth", *J. Political Economy*, **98**(5Pt.2), 103-125.

Brogan,W.L. (1990), *Modern Control Theory*, 3rd Ed., Prentice Hall.

Fujino, Y. and Abé, M. (2007), "Characterization of risk, hazard and vulnerability in natural disasters", *Proceedings of the 10th International Conference on Applications of Statistics and Probability in Civil Engineering*, Tokyo.

Fujino, Y., Siringoringo, D.M. and Abé, M. (2009), "The needs for advanced sensor technology for risk assessment of civil infrastructure", *Smart Struct. Syst.*, **5**(2), 173-191.

Gramlich, E.M. (1994), "Infrastructure investment: a review essay", *J. Economic Literature*, **32**(3), 1176-1196.

ISO 55000 (2014) Asset management - Overview, principles and terminology, International Organization for Standardization.

Kalaitzidakis, P. and Kalyvitis, S. (2004), "On the macroeconomic implications of maintenance in public capital", *J. Public Economics*, **88**(3-4), 695-712.

Meadows, D.H., Meadows, D.L., Randers, J. and Behrens, W.W.III (1972), *The Limits to Growth*, Universe Books.

Uddin, W., Hudson, W. and Haas, R. (2013), Public Infrastructure Asset Management, 2nd Ed.,

McGraw-Hill Professional.
Wenzel, H. (2013), Industrial Safety and Life Cycle Engineering, Technologies/Standards/Applications, IRIS.
Yanev, B. (2007), Bridge Management, Wiley.

Smart Structures and Systems, *Vol. 15, No. 3 (2015) 627-643*
DOI: http://dx.doi.org/10.12989/sss.2015.15.3.627

Cable with discrete negative stiffness device and viscous damper: passive realization and general characteristics

Lin Chen[1a], Limin Sun[1b] and Satish Nagarajaiah[*2]

[1]*State Key Laboratory for Disaster Reduction of Civil Engineering, Tongji University, Shanghai 200092, P.R. China*
[2]*Department of Civil and Environmental Engineering, and Dept. of Mechanical Engineering, Rice University, Houston, TX 77005, USA*

(Received November 27, 2014, Revised February 8, 2015, Accepted February 15, 2015)

Abstract. Negative stiffness, previously emulated by active or semi-active control for cable vibration mitigation, is realized passively using a self-contained highly compressed spring, the negative stiffness device (NSD).The NSD installed in parallel with a viscous damper (VD) in the vicinity of cable anchorage, enables increment of damper deformation during cable vibrations and hence increases the attainable cable damping. Considering the small cable displacement at the damper location, even with the weakening device, the force provided by the NSD-VD assembly is approximately linear. Complex frequency analysis has thus been conducted to evaluate the damping effect of the assembly on the cable; the displacement-dependent negative stiffness is further accounted by numerical analysis, validating the accuracy of the linear approximation for practical ranges of cable and NSD configurations. The NSD is confirmed to be a practical and cost-effective solution to improve the modal damping of a cable provided by an external damper, especially for super-long cables where the damper location is particularly limited. Moreover, mathematically, a linear negative stiffness and viscous damping assembly has proven capability to represent active or semi-active control for simplified cable vibration analysis as reported in the literature, while in these studies only the assembly located near cable anchorage has been addressed. It is of considerable interest to understand the general characteristics of a cable with the assembly relieving the location restriction, since it is quite practical to have an active controller installed at arbitrary location along the cable span such as by hanging an active tuned mass damper. In this paper the cable frequency variations and damping evolutions with respect to the arbitrary assembly location are then evaluated and compared to those of a taut cable with a viscous damper at arbitrary location, and novel frequency shifts are observed. The characterized complex frequencies presented in this paper can be used for preliminary damping effect evaluation of an adaptive passive or semi-active or active device for cable vibration control.

Keywords: stay cable; vibration control; negative stiffness device; viscous damping; frequency loci

1. Introduction

Cable damped by a local damper, since first considered in 1980s (Kovacs 1982), has received

∗Corresponding author, Professor, E-mail: Satish.Nagarajaiah@rice.edu
[a] Ph.D. Candidate, E-mail: l.chen.tj@gmail.com
[b] Professor, E-mail: lmsun@tongji.edu.cn

http://www.techno-press.org/?journal=sss&subpage=8 ISSN: 1738-1584 (Print), 1738-1991 (Online)

considerable attention subsequently, because cable/damper systems are of both theoretical interest and practical significance. In the context of structural control (Spencer and Nagarajaiah 2003), cables are crucial structural components of cable-stayed bridges, but susceptible to problematic vibrations (Hikami and Shiraishi 1988), posing interesting control problems which can be solved analytically due to the homogeneous cable properties and extended to other more complex or discrete systems with local control units (Main and Krenk 2005, Krenk and Høgsberg 2014). Besides, most of cable vibrations of concern can be suppressed by the attached damper, and associated implementations are worldwide (Chen *et al*. 2003, Fujino *et al*. 2012).

The basic problem of a cable/damper system is the achieved cable damping when a linear viscous damper (VD) is attached near cable support, which has been fully solved (Pacheco *et al*. 1993, Krenk 2000, Tabatabai and Mehrabi 2000, Main and Jones 2002a). Further, to simulate real cable/damper systems, other parameters pertaining to the cable have been included, such as cable bending stiffness (Hoang and Fujino 2007, Main and Jones 2007a, b), cable sag (Xu *et al*. 1998, Krenk and Nielsen 2002) and inclination (Xu and Yu 1998); dampers apart from the linear viscous type have also been addressed, such as by taking damper intrinsic stiffness (Zhou *et al*. 2014a), nonlinearity (Main and Jones 2002b, Hoang and Fujino 2009), and damper support flexibility (Sun and Huang 2008, Huang and Jones 2011) into account. Especially, three key parameters, namely cable sag, flexibility and damper support stiffness, have been treated together to formulate general formulas for practical damper design (Fujino and Hoang 2008). In addition, research interest has also extended to a cable with a damper at arbitrary location (Main and Jones 2002a, Main and Jones 2007a, Sun and Chen 2015) or with two dampers (Caracoglia and Jones 2007a, Hoang and Fujino 2008), and hybrid cable networks with both cross-ties and dampers (Caracoglia and Jones 2007b, Zhou *et al*. 2014b).

The aforementioned studies indicate that positive stiffness introduced at the damper location (due to the damper intrinsic stiffness) decreases the relative damper deformation during cable vibrations, and hence impairs the damping effect that can be attained. The negative stiffness realized by active control or equivalently by semi-active control, conversely, enables the increment of the displacement of the cable at the damper location and hence improves the damper performance. Similar findings were presented in Krenk and Høgsberg (2005) where a damper with fractional damping was considered with parameters corresponding to negative stiffness, which indicated that the damper would provide a phase lead instead of phase lag damping force (Høgsberg and Krenk 2006); the added mass due to the damper installation was also found to have an weakening effect, thus increasing the damping effect.

Negative stiffness characteristics were originally observed from the hysteretic loops produced by friction, semi-active or active algorithm for structural protection (Iemura *et al.*2003, 2006), referred to as apparent negative stiffness or pseudo-negative-stiffness (PNS). The important role of PNS played in semi-active and active strategies has been subsequently recognized, and the idea of PNS has therefore been widely resorted to for optimal controller design, associated studies including Iemura*et al*.(2009), Li *et al*. (2008), Ou and Li (2010), Høgsberg (2011), Weber and Boston (2011) and to name a few. Notwithstanding, it is until only recently that true passive negative stiffness (not pseudo-negative stiffness achieved through active or semi-active means) has been achieved by adaptive passive negative stiffness device (NSD) (Sarlis *et al*. 2013, Pasala *et al*. 2013, 2014). The NSD devices have been theoretically and experimentally evaluated for their effectiveness and advantages, when combined with viscous dampers (VD), for seismic protection.

In this study, the passive NSD is applied for the first time to weaken a cable at the damper location and thus improve the damping effect, as a cost-effective alternative of semi-active or active

cable control (Johnson *et al*. 2003, 2007). Besides, noteworthy is that the linear NSD-VD assembly, or a so-called pseudo-viscoelastic (PVE) damper (Li *et al*. 2008) can replace an active or semi-active device for dynamic analysis based on the equivalence of control force-deformation curves corresponding, respectively, to the (semi-) active device and the PVE damper. This simple strategy has adequate accuracy while avoiding the time-consuming numerical integration which is required to solve the responses of a cable equipped semi-active or active devices, such as magneto-rheological (MR) damper or active tuned mass damper (Johnson *et al*. 2003, 2007, Huang *et al*. 2012). However, only the case when the PVE damper located near cable support has been treated in the aforementioned studies. It is also important to evaluate the effect of arbitrary location of such (semi-) active and passive devices along the cable, for example, by hanging a smart tuned mass damper (Nagarajaiah 2009, Weber *et al*. 2011, Sun *et al.* 2014, Sun and Nagarajaiah 2014).Thus the understanding of a taut cable with a NSD-VD assembly at arbitrary location is of theoretical interest, since it can in turn guide the design of an adaptive passive or semi-active or active control device for cable vibration mitigation.

This paper first presents the passive realization of the negative stiffness device at the damper location of a cable, and then deals with the nonlinear behavior of the NSD. The general dynamic characteristics are subsequently discussed for the taut cable with a linear NSD-VD assembly at arbitrary location.

2. Passive negative stiffness device for cable vibration control

2.1 Negative sitffness device

Passively, negative stiffness can be realized in the lateral direction of a pre-compressed spring, and magnification mechanism can be added accordingly (Sarlis *et al*. 2013) in practice. The pre-compressed spring is directly used here without magnification, while associated results can be extended to the case when magnification mechanism is added. The NSD is arranged in parallel with a viscous damper, resulting an assembly illustrated in Fig. 1, where, k_s is the stiffness of the pre-compressed spring; l is the compressed spring length and c_d is the damper coefficient. The force provided by the assembly is

$$F_d(u) = -c_d\dot{u} + k_s\left[\Delta - \left(\sqrt{l^2+u^2} - l\right)\right]\frac{u}{\sqrt{l^2+u^2}} \tag{1}$$

where $u(t)$ is cable displacement at the damper and Δ is the spring initial deformation.

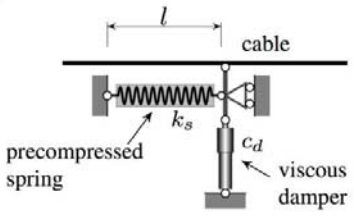

Fig. 1 Schematic of the NSD-VD assembly for cable vibration control

It is worth noting that since the external passive damper is usually installed near one cable anchorage, the displacement at the damper is quite small during cable vibrations, less than 10 mm typically. Considering the length of a compressed spring of l= 1 m, apparently $u<<l$, the negative stiffness is almost a constant and then the force is approximated as

$$F_d(u) \approx -c_d\dot{u} - ku, \quad k = -k_s\frac{\Delta}{l} \tag{2}$$

where k is the approximate negative stiffness coefficient.

2.2 Cable attached with NSD-VD assembly

A taut cable with a NSD-VD assembly is illustrated in Fig. 2, where, m = cable mass per unit, c = cable intrinsic damping, T = cable tension, L = cable length, and x_d denotes the damper location. The cable is still modeled as a taut string owing to practical considerations: cable inclination or sag of practical range for most stay cables has been found insignificant for cable dynamics (Irvine 1981, Tabatabai and Mehrabi 2000); and the bending stiffness of a cable is generally small and difficult to be precisely measured in practice.

2.2.1 Linear approximation

Complex modal analysis (Krenk 2000) can be conducted to appreciate the cable damping due to a linear damper in parallel with a linear spring regardless of the positive or negative spring constant. By defining the following non-dimensional parameters

$$\bar{k} = \frac{kx_d}{T}, \bar{c}_d = \frac{c_d}{\sqrt{Tm}} \tag{3}$$

the maximal modal damping can be then expressed (Krenk and Høgsberg 2005, Li *et al*. 2008) as

$$\zeta_{i,\mathrm{opt}} \approx \frac{1}{1+\bar{k}} \cdot \frac{x_d}{2L} \tag{4}$$

and the corresponding optimal non-dimensional damper coefficient is approximated by

$$\bar{c}_{d,\mathrm{opt}} \approx \left(1+\bar{k}\right) \cdot \frac{1}{i\pi\, x_d/L} \tag{5}$$

Further, following the "universal form" (Krenk and Høgsberg 2005), the additional damping due to an arbitrary damper for mode i is expressed as

$$\zeta_i \approx \frac{x_d/L}{1+\bar{k}} \cdot \frac{\bar{c}_d/\bar{c}_{d,\mathrm{opt}}}{1+\left(\bar{c}_d/\bar{c}_{d,\mathrm{opt}}\right)^2} \tag{6}$$

The preceding equations suggest that when $\bar{k} < 0$ (the system stability requires that $\bar{k} > -1$, Li *et al*. 2008) the additional damping is increased and correspondingly the optimal damper coefficient is decreased for each cable mode, which can be clearly seen from Fig. 3.

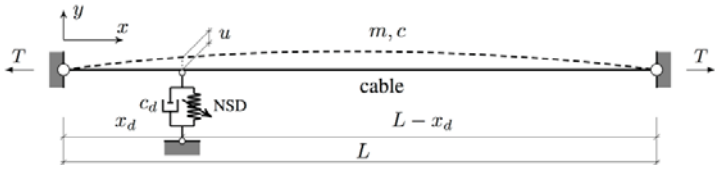

Fig. 2 A taut cable with a NSD-VD assembly

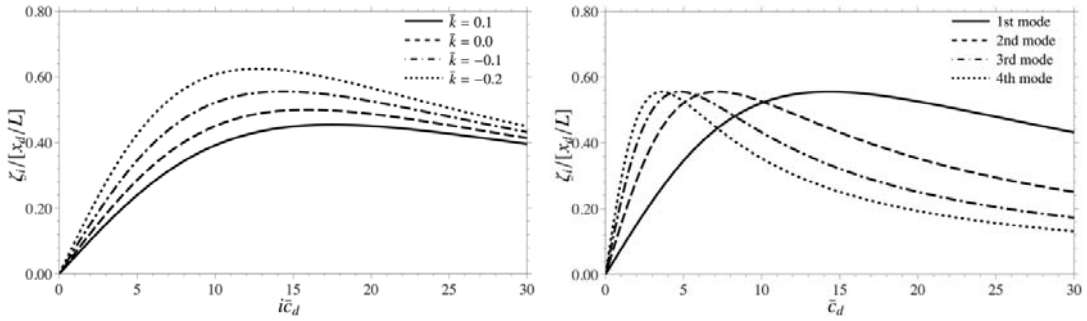

(a) for varied $\bar{k}$ (b) for varied modes when $\bar{k}$ =-0.1

Fig. 3 Damping curves of a cable with a NSD-VD assembly at $\bar{x}_d$ =0.02

2.2.2 Effect of displacement-dependent negative stiffness

Cable discretized by modal decomposition

Taking the nonlinear force generated by the assembly into account, the continuous cable has to be decomposed in modal coordinate for numerical analysis (Pacheco *et al*. 1993, Johnson *et al*. 2007, Li *et al*. 2008). Motions of the cable/damper system are governed by the following non-dimensional equation

$$\ddot{\bar{y}}\left(\bar{x},\bar{t}\right)+\bar{c}\cdot\dot{\bar{y}}\left(\bar{x},\bar{t}\right)-\frac{1}{\pi^2}\bar{y}''\left(\bar{x},\bar{t}\right)=\bar{f}\left(\bar{x},\bar{t}\right)+\bar{F}_d\bar{\delta}\left(\bar{x},\bar{x}_d\right) \tag{7}$$

where those non-dimensional properties, shown with hats, are related to the cable parameters by

$$\bar{t}=\omega_0 t,\bar{x}=\frac{x}{L},\bar{c}=\frac{c}{m\omega_0},\bar{y}\left(\bar{x},\bar{t}\right)=\frac{y\left(x,t\right)}{L},\omega_0=\frac{\pi}{L}\sqrt{\frac{T}{m}} \tag{8}$$

in which ω_0 is the fundamental natural frequency of a taut cable. The excitation force and the damping force are also normalized as

$$\bar{\delta}\left(\bar{x}-\bar{x}_d\right)=L\delta\left(\bar{x}-\bar{x}_d\right),\ \bar{f}\left(\bar{x},\bar{t}\right)=\frac{Lf\left(x,t\right)}{\pi^2 T},\ \bar{F}_d\left(\bar{u}\right)=\frac{F_d\left(u\right)}{\pi^2 T} \tag{9}$$

Substitution of Eqs. (1) and (3) into Eq. (9) leads to

$$\bar{F}_d\left(\bar{u}\right)=-\frac{\bar{c}_d}{\pi}\dot{\bar{u}}-\frac{\bar{k}}{\pi^2\bar{x}_d}\left[\frac{1}{\sqrt{1+\left(\bar{u}/\bar{l}\right)^2}}\left(1+\frac{1}{\bar{\Delta}}\right)-\frac{1}{\bar{\Delta}}\right]\bar{u} \tag{10}$$

with the normalized initial spring deformation $\bar{\Delta}=\Delta/l$ and compressed spring length $\bar{l}=l/L$.

In order to solve Eq. (7), cable transverse deflection is usually approximated using a finite series as $\bar{y}(\bar{x},\bar{t})=\sum_{i=1}^{N}q_i(\bar{t})\phi_i(\bar{x})$, where $q_i(\bar{t})$ is generalized displacement and $\phi_i(\bar{x})$ is the shape function. The subscript *i* indicates the mode number and *N* denotes the total number of cable modes retained. The continuous system is thereby discretized to

$$\mathbf{M}\ddot{\mathbf{q}}+\mathbf{C}\dot{\mathbf{q}}+\mathbf{K}\mathbf{q}=\bar{\mathbf{f}}+\left[\phi_i\left(\bar{x}_d\right)\right]\cdot\bar{F}_d \tag{11}$$

where $q=[q_1\,q_2\,q_3\,\ldots q_N]^{\mathrm{T}}$ and the superscript $^{\mathrm{T}}$ indicates a transpose operation. The mass, damping and stiffness matrices depend on the set of shape functions used: sine series, corresponding to mode shapes of a taut string, were traditionally used (Pacheco *et al*. 1993); Johnson *et al*. (2007) further introduced the static deflection shape of a string with a concentrated force at the damper location in addition to the sine series, to reduce the number of modes needed for numerical convergence; besides, Main (2002) found that two typical mode shapes, namely the undamped mode shape and the mode shape corresponding to the cable clamped at the damper location, are sufficient to capture near resonant responses of that mode. Here, the widely validated shape functions proposed by Johnson *et al*. (2007) are used and the static deflection shape function is designated as mode 1. The mass and stiffness matrices, $\mathbf{M}=[m_{i_1i_2}]$ and $\mathbf{K}=[k_{i_1i_2}]$, are given as

$$m_{i_1i_2}=\begin{cases}\dfrac{1}{3} & i_1=i_2=1\\ \delta_{i_1i_2}/2 & i_1>1,i_2>1,\\ \dfrac{\sin\left(i_m\pi\bar{x}_d\right)}{\bar{x}_d\left(1-\bar{x}_d\right)i_m^2\pi^2} & \text{otherwise}\end{cases}\qquad k_{i_1i_2}=\begin{cases}\dfrac{1}{\bar{x}_d\left(1-\bar{x}_d\right)\pi^2} & i_1=i_2=1\\ \left(i_1-1\right)^2\delta_{i_1i_2}/2 & i_1>1,i_2>1\\ \dfrac{\sin\left(i_m\pi\bar{x}_d\right)}{\bar{x}_d\left(1-\bar{x}_d\right)\pi^2} & \text{otherwise}\end{cases} \tag{12}$$

where i_1 and i_2 are mode indices, and $i_m=\max(i_1,i_2)$-1. The damping matrix is $\mathbf{C}=\bar{c}\mathbf{M}$.

Numerical results

Given cable parameters, external excitations and the control force at damper location, cable responses can be obtained by integrating Eq. (11). It is important to point out that the nonlinearity considered here is light ($u<<l$) and local ($x_d<<L$) so that cable free decay can still be used to capture the additional damping due to the external damping device.

With the focus on cable resonant vibrations, the excitation force is expressed as

$$\bar{f}\left(\bar{x},\bar{t}\right)=p\sin\left(i_p\bar{t}\right)\phi_{i_p+1}\left(\bar{x}\right) \tag{13}$$

$$\bar{\mathbf{f}}=p\sin\left(i_p\bar{t}\right)\left[\phi_p\right] \tag{14}$$

where $\phi_p(1)=\sin(i_p\pi\bar{x}_d)/[\bar{x}_d(1-\bar{x}_d)i_p^2\pi^2]$, $\phi_p(i_p+1)=1/2$ and $\phi_p(i)=0$ otherwise. Index i_p denotes the mode to be excited and *p* represent the amplitude of the excitation.

Since the damper location is much more limited for long cables where NSDs are needed, $\bar{x}_d$ = 0.02 is adopted here for exemplification. A NSD of $\bar{k}$ = -0.33 is attached to increase the attainable damping by 50 percent over that provided by a viscous damper according to Eq. (4), and the corresponding optimum damper coefficient for the first mode is computed from Eq. (5). On the configuration of the NSD, it is considered that $\bar{\Delta}$ = 0.5, namely the pre-compression is half of the compressed spring length, and $\bar{l}$ =0.005 (e.g., *l*=1 m for a cable of *L*=200 m). The resonant responses for the first mode were numerically integrated for the cable with the NSD in parallel with an optimum damper under the excitation $p=1\times10^{-4}$, where N=20 modes were retained (Johnson *et al*. 2007). The cable was excited for 53 periods to reach the stationary vibration and then allowed to freely decay. The response at the mid-span is illustrated in Fig. 4(a), and corresponding damping ratio is computed from the peaks of the free decay response as illustrated in Fig. 4(b), ζ_1=0.0153, which is a bit larger than 0.015 obtained from Eq. (4). Fig. 4(b) also shows that the damping ratio is almost displacement-independent in this case.

As demonstrated by the control force versus the cable velocity at the damper in Fig. 5(b), the assembly is able to provide both dissipative and non-dissipative forces at the damper location, which is advantageous to semi-active control where only dissipative force is generated (Johnson *et al*. 2007). Since the nonlinear force is generated merely by the NSD, the force due to the negative stiffness introduced to the cable, as the second term in Eq. (1) or Eq. (10), denoted as $\bar{F}_{\mathrm{ns}}$, is plotted in Fig. 5(a) with respect to the damper deformation, and the total control force is also showed. It is clearly shown that in this case the negative stiffness is almost constant, because $\bar{u}$ is below 3×10^{-4} that is far less than $\bar{l}$ =0.005.

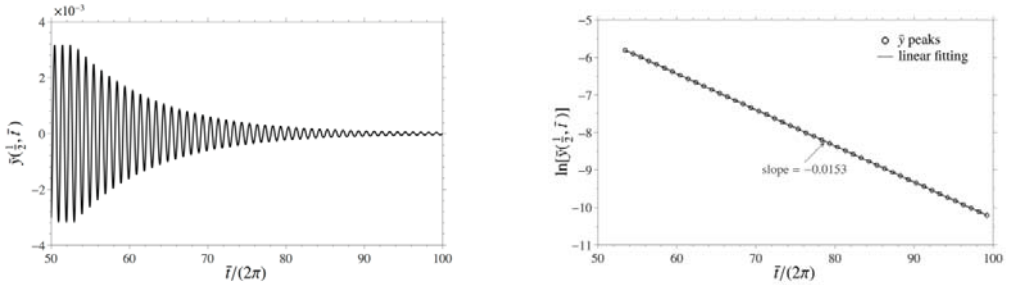

(a) free decay at the mid-span (b) peaks of free decay and corresponding fitted line

Fig. 4 Resonant response of a cable with a NSD and an optimum damper, the first mode case

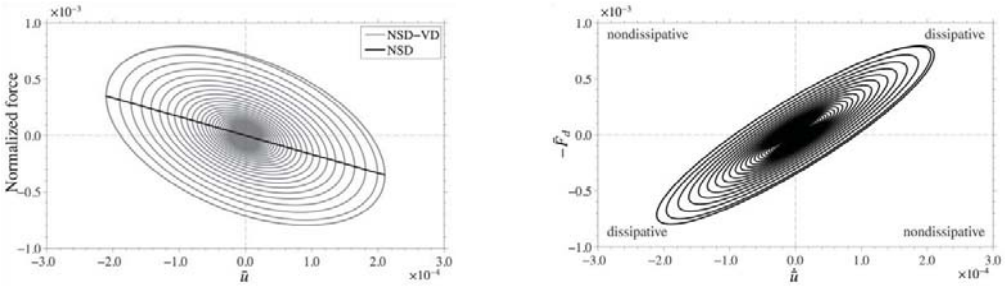

(a) force versus cable displacement at the damper (b) force versus cable velocity at the damper

Fig. 5 Characteristics of the NSD-VD assembly during the cable free decay, the first mode case

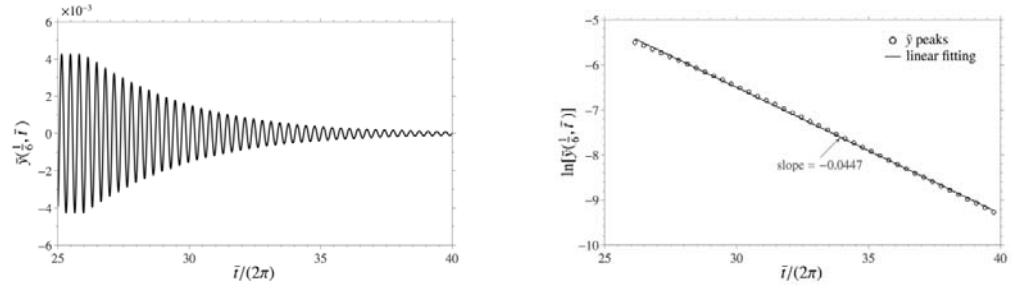

(a) free decay at the 1/6span (b) peaks of free decay and corresponding fitted line

Fig. 6 Resonant response for the third mode case of a cable with a NSD and an optimum damper

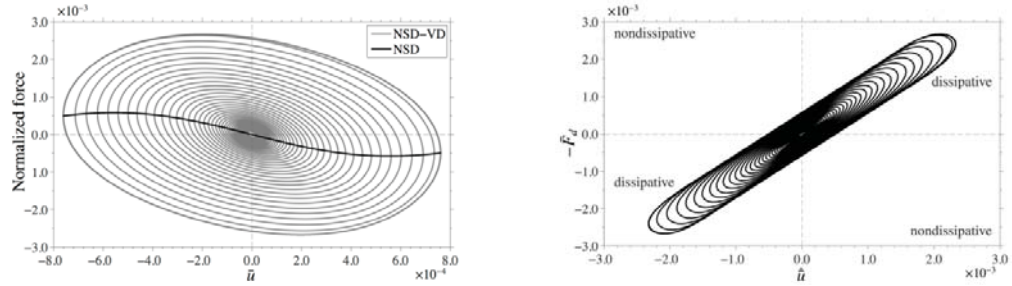

(a) force versus cable displacement at the damper (b) force versus cable velocity at the damper

Fig. 7 Characteristics of the NSD-VD assembly during cable free decay, the third mode case

As also indicated in Eq. (10), the nonlinear force generated by the assembly depends mainly on the ratio $\bar{u}/\bar{l}$. With a reduced $\bar{l}=1\times10^{-3}$l (for instance, *l*=0.5 m for a cable of *L*=500 m) and increasing the excitation amplitude to $p=1\times10^{-3}$ to increase $\bar{u}$ correspondingly, the resulting system was excited during $\bar{t}\in[0,52\pi]$ and then allowed to freely decay. The third mode (i_p=3) free decay is illustrated in Fig. 6(a) and the corresponding modal damping calculation is demonstrated in Fig. 6(b). The additional damping shows visible dependence on the vibration amplitude at the damper compared to the previous case, however, the dependence is still negligible

and the damping can be reliably estimated by the linear fitting as $0.0447/i_p$=0.0149, pretty close to the asymptotic solution from Eq. (4). In this case, the displacement-dependent force due to the NSD is shown in Fig. 7(b) along with the total control force, and the control force versus cable velocity at the damper location is plotted in Fig. 7(b). It is because the damper deformation is comparable to $\overline{l}$.

The passive NSD enables the increment of the displacement of the cable due to negative stiffness at the damper location and hence improves the damper performance. Clearly the larger damping and energy dissipation is evident in Figs. 7(a) and 7(b). It is important to note that even though the negative stiffness is largely dependent on the damper deformation, the linear approximation is still sufficiently accurate for evaluating the additional cable damping. In other words, it can be concluded that for a practical configuration of the NSD for a cable at the damper location, the negative stiffness provided can be safely considered constant, and Eqs. (4)-(6) can be used for the optimum design of the NSD-VD assembly.

2.3 Case study

Based on the approved linear approximation, the relationship between parameters of the NSD with expected stiffness and the cable is obtained by substituting Eq. (3) into Eq. (2)

$$k_s \frac{\Delta}{l} = -\overline{k} \frac{T}{x_d} \tag{15}$$

In the following, a real cable tested by Chen and Sun (2014), with parameters listed in Table 1, is considered to demonstrate the NSD for practical application. The inherent damping ratio of the cable is quite low, ranging from 0.01 to 0.07 of a percent within the vibration amplitudes in the test. To suppress the possible wind/rain-induced variation, it is required that $m\zeta/(\rho D^2) > 10$ (Kumarasena *et al*. 2007) where ρ is the air density (about 1.225 kg/m^3) and D is the cable diameter, that is ζ > 0.43% in this case. Besides, the efficiency factor of a passive device in real-world cable applications can vary from 0.30 to 0.74 (Sun *et al*. 2004). So, the damping ratio of this cable, added by a passive device, is theoretically expected to be larger than 1.17% (considering the mean cable intrinsic damping, 0.04%, and an overall reduction factor of 1/3). When installed at 3.4 m from the cable end, a viscous damper cannot fulfill the requirement, because the maximal damping attainable is 1.01%. A NSD is therefore required with $\overline{k}$ = -0.14 according to Eq. (4), and hence the geometry and stiffness of the pre-compressed spring in Fig. 1is constrained by $k_s \Delta/l$ =157.54 kN/m. This means if a spring with compressed length of 1 meter is chosen, the initial compression force is 157.54 kN, which is feasible from an engineering point of view. Future study is needed to deal with the detailed design of the NSD and the possible magnification mechanism to achieve such a pre-compression force.

Table 1 Parameters of the considered cable

Length L(m)	Mass m(kg/m)	Tension T(kN)	Diameter D(m)	Inherent Damping Ratio (%)	Damper Location x_d(m)
168.25	44.067	3826	0.125	0.01--0.07	3.4

3. General characteristics of a cable with linear NSD-VD at arbitrary location

This section focuses on the general characteristics of a taut cable with a linear NSD-VD assembly at arbitrary location. Hereafter, x_j represents the coordinate originating from each cable end and pointing to the cable center; y_j denotes the transverse displacement of each segment; subscript j is to index the two cable segment divided by the damper; all other parameters are the same as illustrated in Fig. 2.

3.1 Characteristic equation

The characteristic equation of a taut cable with a viscous damper having interior stiffness has been formulated in previous studies, with cable internal damping c=0, as

$$\coth\left[\sqrt{\frac{m}{T}}\lambda x_d\right]+\coth\left[\sqrt{\frac{m}{T}}\lambda\left(L-x_d\right)\right]+\frac{k/\lambda+c_d}{\sqrt{mT}}=0 \tag{16}$$

where λ is the eigen-frequency of the cable/damper system. The above equation is directly used here while the restriction that k>0 (Krenk and Høgsberg 2005, Zhou *et al*. 2014a) or x_d<<L (Li *et al*. 2008) is relieved, and attention is paid to the case where k< 0 and larger frequency shifts are induced, with comparison to the positive and zero stiffness cases.

Introducing the following non-dimensional quantities

$$\mu_1=\frac{x_d}{L},\mu_2=\frac{L-x_d}{L},\tilde{k}=\frac{k\omega_0^{-1}}{\sqrt{mT}},\tilde{\lambda}=\frac{\lambda}{\omega_0} \tag{17}$$

the characteristic equation can then be rewritten in a non-dimensional form

$$\coth\left(\pi\mu_1\tilde{\lambda}\right)+\coth\left(\pi\mu_2\tilde{\lambda}\right)+\tilde{k}/\tilde{\lambda}+\overline{c}_d=0 \tag{18}$$

It is noted that $\overline{k}=\mu_1\pi\tilde{k}$. Correspondingly, the normalized frequency-dependent mode shapes $Y_j(x_j)$ are expressed as

$$Y_j\left(x_j\right)=\gamma\frac{\sinh\left(\pi\tilde{\lambda}\,x_j/L\right)}{\sinh\left(\pi\tilde{\lambda}\mu_j\right)} \tag{19}$$

where γ is the amplitude of $u(t)$.

The complex eigen-frequency can be separated into the real and imaginary parts as

$$\tilde{\lambda}_i=\omega_i\left(\cos\theta_i+\mathrm{i}\sin\theta_i\right)=\sigma_i+\mathrm{i}\varphi_i=-\zeta_i\omega_i+\mathrm{i}\varphi_i \tag{20}$$

where i the square root of -1, and ω_i and θ_i are modulus and phase angle of the complex eigen-frequency; and σ_i and φ_i refer to the real and imaginary parts respectively; the damping ratio and damped frequency then are obtained by $\zeta_i=-\cos\theta_i$ and $\varphi_i=\omega_i\sin\theta_i$.

The system characteristic equation is then separated into the real and imaginary parts as

$$\sum_{j=1,2} \frac{\sinh\left(2\pi\mu_j\omega\cos\theta\right)}{\cosh\left(2\pi\mu_j\omega\cos\theta\right)-\cos\left(2\pi\mu_j\omega\sin\theta\right)} + \frac{\tilde{k}\cos\theta}{\omega} = -\overline{c}_d \tag{21}$$

$$\sum_{j=1,2} \frac{\sin\left(2\pi\mu_j\omega\sin\theta\right)}{\cosh\left(2\pi\mu_j\omega\cos\theta\right)-\cos\left(2\pi\mu_j\omega\sin\theta\right)} + \frac{\tilde{k}\sin\theta}{\omega} = 0 \tag{22}$$

where the subscript *i* indicating mode number is omitted for conciseness. Given certain $\tilde{k}$ and μ_1, possible eigen-frequencies can be determined from Eq. (22); the corresponding $\overline{c}_d$ is determined from Eq. (21); and the mode shape is determined afterwards from Eq. (19). Complex $\tilde{\lambda}_i$ of interest is that with positive imaginary part and negative real part, i.e. $\omega_i \geq 0$ and $\pi/2 \leq \theta_i \leq \pi$, corresponding to positive frequency and negative damping.

3.2 Special solutions

Special solutions of the concerned system are first discussed for further characterizing the system in general.

3.2.1 Nonoscillatory decay

For nonoscillatory decay of the system, $\varphi = 0$, and Eq. (22) is thus trivially satisfied regardless of *k*. Also, with purely real eigen-frequencies, Eq. (21) is reduced to

$$\frac{\sinh\left(-2\pi\sigma\mu_1\right)}{\cosh\left(-2\pi\sigma\mu_1\right)-1} + \frac{\sinh\left(-2\pi\sigma\mu_2\right)}{\cosh\left(-2\pi\sigma\mu_2\right)-1} + \frac{\tilde{k}}{-\sigma} = \overline{c}_d \tag{23}$$

Noting the third term approaches to zero and each of the first two terms approaches to unity with $\sigma \to -\infty$, the critical value for the existence of roots of the preceding equation is still $\overline{c}_d$=2, the same as the case discussed in Main and Jones (2002a).

3.2.2 Nondecaying oscillation

The system oscillates without decaying with purely imaginary eigen-frequencies, e.g., $\tilde{\lambda}_i = \mathrm{i}\varphi_i$. This happens when $\overline{c}_d$=0, substituting which into the characteristic equation leads to

$$\sin\left(\pi\varphi_i\right) = \frac{\tilde{k}}{\varphi_i}\sin\left(\pi\varphi_i\mu_1\right)\sin\left(\pi\varphi_i\mu_2\right) \tag{24}$$

Solutions to the above equation are denoted as φ_{oi}. Obviously: k= 0, $\varphi_{oi} = i$; when k>0, $\varphi_{oi} \geq i$; for k<0, $\varphi_{oi} \leq i$. The equality for the later two cases is fulfilled when $\sin(\pi\varphi_i\mu_1)\sin(\pi\varphi_i\mu_2) = 0$, corresponding to the case when the damper is located at the node of the cable mode *i*.

Similarly, with $\overline{c}_d \to \infty$, the eigen-frequency is also purely imaginary. The characteristic equation is rewritten as

$$\sinh\left(\pi\tilde{\lambda}\right)+\left(\frac{\tilde{k}}{\tilde{\lambda}}+\overline{c}_d\right)\sinh\left(\pi\tilde{\lambda}\mu_1\right)\sinh\left(\pi\tilde{\lambda}\mu_2\right)=0 \tag{25}$$

With bounded $\tilde{k}$ and $\tilde{\lambda}$, solutions for the above equation are cable clamped frequency $\varphi_{ci}^{(j)}=i/\mu_j$, respectively corresponding to the dominant vibration modes of the cable segment *j*.

3.2.3 Critical damping

Oscillatory vibrations approach to critical damping with $\zeta \to 1$ and correspondingly $\sigma \to -\infty$. To discuss the critical damping, the phase equation is rewritten in the form that

$$\sum_{j=1,2}\sin\left(2\pi\varphi\mu_j\right)\cosh\left(2\pi\sigma\mu_{3-j}\right)-\sin\left(2\pi\varphi\right)+\frac{\tilde{k}\varphi}{\omega^2}\prod_{j=1,2}\left[\cosh\left(2\pi\sigma\mu_j\right)-\cos\left(2\pi\varphi\mu_j\right)\right]=0 \tag{26}$$

For bounded φ, when $\sigma \to -\infty$, the above equation is satisfied with $\sin(2\pi\mu_1\varphi)=0$ for $\tilde{k}$ =0 (Main and Jones 2002a), or $\tilde{k}\neq 0$ but $\varphi=0$. In other words, for a damper with positive or negative stiffness, the critical damping cannot be approached for oscillatory vibrations.

3.3 Frequency loci with varied damper location

Complex frequencies have been characterized for a taut cable/damper system (Main and Jones 2002a, Sun and Chen 2015), and the frequency loci with the damper coefficient increasing from zero to infinity have been classified into three distinguished regimes with respect to damper location. The frequency loci of mode *i* originate from the undamped frequency of that mode, while terminate at the frequency corresponding to varied mode with dominant vibration of either cable segment in each regime. In the following, these regimes are extended to a cable with a NSD-VD assembly, where *n* is introduced to denote the node of one mode shape of cable free vibration with *n*=0 referring to the cable end.

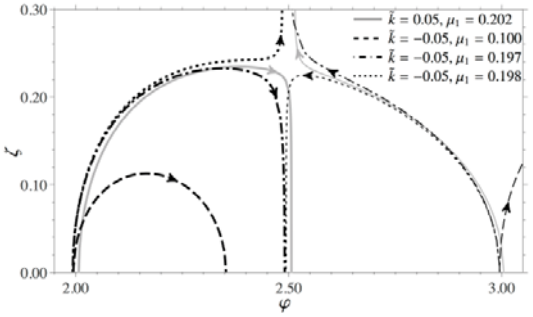

Fig. 8 Frequency loci in regime 1 for mode 2 with varied $\tilde{k}$ and μ_1

3.3.1 Regime 1

In this regime, regardless of the additional stiffness at the damper location, the frequency loci of mode *i* start from the undamped frequency φ_{oi} and terminate at the locked frequency of the longer segment $\varphi_{c(i-n)}^{(2)}$, as illustrated in Fig. 8 for the second mode. However, the upper bound of this regime, which can be analytically expressed only for the zero stiffness case, depends on the stiffness; for positive stiffness, the upper bound is increased while with the negative stiffness, it is decreased. For instance, the upper bound for this regime corresponding to $\tilde{k}$ = 0 is μ_1 =0.2 (Main and Jones 2002a); with a positive stiffness $\tilde{k}$ =0.05, the frequency loci variation is still in this regime for μ_1 =0.202; with a negative stiffness k =-0.05, the frequency loci evolution has already jumped to regime 2 for μ_1 =0.198.

3.3.2 Regime 2

In this regime, variations are observed for the frequency loci evolution of systems where different stiffness is added to the damper, as illustrated in Fig. 9. In particular, when $\tilde{k}$ = 0 (Main and Jones 2002a), the frequency loci in the regime are divided into two distinct branches: one originates from the undamped cable vibration φ_{oi} and terminates at the corresponding critically damped frequency of the longer segment with damping ratio $\zeta \to 1$, and meanwhile $\bar{c}_d$ is increased from zero to 2; the other branch originates from the critically damped frequency of the shorter segment with damping ratio $\zeta \to 1$ and terminates at the fully locked vibration of the short segment, with $\bar{c}_d$ increasing from 2 to infinity. When $\tilde{k}$ > 0, theoretical damping can no longer be approached, as abovementioned, the frequency branch of each mode in this regime originates from the undamped cable vibration φ_{oi} and bends forward to terminate at the clamped vibration of the short cable segment $\varphi_{c(n+1)}^{(1)}$ (Sun and Chen 2015), when the damper is located between the n^{th} node and the $(n+1)^{\text{th}}$ node of the free vibration shape of mode *i*, as illustrated in Figs. 9(a) and 9(b) as a reference.

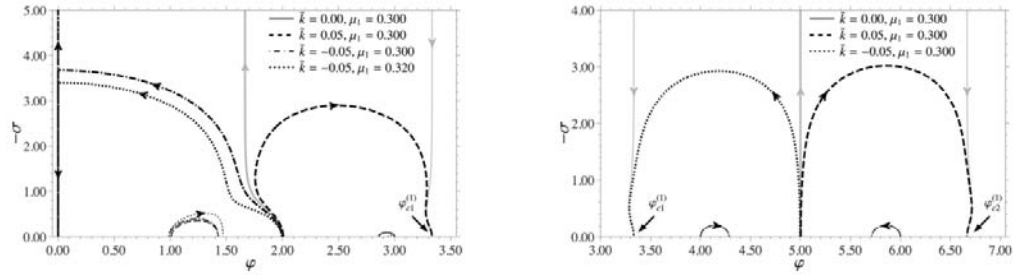

(a) frequency loci of mode 2 with the assembly located between cable end and the first node

(b) frequency loci of mode 5 with the assembly located between the first and second node

Fig. 9 Frequency variation in regime 2 for varied $\tilde{k}$ and μ_1

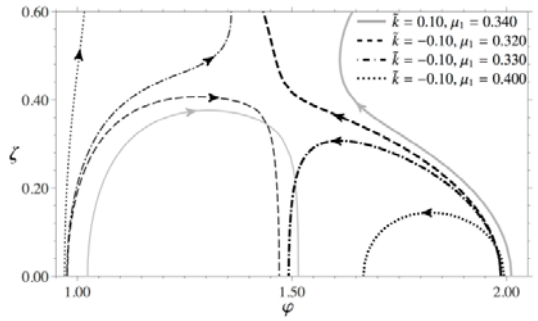

Fig. 10 Frequency loci in regime 3 for mode 2 with varied $\tilde{k}$ and μ_1

With $\tilde{k}$ <0, two sub-cases need to be discussed separately: (1) if the damper is located between the cable support and the first node, the frequency loci starting from φ_{oi} bend leftward to intersect the imaginary axis, as illustrated in Fig. 9(a), and correspondingly terminate at $\varphi = 0$; (2) when the damper is located between the n^{th} node and the $(n+1)^{\text{th}}$ node with n> 0, the frequency loci bend also backward but terminate at the clamped vibration frequency of the short cable segment $\varphi_{cn}^{(1)}$, as illustrated in Fig. 9(b) for the fifth mode with the damper near the second anti-node. It is interesting to note that these characteristics of the frequency loci are found to be similar as those for a tensioned beam with a viscous damper presented in Main and Jones (2007a).

3.3.3 Regime 3

Frequency branch of mode i categorized in regime 3 originates from the undamped vibration frequency φ_{oi} and terminates at the vibration of the longer segment $\varphi_{c(i-n-1)}^{(2)}$. Nevertheless, the lower bound of this regime depends on $\tilde{k}$: the negative stiffness tends to decrease the lower bound and conversely the positive stiffness increase the lower bound, as illustrated in Fig. 10. As above-illustrated, in each regime varied optimum principle applies for the NSD-VD assembly design, which needs to be solved numerically. Besides, the mode shapes in each regime are not presented for the sake of conciseness, and the readers are advised to refer to Main and Jones (2002a, 2007a) and Sun and Chen (2015).

4. Conclusions

Vibrations of a cable with a NSD-VD assembly were investigated for both practical and theoretical purposes. Typically positive stiffness introduced at the damper location (due to the damper intrinsic stiffness) decreases the relative damper deformation during cable vibrations, and hence impairs the damping effect that can be attained. The passive NSD enables the increment of the displacement of the cable due to negative stiffness at the damper location and hence improves the damper performance. A practical NSD was first implemented to produce true negative

stiffness without any energy input, combined with a VD for cable vibration control. Specifically, asymptotic solutions for the cable with a NSD-VD near cable support have been presented and the nonlinear behavior of the NSD has also been evaluated and confirmed to be negligible for practical configurations of the system. Subsequently, general characteristics of a taut cable with the linear NSD-VD assembly at arbitrary location were discussed in the context of semi-active and active cable vibration control. Varied frequency evolutions of the system have been identified with reference to those of the cable with only the viscous damper, which are extensions of the three regimes of frequency loci for taut cable/damper systems. These complex frequency characteristics can be preliminarily used to evaluate the damping effect of an adaptive passive or semi-active or active device for cable vibration control once the NSD-VD (or PVE damper) assembly of equivalence is determined.

Acknowledgments

The scholarship under the State Scholarship Fund granted by the China Scholarship Council (CSC, File no. 201206260012) for supporting the first author's work at Rice University is gratefully acknowledged.

References

Caracoglia, L. and Jones, N.P. (2007a), "Damping of taut-cable systems: Two dampers on a single stay", *J. Eng. Mech. - ASCE*, **133**(10), 1050-1060.

Caracoglia, L. and Jones, N.P. (2007b), "Passive hybrid technique for the vibration mitigation of systems of interconnected stays", *J. Sound Vib.*, **307**(3-5), 849-864.

Chen, L. and Sun, L. (2014), "Laboratory-scale experimental setup for studying cable dampers", *J. Eng. Mech. - ASCE*, 10.1061/(ASCE)EM.1943-7889.0000878, 04014159.

Chen, Z.Q., Wang, X.Y., Ko, J.M., Ni, Y.Q., Spencer Jr., B.F. and Yang, G. (2003), "MR damping system on Dongting Lake cable-stayed bridge", *Proceedings of the SPIE - The Int. Society for Optical Engineering*, 229-235.

Fujino, Y. and Hoang, N. (2008), "Design formulas for damping of a stay cable with a damper", *J. Struct. Eng. - ASCE*, **134**(2), 269-278.

Fujino, Y., Kimura, K. and Tanaka, H., (2012), *Wind Resistant Design of Bridges in Japan*, Springer, Japan.

Hikami, Y. and Shiraishi, N. (1988), "Rain-wind induced vibrations of cables stayed bridges", *J. Wind Eng. Ind. Aerod.*, **29**(13), 409-418.

Hoang, N. and Fujino, Y. (2007), "Analytical study on bending effects in a stay cable with a damper", *J. Eng. Mech. - ASCE*, **133**(11), 1241-1246.

Hoang, N. and Fujino, Y. (2008), "Combined damping effect of two dampers on a stay cable", *J. Bridge Eng.*, **13**(3), 299-303.

Hoang, N. and Fujino, Y. (2009), "Multi-mode control performance of nonlinear dampers in stay cable vibrations", *Struct. Control Health Monit.*, **16**(7-8), 860-868.

Høgsberg, J.R. and Krenk, S. (2006), "Linear control strategies for damping of flexible structures", *J. Sound Vib.*, **293**(1-2), 59-77.

Høgsberg, J. (2011), "The role of negative stiffness in semi-active control of magneto-rheological dampers", *Struct. Control Health Monit.*, **18**(3), 289-304.

Huang, H., Sun, L. and Jiang, X. (2012), "Vibration mitigation of stay cable using optimally tuned MR damper", *Smart Struct. Syst.*, **9**(1), 35-53.

Huang, Z. and Jones, N.P. (2011), "Damping of taut-cable systems: Effects of linear elastic spring support", *J. Eng. Mech. - ASCE*, **137**(7), 512-518.
Iemura, H. and Pradono, M.H. (2003), "Application of pseudo-negative stiffness control to the benchmark cable-stayed bridge", *J. Struct. Control*, **10**(3-4), 187-203.
Iemura, H., Igarashi, A., Pradono, M.H. and Kalantari A. (2006), "Negative stiffness friction damping for seismically isolated structures", *Struct. Control Health Monit.*, **13**(2-3), 775-791.
Iemura, H. and Pradono, M.H. (2009), "Advances in the development of pseudo-negative-stiffness dampers for seismic response control", *Struct. Control Health Monit.*, **16**(7-8), 784-799.
Irvine, H.M. (1981), *Cable Structures*, Cambridge, MA, U.S.A., MIT Press.
Johnson, E., Baker, G., Spencer, B. and Fujino, Y. (2007), "Semiactive damping of stay cables", *J. Eng. Mech. - ASCE*, **133**(1), 1-11.
Johnson, E.A., Christenson, R.E. and Spencer Jr., B.F. (2003), "Semiactive damping of cables with sag", *Comput. - Aided Civil Infrastruct. E.*, **18**(2), 132-146.
Kovacs, I. (1982), "Zurfrage der seilschwingungen und der seildampfung", *Bautechnik*, **59**(10), 325-332.
Krenk, S. (2000), "Vibrations of a taut cable with an external damper", *J. Appl. Mech. - T. ASME*, **67**(4), 772-776.
Krenk, S. and Høgsberg, J. (2014), "Tuned mass absorber on a flexible structure", *J. Sound Vib.*, **333**(6), 1577-1595.
Krenk, S. and Høgsberg, J.R. (2005), "Damping of cables by a transverse force", *J. Eng. Mech. - ASCE*, **131** (4), 340-348.
Krenk, S. and Nielsen, S.R.K. (2002), "Vibrations of a shallow cable with a viscous damper", *P. Roy. Soc. Lond. Series A*, **458**(2018), 339-357.
Kumarasena, S., Jones, N.P., Irwin, P. and Taylor P. (2007), *Wind-Induced Vibration of Stay Cables*, Report.
Li, H., Liu, M. and Ou, J. (2008), "Negative stiffness characteristics of active and semi-active control systems for stay cables", *Struct. Control Health Monit.*, **15**(2), 120-142.
Main, J.A. (2002), *Modeling the vibrations of a stay cable with attached damper*, Ph.D. Dissertation, Johns hopkins University, Baltimore, Maryland.
Main, J.A. and Jones, N.P. (2002a), "Free vibrations of taut cable with attached damper. I: Linear viscous damper", *J. Eng. Mech. - ASCE*, **128**(10), 1062-1071.
Main, J.A. and Jones, N.P. (2002b), "Free vibrations of taut cable with attached damper. II: Nonlinear damper", *J. Eng. Mech. - ASCE*, **128**(10), 1072-1081.
Main, J.A. and Jones, N.P. (2007a), "Vibration of tensioned beams with intermediate damper. I: Formulation, influence of damper location", *J. Eng. Mech. - ASCE*, **133**(4), 369-378.
Main, J.A. and Jones, N.P. (2007b), "Vibration of tensioned beams with intermediate damper. II: Damper near a support", *J. Eng. Mech. - ASCE*, **133**(4), 379-388.
Main, J.A. and Krenk, S. (2005), "Efficiency and tuning of viscous dampers on discrete systems", *J. Sound Vib.*, **286**(1-2), 97-122.
Nagarajaiah, S. (2009), "Adaptive passive, semiactive, smart tuned mass dampers: identification and control using empirical mode decomposition, Hilbert transform, and short-term fourier transform", *Struct. Control Health Monit.*, **16**(7-8), 800-841, DOI: 10.1002/stc.349.
Ou, J. and Li, H. (2010), "Analysis of capability for semi-active or passive damping systems to achieve the performance of active control systems", *Struct. Control Health Monit.*, **17**(7), 778-794.
Pacheco, B.M., Fujino, Y. and Sulekh, A. (1993), "Estimation curve for modal damping in stay cables with viscous damper", *J. Struct. Eng. - ASCE*, **119**(6), 1961-1979.
Pasala, D., Sarlis, A., Nagarajaiah, S., Reinhorn, A., Constantinou, M. and Taylor, D. (2013), "Adaptive negative stiffness: New structural modification approach for seismic protection", *J. Struct. Eng. - ASCE*, **139**(7), 1112–1123, DOI: 10.1061/(ASCE)ST.1943-541X.0000615.
Pasala, D., Sarlis, A., Reinhorn, A., Nagarajaiah, S., Constantinou, M. and Taylor, D. (2014), "Simulated bilinear-elastic behavior in a SDOF elastic structure using negative stiffness device: Experimental and analytical study", *J. Struct. Eng. - ASCE*, **140**(2), 04013049.
Sarlis, A., Pasala, D., Constantinou, M., Reinhorn, A., Nagarajaiah, S. and Taylor, D. (2013), "Negative

stiffness device for seismic protection of structures", *J. Struct. Eng. - ASCE*, **139**(7), 1124-1133.
Spencer, B. and Nagarajaiah, S. (2003), "State of the art of structural control", *J. Struct. Eng. - ASCE*, **129** (7), 845-856.
Sun, C. and Nagarajaiah, S. (2014), "Study on semi-active tuned mass damper with variable damping and stiffness under seismic excitations", *Struct. Control Health Monit.*, **21**(6), 890-906.
Sun, C., Nagarajaiah, S. and Dick, A. (2014), "Family of smart tuned mass dampers with variable frequency under harmonic excitations and ground motions: closed-form evaluation", *Smart Struct. Syst.*, **13**(2), 319-341.
Sun, L. and Huang, H. (2008), *Design, implementation and measurement of cable dampers for large cable-stayed bridges*, IABSE Congress Report, **17**(16), 242-243.
Sun, L. and Chen, L. (2015), "Free vibrations of a taut cable with a general viscoelastic damper modeled by fractional derivatives", *J. Sound Vib.*, **335**(2015), 19-33.
Sun, L., Shi, C., Zhou, H. and Cheng, W. (2004), "A full-scale experiment on vibration mitigation of stay cable", *Proceedings of the IABSE Symp. Rep., IABSE Symp., Shanghai 2004: Metropolitan Habitats and Infrastructure*, IABSE, Zurich, Switzerland.
Tabatabai, H. and Mehrabi, A.B. (2000), "Design of mechanical viscous dampers for stay cables", *J. Bridge Eng.*, **5**(2), 114-123.
Weber, F. and Boston, C. (2011), "Clipped viscous damping with negative stiffness for semi-active cable damping", *Smart Mater. Struct.*, **20**(4), 045007.
Weber, F., Boston, C. and Maślanka, M. (2011), "An adaptive tuned mass damper based on the emulation of positive and negative stiffness with an MR damper", *Smart Mater. Struct.*, **20**(1), 015012.
Xu, Y.L. and Yu, Z. (1998), "Vibration of inclined sag cables with oil dampers in cable-stayed bridges", *J. Bridge Eng.*, **3**(4), 194-203.
Xu, Y.L., Yu, Z. and Ko, J.M. (1998), "Forced vibration studies of sagged cables with oil damper using a hybrid method", *Eng. Struct.*, **20**(8), 692-705.
Zhou, H., Sun, L. and Xing, F. (2014a), "Damping of full-scale stay cable with viscous damper: Experiment and analysis", *Adv. Struct. Eng.*, **17**(2), 265-274.
Zhou, H., Sun, L. and Xing, F. (2014b), "Free vibration of taut cable with a damper and a spring", *Struct. Control Health Monit.*, **21**(6), 996-1014.

Smart Structures and Systems, *Vol. 15, No. 3 (2015) 645-663*
DOI: http://dx.doi.org/10.12989/sss.2015.15.3.645

Displacement estimation of bridge structures using data fusion of acceleration and strain measurement incorporating finite element model

Soojin Cho, Chung-Bang Yun and Sung-Han Sim*

School of Urban and Environmental Engineering, Ulsan National Institute of Science and Technology (UNIST), Ulsan 689-798, Republic of Korea

(Received November 5, 2014, Revised February 10, 2014, Accepted February 12, 2015)

Abstract. Recently, an indirect displacement estimation method using data fusion of acceleration and strain (i.e., acceleration-strain-based method) has been developed. Though the method showed good performance on beam-like structures, it has inherent limitation in applying to more general types of bridges that may have complex shapes, because it uses assumed analytical (sinusoidal) mode shapes to map the measured strain into displacement. This paper proposes an improved displacement estimation method that can be applied to more general types of bridges by building the mapping using the finite element model of the structure rather than using the assumed sinusoidal mode shapes. The performance of the proposed method is evaluated by numerical simulations on a deck arch bridge model and a three-span truss bridge model whose mode shapes are difficult to express as analytical functions. The displacements are estimated by acceleration-based method, strain-based method, acceleration-strain-based method, and the improved method. Then the results are compared with the exact displacement. An experimental validation is also carried out on a prestressed concrete girder bridge. The proposed method is found to provide the best estimate for dynamic displacements in the comparison, showing good agreement with the measurements as well.

Keywords: Displacement; bridge; data fusion; finite element model; modal mapping

1. Introduction

Displacement is an intuitive response that directly results from external loads to a structure. Despite of its close relationship with health of a structure, displacement has not been popularly used in structural health monitoring (SHM) of full-scale civil engineering structures unlike other responses such as acceleration (Doebling *et al*. 1998, Bani-Hani *et al*. 2008, Altunisik *et al*. 2012) and strain (Omenzetter *et al*. 2004, Majumder *et al*. 2008, Sigurdardottir and Glisic 2014); a limited number of literatures have reported the use of displacement for monitoring of civil structures (Faulkner *et al*. 1996, Celibi 2000, Xu *et al*. 2002, Nassif *et al*. 2005, Lee *et al*. 2007). The literatures, however, exhibit that the usage is limited to the measurements at a few locations, which is incapable of providing rich information necessary to assess comprehensive structural

*Corresponding author, Assistant Professor, E-mail: ssim@unist.ac.kr

http://www.techno-press.org/?journal=sss&subpage=8 ISSN: 1738-1584 (Print), 1738-1991 (Online)

health.

The usage of displacement has been restricted in full-scale civil structures due to measurement inconvenience and high cost of measurement devices. The traditional contact-type transducers, such as a linear variable differential transformer (LVDT) and a ring type transducer, measure displacements from the deformation of an elastic part of the transducer that is contacted to the structure. The contact-type transducers are inexpensive, but require reference points to fix the transducer firmly when the host structure is deforming. In many cases, some fixtures such as scaffolds are installed around the structure to bind the transducers, which is labor intensive and often unavailable due to operational condition of the structure. Even the fixtures may be deformed by an external force such as wind. Noncontact-type devices, such as the global positioning system (GPS) and the laser Doppler vibrometer (LDV), have been emerged as alternatives (Nassif *et al*. 2005, Jo *et al*. 2013). However, high cost of the devices up to a few ten thousand dollars per sensing channel still limits their real-world applications with a dense topology.

To overcome the inherent limitations of displacement transducers, indirect displacement estimation approaches have alternatively been studied to use other responses that can be converted to the displacement. Acceleration and strain are the most popular responses in the studies. Acceleration is an absolute response that can be easily captured on a structure without having a fixed reference. Theoretically, acceleration can be converted into displacement by double integration in the time domain, while the numerical integration generally brings a significant signal drift (Park *et al*. 2005, Gindy *et al*. 2008, Kandula *et al*. 2012). Lee *et al*. (2010) successfully proposed an FIR filter-based displacement estimation technique which regularizes the signal drift. However, the acceleration-displacement conversion is based on the low-pass filter that eliminates the signal drift with true low frequency component contained in the displacement signal. Thus, the acceleration-based technique fails to estimate displacement with the static or pseudo-static components. Unlike the acceleration, strain can estimate the static or pseudo-static displacement in nature as the time integration is uninvolved in the conversion. Displacement may be estimated from strain using double spatial integration in space when the strain is measured on a structure in the distributed manner (Chung *et al*. 2008) or using the modal mapping between a strain and displacement (Foss and Hauge 1995). Since the modal mapping may construct dynamic displacement from a few measured dynamic strain data based on the modal information, it is very useful to estimate displacements at arbitrary locations on the structure when its modal information is available. Instead of using modal information measured by densely deployed sensors, Kang *et al*. (2007) used mode shapes from the finite element (FE) model of a structure and Shin *et al*. (2012) used assumed sinusoidal mode shapes for a simple beam-type structure. The strain does not cause the signal drift in time domain during the conversion to displacement, while its measurement is vulnerable to measurement noise in high frequency range. Furthermore, the strain-based method requires determination of neutral axis of the structure (Shin *et al*. 2012).

Park *et al*. (2013) proposed a displacement estimation method using data fusion of acceleration and strain by extending the acceleration-based method proposed by Lee *et al*. (2010). In the regularization term, the displacement converted from strain data by the modal mapping is used to prevent the signal drift. For the modal mapping, the assumed analytical (sinusoidal) mode shapes proposed by Shin *et al*. (2012) are employed. The method by Park *et al*. (2013), however, inherits a limitation in application to more general types of bridges with complex shapes, such as arch and truss bridges, since the method uses assumed sinusoidal mode shapes which may be reasonably obtained only for the girder bridges.

This study proposes an improved method to estimate the accurate displacement using

acceleration and strain for general bridge structures. The proposed method is to extend the method by Park *et al*. (2013) to general types of bridges by using the mode shapes for the modal mapping from the FE model of a structure instead of assumed sinusoidal mode shapes. The performance of the proposed method is evaluated by numerical simulations on a deck arch bridge model and a three-span truss bridge model whose mode shapes are hard to be assumed as sinusoidal functions. The displacements are estimated by acceleration-based method, strain-based method, fusion-based method, and the improved method, and the results are compared with exact displacements to demonstrate the performance of the proposed method. Then, the method is experimentally validated from a field testing on a prestressed concrete bridge. From the comparison of displacements estimated by the four methods to the reference values measured by laser displacement meters, the accuracy of the proposed method has been investigated. The proposed method makes the displacement measurement facilitated (without the reference points), inexpensive, and accurate.

2. Improved displacement estimation method using acceleration and strain

This section describes the principles of the displacement estimation method proposed by Park *et al*. (2013) and the modification made in the proposed method.

2.1 Acceleration-strain-based displacement estimation method

Park *et al*. (2013) have proposed the displacement estimation method by fusing the acceleration and strain. The method uses the basic form of the acceleration-based method proposed by Lee *et al*. (2010), while the regularization term is replaced by the difference between estimated displacements and displacement estimated from the strain by modal mapping method. The method can be formulated for displacement $\mathbf{u}_i$ at the location of x_i as

$$\underset{\mathbf{u}_i}{\text{Min}}\,\Pi = \frac{1}{2}\left\|\mathbf{L}_a(\mathbf{L}_c\mathbf{u}_i - (\Delta t)^2\bar{\mathbf{a}}_i)\right\|_2^2 + \frac{\lambda^2}{2}\left\|\mathbf{u}_i - \bar{\boldsymbol{\varepsilon}}\mathbf{D}_i^{\mathrm{T}}\right\|_2^2 \tag{1}$$

where $\mathbf{u}_i \in \mathbb{R}^{(N+2)\times 1}$ and $\bar{\mathbf{a}}_i \in \mathbb{R}^{N\times 1}$ are the estimated displacement and measured acceleration at the location x_i; $\bar{\boldsymbol{\varepsilon}} \in \mathbb{R}^{(N+2)\times n}$ is the strain measured at n locations; N is the number of acceleration data to be converted into displacement; Δt is the time step; $\mathbf{L}_a \in \mathbb{R}^{N\times N}$ is a diagonal weighting matrix having the first and last entries as $1/\sqrt{2}$ and the other entries as 1; $\mathbf{L}_c \in \mathbb{R}^{N\times(N+2)}$ is the second-order differential operator matrix of the discretized trapezoidal rule (Atkinson 2008); $\|\cdot\|_2$ is2-norm of a vector; λ is a regularization factor; and $\mathbf{D}_i \in \mathbb{R}^{1\times n}$ is the ith row of modal mapping matrix $\mathbf{D} \in \mathbb{R}^{m\times n}$ that converts strain into displacement as

$$\mathbf{u}^{\mathrm{T}} = \mathbf{D}\bar{\boldsymbol{\varepsilon}}^{\mathrm{T}} \tag{2}$$

where $\mathbf{u} \in \mathbb{R}^{(N+2)\times m}$ is the displacement obtained at m locations. The modal mapping matrix can be calculated as

$$\mathbf{D} = \boldsymbol{\Phi}\boldsymbol{\Psi}^{\dagger} \tag{3}$$

where $\mathbf{\Phi} \in ¡^{m \times r}$ and $\mathbf{\Psi} \in ¡^{n \times r}$ denote mode shape vector and strain mode shapes, respectively; the superscript † denotes the pseudo-inverse; and r is the number of used modes that is equal to or smaller than n to avoid an under-determined modal mapping matrix. Note that the number of modes n used in the estimation can be determined based on dominant modes in the displacement being estimated. λ is defined by Lee *et al*. (2010) as

$$\lambda = 46.81N^{-1.95} \tag{4}$$

The mode shapes and strain mode shapes may be directly estimated from measurements, which would be very expensive. Instead, Park *et al*. (2013) employed assumed sinusoidal mode shapes and corresponding strain mode shapes, proposed by Shin *et al*. (2012), as

$$\mathbf{\Phi}^{assumed} = \begin{bmatrix} \sin\dfrac{\pi x_1}{l} & \mathrm{L} & \sin\dfrac{r\pi x_1}{l} \\ \mathrm{M} & \mathrm{O} & \mathrm{M} \\ \sin\dfrac{\pi x_m}{l} & \mathrm{L} & \sin\dfrac{r\pi x_m}{l} \end{bmatrix} \tag{5}$$

$$\mathbf{\Psi}^{assumed} = \frac{y\pi^2}{l^2}\begin{bmatrix} \sin\dfrac{\pi z_1}{l} & \mathrm{L} & r^2\sin\dfrac{r\pi z_1}{l} \\ \mathrm{M} & \mathrm{O} & \mathrm{M} \\ \sin\dfrac{\pi z_n}{l} & \mathrm{L} & r^2\sin\dfrac{r\pi z_n}{l} \end{bmatrix} \tag{6}$$

where x_i $(i = 1, \mathrm{L}, m)$ and z_i $(i = 1, \mathrm{L}, n)$ are the locations where acceleration and strain are measured, respectively; y is the distance from the neutral axis to the surface where strain gauges are installed; and l is length of the structure. The neutral axis y can be determined by the calibration technique that uses both acceleration and strain, which was proposed by Park *et al*. (2013). The solution of Eq. (1) can be expressed as

$$\mathbf{u}_i = (\mathbf{L}^T\mathbf{L} + \lambda^2\mathbf{I})^{-1}(\mathbf{L}^T\mathbf{L}_a\bar{\mathbf{a}}_i\Delta t^2 + \lambda^2\bar{\boldsymbol{\varepsilon}}\mathbf{D}_i^{\mathrm{T}}) \tag{7}$$

where $\mathbf{L} = \mathbf{L}_a\mathbf{L}_c$. Note that Lee *et al*. (2010) suggested a moving-window strategy to address the inaccurate estimation near the boundaries of the finite data, which was also adapted by Park *et al*. (2013). The optimal size of moving window is proposed as three times the number of data points in the first natural period after numerical simulation tests on various systems in Lee *et al*. (2010).

2.2 Improved method using modal mapping from finite element model

The acceleration-strain-based method (described in the previous section) builds the modal mapping matrix $\mathbf{D}$ using the assumed sinusoidal mode shapes as in Eqs. (5) and (6). In the case of prismatic or nearly-prismatic simply-supported beams, the sinusoidal mode shapes approximate the real ones reasonably. For example, Shin *et al*. (2012) successfully estimated displacement from the measured strain on a single-span bridge using the assumed sinusoidal mode shapes. Park *et al*. (2013) also validated their method on a suspension bridge in the experiment. Both bridges have

prismatic or nearly-prismatic sections and large span-to-depth ratios, and thus have the mode shapes quite close to the assumed sinusoidal shapes.

However, possible disagreements of the assumed mode shapes to the real mode shapes can happen in general types of structures, causing significant errors in the displacement estimation. The errors can be minimized by obtaining the real mode shapes and strain mode shapes from a dense array of accelerometers and strain gages, but it is not practical due to high cost. If the mode shapes and strain mode shapes can be assumed reasonably based on the physical insight of the structure, then they can minimize the error up to the acceptable level.

In this paper, an improved method is proposed by employing a modal mapping matrix derived from an FE model of the structure as

$$\mathbf{D} = \mathbf{\Phi}^{FE} (\mathbf{\Psi}^{FE})^{\dagger} \tag{8}$$

where $\mathbf{\Phi}^{FE} \in ¡^{m \times r}$ and $\mathbf{\Psi}^{FE} \in ¡^{n \times r}$ are the mode shapes and the strain mode shapes obtained from the FE model. Since $\mathbf{\Phi}^{FE}$ and $\mathbf{\Psi}^{FE}$ replace $\mathbf{\Phi}$ and $\mathbf{\Psi}$ of Eqs. (5) and (6) in the improved method, the mode shapes and the strain mode shapes need to be estimated from the FE model for locations where the displacement is to be estimated (i.e., the accelerations are measured) and where the strains are measured, respectively.

The accuracy of the estimated displacement can be quantified by employing a percentage root mean square deviation (RMSD) as

$$RMSD\ (\%) = \frac{\sqrt{\sum_{j=1}^{N} (u_{ij}^{est} - u_{ij}^{ref})^2}}{\sqrt{\sum_{j=1}^{N} (u_{ij}^{ref})^2}} \times 100 \tag{9}$$

where u_{ij}^{est} and u_{ij}^{ref} are the estimated and reference displacements at location x_i, respectively.

3. Numerical validation

The improved method is validated from numerical simulations carried out on two example structures: an open-spandrel deck arch bridge model and a 3-span truss bridge model. The displacements excited by a moving load are estimated by four methods: i.e., acceleration-based method (Lee *et al*. 2010), strain-based method (Kang *et al*. 2007), acceleration-strain-based method (Park *et al*. 2013), and the improved acceleration-strain-based method, and the results are compared for the validation.

3.1 Deck arch bridge model

The first example used in this study is a 2D open-spandrel deck arch bridge model shown in Fig. 1. The model has a deck which locates above the arch and the deck is supported by a number of vertical columns rising from the arch. The Rainbow Bridge at Niagara Falls and the Cold Spring Canyon Arch Bridge are the famous examples of the deck arch bridges.

The model is composed of 34 members: 12 deck members, 12 arch members, and 10 vertical columns. All members are modelled as frame elements. N# and A# denote the nodes and supports,

respectively. The span length of the bridge is 120 m, and the height of the arch is 20 m. The sectional properties of members for deck, arch, and vertical columns are shown in Table 1.

The displacement, acceleration, and strain of the beam are simulated using MATLAB Simulink. A vertical load moving from left to right of the deck with a constant speed (v =10 m/s), shown in Fig. 2, is employed to generate non-zero mean displacements. The load is the combination of a moving static load of 43.2 ton (DB24 truck load specified in Korean highway bridge design code) and zero-mean Gaussian random load with a standard deviation of 13 ton simulating dynamic loading effect. Acceleration is assumed to be measured at N6, while strains on the deck are obtained at the mid spans of four deck members between N1-N2, N4-N5, N7-N8, and N10-N11. The simulated acceleration and strains are made artificially contaminated by adding 5% noise in root mean square (RMS) to emulate the practical measurement. The displacement simulated at N6 is used as the reference to evaluate the accuracy of estimated displacements. Note that acceleration and displacement are obtained in the vertical direction, while the strains are obtained on the bottom surfaces of the deck in the longitudinal direction to capture the bending strain.

Since four strain data are available in this example, the first four modes are employed to build the modal mapping relationship. Fig. 3 shows the first four mode shapes of the FE model, compared with the sinusoidal shapes based on the assumption of a simply supported prismatic beam. The visual comparison clearly shows the difference between the two types of mode shapes, particularly for the first and third mode shapes near the supports. Their modal assurance criterion (MAC) values are 0.718, 0.936, 0.651, and 0.988, respectively. Thus, it can be expected that the displacement estimated near the supports may have considerable error when the assumed modes are used.

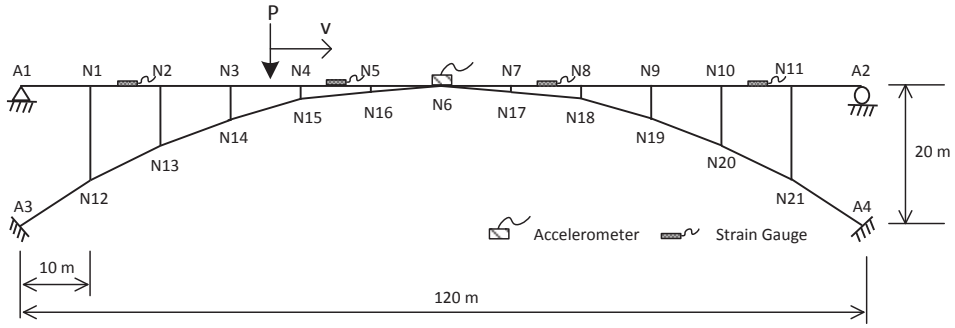

Fig. 1 Deck arch bridge model with sensor topology

Table 1 Structural properties of deck arch bridge model

Members	Deck	Arch	Vertical Column
Sectional area	0.656 m^2	0.280 m^2	0.167 m^2
2nd moment of inertia	1.453×10^{-1} m^4	3.087×10^{-1} m^4	6.535×10^{-2} m^4
Elastic modulus		200 GPa	
Mass density		7850 kg/m^3	

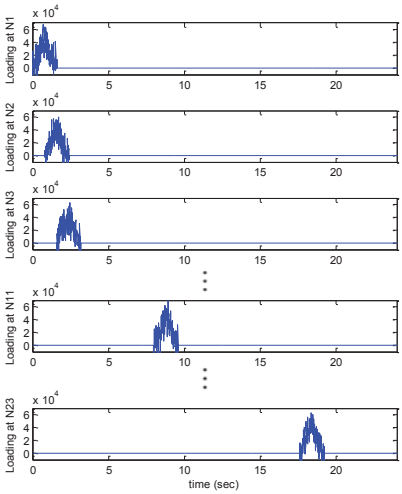

Fig. 2 Simulated vertical moving load

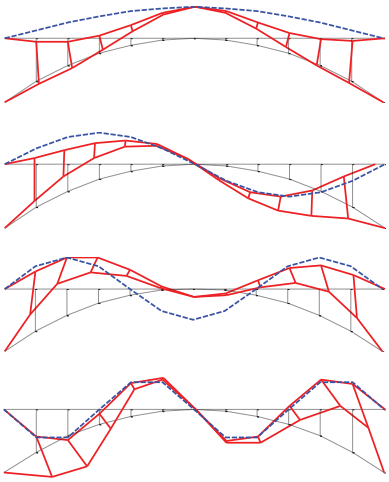

Fig. 3 First four mode shapes of FE model (solid lines) compared with assumed ones (dashed lines)

3.1.1 Comparison of displacements at N6

Fig. 4 shows the comparison of the displacements estimated by four methods with exact one simulated from the MATLAB Simulink. The acceleration-based method can not estimate the nonzero-mean pseudo-static displacement component as shown in Fig. 4(a). The strain-based method can somewhat estimate the static component as shown in Fig. 4(b), while the dynamic component cannot be estimated accurately. The acceleration-strain-based method gives an incorrect displacement due to the incorrect modal mapping as in Fig. 4(c). Meanwhile, the improved acceleration-strain-based method estimates very accurate displacement overlapped with

the exact one as in Fig. 4(d), despite of the complexity of the deck arch model. This clarifies the performance of the improved method for a complex structure whose mode shapes may not be easily assumed as analytical functions.

The accuracy of the estimated displacements can be investigated in the different aspects by looking at the frequency domain. Fig. 5 shows the power spectral density (PSD) of the estimated displacements compared with that of exact one. Figs. 5(a) and 5(b) show errors of the acceleration-based and the strain-based methods in low and high frequency range, respectively. The acceleration-strain-based method shows slightly larger error in estimating the pseudo-static components near 0 Hz than the improved method (see zoomed-ins of Figs. 5(c) and 5(d)).

The peak at 15.4 Hz shown in the PSD of the strain-based method shows a drawback of the strain-based method. The bridge model has a mode at 15.4 Hz, and the corresponding mode shape has a nodal point at N6. This is why there is no peak observed at 15.4 Hz in Fig. 5(a). However, the strains used in the strain-based method were obtained from non-nodal points, and thus the peak is clearly observed. In the acceleration-strain-based and improved methods, the high frequency components contained in the strain were replaced by the components contained in the acceleration, which resulted in the disappearance of the peak at 15.4 Hz in Figs. 5(c) and 5(d). This illustrates that the strain-based method is only effective in estimating the very low-frequency components which have few nodal points.

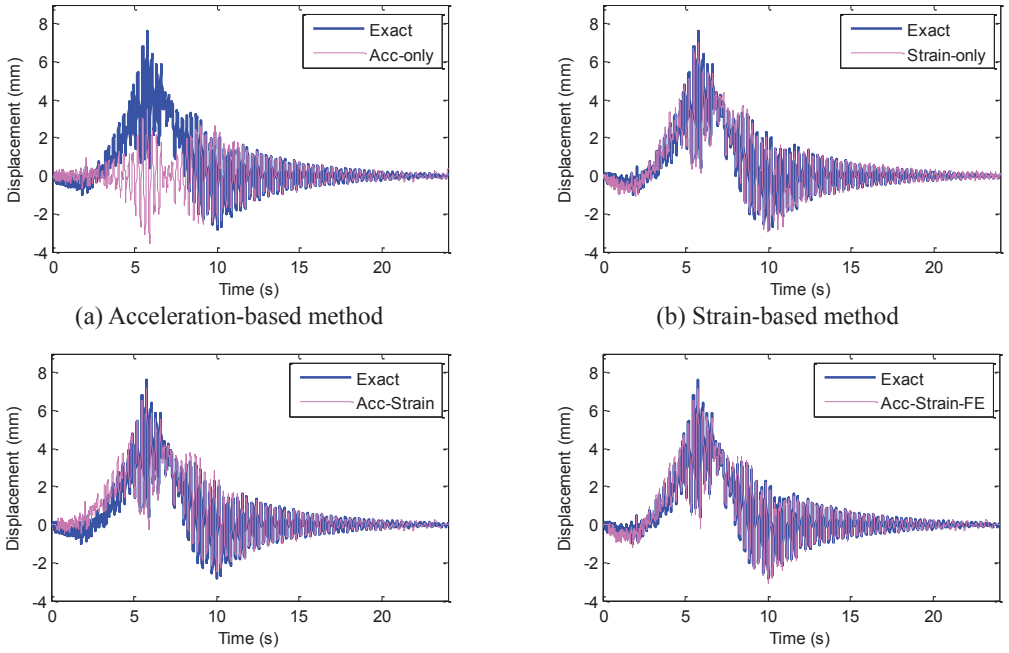

(a) Acceleration-based method (b) Strain-based method

(c) Acceleration-strain-based method (d) Improved acceleration-strain-based method

Fig. 4 Comparison of displacements estimated at N6 for deck arch bridge model by four different estimation methods with exact one

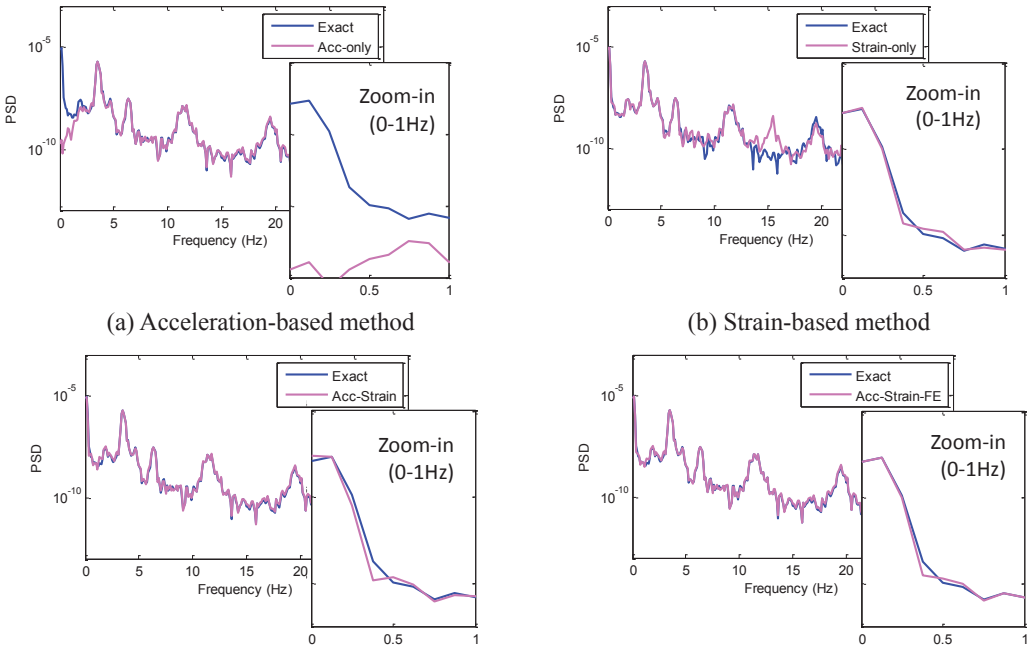

Fig. 5 Comparison of PSD of displacements estimated at N6 for deck arch model by four different estimation methods with exact one

The accuracy of the estimated displacements by the four methods is quantified using the percentage RMSD described in Eq. (12). The acceleration-based method provides the largest RMSD of 85.9% at N6. The strain-based method yields small error of 17.7%, since the method uses accurate modal mapping using the FE mode shapes. The acceleration-strain-based method gives a larger RMSD value of 20.5% than the strain-based method, which means the error in the assumed mode shapes may bring significant error in the estimation due to incorrect modal mapping. The improved method has the smallest RMSD value of 10.6% owing to accurate modal mapping using the FE model. The estimated RMSD values quantitatively show the performance of the improved method compared with the other existing methods for the general types of bridge structures.

3.1.2 Comparison of displacements at other locations

Fig. 6 shows the RMSD values of the displacements estimated by four methods at the left half of the deck: N1-N6. The acceleration-based method shows largest error for all locations due to incorrect estimation of pseudo-static displacements. The incorrect modal mapping significantly increases the error of the acceleration-strain-based method, which is even larger than the strain-based method that uses correct modal mapping. The improved method has the smallest RMSD values for all points.

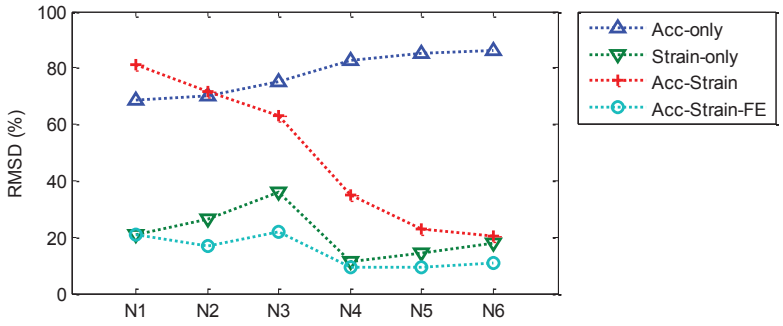

Fig. 6 RMSD of displacements at N1-N6

3.1.3 Effect of FE model inaccuracy

The FE model may be subjected to modelling errors, which may cause estimation errors in the modal properties. To see the effect of the inaccurate FE model to the estimation, the FE model is perturbed by introducing element-level errors in the elastic modulus. Three types of perturbations with 11.5, 23.1, and 34.6% in RMS (i.e., uniform perturbation in the range of ±20%, ±40%, and ±60% of the initial value) are considered. Fig. 7 shows the first four mode shapes of a perturbed FE model with 34.6% errors in RMS in comparison with those from the original FE model. Fig. 7 shows that the perturbation caused considerable discrepancy particularly on the higher mode shapes to be used for the modal mapping.

Fig. 8 shows the RMSDs of the estimated displacements at N6 by the strain-based and the improved methods when the perturbed FE models are used for the modal mapping. The MAC values of the perturbed models are plotted together to show the effect of perturbation to the mode shapes. By the incremental perturbation, the mode shapes are found to change incrementally. However, even with the significant perturbation, the RMSD of the estimated displacement rarely changes for both the strain-based and the improved methods. In the case of with perturbation of 34.6% in RMS, the RMSD by the improved method is 10.8%, which is much smaller than 20.5% by the acceleration-strain-based method in Section 3.1.1. When the exact FE model was used, the RMSDs are 10.6 and 17.7% for the stain-based and the improved methods, respectively. The slight increase by the large perturbation is because the RMS is significantly affected by accuracy of the low frequency components, as shown in the result of the acceleration-based method. The MAC values of Fig. 8 shows that the large perturbation makes bigger change as the mode order increases, and the first mode which significantly affects the RMSDs is barely changed. The inaccuracy in higher modes resulted in inaccurate estimation of dynamic displacements that derives the slight increase of the RMSDs. This illustrates the improved method using the mode shapes of the FE model is very effective when the structure is so complex that its lower mode shapes cannot be easily assumed.

3.1.4 Measurement of strains at load carrying members

In the case of the deck arch bridge, the arch and vertical columns are the major load carrying members to resist the dead loads that comprise majority of the total load applied to the structure, while the deck is designed to transfer the live load to the arch system. Considering the case with strain gauges on the members other than deck, another sensor topology is considered: an

accelerometer is at N6, and four strain gauges are at arch members between N12-N13 and N20-N21, and columns between N3-N14 and N9-N19. Fig. 9 shows the displacement estimated at N6 using the improved method. The result is very close to the exact one with 9.69% in RMSD, which is smaller than the value of 10.6% by the strain measurements on the deck described in Section 3.1.1.

The mode shapes cannot be assumed in an analytical form for the whole structure when the structure has a complex shape. Therefore, the acceleration-strain-based method using the assumed sinusoidal mode shapes is applicable only when the strain gauges are on the deck. This example shows that the proposed improved method based on the FE model has big advantage when the strain sensors are placed on non-deck members.

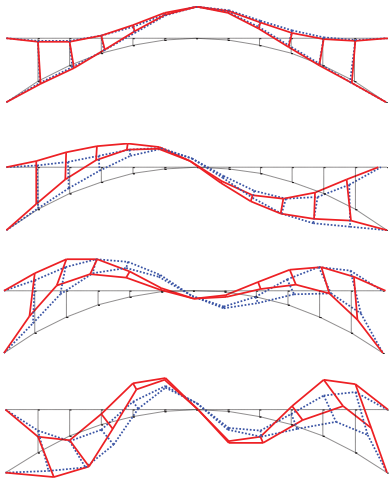

Fig. 7 First four mode shapes of perturbed FE model with 34.6% errors in RMS (dotted lines) compared with those from original model (solid lines)

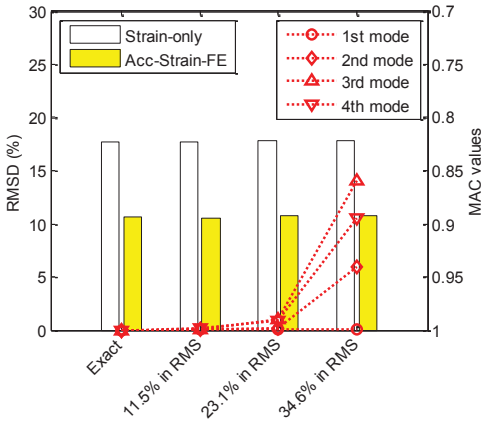

Fig. 8 RMSD of displacements estimated at N5 for perturbed deck arch FE models

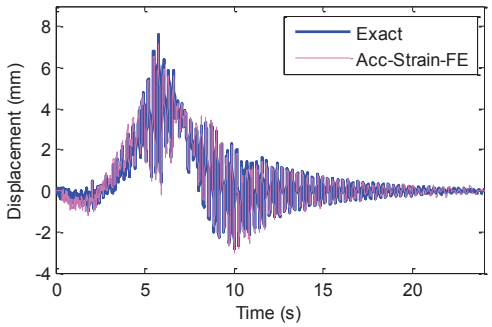

Fig. 9 Displacement estimated at N6 by improved acceleration-strain-based method using strain measurement on load carrying members

3.2 A three-span truss bridge model

The second example is a 2D 3-span truss structure shown in Fig. 10. It is a double-Warren truss model which has intersecting diagonal members to provide the model strength. The model has a total length of 192 m (=56 m+80 m+56 m) with varying heights of 10-18 m. The second support, named A2, is pinned, while the other three supports (A1, A3, and A4) are rollers.

The model is composed of 175 members: 24 lower chords, 24 upper chords, 27 vertical members, and 100 diagonal members. The second span is considered as the monitored span for comparison with acceleration-stain-based method. All members are designed to be made of steel, and to have different sectional areas as shown in Table 2.

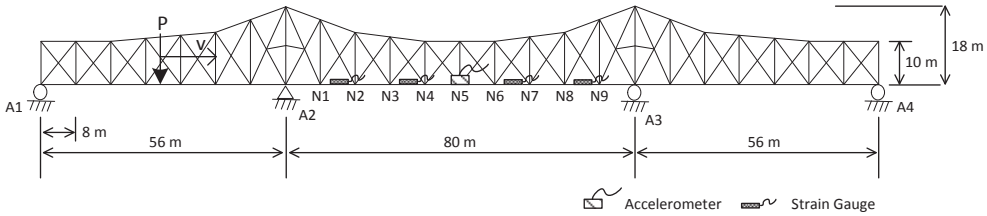

Fig. 10 Three-span truss bridge model with sensor topology

Table 2 Structural properties of truss bridge model

Members	Lower and Upper Chord	Vertical Member	Diagonal Member
Sectional area	0.760 m^2	0.280 m^2	0.360 m^2
Elastic modulus		200 GPa	
Mass density		7850 kg/m^3	

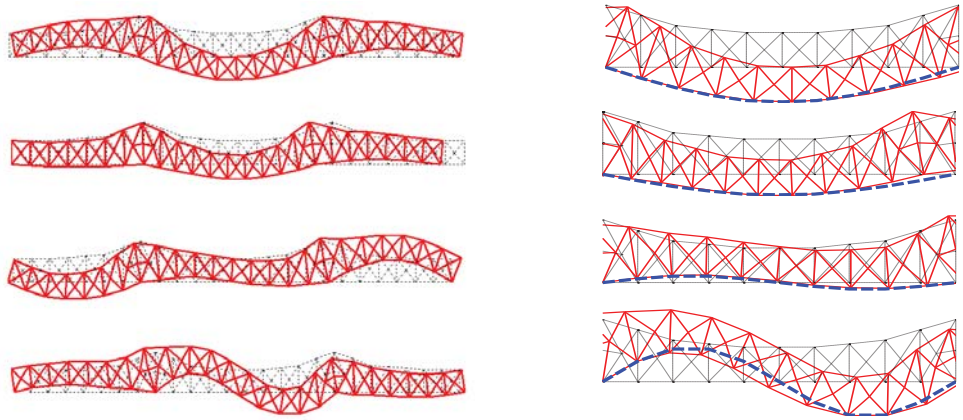

(a) Whole FE model

(b) Second span only: compared with assumed mode shapes

Fig. 11 First four mode shapes of FE model

MATLAB Simulink is used to simulate the displacement, acceleration, and strain of the truss model using a vertical load similar to Fig. 2 moving from left to right on the structure. The acceleration is assumed to be measured at N5, while the strains of the deck are obtained at the mid points of four members between N1-N2, N3-N4, N6-N7, and N8-N9. The simulated acceleration and strains are made contaminated by 5% noise in RMS. Note that acceleration and displacement are obtained in the vertical direction, while the axial strains are obtained on the lower chord members.

Given with 4 strain measurements, the first four mode shapes shown in Fig. 11 are used to build the modal mapping relationship for the strain-based and the improved methods. However, for the acceleration-strain-based method, sinusoidal mode shapes are approximately obtained only for the second span of the continuous truss bridge (Cho *et al*. 2014). Unlike the deck-arch model, the assumed mode shapes are apparently similar to the shapes from the FE model with small discrepancy.

Fig. 12 shows the displacements estimated at N5 by four methods in comparison with the exact ones. The general trends of the results are very similar to those of the deck arch model: the acceleration-based and the strain-based methods show their weakness in pseudo-static and dynamic components of displacement, respectively. Though the acceleration-strain-based method estimates overall shape of the displacement, the amplitude could not be accurately estimated. The improved acceleration-strain-based method estimates the displacement with the best accuracy among the four methods in both low- and high- frequency ranges. The RMSD values of the displacements at N5 are 82.8, 35.1, 34.3, and 22.6% for the four methods, respectively. The error is slightly larger than the deck arch bridge model, but still the proposed improved method gives the smallest error.

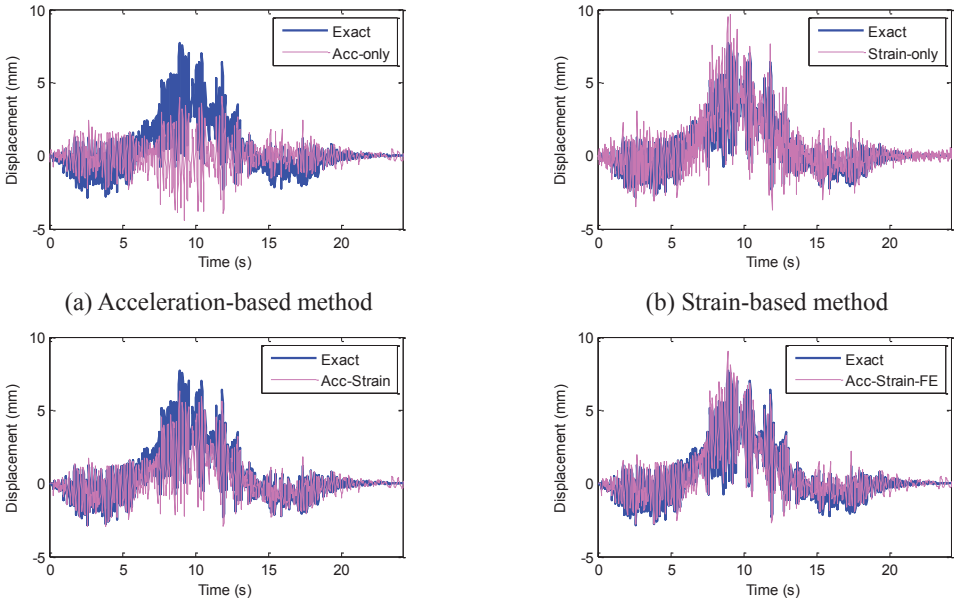

(a) Acceleration-based method

(b) Strain-based method

(c) Acceleration-strain-based method

(d) Improved acceleration-strain-based method

Fig. 12 Comparison of displacements estimated at N5 for three-span truss model by four different estimation methods with exact one

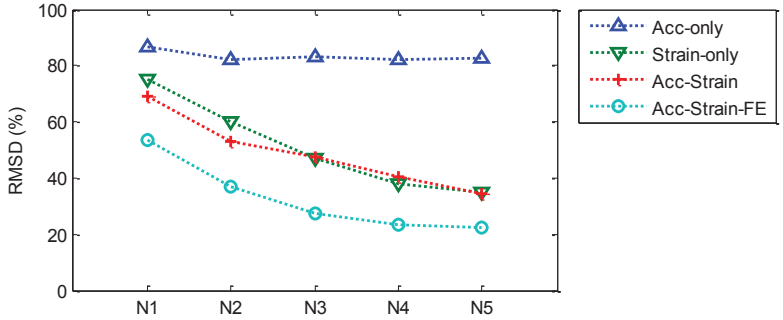

Fig. 13 RMSD of displacements at N1-N5

The RMSD values estimated at 5 locations (N1-N5) by four methods are compared in Fig. 13. Due to the mode shapes assumed similar to the shapes from the FE model (see Fig. 11(b)), the three methods except the acceleration-based method show increasing values as the sensor location gets close to the left support due to smaller amplitude of displacement, while the acceleration-based method shows nearly-constant level of large error due to incorrect estimation of pseudo-static displacements. Similar to the deck arch bridge model, the improved method shows the smallest RMSD values for all locations.

4. Experimental validation

4.1 Test bridge and test setup

To validate the performance of the improved method for a real bridge structure, a field testing was conducted on a prestressed concrete bridge shown in Fig. 14, which was developed as a test-bed of bridge measurement technology by KICT (Korea Institute of Construction Technology). The bridge is a single span prestressed concrete girder bridge with four girders and its span length is 11m.

To estimate the displacement by the improved method, acceleration and strain were measured on the bridge: three strain gages were installed beneath the bridge girder at L1, L3, and L4, and two accelerometers were placed at L2 and L3, as shown in Fig. 14. In addition, two laser displacement sensors were also collocated at L2 and L3 to provide reference displacements. To excite the bridge, a 28.63 ton truck ran on the bridge with the speed of 15 km/h.

4.2 Finite element model of test bridge

To build the modal mapping matrix for the strain-based and the improved methods, an FE model of the bridge was built using ANSYS as shown in Fig. 15. The first three mode shapes for the displacement and strain were extracted from the FE model to build the modal mapping of strain to displacement. Torsional modes have effectively similar shapes to the bending modes for individual girders (Cho *et al*. 2014). Thus, the information of the torsional modes is excluded in the modal mapping procedure.

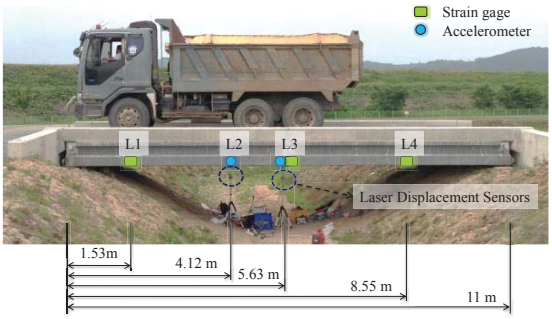

Fig. 14 Test bridge and sensor locations

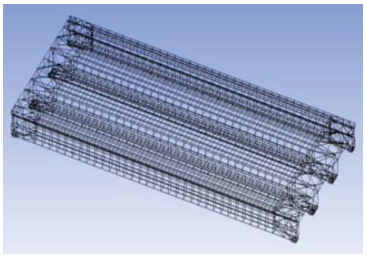

Fig. 15 FE model of test bridge

4.3 Displacement estimation

The displacements at L2 and L3 were estimated by the improved method, and the results were compared with the reference values measured with laser displacement meters. The neutral axis of the bridge was initially assumed to be 0.25 m from the sensor level (bottom of girders) for the strain-based, the acceleration-strain-based, and the improved methods. The neutral axis is compensated in the acceleration-strain-based and the improved methods, but not in the strain-based method. Fig. 16 compares the estimated displacements by four methods with the reference values at L3 when the truck ran. As in the numerical simulations, the acceleration-based method shows weakness in estimating pseudo-static components. The strain-based method cannot estimate accurate pseudo-static component due to the inaccurate neutral axis in the FE model. The acceleration-strain-based and the improved methods estimated displacements very similar to the reference ones as shown in Figs. 16(c) and 16(d).

The RMSD values of the displacements estimated by four methods at L2 and L3 are tabulated in Table 3. While the acceleration-based and the strain-based methods have large errors over 25% in RMSD, the acceleration-strain-based and the improved methods have smaller error. However, the acceleration-strain-based and the improved methods have the smallest measures (less than 6%), since the assumed sinusoidal mode shapes are very good for this beam-type of bridge.

The peak displacement is another important measure for health monitoring of civil infrastructure. Similar to the RMSD, the percentage peak error can be defined as

$$\text{Peak Error } (\%) = \frac{\max u^{est} - \max u^{ref}}{\max u^{ref}} \times 100 \tag{10}$$

The peak errors are calculated and shown in Table 3, which shows that the improved method estimates the peak displacements more accurately than the acceleration-strain-based method: 2.80 and 3.75% versus 3.61 and 6.59% at L2 and L3, respectively. These results indicate that the proposed improved method has better accuracy than the acceleration-strain-based method even for this simply supported bridge. Especially, considering the peak displacement by the moving truck is about 4 mm, the improved method is found to be appropriate for the displacement measurement of civil engineering structures that generally have low displacement levels.

Table 3 RMSD (%) and peak error (%) between estimated and reference displacements

Methods	L2		L3	
	RMSD (%)	Peak Error (%)	RMSD (%)	Peak Error (%)
Acceleration-based method	99.0	-81.4	99.0	-80.3
Strain-based method	28.7	-27.4	33.8	-32.0
Acceleration-strain-based method	5.62	3.61	5.75	6.59
Improved acceleration-strain-based method	5.88	2.80	5.70	3.75

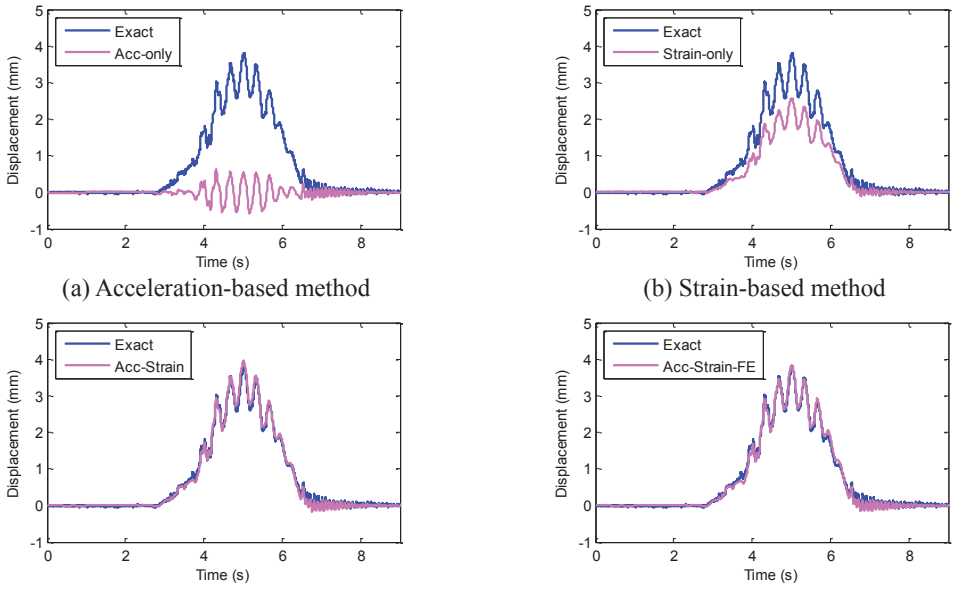

(a) Acceleration-based method (b) Strain-based method

(c) Acceleration-strain-based method (d) Improved acceleration-strain-based method

Fig. 16 Comparison of displacements estimated by improved method with reference: at L3

5. Conclusions

In this paper, an improved displacement estimation method based on data fusion of acceleration and strain has been proposed for the application to general types of bridge structures whose mode shapes may not be assumed in analytical (e.g., sinusoidal) function. The improvement has been made by employing the mode shapes from an FE model in the modal mapping of strain to displacement. The performance of the improved method has been verified by numerical simulations on a deck arch structure and a three-span truss structure with complex shapes. Field experiment on a prestressed concrete bridge has also been carried out. The estimated displacements by four methods, acceleration-based method, strain-based method, acceleration-strain-based method, and improved method, have been compared.

The result of this study can be summarized as:

(1) In the numerical simulations on the deck arch model and the truss model, the proposed method estimated displacements with better accuracy than the other methods at all locations of the structure owing to the accurate modal mapping using the FE model.

(2) The perturbation of the FE model has increased the inaccuracy of the improved method. However, at the center locations, large perturbation (34.6% in RMS) resulted in the RMSD errors of 10.8%, which is less than 20.5% by the acceleration-strain-based method, which shows the effectiveness of the proposed method with somewhat inaccurate FE model.

(3) The proposed method estimated the displacement equivalently well using the strain data on non-beam type members such as truss and arch, which shows its good compatibility of the improved method to more general types of structures.

(4) In the field test on a prestressed concrete bridge, the proposed method accurately estimated the dynamic displacements, whose maximum amplitudes are less than 4mm. The RMSD by the improved method was similar to those by the acceleration-strain-based method, while the peak displacement was estimated more accurately with less than 4% errors.

Acknowledgements

This research was supported by Basic Science Research Program through the National Research Foundation of Korea (NRF) funded by the Ministry of Science, ICT & Future Planning (NRF-2012-R1A1A1-042867). The support is gratefully appreciated.

Reference

Altunisik, A.C., Bayraktar, A. and Ozdemir, H. (2012) "Seismic safety assessment of eynel highway steel bridge using ambient vibration measurements", *Smart Struct. Syst.*, **10**(2), 131-154.

Atkinson, K.E. (2008), *An introduction to numerical analysis*, John Wiley & Sons.

Bani-Hani, K.A., Zibdeh, H.S. and Hamdaoui, K. (2008) "Health monitoring of a historical monument in Jordan based on ambient vibration test", *Smart Struct. Syst.*, **4**(2), 195-208.

Çelibi, M. (2000), "GPS in dynamic monitoring of long-period structures", *Soil Dyn. Earthq. Eng.*, **20**, 477-483.

Cho, S., Sim, S.H., Park, J.W. and Lee, J. (2014), "Extension of indirect displacement estimation method using acceleration and strain to various types of beam structures", *Smart Struct. Syst.*,**14**(4), 699-718.

Chung, W., Kim, S., Kim, N. and Lee, H. (2008), "Deflection estimation of a full scale PSC girder using long-gauge fiber optic sensors", *Constr. Build. Mater.*, **22**(3), 394-401.

Doebling, S.W., Farrar, C.R. and Prime, M.B. (1998), "A summary review of vibration-based damage identification methods", *Shock Vib. Digest*, **30**, 91-105.

Faulkner, B.C., Barton, F., Baber, T.T. and McKeel, W.T. (1996), *Determination of bridge using acceleration data*, Virgina Transportation Research Council. VA, USA.

Foss, G. and Haugse, E. (1995), "Using modal test results to develop strain to displacement transformations", *Proceedings of the 13th Int. Modal Analysis Conf.*

Gindy, M., Nassif, H.H. and Velde, J. (2008), "Bridge displacement estimates from measured acceleration records", *Transport. Res. Rec.*, **2028**, 136-145.

Jo, H., Sim, S.H., Tatkowski, A., Spencer, Jr., B.F. and Nelson, M.E. (2013), "Feasibility of displacement monitoring using low-cost GPS re-ceivers", *Struct. Control Health.*, **20**(9), 1240-1254.

Kandula, V., DeBrunner, L., DeBrunner, V. and Rambo-Roddenberry, M. (2012), "Field testing of indirect displacement estimation using accelerometers", *Proceedings of the Conf. Record of the 46th Asilomar Conf. Signals, Systems, and Computers*.

Kang, L.H., Kim, D.K. and Han, J.H. (2007), "Estimation of dynamic structural displacements using fiber Bragg grating strain sensors", *J. Sound Vib.*, **305**(3), 534-542.

Lee, H.S., Hong, Y.H. and Park, H.W. (2010), "Design of an FIR filter for the displacement reconstruction using measured acceleration in low-frequency dominant structures", *Int. J. Numer. Meth. Eng.*, **82**(4), 403-434.

Lee, J.J., Fukuda, Y., Shinozuka, M., Cho, S. and Yun, C. (2007), "Development and application of a vision-based displacement measurement system for structural health monitoring of civil structures", *Smart Struct. Syst.*, **3**(3), 373-384.

Majumder, M., Gangopadhyay, T.K., Chakraborty, A.K., Dasgupta, K. and Bhattacharya, D.K. (2008), "Fibre Bragg gratings in structural health monitoring—Present status and applications", *Sensor. Actuat.*

A-Phys., **147**(1), 150-164.
Nassif, H.H., Gindy, M. and Davis, J. (2005), "Comparison of laser Doppler vibrometer with contact sensors for monitoring bridge deflection and vibration", *NDT & E Inter.*, **38**, 213-218.
Omenzetter, P., Brownjohn, J.M.W. and Moyo, P. (2004), "Identification of unusual events in multi-channel bridge monitoring data", *Mech. Syst. Signal Pr.*, **18**(2), 409-430.
Park, J.W., Sim, S.H. and Jung, H.J. (2013), "Displacement estimation using multimetric data fusion", *IEEE/ASME Trans. Mechatronics*, **18**(6), DOI: 10.1109/TMECH.2013.2275187.
Park, K.T., Kim, S.H., Park, H.S. and Lee, K.W. (2005), "The determination of bridge displacement using measured acceleration", *Eng. Struct.*, **27**(3), 371-378.
Shin, S., Lee, S.U. and Kim, N.S. (2012), "Estimation of bridge displacement responses using FBG sensors and theoretical mode shapes", *Struct. Eng. Mech.*, **42**(2), 229-245.
Sigurdardottir, D.H. and Glisic, B. (2014), "Detecting minute damage in beam-like structures using the neutral axis location", *Smart Mater. Struct.*, **23**(12), 125042.
Xu, L., Guo, J.J. and Jiang, J.J. (2002), "Time-frequency analysis of a suspension bridge based on GPS", *J. Sound Vib.*, **254**(1), 105-116.

Smart Structures and Systems, *Vol. 15, No. 3 (2015) 665-682*
DOI: http://dx.doi.org/10.12989/sss.2015.15.3.665

Structural identification of Humber Bridge for performance prognosis

R. Rahbari[1], J. Niu[2], J.M.W. Brownjohn[*3] and K.Y. Koo[3]

[1]*Department of Civil Engineering, University of Sheffield, Sheffield, United Kingdom*
[2]*School of Civil Engineering, Southeast University, Nanjing, China*
[3]*College of Engineering, Mathematics and Physical Science, University of Exeter, UK*

(Received November 20, 2015, Revised February 17, 2015, Accepted February 25, 2015)

Abstract. Structural identification or St-Id is 'the parametric correlation of structural response characteristics predicted by a mathematical model with analogous characteristics derived from experimental measurements'. This paper describes a St-Id exercise on Humber Bridge that adopted a novel two-stage approach to first calibrate and then validate a mathematical model. This model was then used to predict effects of wind and temperature loads on global static deformation that would be practically impossible to observe. The first stage of the process was an ambient vibration survey in 2008 that used operational modal analysis to estimate a set of modes classified as vertical, torsional or lateral. In the more recent second stage a finite element model (FEM) was developed with an appropriate level of refinement to provide a corresponding set of modal properties. A series of manual adjustments to modal parameters such as cable tension and bearing stiffness resulted in a FEM that produced excellent correspondence for vertical and torsional modes, along with correspondence for the lower frequency lateral modes. In the third stage traffic, wind and temperature data along with deformation measurements from a sparse structural health monitoring system installed in 2011 were compared with equivalent predictions from the partially validated FEM. The match of static response between FEM and SHM data proved good enough for the FEM to be used to predict the un-measurable global deformed shape of the bridge due to vehicle and temperature effects but the FEM had limited capability to reproduce static effects of wind. In addition the FEM was used to show internal forces due to a heavy vehicle to to estimate the worst-case bearing movements under extreme combinations of wind, traffic and temperature loads. The paper shows that in this case, but with limitations, such a two-stage FEM calibration/validation process can be an effective tool for performance prognosis.

Keywords: suspension bridge; structural; identification model; updating modal; test; temperature; vehicle; wind static

1. Introduction

Trouble-free operation of suspension bridges requires that the design caters for the full range of static and dynamic loads and their combinations and that predicted performance in terms of internal forces and deformations is within tolerable limits.

Each suspension bridge is unique so that unlike mass-produced aircraft or automobiles there are

∗Corresponding author, Professor, E-mail: J.Brownjohn@exeter.ac.uk

http://www.techno-press.org/?journal=sss&subpage=8 ISSN: 1738-1584 (Print), 1738-1991 (Online)

no opportunities to test designs at full-scale before construction. Hence performance is simulated with numerical or finite element models and wind tunnel tests on scaled physical modes. Reliability of such simulations depends on both a good understanding of the loading and the ability of the model to represent the structural behavior. Deficiencies in either can result in expensive, inconvenient or even catastrophic surprises.

By the time 'out of bounds' performance is observed on the as-built structure the only option is a costly retrofit or usage restriction. For example a number of North American bridges (Abdel-Ghaffar and Scanlan 1985, Kumarasena *et al*. 1989) have had to be retrofitted due to lively in-wind performance while for Great Belt Bridge the fix was by aerodynamic modifications through wind vanes (Larsen *et al*. 2000).The other major effect that may be unforeseen is the effect of extreme combinations of thermal, traffic and wind movement on excursions at interfaces among spans, towers and abutments. There have been several surprises at the scale of these movements that have led to premature and costly retrofits.

Hence for an existing structure there are strong motivations to develop a good understanding of the structural behavior and hence the impact of unusual or increased loads. A finite element model (FEM) calibrated or updated (Friswell and Mottershead 1995) using modal properties identified through system identification provides the best tool for simulating such scenarios. It also offers the capability for full understanding and physical interpretation of the causes and effects of the various loading regimes as a form of performance diagnosis.

Models updated based on modal tests should however be used with caution (Brown and Milne, 1985). In principle such models should not be relied on to do more than reproduce the modal properties used to validate them (a form of interpolation) whereas to go beyond those measurements is a risky process akin to extrapolation. This does not always work; one example is the structurally complex Tamar Bridge where a formally updated FE model was unable to reproduce observed effects on modal properties of significant variations in traffic load (Westgate *et al*. 2015).

The aim of this paper is to explore the next step in producing a reliable, updated FE model that justifies faith in extrapolation. Hence in this study, a FEM of Humber Bridge has been developed then calibrated against results of a system identification process using operational modal analysis of dynamic response to ambient dynamic loads measured over a few days of normal operation. In the next step the calibrated FEM has been used to estimate the static response of the bridge to wind, vehicle and thermal loads and to compare the predictions with observations from a structural health monitoring (SHM) system operating on the bridge. This whole process encapsulates the definition of structural identification (St-Id) as 'the parametric correlation of structural response characteristics predicted by a mathematical model with analogous characteristics derived from experimental measurements' (Catbas *et al*. 2013).

Having established that the FEM predicts observed static response reasonably well, the final step was to use the model to predict some results that could not be observed experimentally. These results include global deformations due to wind loads, but more importantly effects of worst-case combinations of extreme loads and even internal forces.

2. Humber bridge: Structural details and previous studies

Humber Bridge (Fig. 1) was opened in July 1981 and has a main span of 1410 m with side spans of 280 m and 530 m. It links the small towns of Hessle (north) and Barton (south), with the

bridge longitudinal axis aligned in an approximate north-south direction. Like its predecessors Severn and Bosporus, Humber has aerodynamic steel box girders and inclined hangers. The spans comprise a total of 124 prefabricated units typically 18.1m long and 4.5m deep. These are 28.5 m wide and include two 3 m walkways and orthotropic deck plates on which road surfacing is applied. The slip-formed reinforced concrete towers rise 155.5 m above the caisson foundations and carry the two main cables with nominal sag of 115.5 m. The bridge is exposed to prevailing south-westerly cyclonic winds that can reach hurricane force (exceeding 32.7 m/sec), with atmospheric temperatures ranging from -10°C to 30°C.

Humber has been the subject of several academic investigations focusing on dynamic performance. Ambient vibration surveys were carried out in 1985 by University of Bristol and Building Research Establishment (BRE), (Brownjohn *et al*. 1987, Littler 1992), BRE again in 1988 (Littler and Woods 1989) and most recently in 2008 by University of Sheffield and helpers (Brownjohn *et al*. 2010).

Observations from the 1985 modal test and the linked finite element analysis (Brownjohn *et al*. 1987) suggested that the pairs of A-frame rocker bearings at each span end, which were designed to prevent translation in vertical and lateral directions but to allow free movement along the bridge longitudinal axis were not functioning quite as expected. The clearest effect of this was the appearance of the first anti-symmetric vertical vibration mode at a higher frequency than that of the first symmetric mode, whereas for a completely free sliding condition it would be the first mode to appear.

Separate from the modal investigations and potentially having greater impact, several campaigns have deployed state of the art technology for tracking static deformation. In particular, in the period 1989 to 1991 a campaign of measurements (Brownjohn *et al*. 1994) led by Politecnico di Milano supported in-wind performance studies of a design for the proposed Stretto di Messina crossing (Brancaleone and Diana 1993). The measurement campaigns included novel optical systems for measuring displacement. The exercise also provided data for identification of aero-elastic flutter derivatives at full scale (Diana *et al*. 1992). There has also been a brief evaluation of GPS technology by Nottingham University (Ashkenazi and Roberts 1997).

Fig. 1 Views of Humber Bridge. Left: View from Barton anchorage, Right: box deck interior

Following the 2008 modal test, a monitoring system comprising GPS antennae, lasers, a tilt-meter, accelerometers, thermistors and an anemometer was installed on the bridge and has operated since early 2011 (Brownjohn et al). With the more sophisticated technology compared to the 1989-1991 campaign, the deformation data available from this system are not only richer but cover a longer period. Hence they represent more extreme conditions and have provided fresh insights into the performance of the bridge. In particular, while the early system predated the era of 'structural health monitoring', the present system is designed to provide automatic data processing, data visualisation and capability for online anomaly detection and load identification. To provide additional capability, a numerical model of the bridge has been developed, for performance interpretation and simulation, providing an effective combination for structural health monitoring of the bridge.

As well as two-dimensional finite element analysis by Freeman Fox & Partners (designers), several numerical models of Humber Bridge have been developed e.g., (Dumanoglu and Severn 1987, Karuna 2002, Hornby *et al*. 2012). The former example provided an opportunity to calibrate novel finite element modeling techniques for suspension bridges to be applied to seismic response analysis of the two bridges crossing the Bosporus in Istanbul.

3. Structural health monitoring, system identification and structural identification (St-Id)

Structural health monitoring offers two approaches for evaluating the present performance (diagnosis) and predicting future performance (prognosis) of structures. One is based on data-driven models (Worden and Manson 2007) that are effectively curve-fits to historic load and performance data. The second is the physics-based approach (Farrar and Lieven 2007) where a finite element model (FEM) is calibrated or adjusted to fit data from measurements of dynamic and/or static response. The whole process of creating and calibrating a physics-based model for performance diagnosis fits the definition of St-Id (Catbas *et al*. 2013) and usually includes system identification to extract modal properties from dynamic response measurements obtained in a modal test.

Both data-driven and physics-based approaches have been applied to the shorter Tamar Bridge (Cross *et al*. 2013). This bridge features a traditional truss girder, with added complexity of retrofitted cantilever lanes and additional stay cables. That exercise demonstrated the limitations of applying a model validated using only modal test data, since using that model (in effect extrapolating) to reproduce the effects of temperature and traffic variations on natural frequencies proved challenging (Westgate *et al*. 2015). The aim here is to demonstrate the power of the physics-based approaches with additional validation from static response data for what is in fact a simpler structure.

4. 2008 modal test and long term monitoring

In July 2008 a team of researchers from University of Sheffield (UK), City University of Hong Kong and Faculty of Engineering, University of Porto used a sequence of 33 one-hour measurements over five days to map out mode shapes and identify natural frequencies and damping ratios for Humber Bridge. The exercise and the operational modal analysis (OMA)

applied for system identification of the modal properties are fully described elsewhere e.g., (Brownjohn *et al*. 2010).

During the campaign winds were moderate and temperature ranges small. Ten autonomous tri-axial accelerometers measured at 76 positions each with a pair of recorders on either side of the bridge, a total of 76×6 degrees of freedom, not all independent. The recorders were synchronized by GPS antennae and used the reference/rover technique to provide for high spatial resolution of mode shapes.

The long term monitoring system was installed as part of the same research project. The system is illustrated in Fig. 2 and comprises three GPS antennae (one base station and two rovers, for real time kinematic operation), three servo accelerometers and one biaxial inclinometer at midspan, and four extensometers in pairs at each end of the main span. The rationale for using only three accelerometers is that having the full set of mode shapes from the modal test, the total dynamic response at any point in the structure can be obtained by modal superposition. There are also temperature and weather sensors at various locations.

The acceleration data are useful for tracking modal parameters and response levels in lowest few modes that are susceptible to buffeting and aero-elastic effects. However it is the quasi-static deformation observed through the GPS, extensometers and DC component of lateral acceleration (interpreted as rotation) that is relevant here and which is usually most important to bridge operators.

The modal survey provided the means to validate and update the FEM described next, while the monitoring system provided deformation signatures for further validation of the updated FEM.

5. Developing the finite element model

In order to provide a reliable physics-based simulator to rationalize observations from the monitoring, a detailed FEM of the bridge was developed. A FEM developed in previous studies (Dumanoglu and Severn 1987) using modified SAPIV software (Bathe *et al*. 1974) assisted development of a more elaborate ANSYS model. Main components of the model are two twin-pylon towers, the bridge deck (main and two unequal side spans), main cables, bearings and expansion joints.

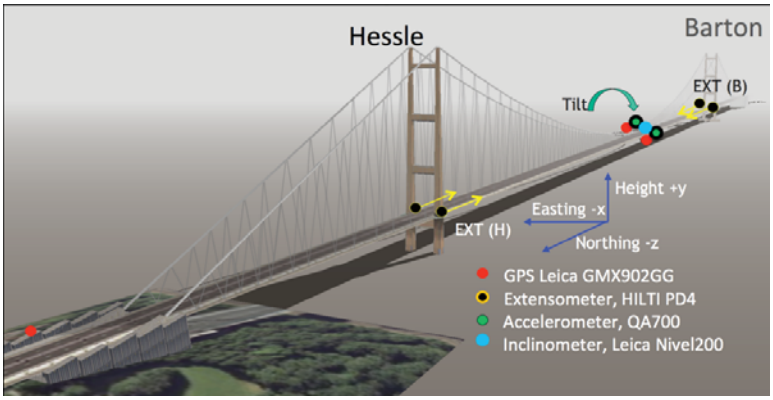

Fig. 2 Humber Bridge instrumentation and directional conventions

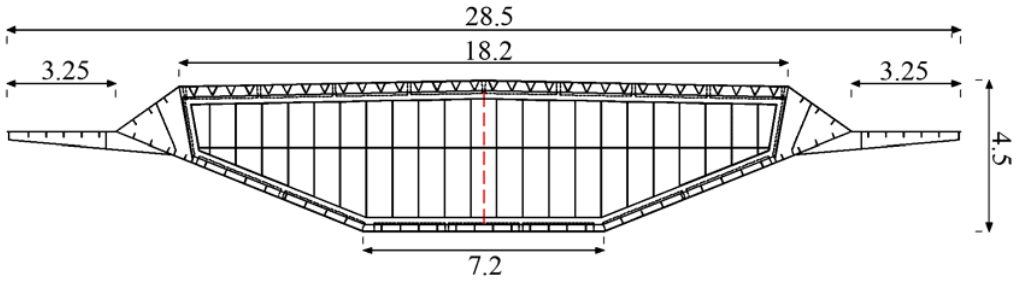

Fig. 3 Deck Section. Dimensions in m

5.1 Box girders

Model creation began with developing an appopriate representation of the box girder, shown in Fig. 3 with typical dimentions and one of the four equi-spaced stiffening bulkheads. A high resolution model with all features of the stiffeners would not necessarily justify the time and computing resources required, so an equivalent section model was created, with appropriate adjustment of thickness and density to represent the stiffening details. Details such as overlap joints and fatigue reducing holes at bulkheads for deck longitudinal stiffeners visible in Fig. 1 were ignored to simplify the model.

5.2 Towers and cables

Hollow reinforced concrete tower columns taper from 30.4 m wide above the base to 26 m under the saddles with a constant 18.4 m between internal faces and wall thickness correspondingly reducing from 3 m at the base. ANSYS SOLID45 elements are used to represent this, assuming full fixity at the caisson foundation levels, with saddles modeled by solid steel elements.

Main span main cables comprise 14948 galvanized 5 mm wires, whereas the shorter Hessle side span uses an extra 800 wire strands that are anchored at the Hessle tower saddle. Hence main cable diameters are about 0.70 m for the main span and Barton side span and 0.71 m for Hessle side span. These cables are modeled using ANSYS BEAM4 elements, with translational fixity at anchorages and saddles and sliding over saddles not allowed.

Steel inclined hangers (8 cm diameter) are modeled using single LINK3 elements, and as such are pinned at each end since they offer no bending resistance in respect of global performance.

5.3 Geometric stiffness and cable tension

With direct access to stiffness matrices e.g., via the FE software source code, the geometric component resulting from the cable tension can be inserted directly, and static and dynamic analyses run in a single step. However, with ANSYS, dynamic analysis of a tension structure such as a suspension bridge involves a prior static analysis to identify a dead load state with equilibrium of gravity and cable axial forces. These axial forces are locked into the global stiffness matrix in subsequent analyses for dynamic and static response.

Fig. 4 A-frame bearings: Left. Conceptualization of arrangement at Hessle tower with bearing pairs connected (left) to main span and (right) to Hessle side span. Right: view of A-frames at west side of Hessle tower

In this first step the initial strains estimated from a parabolic catenary approximation with assumed dead and live load are converted directly to tensions that imperfectly balance gravity forces that are simultaneously applied. The imperfect initial strain estimates may result in configuration (deformed state) too far from both the design condition and a few manual iterations are required. To account for varying total axial load in the main cables these were divided into six region different initial strains. For Humber the final (best) error was about 1 m from the configuration defined in the drawings, a value that has negligible effect on either dynamic or static behavior.

5.4 Movement joints

Supports and expansion joints have a major role in the bridge behavior, an effect observed in other long pan bridges (Fujino and Siringoringo 2013). Figure 4shows the general arrangement at a tower and the physical realization in 2013. Note that the crossbeam of one of the A-frames had collapsed onto the concrete plinth due to internal wear and at the time of writing, A-frame rockers were being replaced using two pendel bearings and a wind shoe (Hornby *et al*. 2012). DEMAG roller bearings provide roadway continuity between the separate spans, accommodating the horizontal movements.

In theory bearings provide only (low) friction but in practice they provide resistance (stiffness), whose effect was studied by changing the hinges progressively from pinned to fixed via a variable stiffness. This produced significant changes in properties (principally natural frequency) for some modes in the modeling, confirming the (first) anti-symmetric mode switching observed in the original SAPIV modeling.

6. Operational modal analysis for model calibration

The traditional basis for calibration and adjustment of a FEM is usually an ambient vibration survey followed by operational modal analysis (OMA). The most recent exercise (2008) provided

a comprehensive set of mode shapes and frequencies for vertical, lateral and torsional. Results from the 1985 exercise could not be used as they were not available in digital form, mode shapes were at a far lower resolution and crude (by 21st century standards) OMA procedures were used. The main disadvantage of the crude 1985 OMA is that it produced positively biased damping estimates, but with smaller non-systematic errors in frequencies and mode shapes.

The 33 sets of one hour recordings from 30 channels of acceleration signals were analysed using a variety of OMA techniques including frequency domain decomposition, stochastic subspace identification and eigensystem realization algorithm (ERA). ERA as deployed in in-house software provided for normalization of cross-spectra in frequency domain that allowed gluing of mode shape pieces to produce the best set of modes, examples of which are shown in Figs. 5-7.

Figs. 5-7 present example comparisons of mode shapes from FEM and OMA. In each plot the dots represent the measured modal ordinates, the curved solid lines the analytical mode shapes and the straight lines the undeformed deck profile. The scatter in points for the lateral and torsional modes reflect the difficulties in OMA at very low frequencies and with modes occurring at extremely close frequencies: the first vertical torsional mode is separated from a vertical mode by as little as 0.003 Hz. The mode shapes shown do not take advantage of summing and differencing of signals from either side of the deck, a process that greatly reduces the scatter in modal ordinates.

The systematic approach to comparing mode shapes uses the modal assurance criterion (MAC) and the more visual Frequency-MAC or 'FMAC' (Fotsch and Ewins 2000). MAC is a simple correlation coefficient between corresponding modal ordinates for experimental and analytical modes such that identical modes have MAC=1, while MAC values close to unity strongly indicate that modes correspond. FMAC takes all combinations of analytical and experimental mode and plots their two frequencies against each other as markers of size and color or shade that indicates the value of the corresponding MAC.

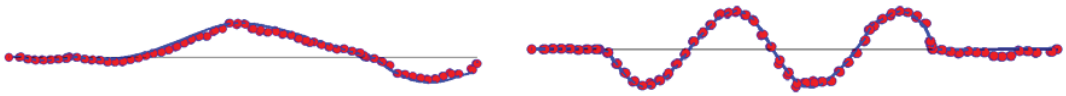

FEM 0.118Hz, OMA 0.117 Hz FEM 0.251 Hz, OMA 0.240 Hz

Fig. 5 Example vertical modes from finite element model (FEM) and operational modal analysis (OMA), viewed from the west

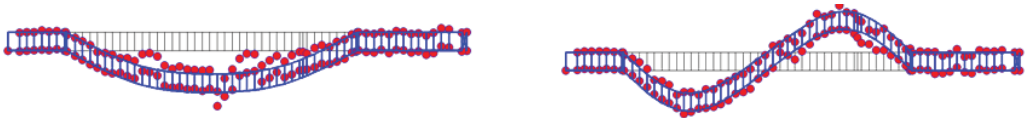

FEM 0.0522 Hz, OMA 0.056 Hz FEM 0.111 Hz, OMA 0.141 Hz

Fig. 6 Example lateral modes from FEM and OMA, viewed from above

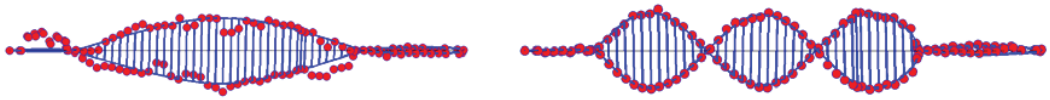

FEM 0.303 Hz, OMA 0.311 Hz FEM 0.646 Hz, OMA 0.650 Hz

Fig. 7 Example torsional modes from FEM and OMA, viewed from the west

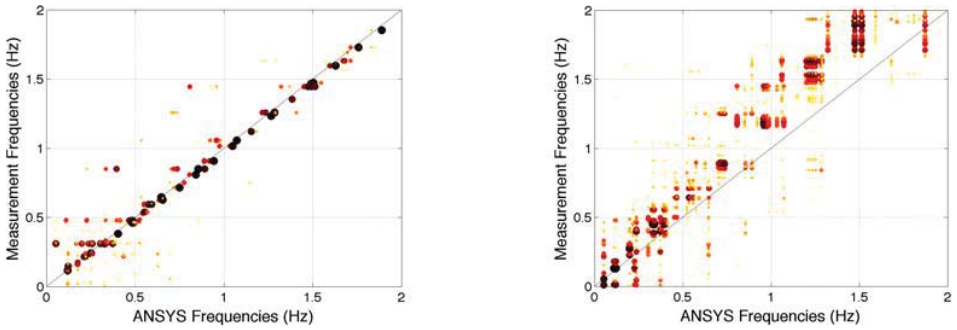

Fig. 8 FMAC comparison of (left) vertical and (right) lateral mode frequencies from FEM and OMA

Hence in Figure 8 FEM frequencies are on the horizontal axis, OMA values on the vertical axis and quality of match is shown as markers whose colour and size increase with MAC. There are many vertical modes with similar shapes (large, dark markers) and frequencies (markers close to the 45° line) up to at least 2 Hz. However for lateral modes the FEM tends to underestimate mode frequencies and to provide relatively few good mode shape matches above 0.5Hz.

While the set of experimental modes identified depends on the parameters used in the identification process and the judgment of the analyst, the final OMA set as reported by (Brownjohn *et al*. 2010) reflects modes that recurred with strong confidence indicators. Likewise the final FEM was the result of several stages of analysis with successive adjustments to parameters having the aim of converging on the best OMA results. Stages of the manual updating involved adjusting factors such as bearing fixity (modeled as stiffness varying from zero to infinity), cable tension and deck girder detail.

7. Comparing predicted and observed quasi-static deformations under operational loads

The FEM variant providing the best match of mode shapes with OMA results, reported in the previous section, was further checked in terms of ability to reproduce observed static performance, for example the movements at the A-frame bearings. Observations (Brownjohn *et al*. 2014) have shown that the large cumulative horizontal girder movement at the A-frames is a combination of dynamic and quasi-static motion due to wind and effects of heavy goods vehicles. SHM data has shown that vertical and lateral movements are both accompanied by horizontal movement at the ends of the main span. The wind and traffic effects on bearing movement are a result of the three-dimensional (3D) deformations due to a single action and which can be understood through simulation with the FEM.

Technology for simultaneous 3D measurement of deformation at all points on a bridge is currently not available in a practical form, although deformations can be sampled with different degrees of spatial and temporal resolution and accuracy (Brownjohn *et al*. 2015). For example a robotic total station can track several dozen markers, but not fast enough to capture quasi-static effects of a heavy vehicle, while one GPS receiver can capture 3D movement with adequate time

resolution but for a single point. Technologies based around optics, radar and lasers are progressing but as yet do not provide a comprehensive and cost-effective solution. Hence the FEM validation through static data is based on the (spatially) sampled GPS and extensometer data, and the double-validated FEM can be used to extrapolate to the whole bridge.
Effects of individual moving vehicles are first considered because the principle of the influence line allows global deformations due to point loads to be observed.

7.1 Vehicle effects

A vehicle passing over the bridge causes downward (negative) deflection at its current location, with corresponding vertical movement in adjacent spans due to the cable continuity and flexible towers. In addition, as revealed by the FEM and corroborated by the SHM system, the bridge configuration is such that significant longitudinal movements accompany the vertical deformation, plus there is a small component of lateral movement and rotation due to the offset from bridge centreline. Humber Bridge occasionally carries extreme heavy goods vehicles (HGVs) of around 100 tonnes (0.98 MN) that provide strong signals compared to effects of wind and passenger cars, making it possible to observe these time and space varying quasi-static deformations with a relatively high signal to noise ratio.

Humber Bridge has a weigh in motion (WIM) system operated independently, with heavy goods vehicles (HGVs) weight and timing data available on request. HGVs travel across the bridge under varied traffic and weather conditions, so that the deformations observed for similar weight vehicles will vary.

7.1.2 Simulated vertical deformations

Because bridge configuration (shape) changes due to a moving vehicle are complex, two different approaches were used to simulate the moving load using the FEM. In the first approach the force was applied to represent the vehicle moving from Hessle to Barton (north to south) on the nearside east lane in 490 steps along the bridge length, noting the midspan deformation. In the second approach the force was applied as a point load at the centre of the mid span, noting the vertical displacement as a function of position along the bridge. According to Betti's theorem and the concept of an influence line, results from these two methods should be same, as shown in Fig. 9 (left). However to be completely convincing as well as to provide animation of a complete set of responses, the single moving force simulation was used to illustrate the complete set of deformations in all axes throughout the deck during vehicle traverse. In fact the single force was realized a set of wheel loads to avoid extreme local deformation and stresses and the two lines are deliberately separated to show equivalence.

7.1.3 Comparison of measured and simulated vehicle-induced vertical deformations

For clearest observation of HGV-induced deformations, data on a calm day are needed. Hence vertical displacement from east GPS receiver on 29/1/2012 was used to verify the procedure. Fig. 9 (right) shows stages in processing the raw GPS data. First the linear trend is removed from the raw GPS data (thinnest line), next a low pass filter was applied to remove vertical vibrations in the lowest modes. Finally a high pass filter with an extremely low cut off frequency (0.0006 Hz) was used to eliminate effects of quasi-static external actions such as wind and temperature, the final result is the thick line. The two traces of Fig. 9 (left and right) do not perfectly overlay due to the varying vehicle speed.

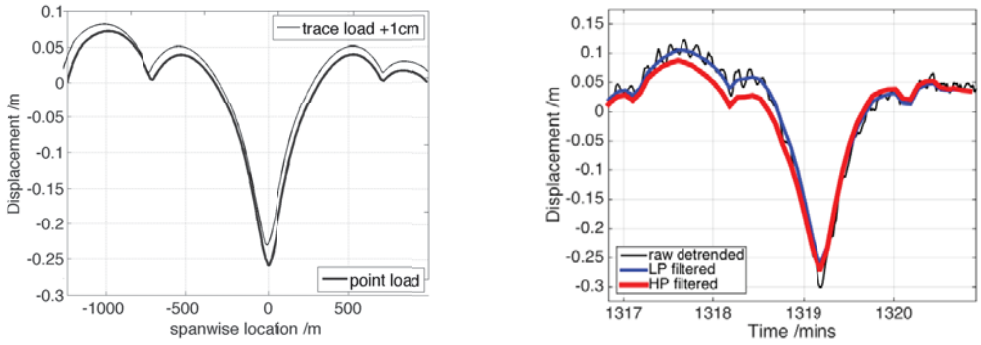

Fig. 9 Left, vertical displacement of bridge main-span from FEM. Trace load is midspan deformation due to moving load, point load is global deformation due to point load at midspan. Right, raw (detrended GPS), low-pass filtered and then high-pass filtered vertical displacement for 100 kN vehicle

7.1.4 Rotation about longitudinal axis measured and simulated

The vehicle path in the nearside (most westerly) lane results in a rotation about the bridge longitudinal axis, illustrated in Fig. 10. The difference between east and west position for maximum deflection is 0.034 m and the agreement between measurement and simulation is a good reflection of the RTK GPS capability, reported as 0.035 m accuracy for three standard deviations (Nickitopoulou *et al*. 2006).

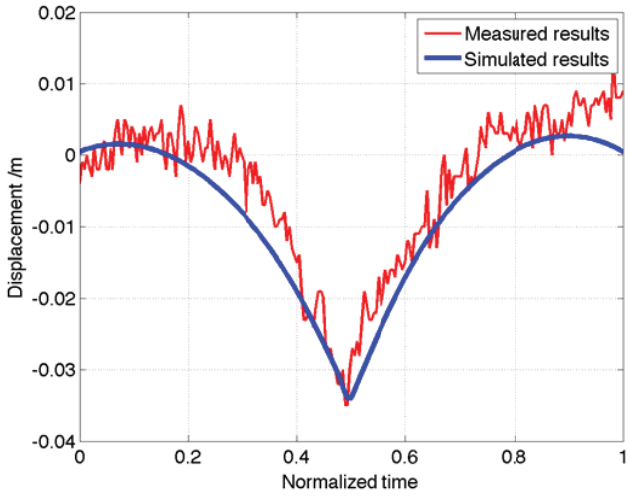

Fig. 10 Comparison between simulated and measured vertical displacement differences between east and west GPS sensor position at midspan

7.1.5 Longitudinal displacement at bearings

Fig. 11 compares simulated movement at Hessle bearing with GPS data for a 98 tonne northbound HGV on 26/4/2012. Both simulation and observation show that the deck shifts towards the tower closer to the vehicle, then moves back to neutral and finally towards the opposite tower as the vehicle crosses. Where extension and GPS data are available simultaneously they confirm the commonality shown in the simulations. Maximum Hessle and Barton simulated bearing movements are 55 mm and 59 mm respectively, minima are 49 mm and 44 mm.

To demonstrate the extrapolation capability of the FEM, the entire vehicle transit was animated to visualise deformations and stresses due to heavy vehicle transit. For example Fig. 12 shows first principal stresses due to a hypothetical 170 tonne vehicle close to the Barton tower. Tension is positive, and close inspection of the area around the A-frame rocker connection to the deck shows expected stress concentration. Vehicles of such size are extremely rare; one was recorded crossing the bridge during the 1990 monitoring (Brownjohn *et al*. 1994).

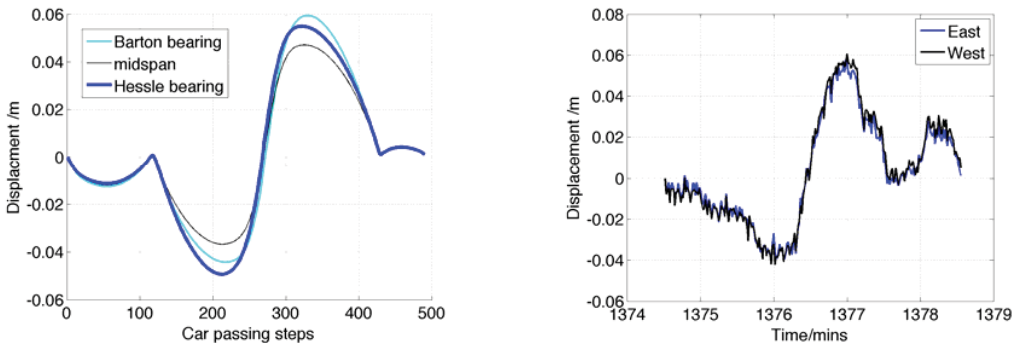

Fig. 11 Comparison betweens imulated and measured longitudinal (northerly) displacement. Left, simulated at three points on main span and right, measured by GPS for northbound 98 tonne vehicle

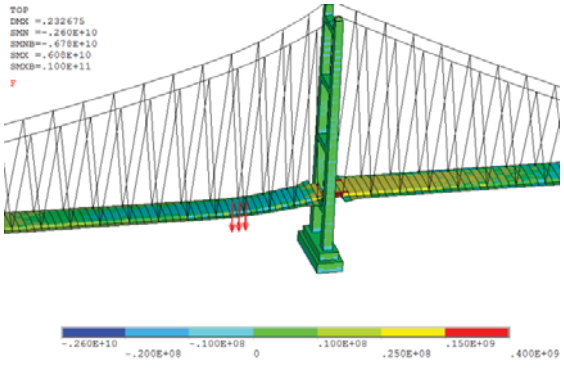

Fig. 12 Stress distribution with 170 tonne vehicle close to Barton tower

7.2 Wind effects

Wind is a critical load condition for a long span bridge due to the uncertain aerodynamic and aeroelastic effects partially explored during the design process via wind tunnel testing. For Humber vertical deformation (both static and dynamic) in wind is found by observation to be significant only in the strongest winds whereas both quasi-static and dynamic lateral deformation have been signficant factors driving bearing wear due to the kinematic link with longitudinal bearing movement. Wind-driven lateral displacement is also more obvious in monitoring data partly because traffic and temperature do not affect it.

7.2.1 Measured wind effects

Several interesting effects of wind loads have been observed during the monitoring, particularly during extreme conditions. Fig. 13 shows measurements of lateral and longitudinal displacement during a hurricane force wind in January 2013 with instantaneous wind speeds reaching 39 m/sec at a compass bearing of 255° i.e., a little south of due west (30 minute mean speed was 26 m/sec). The strong lateral motion (GPS E) is reflected almost exactly in the differential movement of the two bearings and the ratio of lateral displacement to differential bearing longitudinal motion is approximately 30:1. The midspan GPS and bearing extension measurements show that the main span moves bodily to the north along with the lateral drift.

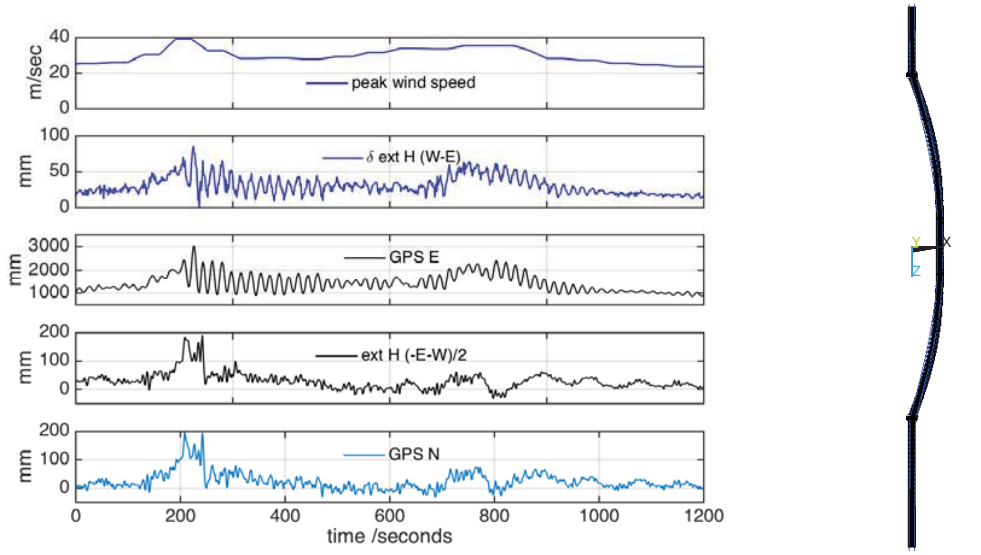

Fig. 13 Wind and horizontal plane man span movements due to hurricane force wind (30/1/2013).Top to bottom: peak gust; difference of east and west extensions at Hessle bearing; midspan GPS eastings (E) (similar trends in the two plots); average northerly movement at Hessle bearing; midspan GPS northings (N)(similar trends in the two plots). GPS data are with respect to datum for neutral conditions. Inset (right) shows the FEM first lateral mode shape

7.2.2 Simulated wind responses

Simulating wind effects is complicated by the unknown distribution of wind forces along the bridge axis and simultaneous effects on rotation about the bridge axis. The original wind tunnel investigation (Walshe and Cowdrey 1972) provided drag coefficient C_D=0.078 for 28.5 m reference width and showed this to be a maximum value, at zero angle of attack. Hence a total lateral force of 100 kN (45 N/m) along the length of the bridge is a reasonable representation of a uniform 5.64 m/sec wind.

Fig. 14 shows the observed and simulated effects of steady winds. The experimental observation is for the relationship of westerly wind component orthogonal to the deck axis and GPS eastings, both for 30 minute averages. For the full range of measured winds the zero wind datum has a 13 cm positive offset, while the quadratic factor 0.0019 sec^2/m is similar to that identified by Stephen *et al*. (1992). With winds limited to maximum 6 m/sec the coefficient rises to 0.0027. Considering only easterly winds (not shown) the coefficients are 0.0022 and 0.0037 (for winds below 6 m/sec), so factors such as wind angle of attack and nonlinearities in the structure or load mechanisms may influence response.

The (low wind) simulation provides a coefficient 0.004 sec^2/m. The simulated deflections in Fig. 14 are for a line along the west side of the bridge between bearings at each end, and the lateral load is applied in the easterly direction (as for a westerly wind). This is an extreme simplification as it assumes that wind is uniform in time and space, perfectly orthogonal to the bridge in the horizontal plane and inducing no rotation due to moment coefficient.

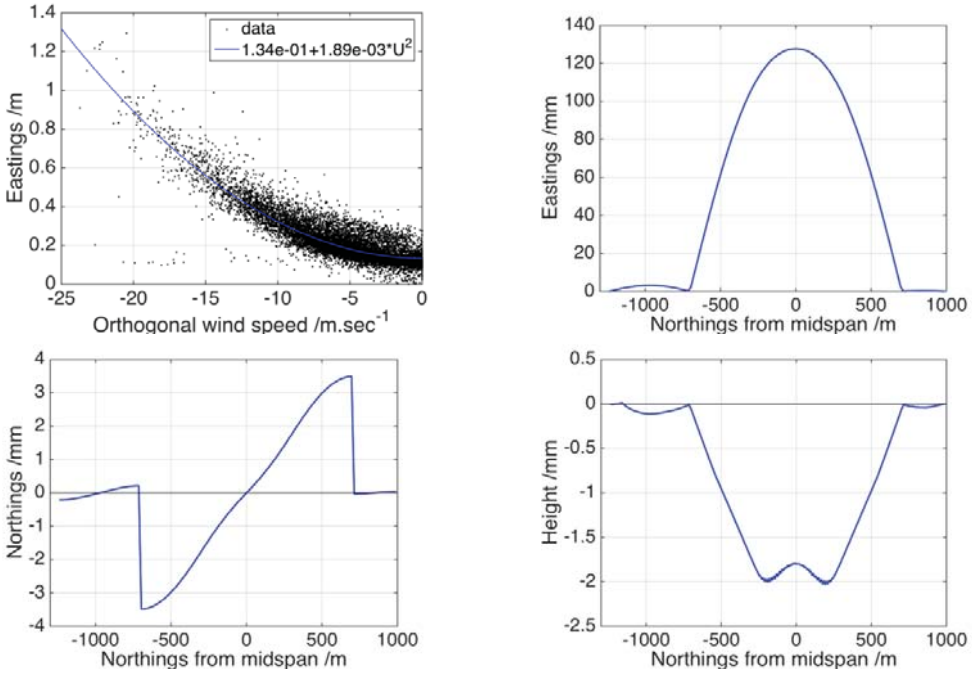

Fig. 14 Clockwise from top left. Observed 30-minute averages of GPS easting and orthogonal wind speeds for westerly winds only; lateral, longitudinal and vertical deflections of west side of bridge due to pure 45 N/m lateral load in +ve east direction

The longitudinal and vertical deformations on the east side are a perfect mirror image of those (shown) on the west side i.e., there is rotation about vertical axes through the towers –as observed experimentally, but no net longitudinal shift in one direction –unlike the observation. This may be due to the northerly component of the hurricane wind force. There is also rotation about the longitudinal axis but that seems to be a pure geometric effect since no aerodynamic moment has been applied.

The midspan lateral displacement is 128 mm for 3.5 mm longitudinal displacement (of one bearing), a ratio of 36:1, 18:1 for the differential movement, smaller than the 30:1 ratio observed at full scale during the hurricane. As already stated it is at present practically impossible to observe such a deformed shape experimentally.

7.3 Temperature effects

Effects of uniform temperature changes can easily be obtained from a single FEM analysis and checked against single point measurements with effects of wind and vehicle loads filtered out.

7.3.1 Measured temperature effects

Temperature effects are very clear, for example Fig. 15 (left) shows the almost linear observed relationship between the temperature on the top surface inside the box and displacement in the northerly direction at both bearings (from extensometers) and midspan (from west GPS antenna), all 30-minute average values thus removing effects of vehicle-induced movement. The datum values for each set are arbitrary but the linear relationships for extensions are crystal clear with e.g., 9.5 mm Hessle bearing movement per 1°C increase in box temperature. There is also a weak trend for the midspan displacement. Unfortunately relationships with temperatures of air, road surface and box deck soffit are varied and nonlinear to differing extents (Fig. 15, right).

Midspan vertical displacement also shows varying relationships with different temperature data, the clearest being with box soffit temperature, with 53 mm sag per 1° increase temperature.

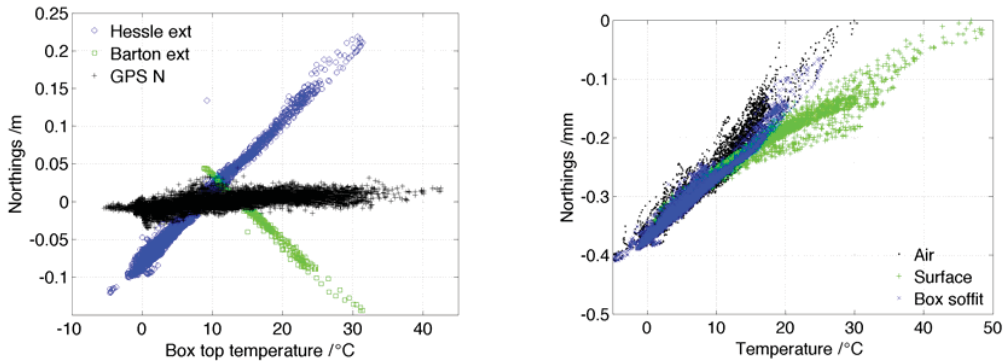

Fig. 15 Temperature effects on longitudinal deformation. Left point displacements with respect to data from a single a single temperature sensor. Right Hessle extension with respect to different temperature data

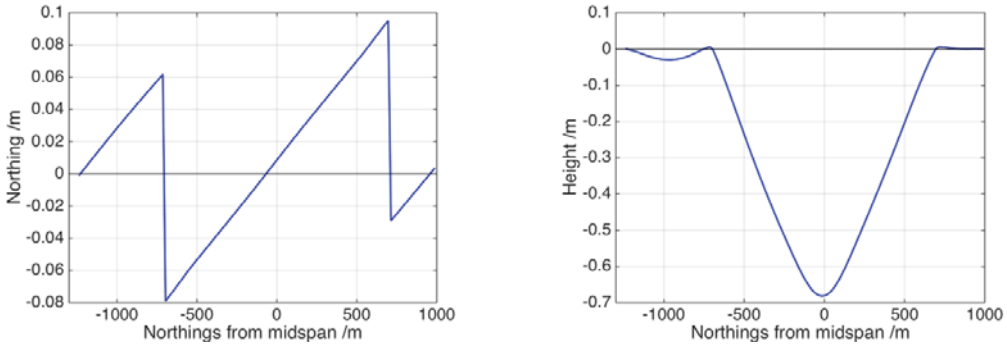

Fig. 16 Vertical and longitudinal deflections due to10°C temperature change throughout the structure

7.3.2 Simulated results

Effect of temperature was simulated with a uniform increase of 10°C, the result is shown in Fig.16 with 9.5 mm longitudinal bearing movement and 68 mm midspan vertical sag per °C. As with the wind simulation, this approach is extremely crude given that temperatures vary with location -throughout the box, on the road surface and in the cables, for which data are not available. There will also be temporal variation due to varying sun azimuth and elevation and radiation intensity (Westgate *at al*. 2014).However the simulation matches the measurement very well for longitudinal deformation. Measuring global deformation of a long span bridge due to temperature is more feasible because of the slow changes, for example using a robotic total station (Brownjohn *et al*. 2015) but was not possible using the sparse instrumentation at Humber.

The simulation also shows that the box moves slightly with temperature at midspan due to the asymmetric bridge configuration, this is in line with the experimental observation in Fig. 15.

8. Performance extrapolation

Bridge movement at supports/bearings is a critical condition. This is clear from studies such as on the Gazela Bridge (Belgrade) (Bojovi *et al*. 2013) where the bridge was strengthened to accommodate extreme combination of traffic and temperature effects, and the Cleddau Bridge (Kromanis and Kripakaran 2014) where transverse temperature differences resulted in serious bearing wear.

Compared to a neutral condition (ambient temperature of 10°C, no wind, no traffic), for Humber the worst-case combinations of bearing extension (*away* from towers) would be at Hessle tower due to an unlikely combination of

- 100 tonne HGV halfway between Barton tower and midspan (49 mm from Fig. 11)
- steady 30 m/sec wind (100 mm from Fig. 14).
- low temperature, e.g. -10°C (190 mm from Fig. 16)

This combination is unlikely since strong winds at Humber generally go with temperate cyclonic winds and the bridge would be closed to high-sided vehicles such as HGVs with wind speeds exceeding 26 m/sec.

A more likely combination would bearing movement *towards* the tower at the Barton end due

to

- 100 tonne HGV halfway between Hessle tower and midspan (59 mm from Fig. 11)
- zero wind
- high temperature e.g., 30°C (190 mm from Fig. 16)

9. Conclusions

A finite element model calibrated in the first instance using the results of a system identification exercise has been further checked against limited observations of static response to wind, traffic and temperature loads. This second stage of validation is rare and authors believe it is an essential step to provide credibility for simulations of extreme quasi-static behavior. The results are encouraging enough to believe in the predicted global deformations that –with present technology- could not be observed.

The whole exercise encapsulates the nature of structural identification (St-Id), which is the characterization of a structure through matching of experimental and analytical observations.

The exercise has shown that for such a landmark structure a St-Id exercise is worth the effort and that a thorough modal test combined with sparse monitoring and parallel analytical modeling is sufficient to understand and predict behavior to ranges and combinations of operational loads.

In terms of the behavior of the bridge, there are no big surprises and the simulations of static response fitted the limited observations of performance. Some differences were observed in the scale of longitudinal vehicle-induced deformation and bodily longitudinal shift observed in a strong lateral wind, for which a possible explanation might be the angle of the wind. In fact the least reliable and most over-simplified predictions are of wind effects.

Acknowledgements

The monitoring system and related research was funded by EPSRC (grants EP/G061130/2 and EP/F035403). Access to Humber Bridge was by kind permission of the Humber Bridge Board.

References

Abdel-Ghaffar, A.M. and Scanlan, R.H. (1985), "Ambient vibration studies of Golden Gate bridge: 1. Suspended structure, and 2. Pier tower structure", *J. Eng. Mech. - ASCE*, **111**(4), 463-482.

Ashkenazi, V. and Roberts, G.W. (1997), "Experimental monitoring of the Humber Bridge using GPS". *ICE Proceedings Civil Eng.*, **120**, 177-182.

Bathe, K.J., Wilson, E.L. and Petersen, F.E. (1974), SAPIV a structural analysis program for static and dynamic response of linear structures.

Bojovi, A. Velov, N. and Toljatija, P. (2013), "Rehabilitation of the Gazelle road bridge in Belgrade", *Proceedings of the 8th International Conference "Bridges in Danube Basin"*.

Brancaleoni, F. and Diana, G. (1993), "The aerodynamic design of the Messina Straits Bridge", *J. Wind Eng. Ind. Aerod.*, **48**(2-3), 395-409.

Brown, T.A. and Milne, R.D. (1985), "Strategies for the verification of a finite element model", In *IMAC III* (pp. 1031-1039). Orlando, Florida.

Brownjohn, J.M.W., Dumanoglu, A.A., Taylor, C.A. and Severn, R.T. (1987), "Ambient vibration

measurements of the Humber Suspension Bridge and comparison with calculated characteristics", *Proceedings Institution of Civil Engineers Part 2*, **83**, 561-600.
Brownjohn, J.M.W. ,Maglhaes, F., Caetano, E. and Cunha, A. (2010), "Ambient vibration re-testing and operational modal analysis of the Humber Bridge", *Eng. Struct.*, **32**(8), 2003-2018.
Brownjohn, J.M.W., Bocciolone, M., Curami, A., Falco, M. and Zasso, A. (1994), "Humber bridge full-scale measurements campaigns 1990-1991", *J. Wind Eng. Ind. Aerod.*, **52**, 185-218.
Brownjohn, J.M.W., Koo, K.Y., Scullion, A. and List, D. (2015), "Operational deformations in long span bridges", *J. Struct. Infrastruct. E.*, **11**(4), 556-574
Catbas, F.N., Correa-Kijewski, T. and Aktan, A.E. (2013), *Structural Identification of Constructed Systems. Approaches, Methods and Technologies for Effective Practice of St-Id.*, ASCE.
Cross, E.J. Koo, K.Y., Brownjohn, J.M.W. and Worden, K. (2013), "Long-term monitoring and data analysis of the Tamar Bridge", *Mech. Syst. Signal Pr.*, **35**(1-2), 16-34.
Diana, G., Cheli, F., Zasso, A., Collina, A. and Brownjohn, J.M.W. (1992), "Suspension bridge parameter identification in full-scale test", *J. Wind Eng. Ind. Aerod.*, **41**(1-3), 165-176.
Dumanoglu, A.A. and Severn, R.T. (1987), "Seismic response of modern suspension bridges to asynchronous vertical ground motion", *Proceedings ICE Part 2*, **83**, 701-730.
Farrar, C.R. and Lieven, N.A.J. (2007), "Damage prognosis: the future of structural health monitoring", *Philos. T. R. Soc. A.*, **365**(1851), 623-632.
Friswell, M.I. and Mottershead, J.E. (1995), *Finite element model updating in structural dynamics*, Springer.
Fujino, Y. and Siringoringo, D.M. (2013), "Lessons learned from structural monitoring of long-span bridges and a tall base-isolated building", *Proceedings of the SHMII-6*. Hong Kong.
Hornby, S.R., Collins, J.H., Hill, P.G. and Cooper, J.R. (2012), "Humber bridge A-frame refurbishment / replacement", *Proceedings of the 6th International Conference on Bridge Maintenance, Safety and Management (IABMAS)*. Stresa, Italy: Taylor & Francis Group, London.
Karuna, R. (2002), *Structural Modelling of Suspension Bridges with Particular Reference to the Humber Bridge* , PhD Thesis, Brunel University.
Koo, K.Y., de Battista, N. and Brownjohn, J.M.W. (2011), "SHM data management system using MySQL databse with MATLAB and Web interfaces", *Proceedings of the SHMII-5*. Cancun, Mexico,
Kromanis, R. and Kripakaran, P. (2014), "Predicting thermal response of bridges using regression models derived from measurement histories", *Comput. Struct.*, **136**, 64-77.
Kumarasena, T., Scanlan, R.H. and Morris, G.R. (1989), "Deer Isle bridge: Efficacy of stiffening systems", *J. Struct. Eng.*, **115**(9), 2297-2312.
Larsen, A., Esdahl, S., Andersen, J.E. and Vejrum, T. (2000), "Storebaelt suspension bridge - vortex shedding excitation and mitigation by guide vanes", *J. Wind Eng. Ind. Aerod.*, **88**(2-3), 283-296.
Littler, J.D. (1992), "Ambient vibration tests on long span suspension bridges", *J, Wind Eng. Ind. Aerod.*, **41-44**, 1359-1370.
Littler, J.D. and Woods, A.R. (1989), *Ambient vibration tests on the Humber Bridge July 1988*, BRE N75/89.
Nickitopoulou, A., Protopsalti, K. and Stiros, S.C. (2006), "Monitoring dynamic and quasi-static deformations of large flexible engineering structures with GPS: Accuracy, limitations and promises", *Eng. Struct.*, **28**, 1471-1482.
Stephen, G.A., Brownjohn, J.M.W. and Taylor, C.A. (1993), "Measurements of static and dynamic displacement from visual monitoring of the Humber Bridge", *Eng. Struct.*, **15**(3), 197-208.
Walshe, D.E. and Cowdrey, C.F. (1972), *A further investigation for the proposed Humber suspension bridge*, Transport Research Laboratory.
Westgate, R.J., Koo, K.Y. and Brownjohn, J.M.W. (2015), "Effect of vehicular loading on suspension bridge dynamic properties", *J. Struct. Infrastruct. E.*, **11**(2), 129-144.
Westgate, R., Koo, K.Y. and Brownjohn, J.M.W. (2014), "Effect of solar radiation on suspension bridge performance", *J. Bridge Eng. - ASCE* (online), 10.1061/(ASCE)BE.1943-5592.0000668.
Worden, K. and Manson, G. (2007), "The application of machine learning to structural health monitoring", *Philos. T. R. Soc. A.*, **365**(1851), 515-537.

Smart Structures and Systems, *Vol. 15, No. 3 (2015) 683-698*
DOI: http://dx.doi.org/10.12989/sss.2015.15.3.683

System identification of an in-service railroad bridge using wireless smart sensors

Robin E. Kim*, Fernando Moreu[a] and Billie F. Spencer, Jr.[b]

Department of Civil and Environmental Engineering,
University of Illinois at Urbana-Champaign, Urbana, IL 61801, USA

(Received November 27, 2014, Revised February 10, 2015, Accepted February 15, 2015)

Abstract. Railroad bridges form an integral part of railway infrastructure throughout the world. To accommodate increased axel loads, train speeds, and greater volumes of freight traffic, in the presence of changing structural conditions, the load carrying capacity and serviceability of existing bridges must be assessed. One way is through system identification of in-service railroad bridges. To dates, numerous researchers have reported system identification studies with a large portion of their applications being highway bridges. Moreover, most of those models are calibrated at global level, while only a few studies applications have used globally and locally calibrated model. To reach the global and local calibration, both ambient vibration tests and controlled tests need to be performed. Thus, an approach for system identification of a railroad bridge that can be used to assess the bridge in global and local sense is needed. This study presents system identification of a railroad bridge using free vibration data. Wireless smart sensors are employed and provided a portable way to collect data that is then used to determine bridge frequencies and mode shapes. Subsequently, a calibrated finite element model of the bridge provides global and local information of the bridge. The ability of the model to simulate local responses is validated by comparing predicted and measured strain in one of the diagonal members of the truss. This research demonstrates the potential of using measured field data to perform model calibration in a simple and practical manner that will lead to better understanding the state of railroad bridges.

Keywords: calibrated numerical model; structural health monitoring system; railroad bridge; system identification; wireless smart sensors

1. Introduction

Railroads have been an important part of the transportation network for over a hundred years in the United States (US).The freight rail industry has been the fastest growing segment since 1980, accounting approximately 40 percent of the total freight moved nationwide in 2010 (FRA, 2010). Due to continuous growth in freight demand, the Association of American Railroad forecasts that rail lines exceeding their capacity will increase from 173.81 km (108 miles) to nearly 25,749 km (16,000 miles; AAR, 2012).In an effort to meet the expected increase in the demand, the private

*Corresponding author, Ph.D. Candidate, E-mail: kim491@illinois.edu
[a] Ph.D. Candidate, Email:moreualo@illinois.edu
[b] Professor, Email: bfs@illinois.edu

http://www.techno-press.org/?journal=sss&subpage=8 ISSN: 1738-1584 (Print), 1738-1991 (Online)

US freight railroads have been emphasizing maintenance of their infrastructure, by organizing the majority of their revenue to ensure or to maintain the good state of their network. To date, as much as 15 to 20 percent of their total capital is used to enhance/maintain the railroad capacity (FRA, 2010). Thus, researches that can appropriately assess such infrastructure are assuming greater importance.

Amongst railroad networks, bridges form a critical link. According to the FRA documents in 2002, the US railroad network contained an average of one bridge for every 2.25 km (1.4 miles) of track (GAO, 2007). Ensuring good conditions for those bridges is important because they are the most expensive pieces of railroad networks; replacement and construction cost of railroad bridges can be 11 to 550 times as much per linear foot as regular track (GAO, 2007). At the same time, those structures are susceptible for severe wear or deterioration when the structures age and serve heavier traffic than their original design to meet the increased demands. Methods for quickly assessing physical states of the railroad bridges whether they can accommodate increased axle loads, train speeds, and greater volumes of freight traffic became of primary needs for railroad engineers (Moreu and LaFave 2012).

Numerous researchers have employed system identification to develop models of highway bridges that can help in assessing the state of bridge infrastructure. Because initial models for the bridge may not be 100% successful for assessing dynamic properties, models are usually updated using measurements from dynamic testing. Various model updating approaches have been proposed (e.g., Brownjohn and Xia 2000, Jaishi and Ren 2005, Deng and Cai 2009, Morassi and Tonon 2008). While aforementioned literature used models that well represent global features of the bridge, Catbas *et al*. (2007) asserted that for accurate and practical condition evaluation of a structure, models should not only be updated with global attributes, but also with local data; when local responses are estimated from global-only calibrated model, results may be render meaningless. As such, in some of applications, global responses are measured from ambient vibration tests using accelerometers. Then, local characteristics, such as strain, are captured from controlled tests; the bridge is usually closed for the revenue traffic while a truck of known mass runs over the bridge (Catbas *et al*. 2008, Brenner *et al*. 2010). Although this type of test strategies is relatively easy to achieve in highway bridges, in the case of railroad bridges, performing such tests can be much expensive and hard. In consequence, railroad bridges received comparably less attention in this topic. Thus, a framework for monitoring railroad bridges that can efficiently reach global and local calibration of a model for system identification under revenue traffic needs to be devised.

To date, only a limited number of studies have conducted system identification of in-service railroad bridges. Ahmadi and Daneshjoo (2012) implemented a full-scale monitoring system on a railroad bridge (Firoozeh Railroad Bridge, Iran). They collected acceleration responses of the bridge under a train of known speed and weight passing and extracted key parameters of the bridge. Giles *et al*. (2011, 2012) implemented a full-scale monitoring system on the Government Bridge at the Rock Island Arsenal using wireless smart sensors (WSSs). The efficient and multi-metric system allowed understanding of the global behavior of the bridge (Cho *et al*. 2014). Local responses are also measured from fiber optic strain sensors. However those sensors were only suitable for static measurements, because of the aliasing effects (Van Damme *et al*. 2007). In their application, however, because the bridge could swing to allow river traffic (i.e., barges) to pass, and thus traffics are closed and static loads governed during the period, use of those sensors were adequate. From the member strain under self-weight, the health of the bridge was assessed. In addition, system identification of the bridge was performed comparing global responses of the

bridge with a finite element (FE) model (Cho *et al*. 2014). While these methods have been successful in monitoring railroad bridges, a framework for dynamic tests and calibrated models that can help practically assess in-service railroad bridges based on global and local responses has not been provided.

This paper demonstrates the use of measured data to identify a railroad bridge and calibrate an FE model to understand the global and local behavior of an in-service railroad bridge. This effort includes three distinct phases: (i) selection of a railroad bridge and implementation of a monitoring system with WSSs; (ii) an FE model development based on original construction design; and (iii) model calibration and validation using global and local responses of the bridge. In the monitoring system, WSS networks were installed on a steel truss railroad bridges. An FE model is developed and updated with field measurements so that the model can well represent the bridge both globally and locally. The results of this study demonstrate a framework, which can be used for understanding an in-service railroad bridges under revenue traffic to help railroad engineers managing their bridges.

2. Description of test bridge and monitoring system

A structural health monitoring (SHM) system was installed on a railroad bridge owned by Canadian National Railway (CN). The system comprised a set of WSSs, which provide services suitable for efficient monitoring system. During the research period, the system was able to collect various measurements. The uniqueness of the test bridge enabled rich collection of the measurements. This section demonstrates a successful layout of the system and examples of field data.

2.1Test bridge

A railroad bridge located over the Little Calumet River near Chicago, IL (see Fig. 1) has been selected in this study for assessing its structural conditions. Among the four bridges shown in the Fig. 1, the instrumented bridge is an intermediate truss bridge (the bridge with an arrow); the West-most bridge in the Fig. 1 is the Metra lane, another truss bridge carrying freight and passenger trains located the East to the test bridge, the East-most bridge is closed for the traffic. The bridge is about 95 m long, 21 m tall, and 10 m wide steel bridge and made of A36 American Society for Testing and Materials (ASTM).The bridge opened for service in 1971, with an expected life of 100 years. The test bridge carries two tracks, CN1 track on the West side and CN2 track on the East side, which both are open for South and North bound freight and passenger trains. About ten freight trains and six Amtrak trains run on either CN1 or CN2 track in a daily basis. Those characteristics of the bridge make the bridge suitable and unique for the test bridge;(i) the test bridge is made of steel, which is the most common type in the US (53% of entire railroad bridge inventory, FRA, 2008); (ii) adjacent bridges are open to the traffic exciting the test bridge without changing mass of the bridge by carrying the train loads; and (iii) high traffic with various types of trains on the test bridge allows rich data collection from the monitoring system.

2.2 Monitoring system

WSS networks implemented on the bridge aimed for an efficient SHM system with various

types of sensors. A wireless platform used in this project is an Imote2 platform (Crossbow Technology, 2009). This platform can stack a sensor board via two external connectors allowing flexible design of the network with any types of sensor boards. Sensor boards used in this project are (i) normal accelerometer board (herein, a set of this sensor board and the Imote2 will be noted as ISM400 sensor; (ii) high sensitivity accelerometer board (denoted as SHM-H sensor); and (iii) strain sensor (denoted as SHM-S sensor). Measurable range for an ISM400 sensor is up to ±2 g, while a SHM-H sensor can provide ten times higher sensitivity (i.e., up to ±200 mg). Each sensor node is equipped with a solar panel and rechargeable battery for energy harvesting. The essential driver and software for monitoring, such as synchronization and sensing are implemented, adopting services from Illinois Structural Health Monitoring Project (ISHMP) Services Tool suite (Rice *et al*. 2010, Jo *et al*. 2011).

Fig. 2 shows the WSS network map used in this paper. Components of the network are listed below with each of their objectives.

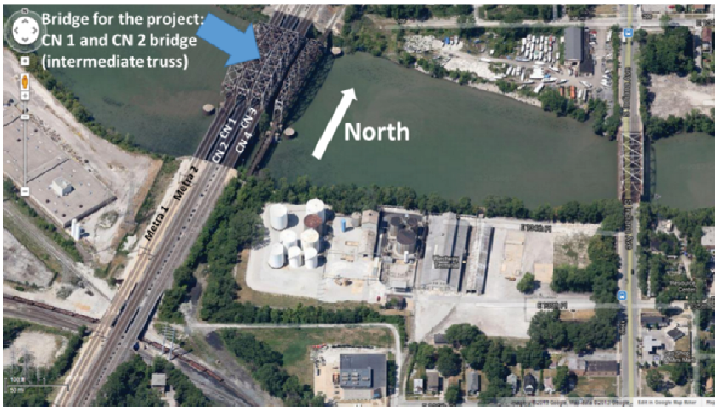

Fig. 1 Selected test bridge, near Chicago, IL*

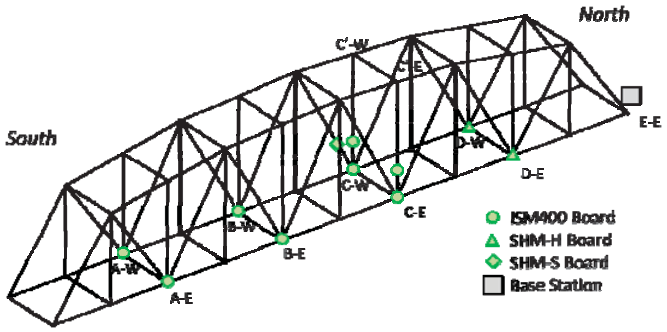

Fig. 2 WSS deployment map on the Calumet Bridge

*Google Maps (2014), www.maps.google.com.

- Six ISM400 sensors at A-E, A-W, B-E, B-W, C-E, and C-W.
- Two ISM400 sensors on 2.1 m higher locations from C-E and C-W, to eliminate the spatial aliasing and to captures way behavior of the bridge.
- Two SHM-H sensors at D-E and D-W to enhance the quality of the network effectively, while keeping total cost of the system low (Jo *et al*. 2012).
- One SHM-S sensor on a diagonal member of the bridge to provide local responses of the bridge. It was placed about 1.2 m South from C-Win Fig. 2. This member was chosen because of its uniqueness; the member experiences both tension and compression as the train passes the bridge.

In the final design of the network, two subnets were prepared; one for acceleration sensor nodes and the other for the strain sensor node. All acceleration sensor nodes were placed symmetrically in longitudinal direction (i.e., East and West), to allow obtaining asymmetric behavior under train loading on one side of the track. Those nodes were synchronized and provided synchronized responses with in a subnet of the truss bridge, which is then used for understanding the global behavior of the bridge. SHM-S sensor measured local responses of the bridge. Other than listed above and shown in Fig. 2, several SHM-S sensors were deployed on the rails both outside and inside the bridge as well. The sensors measured the train wheel loads, but the scope of this study will only cover the measurements from the structure. Finally, a base station PC, located at the North of the bridge (E-E in Fig. 2) controlled and collected data measured from two WSS networks (acceleration sensor network and strain sensor network). Having only 11 sensors, the system realized efficient and cost effective WSS networks tailored to monitor the global and local responses of the bridge under the train traffic.

2.3 Example of measured data

The measurements from the monitoring system under various train traffic formed a database for system identification. Fig. 3 shows an example of the acceleration response of the bridge when northbound Amtrak was passing the bridge on CN1 track at over 80 km/h. On each plot, the first vertical dashed line around 180 seconds indicates when Amtrak is entering the bridge, while the second vertical line near 190 seconds denotes exiting the bridge. As Amtrak passes the bridge, the bridge is excited laterally and vertically at similar degree (±15 mg). However, relatively small accelerations in longitudinal direction inform that Amtrak did not experience much change in acceleration (e.g., neither accelerating nor breaking). Because Amtrak is light and fast, the response of the bridge is similar that under impact tests. The transient responses after Amtrak left the bridge can give rich information of the global characteristics of the bridge.

3. System identification

This section explains the peak-picking method, an output-only system identification method. This method has been chosen due to its advantages over other methods for being fast, simple, and straight forward to extract key features of a structure. The accuracy of the selected method is shown as well, by comparing the results with Natural Excitation Eigensystem Realization Algorithm (NExT ERA).

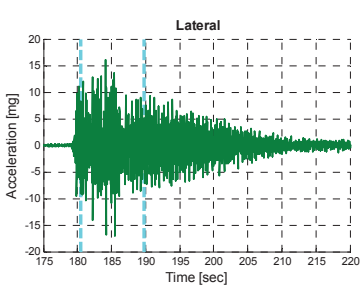

(a) Lateral acceleration.

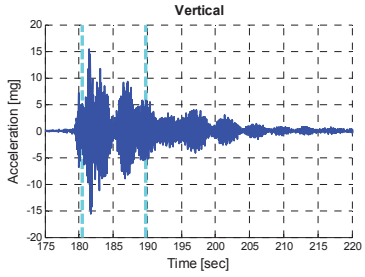

(b) Vertical acceleration.

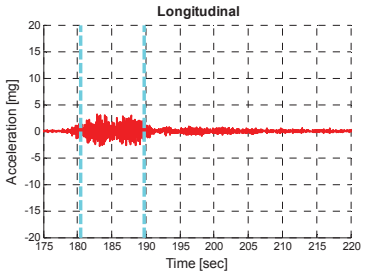

(c) Longitudinal acceleration.

Fig. 3 Bridge responses under northbound Amtrak on CN1 track measured at A-W (located near CN1 track)

3.1 Output-only system ID

In civil engineering structures, measuring input to the structure is difficult in most cases; hence, the modal parameters can identified from output-only system identification. A number of researchers provided frequency domain approaches to estimate the natural frequencies and mode shapes of the structure reasonably. Some widely used techniques are the frequency domain decomposition (FDD), Eigensystem Realization Algorithm (ERA), and peak-picking methods (Brincker *et al*. 2001, Juang and Pappa 1985, Brownjohn 2003). The expansion of those techniques uses acceleration measurement due to the ease of measuring acceleration rather than velocity and displacement of the structure. Among those, the peak-picking method is one of the simplest and fastest implementation for ambient vibration response (Brincker *et al*. 2001).

Felber (1993) introduced the peak-picking method for reliable estimation of modal frequencies and mode shapes for ambient vibration measurements. The basic theory of this method is that the frequency response goes to an extreme around the fundamental frequency. The method assumes that the structure is linear, the excitation is ambient, and the damping of the structure is light with well-separated modes (Felber 1993). The natural frequencies of the structure are identified from the peaks of normalized cross power spectral densities (PSD)s, and the mode shapes are found from the ratio of cross PSDs. Although the theory behind peak-picking may be comprehensive, this method is highly practical and user-friendly. During the process, peaks in the PSDs are selected based on the physical understanding. This feature allows the method to be understood by

a group of variety background. For this reason, this method has been chosen in this study.

To obtain accurate results in the peak-picking method, both low noise levels in the signals and clear, distinctive peaks are essential. Low accuracy in the lower frequencies in the MEMS based low-cost accelerometers may harm the use of the methods for civil structures, where the fundamental frequencies are usually low (Su *et al*. 2010, Nagayama *et al*. 2005). To enhance the accuracy, Nagayama *et al*. (2010), suggested using limited number of high-sensitivity acceleration for the reference signals when calculating cross-PSDs. Such multi-metric network offers cost-effective extraction of the system identification with increased accuracy for peak-picking method.

3.2 Modal identification

In this section, system identification of the bridge using a set of signals from the acceleration network is presented. In the modal analyses, peak-picking and NExT ERA methods are employed to find fundamental characteristics of the bridge. Used measurements are transient responses of the bridge after Amtrak crossed the bridge. This signal is preferred over other records, such as under or after a freight train, because the effect of Amtrak increasing the weight of the bridge is negligible due to its light weight and fast speed (over 80 km/h). Fig. 4(a) shows vertical responses from the West side of WSSs, which are sampled at 25 Hz. Although the vibration level of the measurements are small, due to light damping of the structure, the bridge experienced more than 40 seconds of gradual decrease of the response. Fig. 4(b) shows auto spectral density calculated using Hanning Window with 1024 NFFT. The line with '+' marker corresponds to the lateral vibration collected from a sensor at D-W (see Fig. 2). This SHM-H sensor shows apparently lower noise level within the frequency zone of interest with clear peaks at fundamental frequencies of the bridge. To benefit the modal analyses by reducing the total noise level in the network, auto spectral density of D-W sensor was used as the reference signal in the identification of the lateral mode shapes.

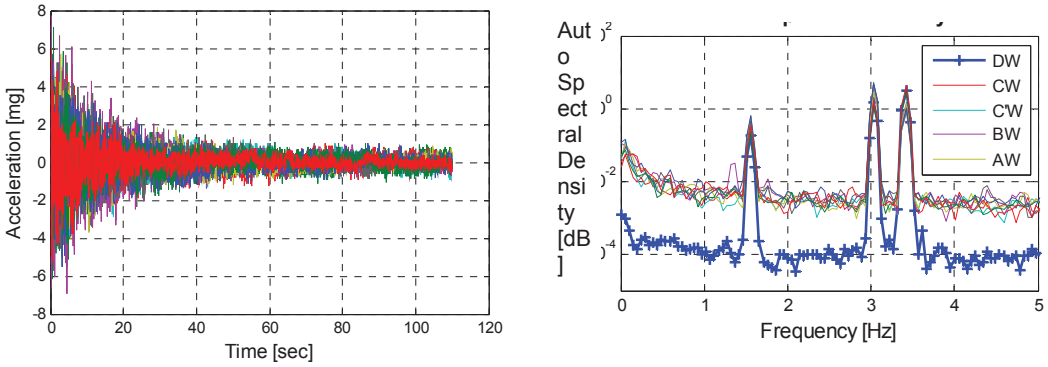

(a) Time history (b)Auto spectral density.

Fig. 4 Vertical responses measured from the West side of the truss bridge

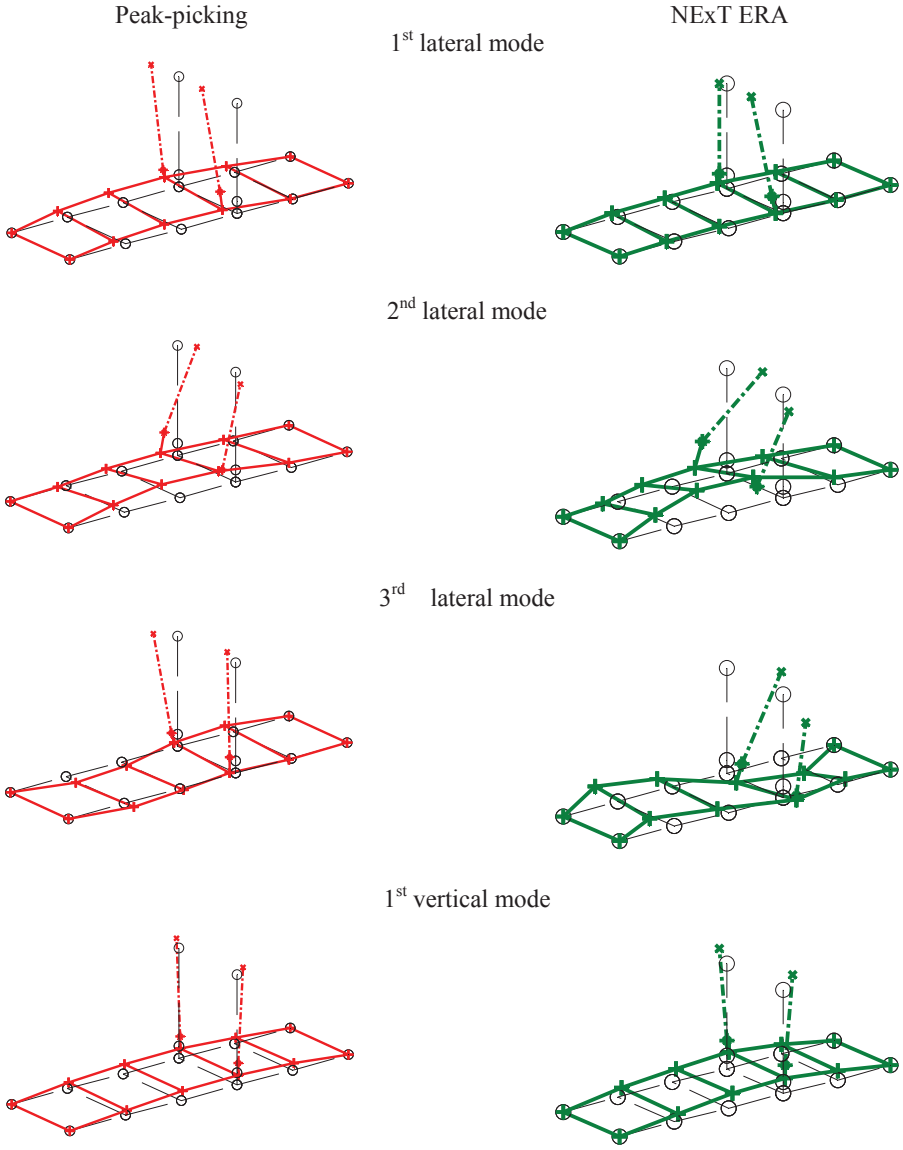

Fig. 5 Mode shape comparison, Peak-picking and ERA comparison

Fig. 5 compares mode shapes from peak-picking and NExT ERA methods. In the peak-picking method, the peaks are manually selected from auto spectral density. For visualization purposes and to ease the task of picking peaks from the reference auto spectral density, signals are regulated and divided by the minimum noise level. As a result, they end up having the same noise level. By doing so, the reference signal shows the highest amplitude at the pick. Then, mode shapes are calculated at the selected frequencies by using the reference auto spectral density.

Table 1 Natural frequency comparisons; Peak-picking and NExT ERA comparison

Candidate Modes	Peak-picking [Hz] (Error [%][†])	NExT ERA [Hz]<EMAC>
1st lateral	1.542(0.065)	1.541<99.84>
2nd lateral	3.014(0.660)	3.034<99.99>
3rd lateral	3.390(0.732)	3.415<99.99>
1st vertical	3.592(1.756)	3.530<99.92>

[†]Absolute error: A (|A-B|/B), where A = Peak-picking; B = NExT ERA

In NExT ERA method, on the other hand, the cross correlation matrix based on the selected reference signals is calculated. Then, the system properties are extracted by employing the eigenvalue problem for the system realization matrix solved through the decomposed of the Hankel matrix (Juang and Pappa 1986, James *et al*. 1993). To select only meaningful modes, those with high Extended Modal Amplitude Coherence (EMAC) are chosen (Pappa *et al*. 1993). Table 1 summarizes differences between natural frequencies identified in two methods. Having less than 2% differences in the results, peak-picking method can be considered as reliable and accurate as NExT ERA method while preserving simplicity and user-friendliness.

4. Finite element model

For several decades, FE models have been widely used for simulating and assessing the structural behavior under arbitrary structural conditions. To build a model with such capability, a preliminary analytical FE model is developed in Matlab® using the shop drawings from CN's construction records. The model contains 345 nodes and 724 elements. The boundary conditions at the North and South bearing supports are pin and expandable, respectively. Nodes are frame connected, which can transfer rotational moments to adjacent elements. The initial FE model developed based on the drawing is shown in Fig. 6. Table 2 summarizes first four modes identified using this model.

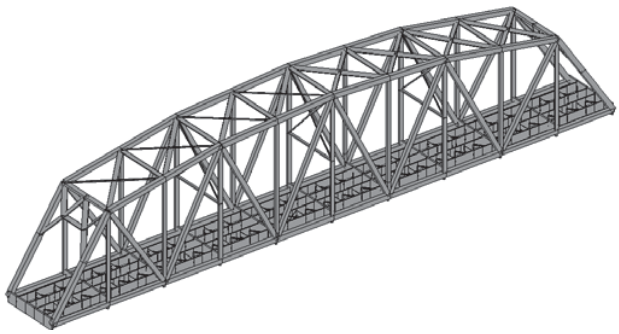

Fig. 6 The bridge model

Table 2 Natural frequency comparisons between peak-picking and initial FE model

Candidate Modes	Peak-picking [Hz]	Initial FE model [Hz]	
		Mode [Hz]	Error [%]†
1st lateral	1.542	1.819	17.96
2nd lateral	3.014	2.875	4.612
3rd lateral	3.390	3.774	11.33
1st vertical	3.592	4.025	12.05

†(|A-B|/A), where A = Peak-picking; B = FE model

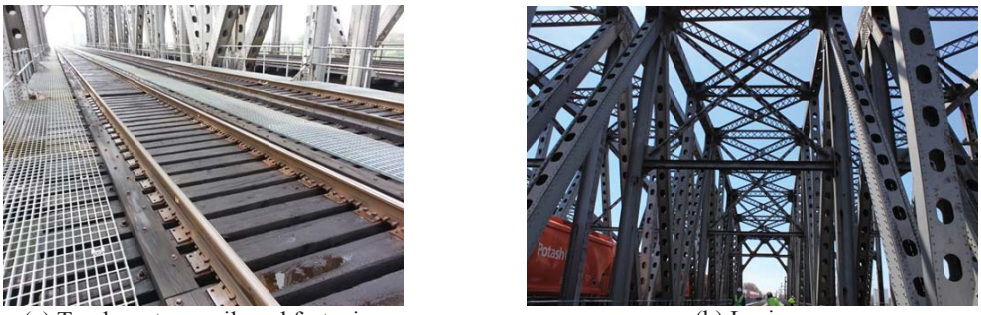

(a) Track system, rail, and fastening (b) Lacings

Fig. 7 Bridge additional mass components

As can be seen from Table 2, the initial FE model does not fully represent the current physical state of the bridge. Part of reasons are:

- The initial model represented only the truss structure and did not include track system.
- Most main sections are built-up sections with holes on each side as shown in Fig. 7. However, those details were excluded to keep the model simple.
- For brevity of the modeling, all floor systems shared the same neutral axes, while they were in fact located at different levels.
- The boundary conditions and joints between elements were modeled as shown in the drawings, but those may have been changed from the time of original construction.

Thus, the model needs to be updated to better represent the bridge. For example, the shop drawing indicated that the total weight of the bridge is approximately 11,120 kN (2500 kips), which was larger than the preliminary FE model. As discussed earlier, these differences arise from neglecting track system, rail and fastening, lacings and other utilities (see Figs. 7(a) and 7(b)). For example, the dead load of rail and fastening elements per track are approximately 889.64 N per meter (200 lb_F per feet, Unsworth 2010). To accommodate the omitted mass, additional mass is distributed and lumped on the floor nodes. After updating the mass, the mass ratio between the bridge and total train represents the actual ratio; a standard Amtrak train composed of one engine and seven cars is about 20% of the bridge weight.

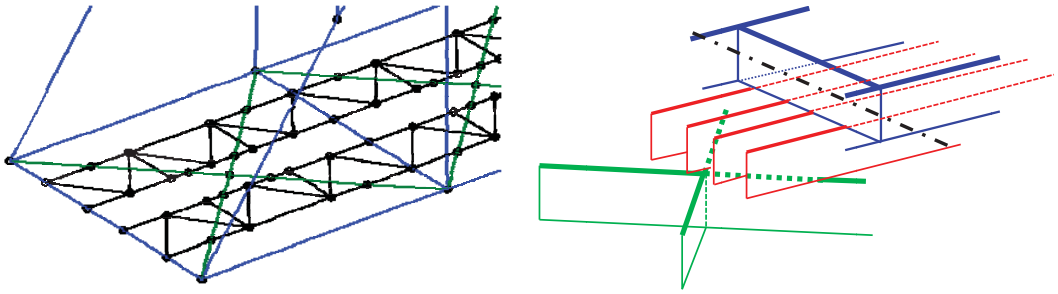

Fig. 8 Floor system in detail

The floor system of the bridge is rigid because three layers are acting as one unit: the lower chords, the floor beams, and the stringers and bottom lateral bracings. To capture such rigidity, the moment of inertias for those layers is calculated about one reference axis, which is the center of lower chords (see Fig. 8). This calculation simplifies the complexity of modeling three layers for the floor system. The following modal analysis of the FE model with updated mass and floor system validates that the model well represents the bridge.

Identified first four modes from the updated FE model show the fundamental dynamic characteristics of the bridge. The first, second and third lateral modes are at 1.551 Hz, 3.054 Hz, and 3.242 Hz, respectively. The first vertical mode is at 3.567 Hz. The next section will show that the model has reached sufficient level of accuracy. Therefore, employing sophisticated model updating techniques such as generic algorithm would be redundant.

5. Model validation

5.1 Model validation with global responses

To validate that the FE model can represent the bridge performance in global sense, numerically identified natural frequencies and their mode shapes are compared with experimentally identified results under transient responses after Amtrak, as shown in Fig. 9. For efficient visualization, the first column shows the deformed mode shapes of global nodes. To reduce the spatial aliasing, the second column shows the deformed mode shapes using the deformations only at the locations of the WSSs. The mode shapes in the third column are experimentally identified, with linear extension of the upper chords where the higher sensors are located 2.1 m higher from the bottom chord (dashed-line in the third column). The mode shapes in the FE model agree well with the mode shapes obtained experimentally.

Table 3 summarizes the frequencies at each mode. The model shows a good agreement with the experimentally derived data, with an error of less than 5% for all modes. In addition, numerically obtained mode shapes are correlated with the experimental ones using the modal assurance criterion (MAC). MAC values obtained between the first four mode shapes are shown in Table 3. All modes show MAC values over 90%, indicating that the model well represents the bridge in a global sense. The following section will demonstrate the accuracy of the model in simulating local

responses of the bridge, which is important for assessing the state of the bridge under an arbitrary trainload.

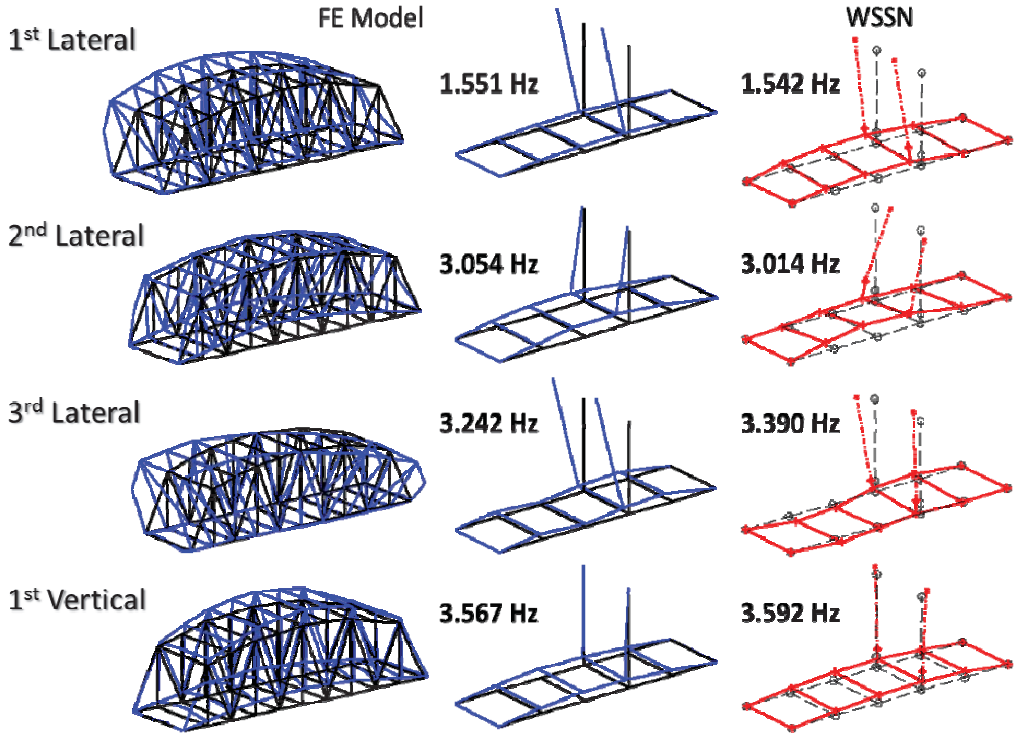

Fig. 9 Modal analysis comparison with FE model

Table 3 Mode comparison

	Peak-picking: WSSN [Hz]	FE model		
		[Hz]	(Error [%])†	MAC [%]
1st Lateral	1.542	1.551	(0.584)	91.34
2nd Lateral	3.014	3.054	(1.327)	94.17
3rd Lateral	3.390	3.242	(4.366)	90.97
1st Vertical	3.592	3.567	(0.696)	98.38

†Absolute error: A (|A-B|/B), where A = Peak-picking; B = FE model

5.2 Model validation using local responses

This section presents the model validation using local responses of the bridge. Here, strain response from SHM-S sensor (Fig. 2) under a train of known mass is used. Collaborating with CN, a test car (Fig. 10) ran over the bridge while the SHM system collected the strain response. During the experiments, the test train ran on CN1 track multiple times with varying speeds (from 8 km/h to 80 km/h) and directions (in the North bound (NB) and the South bound (SB)). The length of the test train was 120 m with total weight of 7,340 kN. A locomotive and seven cars had different wheel loads profile varying from 73 kN/wheel to 143 kN/wheel. Although this tests were performed under a controlled test, for a revenue train, wheel loads and train speed information can be retrieved from a train manifest.

Fig. 11 shows an example of the instrumented member strain collected at 280 Hz when the test train crossed the bridge. The measurements at speeds varying from 8 km/h to 80 km/h indicate that the dynamic component is relatively small and static component dominates the signature of the member strain. Regardless of speeds, the member experiences both compression and tension as the train passes, with the maximum compression near 50 με and the maximum tension around the 60 με.

Fig. 10 Test train wheel loads scheme

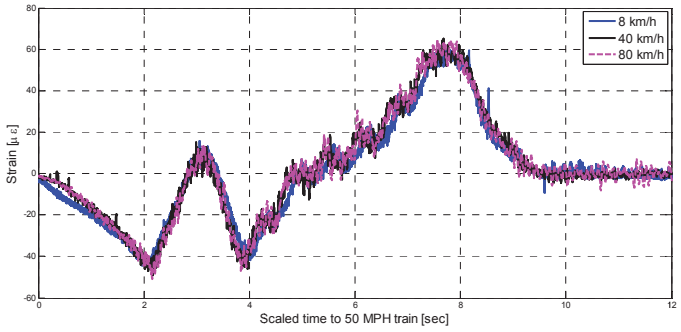

Fig. 11 An instrumented member strain under the test train at speeds 8, 40, and 80 km/h

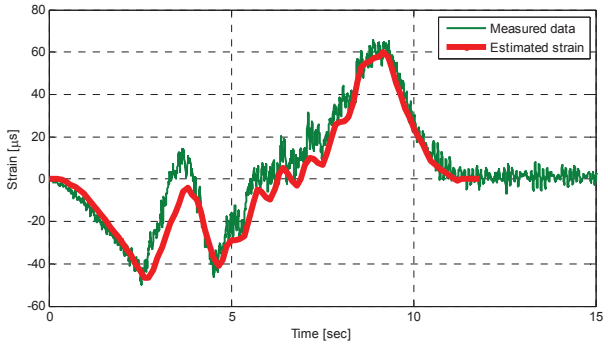

Fig. 12 Member strain comparison with field measured data and static estimation

Static analysis is used to estimate the strain from the FE model, observing that the dynamic component in the measured data is not significant. In the analysis, the location of the train is determined at each time step. For example, the first time step assumes that the head of train is at the South entrance of the bridge. Then, the wheel loads are distributed at the nodal points of the bridge model as a series of point loads. After obtaining the member strain at the time step, train location is re-determined assuming the train headed the North with small amount. This sequence is iterated until the train fully exits the North end of the bridge. Fig. 12 shows the comparison of static estimation and field measurements. Overall, 200 iterative time steps were used in the analysis. The obtained strain well captures the maximum compression and tension that the member actually experienced. For practical purposes, obtaining those maximum values are usually the ones of most concern, exerting that the proposed approach is adequate. Subsequently, one can conclude that this approach has potentials to be expanded for estimating bridge responses under arbitrary revenue train with given wheel loads. However, due to dynamic interactions between the vehicle, track, and the bridge, some discrepancies between the estimated strain and measured strain are observed around 4 seconds. Thus, a further evolution of the model to include dynamic analyses of the model needs to be performed.

6. Conclusions

This paper demonstrated an approach to system identification and dynamic testing with the goal of understanding the in-service response of railroad bridges. High fidelity data has been obtained from a structural health monitoring (SHM) system using wireless smart sensors (WSSs). The final deployment of the system has considered obtaining asymmetric responses and reducing physical aliasing, while retaining cost-effectiveness. Then, a finite element model has been developed based on the shop drawings. Because the initial model did not well represent the bridge, selected parameters are updated. The final model was validated using both global and local responses of the field-measured data; acceleration responses of the bridge validated the global features of the bridge and a member strain demonstrated that the model could well capture the local responses of the bridge. The static analysis proposed in this paper indicated that the approach

could well capture the maximum compression and tension of the selected member, while dynamic approach is still required if reconstructing accurate strain history is of concern. Nonetheless, with this accurately calibrate model and static analysis, a sufficient level of assessment about the bridge can be made. For example, arbitrary wheel loads and train topologies can be determined from the model simulation and allowable member strain. This result showed the potential of turning a model from explanatory in nature to having powerful predictive capabilities that can help assessing the state of the railroad bridge.

Acknowledgements

This study is supported by the Federal Railroad Administration under the BAA 2010-1 project (Cameron Stuart, program manager). In addition, the technical support from CN is greatly appreciated.

References

Association of American Railroads (2012), An Overview of America's Freight RailroadsExternal Link.

Ahmadi, H.R. and Daneshjoo, F. (2012), "A harmonic vibration, output only and time-frequency representation based method for damage detection in Concrete piers of complex bridges", *Int. J. Civil Struct. Eng.*, **2**(3), 987-1002 .

Brenner, B., Bell, E., Sanayei, M., Pheifer, E., Durack, W., Fay, S. and Thorndike, L. (2010), "Structural modeling, instrumentation, and load testing of the Tobin Memorial Bridge in Boston, Massachusetts", *Proceedings of the 2010 Structures Congress*, Orando, Florida, May.

Brincker, R., Zhang, L. and Andersen, P. (2001), "Modal identification of output-only systems using frequency domain decomposition", *Smart Mater. Struct.*, **10**(3), 441-445.

Brownjohn, J. (2003), "Ambient vibration studies for system identification of tall buildings", *Earthq. Eng. Struct. D.*, **32**(1), 71-95.

Brownjohn, J.M. and Xia, P.Q. (2000), "Dynamic assessment of curved cable-stayed bridge by model updating", *J. Struct. Eng.- ASCE*, **126**(2), 252-260.

Catbas, F.N., Ciloglu, S.K., Hasancebi, O., Grimmelsman, K. and Aktan, A.E. (2007), "Limitations in structural identification of large constructed structures", *J. Struct. Eng. - ASCE*, **133**(8), 1051-1066.

Catbas, F.N., Susoy, M. and Frangopol, D.M. (2008), "Structural health monitoring and reliability estimation: Long span truss bridge application with environmental monitoring data", *Eng. Struct.*, **30**(9), 2347-2359.

Cho, S., Giles, R.K. and Spencer, B.F. (2014), "System identification of a historic swing truss bridge using a wireless sensor network employing orientation correction", *Struct. Control Health. Monit.*, **22**(2), 255-272.

Crossbow Technology Inc. (2009), Imote2 - High-performance Wireless Sensor Network Node, Available at http://www.xbow.com/Products/Product_pdf_files/Wireless_pdf/Imote2_Datasheet.pdf

Deng, L. and Cai, C. (2009), "Bridge model updating using response surface method and genetic algorithm", *J. Bridge Eng.*, **15**(5), 553-564.

Federal Railroad Administration (2010), National Rail Plan Progress Report.

Felber, A.J. (1993), *Development of a hybrid bridge evaluation system*, Ph.D. Dissertation, University of British Columbia, British Columbia.

Government Accountability Office (GAO; 2007), Railroad Bridges and Tunnels: Federal Role in Providing Safety Oversight and Freight Infrastructure Investment Could Be Better Targeted. GAO-07-770, August 6, 2007.

Giles, R., Kim, R., Sweeney, S., Spencer, B., Bergman, L., Shield, C. and Olson, S. (2014), "Multimetric monitoring of a historic swing bridge", *Bridges*, **10**, 9780784412374.014.

Giles, R., Kim, R., Spencer Jr, B.F., Bergman, L.A., Shield, C.K. and Sweeney, S.C. (2011), "Structural health indices for steel truss bridges",*Conference Proceedings of the Society for Experimental Mechanics Series*, Jacksonville, Florida, January.

Jaishi, B. and Ren, W.X. (2005), "Structural finite element model updating using ambient vibration test results", *J. Struct. Eng.- ASCE*, **131**(4), 617-628.

James III, G.H., Carne, T.G. and Lauffer, J.P. (1993), *The natural excitation technique (NExT) for modal parameter extraction from operating wind turbines*, NASA STI/Recon Technical Report N, **93**, 28603.

Jo, H., Sim, S.H., Mechitov, K.A., Kim, R., Li, J., Moinzadeh, P., Spencer Jr, B., Park, J.W., Cho, S. and Jung, H.J. (2011), "Hybrid wireless smart sensor network for full-scale structural health monitoring of a cable-stayed bridge", *Proceedings of the SPIE Smart Structures/NDE Conference*, San Diego. California, March.

Jo, H., Sim, S.H., Nagayama, T. and Spencer Jr, B. (2011), "Development and application of high-sensitivity wireless smart sensors for decentralized stochastic modal identification", *J. Eng. Mech. - ASCE*, **138**(6), 683-694.

Juang, J.N. and Pappa, R.S. (1986), "Effects of noise on modal parameters identified by the eigensystem realization algorithm", *J. Guid. Control Dynam.*, **9**(3), 294-303.

Juang, J.N. and Pappa, R.S. (1985), "An eigensystem realization algorithm for modal parameter identification and model reduction", *J. Guid. Control Dynam.*, **8**(5), 620-627.

Morassi, A. and Tonon, S. (2008), "Dynamic testing for structural identification of a bridge", *J. Bridge Eng.*, **13**(6), 573-585.

Nagayama, T., Abe, M., Fujino, Y. and Ikeda, K. (2005), "Structural identification of a nonproportionally damped system and its application to a full-scale suspension bridge", *J. Struct. Eng.- ASCE*, **131**(10), 1536-1545.

Nagayama, T., Ushita, M., Fujino, Y., Ieiri, M. and Makihata, N. (2010), "The combined use of low-cost smart sensors and high accuracy sensors to apprehend structural dynamic behavior", *Proceedings of the SPIE Smart Structures/NDE Conference*, San Diego. California, March.

Pappa, R.S., Elliott, K.B. and Schenk, A. (1993), "Consistent-mode indicator for the eigensystem realization algorithm", *J. Guid. Control Dynam*, **16**(5), 852-858.

Rice, J.A., Mechitov, K., Sim, S.H., Nagayama, T., Jang, S., Kim, R., Spencer Jr, B.F., Agha, G. and Fujino, Y. (2010), "Flexible smart sensor framework for autonomous structural health monitoring", *Smart Struct. Syst*, **6**(5-6), 423-438.

Rice, J.A. and Spencer Jr, B. (2008), "Structural health monitoring sensor development for the Imote2 platform", *Proceedings of the 15th International Symposium on: Smart Structures and Materials & Nondestructive Evaluation and Health Monitoring*, San Diego, California, March.

Su, D., Fujino, Y., Nagayama, T., Hernandez Jr, J.Y. and Seki, M. (2010), "Vibration of reinforced concrete viaducts under high-speed train passage: measurement and prediction including train–viaduct interaction", *Struc.Infrastruct. E.*, **6**(5), 621-633.

Unsworth, J.F. (2010), *Design of modern steel railway bridges Editioned*., CRC Press.

Van Damme, S., Boons, B., Vlekken, J., Bentell, J. and Vermeiren, J. (2007), "Dynamic fiber optic strain measurements and aliasing suppression with a PDA-based spectrometer", *Meas. Sci. Technol.*, **18**(10), 3263-3266.

Smart Structures and Systems, *Vol. 15, No. 3 (2015) 699-715*
DOI: http://dx.doi.org/10.12989/sss.2015.15.3.699

A statistical framework with stiffness proportional damage sensitive features for structural health monitoring

Luciana Balsamo, Suparno Mukhopadhyay and Raimondo Betti*

Department of Civil Engineering and Engineering Mechanics, Columbia University, New York, NY 10027, USA

(Received November 21, 2014, Revised January 27, 2015, Accepted February 5, 2015)

Abstract. A modal parameter based damage sensitive feature (DSF) is defined to mimic the relative change in any diagonal element of the stiffness matrix of a model of a structure. The damage assessment is performed in a statistical pattern recognition framework using empirical complementary cumulative distribution functions (ECCDFs) of the DSFs extracted from measured operational vibration response data. Methods are discussed to perform probabilistic structural health assessment with respect to the following questions: (a) "Is there a change in the current state of the structure compared to the baseline state?", (b) "Does the change indicate a localized stiffness reduction or increase?", with the latter representing a situation of retrofitting operations, and (c) "What is the severity of the change in a probabilistic sense?". To identify a range of normal structural variations due to environmental and operational conditions, lower and upper bound ECCDFs are used to define the baseline structural state. Such an approach attempts to decouple "non-damage" related variations from damage induced changes, and account for the *unknown* environmental/operational conditions of the current state. The damage assessment procedure is discussed using numerical simulations of ambient vibration testing of a bridge deck system, as well as shake table experimental data from a 4-story steel frame.

Keywords: stiffness proportional DSF; empirical complementary CDF; probabilistic damage detection

1. Introduction

Vibration based Structural Health Monitoring (SHM) usually involves either "model based" or "data based" techniques. In model based methods the parameters of an *assumed* analytical model of the true physical system are identified so that the response of the identified model mimics the measured response from the real structure (Friswell 2007). While the identification of an *accurate* parametric model of the structure will allow an *accurate* identification of the existence, location and severity of damage, *accurate* models of true physical systems are seldom available. Moreover, most model based approaches involve some nonlinear optimizations with only a limited number of model parameters to be optimized or identified. This requires a reliable *a priori* analytical model. If the representative model is not very reliable, applying conventional model based methods with all/most of the model parameters as unknowns may not converge to a unique solution (Katafygiotis and Beck 1998, Mukhopadhyay *et al*. 2014a, b).

*Corresponding author, Professor, E-mail: betti@civil.columbia.edu

http://www.techno-press.org/?journal=sss&subpage=8 ISSN: 1738-1584 (Print), 1738-1991 (Online)

Data-based methods rely exclusively on the data recorded from the true structure, and do not require an *a priori* definition of *accurate* physical models (Worden and Farrar 2013). Implemented in a statistical pattern recognition framework, they attempt to identify patterns of Damage Sensitive Features (DSFs) characterizing the structure's condition by analyzing its recorded vibration signatures. The DSFs extracted from the measured responses of a baseline structure are first used to construct a baseline statistical model of the DSFs (training phase), where the baseline structure represents the system in its present conditions. In the following, the baseline system is also referred to as the reference or healthy system, always implying that it represents a system under conditions that have been observed during the training phase. Subsequently, during the testing phase, the DSFs extracted from any new measured response of the structure are compared to the baseline statistical model to identify whether the structure is still in its reference conditions or has undergone any deterioration. Since measured data from different real damage states are not available, data-based SHM involves unsupervised learning, with any new measured data assigned to either the healthy class or a damaged class; questions on the type, location and severity of damage are usually left unanswered. Another challenge in data-based methods is the selection of an appropriate statistical model for the DSFs. The popular normal distribution assumption (Balsamo *et al*. 2014a) may not hold if the number of observations is small, e.g., when instrumentation and data storage/processing costs, faulty instruments etc. lead to small training data set.

In this paper, the comparative advantages of model-based and data-based techniques are combined to a "mixed" approach in vibration based SHM. Due to the intuitive relationship of modal properties to structural characteristics, a modal parameter based DSF may be expected to successfully locate and quantify damage. In fact, several studies have used modal parameters for damage detection (Kim and Stubbs 2003, Yuen *et al*. 2006, Duan *et al*. 2007, Balsamo *et al*. 2013a, b, Huang *et al.* 2012). While modal frequencies, being global features, may be relatively insensitive to local structural damage, mode shapes, being "spatially distributed" features, contain information which may be employed for damage localization (Farrar *et al*. 2001). However, the direct comparison of mode shapes using inner product norms, e.g., the Modal Assurance Criterion, may not provide sufficiently discernible results for structural damage detection, as the differences reflected by such measures are of a lower order than the differences in the structural flexibility matrix (Mukhopadhyay *et al*. 2012). Instead, in (Mukhopadhyay *et al*. 2012, Balsamo *et al*. 2013b) modal parameter comparative measures which mimic changes in the structural flexibility and stiffness matrices are derived. In this paper, we use a stiffness proportional DSF, which gives a measure of the relative difference between the corresponding diagonal elements of the stiffness matrices of two models at comparison. The DSF is defined in terms of experimentally identified modal parameters, which may be identified from the response of the monitored structural system using any modal analysis technique. We consider here the most feasible operational testing scenario (output-only data).

The damage assessment procedure is developed in the statistical pattern recognition paradigm using the DSFs extracted from measured response data. The Empirical Complementary Cumulative Distribution Functions (ECCDFs) of the extracted DSFs are computed, and damage assessment is performed by comparing the ECCDFs obtained during the testing stage with those created during the training stage. The proposed structural health assessment exercise attempts to answer the questions: (1) "Is there a change in the current state of the structure compared to the baseline state?", (2) "Does the change indicate a localized stiffness reduction or increase?", and (3) "What is the severity of the change in a probabilistic sense?". The possible scenario of localized

stiffness increase is intended for applications in retrofitting operations (Nayeri *et al*. 2007).

It has been widely reported that modal parameters are significantly affected by "non-damage" related structural variations, induced, for example, by environmental/operational fluctuations (Sohn2007, Soyoz and Feng 2009). Such effects are taken into account here, using lower and upper bound ECCDFs, obtained from training response time histories measured in different environmental/operational conditions, to define the baseline structural state. Such an approach is intended to decouple normal structural variations from damage induced changes in the values of the proposed DSFs. The lower and upper bound baseline ECCDFs are also used to quantify the uncertainty in damage probability vs. damage severity curves, induced by *unknown* environmental/operational conditions in the testing phase.

The proposed SHM framework addresses several relevant issues. Defining a physically meaningful DSF in a model-based setting allows not only the detection of damage, but also its location and severity estimation. On the other hand, the data-based SHM strategy statistically tests for the existence of damage at any location, and expresses the damage severity through damage probability vs. severity curves, accounting for the different inevitable sources of uncertainty, including those induced by environmental/operational fluctuations. It is worth emphasizing that the proposed algorithm does not require the definition of reliable models describing the effects of environmental/operational conditions on structural parameters, nor does it require the measurements of any operational or environmental variable, e.g., temperature measurements. Hence, the proposed approach may be applied even in those scenarios where measurements of these external conditions are unavailable. While the DSF computation does not require *a priori* knowledge of the mass/stiffness parameter values, limiting the modeling assumptions only to the knowledge of the model class, the use of ECCDFs further avoids the assumption of any particular parametric distribution to statistically model the DSFs. Finally, in addition to damage detection, the proposed approach may also be used to validate retrofitting operations.

The DSF computation is discussed in Section 2. The derivation of the training and testing ECCDFs of the DSFs are discussed in Section 3, and the different levels of damage assessment are discussed in Section 4 using numerical simulations of ambient vibration testing of a bridge deck system. In Section 5, the approach is applied to shake table experimental data from a 4-story steel frame.

2. Stiffness proportional damage sensitive feature

In modeling structural damage as localized stiffness reduction, a DSF which is tailored to measure the deviation of stiffness properties from a baseline state should be ideal. To define such a DSF, consider an N degrees of freedom (DOF) classically damped model of a system, with $N\times N$ mass and stiffness matrices, respectively denoted by $\mathbf{M}$ and $\mathbf{K}$. Let the state of the system described by $\{\mathbf{M}, \mathbf{K}\}$ be the baseline state. Let an alternative state of the system, representing it in an unknown condition, be denoted by $\{\mathbf{M}^*,\mathbf{K}^*\}$. Then, the DSF discussed here measures the departure of the (i,i)th element of $\mathbf{K}^*$ from the (i,i)th element of $\mathbf{K}$

$$\mathrm{DSF}_i = \frac{K_{i,i} - K^*_{i,i}}{K_{i,i}}. \tag{1}$$

Since this DSF measures the relative change in the system's local stiffness properties, it is named *Stiffness Proportional Damage Sensitive Feature* (SPDSF). Since the DSFs discussed in this section are related to the different DOFs constituting the model of the system, these DSFs may be used not only to test for the existence of damage in the system, but also to locate the damage to the neighborhood of any particular DOF. Moreover, since the DSFs provide a measure of the relative change, with respect to the baseline state, in the diagonal elements of the stiffness matrix, they may also be used to assess the severity of any localized damage.

Let λ_j and $\boldsymbol{\phi}_j$ denote the jth eigenvalue and mode shape vector of the model corresponding to the baseline state, and ϕ_{ij} the ith component (corresponding to DOF i) of $\boldsymbol{\phi}_j$. Any appropriate operational modal analysis technique may be used to identify these parameters. In this paper we consider systems which can be represented through lumped mass models, i.e., $\mathbf{M}$ and $\mathbf{M}^*$ are diagonal. The DSF in Eq. (1) can then be written in terms of the modal parameters of the two states of the system as

$$\mathrm{DSF}_i = 1 - \frac{\alpha^*}{\alpha} \frac{\left(\sum_{j=1}^{N} \phi_{i,j}^2 \beta_j^{-1}\right)^2 \left(\sum_{j=1}^{N} \phi_{i,j}^{*2} \lambda_j^* \beta_j^{*-1}\right)}{\left(\sum_{j=1}^{N} \phi_{i,j}^{*2} \beta_j^{*-1}\right)^2 \left(\sum_{j=1}^{N} \phi_{i,j}^2 \lambda_j \beta_j^{-1}\right)} \tag{2}$$

with the superscript * denoting parameters belonging to the alternative $\{\mathbf{M}^*, \mathbf{K}^*\}$ state. In Eq. (2), the β factors $\{\beta_1 = 1, \beta_2, \ldots, \beta_N\}$ are *proportional* mass normalizing factors, which account for the arbitrary scaling of the identified mode shapes in output-only/base excitation situations, while the scalar α is the *true* mass normalizing factor for mode 1; for any mode j, $\alpha\beta_j$ is the *true* mass normalizing factor. In tests with known input forces, with one collocated sensor-actuator pair, it is possible to directly identify the mass normalized mode shapes (e.g., Mukhopadhyay 2014a), and so the α and all β's in Eq. (2) become equal to 1. However, when considering the more feasible output-only/base excitation scenarios, these factors need to be estimated separately. The first factor β_1 is taken as 1, since in output-only situations, for models with diagonal $\mathbf{M}$, one can identify only a model *proportional* to the true model by a single scalar factor without using any *a priori* knowledge of the value of any physical parameter (Mukhopadhyay 2014b). The remaining $(N - 1)$ unknown β_j's may be obtained by imposing any known topological requirements of the $\mathbf{M}$ and $\mathbf{K}$ matrices (Mukhopadhyay 2014b). Imposing the sparsity requirement of a diagonal $\mathbf{M}$, one gets the following linear system of equations whose least squares solution gives the unknown β_j's

$$\sum_{j=2}^{N} \phi_{i,j}\phi_{l,j} / \beta_j = -\phi_{i,1}\phi_{l,1} \qquad \forall\, i,l \in \boldsymbol{S} \text{ and } i \neq l \tag{3}$$

where $\boldsymbol{S}$ is the set of instrumented DOFs (a subset of all the N DOFs), where the output responses are measured. One can similarly obtain a least squares solution for the factors of the alternative system. To evaluate the ratio α^*/α, one would need some assumption on the value of any physical parameter of the system. Assuming that the change in the total mass (= sum of all element masses) of the system in its transition from one state to another is minimum, this ratio may be estimated as

$$\frac{\alpha^*}{\alpha} = \frac{\sum_{i=1}^{N} \left(\sum_{j=1}^{N} \phi_{i,j}^2 \beta_j^{-1}\right)}{\sum_{i=1}^{N} \left(\sum_{j=1}^{N} \phi_{i,j}^{*2} \beta_j^{*-1}\right)} \tag{4}$$

If the system is instrumented with N_s sensors, Eq. (3) will represent $N_s(N_s - 1)/2$ equations, leading to the minimal instrumentation requirement of $N_s \geq [1 + \sqrt{(8N - 7)}]/2$ for estimation of all the $(N - 1)$ β_j's. Even though the DSF in Eq. (2) is written for an identified complete spectrum, in situations where only $N_m<N$ modes are identified from the data, the DSF may still be computed using only these N_m modes in the summation. However, in order to identify the normalizing factors through Eq. (3), all N modes need to be identified at the sensors locations; if $N_m<N$ modes are identified, then other approaches (e.g., Parloo *et al*. 2002) may be used to compute the corresponding β factors.

3. Empirical complementary cumulative distributions of SPDSF

Unlike traditional DSFs, which represent a single state of the system, inherent in the definition of the DSFs in Section 2 is a comparison between two states of the system. For example, a change in the stiffness of an element connecting nodes *i* and *l* would be reflected in a change in the values of the *i*th and *l*th elements in the main diagonal of **K**, and this change would be captured by DSF_i and DSF_l. However, these DSFs, being dependent on the identified frequencies and mode shapes, will not only measure the change in the stiffness properties induced by structural damage, but will also measure stiffness changes induced by environmental and operational variability. Hence, it is pertinent that the damage detection procedure be able to distinguish between damage induced and non-damage induced fluctuations in the DSFs, so as to reduce instances of *false alarms* and *false safety*. This requirement defines an objective of the training phase: to define boundaries for the fluctuations of the DSFs that can be considered normal, and thereby define a reference zone against which new realizations of the DSFs, extracted from the system under unknown conditions, can be compared. To this end, we use the cumulative distribution functions (CDFs) of the DSFs, treating each DSF as a random variable.

The SHM problem can be cast in a probabilistic framework by introducing the "probability of damage" assigned to any model parameter (Yuen *et al*. 2006). Such a probability can be assigned to each diagonal element of **K**, and be defined as the probability that the (i,i)th element of $\mathbf{K}^*$ be less than a prescribed fraction of the (i,i)th element of **K**

$$P_i^{\text{damage}}(d) = P(K_{i,i}^* < (1-d)K_{i,i}) \tag{5}$$

where d is the fractional stiffness reduction (damage). Eq. (5) can be rewritten using Eq. (2) as

$$P_i^{\text{damage}}(d) = P\left(\frac{K_{i,i} - K_{i,i}^*}{K_{i,i}} > d\right) = 1 - P\left(\frac{K_{i,i} - K_{i,i}^*}{K_{i,i}} < d\right) = 1 - \text{CDF}_{\text{DSF}_i}(d) \tag{6}$$

The training procedure to build statistical models of the baseline state DSFs, encompassing the normal variability of the CDFs of the DSFs, can then be performed as discussed herein. Let n_{tr} denote the number of measurement campaigns (i.e., number of sets of measured response data) that have been conducted on the monitored system under *different healthy conditions*; these *different healthy conditions* include different environmental and operational conditions of the healthy state of the system. With N_s sensors, located at the DOFs in $\boldsymbol{\mathcal{S}}$, in each measurement campaign, a set $Y = \{\boldsymbol{\Lambda}^p, \boldsymbol{\Phi}^p\}$, for $p = 1, \ldots, n_{\text{tr}}$, of modal parameters may be identified, where $\boldsymbol{\Lambda}^p$ and $\boldsymbol{\Phi}^p$ respectively contain the N eigenvalues and mode shapes at the N_s measured DOFs

identified from the *p*th set of measured response data. The set Y is then divided into two subsets Y_H and Y_V such that

$$Y_H \bigcup Y_V = Y; \quad Y_H \bigcap Y_V = \varnothing; \quad Y_H, Y_V \neq \varnothing; \quad |Y_H| = n_H; \quad |Y_V| = n_V \tag{7}$$

Now, the modal parameters in Y_H are considered as reference, while those in Y_V are considered to come from an unknown state of the system, i.e., following the terminology used in Section 2, Y_H is treated as the set of modal characteristics identified from baseline states, while Y_V is treated as the set of modal properties identified from the system under unknown conditions. Then, each set of modal parameters in Y_V is compared with each and every set of modal parameters in Y_H using the DSF of Eq. (2); this results in a total of n_V sets DSF_i, $\forall i \in \boldsymbol{S}$, each set containing n_H values. Empirical Cumulative Distribution Functions (ECDFs) of DSF_i are then computed using Eq. (8) (Hanselmann *et al.* 2007), for each of these n_V sets, treating the n_H DSF_i values in each set as random realizations

$$\text{ECDF}_{DSF_i}^{j}(d) = \frac{1}{n_H} \sum_{p=1}^{n_H} U(d - DSF_i^{p,j}) \qquad \forall\ j = 1,..., n_V \tag{8}$$

where $U(z)$ is the Heaviside function: $U(z) = \{0, 0.5, 1\}$ for $z\{<, =, >\}$ 0. Eq. (8) is evaluated over a set of d values such that the computed ECDF(d)'s range from 0 to 1. $\text{ECDF}_{DSF_i}^{j}(d)$ in Eq. (8) can be substituted in place of $\text{CDF}_{DSF_i}(d)$ in Eq. (6); the resulting $P_i^{\text{damage}}(d)$ in Eq. (6), computed as $1 - \text{ECDF}_{DSF_i}(d)$, is then referred to as the *Empirical Complementary Cumulative Distribution Function* (ECCDF) of DSF_i. In this way, we get n_V curves representing $\text{ECDF}_{DSF_i}(d)$, one for each data set in Y_V. The maximum and minimum bounds of these n_V number of $\text{ECCDF}_{DSF_i}(d)$ are then computed, to estimate an acceptable range of d, denoting normal environmental/operational variability, and also to get lower and upper bound exceedance probabilities, given by the lower and upper bound ECCDFs, associated with each value of d in this range, for each DSF_i. At the time of testing, a new set of response data is measured with the N_s sensors from the structure under unknown conditions, and a single set of modal parameters is identified from this data. This new set of modal parameters is compared, using Eq. (2), to each of the n_H sets of parameters in Y_H obtained during the training stage. The resulting n_H values of DSF_i are then used to compute a single $\text{ECCDF}_{DSF_i}(d)$ following the same procedure as in the training stage. This single $\text{ECCDF}_{DSF_i}(d)$ is then compared with the lower and upper bounds of $\text{ECCDF}_{DSF_i}(d)$ obtained in the training stage for damage assessment. This comparison may be performed using different measures, as discussed in the next section with a numerical example.

4. Different levels of damage assessment with numerical example

4.1 Numerical example

To test the validity of the proposed approach and to further define the procedures to identify, locate and define the extent of damage, we consider the simple lumped mass model of a bridge deck of Fig. 1. The model consists of 12 lumped masses and 20 flexural links, and is assumed to vibrate along the z direction. The energy dissipation characteristics of the system are modeled through proportional damping, by assigning 1% damping ratio to each mode.

Table 1 lists the 10 different states considered here. States U1 to U5 represent different healthy

conditions: for example, state U2 may represent a scenario where only the $-y$ side of the bridge deck is subjected to a temperature increase, while state U5 corresponds to a state where only the $+y$ side of the deck is subjected to temperature decrease. States D1 to D4 represent different damage scenarios, with local damages defined with respect to different undamaged states, as may be expected in practice. State R1 represents the condition where a portion of the $-y$ girder is retrofitted.

To construct the training data sets, 50 tests are simulated on each of the five healthy states. Therefore, the set Y defined in Section 3 consists of 250 data sets. For a given test r, the value of the ith stiffness parameter, $k_i^{(r)}$, is chosen as $k_i^{\mathrm{U}m} + U(-0.01,0.01)k_i^{\mathrm{U}m}$, where $k_i^{\mathrm{U}m}$ is the mean value of the flexural stiffness k_i for the undamaged scenario Um, m=1,…,5 (Table 1), and $U(-0.01,0.01)$ is the uniform probability distribution between the limits – 0.01 and 0.01. The variability of the stiffness parameters depicted in Table 1 is adopted to model systematic changes induced, for instance, by environmental effects, while the variability induced by the perturbation obtained via $U(-0.01,0.01)$ is used to mimic the effects of operational and modeling assumptions. The ± 0.01 limits are used as an example, but any range of values producing moderate changes to the structural properties would be similarly acceptable. It should be emphasized that, with the simulated environmental and operational variability, any $(i,i)^{\text{th}}$ element of the healthy stiffness matrix has an approximately ±1.7% variability with respect to the baseline state, which is of the same order as the damage/retrofit induced mean changes (– 5% in states D2 and D4, +8.3% in R1,– 6.6% in D1 and D3); moreover, the difference between the stiffest and the most flexible healthy structure in terms of any $(i,i)^{\text{th}}$ element of the stiffness matrix (approximately 3.3%) is higher than the difference between the most flexible healthy structure and the most stiff damaged structure (approximately 2.4%), thereby including the possibility of damage being masked by environmental/operational variability. Since such a possibility poses a pressing and relevant concern in SHM applications, the performance of the proposed approach is evaluated under such conditions.

Each of the 250 sets of healthy structural parameters is used to simulate the response of the system to Gaussian white noise input force applied at all the DOFs. The resulting response accelerations are corrupted by adding 10% root mean square Gaussian white noise sequences, to represent measurement noise. In this example, only the response accelerations measured at DOFs 4 to 9, 11 and 12 are considered, to represent a partial instrumentation set-up. The set of 250 "measured" acceleration time histories is used to identify the modal frequencies and arbitrarily scaled mode shape components at the instrumented DOFs. In this numerical example, a stochastic subspace identification algorithm is used for this purpose, namely the Enhanced Canonical Correlation Analysis (ECCA) (Hong *et al*. 2013). The 250 sets of identified modal properties are then divided into the subsets $\mathrm{Y_H}$ and $\mathrm{Y_V}$, each of cardinality 125 (n_H and n_V are both equal to 125), both containing 25 realizations from each of the 5 undamaged scenarios. The methods discussed in Sections 2 and 3 are then employed to derive the SPDSFs for the instrumented degrees of freedom and the boundaries of the ECCDFs.

To construct the testing ensemble, 30 tests are performed on each of the 10 states of Table 1, and the structural response is simulated adopting the same procedure used to construct the training data sample. The modal parameters identified through ECCA from each testing data set are compared to the n_H sets of training modal parameters in $\mathrm{Y_H}$, and the resulting testing ECCDF at each measured DOF is constructed.

Fig. 2 compares the 30 *testing* ECCDFs (thin black curves) in states U1, D1 and R1 with the

lower (dashed thick line) and upper (continuous thick line) bound *training* ECCDFs for DSF_6. It may be noted that while the ECCDFs obtained from State U1 are contained within the training boundaries, the testing ECCDFs from State D1 are shifted to the right beyond the upper bound, indicating damage occurrence in one of the elements connected to mass 6 (see Table 1). On the contrary, the testing ECCDFs from State R1 are shifted to the left of the lower bound, validating a retrofitting operation to a portion of the structure in the proximity of sensor 6. Within a deterministic framework, a value of the SPDSF greater than 0 would indicate damage, as only one healthy state would be considered, and would have thus signaled the presence of damage in many of the tests performed on state U1. On the contrary, the initial training phase performed in the currently proposed approach enables us to set a reasonable range of values of *d*, within which the observation of a non-zero *d* can be attributed to the influence of external factors, e.g., temperature, traffic, wind, etc.

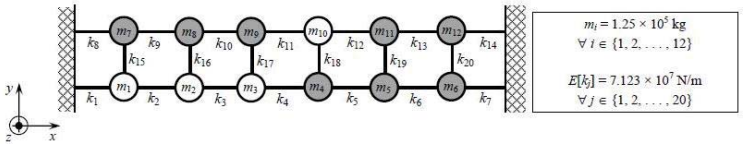

Fig. 1 Bridge model and baseline parameters used in numerical example. Shaded lumped masses denote sensor locations in a partial instrumentation setup.

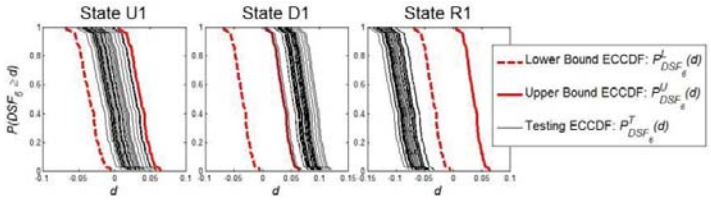

Fig. 2 ECCDFs of SPDSFs at DOF 6 under States U1, D1 and R1

Table 1 Different states of the bridge deck model considered for the numerical example

State	Condition	Description	Affected DOFs
U1	Undamaged	$k_i^{U1} = \mathrm{E}[k_i] \forall\, i \in \{1,\ldots,20\}$	-
U2	Undamaged	$k_i^{U2} = 0.99\,\mathrm{E}[k_i] \forall\, i \in \{1,\ldots,7\}$	1-6
U3	Undamaged	$k_i^{U3} = 1.01\,\mathrm{E}[k_i] \forall\, i \in \{1,\ldots,7\}$	1-6
U4	Undamaged	$k_i^{U4} = 0.99\,\mathrm{E}[k_i] \forall\, i \in \{8,\ldots,14\}$	7-12
U5	Undamaged	$k_i^{U5} = 1.01\,\mathrm{E}[k_i] \forall\, i \in \{8,\ldots,14\}$	7-12
D1	Damaged	$k_6^{D1} = 0.80 k_6^{U1}$	5 and 6
D2	Damaged	$k_6^{D2} = 0.85 k_6^{U2}$	5 and 6
D3	Damaged	$k_{18}^{D3} = 0.80 k_{18}^{U3}$	4 and 10
D4	Damaged	$k_{18}^{D4} = 0.85 k_{18}^{U4}$	4and 10
R1	Retrofitted	$k_6^{R1} = 1.25 k_6^{U5}$	5 and 6

4.2 Damage/retrofit detection and location

In order to identify damage occurrence/retrofitting at a given location, it is necessary to compare the testing ECCDFs with the training boundaries. To fulfill this task, we explore here the use of the Lukaszyk-Karmowski metric (Lukaszyk 2004), which compares two probability distributions as

$$D_{Y,X} = D_{X,Y} = \int_{-\infty}^{+\infty}\int_{-\infty}^{+\infty} | x - y | \, f_X(x) g_Y(y) \, \mathrm{d}x \, \mathrm{d}y \tag{9}$$

where $f_X(x)$ and $g_Y(y)$ are the probability density functions of the random variables x and y. $D_{X,Y}$ is not a distance metric in the strict sense, as $D_{X,X}$ is equal to 0 only if x is an exact value. The property of the Lukaszyk-Karmowski metric that makes it appealing from our perspective is that it satisfies the triangle inequality as an equality: $D_{X,Z} = D_{X,Y} + D_{Y,Z}$. This property may be exploited as follows: let $f_L(d_L)$, $f_U(d_U)$, and $f_T(d_T)$ be the empirical probability density functions (epdfs) corresponding to the lower training bound, the upper training bound and the testing set of SPDSFs, respectively. Then, for example, when the testing ECCDF is obtained from data collected on the structure under undamaged conditions, the Lukaszyk-Karmowski distance of the lower training bound from the upper one satisfies the following relation

$$D_{L,U} = \int_{-\infty}^{+\infty}\int_{-\infty}^{+\infty} | d_L - d_U | \, f_L(d_L) f_U(d_U) \, \mathrm{d}d_L \, \mathrm{d}d_U = D_{L,T} + D_{T,U} \Rightarrow \frac{D_{L,U}}{D_{L,T} + D_{T,U}} \approx 1 \tag{11}$$

Similar relations hold when the system is damaged or retrofitted (Eqs. (12))

$$\frac{D_{L,T}}{D_{L,U} + D_{U,T}} \approx 1 \rightarrow \textbf{Damage} \; ; \quad \frac{D_{U,T}}{D_{L,U} + D_{L,T}} \approx 1 \rightarrow \textbf{Retrofit} \tag{12}$$

In Eqs. (11) and (12) we use $\approx$ to account for numerical errors introduced in the computation of the epdf from the ECCDF, and in the 2-D numerical integration necessary to compute the Lukaszyk-Karmowski metric, which in this paper is performed employing trapezoidal rule.

Table 2 lists the results obtained by employing the said metric to detect and locate damage. In Table 2, for each state, the ratio n/30 indicates the number of tests, n, for which a change in the given diagonal term of the stiffness matrix is identified; the letter in parenthesis indicates whether that change is identified as due to damage (D) or retrofitting (R). Evidently, using said metric it is possible to correctly identify damage between degrees of freedom 5 and 6 (States D1 and D2), and damage around degree of freedom 4 (States D3 and D4), with reasonable accuracy. When dealing with damage scenarios D3 and D4 the detailed estimation of damage location is not possible, owing to incomplete instrumentation, specifically due to the absence of sensors at DOFs 3 and 10. Hence, for such states, we are only able to detect damage around DOF 4, but unable to exactly locate the damaged element. Note, however, that owing to the testing ECCDFs at DOF 5 falling within the training bounds, we can say k_5 is not one of the damaged elements, so that States 3 and 4 would be identified as damage scenarios where damage occurred on element(s) k_4 and /or k_{18}.

In this example, Type II error, i.e. the percentage of damaged instances incorrectly identified as undamaged, is equal to 12.78% (23 out of 180 cases), and it is almost entirely due to missed damage identification of the milder damage conditions (States D2 and D4). Type I error, i.e. the

incorrect identification of an undamaged state as damaged, is much lower and equal to 0.81% (18 out of 2220 cases). The retrofitting operation is correctly validated, with 100% accuracy, between degrees of freedom 5 and 6. The percentage of tests erroneously concluding that a certain area of the system has been retrofitted is 0.56% (13 out of 2340 cases). However, this latter error is of little concern, as the approach here proposed would be used only to verify that a given area of the system has been actually retrofitted. In practice, the retrofitted area is known *a priori*, and the use of the proposed structural health monitoring technique would only validate such an operation. An indication of retrofitting in a non-retrofitted area should be then judged as merely due to testing conditions slightly dissimilar to those attained during training.

4.3 Stiffness change severity assessment

Once changes in stiffness have been identified, it is important to quantify the extent of such changes to conclude whether the identified increase/decrease of the stiffness property is due to an actual change in the structural characteristics or is only due to healthy conditions slightly different from those learnt during training.

At this point, it is important to emphasize the key premise the proposed structural health monitoring strategy is based on. In fact, it is recognized that thinking of the healthy system as represented by a single configuration of the structure is probably inappropriate, but it is rather more realistic to consider the healthy state as a variety of possible conditions where the structural properties might slightly change without leading the structure to perform differently from how it was originally designed. While by itself the testing ECCDF, here onwards denoted as $P^{T}_{DSF_i}(d)$, gives a probabilistic representation of the damage severity, this representation does not account for the inherent variability in the healthy system's ECCDFs. Hence, the damage severity obtained only using $P^{T}_{DSF_i}(d)$ may over/underestimate the actual damage severity. To account for the healthy system variability, the lower and upper training ECCDFs, denoted as $P^{L}_{DSF_i}(d)$ and $P^{U}_{DSF_i}(d)$ respectively, can be exploited as follows. We select a certain percentile from $P^{L}_{DSF_i}(d)$, α_L, and another from $P^{U}_{DSF_i}(d)$, α_U. The values of the stiffness change magnitude, d, corresponding to α_L and α_U should define a *reasonable* range of healthy system's variability, i.e., a range which excludes extreme variations of the healthy system. Since $P^{L}_{DSF_i}(d)$ and $P^{U}_{DSF_i}(d)$ correspond respectively to the stiffest and softest healthy systems, such a reasonable range for d should correspond to a lower percentile from $P^{L}_{DSF_i}(d)$ and a higher percentile of $P^{U}_{DSF_i}(d)$. Reasonable values for α_L would range between 1 and 5, while for α_U between 95 and 99, since such values conform to low and high percentiles, corresponding to a very stiff and a very soft healthy condition, respectively. Here we select α_L equal to 5, and α_U equal to 95. Hence, we subtract the bound defined by the 5th percentile of $P^{L}_{DSF_i}(d)$, $d_L^{5\%}$, and the 95th percentile from $P^{U}_{DSF_i}(d)$, $d_U^{95\%}$ (Fig. 3(a)) from the testing d's: the resulting first ECCDF, $P^{LT}_{DSF_i^S}(d^S)$, gives the exceedance probabilities of damage with respect to the stiffest healthy condition, while the second, $P^{UT}_{DSF_i^S}(d^S)$, quantifies the exceedance probability vs. the damage extent with respect to the softest healthy condition.

Table 2 Results for stiffness change occurrence identification and location

State	$K_{4,4}$	$K_{5,5}$	$K_{6,6}$	$K_{7,7}$	$K_{8,8}$	$K_{9,9}$	$K_{11,11}$	$K_{12,12}$
U1	***1/30 (D)***	0/30	***1/30 (R)***	0/30	0/30	0/30	***1/30 (R)***	***3/30 (D)***
U2	0/30	***1/30 (D)***	***1/30 (D)***	0/30	0/30	***1/30 (D)***	0/30	0/30
U3	***1/30 (R)***	0/30	***1/30 (D)*** ***1/30 (R)***	***1/30 (R)***	0/30	0/30	***1/30 (D)***	***2/30 (D)***
U4	0/30	0/30	***1/30 (D)***	0/30	0/30	0/30	***1/30 (D)*** ***1/30 (R)***	0/30
U5	0/30	0/30	0/30	0/30	0/30	0/30	***1/30 (R)***	0/30
D1	0/30	***29/30 (D)***	***29/30 (D)***	0/30	***1/30 (R)***	0/30	***1/30 (R)***	0/30
D2	0/30	***27/30 (D)***	***20/30 (D)***	0/30	0/30	0/30	***1/30 (D)*** ***1/30 (R)***	0/30
D3	***30/30 (D)***	0/30	0/30	0/30	0/30	0/30	***1/30 (D)***	0/30
D4	***22/30 (D)***	0/30	0/30	0/30	0/30	0/30	0/30	0/30
R1	***1/30 (R)***	***30/30 (R)***	***30/30 (R)***	***2/30 (R)***	0/30	0/30	0/30	***3/30 (D)***

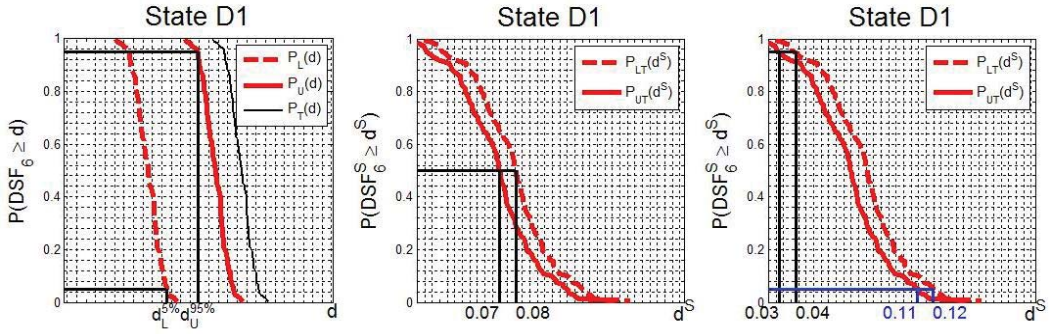

(a) (b) (c)

(a) Definition of $d_L^{5\%}$ and $d_U^{95\%}$, (b) Estimation of damage severity (median) and (c) Estimation of damage severity (5th and 95th percentiles)

Fig. 3 Estimation of damage severity

Fig. 3(b) shows the ECCDFs obtained for a test under state D1 at DOF 6. In Figs. 3(b) and 3(c), the ordinate and abscissa labels display DSF^S and d^S in place of DSF and d, respectively, to emphasize that the values of the random variable are not those evaluated during testing, but those obtained by subtracting $d_U^{95\%}$ and $d_L^{5\%}$ from the testing values. The median amount of damage extent with respect to the stiffest healthy condition is equal to 0.08 (dashed thick red line in Fig. 3(b)), while with respect to the softest healthy state is equal to 0.07 (continuous thick red line in Fig. 3(b)). From the previous results, we know that the element between DOFs 5 and 6 is damaged; if we assume that all spring elements connected to mass 6 have the same stiffness values, we can then estimate the amount of remaining stiffness, γ, of element k_6 according to Eq. (14):

$$P(DSF_6 > d) = P\left(1 - \frac{k_6^* + k_7^* + k_{20}^*}{k_6 + k_7 + k_{20}} > d\right) = P\left(1 - \frac{2k + \gamma k}{3k} > d\right) = P(\gamma < 1 - 3d). \quad (14)$$

It is important to note that, to perform damage severity assessment as in Eq. (14), one needs to know which are the stiffness elements connecting to the node under consideration, i.e., one needs to know the model class representing the system, which is a common assumption in most SHM techniques attempting to quantify damage severity. Using Eq. (14), it is possible to conclude that, under the damage scenario D1, there is 50% probability that the remaining stiffness of the damaged element between DOFs 5 and 6 be less than 0.79(= 1 - 3d = 1 - 3×0.07) when compared to the softest healthy system, and 0.76 (= 1 - 3×0.08) when compared to the stiffest healthy system (see Fig. 3(b)). Moreover, exploiting the 5th and 95th percentile of the ECCDFs of Fig. 3(c), it is possible to assess that there is only 5% probability that the remaining stiffness is lower than 0.67, but 95% probability that is lower than 0.91, with respect to the softest system. On the other hand, when considering the stiffest healthy condition, there is only 5% probability that the remaining stiffness of k_6 be lower than 0.64, but 95% probability that be lower 0.88. Since the actual range of variability of the simulated k_6 is within 0.73 and 0.82, the damage extent estimates are assumed to be reasonably accurate. Performing the same approach for all other tests under damaged cases D1 and D2, and retrofitted case R1, the results are equally accurate. As mentioned in section 4.2, owing to partial instrumentation, it is not possible to estimate with comparable accuracy the damage extent for damage states D3 and D4. If we assume that both elements k_4 and k_{18} are damaged and that the healthy counterparts share the same stiffness values, the stiffness retention of the two elements would range between 0.955 and 0.94; on the contrary, if we assume that only one element is damaged, values similar to those given for the state D1 are obtained.

5. Shake table experimental application

For the experimental application of the proposed SHM approach, a 4-story singlebay laboratory scale A36 steel frame structural model is considered (Fig. 4).The frame has an inter-story height of 533 mm, floor plate dimensions of 610 x 457 x 12.7 mm, and it is diagonally braced in one direction (North-South direction), from here onwards denoted as the strong direction, as opposed to the perpendicular direction (East-West direction), referred to as the weak direction. The columns and the diagonal braces have cross-sectional dimensions of 50.8 x 9.5mm and 50.8 x 6.4 mm, respectively. All the structural connections are bolted using connection plates and angles. The frame is excited along the weak direction of bending. The base excitation is provided using the 1.5 x 1.5 m platform uniaxial hydraulic shaking table facility available at the Carleton Laboratory of Columbia University, New York. The frame is mounted on the table and the structure-table connection is sufficiently bolted to reproduce a fixed-base behavior. The frame is instrumented with 8 piezoelectric accelerometers, located at the plate levels on the column to plate connections, measuring the acceleration along the weak direction of bending (Fig. 4).The sampling rate of all instruments is at least 200 Hz for all the experiments considered herein. In the ensuing discussion, we use the structural acceleration at the centroids of the floors, referred to as $\ddot{u}_i$ in the following, for i= 1,…,4, obtained by averaging the recorded acceleration time histories: $\ddot{u}_1$= (A1 + A8)/2, $\ddot{u}_2$= (A2 + A7)/2, $\ddot{u}_3$= (A3 + A6)/2 and $\ddot{u}_4$= (A4 + A5)/2. Using the assumption of rigid floors and the coincidence of floor centers of mass and centroids, the frame is modeled as a 1-D 4-DOF system. Six different types of input ground motions (band limited white noise, Eurocode 8 compatible, El

Centro, Hachinohe, Kobe and Northridge) are applied to the table. For this application, the OKID/ERA (Luş et al. 1999) algorithm is employed to identify the modal properties of the frame, by using the measured acceleration responses of the floors as outputs and of the table as input.

To assess the applicability of the approaches discussed herein, in addition to the above frame, here onwards referred to as the "healthy" system (U1), an additional healthy condition U2 is considered, by adding two masses at the third floor: one on the south and the other on the north floor edge. The training data set is constituted by 89 input-output sets of acceleration histories. Four different "damaged" frames (D1 to D4) are also tested using the same set of 6 inputs. In these damaged frames, structural damage is simulated as stiffness reduction, by replacing one or more columns of the "healthy" frame with columns of reduced cross-sectional area (50.8 x 7 mm). The testing set consists of 144 data sets: 10 from state U1, 14 from state U2 and 30 from each of the four damaged states. The results of the stiffness change detection and location are presented in Table 4, using the same notation used to present the results for the numerical example. Type I error is again low and equal to 1.6% (5 out of 306 cases). Adversely, Type II error is equal to 25.6% (69 out of 270 cases). In fact, while damage scenarios D2 and D3 are correctly identified and located with 100% accuracy, the method identifies the stiffness change at DOF 3, but fails at identifying such change at DOF 2 for the damage scenario D1; similarly, for state D4, stiffness change at the third inter-story is identified both at DOF 3 and 2, but the stiffness reduction at the second inter-story cannot be identified from these results. One possible reason behind this misidentification is that both damage scenarios D1 and D3 cause torsion in the system, which may not be captured well by the 4 DOFs 1-D model used. Nonetheless, even in these scenarios the overall system is identified as damaged, and the region containing the damaged elements is identified accurately as well.

Fig. 5 shows the results of the stiffness change extent quantification. For any DOF, the plot in Fig. 5 is obtained as follows. Let $d_U^{95\%}$ correspond to the 95th percentile from the upper bound training ECCDF. Such $d_U^{95\%}$ is subtracted from the *d*'s associated with the 144 testing ECCDFs. From the resulting new shifted 144 ECCDFs, the median *d* values, here onwards referred to as $d_{UT}^{50\%}$, are obtained. Finally, for any given state, the average of such $d_{UT}^{50\%}$ values are computed over all the tests performed on that state, e.g. over the 10 tests on State U1. Comparing the average estimated damage extent displayed in Fig. 5 with the theoretical values presented in the last column of Table 3, it is evident that the proposed approach is able to quantify the extent of stiffness change with reasonable accuracy.

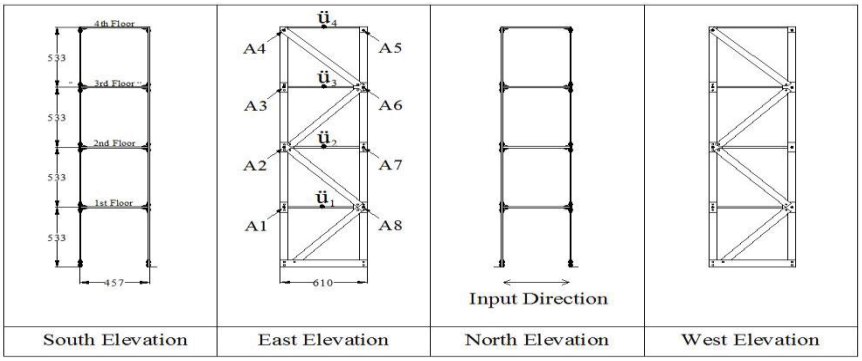

Fig. 4 Elevation views of the steel frame employed in the experimental application. Dimensions are in mm

Table 3 Different states of the steel frame considered for the experimental application

State	Condition	Description	Affected DOFs	Stiffness Reduction at affected DOFs
U1	Undamaged	Baseline condition	-	-
U2	Undamaged	40% mass addition to 3rd floor	-	-
D1	Damaged	15% stiffness reduction at 3rd floor	2 and 3	7.5% at DOFs 2 and 3
D2	Damaged	30% stiffness reduction at 3rd floor	2 and 3	15% at DOFs 2 and 3
D3	Damaged	60% stiffness reduction at 3rd floor	2 and 3	30% at DOFs 2 and 3
D4	Damaged	15% stiffness reduction at 2nd and 3rd floor	1, 2 and 3	7.5% at DOFs 1 and 3, 15% at DOFs 2

Table 4 Results for stiffness change identification and location

State	$\mathbf{K_{1,1}}$	$\mathbf{K_{2,2}}$	$\mathbf{K_{3,3}}$	$\mathbf{K_{4,4}}$
U1	***2/10 (D)***	0/10	***2/10 (R)***	***1/10 (D)*** ***2/10 (R)***
U2	0/14	0/14	0/14	0/14
D1	0/30	0/30	***30/30 (D)***	***2/30 (D)***
D2	0/30	***30/30 (D)***	***30/30 (D)***	0/30
D3	***17/30 (R)***	***30/30 (D)***	***30/30 (D)***	0/30
D4	0/30	***21/30 (D)***	***30/30 (D)***	0/30

An interesting observation from this experiment is the apparent increase in first-story stiffness with damage. The phenomenon may be appreciated in Table 4: at DOF1, for State D3, 17 out of the 30 tests identify an unexpected, systematic increase in stiffness at the first interstory. This is also observed in Fig. 5, which illustrates the estimated stiffness change extents in the different tested states. Such increase in stiffness is less marked for state D4, since the DOF 1 in this state also includes the effect of a damage in the second story; in fact, the average value of the estimated damage extent should be approximately equal to 0.075 in state D4 (Table 3). One possible explanation of the first story stiffness increase may be the activation of some strengthening mechanism (e.g., increased participation of the braces in load resistance, particularly strong torsional component, etc.) in the first story when there is damage at some other story. Such trend is more marked as the damage severity increases. In fact, while for damage scenarios D1 and D2 the average stiffness increase at the first interstory ranges between 4 and 6% (Fig. 5), for damage scenario D3 the increase in stiffness is nearly equal to 8%. This increase of the first interstory stiffness causes more than half of the tests performed on the frame under state D3 to be declared retrofitted at the first inter-story (Table 4). A similar unexpected increase in stiffness has been observed for the same structure also in (Fraraccio *et al.* 2008) where the stiffness properties of the frame structure have been identified using different approaches than the one presented in this paper.

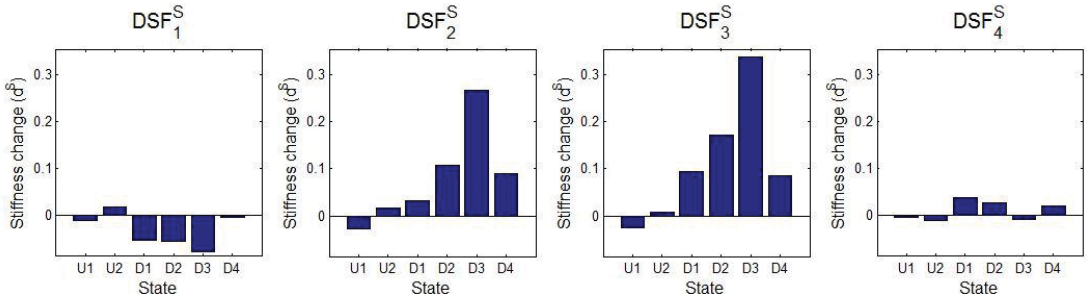

Fig. 5 Average damage extent for the six states of the experimental application

6. Conclusions

In this paper, a "mixed" approach for SHM using operational vibration response measurements is proposed. The DSFs, defined in a model based setting in terms of experimentally identified modal parameters, attempt to measure relative localized stiffness reductions. The health assessment is performed in a statistical pattern recognition framework using the DSFs extracted from response measurements. The features in the training stage, extracted from response measurements on the baseline structure in a wide variety of environmental/operational conditions, are used to compute a range of ECCDFs, from which lower and upper bound training ECCDFs are estimated. Such a training procedure intends to decouple the normal structural variations from damage induced changes, by defining a zone of normal variability of the baseline state through the estimated lower and upper bound training ECCDFs. The ECCDFs of DSFs extracted from the data collected in the testing stage are then compared against the lower and upper bound training ECCDFs to assess the presence, location and severity of any change in the structural stiffness parameters. To detect the existence of a stiffness change a method based on the Lukaszyk-Karmowski metric is exploited, which allows the user to also validate retrofitting operations. The results of a numerical example of ambient vibration testing of a bridge deck system illustrate that, with the localized definition of the DSF, using the aforementioned method, one may detect and locate the existence of any stiffness change with reasonable accuracy. After the existence and location of change detection, the severity of the change is also estimated using the testing and lower and upper bound training ECCDFs. The testing ECCDF is adjusted using different percentiles of the two training ECCDF bounds, resulting in a probability box model to represent the exceedance probability for different stiffness change severity levels. Such a model constitutes of a lower and an upper bound change probability vs. change severity curves, using which, for any given change severity, a lower and upper bound of the probability of exceedance can be estimated, and vice versa. The numerical example of the bridge deck shows that the severity of stiffness reduction/increase induced by damage/retrofitting may be estimated with reasonable accuracy using such curves. The two level uncertainty in the damage severity attempts to segregate: (a) the uncertainty from measurement noise, input variability, and environmental/operational variability in the training state, expressed through a single exceedance probability of change severity, and (b) the uncertainty from unknown environmental/operational conditions in the testing state, expressed through a range of possible values the exceedance

probability may take. If the monitored system is fully instrumented, then the proposed DSF and health assessment method allows also an accurate element level change localization and severity estimation, while for partially instrumented systems it successfully identifies a region within which damage is confined. The proposed health assessment procedure is also applied to experimental data from a 4-story steel frame under base excitation on a shake table and is proved to be capable of identifying the location and severity of stiffness reduction with reasonable accuracy.

Acknowledgments

The authors acknowledge the financial support from Rutgers, Center for Advanced Infrastructure and Transportation - CAIT (Sponsor grant: DTRT12-G-UTC16). The authors also thank Adrian Brügger, Prof. Manolis Chatz is and Prof. Andrew Smyth for their collaboration and support during the experimental phase of the work.

References

Balsamo, L., Mukhopadhyay, S., Betti, R. and Lus, H. (2013a), "Damage detection using flexibility proportional coordinate modal assurance criterion", *Proceedings of the 31stIMAC*, Garden Grove, USA, February.

Balsamo, L., Mukhopadhyay, S., Betti, R. and Lus, H. (2013b), "Modal parameter based damage detection in operational modal analysis: A statistical pattern recognition approach", *Proceedings of the 11th International Conference on Structural Safety and Reliability*, New York, USA, June.

Balsamo, L., Betti, R. and Beigi, H.(2014), "A structural health monitoring strategy using cepstral features", *J. Sound Vib.*, **333**(19), 4526-4542.

Duan, Z., Yan, G., Ou, J. and Spencer, B.F. (2007), "Damage detection in ambient vibration using proportional flexibility matrix with incomplete measured DOFs", *Struct. Control. Health Monit.*, **14**(2), 186-196.

Farrar, C.R., Doebling, S. and Nix, D.A. (2001), "Vibration-based structural damage identification", *Philos. T. R. Soc. A*, **359**(1778), 131-149.

Farrar, C.R. and Worden, K. (2013), *Structural Health Monitoring: A Machine Learning Perspective*, John Wiley & Sons, Ltd., Chichester, UK.

Fraraccio, G., Brugger, A. and Betti, R. (2008), "Identification and damage detection in structures subjected to base excitation", *Exp. Mech.*, **48**(4), 521-528.

Friswell, M.I. (2007), "Damage identification using inverse methods", *Philos. T. R. Soc. A*, **365**, 393-410.

Hanselmann, A., Schrempf, O.C. and Hanebeck, U.D. (2007), "Optimal parametric density estimation by minimizing an analytic distance measure", *Proceedings of the 10th International Conference on Information Fusion*.

Hong, A.L., Ubertini, F. and Betti, R. (2013), "New stochastic subspace approach for system identification and its application to long-span bridges", *J. Eng. Mech. - ASCE*, **139**(6), 724-736.

Huang, Q., Gardoni, P. and Hurlebaus, S. (2012), "A probabilistic damage detection approach using vibration-based nondestructive testing", *Struct. Saf.*, **38**(2012), 11-21.

Katafygiotis, L.S. and Beck, J.L. (1998), "Updating models and their uncertainties. II: Model identifiability", *J. Eng. Mech. - ASCE*, **124**(4), 463-467.

Kim, J. and Stubbs, N. (2003), "Nondestructive crack detection algorithm for full-scale bridges", *J. Struct. Eng. - ASCE*, **129**(10), 1358-1366.

Lukaszyk, S. (2004), "A new concept of probability metric and its applications in approximation of scattered data sets", *Comput. Mech.*, **33**(4), 299-304.

Lus, H., Betti, R. and Longman, R.W. (1999), "Identification of linear structural systems using earthquake-induced vibration data", *Earthq. Eng. Struct. D.*, **28**, 1449-1467.

Mukhopadhyay, S., Lus, H., Hong, A.L. and Betti, R. (2012), "Propagation of mode shape errors in structural identification", *J. Sound Vib.*, **331**, 3961-3975.

Mukhopadhyay, S., Lus, H. and Betti, R. (2014a), "Modal parameter based structural identification using input-output data: Minimal instrumentation and global identifiability issues", *Mech. Syst. Signal Pr.*, **45**(2), 283-301.

Mukhopadhyay, S., Lus, H. and Betti, R. (2014b), "Structural identification with incomplete instrumentation and global identifiability requirements under base excitation", *Struct. Control. Health Monit*., DOI: 10.1002/stc.1732.

Nayeri, R.D., Masri, S.F. and Chassiakos, A.G. (2007), "Application of structural health monitoring techniques to track structural changes in a retrofitted building based on ambient vibration", *J. Eng. Mech. - ASCE*, **133**(12), 1311-1325.

Sohn, H. (2007), "Effects of environmental and operational variability on structural health monitoring", *Philos. T. R. Soc. A*, **365**(1851), 539-560.

Soyoz, S. and Feng, M.Q. (2009), "Long-term monitoring and identification of bridge structural parameters", *Comput-Aided Civ. Inf.*, **24**(2), 82-92.

Yuen, K.V., Beck, J.L. and Katafygiotis, L.S. (2006), "Efficient model updating and health monitoring methodology using incomplete modal data without mode matching", *Struct. Control. Health Monit.*, **13**(1), 91-107.

Smart Structures and Systems, *Vol. 15, No. 3 (2015) 717-733*
DOI: http://dx.doi.org/10.12989/sss.2015.15.3.717

Assessment of modal parameters considering measurement and modeling errors

Qindan Huang*[1], Paolo Gardoni[2] and Stefan Hurlebaus[3]

[1]*Department of Civil Engineering, The University of Akron, Akron, OH 44325-3905, USA*
[2]*Department of Civil and Environmental Engineering, University of Illinois at Urbana-Champaign, Urbana, IL 61801-2352, USA*
[3]*Zachry Department of Civil Engineering, Texas A&M University, College Station, TX 77843-3136, USA*

(Received October 25, 2014, Revised January 17, 2015, Accepted February 3, 2015)

Abstract. Modal parameters of a structure are commonly used quantities for system identification and damage detection. With a limited number of studies on the statistics assessment of modal parameters, this paper presents procedures to properly account for the uncertainties present in the process of extracting modal parameters. Particularly, this paper focuses on how to deal with the measurement error in an ambient vibration test and the modeling error resulting from a modal parameter extraction process. A bootstrap approach is adopted, when an ensemble of a limited number of noised time-history response recordings is available. To estimate the modeling error associated with the extraction process, a model prediction expansion approach is adopted where the modeling error is considered as an "adjustment" to the prediction obtained from the extraction process. The proposed procedures can be further incorporated into the probabilistic analysis of applications where the modal parameters are used. This study considers the effects of the measurement and modeling errors and can provide guidance in allocating resources to improve the estimation accuracy of the modal data. As an illustration, the proposed procedures are applied to extract the modal data of a damaged beam, and the extracted modal data are used to detect potential damage locations using a damage detection method. It is shown that the variability in the modal parameters can be considered to be quite low due to the measurement and modeling errors; however, this low variability has a significant impact on the damage detection results for the studied beam.

Keywords: modal parameters; measurement error; modeling error; bootstrap; sample size

1. Introduction

Modal parameters (e.g., modal frequency and mode shape) are used to describe the characteristics of a structure and have been commonly used in system identification to validate and/or update computer simulated models (Doebling and Farrar 2001, Ching *et al*. 2006). They are also often adopted in vibration-based nondestructive testing (NDT) methods for damage detection, where typically the modal parameters of a damaged system are compared with those of the corresponding undamaged system (Doebling *et al*. 1998). The results of the damage detection are useful for estimating the reliability of existing structures and help schedule condition-based

*Corresponding author, Assistant Professor, E-mail: qhuang@uakron.edu

http://www.techno-press.org/?journal=sss&subpage=8 ISSN: 1738-1584 (Print), 1738-1991 (Online)

maintenance (Ceracolo *et al*. 2009, Zio 2009). To effectively use the modal parameters in these applications, it is critical to know the statistics of the modal parameter estimation.

Modal data are usually extracted from time-history vibration responses obtained from a vibration test. The uncertainties in the modal data mainly come from two sources: one is the vibration test and the other is the modal parameter extraction (identification) process. The epistemic uncertainty in the measurement process in which the structural dynamic responses are recorded is called measurement error. The epistemic uncertainty inherent in the extraction process that reflects the inexactness and assumptions in the process is called modeling error. Currently, studies that assess the uncertainties in the modal parameters are still limited in number, especially in the area of considering the modeling error in the modal parameter extraction process. A typical approach is to assume that modal parameters consist of deterministic quantities and additive random errors with zero means (Liu 1995, Papadopoulos and Garcia 1998, Xia *et al*. 2002, Pothisriri and Hjelmstad 2003). In this approach, regardless of the inaccuracy of the assumption, the contributions to the uncertainties from the measurement and the extraction processes are not clear. Thus such approach is not able to provide the necessary guidance when allocating resources to improve the accuracy of the modal data estimate.

This paper presents a procedure that can be used to assess the modal data extracted from dynamic responses obtained from ambient vibrations considering the effect of the measurement and modeling errors. Particularly, when an ensemble of a limited number of noised time-history response recordings is available, a bootstrap approach is used to estimate the statistics of the modal data. To estimate the modeling error associated with the extraction process, a model prediction expansion approach is adopted where the modeling error is considered as an "adjustment" to the prediction obtained from the extraction process. The modeling error considered in this study is due to a specific modal data extraction process, namely, Time Domain Decomposition (TDD) method (Kim *et al*. 2005). However, the proposed procedure can be extended to other extraction methods. This study is especially useful when the modal parameters are further applied to system identification, damage detection, and other applications, where the uncertainties from various sources should be considered. Moreover, the modeling error is estimated separately and it can help provide guidance in allocating resources to improve the accuracy of the modal data estimate.

In the following, first a brief review of the uncertainty types and the methods for error modeling is given. Next, the procedure to consider the measurement and modeling errors is described. Lastly, in a numerical example, the modal parameters of a damaged two-span, continuous beam are extracted considering measurement and modeling errors following the proposed procedure, and the extracted modal data are used to detect potential damage locations using a damage detection method.

2. Uncertainty types and modeling

To appropriately account for the uncertainties, different types of uncertainties need to be understood. This section first describes the characteristics of different uncertainties associated with the process of extracting modal parameters from the responses. The uncertainty classification follows Gardoni *et al*. (2002). Next a review of the available approaches for handling and propagating those uncertainties is presented.

2.1 Measurement error

Measurement error reflects the difference between the recorded responses and the true responses. It may vary with sensor type, layout, installation of equipment, and environment. In numerical studies, the measurement error is generally modeled by adding random errors into the time-history response signals and the error is often simulated as a random Gaussian noise with zero mean and a specific standard deviation. To provide reasonable upper and lower bounds on the measurement error, absolute error and proportional error are commonly used (Banan *et al*. 1994). For the absolute error, the standard deviation of the measurement error is a fixed value. For the proportional error, the standard deviation of the measurement error is proportional to the value of the amplitude of the true response.

There are two common methods to propagate the measurement error to the modal data. One is the perturbation method or sensitivity method, which requires finding the sensitivity of the measurement error to the modal data. In this respect, Longman and Jung (1987) developed a framework for the eigenrealization algorithm (ERA); Peterson *et al*. (1996) used the perturbation analysis for the fast ERA; and Arici and Mosalam (2005) provided a formulation of sensitivity for the observer Kalman filter identification-ERA with direction correlations method. If the sensitivity can be expressed analytically, the perturbation approach is efficient. However, the sensitivity analysis typically uses a first order approximation that may not be accurate, and the computation required to obtain the sensitivity is not an easy task (Doebling and Farrar 2001). The other approach is the sampling method, where a set of modal data is extracted from a set of time-history responses that are contaminated by the measurement error. Note that using the sampling method the variability in the sets of modal parameters reflects the effect from both the measurement error and the modeling error associated with the modal data extraction process. The sampling method is straightforward but requires a good number of time-history responses.

2.2 Modeling error

Modeling error reflects the error due to model inaccuracy. The sources of the error can come from the abstractions, assumptions, and approximations used in the modeling process. There are two types of modeling errors: parameter error and model error. Parameter error refers to the epistemic uncertainties in the model parameters (e.g., stiffness and mass in a finite element model, FEM) in a given model due to the lack of knowledge of the parameter values. The uncertainties in the model parameters are parameter errors. Model error is associated with the model itself, reflecting the fact that there might not be a perfect numerical model to represent a real-world system and/or from the missing portion that is not included in the model. An example is using an elastic-perfectly-plastic stress-strain relationship to model material behavior.

Oberkampf *et al*. (2002) developed a general framework to deal with modeling error in computational simulations associated with the numerical solution of a set of partial differential equations. Reinert and Apostolakis (2006) gave a review of approaches to handle modeling errors, including model set expansion and model prediction expansion. Model set expansion combines different models to produce a meta-model for a real system, incorporating the advantages of various models. Model prediction expansion, on the other hand, applies an “adjustment” directly to the prediction outcome from one model. In this study, since only one specific extraction method is adopted to extract the modal data, using model prediction expansion is appropriate to estimate the modeling error associated with the extraction process.

3. Estimation of measurement and modelling errors in the extracted modal parameters

3.1 Processes for obtaining modal parameters

Two processes are usually involved in obtaining the modal parameters. One is to record dynamic responses from a vibration test that can be ambient, and the other is to extract the modal parameters from the responses. The ambient vibration test is an attractive option because the excitation can be wind, traffic loading, and any other convenient mechanical exciter and only the output needs to be recorded. When an ambient vibration test is used, an output-only modal parameter identification method is needed to extract the modal parameters. In this paper, an ambient extraction technique called Time Domain Decomposition (TDD) method (Kim *et al*. 2005) is used. For the sake of completeness, a brief review of the TDD method is given next.

3.2 Review of Time Domain Decomposition (TDD) method

Acceleration responses are the commonly recorded quantities in a vibration test. If there are p acceleration sensors and n modes are considered, the acceleration output can be written as

$$\ddot{\mathbf{y}}(t) = \sum_{i=1}^{\infty} \ddot{c}_i(t)\boldsymbol{\varphi}_i = \sum_{i=1}^{n} \ddot{c}_i(t)\boldsymbol{\varphi}_i + \boldsymbol{\varepsilon}_t(t) \tag{1}$$

where $\ddot{\mathbf{y}}(t) = [\ddot{y}_1(t),...,\ddot{y}_p(t)]^T$, $\ddot{c}_i(t) = i$th mode contribution factor at time t, $\boldsymbol{\varphi}_i = i$th modal shape, and $\boldsymbol{\varepsilon}_t(t)$ = truncation error. A mode-isolated response, $\ddot{\mathbf{y}}(t)$, is obtained by filtering the acceleration response using a digital band-pass filter that is designed by estimating the frequency bandwidth for each mode. The filtered acceleration $\ddot{\mathbf{y}}^{(i)}(t)$ for the ith mode can be expressed as

$$\ddot{\mathbf{y}}^{(i)}(t) = \ddot{c}_i(t)\boldsymbol{\varphi}_i + \sum_{j=1}^{p-1} \ddot{d}_j(t)\boldsymbol{\psi}_j \tag{2}$$

where the second term refers to the error due to the truncation and the filtering, $\boldsymbol{\psi}_j$ = orthogonal noise base, and $\ddot{d}_j(t) = j$th mode contribution factor to the total error. The dimension of the mode-isolated acceleration vector, $\ddot{\mathbf{y}}^{(i)}(t)$, at the sample, t, is $p\times 1$, and it contains the modal space and orthogonal noise space. As shown in Eq. (2), the dimension of the modal space is only one (i.e., the ith mode shape vector $\boldsymbol{\varphi}_i$) and the dimension of the noise space is $p - 1$.

With a total time sample N, and assuming that the orthogonal bases in the modal space consists of $\ddot{\mathbf{c}}_i = [\ddot{c}_i(1),...,\ddot{c}_i(N)]$ and the error space consists of $\ddot{\mathbf{d}}_j = [\ddot{d}_j(1),...,\ddot{d}_j(N)]$, a cross-correlation $\mathbf{E}_i = \mathbf{H}_i\mathbf{H}_i^T$ of $\ddot{\mathbf{y}}^{(i)}(t)$, where $\mathbf{H}_i = [\ddot{\mathbf{y}}^{(i)}(1)\ \ddot{\mathbf{y}}^{(i)}(2)\ \ldots\ \ddot{\mathbf{y}}^{(i)}(N)]$, can be calculated as

$$\mathbf{E}_i = \boldsymbol{\varphi}_i q_i \boldsymbol{\varphi}_i^T + \sum_{j=1}^{p-1} \boldsymbol{\psi}_j \sigma_j \boldsymbol{\psi}_j^T \tag{3}$$

where $q_i = \ddot{\mathbf{c}}_i^T\ddot{\mathbf{c}}_i$ and $\sigma_j = \ddot{\mathbf{d}}_j^T\ddot{\mathbf{d}}_j$. Since the energy contributed by the noises is relatively small, then it is appropriate to assume that $q_i > \sigma_1 > \ldots > \sigma_{p-1}$. Thus, by conducting singular value decomposition on

$\mathbf{E}_i$, the first singular vector in the singular vector matrix is the extracted modal shape $\hat{\boldsymbol{\varphi}}_i$ for the *i*th mode. With the obtained $\hat{\boldsymbol{\varphi}}_i$, the contribution factor can be calculated as

$$\ddot{\mathbf{c}}_i^T = \frac{\hat{\varphi}_i^T \mathbf{H}_i}{\hat{\varphi}_i \hat{\varphi}_i^T} \tag{4}$$

The signal, $\ddot{\mathbf{c}}_i$, contains the *i*th modal behavior of the acceleration for the entire set of *p* signals. Therefore, the auto-spectrum of $\ddot{\mathbf{c}}_i$, contains one peak, at which the frequency is the extracted modal frequency $\hat{f}_i$.

3.3 Measurement error in an ambient vibration test

Measurement error in an ambient vibration test can have many causes. The primary sources are listed in the following and the examples of influencing factors are given in the parentheses:

- electromagnetic noises in the sensor (sensor type, signal conditioning type)
- data acquisition and discretization (data-acquisition system, sampling rate)
- data processing and testing economy (signal processing system)

With *p* sensors, one set of time-history responses $\ddot{\mathbf{y}}_1(t) = [\ddot{y}_{1,1}(t),\ldots, \ddot{y}_{p,1}(t)]^T$ is measured in one recording. It is assumed that these *p* series of time-history responses have the same measurement noise level. When such measurement is repeated *m* times, *m* sets of such time-history responses, $\{\ddot{\mathbf{y}}_1(t),\ddot{\mathbf{y}}_2(t),\ldots,\ddot{\mathbf{y}}_m(t)\}$, are obtained and each set of time-history responses is assumed to have the same level of measurement error. Then, for each set of responses, the TDD method is applied to obtain one set of modal data, thus *m* sets of modal data are generated. If *m* is large enough, the statistics of the modal data can be assessed. If *m* is small (e.g., if the vibration testing is conducted by applying a pulse excitation in order to excite out the modal frequencies of interest, then the number of the vibration testing will be limited), a bootstrap method (Efron 1982) is proposed in this paper to generate new sets of responses based on the recorded ones. The basic idea of the bootstrap method is to randomly generate new responses using the original list of responses. The new sets of responses have the same level of measurement error as the recorded ones.

Note that in an ambient vibration test, the excitation is not recorded and it varies for each recording; thus, the Bootstrap method cannot directly be applied to the responses in the time domain. In the frequency domain, the response amplitude varies with frequencies. However, it is legitimate to assume that the amplitude is constant in a narrow bandwidth. In the TDD, the mode-isolated responses are obtained using a frequency bandwidth that can be considered to be narrow. Additionally, as the normalized mode-isolated responses reflect the normalized mode shapes at the sensor locations, they are independent of the excitation. Thus, a Bootstrap method can be applied to the normalized mode-isolated responses in the frequency domain at each sensor node. This principle can be applied to other output only modal data exaction method such as frequency domain decomposition (Brinker *et al*. 2000).

Fig. 1 shows the flowchart of the proposed procedures for estimating the statistics of the modal data considering measurement and modeling errors, where *p* acceleration sensors are used and *m* sets of dynamic responses are collected. In the proposed procedure, firstly the measured responses, $\{\ddot{\mathbf{y}}_1(t),\ddot{\mathbf{y}}_2(t),\ldots,\ddot{\mathbf{y}}_m(t)\}$, are transferred to the frequency domain and normalized, and then are filtered using a digital band-pass filter to obtain the mode-isolated responses in the frequency domain,

$\{\ddot{\mathbf{Y}}_1^{(i)}(\omega),\ddot{\mathbf{Y}}_2^{(i)}(\omega),\ldots,\ddot{\mathbf{Y}}_m^{(i)}(\omega)\}$. Next, the bootstrap technique is applied to $\{\ddot{\mathbf{Y}}_1^{(i)}(\omega),\ddot{\mathbf{Y}}_2^{(i)}(\omega),\ldots,\ddot{\mathbf{Y}}_m^{(i)}(\omega)\}$ to obtain a bootstrap sample $\ddot{\mathbf{Y}}_b^{(i)}(\omega)$. This new bootstrap sample $\ddot{\mathbf{Y}}_b^{(i)}(\omega)$ is then transferred back to the time domain, $\ddot{\mathbf{y}}_b^{(i)}(t)$. For each bootstrap sample, the TDD method is applied to extract a set of modal data. Thus, a pool of modal data is obtained. The procedures can be repeated to obtain more bootstrap samples. As shown in Fig. 1, the proposed procedure involves the extraction process (i.e., the TDD method); therefore, the variability in the pool of modal data shows the influence of the measurement and modeling errors. The advantages of this proposed procedure are: 1) it does not require knowing the measurement noise level in the responses, and 2) the excitation for the vibration can be any ambient conditions as noted previously.

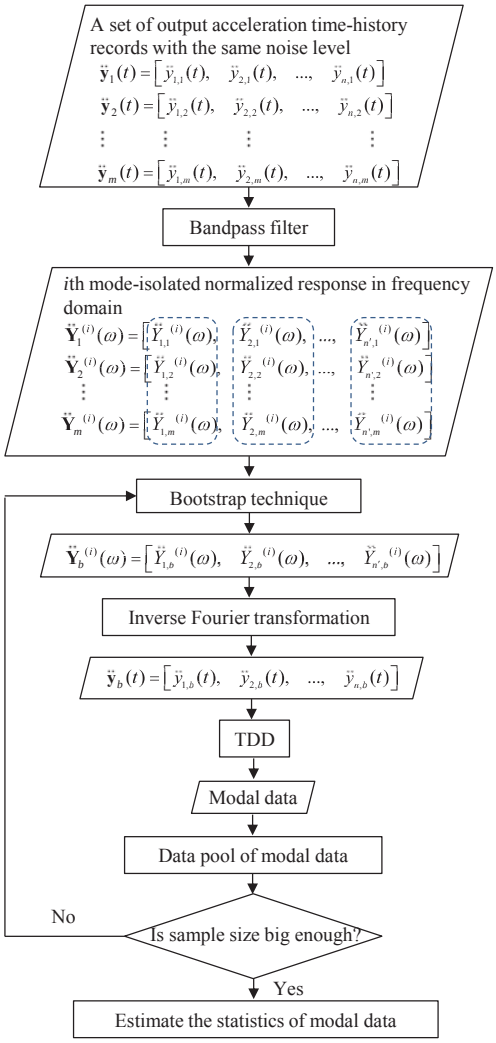

Fig. 1 Flowchart of the proposed procedure to propagate the measurement and modeling errors to the modal data

3.4 Modeling error due to the Time Domain Decomposition (TDD) method

Using the proposed procedure in Fig. 1, the statistics of the modal data reflect the influences from both measurement and modeling errors. However, the effect only due to the modeling error associated with the extraction process sometimes needs to be known. For example, in system identification, the value of the modeling error is important for updating the structural models using the extracted modal parameters if a Bayesian probabilistic framework is applied (Beck and Au 2002, Huang *et al*. 2010). In this study, the modeling error due to TDD alone is investigated. With the use of the TDD method, the modeling error arises mainly from the following sources with the examples of influencing factors given in the parentheses:

- truncating non-dominant modes (excitation type, sensor layout, sampling rate)
- model isolation process (filter width, response length)
- singular value decomposition (noise orthogonal assumption)
- system nonlinearity (excitation type and amplitude)

As discussed previously, it is appropriate to apply model prediction expansion to estimate the modeling error in the TDD method. Specifically, the additive model prediction expansion is adopted here. The relation between the real modal data in the *i*th mode (modal frequencies, f_i, and mode shape, $\boldsymbol{\varphi}_i$) and the extracted modal data ($\hat{f}_i$ and $\hat{\boldsymbol{\varphi}}_i$) can be formulated as follows

$$f_i = \hat{f}_i + e_{f_i} \tag{5}$$

$$\boldsymbol{\varphi}_i = \hat{\boldsymbol{\varphi}}_i + \mathbf{e}_{\varphi_i} \tag{6}$$

where e_{fi} and $\mathbf{e}_{\varphi i}$ are the modeling errors in modal frequency and mode shape due to the TDD process. They can be considered as "adjustments" to the predictions. To assess the "adjustments", e_{fi} and $\mathbf{e}_{\varphi i}$, one can directly compare the extracted modal data from TDD, $\hat{f}_i$ and $\hat{\boldsymbol{\varphi}}_i$, to the real values, f_i and $\boldsymbol{\varphi}_i$.

In system identification or vibration-based NDT, a preliminary FEM usually needs to be constructed and validated by calibrating the unknown structural parameters (such as stiffness and/or mass) using the extracted modal data. The model used for constructing the preliminary FEM is assumed to be correct. Therefore, for given a set values of the unknown structural parameters, the modal parameters obtained from the modal analysis of the preliminary FEM are considered as the actual values, f_i and $\boldsymbol{\varphi}_i$, for this set of structural parameters. If the modeling error in the constructing the FEM needs to be considered, one can follow the methodology and specific implementation proposed by Haukaas and Gardoni (2011).

As the structural parameters are unknown, we can generate a group of n_e FEMs, where n_e is the number of FEMs in the group, constructed in the same way as the preliminary FEM but with different combinations of structural parameter values that are randomly drawn from the parameter ranges. Note that for setting the parameter ranges, the best guess (predictive values, $\mathbf{x}_0$) need to be made based on the engineering judgment and then one can set $[\mathbf{x}_0/k, k\mathbf{x}_0]$ (where $k > 1$) as the parameter ranges. The larger k is chosen, the bigger the range will be. To effectively span the space of the parameters given a specific number of combinations, Latin hypercube sampling (McKay *et al*. 1979) can be used, where each parameter is approximately sampled uniformly from its range. For each FEM, a modal analysis is conducted to find f_i and $\boldsymbol{\varphi}_i$ that are the true modal parameters for the corresponding FEM, while an excitation can be applied to the FEM to obtain the vibration responses,

from which $\hat{f}_i$ and $\hat{\boldsymbol{\varphi}}_i$ can be extracted through TDD. Thus, n_e sets of f_i, $\boldsymbol{\varphi}_i$, $\hat{f}_i$, and $\hat{\boldsymbol{\varphi}}_i$ are obtained; thus e_{fi} and $\mathbf{e}_{\varphi i}$ can be assessed through Eqs. (5) and (6). Note that the estimation of e_{fi} and $\mathbf{e}_{\varphi i}$ are based on the FEMs only and it does not need any measurements from a real structure after the preliminary FEM has been developed.

Using the difference between $f_i$and $\hat{f}_i$, to estimate e_{fi} is straightforward. Given certain influencing factors, the mean, μ_{efi}, and standard deviation, σ_{efi}, of e_{fi} can be estimated from the differences, $f_i - \hat{f}_i$. The differences between $\boldsymbol{\varphi}_i$ and $\hat{\boldsymbol{\varphi}}_i$ for the ith mode are vectors, and can be considered a linear combination of mode shapes of other modes. This is because in the frequency domain the modes are overlapped due to the existence of damping, which makes it impossible to obtain a pure mode-isolated response in the TDD method. Especially, a mode shape is influenced most by the nearest mode shape. A linear regression model is proposed to assess the mode shape error, $\boldsymbol{e}_{\varphi i}$, for the ith mode, and it is written as follows

$$\mathbf{e}_{\varphi_i} = \sum_{j=1}^{N_e}\left[\alpha_{j,i} + \beta_{j,i}\left(f_j - f_i\right)^{\theta_{j,i}}\right]\boldsymbol{\varphi}_j\left(1-\delta_{ij}\right) + \sigma_{\varphi_i}\boldsymbol{\varepsilon} \tag{7}$$

where N_e = number of modes used, $\alpha_{j,i}$, $\beta_{j,i}$, and $\theta_{j,i}$= model parameters for the ith mode, δ_{ij} = Kronecker delta (i.e., $\delta_{ij} = 1$, for $i = j$; $\delta_{ij} = 0$, for $i \neq j$), $\sigma_{\varphi i}$ = standard deviation of $\mathbf{e}_{\varphi i}$, and $\boldsymbol{\varepsilon}$ = a vector of standard normal random variables. The model parameters can be estimated by the Bayesian updating rule (Box and Tiao 1992). One could use locally uniform distributions for the model parameters as the non-informative priors in the Bayesian updating rule. Note that the further a mode is from the ith mode, the less contribution that mode has to $\mathbf{e}_{\varphi i}$. Moreover, the closeness of two modes can be measured by the difference between the corresponding modal frequencies; thus, the term $\beta_{j,i}(f_j - f_i)^{\theta j,i}$ is included in Eq. (7). A stepwise deletion procedure (Gardoni *et al*. 2002) can be also used to eliminate the unimportant terms in Eq. (7) to obtain an accurate but parsimonious model. Fig. 2 summarizes the steps for accessing e_{fi} and $\mathbf{e}_{\varphi i}$, where the modal data extraction process can be general.

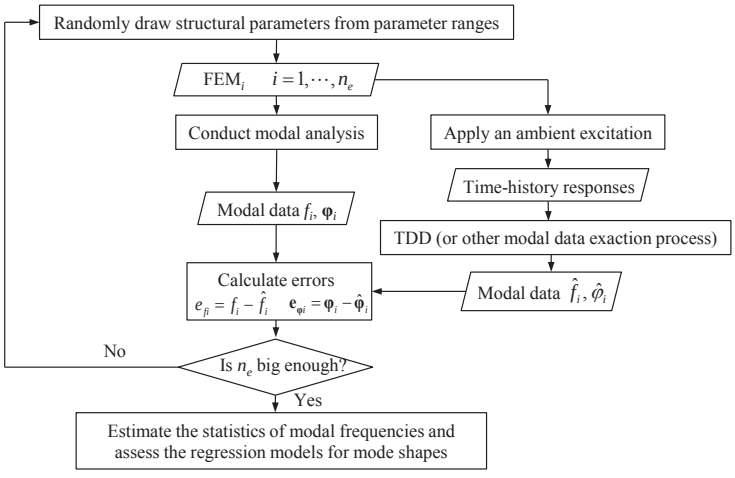

Fig. 2 Flowchart of the proposed procedure to estimate the modeling error in TDD

3.5 Considerations on the sample size for the bootstrap method

In the flowchart shown in Fig. 1, the sample size for the bootstrap method needs to be determined. Efron (1987) suggested 1000 samples for confidence intervals. However, given available computing power and time, it is reasonable to use as many samples as actually needed based on a convergence criterion. The sample size, n_e, in the flowchart in Fig. 2 is determined by the maximum of two sample sizes: a sample size, n_f, for determining the statistical interferences of e_{fi}, and a sample size, n_φ, for assessing the regression models of $\mathbf{e}_{\varphi i}$. Although e_{fi} is unknown, by setting predefined confidence intervals, n_f can be estimated. Assuming that e_{fi} follows a normal distribution, with $100(1-\alpha)\%$ confidence, where α refers to the significance level, the following relationships hold (Ang and Tang 2006)

$$\hat{\mu}_{ef} - t_{\alpha/2}\frac{\hat{S}_{ef}}{\sqrt{n_{\mu f}}} \le \mu_{ef} \le \hat{\mu}_{ef} + t_{1-\alpha/2}\frac{\hat{S}_{ef}}{\sqrt{n_{\mu f}}} \tag{8}$$

$$\frac{n_{\sigma f}}{\chi^2_{1-\alpha/2}}\hat{S}_{ef}{}^2 \le \sigma_{ef}{}^2 \le \frac{n_{\sigma f}}{\chi^2_{\alpha/2}}\hat{S}_{ef}{}^2 \tag{9}$$

where μ_{ef} = mean of e_{fi}, $\hat{\mu}_{ef}$ = sample mean, σ_{ef} = standard deviation of e_{fi}, $\hat{S}_{ef}$ = sample standard deviation, $t_{\alpha/2} = t_{1-\alpha/2} = (1-\alpha/2)$th quantile of the student's t distribution with degree of $n_{\mu f} - 1$, and $\chi^2_{1-\alpha/2}=(1-\alpha/2)$th and $\chi^2_{\alpha/2} = \alpha/2$th quantiles of the χ^2 distribution with degree of $n_{\sigma f} - 1$. When the confidence intervals are given for μ_{ef} and σ_{ef}, then $n_{\mu f}$ and $n_{\sigma f}$ can be calculated through Eqs. (8) and (9) and the sample size n_f is determined as $n_f = \max(n_{\mu f}, n_{\sigma f})$.

The sample size, n_φ, needs to be determined for Eq. (7) to ensure a sufficient statistical power to detect the significant effects. Following Cohen (1988), four input parameters are needed: (1) a significance confidence level, α, (2) a target power level of a F-test, γ, (3) an effect size, ES, and (4) the number of predictors used in the linear regression model, p_e. The power level γ refers to the probability that one rejects the null hypothesis while the alternative hypothesis is true. Type III F-test is used in the procedure, where the null hypothesis states that all coefficients of predictors of interest are zero. To calculate the power of the F-test, the F-distribution and the non-central F-distribution probability density function are used and they are respectively expressed as

$$p(x) = \frac{1}{B\left(\frac{v}{2},\frac{u}{2}\right)}\left(\frac{ux}{ux+v}\right)^{\frac{u}{2}}\left(1-\frac{ux}{ux+v}\right)^{\frac{v}{2}}x^{-1} \tag{10}$$

$$p(g) = \sum_{k=0}^{\infty}\frac{e^{-\lambda/2}(\lambda/2)^k}{B\left(\frac{v}{2},\frac{u}{2}+k\right)k!}\left(\frac{u}{v}\right)^{\frac{u}{2}+k}\left(\frac{v}{u+vg}\right)^{\frac{v+u}{2}+k}g^{\frac{v}{2}-1+k} \tag{11}$$

where $p(\cdot)$ = probability density function, $B(\cdot)$ = Beta function, u = number of predictors or numerator degrees of freedom, v = denominator degrees of freedom, λ = non-centrality parameter, and g = critical value of F-distribution. Note that as no intercept is included in Eq. (7), the sample size is $u + v$; otherwise, the sample size would be $u + v + 1$. The effect size, ES, describes the degree to which the

null hypothesis is false: the larger the effect size indicates the greater degree to which the alternative hypothesis is manifested. Conventionally, *ES* of 0.02, 0.15, and 0.35 are considered as small, medium, and large, respectively. With the four input values, the sample size, n_φ, can be calculated by the following steps:

i) Set a significance confidence level α, a desired power level γ, and an effect size *ES*, and set an initial value $v = p_e$.

ii) Calculate the $(1-\alpha/2)$th quantiles of the *F*-distribution g through Eq. (10), with the given values of α, $u(= p_e)$, and v.

iii) Compute $\lambda = ES(u + v)$.

iv) With the values of g,u $(= p_e)$,v, and λ, estimate the corresponding value of the non-central *F*-distribution through Eq. (11).

v) Compute the power by calculating the cumulative area under the standard normal curve from zero to the value of the non-central *F*-value estimated from the previous step.

vi) If the power computed from step v) is less than the desired power level γ, increase v value and repeat step ii) through step v).

vii) Determine the sample size $n_\varphi = u + v$.

Then, the sample size, n_e, in the flowchart in Fig. 2 is determined as $n_e = \max(n_f, n_\varphi)$.

4. Illustration

This section illustrates the proposed procedures using a numerical example considering a two-span continuous aluminum beam on elastic supports. Modal data is extracted from an ambient vibration test, and then a damage detection method, called Damage Index Method (DIM) developed by Stubbs and Kim (1996) is applied using the extracted modal data to study the effect of the measurement and modeling errors on the damage detection. This example beam has been previously analyzed by Stubbs and Kim (1996). The FEM of the beam is built in OpenSees (Mckenna and Fenves 2002) using 50 elastic beam-column elements with elastic springs for the supports, as shown in Fig. 3, where E_b refers to the flexural stiffness of the beam and K_1 and K_2 are the spring stiffness. Table 1 summarizes the structural properties for the FEM. A damage scenario is simulated by introducing a reduction of 10% of the flexural stiffness in the beam Element 16. The first four modal frequencies of the damaged structure obtained from the modal analysis are 36.56 Hz, 55.11 Hz, and 141.47 Hz, 158.72 Hz, respectively. For the purpose of the illustration, the stiffness properties of the study structure, E_b, K_1, and K_2 are assumed to be unknown. A preliminary FEM is constructed in the same way as the study structure but with different values of E_b, K_1, and K_2 and assuming that all the elements have the same flexural stiffness. The values of E_b, K_1, and K_2 in the preliminary FEM can be arbitrary since they are unknown.

Next, a vibration test is conducted to collect the dynamic responses, from which the modal parameters are extracted. The proposed procedures are applied to estimate the influence of measurement and modeling errors on the modal data. Finally, DIM is applied to identify the damage location using the extracted modal parameters to investigate the influence of measurement and modeling errors on the damage detection.

A vibration test is conducted by collecting the dynamic responses of the element nodes (a total of 51 nodes) under a force excitation. To avoid the issue of not being able to observe some modes due to a narrow-band excitation, a pulse loading that contains a wide range of frequencies is applied. The recording time for each node response measurement is 4 second with a sampling rate

1000 Hz. As the recording time is one of the influencing factors of the modeling error, the modeling error changes when the recording time varies, as shown later. With the 4 second recording time, there are 51 x 4 x 1000 = 204,000 response points obtained and they are noise-free since in this example they are the responses obtained from a numerical analysis.

Measurement noise is simulated using a proportional error and is added to the noise-free responses. Three different noises levels are considered and they are 0.5%, 1.0%, and 2.0%. Specifically, the measurement noises that are added to the 204,000 response points are assumed to follow independent Gaussian distributions with zero mean and specific standard deviations that are proportional to the amplitudes of the responses. The standard deviations are calculated by multiplying the amplitudes of the responses with the measurement noise level (i.e., based on a 0.5%, 1.0%, and 2.0% coefficient of variation). For each noise level, the procedures of adding the simulated measurement noise to the noise-free responses are repeated 10 times (m = 10 is used in this study just to illustrate a case when a limited number of records is available). Thus 10 sets of responses at each noise level are generated and they can be considered as the recorded responses, $\{\ddot{\mathbf{y}}1(t),\ddot{\mathbf{y}}2(t),\ldots,\ddot{\mathbf{y}}m(t)\}$, obtained from the vibration testing. With the recorded responses, the statistics of the modal parameters considering the measurement and modeling errors can be estimated following the flowchart shown in Fig. 1. Particularly, 1000 bootstrap samples (suggested by Efron 1987) are generated for each measurement noise level. Note that the measurement noise level does not need to be known when using the flowchart in Fig. 1.

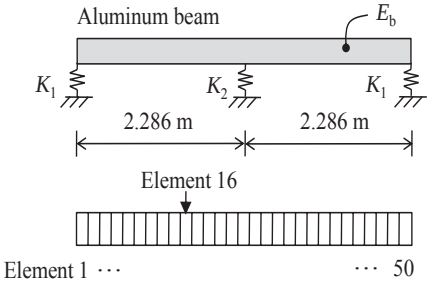

Fig. 3 Schematic of the example beam and the FEM

Table 1 FEM properties for the example beam

Property	Value
Cross section area, A	1.05×10^{-3}m^2
Second moment of area about vertical axis z, I_z	9.57×10^{-7}m^4
Second moment of area about transverse axis y, I_y	7.23×10^{-7} m^4
Mass density, ρ	2710 kg/m^3
Young's modulus, E_b	70 GPa
Poisson's ratio, v	0.33
Stiffness for support springs, K_1	6.0×10^{-5} N/m
Stiffness for support spring, K_2	1.2×10^{-4} N/m

To estimate the modeling error due to the TDD method following the flowchart in Fig. 2, the minimum sample size, ne, needs to be determined first. If a significance confidence level 5% is chosen, and the desired confidence intervals for μ_{ef} and σ_{ef} are set to be $\left[\hat{\mu}_{ef} - \hat{S}_{ef}/5, \hat{\mu}_{ef} + \hat{S}_{ef}/5\right]$ and $\left[0.864\%\hat{S}_{ef}{}^2, 1.164\%S_{ef}{}^2\right]$ respectively, one can obtain $n_{\mu f} = 97$ and $n_{\sigma f} = 349$ through Eqs. (8) and (9). Following the steps for determining nφ, with selected $\alpha = 0.05$, $\gamma = 0.9$, ES = 0.15, and $p_e = 6$, then $n_\varphi = 123$ is obtained. Thus, $ne = \max(n_f, n_\varphi) \geq 350$. In this study, $n_e = 400$ is used. As mentioned previously, E_b, K_1, and K_2 are unknown. Then 400 FEMs are generated with the same configurations as the preliminary FEM by varying the three stiffness properties of the structures. In this study, we use $[0.5\mathbf{x}_0, 2\mathbf{x}_0]$ as the ranges for E_b, K_1, and K_2, where x_0 are the best guessed values for E_b, K_1, and K_2. Particularly, we let $\mathbf{x}_0 = [1.1E_{b,\,\text{true}}, 1.05K_{1,\text{true}}, 1.05K_{2,\text{true}}]$, where $E_{b,\text{true}}$, $K_{1,\text{true}}$, $K_{2,\text{true}}$ are the values used for the damaged beam are listed on Table 1.

For each of the 400 FEMs, the modal analysis is conducted to obtain f_i and φ_i, and a pulse excitation is applied to the FEM to obtain the vibration responses, from which $\hat{f}_i$ and $\hat{\boldsymbol{\varphi}}_i$ are extracted through TDD. Then, the modeling errors, e_{fi} and $\mathbf{e}_{\varphi i}$, are assessed using Eqs. (5) and (6). As described previously, the modeling error due to the TDD method is a function of the corresponding influence factors. Given the influence factors, the statistics of modeling error can be estimated. In this illustration, the recorded response length is 4 s and the sampling rate is 1000 Hz, and we use ±1 Hz for the filter width in the TDD method. By changing only one influence factor, we can observe how the modeling errors vary with that influence factor. Fig. 4 shows how the mean and standard deviation of modeling error e_{fi} for the first four frequencies varies when one of the influencing factors, the recorded response length in the vibration test, increases. As the lower modes have the longer periods, given the same response length, the standard deviation of the modeling errors are higher for the lower modes. In other words, longer the response length, more reliable the extracted modal frequencies is. However, after exceeding a certain response length, the error does not change significantly. Other influencing factors can be studied similarly.

The regression models for the mode shape error $\mathbf{e}_{\varphi i}$ of the first three modes are written following the formulation given in Eq. (7) as

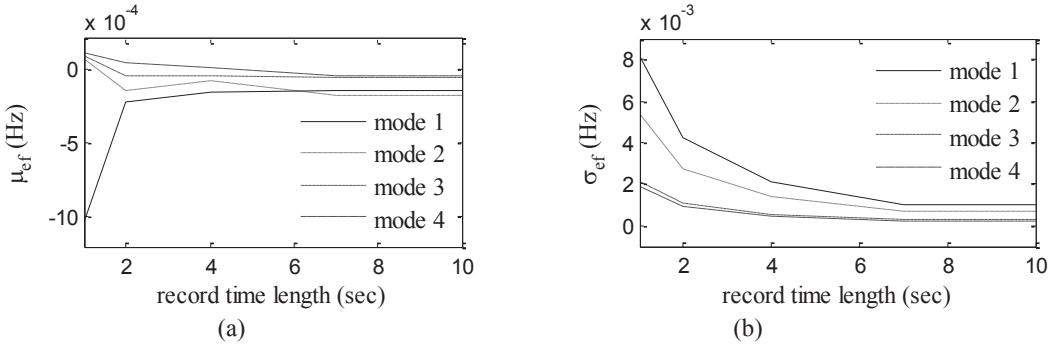

Fig. 4(a) Mean and (b) standard deviation of the estimated modeling error in modal frequencies

$$\mathbf{e}_{\boldsymbol{\varphi}_1} = \alpha_{1,1}\boldsymbol{\varphi}_2 + \alpha_{2,1}\boldsymbol{\varphi}_3 + \alpha_{3,1}\boldsymbol{\varphi}_4 + \beta_{1,1}\left(f_2 - f_1\right)^{\theta_{1,1}}\boldsymbol{\varphi}_2 + \left(\sigma_{0,1}\mathbf{I} + \sigma_{1,1}\left|\boldsymbol{\varphi}_2\right|\right)\varepsilon + \sigma_1\boldsymbol{\varepsilon} \tag{12}$$

$$\mathbf{e}_{\boldsymbol{\varphi}_2} = \alpha_{1,2}\boldsymbol{\varphi}_1 + \alpha_{2,2}\boldsymbol{\varphi}_3 + \alpha_{3,2}\boldsymbol{\varphi}_4 + \beta_{1,2}\left(f_2 - f_1\right)^{\theta_{1,2}}\boldsymbol{\varphi}_1 + \left(\sigma_{0,2}\mathbf{I} + \sigma_{1,2}\left|\boldsymbol{\varphi}_1\right|\right)\varepsilon + \sigma_2\boldsymbol{\varepsilon} \tag{13}$$

$$\mathbf{e}_{\boldsymbol{\varphi}_3} = \alpha_{1,3}\boldsymbol{\varphi}_1 + \alpha_{2,3}\boldsymbol{\varphi}_3 + \alpha_{3,3}\boldsymbol{\varphi}_4 + \beta_{1,3}\left(f_4 - f_3\right)^{\theta_{1,3}}\boldsymbol{\varphi}_4 + \left(\sigma_{0,3}\mathbf{I} + \sigma_{1,3}\left|\boldsymbol{\varphi}_4\right|\right)\varepsilon + \sigma_3\boldsymbol{\varepsilon} \tag{14}$$

where the statistics of the model parameters $\alpha_{i,i}$, $\beta_{i,i}$, $\theta_{i,i}$, and $\sigma_{i,i}$ are shown in Table 2 and they are estimated using the Bayesian updating rule (Box and Tiao 1992).

With the consideration of the measurement and modeling errors, the DIM (Stubbs and Kim 1996) is applied using the extracted modal parameters. Since the stiffness properties of the structures, E_b, K_1, and K_2, are unknowns, one could use the extracted modal frequencies to identify a baseline FEM for the study structure following a system identification method proposed by Huang *et al*. (2010). The DIM calculates a damage index, Z, for each element in the FEM based on the mode shapes from the baseline FEM and the mode shapes extracted from the dynamic responses of the study structure. The damage indexes of the damaged elements can be differentiated from the ones of the undamaged elements through statistical approaches, such that the damage location can be identified.

The normalized damage index, Z, is calculated for 50 elements of the beam. For brevity, the procedure for calculating Z is not included here but it can be found in Stubbs and Kim (1996). The left column plots in Fig. 5 give the normalized damage index of each element for the beam under different levels of measurement noise, while the left plot in Fig. 6 shows the damage indexes when only the modeling error due to TDD is considered. The solid lines and the dotted lines are the mean and mean ± 1 standard deviation of Z, respectively.

The variability of Z shown in the left column plots of Fig. 5 reflects the influences of the measurement and modeling errors, which are not negligible. This result is consistent with the conclusion drawn from the study conducted by Doebing and Farrar (1997), where they found that the statistical significance of the modal parameters could not be ignored when the modal data are used in the damage detection applications. Moreover, with the increment of the noise level shown in the left column plots of Fig. 5, the mean value of Z of the damaged element decreases, while the standard deviation of Z increases. The larger the standard deviation is, the more uncertainties are brought into the damage detection. Under the high noise level 2%, the Z value of the damaged element is hardly differentiated from other elements, which might make the damage detection difficult. The results show that it is important to account for the statistical significance of modal parameters when modal data are applied for damage detection.

Table 2 Statistics of model parameters

		α_1	α_2	α_3	β_1	θ_1	σ_0	σ_1	σ
Mode 1	Mean	-1.41E-04	-2.57E-05	-1.96E-05	-2.03E+00	1.41E-01	5.38E-05	2.68E-04	8.51E-07
	St. Dev	-9.38E-07	-2.80E-07	-2.70E-07	-2.15E-03	4.82E-04	2.98E-07	2.13E-06	–
Mode 2	Mean	9.10E-05	-4.10E-05	-2.59E-05	-1.70E+00	1.51E-01	1.23E-05	1.08E-03	1.61E-06
	St. Dev.	1.71E-06	-4.26E-07	-3.60E-07	-1.32E-03	3.31E-04	1.19E-07	8.50E-07	–
Mode 3	Mean	1.68E-04	2.20E-04	-1.34E-03	-3.86E+00	-3.55E+01	8.98E-04	6.70E-03	4.10E-05
	St. Dev..	3.21E-05	3.19E-05	-3.56E-05	-2.55E-02	-1.44E+00	8.55E-06	6.11E-05	–

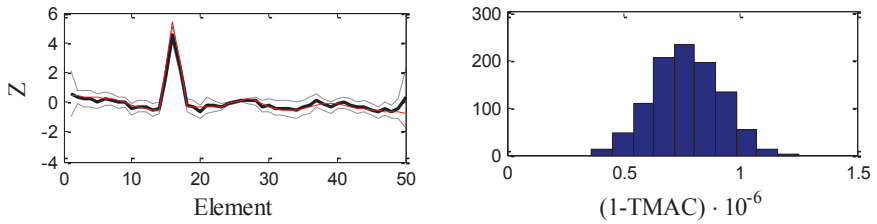

(a) measurement noise level 0.5%

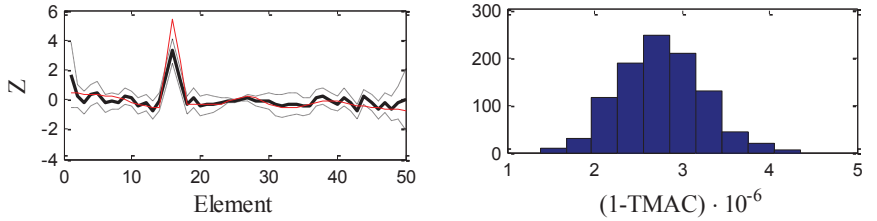

(b) measurement noise level 1.0%

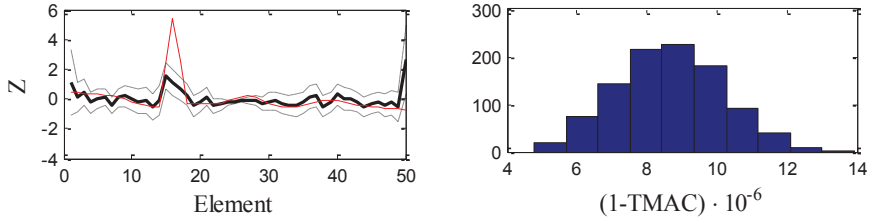

(c) measurement noise level 2.0%

Fig. 5 (left) Z values (thick solid line: mean, dotted line: mean ± 1 standard deviation, thin solid line: no error considered) for the beam elements and (right) 1 − TMAC for mode shapes

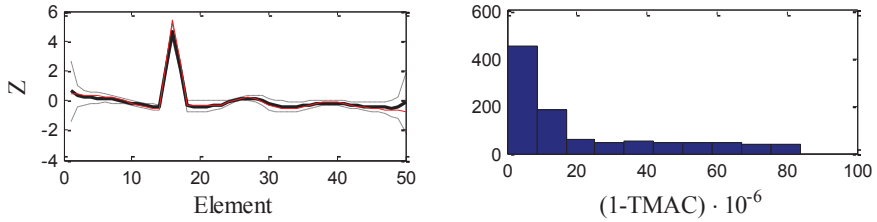

Fig. 6 (left) Z values (thick solid line: mean, dotted line: mean ± 1 standard deviation, thin solid line: no error considered) for the beam elements and (right) 1 − TMAC for mode shapes considering the estimated modeling error due to TDD

Another observation is that the influence on Z from the measurement and the modeling errors shown in the left column plots of Fig. 5 is larger than the influence from the estimated modeling error due to the TDD method alone shown in the left plot of Fig. 6. Therefore, more emphasis needs to be put on reducing the measurement noise when the dynamic responses are collected.

To exam the influence of the measurement and modeling errors on the mode shape only, the modal assurance criteria (MAC) (Allemang and Brown 1982) is used for estimating the degree of correlation between two mode shape vectors. When N_T modes are considered, a Total MAC (TMAC) between two sets of mode shapes from two records, records *a* and *b*, can be calculated by

$$\mathrm{TMAC} = \prod_{i}^{N_T} \frac{\left|\boldsymbol{\varphi}_{i,a}^T \boldsymbol{\varphi}_{i,b}\right|^2}{\left(\boldsymbol{\varphi}_{i,a}^T \boldsymbol{\varphi}_{i,a}\right)\left(\boldsymbol{\varphi}_{i,b}^T \boldsymbol{\varphi}_{i,b}\right)} \tag{15}$$

The value of TMAC is between 0 and 1. When TMAC is close to 1, it indicates the mode shapes obtained from the two records *a* and *b* are very similar. In other words, the bigger the value of (1 − TMAC) is, the bigger the difference between the mode shapes influenced by the measurement and modeling errors is. Thus, (1 − TMAC) reflects the variability in mode shapes in an overall sense.

The right column plots in Fig. 5 show the values of (1 − TMAC) for the mode shapes of the beam under different levels of measurement noise. The right plot in Fig. 6 shows the values of (1 − TMAC) considering the modeling error due to TDD alone. All the values of (1 − TMAC) are smaller than 1.5×10^{-4}, indicating that TMAC is close to 1. Therefore, the variability in the mode shapes due to measurement and modeling errors can be considered to be low. However, as discussed previously and shown in the right plots of Figs. 5 and 6, this low variability has a significant impact on the damage detection results. Moreover, as expected, when the measurement noise level becomes higher the values of TMAC become smaller, which means the variability in mode shapes is higher as shown in the right column plots of Fig. 5.

Interestingly, the values of TMAC in the right column plots of Fig. 5 are much larger than the values in the right plot of Fig. 6, indicating that the different sets of mode shapes due to measurement and modeling errors are more similar to each other than the sets of mode shapes considering only the modeling errors. However, the Figs. 5 and 6shows that the influence on the damage detection due to measurement and modeling errors (shown in the right column plots of Fig. 5) is significantly larger than the influence due to modeling error (shown in the right plot of Fig. 6). Therefore, using the TMAC values cannot be used for measuring the influence of the measurement and modeling errors on the damage detection.

As discussed previously, when the measurement noise level becomes high, the damage detection may become impossible. Since the level of the measurement noise is unknown in reality, it is desire to have a quality that can be used to measure the variability of mode shapes so that by examining this quality one can determine whether the extracted modal parameters are useful for the damage detection and how reliable the damage detection results are. One option of such quantity could the standard deviation of the damage index and the standard deviation can be calculated using the data pool of modal shapes generated following the proposed procedure shown in Fig. 1. However, the further study in this regard is needed.

5. Conclusions

This paper presented procedures to account for the uncertainties in the modal parameters extracted from ambient vibration tests. In particular, the focus is on the measurement errors and the modeling error resulting from Time Domain Decomposition (TDD). To estimate the statistics of the extracted modal parameters considering these errors, a bootstrap approach is used to generate artificial records based on limited number of response records obtained from the ambient vibration

test. As it is critical to estimate the modeling errors associated with the extraction process particularly for system identification applications, the model prediction expansion is adopted in this study to assess the modeling errors. The proposed procedure to evaluate the modeling error associated with TDD can be extended to other extraction methods.

The proposed procedures are illustrated by a numerical example of a two-span continuous aluminum beam. The influences from measurement and the modeling errors are studied by applying a damage detection method, the Damage Index Method (DIM), on the example beam using the extracted modal parameters. Future work should include applying the proposed procedures using laboratory or field data.

References

Allemang R.J. and Brown, D.L. (1982), "A correlation coefficient for modal vector analysis", *Proceedings of the 1st Int. Modal Analysis Conference*, Orlando, FL, Nov.

Ang, H.S. and Tang, W. (2006), *Probability Concepts in Engineering: Emphasis on Applications to Civil and Environmental Engineering*. 2nd Ed., New York, NY: John Wiley & Sons.

Arici, Y. and Mosalam, K.M. (2005), "Statistical significance of modal parameters of bridge systems identified from strong motion data", *Earthq. Eng. Struct. D.*, **34**(10), 1323-1341.

Banan, M.R., Banan, M.R. and Hjelmstad, K.D. (1994), "Parameter estimation of structures from static response.II. Numerical simulation studies", *J. Struct. Eng. – ASCE*, **120**(11), 3259-3283.

Beck, J.L. and Au, S.K. (2002), "Bayesian updating of structural models and reliability using Markov chain Monte Carlo simulation", *J. Eng. Mech. – ASCE*, **128**(4), 380-391.

Brinker, R., Zhang, L. and Andersen, P. (2000), "Modal identification from ambient responses using frequency domain decomposition", *Proceedings of the 18th International Modal Analysis Conference*, San Antonio, TX.

Box, G.E.P. and Tiao, G.C. (1992), *Bayesian Inference in Statistical Analysis*, Wiley, New York, New York, USA.

Ceracolo, R., Pescatore, M. and De Stefano A. (2009), "Symptom-based reliability and generalized repairing cost in monitored bridges", *Reliab. Eng. Syst. Safe.*, **94**(8), 1331-1339.

Ching, J., Muto, M. and Beck, J.L. (2006), "Structural modal updating and health monitoring with incomplete modal data using gibbs sampler", *Comput. - Aided Civil Infrastruct. E.* , **21**(4), 242-257.

Cohen, J. (1988), *Statistical Power Analysis for the Behavioral Sciences* (2nd Ed.), Lawrence Earlbaum Associates, Hillsdale, New Jersey, USA.

Doebling, S.W. and Farrar, C.R. (1997), "Effects of measurement statistics on the detection of damage in the Alamosa Canyon Bridge", *Proceedings of the 15th International Modal Analysis Conference*, Orlando, FL, Feb.

Doebling, S.W., Farrar, C.R. and Prime, M.B. (1998), "A summary review of vibration-based damage identification methods", *Shock Vib. Digest*, **30**(2), 91-105.

Doebling, S.W. and Farrar, C.R. (2001), "Estimation of statistical distribution for modal parameters identified from average Frequency response function data", *J. Vib. Control*, **7**, 603-624.

Efron, B. (1982), *The Jackknife, the Bootstrap and Other Resampling Plans*, Society for industry and Applied Mathematics, Philadelphia, Pennsylvania, USA.

Efron, B. (1987), "Better bootstrap confidence intervals (with discussion)", *J. American Statistical Association*, **82** (397), 171-185.

Gardoni, P., Der Kiureghian, A. and Mosalam, K.M. (2002), "Probabilistic capacity models and fragility estimates for RC columns based on experimental observations", *J. Eng. Mech. – ASCE*, **128**(10), 1024-1038.

Haukaas, T. and Gardoni, P. (2011), "Model uncertainty in finite-element analysis: Bayesian finite elements", *J. Eng. Mech. – ASCE*, **137** (8), 519-526.

Huang, Q., Gardoni, P. and Hurlebaus, S. (2010), "A probabilistic damage detection approach using

vibration-based nondestructive testing", *Struct. Saf*., **38**, 11-21.
Kim, B., Stubbs, N. and Park, T. (2005), "A new method to extract modal parameters using output-only responses", *J. Sound Vib*., **282**, 215-230.
Liu, P.L. (1995),"Identification and damage detection of trusses using modal data", *J. Struct. Eng. - ASCE*, **121**(4), 599-608.
Longman, Rw and Juang, J.N. (1987), "A variance based confidence criterion for ERA identified modal parameters", *Proceedings of the AAS/AIAA Astrodynamics Specialist Conference*, Kalispell, MT, August.
Mckay, M.D., Beckman, R.J. and Conover, W.J. (1979), "Comparison of three methods for selecting values of input variables in the analysis of output from a computer code", *Technometrics*, **21**, 239-245.
McKenna, F. and Fenves, G.L. (2002), *The Open Sees Command Language Primer*, Department of Civil and Environmental Engineering, University of California, Berkeley, California, USA.
Oberkampf, W.L., DeLand, S.M., Rutherford, B.M., Diegert, K.V. and Alvin, K.F. (2002), "Error and uncertainty in modeling and simulation", *Reliab. Eng. Syst. Safe*, **75**(3), 333-357.
Papadopoulos, L. and Garcia, E. (1998), "Structural damage identification: a probabilistic approach", *AIAA J*., **36**(11), 2137-2145.
Peterson, L.D., Bullock, S.J. and Doebling, S.W. (1996), "The statistical sensitivity of experimental modal frequencies and damping ratio to measurement noise", *Modal Anal*., **11**(1), 63-75.
Pothisiri, T. and Hjelmstad, K.D. (2003), "Structural damage detection and assessment from modal response", *J. Eng. Mech. - ASCE* , **129**(2), 135-145.
Reinert, J.M. and Apostolakis, G.E. (2006), "Including model uncertainty in risk-informed decision making", *Ann. Nucl. Energy*, **33**, 354-369.
Stubbs, N. and Kim, J.-T.(1996), "Damage localization in structures without baseline modal parameters", *,AIAA J*., **34**(8), 1644-1649.
Xia, Y., Hao, H., Brownjohn, J.M.W. and Xia, P.Q. (2002), "Damage identification of structures with uncertain frequency and mode shape data", *Earthq. Eng. Struct. D*., **31**, 1053-1066.
Zio, Z. (2009), "Reliability engineering: Old problems and new challenges", *Reliability Engineering & System Safety* 94(2), 125-141.

Smart Structures and Systems, *Vol. 15, No. 3 (2015) 735-749*
DOI: http://dx.doi.org/10.12989/sss.2015.15.3.735

Posterior density estimation for structural parameters using improved differential evolution adaptive Metropolis algorithm

Jin Zhou*, Akira Mita[a] and Liu Mei[b]

Department of System Design Engineering, Keio University, 3-14-1 Hiyoshi, Kohoku-ku, Yokohama 223-8522, Japan

(Received November 27, 2014, Revised January 20, 2015, Accepted January 28, 2015)

Abstract. The major difficulty of using Bayesian probabilistic inference for system identification is to obtain the posterior probability density of parameters conditioned by the measured response. The posterior density of structural parameters indicates how plausible each model is when considering the uncertainty of prediction errors. The Markov chain Monte Carlo (MCMC) method is a widespread medium for posterior inference but its convergence is often slow. The differential evolution adaptive Metropolis-Hasting (DREAM) algorithm boasts a population-based mechanism, which runs multiple different Markov chains simultaneously, and a global optimum exploration ability. This paper proposes an improved differential evolution adaptive Metropolis-Hasting algorithm (IDREAM) strategy to estimate the posterior density of structural parameters. The main benefit of IDREAM is its efficient MCMC simulation through its use of the adaptive Metropolis (AM) method with a mutation strategy for ensuring quick convergence and robust solutions. Its effectiveness was demonstrated in simulations on identifying the structural parameters with limited output data and noise polluted measurements.

Keywords: structural identification; differential evolution; adaptive metropolis-hastings; Markov chain Monte Carlo; structural parameter estimation; Bayesian posterior probability density

1. Introduction

Most of the structural identification approaches based on heuristic optimization algorithms are formulated as deterministic models in which the residual errors are built-up optimization functions to be minimized so that the candidate model can provide relatively accurate predictions of the system response. Heuristic algorithms, such as the genetic algorithm (GA) (Koh *et al*. 2007 and Perry *et al*. 2006), particle swarm optimization (PSO) (Xue *et al*. 2009), and differential evolution (DE) (Tang *et al*. 2008), have been used as global-optimum searches for the fitness function of the prediction errors. Recently, there has been an increasing need for structural identification to quantify the uncertain prediction errors associated with noise or model errors.

As is shown by Beck *et al*. (2010), no candidate model can exactly represent the I/O behavior of an actual system. It is a quixotic notion to choose only one biased model in a quest for the

*Corresponding author, Ph.D. Student, E-mail: zhoujin5120@gmail.com
[a] Professor, E-mail: mita@sd.keio.ac.jp
[b] Ph.D. Student, E-mail: meiliumail@gmail.com

http://www.techno-press.org/?journal=sss&subpage=8 ISSN: 1738-1584 (Print), 1738-1991 (Online)

output of the true system with uncertain prediction errors. Bayesian probabilistic inference provides a rigorous way of quantifying this uncertainty based on a probabilistic model that is defined by stochastic model classes. The model set, M, is a class of parameterized probability models, each of which predicts the behavior of the actual system with a prior probability density. The prior probability of each model indicates the initial plausibility of the individual model. In Bayesian parametric posterior density estimation, the identification problem is to infer the plausibility of each candidate model with a posterior density conditioned by the measured data; it is not a quest for the true structural parameters. It is usually difficult for Bayesian probabilistic inference identification to obtain the posterior probability density function (PDF) of the structural parameters, $P(\hat{x}(\theta)|Y^m)$, conditioned by the measured response, Y^m, where $\hat{x}(\theta)$ is a stochastic parameter vector defining each possible model within the model set (θ is a random variable in a probability space Ω). The posterior PDF describes how plausible each model is if one accounts for the uncertainty of the prediction errors. The posterior density, $P(\hat{x}(\theta)|Y^m)$, is needed to make robust predictions of the performance of the system based on past observations, as was illustrated by Papadimitriou *et al*. (2001) and Beck *et al*. (2002). Many studies have focused on obtaining the posterior PDF because its calculation often requires an evaluation of multidimensional integrals that cannot be easily obtained. In particular, Laplace's method of asymptotic approximation was utilized by Beck *et al*. (2002) to obtain a posterior PDF with a small-dimensional parameter space. To solve higher dimensional problems, an adaptive Markov chain Monte Carlo (MCMC) simulation method, the Metropolis-Hastings (MH) algorithm, was developed to be used in the Bayesian model update (Muto and Beck 2008). Since the advent of the MH algorithm, MCMC methods have become the primary means to obtain the posterior PDF in structural identification. Gibbs sampling and transitional Markov Chain Monte Carlo (TMCMC) were used by Ching *et al*. (2007). Cheung *et al*. (2009) used a hybrid Monte Carlo method, known as the Hamiltonian Markov chain method, to solve the higher dimensional Bayesian model updating problems.

However, all of these MCMC-based identification methods use a single Markov Chain, which may be inefficient and unreliable when the posterior surface is complicated. It is known that because of the noise corrupted system response, the surface of the prediction error lies in a hyper-surface of a multi-dimensional parametric space. The complicated surface of the prediction error will definitely cause the surface of the posterior model samples to have multiple regions of attraction and numerous local optima. To surmount this difficulty, the ability of heuristic algorithms to search for the global optimum will have to be merged with the advantage of the MH algorithm for inferring the posterior PDF. The first combining of DE and MCMC was proposed by Ter Braak. (2006) in Bayesian computing; it was named the DE-MC algorithm. Vrugt *et al*. (2009) proposed a differential evolution adaptive metropolis algorithm for solving the problem of flood forecasting.

In this paper, an improved differential evolution adaptive Metropolis-Hastings algorithm (IDREAM) is proposed for updating the posterior PDF of the structural identification model. Compared with other MCMC based identification methods, it runs different parallel Markov chains simultaneously and the posterior samples mutually exchange information along the iteration. Numerical examples of updating the posterior PDF of a linear structural system are presented, with which the effectiveness and efficiency of IDREAM are investigated. The influence of the incomplete measurements and noise errors on the posterior PDF of the parameters is discussed.

2. Problem statement

In the Bayesian probability logic identification framework, the measured response is used to estimate the posterior density of the plausibility for each I/O model in a model set instead of estimating biased parameters for only misrepresentative models (models with biased parameters that cannot represent the actual behavior of the true system). Here, let $y^m(t)$ denote the measured response at each time step ($\mathrm{t} = 1, \dots, \mathrm{N_t}$). The stochastic model set, M, is defined by a structural parameter vector, $\hat{x}(\theta) = \left(\hat{x}_1(\theta), \hat{x}_2(\theta), \cdots, \hat{x}_{n_m}(\theta)\right) \in \mathbb{R}^{\mathrm{n}}$ ($\theta_{N_s} \in \Omega$, θ is a random variable in a probability space Ω), where n_m is the number of parameters for model $M_m \in M$, and N_s is the number of stochastic samples. The initial plausibility of each model parameterized by $\hat{x}(\theta_k)$ $(k = 1,2, \dots, N_s)$ is defined as a prior density function, $P(\hat{x}(\theta)|M)$. The updated plausibility of each I/O model considering the uncertainty of the measured response is defined as the posterior density, $P(\hat{x}(\theta)|y^m, M)$, which from Bayes' Theorem gives

$$P(\hat{x}(\theta)|y^m, M) = P(y^m|\hat{x}(\theta), M) \cdot P(\hat{x}(\theta)|M)/P(y^m|M) \tag{1}$$

where $\mathrm{P}(\mathrm{y^m}|\hat{\mathrm{x}}(\theta), \mathrm{M})$ is obtained from a probabilistic model that accounts for the uncertainty of the prediction errors between the measured response and the stochastic output of the model set specified by each random model variable, $\hat{y}(\hat{x}(\theta), t)$. Let $e_j^k(t) = y_j^m(t) - \hat{y}_j^k(\hat{x}(\theta_k), t)$ denote the prediction error at each time interval ($t = 1, 2, \dots, N_t$, $k = 1,2, \dots, N_s$, and $j=1, \dots, m$, where m is the number of available measurements). The predictive PDF for the model output (white noise is considered as the measurement error; it thus obeys a normal distribution) at each time interval is

$$P\left(y_j^m(t)\middle|\hat{x}(\theta), M\right) = P\left(e_j(t)\middle|\hat{x}(\theta), M\right) = \frac{1}{\sqrt{2\pi}\sigma_j} e^{\left[-\frac{1}{2{\sigma_j}^2}(y_j^m(t) - \hat{y}_j(\hat{x}(\theta),t))^2\right]}, j=1,\dots, m \tag{2}$$

Hence, the predictive PDF (which is the likelihood function) seen from the whole time history is

$$P(y^m|\hat{x}(\theta), M) = \frac{1}{(\prod_{j=1}^m \sqrt{2\pi}\sigma_j)^{N_t}} e^{\left[-\sum_{j=1}^m \frac{1}{2{\sigma_j}^2}\sum_{t=1}^{N_t}(y_j^m(t) - \hat{y}_j(\hat{x}(\theta),t))^2\right]} \tag{3}$$

The vector of the prediction error variance, σ_j^2, is an independent parameter corresponding to each candidate model in the model class, M. The term, $P(y^m|M)$, is called the evidence of the model class, and it equals

$$P(y^m|M) = \int P(y^m|\hat{x}(\theta), M) \cdot P(\hat{x}(\theta)|M) d\theta \tag{4}$$

The difficulty in estimating the Bayesian posterior density is none other than approximating this multi-modal and high-dimensional integral. A direct and easy-to-understand approach would be the Monte-Carlo method. However, a direct MC simulation usually requires a large number of MC samples, which makes it inefficient. On the other hand, the Metropolis-Hastings (MH) algorithm (Chib *et al*. 1995) is a new Markov-chain Monte-Carlo simulation tool, and it can meet this challenge. In the MH algorithm, it is unnecessary to accurately calculate the model evidence in Eq. (4). The Markov chain samples are initially distributed according to the prior PDF and updated with a jumping distribution. The samples in the Markov chain are selected according to the MH acceptance rate and eventually converge to a stationary probability density which can be seen to be the desired posterior PDF of the model parameters. However, the scale of the jumping distribution

is hard to decide for the MH algorithm. This is an important problem because choosing a suitable transition strategy for the samples in the Markov chain influences not only the convergence speed but also the robustness of the solutions.

3. IDREAM for Bayesian inference of parameter estimation

This study presents an improved differential evolution adaptive Metropolis-Hastings algorithm (IDREAM) aimed at overcoming the difficulty of choosing a suitable jumping scale in the algorithm. The IDREAM algorithm starts by choosing samples represented as a dimensional vector $\hat{x}$, and the k^{h} sample is denoted as $\hat{x}^k$ $(k = 1,2, \ldots N_s)$. The number of samples is twice the parametric dimension, as is proposed in J. Vrugt *et al*. (2009). The initial states of the Markov chain samples are drawn from the search domain by using Latin hypercube sampling (LHS). The density function of each sample in the initial state can be computed as a prior density $p(\hat{x}_0^k)$ for $k = 1,2, \ldots N_s$.

3.1 DE mutation of the MC samples

In the differential evolution adaptive Metropolis-Hastings (DREAM) algorithm (Vrugt *et al.* 2009), the samples are updated by using the difference between randomly chosen pairs of samples in the current state. Let $\Delta_{\hat{x}}^k = \hat{x}_{s+1}^k - \hat{x}_s^k$ denote the jump scale between the updating state (s+1) and current state (s) of the sequence k in the Markov chain. In the DREAM algorithm, the samples are updated as

$$\Delta_{\hat{x}}^k = (u_d + e_d)\gamma(\delta, d)\left[\sum_{j=1}^{\delta} \hat{x}_s^{r_1(j)} - \sum_{n=1}^{\delta} \hat{x}_s^{r_2(n)}\right] + \varepsilon \quad (5)$$

where ε is a small random vector that is drawn from $N_d(0, \hat{\Sigma})$. This variable is the same as the jumping scale vector in the classic MH algorithm, which is called the random-walk strategy. In the MH algorithm, the jump scale ε obeys a Gaussian distribution in which the variance, $\hat{\Sigma}$, decides the jumping direction and scale of the MC samples. It is clear that the efficiency of this algorithm is strongly affected by ε. So how we choose an appropriate jumping scale for the samples transition is a difficulty especially for high-dimensional problems. This problem can be solved with Eq. (5), where the jumping scale equals an adaptive multiple of the difference between pairs of randomly chosen samples in the current state. δ is the number of chosen pairs, and $r_1(j)$ and $r_2(n)$ are respectively different and random integers that are chosen from the integer set {1,2,…k-1,*k*+1,…,N_s}. The term u_d us the d-dimensional unit vector, and e_d signifies a small random vector drawn from a uniform distribution to assure the ergodicity of each individual Markov chain. The scaling factor γ is decided by the values of δ and d, where d is the parametric dimension. From Eq. (5), it is clear that in DREAM, only the sequences in the current state are used to update the samples in the Markov chain. In this study, we propose a new update pattern in which the sequence having the largest plausible density in the current state k and the one with the maximum posterior PDF from the initial state to the current state are used for the updating of the Markov chain samples

$$\Delta_{\hat{x}}^k = w_1^k\left(\hat{x}_s^{cbest} - \hat{x}_s^k\right) + w_2^k\left(\hat{x}_{1-s}^{gbest} - \hat{x}_s^k\right) + (u_d + e_d)\gamma(\delta, d)\sum_{j=1}^{\delta} w^{*k}_j\left(\hat{x}_s^{r_1(j)} - \hat{x}_s^{r_2(j)}\right) + \varepsilon \quad (6)$$

where $\hat{x}_s^{cbest}$ denotes the sample with the maximum density in the current state (s^{th} state) and is called the "current-best individual", and $\hat{x}_{1-s}^{gbest}$ denotes the sequence with the maximum density in the previous states (from the initial state to the s^{th} state) and is called the "global-best individual". $\hat{x}_s^{r_1(j)}$ and $\hat{x}_s^{r_2(j)}$ are randomly chosen individuals in the current state and are different from each other. The weighting factors, w_1^k, w_2^k and w_j^k, are the distance between the individuals

$$\begin{cases} w_1^k = d_1^k/d_{sum}^k, w_2^k = d_2^k/d_{sum}^k, w^{*k}_j = d_j^k/d_{sum}^k \\ d_{sum}^k = d_1^k + d_2^k + \sum_{j=1}^{\delta} d_j^k \end{cases} \tag{7}$$

where d_1^k and d_2^k are respectively the Euclidean distance from sequence $\hat{x}_s^k$ to the "current-best" sample $\hat{x}_s^{cbest}$ and the distance from the sequence $\hat{x}_s^k$ to the "global-best" sample $\hat{x}_s^{gbest}$, and d_s^k is the Euclidean distance of are randomly chosen sample pairs excluding the individual $\hat{x}_s^k$ in the Markov chain. From Eq. (6), one can see that the biggest difference of IDREAM from DREAM is that the posterior samples are updated using both the maximum PDF in the current state and that of the previous states, while the updated samples of DREAM are orientated between the chosen pairs of samples only in the current state. IDREAM enhances the convergence speed especially in the early stage because the difference between the individual and the "best" sample is definitely large owing to the diversity of samples in the initial state. From Eq. (7), it is clear that samples farther away from the "best" sample possess a larger jumping scale because the weight factor is positively propositional to the distance. As for the "best" sample, the update method is the same as in DREAM, i.e., Eq. (5). The convergence becomes slower in the later stages when the diversity of the samples in the Markov chain decreases. Because of this, a crossover strategy (Storn *et al.* 1997) is used to keep the diversity of the MC samples high.

Assertion: IDREAM yields a Markov chain which is irreducible and aperiodic with a unique stationary distribution with the target *pdf* $\pi(\cdot)^{N_s}$. *Proof*: the proof consists of two parts:

1. If the sample of the k^{th} chain coincides with the position of the global-best and the current-best individual, the probability of a jump from sample in the state s of the chain to the sample in the state s+1 is the same as in the DREAM algorithm, in which the conditional probability of jumping forward, $\mathrm{p}\left(\hat{\mathrm{x}}_{\mathrm{s}}^{\mathrm{k}} \rightarrow \hat{\mathrm{x}}_{\mathrm{s+1}}^{\mathrm{k}}\right)$, is equal to that of jumping back, $\mathrm{p}\left(\hat{\mathrm{x}}_{\mathrm{s+1}}^{\mathrm{k}} \rightarrow \hat{\mathrm{x}}_{\mathrm{s}}^{\mathrm{k}}\right)$. For the individuals who are different from the "best" sample in the current state, *s*, the distance and the corresponding weighting factor decrease quickly in the later stages (especially following a sufficient burn-in period) as the populations converge. The deviations (random walks) of the randomly chosen sample pairs mainly decide the transitions of each chain. The $N_s - 1$ samples can been seen as updated conditionally on the other chains obeying the reversibility property of the Markov chain, because the Jacobian of the transformation (Hastie 2012) implied in Eq. (6) is close to 1 in absolute value, (Vrugt *et al.* 2009), and the first two items of Eq. (6) play limited roles in the transition Markov chains during the later stages (*Note*: $\hat{x}_s^{cbest}$ is equal to $\hat{x}_{1-s}^{gbest}$ in the later stages). 2. Detailed balance is achieved with an accepting rule having probability $min(p(\hat{x}_{s+1})/p(\hat{x}_s), 1)$. Each chain maintains conditional detailed balance, because the chains are aperiodic and not transient with the random walk generated by Eq. (6). The N_s chains are irreducible with the unbounded support of the distribution of ε in Eq. (6). This concludes the assertion.

3.2 DE crossover strategy for the MC samples

The crossover strategy is implemented in d dimensions of the current samples, $\hat{x}_s^k$, and the updated posterior samples, $\hat{x}_{s+1}^k$, and a trial sample $\hat{x}_{s+1}^{kj}$ is generated with

$$\hat{x}_{s+1}^{kj}=\begin{cases}\hat{x}_s^{kj} & if\ U_j \le 1-CR\\ \hat{x}_{s+1}^{kj} & otherwise\end{cases} \tag{8}$$

where j=1,2,…,d; U_j is the j^{th} independent random number uniformly distributed in the range of [0,1]. CR is a crossover probability defined by the user.

3.3 Metropolis acceptance

The density of the new sample, $p\left(\hat{x}_{s+1}^k\right)$, and the Metropolis acceptance (Haario *et al.* 2001) can be calculated with the updated samples in the Markov chain

$$\alpha(\hat{x}_s,\hat{x}_{s+1}) = min\left[\frac{p(\hat{x}_{s+1})}{p(\hat{x}_s)},1\right] \tag{9}$$

The algorithm accepts the candidate state $\hat{x}_{s+1}$ with probability min(1,$\alpha(\hat{x}_{s+1},\hat{x}_s)$), and keeps the current state $\hat{x}_s$ with probability 1-min(1, $\alpha(\hat{x}_{s+1},\hat{x}_s)$). This process is repeated in several iterations, and after a burn-in period, the chain of samples approaches a stationary distribution. The desired posterior PDF can be obtained from these Markov-chain samples, excluding the ones in the burn-in period.

3.4 Gelman-Rubin convergence condition

The IDREAM algorithm ends by checking the Gelman-Rubin convergence condition (A. Gelman *et al.* 1992), and calculates the $\widehat{\mathrm{R}}_j$-statistic by using the last 50% of the samples in each chain. Let k be the number of the sequences used to calculate $\widehat{\mathrm{R}}_j$, and let B be the variance between the sequence means and W signify the average of the within sequence variances (B=$N_s \times \sum_{i=1}^{k}(\hat{x}_i-\bar{\hat{x}})^2/(\mathrm{k}-1)$, and W=$\sum_{i=1}^{k} s_i^2/k$, where s_i^2 is the variance of the sequence). Furthermore, the target posterior variance is estimated as $\hat{\sigma}^2$=$\frac{n-1}{n}W+\frac{1}{n}B$. The Gelman-Rubin convergence parameter, $\widehat{\mathrm{R}}$, can be calculated as

$$\widehat{\mathrm{R}}=\sqrt{\frac{k+1}{k}\times\frac{\hat{\sigma}^2}{W}-\frac{N_s-1}{k\times N_s}} \tag{10}$$

If $\widehat{\mathrm{R}}_j < 1.2$ for all dimensions (Gelman *et al.* 1992), it means that the Markov chain has converged to a stationary distribution; otherwise, the posterior sample is updated with Eq. (6).

3.5 IDREAM based parametric posterior density estimation

The procedure of IDREAM-based Bayesian probability inference parameter estimation is as follows:

Step 1: The initial N_s sequences for the Markov chain are drawn by Latin hypercube sampling with the predefined maximum and minimum boundary of the structural parameters and number of

samples, N_s, while respecting the prescribed limits of the search space. Calculate the prior density and the likelihood function using Eqs. (2) and (3).

Step 2: Update the posterior sample of the Markov chain by using Eqs. (6) and (7).

Step 3: The samples are updated according to the crossover probability calculated with Eq. (8). Calculate the density for the each updated sample in the Markov chain.

Step 4: Use the Metropolis acceptance (Eq. (9)) to decide whether to accept the new samples.

Step 5: Return to Step 2 to Step 4, considering the burn-in period and calculate the Gelman statistic condition using Eq. (10) for each dimension of the stochastic parameter. If the stopping criteria are met, ($\widehat{\mathrm{R}}_j < 1.2$ or the max. iteration number is reached) stop the algorithm; otherwise, return to Step 2.

4. Numerical study

A numerical simulation of a 5-DOF linear time invariant (LTI) system was carried out to verify the IDREAM algorithm. The actual system output was simulated from a linear structural system (a one-dimensional shear frame structure). For sake of clearly exhibiting that only the measurement uncertainty is considered, the second-order differential dynamic equation of the structural system is described by the state-space representation as

$$\begin{bmatrix}\dot{v}_1(t)\\ \dot{v}_2(t)\end{bmatrix} = \begin{bmatrix}0 & \mathrm{I}\\ -M^{-1}K & -M^{-1}C\end{bmatrix}\begin{bmatrix}v_1(t)\\ v_2(t)\end{bmatrix} + \begin{bmatrix}0\\ -\mathrm{I}\end{bmatrix}\Gamma^T u(t) \tag{11}$$

where M, C, and K are mass, damping, and stiffness matrices, I is a $n \times n$ identity matrix, $\Gamma = [1,1,\ldots,1]^T$ is a $1 \times n$ position vector. $v_1(t)$ and $v_2(t)$ are state space vectors respectively representing the displacement and velocity, and $u(t)$ is the input of the system. Equation (11) includes a Rayleigh damping matrix C, where the modal damping ratio (ζ_r) is set to 5% in the first two modes (r=1, 2) (Mita 2003).

$$C = \alpha M + \beta K, \quad \zeta_r = \frac{\alpha}{2\omega_r} + \frac{\beta\omega_r}{2} \tag{12}$$

The system output is an acceleration value that is assumed to be contaminated by Gaussian white noise w_j(t)~N(0, $\sigma_j(\theta)$), (j=1,.. m). The measured output vector is thus

$$y(t) = [-M^{-1}K \quad -M^{-1}C]\begin{bmatrix}v_1(t)\\ v_2(t)\end{bmatrix} - \Gamma^T \cdot u(t) + w(\sigma(\theta), \mathrm{t}) \tag{13}$$

The input was the 1940 El Centro ground motion (N-S acceleration measured at the Imperial Valley Irrigation District substation in El Centro, CA, during the 1940 Imperial Valley earthquake) lasting 40 s. It was normalized so that its peak was 10 cm/s^2, and the sampling frequency was decimated as 50 Hz (Fig. 1). The Newmark-beta method was used to calculate the structural response. An output acceleration (*acc.*) with different Gaussian white noise levels (Eq. (13)) was assumed. To show the effectiveness of the method for an identification problem with a large noise level, the noise level (*nl.*) was chosen to have a standard deviation of 30% or 100% of the corresponding signal; i.e., if $\sigma_{acc.,i}$ is the standard deviation of the i^{th} floor acceleration (relative to the ground), then the noise affecting the measurement of that floor's acceleration has an RMS $\sigma_i = nl. \times \sigma_{acc.,i}$. The response of the 5$^{\text{th}}$ DOF with and without 100% noise is shown in Fig. 1.

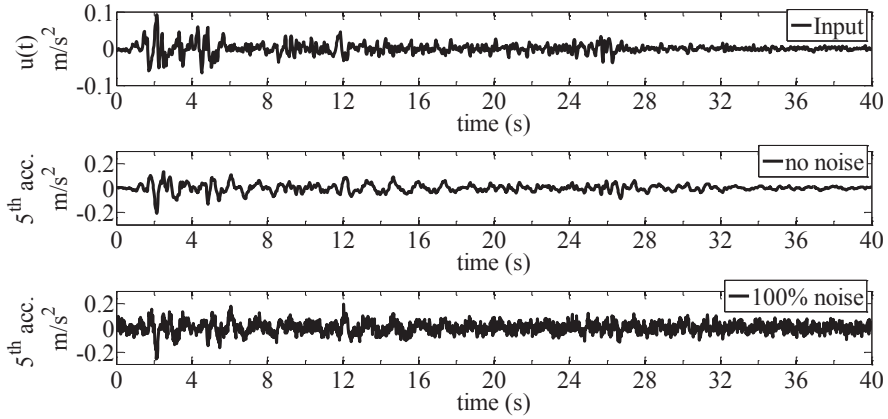

Fig. 1 Input and measured noise

The influence of the limited availability of measurements was also assessed. In the "full output" scenario, measurements of all DOFs were available, whereas in the "partial output" scenario, only data from floors 3 and 5 were available. The mass was assumed to be known and deterministic; hence, an *n*-DOF system with *m*-available measurements can be described by a model set, of which the stochastic parameterized vector for each model is

$$\hat{\boldsymbol{x}}(\theta)=\{k_1(\theta),\dots,k_n(\theta),\zeta_1(\theta),\zeta_2(\theta),\sigma_1(\theta),\dots,\sigma_m(\theta)\} \tag{14}$$

where k_i denotes the stiffness of i^{th} -DOF, n is the number of structural DOFs; ζ_1 and ζ_2 are the damping ratio of the first two modes; σ_i denotes the standard deviation of the i^{th} measurement noise, m is the number of measurements; θ denotes the random variables in the sample space, Ω_θ.

Table 1 lists the structural properties together with the simulated measurement error for each available DOF. The parametric dimension was 12 for the full output scenario and 9 for the partial output scenario. The parameters of the IDREAM algorithm were set as follows: the number of Markov chain samples (N_s) was 20, the crossover probability (CR) was 0.85, and the number of sample pairs (δ) was 5. These prescribed parameters were tested and also suggested by the developer of the algorithm. If the number of samples is increased, such as to 50 or 100, the results may improve a little at the expense of a higher computing cost. The search domain was 0.5 to 2.0 times the true value, which depends on prior knowledge about the structural system. The prior distribution followed a uniform distribution at the search boundary.

The results obtained by the original DREAM algorithm are shown for comparison in the full output scenario (Tables 2(a) and 2(b)) and partial output scenario (Tables 3(a) and 3(b)). From Tables 2 (a) and 2(b), it is clear that both algorithms performed very well in the noise-free scenario. As the magnitude of the measured noise increased, the relative errors of the identified solutions remained small. The maximum relative error for the most plausible value of structural stiffness, i.e., the sample with the maximum posterior density ($\hat{x}_{MAP}$), ranged from zero in the no-noise case to 0.502% in the 30% noise case and up to 1.987% in the 100% noise case when using the DREAM algorithm.

Table 1 Structural properties and measurement errors

Stiffness	(10^4N/m)		(σ_i) m/s^2	30% noise	100% noise
Levels 1	2.000	Case 1	Levels 1	0.0049	0.0162
Level 2-5	1.000		Levels 2	0.0074	0.0248
Mass	(kg)		Levels 3	0.0076	0.0252
Levels 1-4	50		Levels 4	0.0077	0.0256
Level 5	45		Levels 5	0.0095	0.0317
Damping ratio		Case 2			
ζ_1	0.05		Levels 3	0.0076	0.0252
ζ_2	0.05		Levels 5	0.0095	0.0317

Table 2 (a) Identified results of structural parameters (full output scenario)

		no noise		30% noise		100% noise	
		DREAM	IDREAM	DREAM	IDREAM	DREAM	IDREAM
k_1	*error*	0.000	0.000	0.352	0.164	0.656	0.250
	cov.	0.000	0.000	0.906	0.533	3.263	1.641
k_2	*error*	0.000	0.000	0.324	0.242	1.558	0.114
	cov.	0.000	0.000	0.683	0.399	2.462	1.286
k_3	*error*	0.000	0.000	0.298	0.353	1.987	0.198
	cov.	0.000	0.000	0.812	0.459	2.946	1.474
k_4	*error*	0.000	0.000	0.172	0.045	0.658	0.717
	cov.	0.000	0.000	0.813	0.465	2.789	1.564
k_5	*error*	0.000	0.000	0.502	0.299	1.155	1.083
	cov.	0.000	0.000	0.937	0.530	3.227	1.835
ζ_1	*error*	0.000	0.000	1.307	0.813	3.442	2.035
	cov.	0.000	0.000	1.591	0.871	5.545	2.946
ζ_2	*error*	0.000	0.000	0.887	1.217	1.677	0.499
	cov.	0.000	0.000	1.158	0.635	3.951	2.095

* the error is in %; the cov. (the ratio of the standard deviation to the mean) is in %

Table 2 (a) shows that the accuracy of $\hat{x}_{MAP}$ when using IDREAM was better than that of DREAM. The maximum relative error fell to 0.353% in the 30% noise case and 1.083% in the 100% noise case. The parameter with the largest uncertainty obtained by the two algorithms was in the damping ratio. The largest coefficient of variance (*cov.*) of the damping ratio was 1.591% in the 30% noise case, and it increased to 5.545% in the 100% noise case for the DREAM algorithm. For IDREAM, the coefficient of variance (*cov.*) of the damping ratio ranged from 0.871% to 2.946%. It is clear that the parametric uncertainty was additive as the measurement error increased. Table 2 (b) shows that the two algorithms can identify the exact value of the noise standard

deviation, σ_i in Table 1. In the noise-free scenario, both solutions were as small as zero. For the 100% noise case, the maximum error emerged in the third DOF at 2.341% for DREAM and at 2.562% for IDREAM. The identified results for the partial output case are listed in Tables 3(a) and 3(b).

From Table 3(a), it can be seen that when there was a noise error, the maximum relative errors of $\hat{x}_{MAP}$ were smaller for IDREAM than for DREAM. In the 30% noise case, the maximum relative error for DREAM was 1.855%, but only 1.501% for IDREAM, while in the 100% noise case, the maximum error decreased from 5.602% to 5.214%.

Table 2 (b) Identified results of prediction errors (full output scenario)

		no noise		30% noise		100% noise	
		DREAM	IDREAM	DREAM	IDREAM	DREAM	IDREAM
σ_1	*error*	0.000	0.000	0.967	0.080	2.060	0.204
	cov.	0.000	0.000	0.136	0.082	0.172	0.055
σ_2	*error*	0.000	0.000	0.966	0.034	0.725	2.562
	cov.	0.000	0.000	0.074	0.042	0.183	0.043
σ_3	*error*	0.000	0.000	0.445	0.731	2.341	0.678
	cov.	0.000	0.000	0.088	0.051	0.084	0.032
σ_4	*error*	0.000	0.000	0.185	1.879	1.302	1.128
	cov.	0.000	0.000	0.075	0.049	0.070	0.042
σ_5	*error*	0.000	0.000	1.108	1.741	2.237	0.128
	cov.	0.000	0.000	0.096	0.022	0.111	0.048

* the error is in %; the cov. (the ratio of the standard deviation to the mean) is in %

Table 3 (a) Identified results of structural parameters (partial output scenario)

		no noise		30% noise		100% noise	
		DREAM	IDREAM	DREAM	IDREAM	DREAM	IDREAM
k_1	*error*	0.019	0.010	1.404	1.501	2.227	2.546
	cov.	0.000	0.000	4.267	2.606	16.58	7.761
k_2	*error*	0.082	0.025	1.025	0.794	4.372	1.450
	cov.	0.000	0.000	2.216	1.351	10.33	4.584
k_3	*error*	0.072	0.018	1.855	0.196	5.602	0.725
	cov.	0.000	0.000	2.710	1.530	12.69	5.538
k_4	*error*	0.089	0.014	1.041	0.511	2.722	2.376
	cov.	0.000	0.000	2.145	1.222	8.633	4.224
k_5	*error*	0.106	0.028	1.233	1.189	0.859	4.485
	cov.	0.000	0.000	2.243	1.358	12.32	4.171
ζ_1	*error*	0.050	0.030	1.066	0.406	1.667	5.214
	cov.	0.000	0.000	2.110	1.179	6.774	4.024
ζ_2	*error*	0.016	0.006	1.564	1.067	0.273	0.972
	cov.	0.000	0.000	2.142	1.258	7.930	4.020

* the error is in %; the cov. (the ratio of standard deviation to the mean) is in %

Table 3(b) Identified results of prediction errors (partial output scenario)

		no noise		30% noise		100% noise	
		DREAM	IDREAM	DREAM	IDREAM	DREAM	IDREAM
σ_3	*error*	0.000	0.000	0.950	2.406	2.675	0.669
	cov.	0.000	0.000	0.145	0.114	0.207	0.089
σ_5	*error*	0.000	0.000	1.240	0.982	0.490	0.557
	cov.	0.000	0.000	0.096	0.094	0.116	0.091

* the error is in %; the cov. (the ratio of standard deviation to the mean) is in %

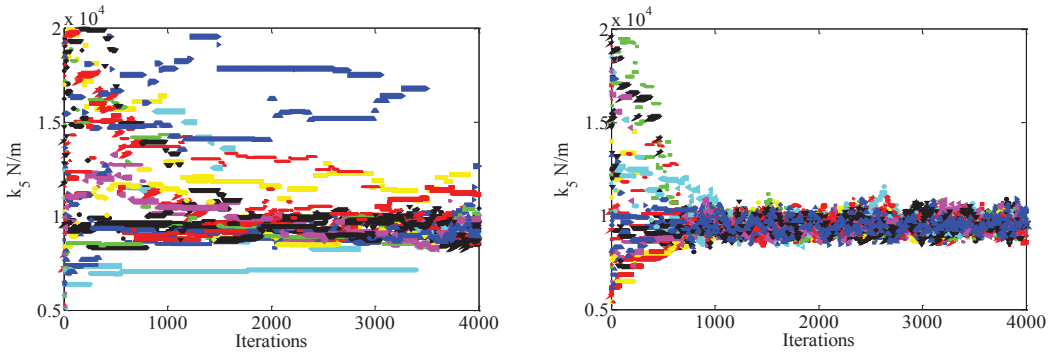

Fig. 2 Progress of identification of stiffness of 5th floor (partial output, 100% noise)

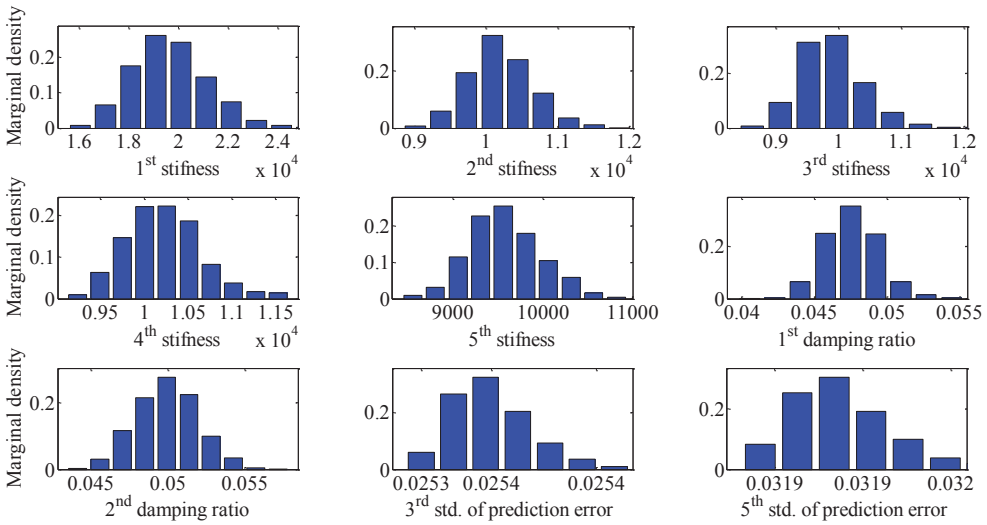

Fig. 3 Histogram of marginal density for each parameter (100% noise, partial output)

Comparing Table 3(a) with Table 2(a), it is clear that the loss of available measurements leads to an increase in parametric uncertainty, because the maximum coefficient of variance for the structural parameters adds from 2.946% to 7.761% at the same noise level. Table 3(b) shows that the actual prediction error standard deviation can be well estimated even if only measurements of the 3rd and 5th DOFs are available. The maximum error of the estimated prediction errors, $\hat{x}_{MAP}$, was 2.406% in the 30% noise case and 0.669% in the 100% noise case. For the DREAM algorithm, the corresponding errors were 1.240% in the 30% noise case and 2.675% in the 100% noise case. (Note that the maximum error of the estimator prediction errors seems larger for the 30% noise scenario than for the 100% noise scenario. The reason for this phenomenon is the denominator for calculating the relative error in the case of 30% noise is smaller than that in the case of 100% noise.)

Fig. 2 shows the progress of identification of the stiffness of the 5th DOF at the 100% noise level in the partial output scenario. In Fig. 2, each plot with a different color denotes the progress of a Markov Chain, which means there were 20 posterior MC samples at each iteration. We can see that the posterior samples of the Markov chain obtained by IDREAM were more stable than those of DREAM, which leads to a smaller uncertain range. The marginal posterior density of the parameters using IDREAM can be obtained by using kernel density estimation on the stationary Markov chain samples excluding the sequence during the burn-in period, as is shown in Fig. 3.

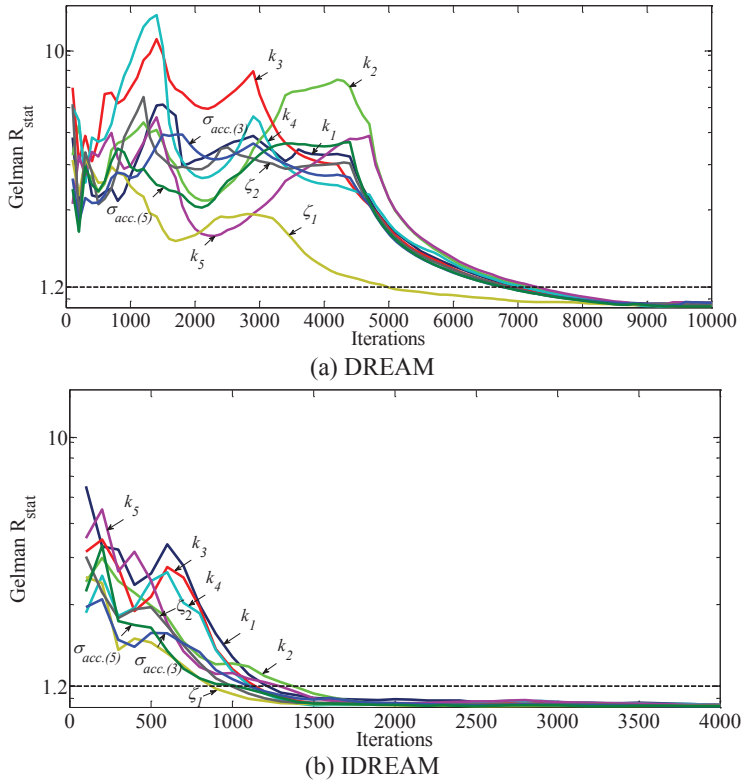

Fig. 4 Convergence of Markov Chain (100% noise, partial output)

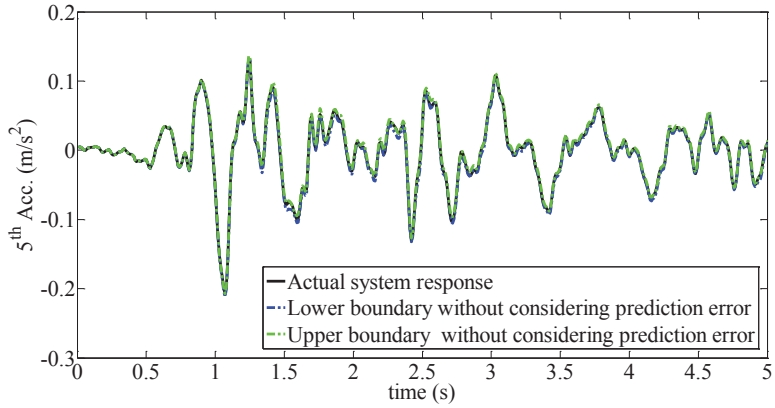

(a) Response range considering the identified parametric uncertainty

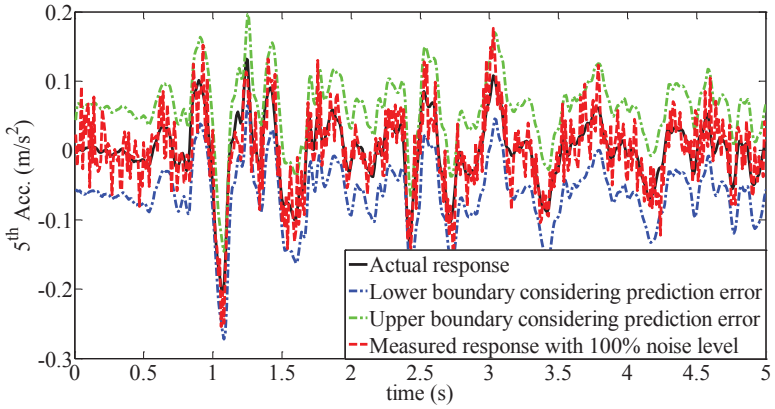

(b) Response range considering the identified std. of prediction error

Fig. 5 95% uncertainty ranges for acceleration of 5th DOF (100% noise, partial output)

Figs. 4(a) and 4(b) indicate that the Markov chain converged for each identified parameter when using DREAM and IDREAM in the scenario of partial outputs and 100% noise. Comparing Fig. 4(a) with Fig. 4(b), however, makes it clear that IDREAM already converged by the time 4000 iterations were reached, but the Markov chains of DREAM were still unstable. Therefore, IDREAM converged faster than DREAM. Combing the solutions in Tables 2 and 3, we can conclude that IDREAM outperformed DREAM because of its earlier convergence and robustness of the posterior samples without decreasing the accuracy of the results.

The posterior uncertain range that assures a reliability of 95% can be obtained from the posterior samples of the model class which denotes the plausibility of each I/O system. Fig. 5 shows the ranges for part of the time history (5 seconds). Fig. 5 (a) is the uncertain response range of a stochastic I/O system parameterized by identified parameters of the posterior candidate model set with 95% assurance and without prediction errors at each time interval. On the other hand, Fig. 5(b) shows the uncertain range of the response with 95% assurance and with measurement errors at each time interval by incorporating the identified standard deviation of the prediction error. Fig.

5(a) illustrates the effectiveness of the Bayesian identification method because the parametric uncertain response range is close to the actual system response. Moreover, in Fig. 5(b), the percentage of the response considering a 100% measurement error within the uncertain range that covers the prediction error is 94.75%.

5. Conclusions

A framework of Bayesian probability inference for identification based on an improved differential evolution adaptive Metropolis-Hasting (IDREAM) algorithm was proposed. Compared with the DREAM algorithm, its novelty lies in a new sample updating pattern that speeds convergence and improves the stability of the posterior samples. IDREAM runs MCMC simulations in parallel and keeps the diversity of samples by using a DE crossover strategy. This gives it a strong ability to search for the global optimum and to resolve the problem that the MH algorithm has in choosing an approximate jump scale. A numerical simulation of a 5-DOF system demonstrated its potential for solving identification problems with a high noise level and with partial output data. In conclusion, IDREAM is a new approach to obtaining the posterior density of a model class that cannot be easily found with the classic Monte-Carlo method due to the difficulty in calculating high-dimensional integrals.

Acknowledgments

This work was supported in part by a grant for the project "Implementation of shelter guidance system for commuters who are unable to return home based on Structural Health Monitoring of tall buildings after large-scale earthquake," (FY2013-2016, PI: Mita) from the Japan Science and Technology Agency.

References

Beck, J.L. (2010), "Bayesian system identification based on probability logic", *J. Struct. Control Health Monit.*, **17**(7), 825-847.

Beck, J.L. and Au, S.K. (2002), "Bayesian updating of structural models and reliability using Markov-Chain Monte-Carlo simulation", *J. Eng. Mech. - ASCE*, **128**(4), 380-391.

Beck, J.L. and Yuen, K.V. (2004), "Model selection using response measurements: A Bayesian probabilistic approach", *J. Eng.Mech. -ASCE*, **130**(2), 192-203.

Cheung, S.H. and Beck, J.L. (2009), "Bayesian model updating using Hybrid Monte Carlo simulation with application to structural dynamic models with many uncertain parameters", *J. Eng. Mech. - ASCE*, **135**(4), 243-255.

Chib, S. and Greenberg, E. (1995), "Understanding the Metropolis-Hasting algorithm", *Am. Statist. Association*, **49**(4), 327-335.

Ching, J. and Chen, Y.C. (2007), "Transitional Markov Chain Monte Carlo method for Bayesian model updating, model class selection and model averaging", *J. Eng.Mech. - ASCE*, **133**(7), 816-832.

Gelman, A. and Rubin, D.B. (1992), "Inference from iterative simulation using multiple sequence", *Statistical Sci.*, **7**(4), 457-472.

Haario, H., Saksman, E. and Tamminen, J. (2001), "An adaptive Metropolis algorithm", *J. Bernouli*, **7** (2),

223-242.
Hastie, D.I. (2012), "Model choice using reversible jump Markov chain Monte Carlo", *Statistica Neerlandica*, **66**(3), 309-338.
Koh, C.G and Perry, M.J. (2007), "Structural damage quantification by system identification", *J. Earthq. Tsunami*, **1**(3), 211-231.
Mita, A. (2003), *Structural Dynamics for Health Monitoring*, Sankeisha Co., Ltd, Nagoya , Japan.
Muto, M. and Beck, J.L. (2008), "Bayesian updating and model class selection for hysteretic structural models using stochastic simulation", *J. Vib. Control*, **14**(1-2), 7-34.
Papadimitriou,C., Beck, J.L and Katafygiotis, L.S. (2001), "Updating robust reliability using structural test data", *Probabilist. Eng. Mech.*, **16** (2), 103-113.
Perry, M.J., Koh, C.G. and Choo, Y.S. (2006), "Modified genetic algorithm strategy for structural identification", *Comput. Struct.*, **84**(8-9), 529-540.
Storn, R. and Price, K. (1997), "Differential evolution-a simple and efficient heuristic for global optimization over continuous spaces", *J. Global Optim.*, **11**(4), 341-359.
Tang, H.S., Xue, S.T. and Fan, C.X. (2008), "Differential evolution strategy for structural system identification", *Comput. Struct.*, **86**(21-22), 2004-2012.
Ter Braak, C.J.F. (2006), "A Markov Chain Monte Carlo version of the genetic algorithm differential evolution: easy Bayesian computing for real parameter spaces", *Statistics Comput.*, **16**(3), 239-249.
Vrugt, J.A., Ter Braak, C.J.F., Diks, C.G.H. et al. (2009), "Acceleration Markov Chain MonteCarlo simulation by differential evolution with self-adaptive randomized subspace sampling", *Int. J. Nonlinear Sci. Numerical Simulation*, **10**(3), 273-290.
Xue, S., Tang, H. and Zhou, J. (2009), "Identification of structural systems using particle swarm optimization", *J. Asian Architect. Build. Eng.*, **8**(2), 101-112.

Smart Structures and Systems, *Vol. 15, No. 3 (2015) 751-767*
DOI: http://dx.doi.org/10.12989/sss.2015.15.3.751

Probabilistic condition assessment of structures by multiple FE model identification considering measured data uncertainty

Hyun-Joong Kim[a] and Hyun-Moo Koh[*]

Department of Civil and Environmental Engineering, Seoul National University, 1 Gwanak-ro, Gwanak-gu, Seoul 151-742, Republic of Korea

(Received October 17, 2014, Revised January 15, 2015, Accepted January 22, 2015)

Abstract. A new procedure is proposed for assessing probabilistic condition of structures considering effect of measured data uncertainty. In this procedure, multiple Finite Element (FE) models are identified by using weighting vectors that represent the uncertainty conditions of measured data. The distribution of structural parameters is analysed using a Principal Component Analysis (PCA) in relation to uncertainty conditions, and the identified models are classified into groups according to their similarity by using a *K*-means method. The condition of a structure is then assessed probabilistically using FE models in the classified groups, each of which represents specific uncertainty condition of measured data. Yeondae bridge, a steel-box girder expressway bridge in Korea, is used as an illustrative example. Probabilistic condition of the bridge is evaluated by the distribution of load rating factors obtained using multiple FE models. The numerical example shows that the proposed method can quantify uncertainty of measured data and subsequently evaluate efficiently the probabilistic condition of bridges.

Keywords: condition assessment; FE Model update; measurement uncertainty; principal component analysis; *K*-means clustering; load rating

1. Introduction

The purpose of condition assessment is to provide a diagnosis of its current state, predict upcoming performance degradation, and ultimately prevent gradual or sudden failure. The accuracy of an assessment can be assured by a reliable Finite Element analysis. However, FE models frequently lack accuracy in terms of the actual behavior of a structure. The discrepancies between predicted and observed behavior are mainly accounted by modeling uncertainty, which is a combination of various factors including assumptions in the design process, deterioration of the structures, variability of material properties, and the limited resolution of the FE model and numerical errors in discretization using finite number of elements.

The modeling uncertainty can be reduced by updating the FE model using measured data, of which procedure mostly involves solving an optimization problem (Park *et al*. 2012). The conventional updating procedure usually assumes that the measured data is accurate and involves deterministic values, thus a single optimal FE model is identified. However, measured data is also

*Corresponding author, Professor, E-mail: hmkoh@snu.ac.kr
[a] Ph.D., E-mail: hjkim@sel.snu.ac.kr

http://www.techno-press.org/?journal=sss&subpage=8 ISSN: 1738-1584 (Print), 1738-1991 (Online)

deterministic values, thus a single optimal FE model is identified. However, measured data is also known to exhibit considerable variability due to non-stationary behavior of structure, noise and bias during data acquisition, numerical error in data processing, and influence of adverse environmental conditions such as temperature and humidity variation. The risk of an error in the identification of single updated model under the existence of data uncertainties has been reported (Robert-Nicoud *et al.* 2000, Schuëller *et al*. 2008).

Variability of FE model caused by data uncertainty can be dealt by using a probabilistic approach such as inverse Stochastic FEM (Mares *et al*. 2006, Soize *et al*. 2008, Govers and Link 2009). Bayesian model updating has also been proposed to find the most plausible posterior PDF of structural parameters (Katafygiotis *et al*. 1998, Beck and Au 2002, Park *et al*. 2010). Uncertainty of measured data can also be represented by variation of weighting factors for optimization problem (Friswell and Mottershead 1999, Steenackers and Guillaume 2006). The non-uniqueness of optimal model due to uncertainties has also been dealt by identification of multiple models (Zarate and Caicedo 2008, Groulet *et al*. 2010).

This paper proposes a procedure for a probabilistic condition assessment of structures considering measured data uncertainty. In this procedure, multiple Finite Element (FE) models are identified through successive optimizations by using sets of weighting vectors. The successive optimizations can overcome the limitation of conventional single model update to deal with the uncertainty of measured data, and estimate probabilistic information about the structural condition. The distribution of multiple FE models is analysed using the Principal Component Analysis (PCA) in relation to uncertainty conditions of measured data. The PCA is utilized for dimension reduction and feature extraction of the multiple models, and improving the clustering accuracy. The multiple FE models can be classified into groups according to their similarity by using a *K*-means clustering. Combined use of PCA and *K*-means clustering can provide probabilistic information about state of the structure, and reduce subjectivity in the interpretations and assessments. Finally, the condition of a structure can be expressed probabilistically by the distribution of performance indices such as load rating factor using FE models in the classified groups, each of which represents specific uncertainty condition of measured data. Furthermore, probability of failure is also estimated using multivariate normal distribution function describing the distribution of structural parameters. Yeondae bridge, a steel-box girder expressway bridge in Korea, is used as an illustrative example. In the example, the distribution of load rating factors and the probability of a bridge failure are evaluated for probabilistic assessment of bridge condition. Numerical example shows that the proposed method can quantify uncertainty of measured data and subsequently evaluate efficiently the probabilistic condition of bridges.

2. Updating multiple finite element models

2.1 Formulation of successive optimization problems

A procedure for updating a FE model involves different types of measured data, e.g., natural frequencies, mode-shapes, damping ratios, displacement, strain, and so on, in order to prevent the occurrence of under-fitted solutions. This represents the multi-objectivity of a FE model update problem. However, it was pointed out that the multi-objective optimization of more than three objectives would be computationally too expensive, and may converge to the wrong solution (Jung *et al.* 2010). Especially in case of the large-scale structure examples, the problem of convergence

and the credibility of a solution may be worsened because sufficient number of structural parameters and target responses should be considered. As an alternative, the problem of finding an optimal FE model satisfying various types of responses can be formulated as an aggregated single-objective function by assigning a weighting factor for each residual. Typically, a single FE model is updated by optimization of the objective function. The single updated model can reflect specific structural condition and is not suitable to represent probabilistic condition of the structure considering uncertainty of the measured data.

In this paper, successive optimization is proposed to deal with the uncertainty of measured data, and to estimate probabilistic condition of structure. For the purpose, a set of optimization problems with each member in the set corresponding to a different choice of the weights are constructed. Varying weighting factors represent different levels of measurement uncertainties. Accordingly, multiple FE models are updated from the optimization problems incorporating measurement uncertainties. An optimization problem corresponding to a specific choice of the weight factors is expressed as follows

$$\min \; J_i(\boldsymbol{\theta}_i) = \mathbf{W}_i^T \mathbf{r}(\boldsymbol{\theta}_i) = \sum_{j=1}^{M} w_{ji} r_j(\boldsymbol{\theta}_i) \;\; \text{subjected to} \;\; \boldsymbol{\theta}_{lb} \le \boldsymbol{\theta}_i \le \boldsymbol{\theta}_{ub} \tag{1}$$

The objective function J_i, denoted by the index i, is a component in the sets of optimization problems corresponding to a different choice of the weights $\mathbf{W}_i$, by which specific uncertainty condition is represented. The subscript j denotes different type of measurements. The $\boldsymbol{\theta}$ is a vector of updated structural parameters that are normalized to the initial values. Structural parameters of different units and magnitudes can be considered effectively by the normalization. The vector of updated structural parameters for the i-th optimization problem is expressed as $\boldsymbol{\theta}_i = [\theta_{1i}, \theta_{2i}, \ldots, \theta_{Pi}]^T$ where P is the number of parameters. The optimal value of $\boldsymbol{\theta}_i$ that can minimize the objective function is identified within a reasonable range defined by $\boldsymbol{\theta}_{lb}$ and $\boldsymbol{\theta}_{ub}$, a lower and upper bound vector, respectively. Weighting factor w_{ji} in Eq. (1) represents weight for the residual of j-th response. An weighting vector $\mathbf{W}_i = [w_{1i}, w_{2i}, \ldots, w_{Mi}]^T$, composed by M weighting factors, represents specific uncertainty condition of measured data in the i-th optimization. The residual r_j represents discrepancy between the analytical model and a real structure with respect to the j-th type of measurement.

$$r_j(\boldsymbol{\theta}_i) = \sqrt{\frac{1}{N_u} \sum_{n=1}^{N_u} \left(\frac{u_{a,n}(\boldsymbol{\theta}_i) - u_{m,n}}{u_{m,n}} \right)^2} \tag{2}$$

where u is the concerned responses such as displacement and natural frequency, subscript n represents the n-the measurement within the N_u total measurements, subscripts a and m represent the analyzed and measured values, respectively. When calculating mode-shape residual $r_{i\phi}$, Modal Assurance Criterion (MAC) is generally adopted.

$$r_\phi = 1 - \mathrm{MAC}(\theta_i) = 1 - \frac{[\phi_m{}^T \phi_a(\theta_i)]^2}{[\phi_m{}^T(\theta_i)\phi_m(\theta_i)] \cdot [\phi_a{}^T \phi_a]} \tag{3}$$

where ϕ_m and ϕ_a are mode-shape of real structure and analysis model, respectively.

The Sequential Quadratic Programming (SQP) is utilized to find optimal FE models for the

constrained non-linear optimization problems, each of which is characterized by a weighting vector $\mathbf{W}_i$ representing specific uncertainty condition. The SQP method approximates the objective function to a quadratic model, and solves a sequence of optimization sub-problems iteratively until convergence is achieved. Karush-Kuhn-Tucker (KKT) conditions and the rate of change of the $\boldsymbol{\theta}$ are considered to check convergence.

2.2 Identification of multiple FE models from sets of weighting vectors

Weighting factors can be determined by the reciprocals of the variance of the corresponding measurements (Friswell and Mottershead 1999). In this paper, various levels of measurement uncertainty are represented by variation of the weighting vector $\mathbf{W}_i$. Varying relative magnitude of weighting factors for different responses account for different level of uncertainty. For example, smaller weight factor can be assigned to the measured data that is expected to contain large uncertainty. On the other hand, large weighting factor of a residual implies that the related data contain small uncertainty. In this way, a weighting vector $\mathbf{W}_i$ can represent specific condition of measurement uncertainties. Accordingly, various conditions of data uncertainty can be reflected by sets of weighting vectors as $\mathbf{W} = [\mathbf{W}_1, \mathbf{W}_2, \ldots, \mathbf{W}_N]$.

To include all possible conditions of measurement uncertainties, the generated weighting vectors are uniformly distributed in feasible space. The directional angles of the weighting vector are taken as variables. For example, if we deal with FE model update associated with three types of responses, a weighting vector $\mathbf{W}_i$ include three weighting factors. The $\mathbf{W}_i$ can be expressed by the three directional angles as Eq. (4).

$$\mathrm{W}_i = [w_{i1}, w_{i2}, w_{i3}]^T = \|\mathrm{W}_i\| \cdot \left[\frac{w_{i1}}{\|\mathrm{W}_i\|}, \frac{w_{i2}}{\|\mathrm{W}_i\|}, \frac{w_{i3}}{\|\mathrm{W}_i\|}\right]^T = \|\mathrm{W}_i\| \cdot [\cos\alpha_i, \cos\beta_i, \cos\gamma_i]^T \tag{4}$$

where α_i, β_i and γ_i are directional angles between the $\mathbf{W}_i$ and three axes for the responses. By setting the norm of the $\mathbf{W}_i$ as one and considering dependency between directional angles, the Eq. (4) can be expressed with two variables as

$$\mathbf{W}_i = \left[\cos\alpha_i, \cos\beta_i, \sqrt{1-\cos^2\alpha_i - \cos^2\beta_i}\right]^T \tag{5}$$

Therefore, generating weighting vectors for three types of responses is equivalent to sampling two directional angles α and β uniformly in 2-D Euclidean space (Fig. 1(a)). The direction angles are acute, i.e., $0 \le \alpha \le \pi/2$ and $0 \le \beta \le \pi/2$ because the weighting factors should be larger than or equal to zero. Fig. 1(b) shows the consequent weighting vectors that compose surface of 1/8 sphere in the first octant.

In case N weighting vectors are generated as $\mathbf{W} = [\mathbf{W}_1, \mathbf{W}_2, \ldots, \mathbf{W}_N]$, N optimal FE models are finally identified by N successive optimizations and compose a matrix of optimal structural parameters $\boldsymbol{\Theta} = [\boldsymbol{\theta}_1, \boldsymbol{\theta}_2, \ldots, \boldsymbol{\theta}_N]$. The i-th column vector $\boldsymbol{\theta}_i$ indicates the properties of the i-th updated model, and each of the p rows corresponds to considered structural parameter. Thus, the matrix $\boldsymbol{\Theta}$ expresses the variability of multiple FE models by the distribution of structural parameter values. Fig. 2 shows an example of updated multiple FE models distributed in the space of structural parameters. Each point represents probable status of structure under the employed uncertainty condition, which is represented by a corresponding weighting vector. Accordingly,

distribution of the updated FE models provides probabilistic information about the structural condition due to the measurement uncertainties.

3. Probabilistic structural condition assessment using multiple FE models

3.1 Analysis of structural parameters distribution of multiple FE models

The Principal Component Analysis (PCA) is utilized for the purposes of dimension reduction and feature extraction of the multiple models. Applying the PCA is also beneficial to improve the clustering accuracy (Ding and He 2004). In addition, the PCA enables to visualize multiple FE models using a couple of principal components only, thus analysis on the grouped models becomes easier.

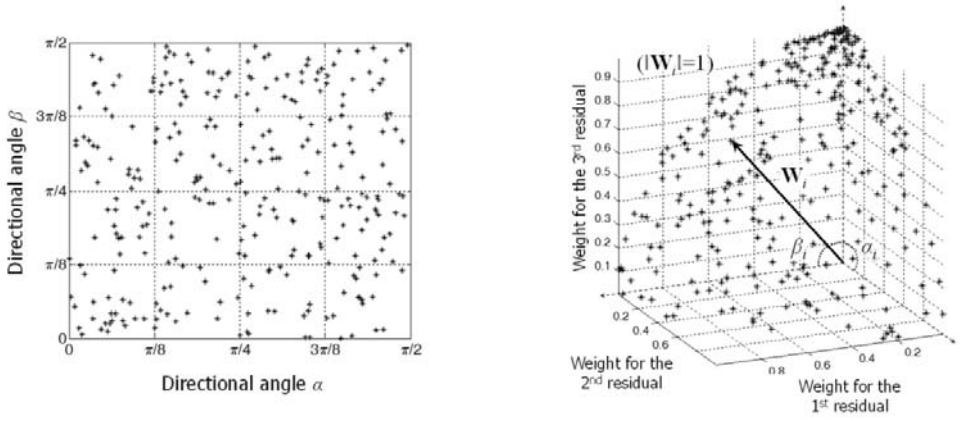

(a) Uniform sampling of two directional angles (b) Generating sets of weighting vectors

Fig. 1 Example of weighting vector generation for three types of responses

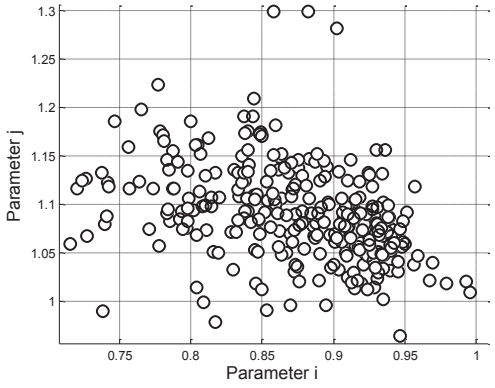

Fig. 2 Distribution of multiple FE models in the space of structural parameters

As a first step to find principal components, the covariance of structural parameters for the N optimal FE models are computed.

$$\mathbf{S} = E[(\mathbf{\Theta} - E[\mathbf{\Theta}])(\mathbf{\Theta} - E[\mathbf{\Theta}])^T] \tag{6}$$

Each entry of the covariance matrix $\mathbf{S}$ is calculated as

$$S_{pq} = \frac{1}{N}\sum_{i=1}^{N}\left(\theta_{pi} - \bar{\theta}_p\right)\left(\theta_{qi} - \bar{\theta}_q\right) \tag{7}$$

where θ_{pi} is p-th component of optimal structural parameter vector $\boldsymbol{\theta}_i$, and $\bar{\theta}_p$ is a mean value given by Eq. (8).

$$\bar{\theta}_p = \frac{1}{N}\sum_{i=1}^{N}\theta_{pi} \tag{8}$$

By applying eigenvector decomposition on $\mathbf{S}$, eigenvector matrix $\mathbf{u}$ and eigenvalue matrix $\mathbf{\Lambda}$ are obtained.

$$\mathbf{S} = \mathbf{u}\mathbf{\Lambda}\mathbf{u}^T \tag{9}$$

The eigenvector matrix $\mathbf{u}$ contains principal components in its column vectors, which are bases of transformed space. The contribution of principal components to explain the variance of the distribution of structural parameters is calculated from diagonal components of $\mathbf{\Lambda}$.

Finally, the coordinate of each model in the transformed space is calculated as

$$\hat{\boldsymbol{\theta}}_i = \mathbf{u}^T\left(\boldsymbol{\theta}_i - \bar{\boldsymbol{\theta}}\right) \tag{10}$$

where $\bar{\boldsymbol{\theta}} = \left[\bar{\theta}_1, \bar{\theta}_2, \ldots, \bar{\theta}_P\right]^T$.

The relationship between the distribution of structural parameters and uncertainty conditions of the measured data can be characterized by the principal components on the transformed space.

3.2 Grouping of multiple FE models according to similarity

The K-means method is further implemented in order to classify the multiple FE models into several groups according to the similarity, which is now revealed by the application of PCA. Combined use of PCA and K-means clustering can group the multiple models, and reduce subjectivity in the interpretations and assessments. The objective function for the clustering is given by

$$J = \sum_{k=1}^{K}\sum_{i=1}^{N} r_{ik}\left\|\hat{\boldsymbol{\theta}}_i - \boldsymbol{\mu}_k\right\|^2 \tag{11}$$

where $\boldsymbol{\mu}_k$ is the centroid of the k-th cluster and r_{ik} indicates membership of the i-th model in the k-th cluster. If the i-th model is assigned to cluster k then $r_{ik} = 1$, otherwise $r_{ik} = 0$. Term inside Σ measures the sum of the inner-distances of data points that are assigned to the k-th cluster. The algorithm iteratively finds centroids of clusters $\boldsymbol{\mu}_k$ and r_{ik} for each of N updated models. The number of clusters K is determined by calculating score function which evaluates the quality of

clustering by two quantities: the Between Cluster Distance (*BCD*) and the Within Cluster Distance (*WCD*). The former one indicates the degree of separation of clusters from each other, whereas the second term indicates the degree of compactness of each cluster. The score function is thus defined as

$$S.F. = BCD/WCD \tag{12}$$

where

$$BCD = \frac{1}{NK}\sum_{k=1}^{K}\left\|\overline{\boldsymbol{\mu}} - \boldsymbol{\mu}_k\right\|^2 n_k \tag{13}$$

$$WCD = \frac{1}{K}\sum_{k=1}^{K}\sqrt{\frac{1}{n_k}\sum_{i=1}^{N} r_{ik}\left\|\hat{\boldsymbol{\theta}}_i - \boldsymbol{\mu}_k\right\|^2} \tag{14}$$

where n_k is the number of FE models in the k-th cluster, and $\overline{\boldsymbol{\mu}}$ is the mean of centroids of all K clusters. Score function values are calculated for different number of clusters, and optimal number of clusters for the maximum score is chosen.

The FE models in each identified group may be characterized by similar property of weighting vectors each of which represents specific uncertainty condition of measured data. Thus, depending on the features of the groups and characteristic of concerned assessment, a specific group of FE models is selected to assess the condition of structures probabilistically.

3.3 Probabilistic assessment of condition using the multiple FE models

A set of FE models provides the probabilistic information about the structural condition considering measurement uncertainties. Thus, the variability of multiple models indicates a likelihood of status that the structure may exhibit under the employed uncertainty of measured data, rather than modeling uncertainty. Accordingly, the updated models can be used for probabilistic assessment of structural condition.

The condition of structure can be expressed as distribution of any types of structural performance index, such as load rating factor, seismic fragility and safety index. In this paper, distribution of Load Rating Factors (RF) is calculated by numerical simulations with the multiple FE models. The distribution of RFs provides statistical information about vehicle load carrying capacity of bridge. When all models are used, the estimated distribution can consider overall variability of multiple models caused by all possible conditions of data uncertainty. A group of similar models can also be selected to consider specific status of structure according to the classified conditions of data uncertainty.

When the statistical information is not necessary, a model representing each cluster can also be selected from the centroids of clusters by Eq. (15).

$$\boldsymbol{\theta}_c = \left[\mathbf{u}^T\right]^{-1}\boldsymbol{\mu}_c + \overline{\boldsymbol{\theta}} \tag{15}$$

where $\boldsymbol{\mu}_c$ is the coordinate of centroid of selected group in the principal component space, and $\boldsymbol{\theta}_c$ the corresponding structural parameters. Structural assessment using the representative model yields the average condition of the structure.

Probability of bridge failure is also evaluated for rigorous probabilistic assessment. A

probability model for multiple FE models is obtained by fitting a multivariate normal distribution to the matrix of transformed structural parameters $\hat{\boldsymbol{\Theta}}$. Once the mean vector $\boldsymbol{\mu}_{\hat{\theta}}$ and covariance matrix $\boldsymbol{\Sigma}_{\hat{\theta}}$ are identified, a set of offspring models are sampled from the PDF $p(\hat{\boldsymbol{\theta}}) = N(\boldsymbol{\mu}_{\hat{\theta}}, \boldsymbol{\Sigma}_{\hat{\theta}})$ and expressed by a matrix $\hat{\boldsymbol{\Theta}}_{offspring}$. The offspring models in principal component space is inversely transformed to the space of structural parameters as $\boldsymbol{\Theta}_{offspring} = \mathbf{u}^{-T}\hat{\boldsymbol{\Theta}}_{offspring} + \overline{\boldsymbol{\theta}}\vec{\mathbf{1}}$, where $\vec{\mathbf{1}}$ is a row vector of which components are 1, and $\boldsymbol{\Theta}_{offspring}$ indicates structural parameters of offspring models. Through the numerical simulation using the offspring models, probabilistic assessment of structural condition can be conducted rigorously. In this paper, probability that the bridge does not meet the safety criteria with respect to the rating factor (RF) is calculated by using the offspring models. The RF equals to 1 defines a safety criteria indicating necessity of bridge reinforcement or vehicle regulation due to insufficient load carrying capacity, rather than actual collapse of the bridge.

The overall procedure for multiple FE model identification, grouping and probabilistic condition assessment is shown in the flow chart (Fig. 3).

4. Application to the assessment of bridge condition

4.1 Application to Yeondae bridge

Yeondae bridge is comprised of a composite steel box girder with two cells as shown in Fig. 4. The bridge is located in a test road section of the expressway 45 in Korea.

Static loading tests were carried out under various load cases using two test trucks, and dynamic loading tests were conducted by running test trucks on the bridge with a varying speed from 5 km/h to 100 km/h. Natural frequencies, mode-shapes and dynamic amplification factor were identified from the instrumented accelerations and dynamic displacements (Kim *et al*. 2013). In this study, three types of measured data are employed: the first 3 natural frequencies and the associated mode-shapes, and vertical displacements of box girders obtained by 3 static load cases (Figs. 5 and 6).

4.2 Identification of multiple FE models

A baseline FE model has been developed based on the design documents. The box girders, cross frames and bracings are modeled using three-dimensional frame elements, and elastic spring support elements are used to represent the bearings. The equivalent sectional properties of each box girder are calculated considering the composite concrete deck. The structural behavior computed by using this FE model was proven to be in good accordance with the actual one measured at the completion of construction (Kim *et al*. 2013).

The baseline FE model is updated by the proposed procedure in order to evaluate condition of the bridge. In the optimization process, 37 structural parameters are considered including the coefficient of spring support elements, the mass of structural and substructural members, Young's modulus of the composite box-girder, cross frame and slab, moment of inertia of girder and cross frame. Table 1 summarizes the structural parameters and their allowable bounds considered in the optimization.

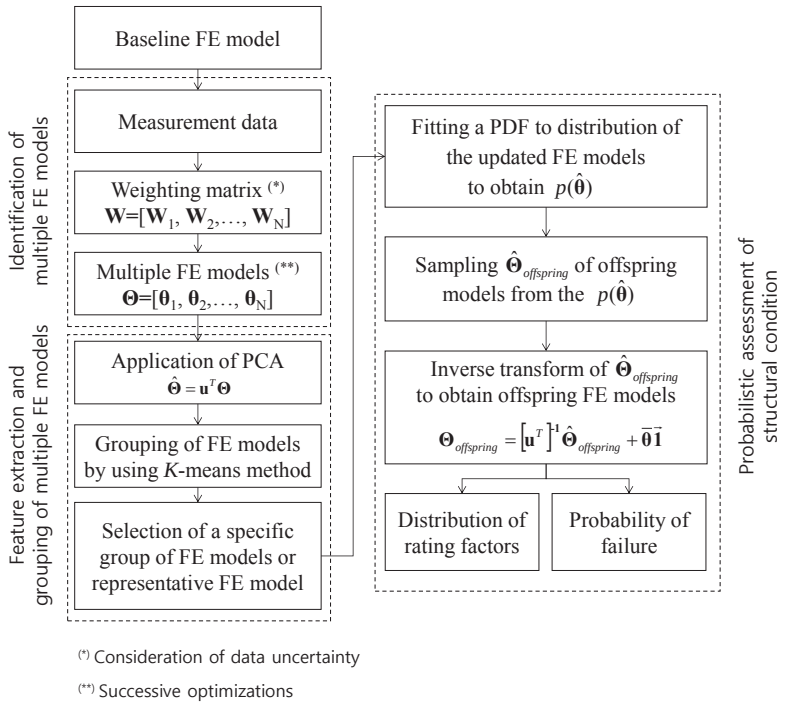

Fig. 3 Overall schema of multiple FE model identifications, feature extraction, and probabilistic assessment of structural condition considering data uncertainty

(a) Composite twin box-girders

(b) Side view

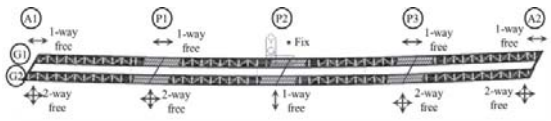

(c) Plan view

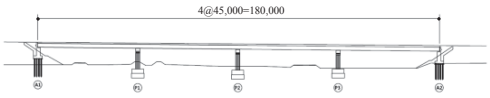

(d) Elevation

Fig. 4 Yeondae bridge

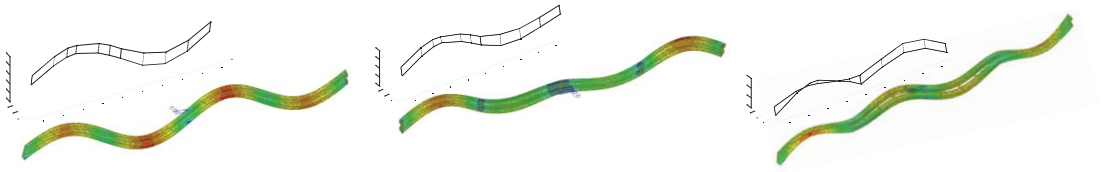

(a) The 1st mode (2.32Hz) (b) The 2nd mode (2.61Hz) (c) The 3rd mode (3.42Hz)

Fig. 5 Measured modal properties

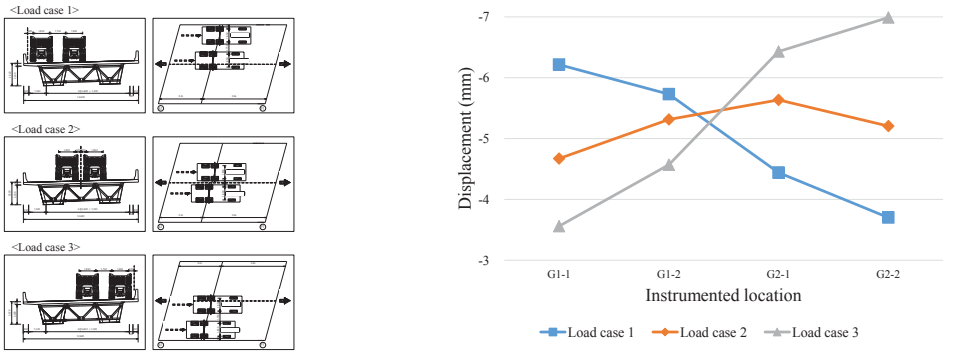

(a) Three load cases (b) The measured displacements of box girders (mm)

Fig. 6 Measured static displacements

The objective function for the *i*-th optimal FE model is formulated as Eq. (16) considering three types of responses.

$$\min\ J_i(\boldsymbol{\theta}) = \mathbf{W}_i^T \mathbf{r}_i(\boldsymbol{\theta}) = w_{if} r_{if} + w_{i\phi} r_{i\phi} + w_{i\delta} r_{i\delta} \tag{16}$$

where r_{if} is the natural frequency residual, $r_{i\phi}$ the mode-shape residual, and $r_{i\delta}$ the displacement residual. The 300 sets of weighting vectors are sampled to represent uncertainty of the responses and, accordingly, a matrix of structural parameters $\boldsymbol{\Theta} = [\boldsymbol{\theta}_1, \boldsymbol{\theta}_2, \ldots, \boldsymbol{\theta}_{300}]$ for the 300 updated FE models are identified by successive optimizations.

4.3 Analysis of structural parameters distribution of multiple FE models

A matrix of transformed coordinate of 300 FE models $\hat{\boldsymbol{\Theta}}$ is obtained along with eigenvector matrix u and eigenvalue matrix Λ by applying PCA to the by applying PCA to the $\boldsymbol{\Theta}$. The Fig. 7 shows the contribution of a few dominant principal components for the variance of the FE models in the case of Yeondae bridge, which indicates that more than 90% of the variance of the multiple FE models can be explained by the first 9 principal components.

Table 1 Structural parameters and their allowable bounds considered in the optimization

Structural parameters	Allowable bounds (%)
Coefficients of spring support elements in translation and rotational direction	±30
Mass of girders (span 1, 2, 3, 4), cross frame	±10
Young's modulus of girders (span 1, 2, 3, 4), cross frame, and slab	±20
Torsional stiffness of girders (span 1, 2, 3, 4), cross frame, and slab	±25
Moment of inertia (I_{yy}) of girders (span 1, 2, 3, 4), cross frame, and slab	±10
Moment of inertia (I_{zz}) of girders (span 1, 2, 3, 4), cross frame, and slab	±10
Area of transverse slab	±30
Mass of substructural member (vertical, rotational)	±30

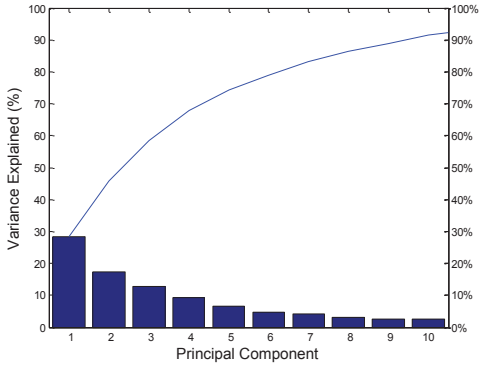

Fig. 7 Contribution of each principal component in the variance of multiple FE models

The relationship between the distribution of structural parameters and uncertainty conditions of the measured data can be characterized sufficiently by the two largest principal components in this example, as represented by gradual variation of weighting factors along the principal axes in Fig. 8. Although not presented here, we found that the relationship between the distribution of structural parameters and uncertainties does not reveal any specific characteristics in the spaces defined by other remaining higher-order principal components. Each point represents each of multiple FE models in the orthogonal space. The 2nd principal axis obviously explains the relationship between multiple FE models and the weighting factor for natural frequency residual (Fig. 8(a)). Variation of the weighting factor for mode-shape residual is also well represented by combination of the 1st and 2nd principal axes in Fig. 8(b). In the meantime, wide dispersion of higher weightage of mode-shape may suggest the insignificance of MAC based residual due to different orders of identified modal parameter and the structural matrices as discussed in Mukhopadhyay *et al*. (2012). The variation of weighting factor for displacement residual is less apparent than others (Fig. 8(c)).

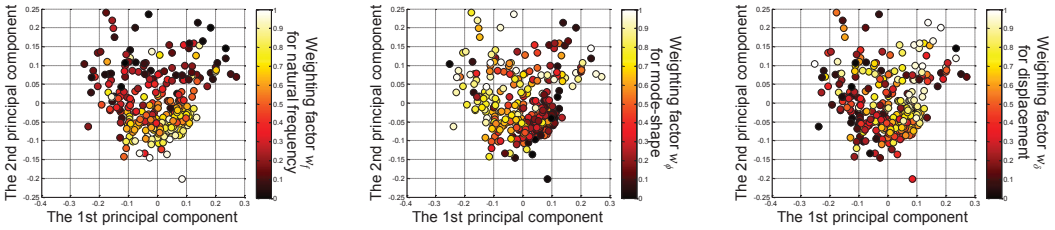

(a) Natural frequency (b) Mode-shape (c) Static displacement

Fig. 8 Variation of the weighting factors of each measured data for updated FE models

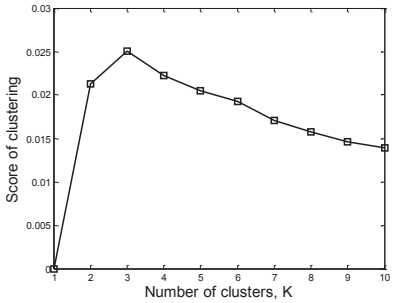

Fig. 9 Scores of clustering for different number of clusters

K-means method is then applied to the $\hat{\boldsymbol{\Theta}}$ to classify models according to similarity. The value of score function is evaluated to assure the quality of cluster results while varying the number of clusters from 1 to 10, where the optimal number of clusters is found to be three (Fig. 9). According to the estimated scores, the multiple FE models are classified into three groups as shown in Fig. 10.

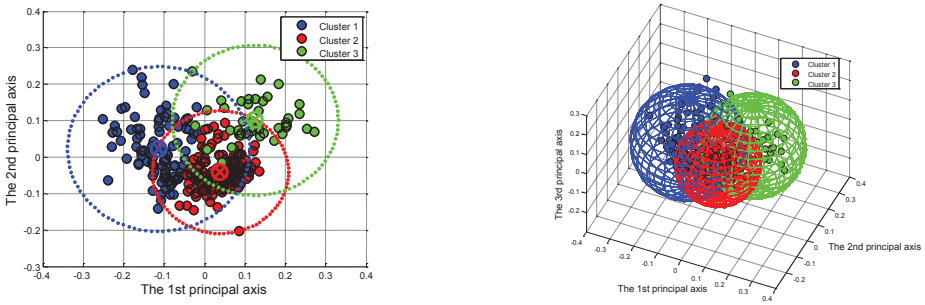

Fig. 10 Classification of multiple FE models into 3 groups

Table 2 Number of FE models in each cluster and characteristics of clusters

	Cluster 1	Cluster 2	Cluster 3
Number of FE models	99	160	41
Characteristic of cluster	Higher weighting factor for mode-shape residual	Higher weighting factor for natural frequency residual	Higher weighting factor for displacement residual

Each group, or cluster, can be characterized by the variation of weighting factors. For example, FE models characterized by higher weighting factor for natural frequency residual, shown in more bright yellow color in Fig. 8(a), are grouped together in the cluster 2. The cluster 2 also includes the models for which all the measurement types are weighted equally. Thus, the FE models in the cluster are expected to be suitable for the evaluations requiring good prediction on the natural frequency, such as seismic fragility analysis. Similarly, the cluster 1 and cluster 3 are characterized by higher weighting for mode-shape and displacement residuals, respectively (Figs. 8(b) and 8(c)). The multiple FE models can be classified into distinct groups without subjectivity by the combined use of PCA and *K*-means. Table 2 shows the number of FE models in three clusters, and their characteristics with respect to weighting factor.

4.4 Probabilistic assessment of bridge condition using load rating factor

Condition assessment of bridges evaluates the remaining resistance capacity of major structural components of bridge against external loads. Especially, the vehicle load carrying capacity is quantified by evaluating load rating factor. The Rating Factor (RF) is usually computed by using a single updated FE model by which bridge condition is reflected restrictively. On the contrary, the proposed procedure utilizes multiple updated FE models that can represent possible states of structural conditions, and the estimated rating factors provides statistical information on bridge condition.

The rating factors are evaluated with respect to the maximum positive bending moment for the strength limit state I (MLTM 2012). Table 3 shows the results obtained by using different sets of FE models: all the identified FE models and FE models in each of the three clusters. Since rating factors are highly dependent on the stiffness of the bridge, it can be concluded that the mean value of 2.16, computed by using FE models in the cluster 3 that is characterized by higher weighting factors for displacement residual, represents properly the current condition of the bridge. This is also confirmed by more rigorous analysis where highly refined updated FE model based on measured data produced a rating factor of 2.15 (Kim *et al.* 2013). It is noteworthy that, when 50% of the FE models closest to the centroid of each cluster are used, all the standard deviations have decreased considerably while the mean values have not changed much. Fig. 11 also shows that using the FE models of cluster 3 results in narrower and shifted distribution of rating factor compared to the case of using all the identified FE models.

Table 3 Rating factors using different set of FE models

	All identified FE models	Cluster 1	Cluster 2	Cluster 3
Mean value	2.06	2.06 (1.98)*	2.03 (2.03)*	2.16 (2.18)*
Standard deviation	0.129	0.153 (0.104)*	0.089 (0.064)*	0.128 (0.081)*

( )* : values estimated by using 50% closest FE models to the centroid of each cluster

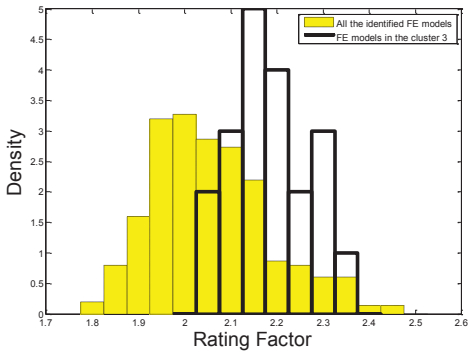

Fig. 11 Distribution of rating factors estimated by using all identified FE models and FE models in the cluster 3

When probabilistic information is not necessary, the proposed procedure can simply use one representative FE model located at the centroid of each cluster. In this case, the rating factors are evaluated as 2.01, 2.01 and 2.11 for cluster 1, 2 and 3, respectively, which are close to the mean values for each cluster. Thus, the evaluation of bridge condition using the representative FE model can also reflect each cluster's characteristics in this procedure.

The probability of bridge failure is computed as $p_f = P[RF \le 1]$. Here, the limit state function indicates insufficient load carrying capacity. To evaluate the probability, a distribution of rating factors is estimated by numerical simulations with 10,000 offspring FE models, which are generated from a multivariate normal distribution for the updated FE models. Then, the probability of insufficient load carrying capacity is evaluated by using a Gaussian PDF that is fitted to the distribution of rating factors. The evaluations are repeated by using FE models of each cluster, respectively. Table 4 lists statistical properties of the rating factors estimated by using the offspring models, and the probability of bridge failure for the identified clusters. The probability computed by using FE models in each cluster is significantly small compared to the one using all the identified FE models because data uncertainties are well taken care by clustering. The probabilistic assessment of the current structural condition by the proposed procedure can provide useful and efficient information for optimizing repair and maintenance plan in terms of lifetime cost and safety.

Table 4 Statistical parameters of rating factors obtained by using 10,000 offspring models and probability of insufficient load carrying capacity

	All identified FE models	Cluster 1	Cluster 2	Cluster 3
Mean value of RF	2.01	2.09	2.06	2.15
Standard deviation of RF	0.39	0.26	0.24	0.26
p_f	2.54×10^{-3}	1.57×10^{-5}	4.38×10^{-6}	4.18×10^{-6}

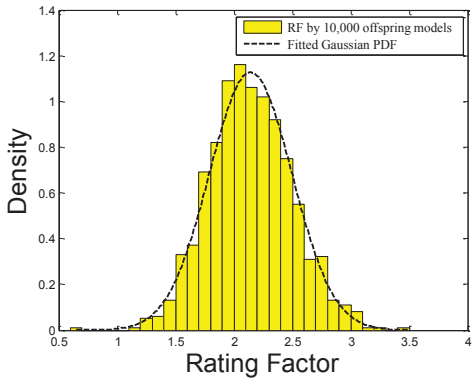

Fig. 12 Fitting of a Gaussian distribution ($\mu = 2.01$, $\sigma = 0.39$) to the distribution of rating factors estimated by considering all identified FE models

5. Conclusions

In this paper, a new procedure for assessing probabilistic condition of bridge considering measured data uncertainty has been proposed. The uncertainty of measured data is represented by the variation of weighting vectors. Multiple updated FE models are identified by successive optimizations using varying weighting vectors for specific measured data, and are classified into groups according to their similarity by using Principal Component Analysis (PCA) and *K*-means clustering. Probabilistic condition of a structure is properly assessed by using a selected group of updated FE models depending on the degree of data uncertainties. It is shown in the application example of Yeondae bridge that the proposed procedure can effectively evaluate probabilistic distribution of load rating factors for representing the current remaining resistance capacity of the bridge. The probabilistic assessment of the current structural condition by the proposed procedure can provide useful and efficient information for optimizing repair and maintenance plan in terms of lifetime cost and safety.

Acknowledgments

This research was supported by grants (09CCTI-A052531-05-000000) from the Ministry of Land, Transport and Maritime (MLTM) of Korean government as the Core Engineering Technology Development Project at Seoul National University through Super Long Span Bridge R&D Center, and also partially supported by Integrated Research Institute of Construction and Environmental Engineering (IRICEE) at Seoul National University.

References

Beck, J.L. and Au, S.K. (2002), "Bayesian updating of structural models and reliability using Markov chain Monte Carlo simulation", *J. Eng. Mech. -ASCE*, **128**(4), 380-391.

Bishop, C.M. (2006), *Pattern Recognition And Machine Learning*, New York: springer, NY, USA.

Ding, C. and He, X. (2004), "K-means clustering via principal component analysis", *Proceedings of the 21th International Conference on Machine Learning*, ACM.

Friswell, M. and Mottershead, J.E. (1995), *Finite Element Model Updating In Structural Dynamics*, Kluwer Academic Publishers, Dordrecht, The Netherlands.

Govers, Y. and Link, M. (2010), "Stochastic model updating—Covariance matrix adjustment from uncertain experimental modal data", *Mech. Syst. Signal Pr.*, **24**(3), 696-706.

Goulet, J.A., Kripakaran, P. and Smith, I.F. (2010), "Multimodel structural performance monitoring", *J. Struct. Eng. - ASCE*, **136**(10), 1309-1318.

Jung, S., Ok, S.Y. and Song, J. (2010), "Robust structural damage identification based on multi-objective optimization", *Int. J. Numer. Meth.Eng,*, **81**(6), 786-804.

Katafygiotis, L.S., Papadimitriou, C. and Lam, H.F. (1998), "A probabilistic approach to structural model updating", *Soil Dyn. Earthq. Eng.*, **17**(7), 495-507.

KCI (2010), *Guide Specification for Assessment of Concrete bridges*, Korea Concrete Institute, Seoul, Korea.

Kim, H.J., Kim, H.K. and Park, J.Y. (2013), "Reliability-based evaluation of load carrying capacity for a composite box girder bridge", *J. Civil Eng. - KSCE*, **17**(3), 575-583.

Kim, H.J., Park, W., Koh, H.M. and Choo, J.F. (2013), "Identification of structural performance of a steel-box girder bridge using machine learning technique", *Proceedings of the IABSE Symposium Report*, **99**(12), 1313-1320, International Association for Bridge and Structural Engineering.

Kim, H.J., Park, W. and Koh, H.M. (2014), "Probabilistic performance assessment of highway bridges using operational monitoring data", *Proceedings of IABSE Symposium Report*, **102**(9), 2650-2657, International Association for Bridge and Structural Engineering.

Mares, C., Mottershead, J.E. and Friswell, M.I. (2006), "Stochastic model updating: part 1—theory and simulated example", *Mech. Syst. Signal Pr.*, **20**(7), 1674-1695.

MLTM (2012), *Highway Bridge Design Code*, Korea Ministry of Land, Transportation and Maritime Affairs, Seoul, Korea.

Mottershead, J.E., Mares, C., James, S. and Friswell, M.I. (2006), "Stochastic model updating: part 2—application to a set of physical structures", *Mech. Syst. Signal Pr.*, **20**(8), 2171-2185.

Mottershead, J.E., Link, M. and Friswell, M.I. (2011), "The sensitivity method in finite element model updating: a tutorial", *Mech. Syst. Signal Pr.*, **25**(7), 2275-2296.

Mukhopadhyay, S., Lus, H. and Betti, R. (2014), "Modal parameter based structural identification using input–output data: Minimal instrumentation and global identifiability issues", *Mech. Syst. Signal Pr.*, **45**(2), 283-301.

Mukhopadhyay, S., Luş, H., Hong, A.L. and Betti, R. (2012), "Propagation of mode shape errors in structural identification", *J. Sound Vib.*, **331**(17), 3961-3975.

Park, I., Amarchinta, H.K. and Grandhi, R.V. (2010), "A Bayesian approach for quantification of model uncertainty", *Reliab. Eng. Syst. Safe.*, **95**(7), 777-785.

Park, W., Kim, H. K. and Jongchil, P. (2012), "Finite element model updating for a cable-stayed bridge using manual tuning and sensitivity-based optimization", *Struct. Eng. Int.*, **22**(1), 14-19.

Robert-Nicoud, Y., Raphael, B. and Smith, I.F.C. (2000), "Decision support through multiple models and probabilistic search", *Proceedings of the Construction Information Technology*, Icelandic Building Research Institute, Reykjavik.

Saitta, S., Raphael, B. and Smith, I.F. (2007), "A bounded index for cluster validity", *Proceedings of the 5th International Conference MLDM 2007*, Leipzig, Germany, July.

Schuëller, G.I. and Jensen, H.A. (2008), "Computational methods in optimization considering uncertainties–an overview", *Comput. Method. Appl. M.*, **198**(1), 2-13.

Soize, C., Capiez-Lernout, E., Durand, J.F., Fernandez, C. and Gagliardini, L. (2008), "Probabilistic model identification of uncertainties in computational models for dynamical systems and experimental validation", *Comput. Method. Appl. M.*, **198**(1), 150-163.

Steenackers, G. and Guillaume, P. (2006), "Finite element model updating taking into account the uncertainty on the modal parameters estimates", *J. Sound Vib.*, **296**(4), 919-934.

Smart Structures and Systems, *Vol. 15, No. 3 (2015) 769-785*
DOI: http://dx.doi.org/10.12989/sss.2015.15.3.769

Performance monitoring of timber structures in underground construction using wireless SmartPlank

Xiaomin Xu*[1], Kenichi Soga[1], Sarfraz Nawaz[1], Neil Moss[2], Keith Bowers[2] and Mohammed Gajia[2]

[1]*Department of Engineering, University of Cambridge, Cambridge, UK*
[2]*Transport for London, London, UK*

(Received November 8, 2014, Revised January 20, 2015, Accepted February 21, 2015)

Abstract. Although timber structures have been extensively used in underground temporary supporting system, their actual performance is poorly understood, resulting in potentially conservative and over-engineered design. In this paper, a novel wireless sensor technology, SmartPlank, is introduced to monitor the field performance of timber structures during underground construction. It consists of a wooden beam equipped with a streamlined wireless sensor node, two thin foil strain gauges and two temperature sensors, which enables to measure the strain and temperature at two sides of the beam, and to transmit this information in real-time over an IPv6 (6LowPan) multi-hop wireless mesh network and Internet. Four SmartPlanks were deployed at the London Underground's Tottenham Court Road (TCR) station redevelopment site during the Stair 14 excavation, together with seven relay nodes and a gateway. The monitoring started from August 2013, and will last for one and a half years until the Central Line possession in 2015. This paper reports both the short-term and long-term performances of the monitored timber structures. The grouting effect on the short-term performance of timber structures is highlighted; the grout injection process creates a large downward pressure on the top surface of the SmartPlank. The short and long term earth pressures applied to the monitored structures are estimated from the measured strains, and the estimated values are compared to the design loads.

Keywords: wireless sensor network; timber structure; underground construction; grouting; earth pressure

1. Introduction

Integrated in modern excavation and supporting systems, timber remains an important ground supporting material since the inception of underground construction (Mark and Barczak 2000, Mackenzie 2014). In early tunnels, timber was used for the initial or temporary support, followed by a permanent lining of brick or stone masonry. At present, timber support of temporary work continues to be an effective system for ground support, due to its availability, flexibility and ease of installation. It is preferred over steel mainly as: (1) it has a lower density (~420 kg/m^3) for transportation; and (2) it offers more flexibility, as it can be easily sawn, manipulated and put in the form of a support on site to suit specific local requirements whenever arise. As a construction material, timber requires none of the special equipments necessary for the placement of concrete or

*Corresponding author, Ph.D., E-mail: xx787@cam.ac.uk

http://www.techno-press.org/?journal=sss&subpage=8 ISSN: 1738-1584 (Print), 1738-1991 (Online)

steel support, which demands a carefully dimensioned and engineered excavation for their installation. Nevertheless the principal disadvantage of timber as a support method is higher material cost and labor cost associated with its labor-intensive installation. This not only poses health and safety risks to workers, but also increases the cost and construction time. Therefore, in any situation if used, it should be able to bear the load safely and its consumption should be minimized /optimized to economize on its material and construction costs.

Despite its extensive usage in underground construction, the actual performance of the timber supporting temporary works has not been thoroughly understood, resulting in often conservative and over-engineered design. Until recently, temporary timbering support is solely relying on the experience of the contractor and analogies from the mining industry. An estimation of loads on underground temporary structures is principally based on the classical recommendations by Terzaghi (1946) and some historic practices. The former is probably only adequate for relatively shallow tunnels in favorable ground conditions (Kavvadas 2003), while the latter is considered by the industry to lead to over-engineered structures. For instance, the short-term and long-term horseheads in the London Underground are designed to carry at least 25% and 40% of the soil overburden, respectively (Mackenzie 2014). In order to cater for the different loading conditions in the field and in the laboratory, the strength of timber in the underground environment is commonly derived from laboratory compression tests based on the generalized de-rating factor, which was originally developed from gold mines in the 1980's (Robert *et al*. 1987). Following these industrial guidelines, no incident has been reported in the past that any of these timbers failed in the London Underground, except the cross-passage incident at Victoria, where the full overburden loading induced by the train vibration was carried (Mackenzie 2014).

Timbers are often used in underground mining. Szwedzicki (1989) argued that the safety factor for timber supports in underground mining was too high, as no sign of stress was observed in many timber packs. Recently, in-situ load measurement has enabled better understanding of the real performance of elongate support units. For example, Daehnke *et al*. (2000) evaluated the performance characteristics of eighteen 140 mm diameter mine poles instrumented with standard pre-stressing units, and six 170 mm diameter mine poles without pre-stressing units spread at four locations of two mines. Direct comparison between the field and laboratory testing results subjected to oblique loading conditions indicated that the relationship proposed by Robert *et al*. (1987) had overestimated the strength of mine poles installed in situ, attributing this overestimation to the effects of installation angle and rotation during the loading process. Piper and Malan (2008) used a wired load logger to measure the in-situ loads on four types of timber elongates with diameters ranging from 160 mm to 180 mm in a shallow platinum mine under very low rates of closure. Their measurements indicated that the original de-rating factor was too conservative; a de-rating factor of up to 40% for low closure areas may be appropriate to take into account of the differences between laboratory and field conditions. Bierman *et al*. (2013) proposed a revised de-rating methodology for timber elongates by recognizing that the original de-rating factor may underestimate their in-situ performance.

These past studies imply that the real performance of timber structures in underground construction could be very site-specific, and can only be understood in conjunction with the environment and real-time ground behavior that they support. The design of timber-based support system should be based on the measurements at that site, and not on the de-rating factors or measurements from others (Piper and Malan 2008). The use of timber for temporary ground support in tunnelling in London Clay has been extensively adopted for over one hundred years, due to the satisfactory physical properties of London Clay. Large components of the face timbering

are used to manage the stability of advancing tunnel faces. Cement grout is then pumped into voids between the irregular excavated clay surfaces and the close timbering to avoid soil softening and loss of ground, and to act as a primitive seal by preventing clay to be exposed to the air in the tunnel. These London practices have heavily influenced the traditional timbering in other cohesive soil in the UK (Mackenzie 2014). Unfortunately, based on our best knowledge, there has been no in-situ measurement or evidence made in underground construction to validate its timbering design philosophy.

With the advances in sensor technology, the wireless sensor system has emerged as an alternative to the traditional sensor system. The use of wireless sensor network allows faster deployment, less complication in maintaining the system and better Signal-to-Noise Ratio (SNR) compared to a wired solution. It can facilitate continuous monitoring of critical underground infrastructures with minimum human involvement (Bhalla *et al*. 2005, Hoult *et al*. 2009, Bennnet *et al*. 2010a, b). However there are other challenges such as robust wireless communication to overcome (Akyildiz and Stuntebeck 2006, Stajano *et al*. 2010, Kennedy and Bedford 2014). In this paper, a novel monitoring technology, wireless SmartPlank system, is introduced. Monitoring on a London Underground temporary supporting system is ongoing, using this new technology to understand the actual field behavior of these timber structures.

2. Wireless sensor network

A wireless SmartPlank system measures the field performance of temporary timber structures used in manual underground construction in order (i) to examine the validity engineering assumptions made in design and (ii) to use it as real time monitoring system for safety of construction workers. It consists of an instrumented plank (SmartPlank), some relay sensors and a gateway. The engineering information measured by SmartPlank is transmitted in real-time over an IPv6-based multi-hop wireless mesh network and Internet while the underground construction is taking place. The main advantages of wireless against wired are (i) its ease to be installed in confined space by construction workers due to safety reason and (ii) continuous monitoring of the structures from the installation stage.

2.1 SmartPlank

SmartPlank is a wooden beam equipped with a streamlined wireless sensor node, and two thin foil strain gauges accompanied with two temperature sensors. It measures the strain and temperature experienced by the beam, and transmits this information in real-time through a multi-hop mesh network.

A typical installation of SmartPlank consists of a horizontal head tree supported by two vertical side trees using Yankee brob (see Fig. 1). The top tree takes bending load while the side trees hold the vertical load axially and the lateral bending load. With this layout, strain gauges and temperature sensors are attached on both the top and bottom surfaces of the timber plank. A wireless sensor node is attached to the underside to allow wireless communication. A load cell can be placed at the top of the side tree at the Yankee brob and connected to another wireless sensor node (this was not done in this study). The top tree is countersunk by having the side trees shortened to accommodate the load cells, which enables a constant height for all timber frames.

A 5 mm wire lead strain gauge was used in this study. To avoid the usage of inflammable epoxy

adhesives on site, a special mounting plate (60 mm×20 mm×5 mm) using Aluminum alloy 6082 (see Fig. 2(a)) was designed and manufactured. The ends of the plate were made to be thick to ensure a good load transfer from the plank to the gauge. Strain gauges were glued onto the middle thin part of the plate to minimize its local reinforcement effect, and flexible wiring was soldered onto the strain gauge electrical leads. The mounting plate equipped with strain gauge was then mounted to the timber surface on the bottom and top sides to measure both tension and compression during the bending.

A temperature gauge MCP9700A (see Fig. 2(b)) was also attached to the plank surface alongside with each strain gauge to account for any effects that temperature variation might have on the strain gauge. It is a low-cost analog temperature sensor that converts temperature to analog voltage and then digitized by the sensor node. The accuracy of the sensor is ±2˚C for a temperature range from 0˚C to 70˚C, and the operating current is only $6\mu A$.

The electrical wiring from all strain gauge units and temperature gauges is connected to the wireless sensor node attached to the bottom side of the timber plank. The sensor node has 4 input channels, each of which can accept a resistive sensor. Each input channel forms one leg of a Wheatstone bridge and is also connected to ADS7795 Analogue to Digital converter (ADC). ADS7795 is a multi-channel ADC and has an internal amplifier with software selectable gain in powers of 2 from 1 to 128. Each channel can be individually powered and read to keep the total power consumption down to meet the limitations of the battery. The gain of each channel can also be set individually. ADS7795 also has an internal temperature sensor that measures ambient temperature. Each wireless sensor node is powered by either 2 AA size batteries mounted directly on the PCB of the sensor node or by an external pack of 2 D sized Lithium-thionyl Chloride batteries to provide extended operating lifetime. Each sensor node starts sampling the strain gauges and the temperature sensors, and transmits this information through its radio interface. There is a trade-off between the frequency of readings and the battery life. The reading frequency is set in software, and is typically chosen to take a set of readings every 15 minutes for the first week, and then take hourly readings afterwards. It is expected that the nodes will remain in place and will not be recoverable.

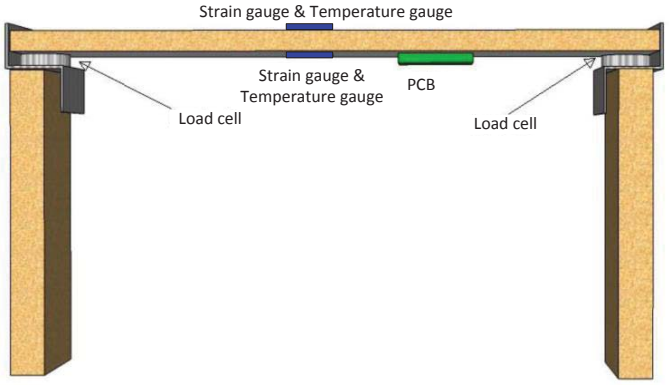

Fig. 1 Idealized SmartPlank prototype

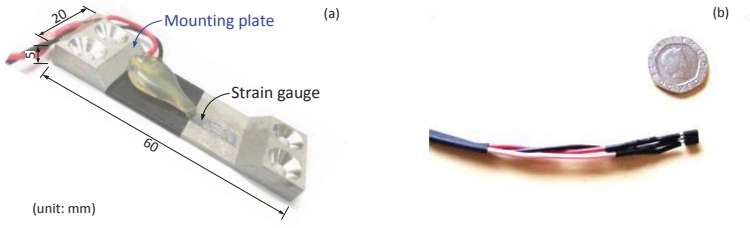

Fig. 2 Sensors mounted on the SmartPlank: (a) strain gauge mounting plate and (b) temperature gauge

2.2 Wireless network

Each wireless sensor node is programmed with application software that has been developed in Contiki OS, an open source operating system for embedded and resource constrained devices. This application software periodically switches on individual channels, powers up the ADS7795, writes configuration commands to it to set input channel and amplifier gain and then samples 10 measurements from each channel. It computes the mean and median values of these measurements and then transmits this information over the wireless network. The input channel and ADS7795 are then powered down. Each sensor nodes uses the IPv6 (6LowPan) stack provided by Contiki OS to form a multi-hop network with nearby SmartPlank nodes and relay nodes.

A relay node is identical to a SmartPlank sensor node except that it does not include any strain gauge or temperature sensors. Its role is to provide connectivity between SmartPlank sensor nodes and the gateway. The 6LowPan network layer includes neighbor discovery, address configuration and packet routing capabilities. It discovers neighboring nodes and maintains the shortest route to the gateway based on link layer packet loss to neighboring nodes. When a data packet destined for the gateway is passed down to the network layer, it looks up the next hop node in its routing table and transmits it to this neighbor. At each node this process continues until the data packet is delivered to the gateway.

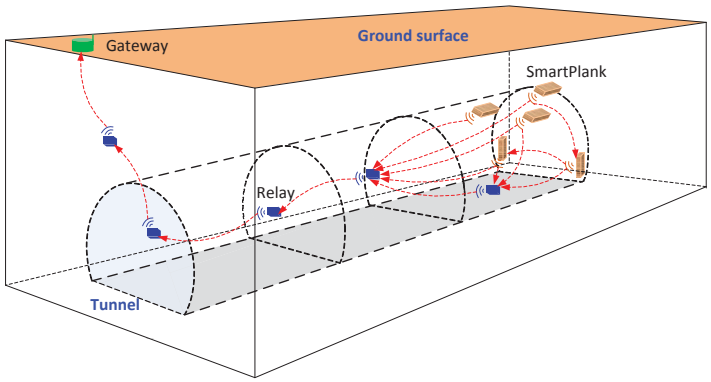

Fig. 3 Wireless sensor network in underground tunnel

The gateway provides local data storage and connectivity to the Internet via a 3G modem. The IPv6 based network allows each sensor node to send data to any host machine over the Internet. It also becomes a host to connect to individual sensor nodes as well. Each node also implements radio duty cycling in software, and switches its radio on with a frequency of 8Hz to sample the radio channel. If it senses any radio transmission, it keeps the radio on to receive the entire packet, otherwise the radio is switched off to save energy.

The received sensor data from strain gauges and temperature sensors is first converted into voltage, and then into strain and temperature measurements. The strain is obtained by using gauge resistance (e.g., 120 Ω for RS strain gauge), and gauge factor (GF) which is a fundamental parameter of the strain gauge defined as the ratio of fractional change in electrical resistance to the fractional change in length. The typical GF for foil strain gauges is around 2.1. The measurement from the temperature sensor can be translated by using the temperature coefficient (10mV/℃ for MCP9700A) and the output voltage at zero degrees (500mV for MCP9700A). Note that temperature compensation is essential to obtain the real strain.

It is vital that the whole system is connected together and tested prior to the real deployment. This is not only to check the network connectivity, but also to assess the capability of each SmartPlank (e.g., strain gauge attachment). To replace the installed problematic planks on real site would become rather difficult, as most of the sites will be inaccessible and unreachable during the excavation period. Calibration of SmartPlank was also conducted in the laboratory to understand the relationship between the actual desired measurements and the collected signal data. Loading tests were conducted with strain gauges directly attached to the wooden beam and with the strain gauge holders next to the directly attached gauges. Results show that the system measures the strain of the instrumented beam accurately.

3. SmartPlank deployment at TCR

London Underground's Tottenham Court Road (TCR) station is currently being upgraded to meet the expected rise in passenger numbers interchanging between London Underground services and Crossrail in 2018. One sub-project is to provide a new access from Stair 14 to the Central Line platforms to reduce congestion. Temporary works have been installed from the Stair 14 upper landing since August 2013, in order to create space and lifting facilities for the installation of the modular channels and top strut above the platform tunnel shoulder during the Central Line possession in 2015. The reinforced concrete, and steel frames together with timber were employed to support the ground after excavation. The deployment of wireless SmartPlank system was carefully designed to comply with the site conditions and the timber temporary system.

3.1 Geological conditions

The geological sequence at Stair 14 comprises of a thin layer of Made Ground and Thames River Terrace Gravels, underlain by the London Clay formation, Harwich formation, the Lamebth Group formation, the Thanet Sand formation then the Chalk, as shown in Fig. 4. The Central Line platform tunnels are entirely within London Clay. The proposed platform level at the Stair 14 opening is 100.445 m TD (tunnel datum), and the existing platform tunnel axis levels varies between 101.6 mTD and 101.9 mTD. The borehole data shows that the reduced levels of the boundaries between strata are similar with no noticeable dipping or faulting. The pore pressure

profile is likely to be severely under-drained at this location as the site lies in the middle of the main cone of depression caused by abstraction from the deep aquifer in central London. Therefore, groundwater levels are expected to be around 65 mTD. Further details of the site can be found in Yeow *et al*. (2014).

3.2 SmartPlank deployment

From the completed Stair 14 upper landing, the temporary works were constructed in sequence from stage I to stage VI, as shown in Fig. 5. At each cross-section, up to 20 frames of heading timber were constructed along the line of the modular channels, resting on the H-shaped steel beam frames which were bolted into the concrete walls. The siding and heading H-shaped steel beams are UC 152×152×37 and UC 203×203×46, respectively. The grade of timber used in the temporary support system was C24, with Young's modulus of 9GPa.

Four SmartPlanks numbered as SP51, SP52, SP53 and SP54 were deployed at TCR Stair 14, as shown in Fig. 5(a), each with a rectangular cross-section of 200 mm×100 mm (see Fig. 5(b)). For each SmartPlank, the designed locations for each support were first marked. A strain gauge and a temperature sensor were then attached in the mid-span of both the top and bottom surfaces of the plank, and the wireless sensor node was attached on the bottom side of the timber, as shown in Fig. 6(a). The electrical wiring that connects all the sensing units and the wireless sensor node was wrapped to the side of the plank. This is to avoid direct damage to the wiring during the H-beam installation. Once prepared, each SmartPlank was tested to check its connectivity, and take the baseline readings prior to being installed. The instrumented SmartPlanks were then wrapped with tape to protect them from any physical damage.

The SmartPlanks were installed together with the other planks once the designated location was ready, and were switched on immediately after the installation. Although the planks were supposed to be supported by four bearings (as shown in Fig. 5(a) for SP54), in reality there were only the first and fourth ones available at the initial stage. Wedges were used to stabilize all the planks, which could induce a certain amount of axial force in the planks. It was witnessed that the soil could actually hold itself without failing before the planks were installed. Grouting was then carried out immediately after the timber heading at each stage, to prevent softening and loss of ground (see Fig. 5(a)). The grout also acts as a primitive seal to prevent the clay being exposed to the air in the tunnel. All the bolt holes on the timber head trees were protected during the grouting. The other two steel bearings in the middle were then added a week or so later after the plank installation. Fig. 6(b) gives a picture of SP52 installed at Stair 14 TCR. It is worth noting that the antenna had to be extended and hung down to provide good wireless communication among each node.

3.3 Wireless sensor network at TCR

The wireless monitoring system was deployed at TCR Stair 14 to monitor the field performance of timber heading, including 4 SmartPlanks, 7 relays and a gateway, as shown the plan view in Fig. 7. The initial plan was to spread the relays along the tunnel and connect the gateway with 3G signal, so the data can be sent back to a server in Cambridge. Unfortunately there was very poor 3G signal coverage in the vicinity of the station. As a result, the gateway was moved to the current position shown in Fig. 7, and formed a wireless network. In the mean time, SP51 was not properly installed at the very beginning, and thus became unrecoverable and useless in the end. Monitoring

with the other three SmartPlanks is still ongoing.

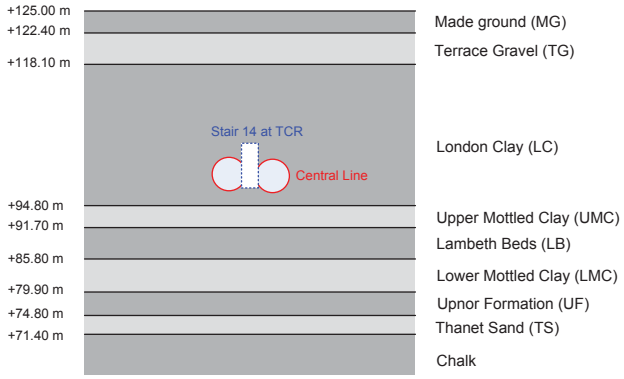

Fig. 4 Geological strata levels at Stair 14, Tottenham Court Road Station, London

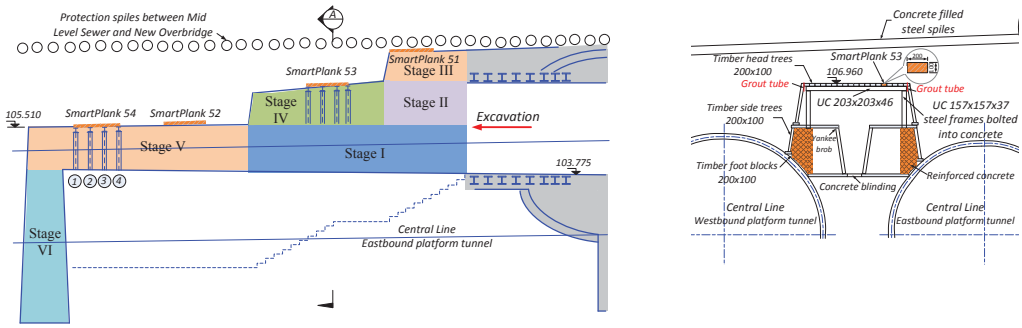

(a) Longitudinal view (b) Sectional view (A-A)

Fig. 5 SmartPlank deployment TCR Stair 14

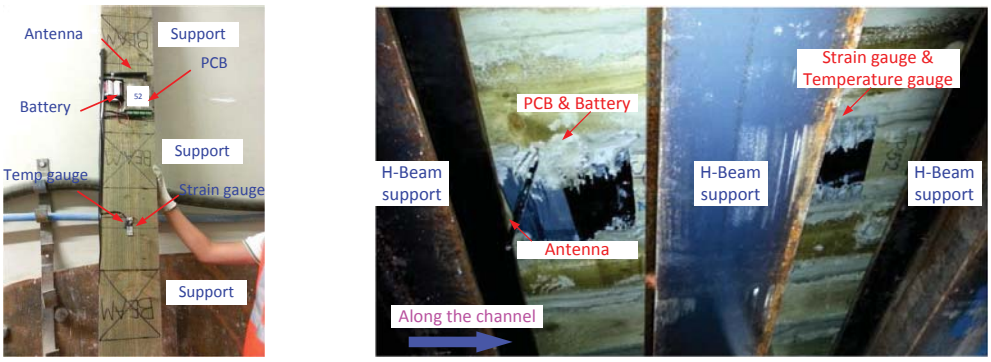

(a) before installation (b) after installation

Fig. 6 Instrumented SmartPlank at TCR Stair 14

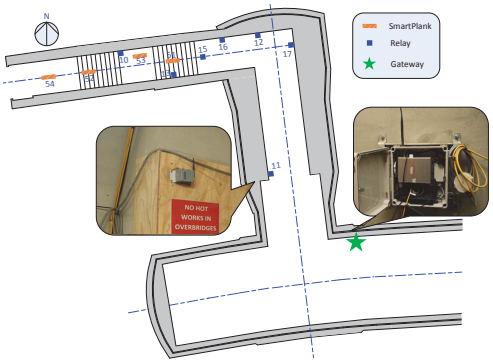

Fig. 7 Wireless sensor network deployment at TCR Stair 14 (plan view)

4. Field performance of SmartPlanks

The SmartPlank monitoring at TCR Stair 14 does indicate movement of the timber supporting system, which will be discussed more in detail here, including observations on both the short-term and long-term performance.

4.1 Cement hydration

Fig. 8 presents the temperature variations captured by the temperature sensors attached on SP52. The first packet of data was received just before the grouting. From Fig. 8, it is observed that the temperature on the top surface of SP52 rose up to 33 degrees around 10 hours after the grouting, and it then gradually decreased to about 25.6 degrees. This is consistent with the classical hydration process of Portland cement. Meanwhile, the temperature variation inside the tunnel is also being monitored by both the temperature sensor in PCB and temperature gauge, with very close measurements. Most of the time, the temperature experienced on the top surface was much higher than the one measured at the bottom, except one occasion on 27th September 2013 probably attributed to the lighting nearby. The maximum and residual temperature differences were up to 10.5 and 2.8 degree respectively.

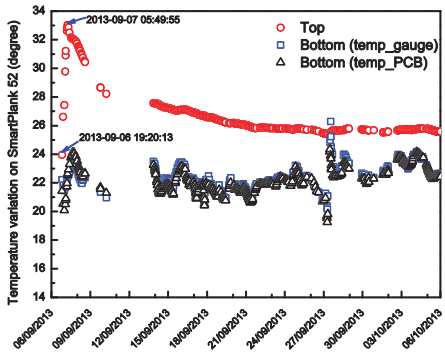

Fig. 8 Temperature variations on SmartPlank 52

4.2 Short-term mechanical performance

Fig. 9(a) illustrates the strain variations experienced on both the top and bottom surfaces of S52 within one month from its installation. The negative strain means compression. It can be clearly observed from Fig. 9(a) that the top surface initially suffered from a very large compression immediately after its installation and then gradually recovered, while the strain happened on the bottom part was much smaller than that of the top part. During the grouting, the peak compression strain was up to 2139.4 micro-strains. This suggests that the grouting had created a downward pressure from the top surface of the plank, together with a pair of extra axial forces, as indicated in Fig. 10. In the meantime, the observed peak compression strain may well exceed the elastic range of the timber, inducing some plastic or permanent damage (Buchanan 1990, Fiorelli and Dias 2003).

The strain on the top surface then dropped rapidly to 41.4% of the peak compression strain when the corresponding temperature reached its maximum value (see Fig. 9). It continued to recover another 24.9% of the maximum compression strain during the cement hardening and shrinking, resulting in a residual compression strain of about 352.8 micro-strains. The SmartPlank was not experiencing pure bending, as there was a residual axial force induced by its installation using wedges. Very similar recovery phenomenon of the compression strain on the top surface of the SmartPlank was also observed from our first pre-trial at Victoria Station (not reported here).

Another instrumented plank, SP54, was the last one installed. At the very beginning of the grouting, the collected strain data on both the top and bottom surfaces indicated that the SmartPlank was largely compressed on both sides, as shown in Fig. 9(b). Unfortunately, a few days after the grouting, it was discovered that there were significant amount of oxidized components in the sensor nodes, caused by unexpected grouting-induced corrosion. The motes stopped working. The oxidized components and the batteries were replaced 24 days after the sensor corrosion due to site inaccessibility. Clearly, extra waterproof precautions must be employed to better protect the sensor nodes. Nevertheless, on the basis of previous analysis, the performance of SP54 was reconstructed, as shown in Fig. 9(b).

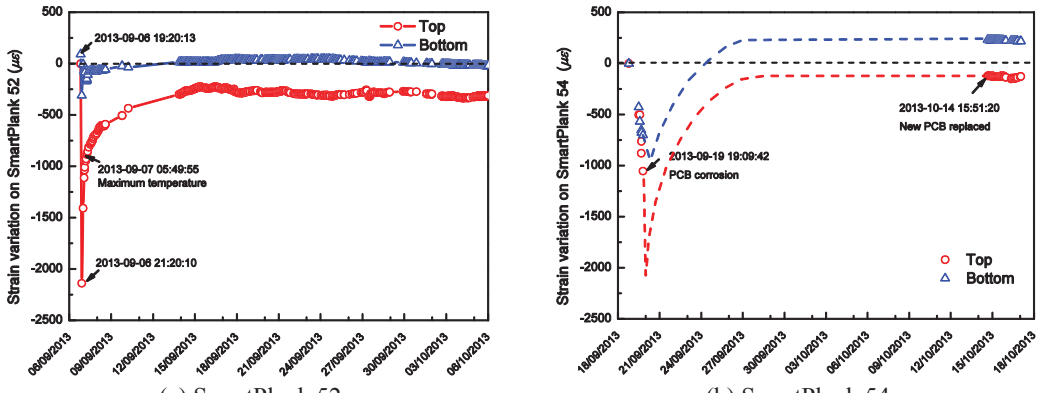

(a) SmartPlank 52 (b) SmartPlank 54

Fig. 9 Short-term performance of SmartPlanks

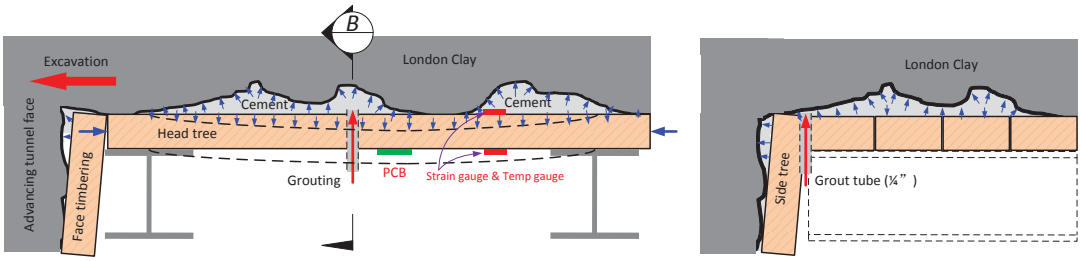

(a) longitudinal view (b) cross-section view (B-B)

Fig. 10 Grouting effect on SmartPlanks

4.3 Long-term mechanical performance

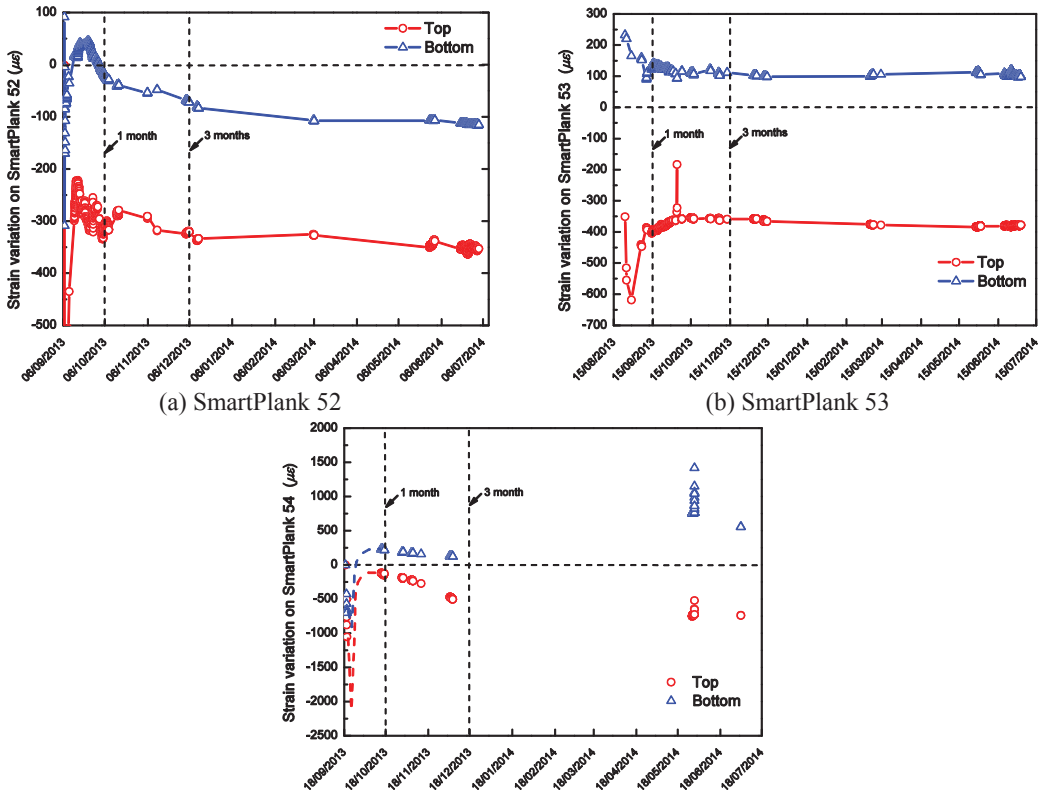

(a) SmartPlank 52 (b) SmartPlank 53

(c) SmartPlank 54

Fig. 11 Long-term performance of timber structures

Fig. 11 presents the long-term performance of SmartPlanks at Stair 14 over a period of 10 months after the installation. It can be observed the figure that all three SmartPlanks continued to deform after the short-term. From December 2013 to May 2014, the data delivery was limited due to antenna damage as well as Contiki software and gateway problems. Despite this, on the basis of the strain rate, their deforming characteristics can be divided into two stages: (1) from 1 month to 3 months; (2) after 3 months. At the first stage, the strain varies in a more rapid way compared to that of the second stage, together with some strain fluctuations. Taking SP52 for an example, the strains on the top and bottom surface vary in a very similar slope, and the average strain rates for both stages are about -0.89 με/day and -0.19 με/day respectively, as shown in Fig. 11(a). For SP53, Fig. 11(b) indicates that there were no clear differences between the strain rates of the two stages mentioned above. Instead, the second stage seems to start from the 1st month, rather than the 3rd one. This is probably due to the relatively high location of SP53, and the protection of the spiles, as shown in Fig. 5.

For SP54, it is obvious from Fig. 11(c) that the strain rates at the 1st stage were much higher than that of the other two. The averaged strain rates for the bottom and top surfaces were up to 1.91 με/day and 7.91 με/day respectively. This attributed to the adjacent deep excavation at stage VI, as shown in Fig. 5(a). At the second stage, although there was not much data collected, some large strain fluctuations were observed at the end of May 2014. Two continuous cracks developed on each side of the walls from November 5th, 2013, between the 2nd and 3rd supports for SP54 (see Fig. 5(a)). The width of the cracks is up to 1mm. This suggests that SP54 experienced some localized movement which may result in the large strain measured.

5. Earth pressure

By assuming a uniformly distributed load, the earth pressure acting on the instrumented planks was estimated using the measured strain according to the beam theory. Two models were adopted to consider different support conditions, and the results are then compared with the current design.

5.1 Simplified model

In this study, a uniformly distributed load is assumed, and two different supporting conditions, namely a simply supported beam (Case 1) and a three-span continuous beam (Case 2), are taken into account, as shown in Fig. 12. All the supports are modeled as elastic bearings, rather than fixed supports, to characterize the contribution from their supporting H-beam frames. The vertical stiffness k_v of the elastic support is obtained by calculating the deformation of the steel frame using the virtual displacement method, and the results are: 42.85 MN/m, 85.69 MN/m and 43.52 MN/m for SP52, SP53 and SP54, respectively. The relatively higher value of stiffness for SP53 is due to its eccentric location, as illustrated in Fig. 7. The horizontal stiffness k_h of the support is simply assumed to be ten times of the vertical ones, but the selection of k_h will not affect the following results in this study.

In Case 1 (see Fig. 12(a)), we assume that each SmartPlank is a simply supported beam during the whole loading process. This implies that the two additional supports placed later (as stated in section 3.2) were not activated at any time. The earth pressure time history $p(t)$ for each SmartPlank is then obtained using the purely bending strain $\varepsilon(t)$. In Case 2 (see Fig. 12(b)), on the other hand, the strain history of each SmartPlank is first divided into two parts: $\varepsilon(t_1)$ for the purely

bending strain measured within the first week of installation and $\varepsilon(t_2)$ for additional strain measured from the second week after its installation. Note that their interpretations toward to the earth pressure are performed separately. The first part of earth pressure time history $p(t_1)$ is calculated in the same way as that in Case 1, using $\varepsilon(t_1)$. However, the second part of earth pressure time history $p(t_2)$ depends on the incremental strain $\Delta\varepsilon(t_2)$, which is taken as the difference between $\varepsilon(t_2)$ and the purely bending strain in a week after the installation ε_0. If $\Delta\varepsilon(t_2)$ is negative, $p(t_2)$ is calculated as the superposition of the earth pressure in a week p_0 and the incremental earth pressure $\Delta p(t_2)$. The former is obtained based on the simply supported beam using ε_0, while the latter is calculated based on the three-span continuous beam using $\Delta\varepsilon(t_2)$. Otherwise, $p(t_2)$ is computed in the same way as that in Case 1, using $\varepsilon(t_2)$.

5.2 Earth pressure

Fig. 13 presents the back calculated vertical earth pressure histories on the two of three SmartPlanks based on the abovementioned two cases. For SP52 as shown in Fig. 13(a), the estimated pressure within the grouting period is 100.60kPa. This matches well to the actual grouting pressure measured (approximately 100 kPa). For the post-grouting stage, there was almost no difference between the two cases, except the period between 21st and 26th September 2013, as indicated in the inset of Fig. 13(a). This is probably due to the adjacent construction work (e.g., prop installation) during that period. The residual earth pressure is estimated to be 13.06 kPa, which corresponds to 3.53% of the total overburden vertical stress σ_v.

For SP53, as shown in Fig. 13(b), most of the data was lost during the grouting stage. The estimated residual earth pressure is 26.92kPa (7.87% of σ_v) for Case 1 and 27.13kPa (7.93% of σ_v) for Case 2. For SP54, the estimated pressure is 75.37kPa (20.34% of σ_v) for Case 1 and 594.92kPa (160.57% of σ_v) for Case 2. The result from Case 2 for SP54 seems to be significantly over-estimated, which is possibly due to some localized pressure with two major cracks observed on the siding walls, as discussed earlier. Therefore, for SP54, the assumption of uniformly distributed load may not be appropriate. Further investigation is needed.

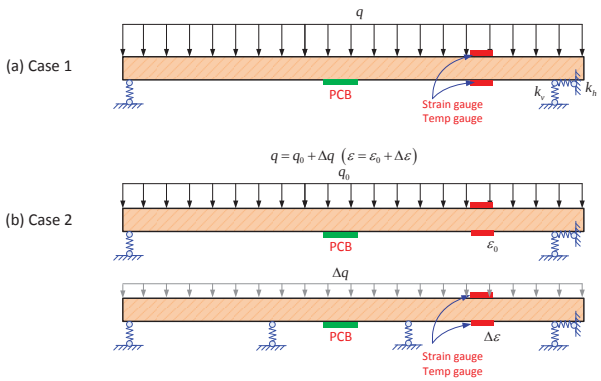

Fig. 12 Longitudinal section of TCR Stair 14

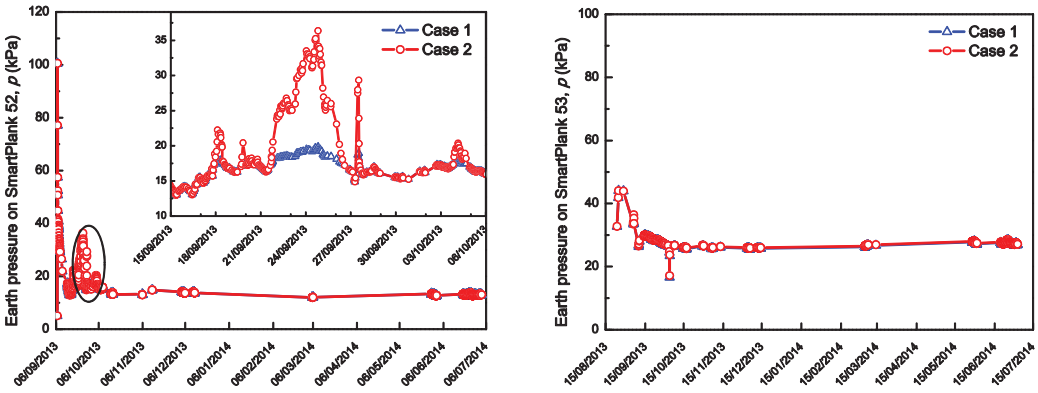

(a) SmartPlank 52 (b) SmartPlank 53

Fig. 13 Calculated earth pressure

5.3 Discussions

Considering the embedded depth, the total vertical overburden pressures σ_v for SP52/SP54 and SP53 are 370.5kPa and 342kPa, respectively. In the design, using Terzarghi's arching theory, the short-term load varies between 15% and 25% of the full overburden for the proposed excavation width at Stair 14. These loads then increase to around 40% of the overburden for the long-term loading condition. The temporary works design comprises of short-term components, timber headings, used to create sufficient space to install the longer-term support elements, steel frames and reinforced concrete. At the design stage, the design load using 25% of the full overburden for short-term ground load was considered to be too conservative, as the installation of stiff concrete filled steel spiles in the Mid-level Sewer in Oxford Street would limit the ground loads acting on the timber headings constructed below (see Fig. 5). Therefore, the design loads for Stair 14 were taken as 15% and 40% respectively, rather than 25% and 40% (Mackenzie 2014).

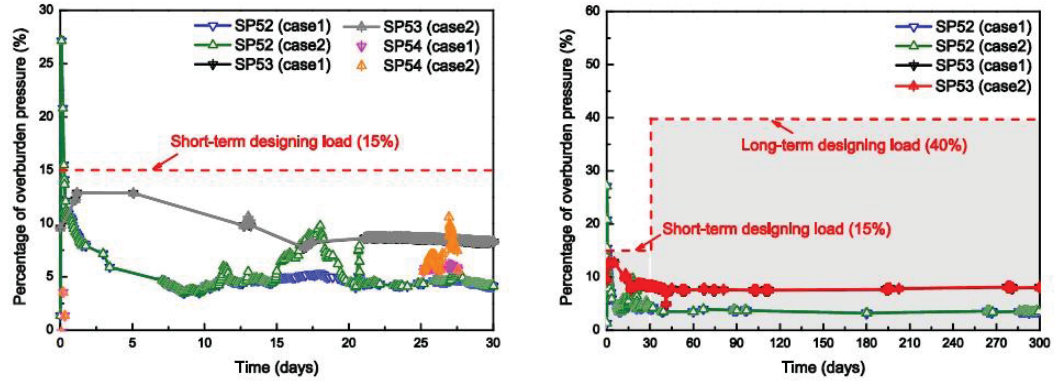

(a) Short-term (b) Long-term

Fig. 14 Comparison between the calculated earth pressure and the designing load

Fig. 14(a) presents a comparison between the estimated earth pressure ratio for the three SmartPlanks and the short-term designing load. As shown in Fig. 14(a), there is not much difference for all three SmartPlanks. The measurements from SP52 rose up to 27.15% during the grouting stage. After that, all the measurements became well below the design load 15%. This indicates that the short term performance of the planks is governed by the grouting process, which is not considered as part of the short-term earth pressure design.

For the long-term earth pressure, as shown in Fig. 14(b), the data recorded so far for the past 10 months indicates that the straining of SP52 and SP53 has stabilized, and hence it is difficult to evaluate whether there are any differences in short and long-term design loads. After 10 months of tunneling, the normalized earth pressures estimated using Case 1 and Case 2 are 3.53% and 3.53% for SP52, and 7.87% and 7.93% for SP53, which appear to be much smaller than the design value of 40%. However, for SP54, the uncertainty in the support made it difficult to evaluate whether the applied earth pressure is within the range of the design value. The effect of localized deformation observed at this location was discussed earlier.

Given the underestimation and overestimation of the short-term and long-term earth pressures on the timber structures respectively, there is an opportunity to improve their design. A set of simple empirical rules for timbering (e.g., an optimized grouting pressure) could largely reduce the timbering components in mass and dimension, and thus reduce the health and safety risks, as well as the construction time and cost. Further investigation is ongoing.

5. Conclusions

This paper proposed a novel wireless sensor network technology to monitor the field performance of timber structures in underground construction. The capability of the system developed was demonstrated through a case study at Stair 14 temporary works, TCR, London. The use of SmartPlank offers an opportunity to improve our understanding on the field performance of the timber structures, which could lead to an optimized design, and a reduced health and safety risk to workers. Ultimately it can be used for real-time monitoring of timber structures to ensure safety of the workers. The key findings are summarized as follows.

- Grouting effect on the short-term performance of timber: the top surface of SP52 experienced a large compression strain during the grouting, and it then gradually recovered even after the hydration rate reaches the peak. The grouting-induced compression strain could be up to 0.22%, which may cause some plastic or permanent damage on the timber. The grouting effect may be minimized by reducing the grouting pressure, or strengthening the support before grouting.
- Cement hydration: the cement hydration process was observed, with temperature rising up to 33 degrees around 10 hours after grouting.
- Timber long-term performance: all three SmartPlanks continued to deform over a period of 10 months after their installation. The deforming process can be divided into two stages: from 1 month to 3 months and after 3 months. For SP52, the strain change at the first stage was around 4.7 times faster than that of the second stage. Much quicker strain change was observed on SP54 probably due the localized deformation caused by nearby construction.
- Earth pressure: results from all three SmartPlanks indicate that the short term performance of the planks was governed by the grouting process, which is not considered as part of the short-term earth pressure design. For the long-term earth pressure, the normalized pressures

estimated from the strain data of SP52 and SP53 were between 3% and 8%, which are much smaller than the design value of 40%. Although the strain development at present is rather small, the planks will be monitored until 2015 to further evaluate their long-term performance.

Acknowledgments

The authors acknowledge the technical assistance from Dr. Jize Yan, Mr. JJ Tang, Dr. Loizos Pelecanos, Mr. Peter Knott, Mr. Samondra Boodhoo and Mr. Alex Alchin. The funding of this project comes from London Underground Limited and the Cambridge Centre for Smart Infrastructure and Construction supported by EPSRC and TSB. The second author acknowledges the support from the Major State Basic Research Development Program of China (973 Program) (No. 2011CB013803).

References

Akyildiz, I.F. and Stuntebeck, E.P. (2006), "Wireless underground sensor networks: research challenges", *Ad Hoc Networks*, **4**, 669-686.

Bennnet, P.J., Kobayashi, Y., Soga, K. and Wright, P. (2010a), "Wireless sensor network for monitoring of underground tunnel", *Proceedings of the ICE, Geotechnical Engineering GE3*, **163**, 147-156.

Bennnet, P.J, Soga, K., Wassell, I.J., Fidler, P., Abe, K., Kobayashi, Y. and Vanicek, M. (2010b), "Wireless sensor networks for underground railway applications: case studies in Prague and London", *Smart Struct. Syst.*, **6**(5-6), 619-639.

Bhalla, S, Yang, Y.W., Zhao, J. and Soh, C.K. (2005), "Structural health monitoring of underground facilities – Technological issues and challenges", *Tunn. Undergr. Sp. Tech.*, **20**, 487-500.

Bierman, R., Piper, P., Carstens, R. and Priest, G. (2013), "A revised timber elongate de-rating factor for platinum mines", *Proceedings of the South African National Institute of Rock Engineering Symposium*.

Buchanan, A.H. (1990), "Bending strength of lumber", *J. Struct. Eng. - ASCE*, **116**(5), 1213-1229.

Daehnke, A., Watson, B.P., Roberts, D., Acheampong, E. and van Zyl, M. (2000), *The impact of soft loading conditions on the performance of elongate support elements*, Safety in Mines Research Advisory Committee, Final Project Report.

Fiorelli, J. and Dias, A.A. (2003), "Analysis of the strength and stiffness of timber beams reinforced with carbon fiber and glass fiber", *Mater. Rese.*, **6**(2), 193-202.

Hoult, N.A., Bennnet, P.J., Stoianov, I., Maksimović, C., Middleton, C.R., Graham, N.J.G. and Soga, K. (2009), "Wireless sensor networks: creating 'Smart Infrastructure'", *Proceedings of ICE, Civil Engineering*, **162**, 136-143.

Kavvadas, M.J. (2003), "Monitoring and modelling ground deformations during tunneling", *Proceedings of the 11th FIG Symposium on Deformation Measurements*, Santorini, Greece.

Kennedy, G.A. and Bedford, M.D. (2014), "Underground wireless networking: A performance evaluation of communication standards for tunneling and mining", *Tunn. Undergr. Sp. Tech.*, **43**, 157-170.

Mackenzie ,C.N.P. (2014), "Traditional timbering in soft ground tunneling", *The British Tunnelling Society*.

Mark, C. and Barczak, T.M. (2000), "Fundamentals of coal mine roof support", *Proceedings of the New technology for coal mine roof support*, Pittsburgh, USA.

Piper, P.S. and Malan, D.F. (2008), "The in-situ performance of elongate support – myths and realities", *Proceedings of the 6th International Symposium on Ground Support in Ming and Civil Engineering Construction*, Cape town, South Africa.

Robert, M.K.R., Riemann, K. and Jager, A.J. (1987), *The performance characteristics of timber props*, Chamber of Mines Research Organisation, Research Report.

Stajano, F., Hoult, N.A., Wassell, I.J., Bennett, P.J., Middleton, C.R. and Soga, K. (2010), "Smart bridges, smart tunnels: transforming wireless sensor networks from research prototypes into robust engineering infrastructure", *Ad Hoc Networks*, **8**, 872-888.

Szwedzicki, T. (1989), "Geotechnical assessment deficiencies in underground mining", *Mining Sci. Technol.*, **9**, 23-37.

Terzaghi, K. (1946), *An introduction to tunnel geology*, in Rock Tunnelling with Steel Supports, (Eds., Proctor R.V. and White T.L.), The Commercial Shearing and Stamping Co, Youngstown, Ohio, USA.

Yeow, H.C., Nicholson, D. and Man, C.L. (2014), "Application of observational method at Crossrail Tottenham Court Road station, UK", *Geotech. Eng.*, **167**(2), 182-193.

Smart Structures and Systems, *Vol. 15, No. 3 (2015) 787-806*
DOI: http://dx.doi.org/10.12989/sss.2015.15.3.787

Damage identification of belt conveyor support structure using periodic and isolated local vibration modes

Amin Honarbakhsh[1a], Tomonori Nagayama[*2], Shohel Rana[2b], Tomonori Tominaga[3], Kazumasa Hisazumi[3] and Ryoichi Kanno[3]

[1]*Honarbakhsh Construction Office, Iran*
[2]*Department of Civil Engineering, the University of Tokyo, Tokyo, Japan*
[3]*Nippon Steel and Sumitomo Metal Corporation, Tokyo, Japan*

(Received October 22, 2014, Revised January 11, 2015, Accepted January 15, 2015)

Abstract. Due to corrosion, a large number of belt conveyors support structure in industrial plants have deteriorated. Severe corrosion may result in collapse of the structures. Therefore, practical and effective structural assessment techniques are needed. In this paper, damage identification methods based on two specific local vibration modes, named periodic and isolated local vibration modes, are proposed. The identification methods utilize the facts that support structures have many identical members repeated along the belt conveyor and there exist some local modes within a small frequency range where vibrations of these identical members are much larger than those of the other members. When one of these identical members is damaged, this member no longer vibrates in those modes. Instead, the member vibrates alone in an isolated mode with a lower frequency. A damage identification method based on frequencies comparison of these vibration modes and another method based on amplitude comparison of the periodic local vibration mode are explained. These methods do not require the baseline measurement records of undamaged structure. The methods is capable of detecting multiple damages simultaneously. The applicability of the methods is experimentally validated with a laboratory model and a real belt-conveyor support structure.

Keywords: damage Identification; belt conveyor; local vibration mode; periodic structure; sensitivity analysis

1. Introduction

A large number of belt conveyor support structures in industrial plants have deteriorated due to corrosion. The corrosion may cause structural failure endangering the safety of the working conditions. The failure may also result in significant social and economic loss. In case of ironworks, the total length of belt conveyors, carrying iron-ore and other materials, often reaches tens of kilometers. Dust falls from the belt and adheres to the support structure. Kilograms of dust accumulates on support structure members. Accumulated dust, which is sometimes wet due to rain, causes severe corrosion. The corrosions occasionally result in the complete loss of cross section.

∗Corresponding author, Associate Professor, E-mail: nagayama@bridge.t.u-tokyo.ac.jp
[a] Ph.D., E-mail: amin_honarbakhsh@yahoo.com
[b] Ph.D. Student, E-mail: rana@bridge.t.u-tokyo.ac.jp

http://www.techno-press.org/?journal=sss&subpage=8 ISSN: 1738-1584 (Print), 1738-1991 (Online)

Furthermore, the occurrence of multiple corrosion damages is not rare. Effective monitoring and assessment of such structures are needed.

For the condition assessment of structures, a significant amount of research efforts have been made in the field of structural health monitoring (SHM). Some research has been performed on the health monitoring of belts or machinery parts of belt conveyors (Harrison 1980, Mazurkiewicz 2008). However, structural condition assessment of the support structure has not been studied in details.

Condition assessment based on dynamic property changes has been studied by many researchers in the last three decades (Ewins 1985, Ojalvo and Pilon 1988, Mottershead and Friswell 1993, Salawu 1997, Law *et al*. 1998, Shi and Law 1998, Kim and Bartkowicz 2000, Shi *et al*. 2000, Ricci 2000, Park and Kim 2002, Ren and De Roeck 2002, Gao and Spencer 2008, Yang *et al*. 2009, Dinh *et al*. 2012). Comprehensive reviews of existing techniques are available (Doebling *et al*. 1996, Chang *et al*. 2003, Sohn *et al*. 2004, Carden and Fanning 2004, Farrar and Worden 2007). However, these techniques have not seen practical usage in belt conveyor support structure monitoring. The damage introduced and identified were limited to only a few elements while the corrosion damages on the support structures are not. Moreover, before-and-after comparison of structures, which is often impractical for the support structure assessment, has been assumed. In addition, the non-structural members of belt conveyor such as machinery parts and sidewalks affect the global vibration modal properties because the size of these members are not small as compared to the size of support structures.

In this paper, new damage identification methods for secondary members of belt conveyor support structures based on local vibration modes are proposed. Periodic Local Vibration Modes (PLVM) and Isolated Local Vibration Modes (ILVM) are utilized to overcome the difficulties in identifying a large number of damage elements in the absence of baseline measurement records of undamaged structures. Local vibration modes are difficult to observe because the modes usually appear in high frequency ranges and are small in amplitude. The differentiation of specific local modes among numerous local modes is also difficult. To enable observation and differentiation of local vibration modes efficiently, the Laser Doppler Vibrometer (LDV), capable of non-contact measurement of small vibration with a high resolution in a wide frequency range, is utilized. First, a finite element model of the support structure is constructed using commercial FE software, ABAQUS (Abaqus FEA 2015) and dynamic characteristics of the structure are investigated. Then the sensitivity analyses of the frequencies of PLVM and ILVM to several parameters are carried out. The applicability of these modes in damage identification is investigated. Finally, the proposed methods are experimentally validated in a laboratory model as well as in a real belt conveyor structure.

2. Finite element model of the beltconveyor support structure

A design drawing of a typical belt conveyor is shown in Fig. 1(a). One representative span of this support structure is modeled in ABAQUS (Fig. 1(b)). The support structure consists of the main frame and columns. The main frame consists of main and secondary members. The main members include continuous longitudinal members. The secondary members include braces, lateral members, and vertical members; these members are connected to the longitudinal members. The connections between the columns and the ground and those between the main frame and columns are modeled as fixed. Three-dimensional linear beam element are employed for all

members.

3. Local vibration modes of the main frame

The eigenvalue analysis shows that there are some modes within a small frequency range where all identical members strongly vibrate. Here, the identical members are defined as the secondary members of the same cross sections, lengths, and local boundary conditions. Because these members have nearly the same intervals along the longitudinal direction, the modes are named Periodic Local Vibration Modes (PLVM). As an example, one of the PLVM of the top and bottom braces is shown in Fig. 2. The mode shape amplitudes at the identical members are much larger than those at the other members; the amplitudes at connection points are small. On the other hand, no PLVM of the continuous main members exists. The damage identification methods discussed in this paper utilize PLVM and are not applicable to the main members.

If one of the identical members is damaged, this damaged member does not vibrate in the PLVM; instead, only this damaged member vibrates in another mode named Isolated Local Vibration Modes (ILVM). In fact, the damaged member is no longer identical with the other members and the dominant frequency shifts. Example PLVM and ILVM are shown in Fig. 3. The damaged member, shown in red, is under isolated vibration in the ILVM and does not vibrate in the PLVM. Other than PLVM and ILVM, there are many local modes, such as combination of local and global vibration modes, and other modes, where all or some of non-identical members vibrate.

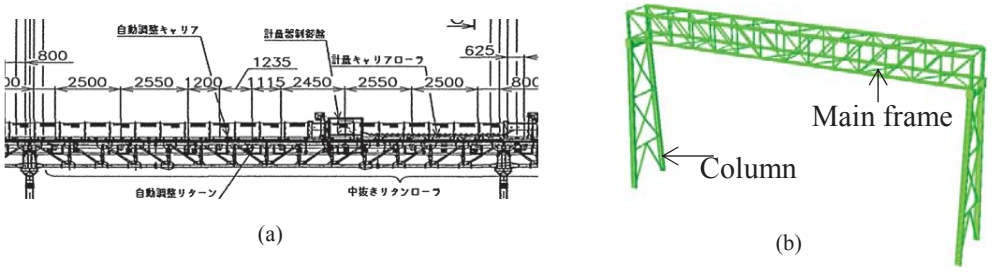

Fig. 1 Modeled span of the belt conveyor; (a) Design drawing of main frame and (b) FE Model

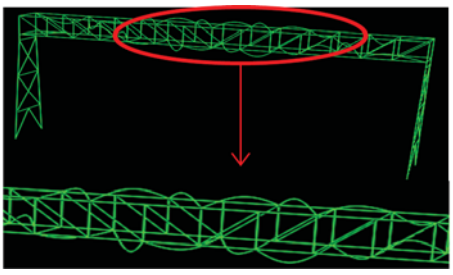

Fig. 2 One of the PLVM of the undamaged structure

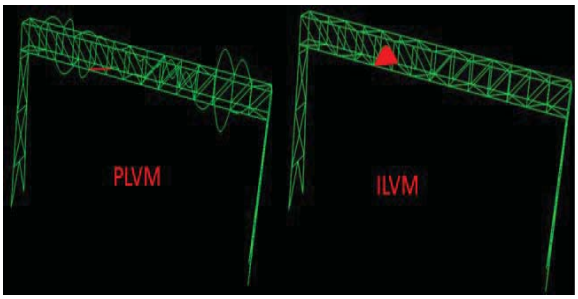

Fig. 3 PLVM and ILVM of the damaged structure

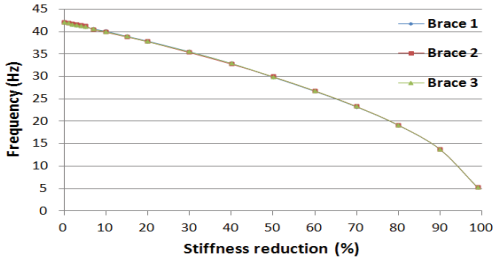

Fig. 4 Frequency changes of ILVM versus stiffness reduction

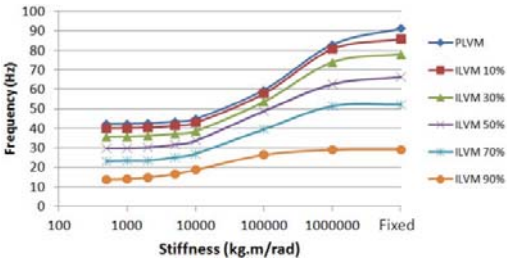

Fig. 5 Frequency changes of PLVM and ILVM versus stiffness change of the rotational springs

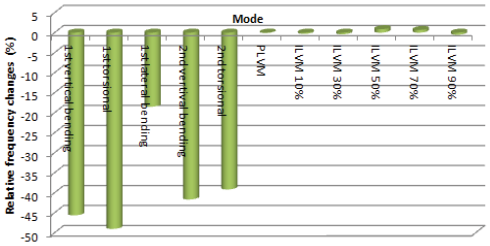

Fig. 6 Relative frequency change versus stiffness reduction of the longitudinal members

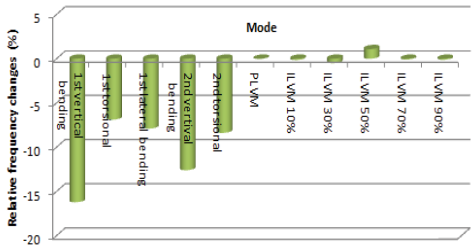

Fig. 7 Relative frequency change versus stiffness reduction of the two columns

4. Sensitivity of PLVM and ILVM to parameter changes

The sensitivity of PLVM and ILVM frequencies to various structural parameters is investigated herein. The parameters include the properties of the secondary member, local boundary conditions (i.e., stiffness of rotational springs at the connection points), the properties of the longitudinal members and the global boundary conditions of the main frame (i.e., properties of the columns).

To investigate the sensitivity of the ILVM frequency to the secondary member stiffness changes, the Young's moduli of three identical braces, i.e., brace 1, 2 and 3, at the bottom and top are changed. The sensitivity is large and almost the same for all identical members (Fig. 4).

The sensitivity to the rotational springs at the ends of secondary members is then investigated. The frequency of PLVM and ILVM significantly changes when the rotational spring stiffness at the ends of bottom brace members changes (see Fig. 5).

Next, the sensitivity to the stiffness of the main longitudinal members is examined. The stiffness of all longitudinal members is reduced by 80%. In addition, the frequency change of some global vibration modes are shown for comparison. The frequency change of PLVM and ILVM are always less than 0.8% (see Fig. 6).On the other hand, the frequencies of global vibration modes are much more sensitive than the frequencies of PLVM and ILVM.

As for the boundary conditions of the main frame, the stiffness of all members of the two columns is reduced by 80%. The frequency changes of PLVM and ILVM, as well as those of global modes, are shown in Fig. 7. The changes of PLVM and ILVM are always less than 1%.

Thus, the PLVM and ILVM frequencies are sensitive to the properties of the secondary members and their local connections. The effects of global boundary conditions and the properties of the main longitudinal members are negligible. These local modes are considered equivalent to the modes of the simply supported beam. The secondary member properties and their connections can therefore be updated based upon the frequencies of the local modes. Next, damage identification methods using PLVM and ILVM are discussed.

5. Damage identification by comparing the frequencies of local vibration modes

5.1 Damage identification principle

Consider a uniform simply supported beam with two rotational springs with stiffness, k_{r1} and

k_{r2}, as shown in Fig. 8. The hinge corresponds to the stiffness of $k_r=0$ and the clamped end corresponds to the stiffness of $k_r=\infty$.

The n^{th} natural frequency, ω_n, of the elastic beam can be represented as the square of a dimensionless coefficient, λ_n multiplied by the fundamental frequency of the hinged end beam

$$\omega_n = \lambda_n^2 \sqrt{\frac{EI}{\rho A L^4}} \tag{1}$$

in which, EI is the flexural rigidity, ρA is mass per unit length and L is the span length. λ_n is the n^{th} non-zero root of the following equation (Maurizi *et al*. 2003)

$$2R_1R_2\phi_1(\lambda)\lambda^2 + (R_1 + R_2)\phi_6(\lambda)\lambda - \phi_4(\lambda) = 0 \tag{2}$$

where

$$R_1 = \frac{EI}{k_{r_1}L},\ R_2 = \frac{EI}{k_{r_2}L}\ ,\ \phi_1(\lambda) = \sin(\lambda)\sinh(\lambda), \phi_4(\lambda) = \cos(\lambda)\cosh(\lambda) - 1,$$

$$\phi_6(\lambda) = \sin(\lambda)\cosh(\lambda) - \sin h(\lambda)\cos(\lambda) \tag{3}$$

The frequencies of PLVM and ILVM are used in the above equations to evaluate the stiffness parameters. From Eq. (1), λ_n is

$$\lambda_n = \left(\frac{\omega_n}{\sqrt{\frac{EI}{\rho A L^4}}}\right)^{0.5} \tag{4}$$

The frequency of PLVM, ω_n, is measured and ρA, EI, and L are obtained from the design drawings. Thus, λ_n is calculated. When the connection designs at both ends of each secondary member are identical, the stiffness of rotational springs at the ends of each member has the same values. Eq. (2) is written as

$$2R^2\phi_1(\lambda)\lambda^2 + 2R\phi_6(\lambda)\lambda - \phi_4(\lambda) = 0 \tag{5}$$

where $R = \frac{EI}{k_r L}$ and $k_r = k_{r1} = k_{r2}$. The only unknown parameter, k_r, which is the rotational spring stiffness at the ends, is obtained numerically from this equation.

For damaged members, the frequency of ILVM, ω_n is known. The damage is assumed to occur only on the members. The stiffness of rotational springs at the ends is thus the same as that of undamaged members. Therefore, the only unknown parameter in Eq. (5), *EI*, is identified numerically.

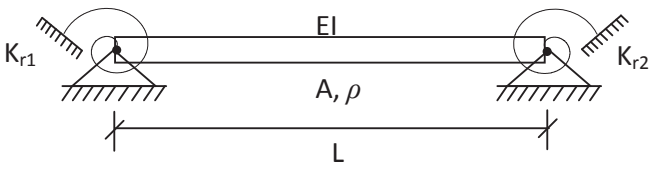

Fig. 8 A simply supported beam with two elastic rotational springs at the ends

In practice, observation of PLVM and ILVM is difficult unless these modes are strongly excited. Direct excitations effectively excite the corresponding PLVMs or ILVMs and help identification of the PLVM frequencies among many other modes. In experiments, a secondary member is directly hit by Hammer while its response is measured by the non-contact LDV. This process is repeated for all the secondary members by moving the Hammer and LDV. Note that the responses of nodal points and some secondary members of different design are also measured; by comparing the power spectrums of responses of identical design secondary members and others, PLVM, ILVM, and other modes are distinguished. The frequencies of the modes are identified by the peak-picking method.

5.2 Application to a numerical model

Damages introduced to the finite element model of a support structure are identified using the proposed method (see Fig. 9).There are four identical member sets in the main frame. In total, 18 members have been damaged with different severities. The percentage of stiffness reduction is shown in Table 1. These reductions of stiffness are considered as damages. Note that the introduced stiffness reductions are of realistic damage level. There are support structures of belt conveyors with severely corroded members. Even a complete loss of cross section is not rare.

The velocity time history of the main frame of the support structure are obtained through dynamic implicit analysis with a sampling frequency of 5000 Hz after both columns are hit near the bottom. Because no noise is introduced, the excitation even at the columns, instead of the excitation at each secondary member, resulted in sufficient observability of the local modes. The power spectrum of the bottom and top braces and one lateral member are shown in Fig. 10. There are five ILVM corresponding to the damaged members and one PLVM frequency range. In the PLVM range, the amplitude of the undamaged bottom and top braces are much larger than the other members. The other peaks correspond to global vibration modes or other modes in which all or some parts of the structure vibrate. The PLVM range is zoomed in and shown in Fig. 11(a). The PLVM frequency range is defined as the frequency range between the lowest PLVM frequency and the highest PLVM frequency. Note that the rightmost bottom brace and the lateral member are not of the identical design with the other bottom and top braces.

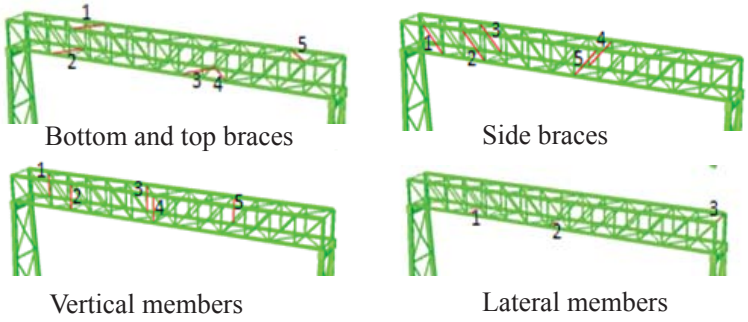

Fig. 9 Damaged members in different member sets

Table 1 Stiffness reductions introduced in the FE model and their estimation

Member sets	Member 1		Member 2		Member 3		Member 4		Member 5	
	*a	*b	a	b	a	b	a	b	a	b
Bottom and top braces	75	74.81	5	4.50	10	10.10	20	19.70	35	35.19
Side braces	90	89.86	5	5.15	65	64.38	25	25.39	25	25.39
Vertical members	85	85.11	5	5.27	55	55.32	15	15.86	30	31.74
Lateral members	5	4.28	15	14.06	40	39.69	-	-	-	-

*a = Stiffness reduction (%) introduced in the FE model; b = Estimated stiffness reduction (%)

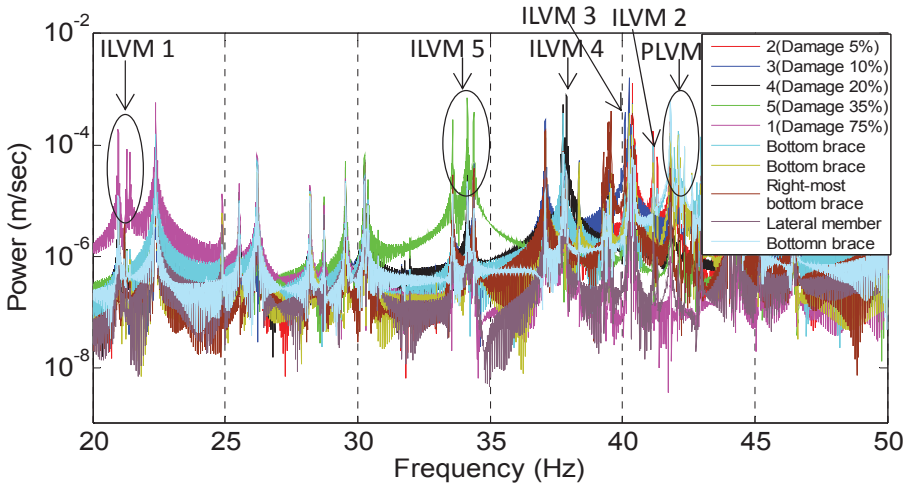

Fig. 10 Fourier spectrum indicating PLVM and ILVM frequency peaks of the bottom and top braces

The ILVM peak corresponding to member 5 is shown in Fig. 11(b). There are three peaks where the amplitude of member 5 is much larger than the other members. Only one of these three peaks is considered to be the ILVM of member 5; however, because the frequency of ILVM is at the vicinity of two other modes, there are, in total, three peaks. In case of existence of many peaks, the mean value of frequencies of these peaks is defined as the frequency of ILVM.

Likewise, based on PLVM and ILVM frequencies, damages of the other members are identified (see Table 1). The maximum error is 1.74% at vertical member 5. For the other damaged members, the error is less than 1%. The main cause of the damage quantification error is considered the coupling of closely spaced modes. As the signal to noise ratio can be improved by adjusting the impact force, the observation noise is not considered in this analysis.

If damage is considered both on the members and the local connections of the members, the higher PLVM and ILVM needs to be utilized to distinguish and quantify these damages. When Eq.

(2) or (5) are not directly applicable (e.g., three dimensional model), model updating can be performed; the boundary conditions are first identified from frequencies of undamaged members and then damage member stiffness is identified from those of damaged members.

6. Damage identification by comparing the amplitudes of local modes in the PLVM range

6.1 Damage identification principle

The damage quantification method introduced in previous section requires local mode frequency identification of each member, which is typically realized by directly hitting each member. However, direct hit of every member is oftentimes impractical. Damage identification without the need of direct hit of every member is introduced herein. The method can localize damages and evaluate their relative severity.

Consider the impact load, $P_0\delta(t)$, applied at location l

$$\{P(t)\} = P_0\delta(t)E_l \tag{6}$$

where E_l is a unit vector whose elements except for the location of impact are all zero. The impulse response in the modal coordinate, $q_i(t)$, is written as

$$q_i(t) = \frac{P_0\phi_{i,l}}{m_i\omega_i} sin\omega_i t \tag{7}$$

where $\phi_{i,l}$ is the i-th mode shape at the location l, m_i is the generalized mass and ω_i is the i-th natural frequency. The response in the PLVM frequency range at the location $m$in the physical coordinate, $x_m(t)$ is approximately obtained by summing all PLVM components as follows

$$x_m(t) = \sum_i \frac{P_0\phi_{i,m}\phi_{i,l}}{m_i\omega_i} sin\omega_i t \cong \sum_{i\in PLVM} \frac{P_0\phi_{i,m}\phi_{i,l}}{m_i\omega_i} sin\omega_i t \tag{8}$$

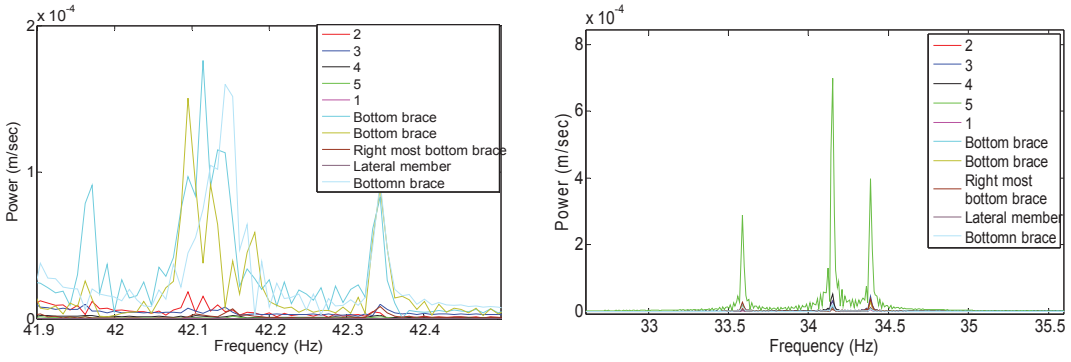

Fig. 11 (a) Fourier spectrum of the PLVM frequency range of the bottom and top braces (b) Fourier spectrum of the ILVM of member 5

The maximum modal amplitude at the location m in its PLVM range, x_{ml}, is

$$x_{ml} = \max_i \frac{P_0 \phi_{i,m} \phi_{i,l}}{m_i \omega_i} \tag{9}$$

When the mode shape amplitude is large both at location l and m, as in PLVMs of undamaged members, the maximum modal amplitude is large. When the member at the location m is damaged, the PLVM mode shape is small at this point. Therefore, the maximum modal amplitude at the damaged member is small. Thus, the location of damage is indicated by the maximum modal amplitude. This maximum modal amplitude is approximately obtained as the peak values of frequency spectrum of $x_m(t)$ in the PLVM range. The differences come from closely spaced modes.

In practice, the location of damage is identified by comparing the spectrum peak values in the PLVM range when an impact load is applied at one undamaged member. One undamaged member is identified first. In case of the belt conveyor support structure, some undamaged members are easily identified by visual inspection. One of these undamaged member is hit by a Hammer equipped with a load cell while the response of an identical design secondary member is measured by LDV. This measurement is repeated for all of the identically designed secondary members while the Hammer hit location is unchanged. The response signals are normalized by the input force. Then the frequency spectrum amplitudes of all the identical design members are compared to identify the PLVM frequency range. In the identified range, the spectrum amplitudes are compared with each other to identify the damaged members and their severity.

6.2 Application to a numerical model

The proposed method is numerically examined using the same model (see Fig. 9). There are 24 identical bottom and top braces in the main frame and damage is introduced at five members. Brace 1is hit and the velocity time histories of all 24 identical bottom and top braces are obtained. The maximum Fourier amplitudes of the velocity responses in their PLVM range are shown in Fig. 12. The maximum amplitudes for damaged members, 2, 8,9,13, and 22, are much smaller than those of the other members. Moreover, severer damages results in smaller amplitudes. By comparing the value of maximum amplitude of Fourier spectrum in the PLVM range, the damage degree is estimated. The damaged members are ordered from the member with the smallest amplitude as 22, 13, 9, 8 and 2 in Table 2. This order is consistent with the damage degree (see Table 1).

The observation noise is not considered in this analysis either because the signal to noise ratio can be improved by adjusting the impact force. The coupling of closely spaced modes is considered the main source of the estimation error.

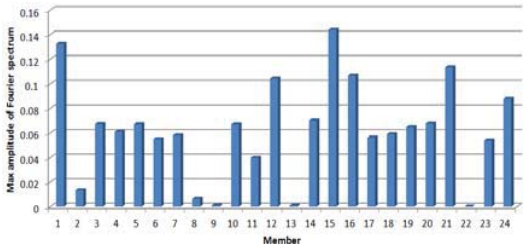

Fig. 12 Maximum Fourier spectrum amplitude of the 24 bottom and top braces in their PLVM range when brace No 1 is hit

Table 2 Maximum amplitude of damaged members in PLVM range

Member	Damage degree	Max amp. in PLVM
2	5%	0.01338
8	10%	0.006375
9	20%	0.001191
13	35%	0.000918
22	75%	0.000201

7. Local mode property changes of a laboratory truss structure

The proposed damage identification techniques are applied to a laboratory truss model and the identification performances are examined. The scale model is 5-bay truss frame shown in Fig. 13. The model is 2 m tall from its base plate and the dimension of each bay is 41×41×40 cm. The four vertical continuous main members are made of 1.5 cm steel solid rods. The model has diagonal and lateral secondary members made of aluminum pipes. Their external and internal diameters are 1.0 cm and 0.8 cm, respectively. The vertical member go through the connection element while the other members are connected to the elements via thinner threaded rods and nuts (see Fig. 13).

To simulate damage, several secondary members are replaced with rods with various diameters. Also some secondary members are partially cut. Locations of simulated damage members are shown in Fig. 14(a). The detail of damage members are provided in Table 3.

7.1 The frequencies of local vibration modes

In order to localize and quantify the damage using frequencies of PLVM and ILVM of the secondary members, each member is directly hit and its velocity time history is measured by Laser Doppler Vibrometer (LDV) (see Fig. 13). The sampling frequency is 10,000 Hz. In order to compare the local vibration modes with the vibration of a simply supported beam, the truss is also disassembled and each member is separately installed on the two connection elements which are fixed to the base plate (see Fig. 14(b)).

As for the undamaged diagonal and lateral members, there are PLVMs, in which only undamaged members vibrate. The power spectrum of some undamaged diagonal members are shown in Fig. 15. The PLVM ranges of diagonal members are 104-114Hz. All undamaged members, including those not shown, strongly vibrate in the PLVM range.

The ILVM frequencies of the damaged diagonal member, member 13, is shown in Fig. 16. The damage members do not vibrate in PLVM range. The ILVM frequency peak below the PLVM ranges is clearly observable. Then the model is disassembled so that each secondary member is measured separately. The frequency peak of the local vibration mode and that of the separate simple beam are close with each other (see Fig. 16). The 1st PLVM and ILVM of the secondary members and the 1stnatural frequencies of the corresponding simple beams are summarized in Table 3. The frequencies of the local modes are nearly the same as the natural frequencies of the corresponding simple beams.

Fig. 13 Laboratory truss structure

(a) (b)

Fig. 14 (a) Location of the damaged members and (b)Measurement of each member with LDV

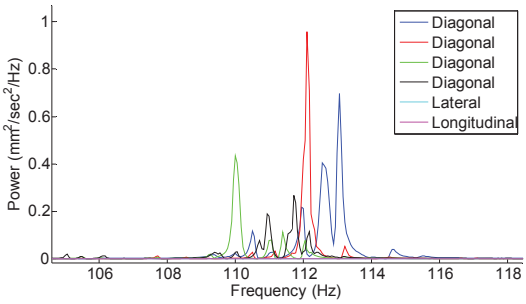

Fig. 15 PLVM range (undamaged diagonal members)

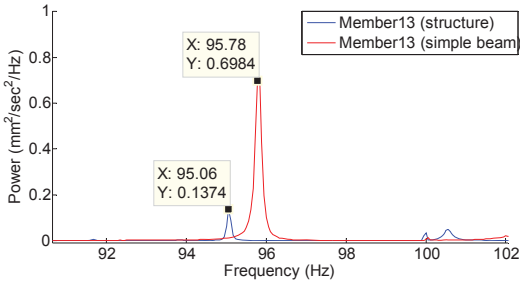

Fig. 16 Power spectrums of member 13 in the structure and the member fixed on the base plate

Table 3 Frequencies of ILVM and PLVM of secondary members and their corresponding simple beams

Member No.	Cross section	Type	Freq (Hz) Structure	Freq (Hz) Simple Beam	Member No.	Cross section	Type	Freq (Hz) Structure	Freq (Hz) Simple Beam
1	Φ13×1	ILVM	132.2	130.8	9	Φ10×1 (1/3 cut)	ILVM	201	198.6
2	Φ12×1	ILVM	230.82	233.6	10	Φ10×1 (1/2 cut)	ILVM	92.22	93.44
3	Φ11×1	ILVM	115.5	114.1	11	Φ9.5×1	ILVM	109.3	107.7
4	Φ10×1 (1/2 cut)	ILVM	186.2	188.1	12	Φ13×1	ILVM	245.2	247.6
5	Φ12×1	ILVM	228.4	233.6	13	Φ8×1	ILVM	95.06	95.83
6	Φ13×1	ILVM	127.4	126	Undamaged Diagonal elements	Φ10	PLVM	104~114	112.1
7	Φ10×1 (2/3 cut)	ILVM	89.61	90.06	Undamaged Lateral elements	Φ10	PLVM	204~213	207.6
8	Φ8×1	ILVM	167	167.1					

7.2 The amplitude of local modes in the PLVM range

The amplitudes of local modes in the PLVM frequency ranges are examined using the scale model. The damaged structure considered here is same as that in Fig. 14(a). The maximum power spectrum amplitudes of diagonal members in the PLVM frequency range (i.e., 104 to 114 Hz) are summarized in Fig. 17 when one of the undamaged diagonal members is hit. The damaged members generally have smaller amplitudes than intact members. The exception is member 11 (Φ9.5×1). Because the damage severity is small, its frequency of ILVM remains in the PLVM frequency range. The local mode amplitudes of member 11 in the PLVM frequency range is therefore large.

Fig. 18 shows the maximum power spectrum amplitude for lateral members in PLVM range when one of the undamaged lateral members is hit. The maximum amplitude of the damaged lateral members in PLVM range is smaller than intact lateral members. The exception is member 9. Because the damage severity is small, its frequency of ILVM is close to the PLVM range. Thus, damaged lateral members are identified by comparing amplitudes except for small damage. Note that the input force was not measured through this analysis due to limitation in experimental setup. Measurment of the input force and normalization of the output data are expected to result in better identification.

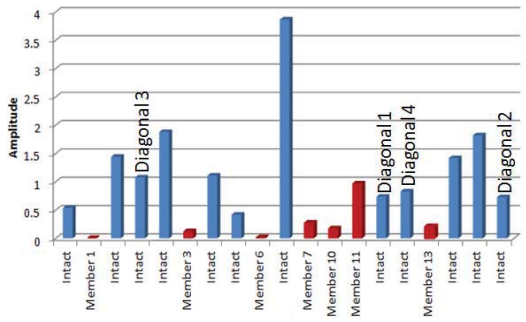

Fig. 17 Maximum power spectrum amplitude of the diagonal members in PLVM range

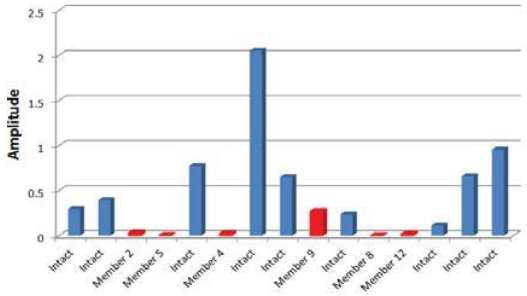

Fig. 18 Maximum power spectrum amplitude of the lateral members in PLVM range

8. Damage identification of a real belt conveyor

8.1 Damage identification by comparing the frequencies of local vibration modes

Damage identification is performed on a real belt conveyor shown in Figs. 19(a) and 19(b). This structure contains a support structure of the belt conveyor, walkways, machinery parts and some non-structural segments protecting the machinery parts. The length is 10 m. All members are of L50×50×6 made of SS400. Lateral members are 1.3 m long while side braces are 1.06 m long.

To identify PLVM and ILVM among various local vibration modes, the velocity time histories of points shown in Fig. 19(b) are obtained by LDV while each member is directly hit. The sampling frequency is 10,000 Hz. Note that the lateral members are measured along the vertical direction while longitudinal members, side braces and vertical members are measured along the horizontal direction.

The identification results of lateral members are discussed herein. The members 1 to 5 indicated by the sensor location number in Fig. 19(b) are assessed. The power spectrums of the lateral members together with other members are shown in Fig. 20. Each member is directly hit during the measurement. There is a range in which only members 3 and 4 strongly vibrate. This range corresponds to the 1stPLVM of the undamaged lateral members. Moreover there are three

peaks corresponding to the1stILVM of member 1, 2 and 5. These members are considered damaged. Also, the severity of the damage, in terms of the frequency change, is in the order of member 2, 1 and 5. This severity is consistent with visual inspection results. Member 2, shown in Fig. 21, clearly has the severest corrosion.

Note that higher order PLVM and ILVM are also observed (see Fig. 22). The measurement are performed at the quarter point of the lateral members (see Fig. 19(b)). The frequency ranges of PLVMs of lateral members and the ILVM frequencies of the damaged members are shown in Tables4 and 5, respectively.

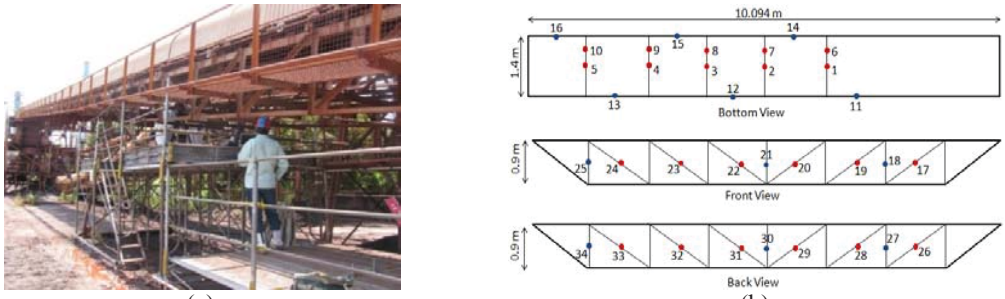

(a) (b)

Fig. 19 (a) A real belt conveyor and (b)Measurement points of the belt conveyor

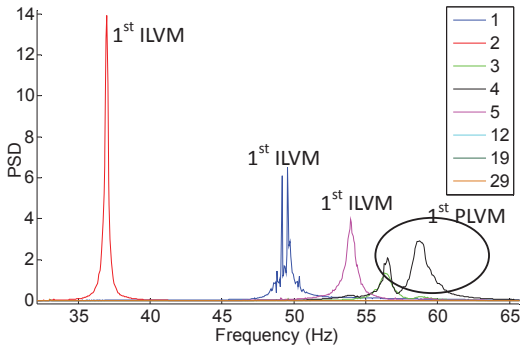

Fig. 20 Power spectrums of the lateral members together with some other members

Fig. 21 A corroded part of member 2

Then, the absolute severity of the damage is evaluated assuming the connections are undamaged as in section 5.1. First, the frequencies of PLVM for the two undamaged members are utilized to evaluate the stiffness of springs at the ends of the undamaged members. The rotational springs are identified by model updating. Table 6shows the estimated values of the springs at the ends of the lateral members. The natural frequencies and mode shapes of a beam with the same springs at two ends are shown in Fig. 23. The natural frequencies are close to those of PLVMs, which indicates the similarity of PLVM to vibration of an independent beam.

Then, the stiffness reduction, i.e., reduction of *EI*, of the damaged members is estimated. The estimated stiffness reduction values are summarized in Table 7. The natural frequencies of the simple beam with the identified stiffness reduction and the rotational spring at the ends are also shown in Table 7. The frequencies are close to the observed ILVM frequencies in Table 5. Note that the assumption of uniform damage is not necessarily satisfied. This assumption is considered a source of damage identification errors.

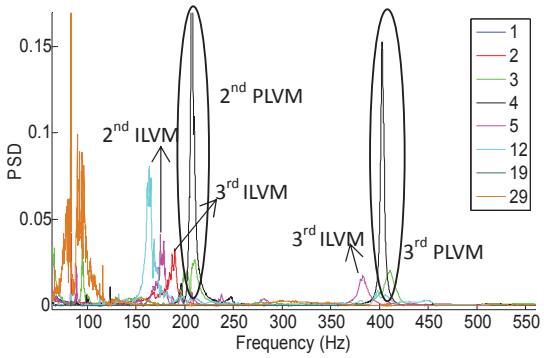

Fig. 22 Some higher PLVM and ILVM of the lateral members

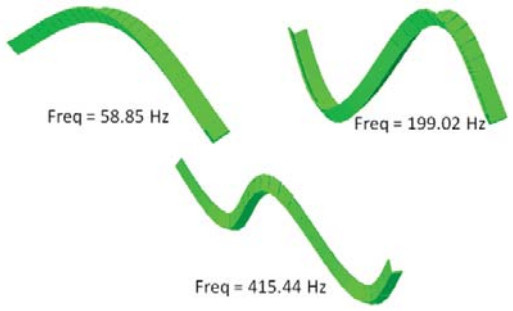

Fig. 23 Corresponding modes of the beam with the estimated spring values

Table 4PLVM frequency ranges of lateral members (Hz)

Member	1st PLVM	2nd PLVM	3rd PLVM	Condition
3 , 4	56.33 - 58.94	199.2 – 207.4	402.4 – 411.4	Undamaged

Table 5 ILVM frequencies of the damaged lateral members (Hz)

Member	1st ILVM	2nd ILVM	3rd ILVM	Condition
1	49.37	154.3	353.5	Damaged
2	37	116.1	188.3	Damaged
5	53.94	176.7	381.7	Damaged

Table 6 Estimated values of the stiffness of springs at the ends of the lateral members

Spring	Direction	Value of stiffness
Rotational	Transversal	$15000\ N.m/rad$
Rotational	Vertical	$15000\ N.m/rad$

Table 7 Stiffness reduction of damaged members and calculated natural frequencies

Member	Stiffness reduction (%)	1st Freq. (Hz)	2nd Freq.(Hz)	3rd Freq.(Hz)
1	42%	49.37	157.76	324.48
2	77%	37.12	108.98	209.67
5	23%	53.99	177.75	369.44

8.2 Damage identification by comparing the amplitudes of local modes in the PLVM range

The relative severity of the damage on the support structure is determined by comparing the maximum amplitude of frequency spectrum of identical design members in the PLVM range. This method does not require hitting each identical design members and thus, is more practical.

The velocity response of each member is measured by LDV while member 4, which was identified as undamaged in the previous section, is hit. A hammer equipped with a load cell (model PCB 086C03) is used to measure the input force.

The Fourier spectrums of normalized velocity responses of lateral members are shown in Fig. 24. The maximum amplitudes of Fourier spectrums of members 3 and 4 are much larger than the other members. The maximum amplitudes of Fourier spectrum of the lateral members are summarized in Fig. 25. The damaged members, 1, 2, and 5 have much smaller Fourier spectrum amplitudes. Moreover, the severer the damage is, the smaller the amplitude is. The damage identification capability is thus experimentally confirmed on the real belt conveyor support structure.

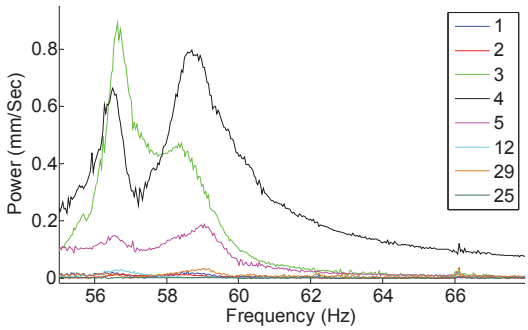

Fig. 24 Fourier spectrums in PLVM range of the lateral members

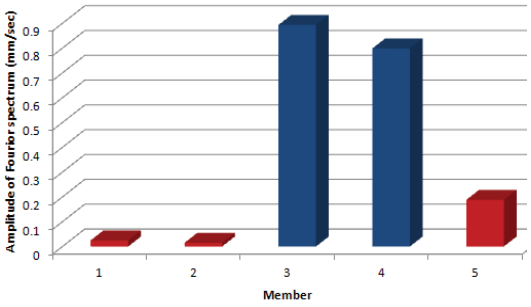

Fig. 25 Maximum amplitude of Fourier spectrum of the lateral members intheir PLVM range

9. Conclusions

Damage localization and quantification methods based on two specific local vibration modes, i.e., PLVM and ILVM, are proposed for the structural assessment of belt conveyor support structures and examined numerically and experimentally. Both methods can deal with a large number of damages on a single structure and do not require the baseline measurement records of undamaged structure. The first method utilizes the frequency change of the local vibration modes. The numerical and experimental studies show that the frequency of PLVM significantly change due to damage. The degree of damage is shown to be quantified accurately. The limitation in practice is that direct Hammer hit of each member is required to excite the local vibrations. The second method utilizes the amplitude comparison of PLVM. By hitting only one of undamaged members and measuring vibration of identical design members, damaged members are localized. Though the degree of damage cannot be quantified, the relative severity among identical design members are evaluated.

The applicability of these methods is limited to secondary members because the PLVM and ILVM exist only on these members. The extension of this approach to the main frame members is important from a perspective of belt conveyors structural assessment.

References

Abaqus FEA (2015), Dassault Systèmes Simulia Corp., Providence, RI, USA.

Chang, P.C., Flatau, A. and Liu, S.C. (2003), "Review paper: health monitoring of civil infrastructure", *Struct. Health Monit.*, **2**(3), 257-267.

Carden, E.P. and Fanning, P. (2004), "Vibration based condition monitoring: A review", *Struct. Health Monit.*, **3**(4), 355-377.

Doebling, S.W., Farar, C.R., Prime, M.B. and Shevitz, D.W. (1996), *Damage identification and health monitoring of structural and mechanical systems from changes in their vibration characteristics: a literature review*, Los Alamos National Laboratory Report LA-13070-MS, USA.

Dinh, H.M., Nagayama, T. and Fujino, Y. (2012), "Structural parameter identification by use of additional known masses and its experimental application", *Struct. Control Health Monit.*, **19**(3), 436-450.

Ewins, D.J. (1985), Modal Testing: Theory and Practice, John wiley & sons, Inc., New York, USA.

Farrar, C.R. and Worden, K. (2007), "An Introduction to Structural Health Monitoring", *Philos. T. R. Soc. A*, **365**, 303-315.

Gao, Y. and Spencer Jr., B.F. (2008), *Structural Health Monitoring Strategies for Smart Sensor Networks*, *Newmark Structural Engineering Laboratory Report Series, No. 011*, University of Illinois at Urbana-Champaign.

Harrison, A. (1980), "Non-destructive testing of industrial steel cord conveyor belts", *Process. Eng.*, **6**, 22-25.

Kim, H.M. and Bartkowicz, T.J. (2000), "An experimental study for damage detection using a hexagonal truss", *J. Comput. Struct.*, **79**(2), 173-182.

Law, S.S., Shi, Z.Y. and Zhang, L.M. (1998), "Structural damage detection from incomplete and noisy modal test data", *J. Eng. Mech. - ASCE*, **124**(11), 1280-1288.

Mottershead, J.E. and Friswell, M.I. (1993), "Model updating in structural dynamics: a survey", *J. Sound Vib.*, **167**(2), 347-375.

Maurizi, M.J., Belles, P.M. and Martin, H.D. (2003), "An almost semi centennial formula for a simple approximation of the natural frequencies of Bernoulli–Euler beams", *J. Sound Vib.*, **260**,191-194.

Mazurkiewicz, D. (2008), "Analysis of the ageing impact on the strength of the adhesive sealed joints of conveyor belts", *J. Mater. Process. Tech.*, **208**(1-3), 477-485.

Ojalvo, I.U. and Pilon, D. (1988), "Diagnostics for geometrically locating structural math model errors from modal test data", *Proceedings of the 29th AIAA/ASME/ASCE/AHS/ ASC Structures, Structural Dynamics, and Materials Conference*, Williamsburg, Virginia, April.

Park, S. and Kim, Y.B. (2002), "Nondestructive damage detection in large structures via vibration monitoring", *Electronic J. Struct. Eng.*, **2**, 59-75.

Ricci, S. (2000), "Best achievable modal eigenvectors in structural damage detection", *J. Exper. Mech.*, **40**(4), 425-429.

Ren, W.X. and De Roeck, G. (2002), "Structural damage identification using modal data. I: Simulation verification", *J. Struct. Eng .- ASCE*, **128**, 87-95.

Salawu, O.S. (1997), "Detection of structural damage through changes in frequency: a review", *Eng. Struct.*, **19**(9), 718-723.

Shi, Z.Y. and Law, S.S. (1998), "Structural damage localization from modal strain energy change", *J. Sound Vib.*, **218**(5), 825-844.

Shi, Z.Y., Law, S.S. and Zhang, L.M. (2000), "Damage localization by directly using incomplete mode shapes", *J. Eng. Mech. - ASCE*, **126**(6), 656-660.

Sohn, H., Farrar, C.R., Hemez, F.M., Shunk, D.D., Stinemates, D.W. and Nadler, B.R. (2004), *A review of structural health monitoring literature: 1996-2001*, Los Alamos National Laboratory Report LA-13976-MS, USA.

Yang, H., Wu, Z. and Yan, Y. (2009), "A study on structural damage identification method based on model updating", *Proceedings of the 2nd International Conference on Image and Signal Processing*, IEEE, Tianjin, October.

Smart Structures and Systems, *Vol. 15, No. 3 (2015) 807-830*
DOI: http://dx.doi.org/10.12989/sss.2015.15.3.807

Integration of health monitoring and vibration control for smart building structures with time-varying structural parameters and unknown excitations

Y.L. Xu[1], Q. Huang[*1,2], Y. Xia[1] and H.J. Liu[2]

[1]*Department of Civil and Environmental Engineering, The Hong Kong Polytechnic University, Hong Kong*
[2]*Shenzhen Graduate School, Harbin Institute of Technology, Shenzhen, China*

(Received November 28, 2014, Revised January 19, 2015, Accepted January 21, 2015)

Abstract. When a building structure requires both health monitoring system and vibration control system, integrating the two systems together will be cost-effective and beneficial for creating a smart building structure with its own sensors (nervous system), processors (brain system), and actuators (muscular system). This paper presents a real-time integrated procedure to demonstrate how health monitoring and vibration control can be integrated in real time to accurately identify time-varying structural parameters and unknown excitations on one hand, and to optimally mitigate excessive vibration of the building structure on the other hand. The basic equations for the identification of time-varying structural parameters and unknown excitations of a semi-active damper-controlled building structure are first presented. The basic equations for semi-active vibration control of the building structure with time-varying structural parameters and unknown excitations are then put forward. The numerical algorithm is finally followed to show how the identification and the control can be performed simultaneously. The results from the numerical investigation of an example building demonstrate that the proposed method is feasible and accurate.

Keywords: building structure; identification; time-varying parameters; unknown excitation; vibration control; semi-active dampers; integration; smart building

1. Introduction

In the last few decades, a great deal of research has been conducted on health monitoring and vibration control of building structures subject to earthquakes, strong winds, and other natural or man-made hazards. Comprehensive reviews on vibration control technologies for civil structures were given by Housner *et al*. (1997), Nishitani and Inoue (2001), and Spencer *et al*. (2003). There are also many state-of-the-art reports on health monitoring technologies for civil structures (e.g., Doebling *et al.* 1996, Mufti 2001, Sohn *et al.* 2003, Wenzel 2009, Xu and Xia 2012). However, the areas of vibration control and health monitoring have mostly been investigated separately although both vibration control system and health monitoring system need similar sensors, data acquisition, transmission and processing devices. When a building structure requires both vibration control system and health monitoring system, integrating both systems together will be cost-effective by

*Corresponding author, Ph.D., Research Assistant, E-mail: tmxhq@126.com

http://www.techno-press.org/?journal=sss&subpage=8 ISSN: 1738-1584 (Print), 1738-1991 (Online)

sharing the same hardware devices and beneficial for creating a smart structure with its own sensors (nervous system), processor (brain system), and actuators (muscular system).

In mechanical engineering, Ray and Tian (1999) introduced a method of enhancing modal frequency sensitivity to damage using a feedback control that intended for smart structures embodying self-actuation and self-sensing capabilities. Gattulli and Romeo (2000) presented an integrated procedure based on a direct adaptive control algorithm for uncertain multi-degree-of-freedom (MDOF) systems. Viscardi and Lecce (2002) proposed an integrated system for active vibro-acoustic control and damage detection on a typical aeronautical structure based on piezoelectric devices. Deng *et al.* (2011) proposed a self-adaptive modal control including both identification and control update in real-time. However, these studies focused on actively controlled mechanical systems that are different from civil structures where structural systems are more complicated with uncertainties and active control may become problematic.

In civil engineering, Nagarajaiah and Jung (2014) reviewed a number of recent papers on vibration frequency tracking and semi-active control of building structures using smart tuned mass dampers. Xu and Chen (2008), Chen and Xu (2008), and Chen *et al.* (2010) proposed an integrated procedure of vibration control and health monitoring of building structures in the frequency-domain and the time-domain respectively, using semi-active friction dampers to fulfill model updating, seismic response control and damage detection of the building structure based on the change of natural frequencies and mode shapes. Huang *et al.* (2012) and Xu *et al.* (2014) extended their methods in the frequency domain based on the change of frequency response functions. Nevertheless, these procedures cannot realize real-time integration of vibration control and health monitoring of building structures. Recently, Yang *et al.* (2013) presented a hybrid real-time structural health monitoring and control system for building structures, in which a model-reference adaptive control algorithm was integrated with an inter-story drift-based acceleration feedback method for health monitoring. In their study, the earthquake-induced ground excitation to a building structure was assumed to be known for both vibration control and health monitoring, and structural vibration control was implemented using active control technology.

For civil structures, external excitations such as earthquake-induced ground motion and typhoon-induced buffeting forces are difficult, if not impossible, to be measured directly and accurately on site. The real-time identification of external excitation for both vibration control and health monitoring is necessary. Moreover, even for a building structure with control devices, structural damage may occur during an extreme event and structural parameters of damaged components are actually varying with time. To ensure control performance, time-varying structural parameters shall be identified and control parameters shall be adjusted accordingly. It shall be noted that the identification of time-varying structural parameters in such a case is for a controlled building structure and thus real-time control forces shall be taken into consideration in the identification.

This paper presents a real-time integrated procedure to demonstrate how health monitoring and vibration control can be integrated in real time to accurately identify time-varying structural parameters and unknown excitations on one hand, and to optimally mitigate excessive vibration of the building structure on the other hand. The basic equations for the identification of time-varying structural parameters and unknown excitations of a magneto-rheological (MR) damper-controlled building structure under earthquake excitation are first presented based on the least-squares estimation method as well as the measured structural responses and control forces. The basic equations for semi-active control of the building structure with MR dampers and clipped optimal displacement control algorithm are put forward based on the updated time-varying structural

parameters and unknown excitations. The numerical algorithm is then followed to perform both identification and control simultaneously. The feasibility and accuracy of the proposed method is finally examined through the numerical investigation of an example building.

2. Structural health monitoring

For a building structure subject to earthquake-induced ground excitation (see Fig. 1), damage may occur and the structural parameters of damaging structural components may vary with time during the ground excitation. To detect damage and identify time-varying structural parameters on-line in the time domain, a structural health monitoring system including sensors, data transmission system, data acquisition system and data analysis system should be installed in the building structure to provide essential and correct information. If the earthquake-induced ground excitation cannot be directly measured, the identification of ground excitation is also necessary. In some cases, the building structure is equipped with control devices to mitigate seismic-induced vibration. Therefore, the identification of time-varying structural parameters and ground excitation of a controlled building structure is an important part of structural health monitoring. In this section, the basic equations for the identification of time-varying structural parameters and unknown excitations of a MR damper-controlled building structure under earthquake excitation are presented based on the least-squares estimation method as well as the measured structural responses and control forces. Although the identification of time-varying structural parameters and unknown excitation was investigated before using the wavelet analysis (Basu *et al*. 2008), neural estimation method (Kosmatopoulos *et al*. 2001), least-squares estimation method (Yang and Huang 2007, Yang *et al.* 2007), and the extended Kalman filter method (Lei *et al.* 2012a, Lei *et al.* 2012b), the method proposed in this study is more accurate and efficient.

2.1 Equation of motion

In this study, the structural mass matrix $\mathbf{M}$ is assumed to be known and constant for the simplicity of presentation although it is not absolutely necessary. Other structural parameters, such as damping and stiffness coefficients, are time-varying as structural damage occurs with time. Excitations on a controlled building structure can be separated into two parts: control forces and unknown excitations. Consequently, the second-order differential equation of motion of a building structure with *n* degrees-of-freedom (DOF) is given by

$$\mathbf{M}\ddot{\mathbf{X}}(t)+\mathbf{C}(t)\dot{\mathbf{X}}(t)+\mathbf{K}(t)\mathbf{X}(t)=\boldsymbol{\varphi}^{*}\mathbf{f}^{*}(t)+\boldsymbol{\varphi}\mathbf{f}(t) \tag{1}$$

where $\mathbf{M}$, $\mathbf{C}(t)$ and $\mathbf{K}(t)$ represent the $n\times n$ mass, damping and stiffness matrices of the building structure, respectively; $\ddot{\mathbf{X}}(t)$, $\dot{\mathbf{X}}(t)$ and $\mathbf{X}(t)$ are the $n\times 1$ structural acceleration, velocity and displacement response vectors, respectively; $\mathbf{f}^{*}(t)$ is the $r\times 1$ measured control force vector with the influence matrix $\boldsymbol{\varphi}^{*}$ ($n\times r$); and $\mathbf{f}(t)$ is the $s\times 1$ unknown excitation vector with the influence matrix $\boldsymbol{\varphi}$ ($n\times s$).

For the controlled building structure with semi-active MR dampers and subjected to earthquake excitation, the semi-active control forces could be measured by force transducers to form the measured control force vector, while the earthquake-induced ground acceleration could be treated

as the unknown excitation vector.

2.2 Multiple linear regression equation

Suppose that $\mathbf{Z}$ is an $m\times 1$ unknown time-varying structural parameter vector, which can include both structural stiffness and damping parameters. The unknown time-varying structural parameter vector at time $t=k\Delta t$ is denoted as $\mathbf{Z}_k$, in which Δt is the sampling interval.

The observation (measurement) equation associated with Eq. (1) at time $t=k\Delta t$ can be described as

$$\mathbf{y}_k=\mathbf{H}_k\mathbf{Z}_k-\boldsymbol{\varphi}\mathbf{f}_k+\mathbf{v}_k \tag{2}$$

where $\mathbf{y}_k=-\mathbf{M}\ddot{\mathbf{X}}_k+\boldsymbol{\varphi}^*\mathbf{f}_k^*$ is a $n\times 1$ measurement vector which can be obtained by the measured structural acceleration responses $\ddot{\mathbf{X}}_k$ and the measured control forces $\mathbf{f}_k^*$; $\mathbf{H}_k$ is an $n\times m$ observation matrix composed of the measured structural velocity and displacement responses $\dot{\mathbf{X}}_k$ and $\mathbf{X}_k$; $\mathbf{v}_k$ represents a $n\times 1$ noise vector, taking into consideration the model uncertainty of the structure and the measurement noise. The noise vector can be assumed as a white noise with a normal probability distribution. The subscript k represents the values of matrices or vectors at time $t=k\Delta t$.

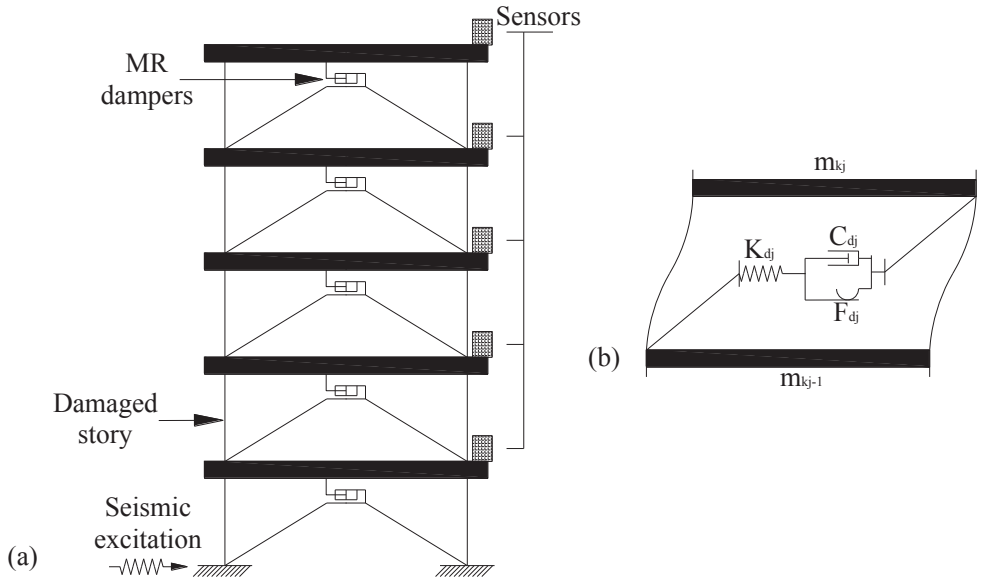

Fig. 1 Schematic diagram of a building structure with integrated health monitoring and vibration control system. (a) sensors and MR dampers and (b) mechanical model of MR damper-brace system

There are two variable vectors $\mathbf{Z}_k$ and $\mathbf{f}_k$ in Eq. (2) to be predicted. Therefore, Eq. (2) is a multiple linear regression equation. Furthermore, the elements in the predictor variable vectors are time-varying. The traditional least-squares estimation method for solving the simple linear regression equation to find constant structural parameters cannot be directly applied to Eq. (2).

2.3 Transformation to simple linear regression equation

From Eq. (2), one can obtain

$$\boldsymbol{\varphi}\mathbf{f}_k = -\mathbf{y}_k + \mathbf{H}_k\mathbf{Z}_k + \mathbf{v}_k \tag{3}$$

The closest solution of $\mathbf{f}_k$ in Eq. (3) can be given by the following projection matrix.

$$\mathbf{f}_{k,LS} = (\boldsymbol{\varphi}^T\boldsymbol{\varphi})^{-1}\boldsymbol{\varphi}^T(-\mathbf{y}_k + \mathbf{H}_k\mathbf{Z}_k + \mathbf{v}_k) \tag{4}$$

The error of the solution from Eq. (4) is given by

$$\begin{aligned} err &= \boldsymbol{\varphi}\mathbf{f}_k - \boldsymbol{\varphi}\mathbf{f}_{k,LS} \\ &= (-\mathbf{y}_k + \mathbf{H}_k\mathbf{Z}_k + \mathbf{v}_k) - \boldsymbol{\varphi}(\boldsymbol{\varphi}^T\boldsymbol{\varphi})^{-1}\boldsymbol{\varphi}^T(-\mathbf{y}_k + \mathbf{H}_k\mathbf{Z}_k + \mathbf{v}_k) \\ &= (\mathbf{I}_n - \boldsymbol{\varphi}(\boldsymbol{\varphi}^T\boldsymbol{\varphi})^{-1}\boldsymbol{\varphi}^T)(-\mathbf{y}_k + \mathbf{H}_k\mathbf{Z}_k + \mathbf{v}_k) \end{aligned} \tag{5}$$

in which $\mathbf{I}_n$ is the $n \times n$ identity matrix; and the matrix $\boldsymbol{\varphi}(\boldsymbol{\varphi}^T\boldsymbol{\varphi})^{-1}\boldsymbol{\varphi}^T$ is the projection matrix that projects the vector $-\mathbf{y}_k + \mathbf{H}_k\mathbf{Z}_k + \mathbf{v}_k$ on to the space spanned by the columns of $\boldsymbol{\varphi}$. As a limit, the error in Eq. (5) tends to be zero, leading to

$$\boldsymbol{\Phi}\mathbf{y}_k = \boldsymbol{\Phi}\mathbf{H}_k\mathbf{Z}_k + \boldsymbol{\Phi}\mathbf{v}_k \tag{6}$$

where $\boldsymbol{\Phi} = \mathbf{I}_n - \boldsymbol{\varphi}(\boldsymbol{\varphi}^T\boldsymbol{\varphi})^{-1}\boldsymbol{\varphi}^T$ for the simplicity of presentation. It is noted that the projection matrix and naturally the matrix $\boldsymbol{\Phi}$ has the two properties: (1) $\boldsymbol{\Phi}$ is a symmetric matrix, $\boldsymbol{\Phi}^T = \boldsymbol{\Phi}$; and (2) $\boldsymbol{\Phi}^2 = \boldsymbol{\Phi}$. As a result, the multiple linear regression equation expressed by Eq. (2) is transformed into the simple linear regression equation expressed by Eq. (6).

2.4 Recursive least-squares estimation for time-varying parameters

When a structure is being damaged, the structural parameters vary with time. To track the parametric variation due to damage with unknown inputs, Yang *et al*. (2007) implemented the adaptive tracking technique into their recursive least-squares estimation with unknown inputs (ARLSE-UI). In this study, a simple time-varying correction factor is introduced together with Eq. (6) to identify the parametric variations due to structural damage. The recursive least squares estimation of Eq. (6) yields

$$\hat{\mathbf{Z}}_k = \hat{\mathbf{Z}}_{k-1} + \mathbf{K}_k(\boldsymbol{\Phi}\mathbf{y}_k - \boldsymbol{\Phi}\mathbf{H}_k\hat{\mathbf{Z}}_{k-1}) = \hat{\mathbf{Z}}_{k-1} + \mathbf{K}_k\boldsymbol{\Phi}(\mathbf{y}_k - \mathbf{H}_k\hat{\mathbf{Z}}_{k-1}) \tag{7}$$

where $\hat{\mathbf{Z}}_k$ and $\hat{\mathbf{Z}}_{k-1}$ are the estimated values of $\mathbf{Z}$ at time $t=k\Delta t$ and $t=(k-1)\Delta t$ respectively; $\mathbf{K}_k$ is the least-squares estimation (LSE) gain matrix for $\hat{\mathbf{Z}}_k$ at time $t=k\Delta t$ with a size of $m\times n$;and the term $\mathbf{\Phi y}_k-\mathbf{\Phi H}_k\hat{\mathbf{Z}}_{k-1}$ is the correction term.

The current estimation error $\boldsymbol{\varepsilon}_k$ of the unknown parameter vector $\mathbf{Z}_k$ at time $t=k\Delta t$ can be obtained as follows

$$\begin{aligned}\boldsymbol{\varepsilon}_k &= \mathbf{Z}_k-\hat{\mathbf{Z}}_k \\ &= \mathbf{Z}_k-\hat{\mathbf{Z}}_{k-1}-\mathbf{K}_k(\mathbf{\Phi y}_k-\mathbf{\Phi H}_k\hat{\mathbf{Z}}_{k-1}) \\ &= \mathbf{Z}_k-\hat{\mathbf{Z}}_{k-1}-\mathbf{K}_k(\mathbf{\Phi H}_k\mathbf{Z}_k+\mathbf{\Phi v}_k-\mathbf{\Phi H}_k\hat{\mathbf{Z}}_{k-1}) \\ &= (\mathbf{I}_m-\mathbf{K}_k\mathbf{\Phi H}_k)(\mathbf{Z}_k-\hat{\mathbf{Z}}_{k-1})-\mathbf{K}_k\mathbf{\Phi v}_k\end{aligned} \tag{8}$$

in which $\mathbf{I}_m$ is the $m\times m$ identity matrix. If the structural parameters are constants, i.e., $\mathbf{Z}_k=\mathbf{Z}_{k-1}$, one can then have $\mathbf{Z}_k-\hat{\mathbf{Z}}_{k-1}=\mathbf{Z}_{k-1}-\hat{\mathbf{Z}}_{k-1}=\boldsymbol{\varepsilon}_{k-1}$. However, the structural parameters vary with time such as a degradation of stiffness when structural damage occurs. To track the structural parametric variations and consequently detect structural damage on-line, a time-varying correction factor matrix $\boldsymbol{\lambda}_k$ is introduced to reflect the structural parametric variations as follows

$$\mathbf{Z}_k-\hat{\mathbf{Z}}_{k-1}=\boldsymbol{\lambda}_k(\mathbf{Z}_{k-1}-\hat{\mathbf{Z}}_{k-1})=\boldsymbol{\lambda}_k\boldsymbol{\varepsilon}_{k-1} \tag{9}$$

in which $\boldsymbol{\lambda}_k$ is a diagonal matrix with size of $m\times m$. By substituting Eq. (9) into Eq.(8), the current estimation error $\boldsymbol{\varepsilon}_k$ could be calculated by

$$\boldsymbol{\varepsilon}_k=(\mathbf{I}_m-\mathbf{K}_k\mathbf{\Phi H}_k)\boldsymbol{\lambda}_k\boldsymbol{\varepsilon}_{k-1}-\mathbf{K}_k\mathbf{\Phi v}_k \tag{10}$$

It is noted that $\mathbf{\Phi}$ is a symmetric matrix. The estimation error covariance can be obtained as

$$\begin{aligned}\mathbf{P}_k &= \mathrm{E}(\boldsymbol{\varepsilon}_k\boldsymbol{\varepsilon}_k^T) \\ &= \mathrm{E}\{[(\mathbf{I}_m-\mathbf{K}_k\mathbf{\Phi H}_k)\boldsymbol{\lambda}_k\boldsymbol{\varepsilon}_{k-1}-\mathbf{K}_k\mathbf{\Phi v}_k][(\mathbf{I}_m-\mathbf{K}_k\mathbf{\Phi H}_k)\boldsymbol{\lambda}_k\boldsymbol{\varepsilon}_{k-1}-\mathbf{K}_k\mathbf{\Phi v}_k]^T\} \\ &= (\mathbf{I}_m-\mathbf{K}_k\mathbf{\Phi H}_k)\boldsymbol{\lambda}_k\mathrm{E}(\boldsymbol{\varepsilon}_{k-1}\boldsymbol{\varepsilon}_{k-1}^T)\boldsymbol{\lambda}_k^T(\mathbf{I}_m-\mathbf{K}_k\mathbf{\Phi H}_k)^T-\mathbf{K}_k\mathbf{\Phi}\mathrm{E}(\mathbf{v}_k\boldsymbol{\varepsilon}_{k-1}^T)\boldsymbol{\lambda}_k^T(\mathbf{I}_m-\mathbf{K}_k\mathbf{\Phi H}_k)^T \\ &\quad -(\mathbf{I}_m-\mathbf{K}_k\mathbf{\Phi H}_k)\boldsymbol{\lambda}_k\mathrm{E}(\boldsymbol{\varepsilon}_{k-1}\mathbf{v}_k^T)(\mathbf{K}_k\mathbf{\Phi})^T+\mathbf{K}_k\mathbf{\Phi}\mathrm{E}(\mathbf{v}_k\mathbf{v}_k^T)(\mathbf{K}_k\mathbf{\Phi})^T \\ &= (\mathbf{I}_m-\mathbf{K}_k\mathbf{\Phi H}_k)\boldsymbol{\lambda}_k\mathbf{P}_{k-1}\boldsymbol{\lambda}_k^T(\mathbf{I}_m-\mathbf{K}_k\mathbf{\Phi H}_k)^T+\mathbf{K}_k\mathbf{\Phi R}_k\mathbf{\Phi K}_k^T\end{aligned} \tag{11}$$

where $\mathbf{R}_k=\mathrm{E}(\mathbf{v}_k\mathbf{v}_k^T)$ is the covariance of noise $\mathbf{v}_k$. Moreover, the estimation error $\boldsymbol{\varepsilon}_{k-1}$ at time $t=(k-1)\Delta t$ can be assumed to be independent of the noise vector $\mathbf{v}_k$ at time $t=k\Delta t$, and accordingly $\mathrm{E}(\mathbf{v}_k\boldsymbol{\varepsilon}_{k-1}^T)=\mathrm{E}(\boldsymbol{\varepsilon}_{k-1}\mathbf{v}_k^T)=0$ in Eq. (11).

The time-varying correction factor matrix $\boldsymbol{\lambda}_k$ can be calculated based on the current measurements. It is noted from Eq. (7) that the current correction term at time $t = k\Delta t$ can be calculated based on the current measurements as follows

$$\mathbf{r}_k = \boldsymbol{\Phi}\mathbf{y}_k - \boldsymbol{\Phi}\mathbf{H}_k\hat{\mathbf{Z}}_{k-1} = \boldsymbol{\Phi}\mathbf{H}_k(\mathbf{Z}_k - \hat{\mathbf{Z}}_{k-1}) + \boldsymbol{\Phi}\mathbf{v}_k = \boldsymbol{\Phi}\mathbf{H}_k\boldsymbol{\lambda}_k\boldsymbol{\varepsilon}_{k-1} + \boldsymbol{\Phi}\mathbf{v}_k \tag{12}$$

Hence, the time-varying factor correction matrix $\boldsymbol{\lambda}_k$ can be determined by the following equation

$$\mathbf{P}_{r,k} = \mathrm{E}(\mathbf{r}_k\mathbf{r}_k^T) = \boldsymbol{\Phi}\mathbf{H}_k\boldsymbol{\lambda}_k\mathbf{P}_{k-1}\boldsymbol{\lambda}_k\mathbf{H}_k^T\boldsymbol{\Phi} + \boldsymbol{\Phi}\mathbf{R}_k\boldsymbol{\Phi} \tag{13}$$

To obtain the optimal value of the gain matrix $\mathbf{K}_k$ that can minimize the estimation error covariance $\mathbf{P}_k$ at time $t = k\Delta t$, the differentiation of $\mathbf{P}_k$ in Eq. (11) with respect to $\mathbf{K}_k$ produces

$$\begin{aligned}\partial\mathbf{P}_k / \partial\mathbf{K}_k &= 2(\mathbf{I}_m - \mathbf{K}_k\boldsymbol{\Phi}\mathbf{H}_k)\boldsymbol{\lambda}_k\mathbf{P}_{k-1}\boldsymbol{\lambda}_k^T(-\boldsymbol{\Phi}\mathbf{H}_k)^T + 2\mathbf{K}_k\boldsymbol{\Phi}\mathbf{R}_k\boldsymbol{\Phi} \\ &= 2\mathbf{K}_k\boldsymbol{\Phi}(\mathbf{H}_k\boldsymbol{\lambda}_k\mathbf{P}_{k-1}\boldsymbol{\lambda}_k^T\mathbf{H}_k^T + \mathbf{R}_k)\boldsymbol{\Phi} - 2\boldsymbol{\lambda}_k\mathbf{P}_{k-1}\boldsymbol{\lambda}_k^T\mathbf{H}_k^T\boldsymbol{\Phi}\end{aligned} \tag{14}$$

By setting the value of the partial derivative to zero, one can obtain

$$\mathbf{K}_k = \boldsymbol{\lambda}_k\mathbf{P}_{k-1}\boldsymbol{\lambda}_k^T\mathbf{H}_k^T\boldsymbol{\Phi} / [\boldsymbol{\Phi}(\mathbf{H}_k\boldsymbol{\lambda}_k\mathbf{P}_{k-1}\boldsymbol{\lambda}_k^T\mathbf{H}_k^T + \mathbf{R}_k)\boldsymbol{\Phi}] \tag{15}$$

It is noted that $\mathbf{P}_{k-1}$, $\mathbf{R}_k$ and $\boldsymbol{\Phi}$ are symmetric matrices, the estimation error covariance expressed by Eq. (11) could be simplified in terms of Eq. (15) as

$$\begin{aligned}\mathbf{P}_k &= (\mathbf{I}_m - \mathbf{K}_k\boldsymbol{\Phi}\mathbf{H}_k)\boldsymbol{\lambda}_k\mathbf{P}_{k-1}\boldsymbol{\lambda}_k^T(\mathbf{I}_m - \mathbf{K}_k\boldsymbol{\Phi}\mathbf{H}_k)^T + \mathbf{K}_k\boldsymbol{\Phi}\mathbf{R}_k\boldsymbol{\Phi}\mathbf{K}_k^T \\ &= (\mathbf{I}_m - \mathbf{K}_k\boldsymbol{\Phi}\mathbf{H}_k)\boldsymbol{\lambda}_k\mathbf{P}_{k-1}\boldsymbol{\lambda}_k^T - \boldsymbol{\lambda}_k\mathbf{P}_{k-1}\boldsymbol{\lambda}_k^T\mathbf{H}_k^T\boldsymbol{\Phi}\mathbf{K}_k^T + \mathbf{K}_k\boldsymbol{\Phi}(\mathbf{H}_k\boldsymbol{\lambda}_k\mathbf{P}_{k-1}\boldsymbol{\lambda}_k^T\mathbf{H}_k^T + \mathbf{R}_k)\boldsymbol{\Phi}\mathbf{K}_k^T \\ &= (\mathbf{I}_m - \mathbf{K}_k\boldsymbol{\Phi}\mathbf{H}_k)\boldsymbol{\lambda}_k\mathbf{P}_{k-1}\boldsymbol{\lambda}_k^T\end{aligned} \tag{16}$$

Once the estimate value $\hat{\mathbf{Z}}_k$ of the unknown parametric vector at time $t = k\Delta t$ is calculated by Eq. (7), the estimate value of the unknown excitation vector at time $t = k\Delta t$ can be estimated by

$$\hat{\mathbf{f}}_k = -(\boldsymbol{\varphi}^T\boldsymbol{\varphi})^{-1}\boldsymbol{\varphi}^T(\mathbf{y}_k - \mathbf{H}_k\hat{\mathbf{Z}}_k) \tag{17}$$

Eqs. (7), (13), (15) (16) and (17) form the recursive least-squares estimation for identifying both time-varying structural parameters and unknown excitations. If all the external excitations can be measured and the unknown parametric vector is constant (the influence matrix of the unknown excitation vector $\boldsymbol{\varphi}$ in Eq. (1) is a null matrix leading to $\boldsymbol{\Phi} = \mathbf{I}_n$ and the time-varying correction factor matrix $\boldsymbol{\lambda}_k = \mathbf{I}_m$), the proposed algorithm becomes the same as the traditional recursive least-squares estimation method.

The proposed algorithm canidentify the unknown inputs and time-varying structural parameters simultaneously, and the flow chart of the proposed recursive least-squares estimation algorithm is shown in Fig. 2.

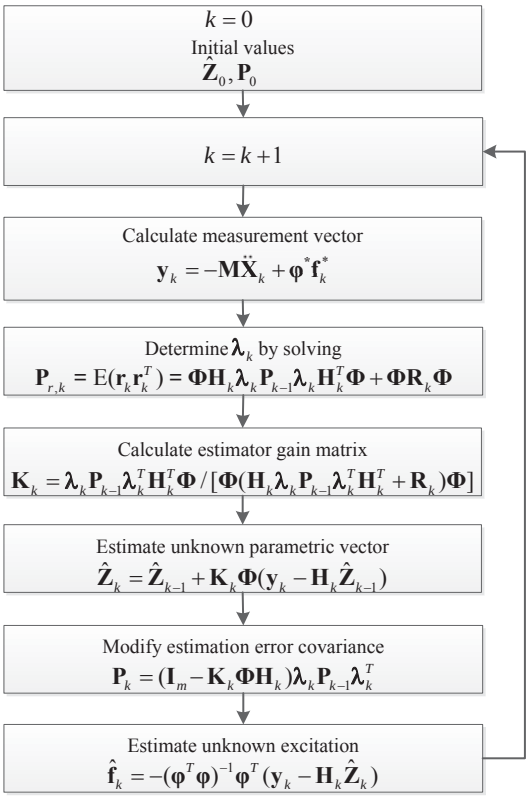

Fig. 2 Flowchart of the proposed method for identifying time-varying structural parameters and unknown excitations

3. Structural vibration control

When a building structure is subject to earthquake excitation, excessive vibration may occur and cause damage (see Fig. 1). Semi-active dampers can be installed in the building structure to reduce the excessive vibration and damage. The vibration control system, including sensors, semi-active dampers, data transmission system, data acquisition system, control algorithm, and data analysis system, should be installed in the building structure to provide essential feedback information and form a close loop control. The semi-active vibration control is then implemented based on the measured structural responses and the identified time-varying structural parameters to generate optimal control forces and achieve the maximum building response reduction. In this section, the basic equations for semi-active control of the building structure with MR dampers and clipped optimal displacement control algorithm are put forward based on the updated time-varying structural parameters and unknown excitations.

3.1 Mechanical model of a MR damper

There are a number of mechanical models available to describe the relationship between force and motion of a MR damper. For the sake of simplicity to illustrate the integration of structural control and health monitoring in this study, the simple Bingham model is adopted. For a steady and fully developed flow, the Bingham model can be used for the shear resistance of MR fluids, which has a friction component augmented by a Newtonian viscosity component. The relationship between the force P_d and velocity $\dot{e}$ of the MR damper can be expressed as follows (Gavin *et al.* 1996, Xu *et al*. 2000, Qu and Xu 2001)

$$P_d(t) = C_d\dot{e} + F_d \operatorname{sgn}(\dot{e}) \tag{18}$$

in which

$$C_d = C_1 \frac{12\varsigma L A_p}{bh^3} A_p, \quad F_d = C_2 \frac{L\tau_y}{h} A_p + P_y \tag{19}$$

For the flow-type damper

$$C_1 = 1.0, \quad C_2 = 2.07 + \frac{1.0}{1.0 + 0.4T}, \quad T = \frac{bh^2\tau_y}{12A_p\varsigma\dot{e}} \tag{20}$$

For the mixed-type damper

$$C_1 = 1.0 - \frac{bh}{2A_p}, \quad C_2 = 2.07 + \frac{1.0}{1.0 + 0.4T} - \frac{1.5V_2}{1.0 + 0.4T^2}, \quad V = \frac{bh}{2A_p} \tag{21}$$

where b is the width of the rectangular plate; h is the gap between two parallel plates; L is the effective axial pole length; A_p is the cross-sectional area of the piston; τ_y represents the yielding shear stress controlled by the applied field; and P_y is the mechanical friction force in the damper. Clearly, F_d is the function of yielding shear stress and it can be controlled through the applied field but C_d is independent of the applied field.

Let us consider a multi-story shear building subjected to earthquake excitation as shown in Fig. 1(a), semi-active MR dampers can be positioned between the chevron braces and the rigid floor diaphragms to enhance its vibration energy dissipation capacity. In consideration of the stiffness of chevron brace, the mechanical model for the MR damper-chevron brace system can be seen as a damper and a spring being connected in series as shown in Fig. 1(b). When considering the MR damper and the chevron brace to be connected in series, the spring force in the brace is equal to the force on the piston of the damper. Eq. (18) should thus be correspondingly changed to

$$C_d\dot{e} + F_d \operatorname{sgn}(\dot{e}) = K_d(u - e) \tag{22}$$

where u is the relative displacement between the two floors with the damper installed and K_d is the horizontal stiffness of the chevron brace.

3.2 Equation of motion

In terms of Eq. (22), the equation of motion of an *n*-story frame structure with *m* dampers subject to earthquake excitation can be expressed as

$$\mathbf{M}\ddot{\mathbf{X}}(t)+\mathbf{C}(t)\dot{\mathbf{X}}(t)+(\mathbf{K}(t)+\mathbf{H}_c\mathbf{K}_d\mathbf{H}_c^{T})\mathbf{X}(t)+\mathbf{H}_c\mathbf{K}_d\mathbf{e}(t)=\mathbf{H}_e\ddot{\mathbf{x}}_g(t) \tag{23}$$

$$\frac{C_{d_j}}{K_{d_j}}\dot{e}_j+e_j+\frac{F_{d_j}}{K_{d_j}}\mathrm{sgn}(\dot{e}_j)=\mathbf{H}_{cj}^{T}\mathbf{X}=X_{kj}-X_{kj-1}\ (j=1,2,\cdots,m) \tag{24}$$

where $\mathbf{C}(t)$ and $\mathbf{K}(t)$ are the $n\times n$ mass, damping, and stiffness matrices of the frame structure, respectively, which are the same as those in Eq. (1); $\mathbf{C}(t)$ and $\mathbf{K}(t)$ are the time-varying structural damping and stiffness matrices which are updated by the health monitoring system with time; $\mathbf{K}_d$ is the $m\times m$ diagonal stiffness matrix, of which the element is the stiffness coefficient of the chevron brace; *m* is the number of stories with MR dampers installed; $\mathbf{H}_c$ is the $n\times m$ matrix converting the brace stiffness matrix into the global co-ordinate system; the superscript T means the transposition of a matrix; $\mathbf{X}$, $\dot{\mathbf{X}}$, and $\ddot{\mathbf{X}}$ are the $n\times 1$ relative displacement, velocity, and acceleration vectors of the frame structure with respect to the ground, respectively; $\mathbf{e}$ is the $m\times 1$ displacement vector of the MR dampers; $\mathbf{H}_{cj}$ is the *j*th column vector of the matrix $\mathbf{H}_c$; X_{kj} and X_{kj-1} are the displacements of the top and bottom floors of the *k* th story where the *j*th damper is installed.

Eq. (23) can be written to the same form as Eq. (1) by using the following substitutions.

$$\boldsymbol{\varphi}^{*}=\mathbf{H}_c,\quad \mathbf{f}^{*}(t)=-\mathbf{K}_d[\mathbf{H}_c^{T}\mathbf{X}(t)+\mathbf{e}(t)],\quad \boldsymbol{\varphi}=\mathbf{H}_e,\quad \mathbf{f}(t)=\ddot{\mathbf{x}}_g(t) \tag{25}$$

Eq. (23) can also be replaced by an equivalent first-order differential equation of the state-space form

$$\dot{\mathbf{Z}}_{MR}(t)=\mathbf{A}_{MR}(t)\mathbf{Z}_{MR}(t)+\mathbf{B}_{MR}\mathbf{e}(t)+\mathbf{D}_{MR}\ddot{\mathbf{x}}_g(t) \tag{26}$$

in which

$$\mathbf{A}_{MR}(t)=\begin{bmatrix}\mathbf{0} & \mathbf{I}\\ -\mathbf{M}^{-1}(\mathbf{K}(t)+\mathbf{H}_c\mathbf{K}_d\mathbf{H}_c^{T}) & -\mathbf{M}^{-1}\mathbf{C}(t)\end{bmatrix},$$
$$\mathbf{B}_{MR}=\begin{bmatrix}\mathbf{0}\\ \mathbf{M}^{-1}\mathbf{H}_c\mathbf{K}_d\end{bmatrix},\boldsymbol{D}_{MR}=\begin{bmatrix}\mathbf{0}\\ \mathbf{M}^{-1}\mathbf{H}_e\end{bmatrix},\boldsymbol{Z}_{MR}(t)=\begin{bmatrix}\mathbf{X}(t)\\ \dot{\mathbf{X}}(t)\end{bmatrix} \tag{27}$$

In this study, the stiffness matrix and damping matrix of the building structure is constructed using the stiffness coefficients and damping coefficients that are identified from the health monitoring system in real time. Accordingly, the matrix $\mathbf{A}_{MR}(t)$ in Eq. (27) is reconstructed at each time step of the computation.

3.3 Semi-active control algorithm

Xu *et al*. (2000) presented a clipped optimal displacement control approach in terms of the linear quadratic regular (LQR) control theory that minimizes

$$J = \int_0^{t_f} [\mathbf{Z}_{MR}^T(t)\mathbf{Q}_{MR}\mathbf{Z}_{MR}(t) + \mathbf{e}^T(t)\mathbf{R}_{MR}\mathbf{e}(t)]dt \tag{28}$$

to control the displacement vector $\mathbf{e}_T(t)$ as

$$\mathbf{e}_T(t) = -\mathbf{R}_{MR}\mathbf{B}_{MR}\mathbf{P}_{MR}(t)\mathbf{Z}_{MR}(t) \tag{29}$$

where $\mathbf{Q}_{MR}$ is the weighting matrix for the structure response in the optimal displacement control, it is an $n \times n$ positive semi-definite matrix; $\mathbf{R}_{MR}$ is the weighting matrix for the damper displacement in the optimal displacement control, it is an $m \times m$ positive definite matrix; the two weighting matrices $\mathbf{Q}_{MR}$ and $\mathbf{R}_{MR}$ are often determined by trial and error for the concerned problem; and $\mathbf{P}_{MR}(t)$ is the positive definite solution of the following Riccati equation

$$\mathbf{P}_{MR}(t)\mathbf{B}_{MR}^T\mathbf{R}_{MR}^{-1}\mathbf{B}_{MR}\mathbf{P}_{MR}(t) - \mathbf{A}_{MR}^T(t)\mathbf{P}_{MR}(t) - \mathbf{P}_{MR}(t)\mathbf{A}_{MR}(t) - \mathbf{Q}_{MR} = 0 \tag{30}$$

The strategy in the clipped optimal displacement control approach (Xu *et al*. 2000) can be described as follows. When the *j*th damper displacement e_j is approaching the desired optimal damper displacement vector e_{Tj}, the friction force F_{dj} in the damper is set to its minimum value. When the *j*th damper moves in the opposite direction to the optimal damper displacement, the friction force F_{dj} in the damper should be set to a smaller value of the two quantities: $F_{\max}$ and the actual damper force $K_{dj}(X_{kj} - X_{kj-1} - e_j)$ minus a small quantity F_0. In this way, the damper is always in motion to dissipate vibration energy. This strategy can be stated as

$$F_{dj} = \begin{cases} F_{\min} & when\ e_j(e_{Tj} - \dot{e}_j) > 0 \\ \min\{abs[K_{dj}(X_{kj} - X_{kj-1} - e_j)] - F_0, F_{\max}\} & when\ e_j(e_{Tj} - \dot{e}_j) < 0 \end{cases} \quad (j = 1, 2, \cdots, m) \tag{31}$$

The flow chart of the proposed semi-active control with MR dampers is shown in Fig. 3.

4. Integrated numerical algorithm

Based on the equations presented in the previous two sections, an integrated numerical algorithm can be implemented for real-time system identification and vibration control of the building structure step by step as follows:

Step 1: Obtain time-varying factor correction matrix $\boldsymbol{\lambda}_k$ at time $t = k\Delta t$ by solving Eq. (13) based on the current measurements $\mathbf{y}_k$.

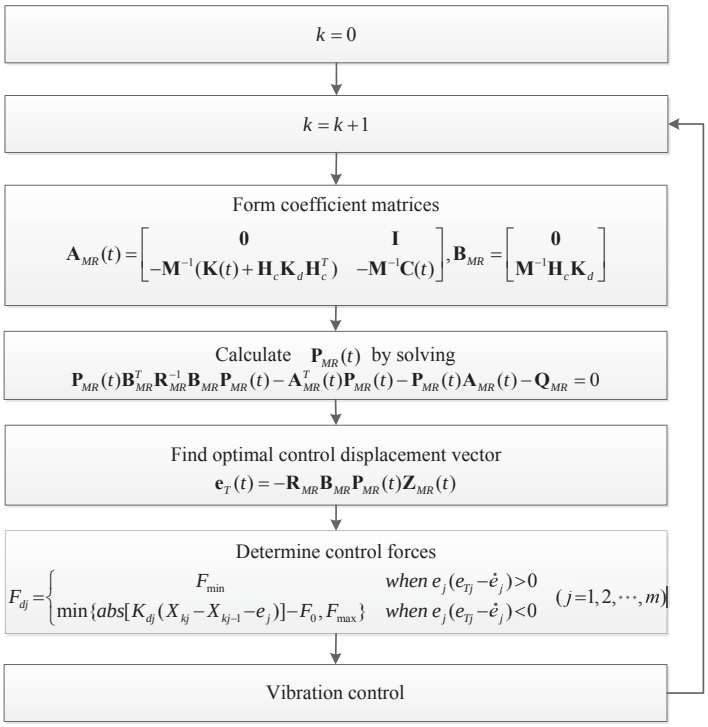

Fig. 3 Flowchart of semi-active control with MR dampers

Step 2: Calculate estimator gain matrix $\mathbf{K}_k$ using Eq. (15) with the time-varying factor correction matrix determined in Step 1.

Step 3: Generate unknown parametric vector $\hat{\mathbf{Z}}_k$ using Eq. (7) based on the estimator gain matrix calculated in Step 2 and the current correction term.

Step 4: Update estimation error covariance matrix $\mathbf{P}_k$ by Eq. (16).

Step 5: Estimate unknown excitation $\hat{\mathbf{f}}_k$ using Eq. (17) with the unknown parametric vector identified in Step 3.

Step 6: Take the increment $k=k+1$. Form coefficient matrices $\mathbf{A}_{MR\,k+1}$ and $\mathbf{B}_{MR}$ based on Eq. (27) as follows

$$\mathbf{A}_{MR\,k+1}=\begin{bmatrix}\mathbf{0} & \mathbf{I}\\ -\mathbf{M}^{-1}(\mathbf{K}_{id\,k}+\mathbf{H}_c\mathbf{K}_d\mathbf{H}_c^T) & -\mathbf{M}^{-1}\mathbf{C}_{id\,k}\end{bmatrix},\mathbf{B}_{MR}=\begin{bmatrix}\mathbf{0}\\ \mathbf{M}^{-1}\mathbf{H}_c\mathbf{K}_d\end{bmatrix} \tag{32}$$

where the stiffness matrix $\mathbf{K}_{id\,k}$ and damping matrix $\mathbf{C}_{id\,k}$ of the building structure are constructed using the stiffness coefficients and damping coefficients identified from the health monitoring

system in Step 3 at time $t = k\Delta t$.

Step 7: Calculate the matrix $\mathbf{P}_{MR\,k+1}$ by solving the following Riccati equation

$$\mathbf{P}_{MR\,k+1}\mathbf{B}_{MR}^{T}\mathbf{R}_{MR}^{-1}\mathbf{B}_{MR}\mathbf{P}_{MR\,k+1} - \mathbf{A}_{MR\,k+1}^{T}\mathbf{P}_{MR\,k+1} - \mathbf{P}_{MR\,k+1}\mathbf{A}_{MR\,k+1} - \mathbf{Q}_{MR} = 0 \tag{33}$$

where the coefficient matrices $\mathbf{A}_{MR\,k+1}$ and $\mathbf{B}_{MR}$ are formed in Step 6.

Step 8: Find optimal control displacement vector $\mathbf{e}_{T\,k+1}$ at time $t = (k+1)\Delta t$ as

$$\mathbf{e}_{T\,k+1} = -\mathbf{R}_{MR}\mathbf{B}_{MR}\mathbf{P}_{MR\,k+1}\mathbf{Z}_{MR\,k+1} \tag{34}$$

where the matrix $\mathbf{P}_{MR\,k+1}$ is calculated in Step 7 and the state vector $\mathbf{Z}_{MR\,k+1}$ is composed of structural displacement and velocity responses at time $t = (k+1)\Delta t$.

Step 9: Determine control forces based on the semi-active control strategy as shown in Eq. (31).

Step 10: Calculate measurement vector at time $t = (k+1)\Delta t$ for the identification of structural parameter and excitation as well as damage detection based on the measured structural acceleration responses $\ddot{\mathbf{X}}_{k+1}$ and the measured control forces $\mathbf{f}_{k+1}^{*}$

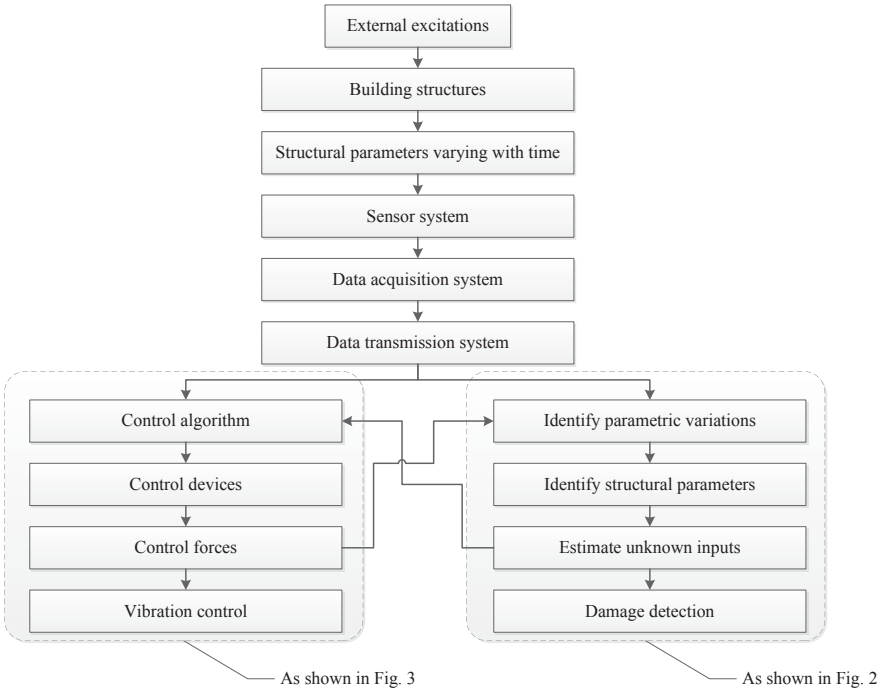

Fig. 4 Flowchart of a real-time integrated procedure for both structural health monitoring and vibration control

$$\mathbf{y}_{k+1} = -\mathbf{M}\ddot{\mathbf{X}}_{k+1} + \boldsymbol{\varphi}^* \mathbf{f}^*_{k+1} \tag{35}$$

where $\boldsymbol{\varphi}^* = \mathbf{H}_c$. Return to Step 1 until the discrete time $t = (k+1)\Delta t$ is the last datum.

A flow chart of the integrated health monitoring and vibration control system for the building structure is shown in Fig. 4. In this integrated system, the health monitoring system and vibration control system are combined together for both system identification and vibration control. The control forces are first measured and transmitted to the health monitoring system in real-time for the identification of structural parameter and excitation as well as damage detection. The time-varying structural parameters and ground excitation, identified from the health monitoring system in real time, are then transmitted to the vibration control system on line to determine optimal control forces to mitigate the structural responses in the next step. The iteration of the above two steps of system identification and vibration control forms the on-line integrated structural health monitoring and vibration control.

5. Numerical example

5.1 Description of example building structure

A simple five-story shear building is chosen as the example building structure. It has the identical story height of 3 meters (see Fig. 1(a)). The building structure has uniform mass $m = 5.1\times10^3\ kg$ and uniform horizontal story (shear) stiffness $k = 1.334\times10^7\ N/\mathrm{m}$ for all five stories. The five natural frequencies of the building structures are calculated as 2.317, 6.762, 10.661, 13.695, and 15.620 Hz. The acceleration responses of the building structure are measured by five accelerometers with one on each floor of the building structure. From a practical viewpoint, the white noise of 2% intensity is added to the calculated acceleration response as the measured acceleration response. The noise intensity is defined as the ratio of the root mean square of the noise to the root mean square of the acceleration response. Since the highest natural frequency of the building is 15.620 Hz, a low-pass filter with a cut off frequency of 30 Hz is applied to the noise-polluted acceleration responses. The displacement and velocity responses of the building are obtained from the measured noise-polluted acceleration responses through numerical integrations. On each story of the building, a semi-active MR damper is installed with a chevron brace that connects two neighboring floors. The ratios of the brace horizontal stiffness to the structure horizontal stiffness k_d/k are selected as one and the same for all the building stories. The properties of the MR dampers are listed in Table 1. Damper forces are measured by five force transducers with one for each MR damper, and the RMS-noise of 1% intensity is added to the calculated control force as the measured control force.

Table 1 Basic parameters of MR damper and fluid

Parameters of MR damper					Parameters of smart material		
L(m)	h (m)	b (m)	A_p(m^2)	P_y (kN)	η (k Pa s)	$\tau_{y\,min}$ (k Pa)	$\tau_{y\,max}$ (k Pa)
0.5	0.002	0.75	0.04	0.05	0.0002	0.05	10

To examine the feasibility and accuracy of the proposed integrated system, the building structure subject to earthquake-induced ground acceleration is considered. The ground acceleration is taken as the EI Centro earthquake with scaled peak ground acceleration (PGA) of 4.0 m/s^2. A single damage occurs in the second story with a linear 5% degradation of the story stiffness from t=8s to t=9s; and the structural damping matrix is assumed to be the Rayleigh damping matrix $\mathbf{C}(t)=\alpha\mathbf{M}+\beta\mathbf{K}(t)$ where α and β are the two constant coefficients decided by the first and second modal damping ratios of 2% and the original mass and stiffness matrixes in this study. It is noted that the damping matrix is also time varying because the stiffness matrix is time varying. It is also noted that the proposed method can also identify the instantaneous change of stiffness.

5.2 Accuracy of time-varying parameter and excitation identification

In this study, the building structure is subjected to earthquake-induced ground acceleration $\mathbf{f}(t)=\ddot{x}_g(t)$. The unknown parameter vector at time $t=k\Delta t$ can be written as $\mathbf{Z}_k=\begin{bmatrix}\mathbf{K}_\theta\\ \beta\mathbf{K}_\theta\\ \alpha\end{bmatrix}_k$, where $\mathbf{K}_\theta=[k_1\ k_2\ \cdots k_n]^T$ is the time varying stiffness coefficients and n=5. The observation matrix can be worked outas

$$\mathbf{H}_k=\begin{bmatrix}\mathbf{H}_{1,k} & \mathbf{H}_{2,k} & \mathbf{H}_{3,k}\end{bmatrix} \tag{36}$$

in which

$$\mathbf{H}_{1,k}=\begin{bmatrix} x_{1,k} & x_{1,k}-x_{2,k} & & & \\ & x_{2,k}-x_{1,k} & x_{2,k}-x_{3,k} & & \\ & & \cdots & \cdots & \\ & & & x_{n-1,k}-x_{n-2,k} & x_{n-1,k}-x_{n,k} \\ & & & & x_{n,k}-x_{n-1,k}\end{bmatrix}$$

$$\mathbf{H}_{2,k}=\begin{bmatrix} \dot{x}_{1,k} & \dot{x}_{1,k}-\dot{x}_{2,k} & & & \\ & \dot{x}_{2,k}-\dot{x}_{1,k} & \dot{x}_{2,k}-\dot{x}_{3,k} & & \\ & & \cdots & \cdots & \\ & & & \dot{x}_{n-1,k}-\dot{x}_{n-2,k} & \dot{x}_{n-1,k}-\dot{x}_{n,k} \\ & & & & \dot{x}_{n,k}-\dot{x}_{n-1,k}\end{bmatrix} \quad \mathbf{H}_{3,k}=\begin{bmatrix}\mathbf{M}\ddot{\mathbf{X}}_k\end{bmatrix}$$

The sampling interval Δt is set as 0.002s, and accordingly the sampling frequency is 500 Hz for all the measurement responses. The initial values of time-varying story stiffness coefficients are taken as 1.25 times the original stiffness coefficients. The initial values for the two constant coefficients α and β are unit but the actual values are 0.4335 and 7.015×10^{-4} respectively. As a result, the initial estimated unknown parametric vector can be written as

$\hat{\mathbf{Z}}_0 = [1.25\mathbf{K}_\theta \quad 1\times 1.25\mathbf{K}_\theta \quad 1]^T$. The initial estimation error covariance matrix is set as $\mathbf{P}_0 = 10^7 \times \mathbf{I}_{2n+1}$, where $\mathbf{I}_{2n+1}$ represents a $(2n+1)\times(2n+1)$ identity matrix. For the controlled building structure with semi-active MR dampers subjected to earthquake excitation, the semi-active control forces could be measured by force transducers as the measured excitation $\mathbf{f}^*(t)$, while the earthquake ground acceleration $\ddot{x}_g(t)$ could be treated as the unknown excitation $\mathbf{f}(t)$. The influence matrix of the unknown excitations can be set as $\boldsymbol{\varphi} = \mathbf{H}_e = -\mathbf{M}[1 \quad 1 \quad 1 \quad 1 \quad 1]^T$. The influence matrix of the known inputs $\boldsymbol{\varphi}^* = \mathbf{H}_c$ reflects the location of the semi-active MR dampers. The time-varying correction factor matrix is set as $\boldsymbol{\lambda}_k = \mathbf{I}_m$ during the time period from $t = 0s$ to $t = 2s$ in order to obtain the covariance matrix of noise $\mathbf{R} = 1/(1000-1)\times\sum_{i=1}^{1000}[(\boldsymbol{\Phi}\mathbf{y}_k - \boldsymbol{\Phi}\mathbf{H}_k\hat{\mathbf{Z}}_k)(\boldsymbol{\Phi}\mathbf{y}_k - \boldsymbol{\Phi}\mathbf{H}_k\hat{\mathbf{Z}}_k)^T]$. The noise covariance matrix calculated is then used for every time step subsequently.

Fig. 5 presents the identified results of time varying stiffness coefficients of the five stories of the building structure. Fig. 6 shows the identified results of two coefficients α and β. In Figs. 5 and 6, the identified results are presented as dash lines but the real values are presented as solid lines for comparison. The initial values of time-varying story stiffness coefficients at t=0 are taken as 1.25 times the original stiffness coefficients in the calculation. It can be seen that after a very short time period (less than 1.25s), the identified results converge to the actual ones and some spikes appear near t=0. It can also be seen from Fig. 5 that the proposed algorithm has a very good tracking ability for capturing slightly changed stiffness in a very short time period from 8s to 9s.

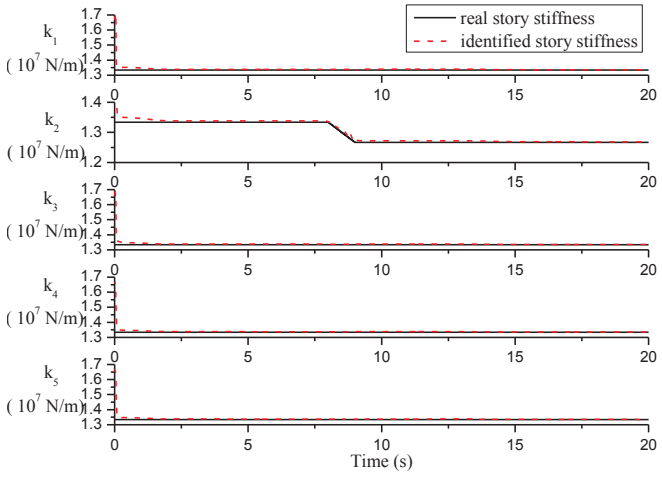

Fig. 5 Identified results of story stiffness

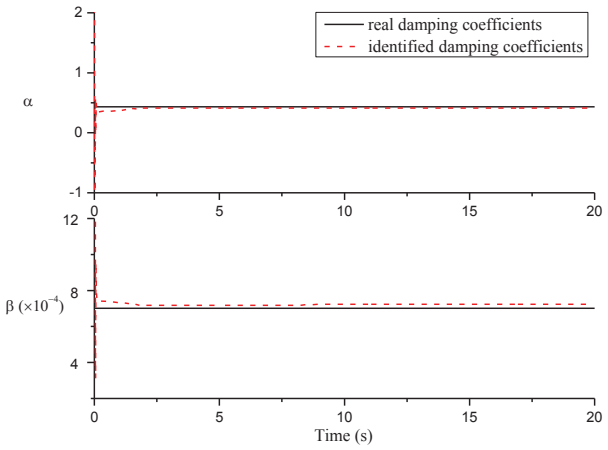

Fig. 6 Identified results of Rayleigh damping coefficients

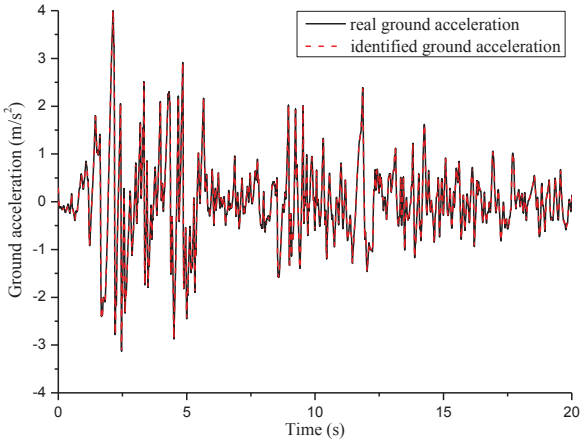

Fig. 7 Identified results of unknown earthquake-induced ground acceleration

The results presented in Fig. 6 also show that the proposed algorithm can identify the two damping coefficients accurately. In summary, the proposed algorithm can identify time-varying structural stiffness and damping coefficients accurately and therefore can detect structural damage precisely on-line. The identified results of the unknown earthquake-induced ground acceleration are presented in Fig. 7 with dash lines and compared with the actual ones with solid lines, and the average identification error of the ground acceleration is only 3.25%. Clearly, the proposed algorithm is capable of identifying the unknown excitation very well.

5.3 Performance of semi-active control with MR dampers

To evaluate the semi-active control performance, the seismic record El Centro NS (1940) is selected as input to the example building. The peak ground acceleration of the seismic records is scaled from 3.417 m/s^2 to 4.0 m/s^2. The stiffness matrix and damping matrix of the example building is constructed using the stiffness coefficients and damping coefficients identified from the health monitoring system accordingly. The matrix $\mathbf{A}_{MR}(t)$ in Eq. (27) and the matrix $\mathbf{P}_{MR}(t)$ in Eq. (30) are reconstructed at each time step. The ratios of the brace horizontal stiffness to the structure horizontal stiffness of all the five semi-active MR dampers are assigned of the same value of 1. Five accelerometers and five force transducers with one accelerometer and one force transducer for each story are necessary to realize the feedback control. In the numerical investigation of semi-active control performance, the corresponding computed building responses and damper forces are taken as the relevant feedback instead of the signals from the sensors in practice. In the implementation of the clipped optimal displacement control strategy, the two weighting matrices $\mathbf{Q}_{MR}$ and $\mathbf{R}_{MR}$ are selected as the unit diagonal matrix multiplied by a factor 1×10^5 and 0.00001, respectively, after a trial and error study.

Demonstrated in Fig. 8 are the variations of the peak displacement, velocity, and acceleration responses of the example building without control, with passive-on control, and with semi-active control. The passive-on control is actually a passive control by setting the maximum damping in the MR damper. It can be seen that the peak responses of all the building floors under semi-active control are substantially reduced in comparison with those with passive-on control and without control. Clearly, the semi-active control with the clipped optimal displacement control algorithm can effectively suppress the seismic responses of the building structure.

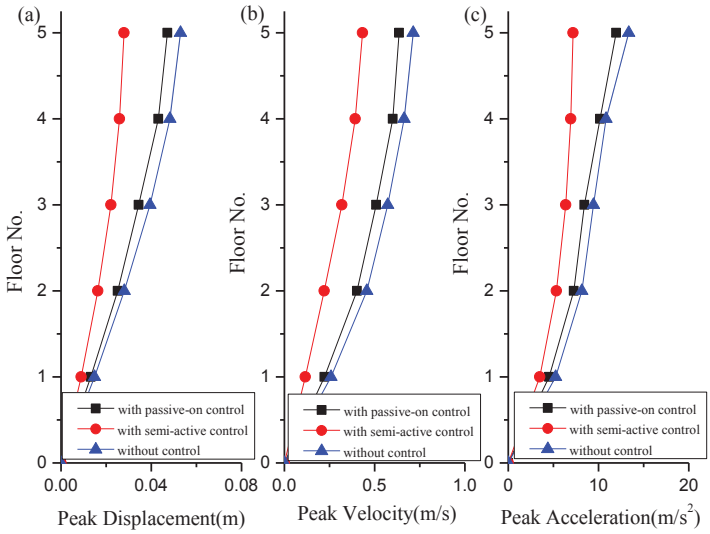

Fig. 8 Comparison of control performance without control and with semi-active control and passive-on control

5.4 Comparison

To further demonstrate the necessity and advantage of the proposed integrated procedure, the performance of semi-active control using on-line updated structural parameters is compared with that without updating structural parameters and that with passive-on control. Moreover, the accuracy of the parameter and excitation identification of the building structure with time-varying structural parameters in control algorithm is compared to that with constant structural parameters in control algorithm.

The semi-active control performance is evaluated in terms of two widely-accepted sets of normalized performance indices. The first set of the performance indices is related to the building responses, which include peak- and RMS-based inter-story drift ratios (J_1 and J_3) and peak- and RMS-based absolute acceleration responses (J_2 and J_4) expressed by

$$J_1 = \frac{\max\limits_{t,i} \left| dx_i^c(t) \right| / h_i}{\max\limits_{t,i} \left| dx_i^n(t) \right| / h_i} \tag{37}$$

$$J_2 = \frac{\max\limits_{t,i} \left| \ddot{x}_i^c(t) \right|}{\max\limits_{t,i} \left| \ddot{x}_i^n(t) \right|} \tag{38}$$

$$J_3 = \frac{\max\limits_{t,i} \left\| dx_i^c(t) \right\| / h_i}{\max\limits_{t,i} \left\| dx_i^n(t) \right\| / h_i} \tag{39}$$

$$J_4 = \frac{\max\limits_{t,i} \left\| \ddot{x}_i^c(t) \right\|}{\max\limits_{t,i} \left\| \ddot{x}_i^n(t) \right\|} \tag{40}$$

where $dx_i^c(t)$ and $dx_i^n(t)$ are the inter-story drifts of the i th story of the building with and without control, respectively; h_i is the height of the i th story; $\left| dx_i^c(t) \right| / h_i$ and $\left| dx_i^n(t) \right| / h_i$ are the inter-story drift ratios of the i th story of the building with and without control, respectively; $\ddot{x}_i^c(t)$ and $\ddot{x}_i^n(t)$ are the absolute acceleration responses of the i th floor of the building with and without control, respectively. The RMS response quantities within the time duration t_f under earthquake excitation are calculated by $\|\bullet\| = \sqrt{\frac{1}{t_f}\int_0^{t_f} [\bullet]^2 dt}$. The sign $\max\limits_{t,i}$ means to find the maximum value within the given time duration first and among all the building stories afterwards. The second set of performance indices are related to the capacity of control devices. The peak-based control force (J_5) is

$$J_5 = \frac{\max\limits_{t,k} \left| u_k(t) \right|}{W} \tag{41}$$

Table 2 Performance indices for semi-active vibration control using MR dampers

Index	J_1	J_2	J_3	J_4	J_5
Passive-on control	0.8703	0.6611	0.8806	0.7532	0.076
Semi-active control without parametric updating	0.8117	0.5744	0.8301	0.6951	0.068
Semi-active control with parametric updating	0.5766	0.5376	0.2439	0.3127	0.054

where $u_k(t)$ is the control force generated by the k th control device (MR damper); and W is the total weight of all the building floors.

Table 2 shows the performance indices of the controlled building with semi-active control (with and without parameter updating) and passive-on control. It can be seen that the proposed semi-active control using MR dampers and considering on-line parameter updating can effectively reduce both the peak and RMS responses of the example building under seismic excitation. The reduction of the RMS responses (J_3 and J_4) is even more than that of the peak responses (J_1 and J_2). It can also be seen that the semi-active control with on-line parameter updating has much higher control performance than that with passive-on control. The control force index further shows that with passive-on control, the control force required is also more than that using semi-active control with on-line parameter updating. Therefore, the on-line parameter updating is necessary to ensure higher control performance and less control force. The above observation can be further confirmed through the comparison of the time histories of displacement, velocity and acceleration responses of the top floor of the building without control, with passive-on control, and with semi-active control. Fig. 9 shows the time histories of acceleration responses of the top floor of the building for various cases as an example.

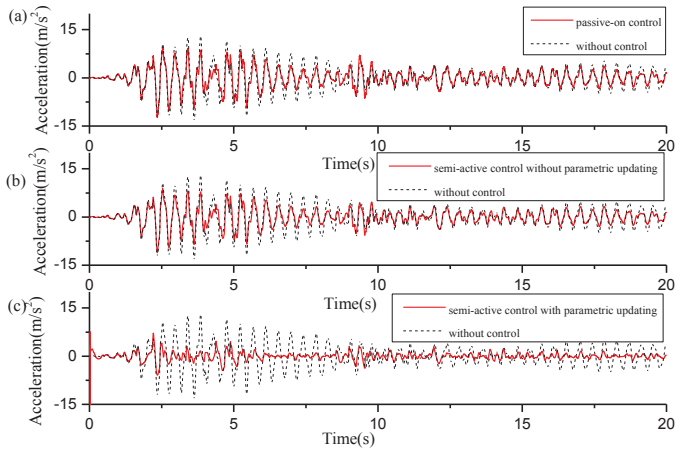

Fig. 9 Comparison of acceleration response time histories of the building structure at the top floor

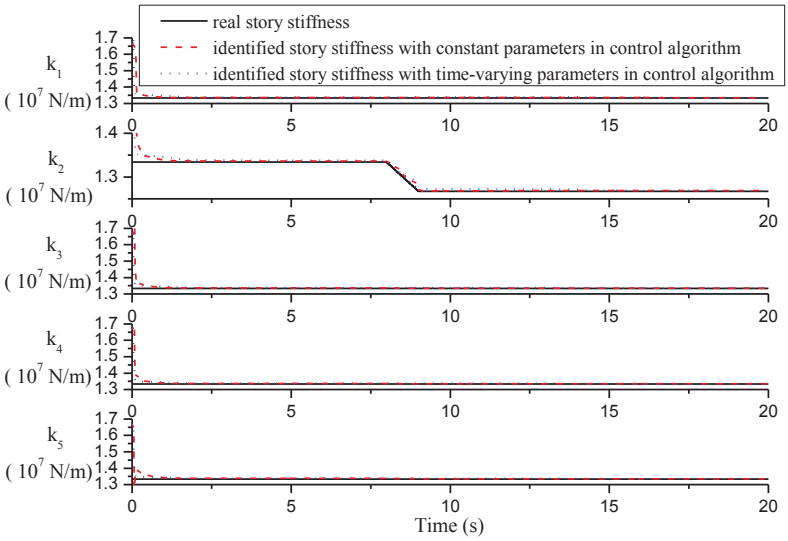

Fig. 10 Comparison of identified results of story stiffness

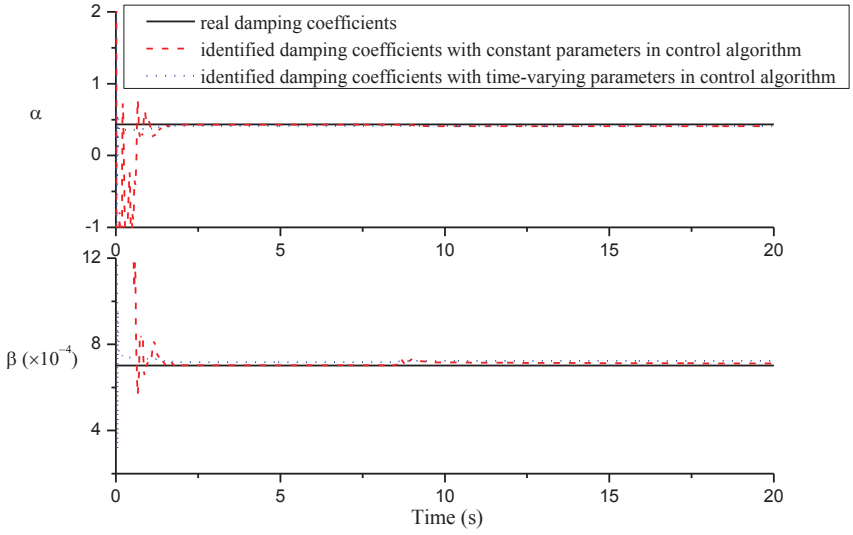

Fig. 11 Comparison of identified results of Rayleigh damping coefficients

Figs. 10 and 11 present the identified results of time-varying stiffness coefficients of the five stories of the controlled building and the two coefficients α and β, respectively, with and without considering time-varying structural parameters in control algorithm. In Figs. 10 and 11, the identified results for the controlled building without considering time-varying structural parameters in control algorithm are presented as dash lines, whereas those with considering time-varying structural parameters in control algorithm are presented as dot lines and the real values are presented as solid lines for comparison. It can be seen that structural parameter identification of the building with and without considering time-varying structural parameters in control algorithm both have very good tracking ability for capturing time-varying stiffness. Moreover, the identified results of the earthquake-induced ground acceleration are almost the same for the two cases. However, the results presented in Figs. 10 and 11 show that structural parameter identification of the building with considering time-varying structural parameters in control algorithm converges much faster to the real value than that without considering time-varying structural parameter in control algorithm. This is particularly true in the identification of damping coefficients.

6. Conclusions

A real-time integrated procedure for both health monitoring and vibration control of a building structure has been presented in this paper so that on one hand, the time-varying structural parameters and unknown excitations of the building structure during earthquake excitation can be identified and, on the other hand, the excessive vibration of the building structure can be effectively mitigated. The time-varying parameter and excitation identifications are based on the least-squares estimation method and the measured structural responses and control forces, whereas the vibration control is fulfilled using semi-active MR dampers, a clipped optimal displacement control algorithm, and on-line identified time varying structural parameters and excitation. The numerical study of an example building shows that the proposed real-time integrated method does effectively suppress the seismic responses of the building compared with the passive-on control and at the same time accurately identify unknown excitations and time-varying structural parameters. The numerical study also manifests that the control performance will deteriorate if only the initial constant structural parameters are taken into account in the semi-active control. However, this does not affect the accuracy of identification of time-varying structural parameters and excitation except for the initial convergent rate.

Acknowledgements

The authors wish to acknowledge the financial supports from the Research Grants Council of Hong Kong (PolyU 5319/10E). Any opinions and concluding remarks presented in this paper are entirely those of the authors.

References

Basu, B., Nagarajaiah, S. and Chakraborty, A. (2008), “Online identification of linear time-varying stiffness

of structural systems by wavelet analysis", *Struct. Health Monit.*, **7**(1), 21-36.
Chen, B. and Xu, Y.L. (2008), "Integrated vibration control and health monitoring of building structures using semi-active friction dampers: Part Ⅱ - Numerical investigation", *Eng. Struct.*, **30**(3), 573-587.
Chen, B., Xu, Y.L. and Zhao, X. (2010), "Integrated vibration control and health monitoring of building structures: a time-domain approach", *Smart Struct. Syst.*, **6**(7), 811-833.
Deng, F., Rémond, D. and Gaudiller, L. (2011), "Self-adaptive modal control for time-varying structures", *J. Sound Vib.*, **330**, 3301-15.
Doebling, S.W., Farrar, C.R., Prime, M.B. and Shevitz, D.W. (1996), "Damage identification and health monitoring of structural and mechanical systems from changes in their vibration characteristics: a literature review", Los Alamos National Lab., NM (United States).
Gattulli, V. and Romeo, F. (2000), "Integrated procedure for identification and control of MDOF structures", *J. Eng. Mech.- ASCE*, **126**(7), 730-737.
Gavin, G.P, Hanson, R.D andFilisko, F.E. (1996), "Electrorheological dampers. Part I: analysis and design", *J. Appl. Mech. - T ASME*, **63**, 669-675.
Housner, G.W., Bergman, L.A., Caughey, T.K., Chassiakos, A.G., Claus, R.O., Masri, S.F., Skelton, R.E., Soong, T.T., Spencer, B.F. and Yao, J.T.P. (1997),"Structural control: past present, and future", *J. Eng. Mech. - ASCE*, **123**, 897-971.
Huang, Q., Xu, Y.L., Li, J.C., Su, Z.Q. and Liu, H.J. (2012), "Structural damage detection of controlled building structures using frequency response functions", *J. Sound Vib*, **331**, 3476-3492.
Kosmatopoulos, E.B., Smyth, A.W., Masri, S.F. and Chassiakos, A.G. (2001), "Robust adaptive neural estimation of restoring forces in nonlinear structures", *J. Appl.Mech. - T ASME*, **68**(6), 880-893.
Lei, Y., Jiang, Y. and Xu, Z. (2012a), "Structural damage detection with limited input and output measurement signals", *Mech. Syst. Signal Pr.*, **28**, 229-243.
Lei, Y., Wu, Y. and Li, T. (2012b), "Identification of non-linear structural parameters under limited input and output measurements", *Int. J.Nonlinear. Mech.*, **47**(10), 1141-1146.
Mufti, A.A. (2001), *Guidelines for Structural Health Monitoring*, Winnipeg, Manitoba: ISIS Canada.
Nagarajaiah, S. and Jung, H.J. (2014), "Smart tuned mass dampers: recent developments", *Smart Struct. Syst.*, **13**(2), 173-176.
Nishitani, A. and Inoue, Y. (2001), "Overview of the application of active/semiactive control to building structures in Japan", *Earthq. Eng. Struct. D.*, **30**, 1565-1574.
Qu, W.L. and Xu, Y.L. (2001), "Semi-active control of seismic response of tall buildings with podium structure using ER/MR dampers", *Struct. Des. Tall Buil.*, **10**(3), 179-192.
Ray, L.R. and Tian, L. (1999), "Damage detection in smart structures through sensitivity enhancing feedback control", *J. Sound Vib.*, **227**(5), 987-1002.
Sohn, H., Farrar, C.R., Hemez, F.M., Shunk,D.D., Stinemates, D.W. and Nadler, B.R. (2003), *A review of structural health monitoring literature: 1996-2001*, Los Alamos National Laboratory Report, LA-13976-MS.
Spencer, B.F. and Nagarajaiah, S. (2003), "State of the art of structural control", *J. Struct. Eng. - ASCE*, **129**(7), 845-56.
Viscardi, M. and Lecce, L. (2002), "An integrated system for active vibro-acoustic control and damage detection on a typical aeronautical structure", *Proceedings of the 2002 IEEE International Conference on Control Applications 2002*, Glasgow, Scotland, U.K.
Wenzel, H. (2009), *Health Monitoring of Bridges*, John Wiley & Sons.
Xu, Y.L. and Chen, B. (2008), "Integrated vibration control and health monitoring of building structures using semi-active friction dampers: Part Ⅰ - Theory", *Eng. Struct.*, **30**(7), 1789-1801.
Xu, Y.L., Huang, Q., Zhan, S. Su, Z.Q. and Liu, H.J. (2014), "FRF-based structural damage detection of controlled buildings with podium structures: Experimental investigation", *J. Sound Vib.*, **333**(13), 2762-2775.
Xu, Y.L., Qu W.L. and Ko J.M. (2000), "Seismic response control of frame structures using magnetorheological/electrorheological dampers", *Earthq. Eng. Struct. D.*, **29**(5), 557-575.

Xu, Y.L. and Xia, Y. (2012), *Structural Health Monitoring of Long-span Suspension Bridges*, CRC Press.
Yang, H.T.Y., Shan, J.Z., Randall, C.J., Hansma, P.K. and Shi, W.X. (2013), "Integration of health monitoring and control of building structures during earthquakes", *J. Eng. Mech. - ASCE*, DOI: 10.1061/(ASCE)EM.1943-7889.0000718.
Yang, J.N. and Huang, H. (2007), "Sequential non-linear least-square estimation for damage identification of structures with unknown inputs and unknown outputs", *Int. J.Nonlinear. Mech.*, **42**(5), 789-801.
Yang, J.N., Pan, S. and Lin, S. (2007), "Least-squares estimation with unknown excitations for damage identification of structures", *J. Eng. Mech. - ASCE*, **133**(1), 12-21.

Smart Structures and Systems, *Vol. 15, No. 3 (2015) 831-846*
DOI: http://dx.doi.org/10.12989/sss.2015.15.3.831

An innovative hardware emulated simple passive semi-active controller for vibration control of MR dampers

Jianqiu Zhang[1] and Anil K. Agrawal[*2]

[1]*Noise, Vibration and Hardness Expert, HELLA Group, Lippstadt, Germany*
[2]*Department of Civil Engineering, The City College of New York, NY 10031, USA*

(Received November 27, 2014, Revised January 27, 2015, Accepted February 18, 2015)

Abstract. Magneto-Rheological (MR) dampers are being used increasingly because of their adaptability to control algorithms and reliability of passive systems. In this paper, an extensive investigation on performance of MR dampers in semi-active and passive modes has been carried out. It is observed that the overall energy dissipation by MR dampers in passive-on modes is higher than that in semi-active modes for most of the competitive semi-active controllers. Based on the energy dissipation pattern, a novel semi-active controller, termed as "Simple Passive Semi-Active Controller", has been proposed for MR dampers. This controller can be emulated by a simple passive hardware proposed in this paper. The proposed concept of controller "hardware emulation" is innovative and can also be implemented for other semi-active devices for control algorithms of certain form. The effectiveness and reliability of the proposed controller has been investigated extensively through numerical simulations. It has been demonstrated that the proposed controller is competitive to or more effective than other widely used / investigated semi-active controllers.

Keywords: structural response control; passive dampers; semi-active dampers; MR dampers

1. Introduction

Structural control systems, such as passive, semi-active and active control systems, have been investigated extensively during last four decades because of their effective wind and seismic hazard mitigation of civil infrastructures (Spencer and Nagarajaiah 2003). Among the three types of structural control systems, fluid viscous dampers have been used the most extensively in buildings and bridges. For example, 18,338 Taylor fluid viscous dampers have been installed in 484structures for wind and seismic hazard mitigations till 2013 (Taylor Devices 2012).

Significant research efforts have been focused on the semi-active protective systems during the last decade because of their reliability and capability to achieve performance similar to those of fully active systems (He and Agrawal 2006). Semi-active protective systems are able to function as passive devices in the event of failure of the control system or power. These systems are also inherently stable and dissipative, since they cannot input mechanical energy into the structural system. They also require significantly smaller amounts of power compared to an active control system because of parametric nature of the control mechanisms.

*Corresponding author, Professor, E-mail: Agrawal@ccny.cuny.edu

http://www.techno-press.org/?journal=sss&subpage=8 ISSN: 1738-1584 (Print), 1738-1991 (Online)

Among various types of semi-active protective systems, magneto-rheological (MR) dampers have been considered to be particularly promising for both wind and seismic hazard mitigation of structures. MR dampers are similar to conventional fluid dampers in construction. However, they contain MR fluids in place of hydraulic oil in conventional fluid dampers. MR fluids consist of oil with suspended fine iron particles and can change their state from liquid to semi-solid to solid almost instantly in the presence of a magnetic field. Compared to other smart fluids, MR fluids have a large maximum yield stress (50 kpa to 100 kPa), a wide operable temperature range (-50˚C to 150˚C), and a fast response time (milliseconds) (Carlson and Spencer 1996). The performance of MR dampers isn't affected by impurities and contaminants. However, MR dampers are operated in passive-on (PON) mode in majority of applications. In this mode, they are provided with a constant voltage (Chen *et al*. 2003).

Commercial MR fluid devices have been available in the market since middle 1990s (Carlson *et al*. 1996b). However, these devices were considered small scale devices because of force capacity of the scale of 10^3 N. More recently, a large scale 20-ton MR damper was designed and produced by Lord Corporation for full scale seismic applications (Spencer *et al*. 1998a).Mechanical simplicity, high dynamic range, low power requirement, large force capacity and inherent robustness have made large scale MR dampers quite suitable for full-scale structural applications.

A Bouc-Wen model exhibiting hysteretic behavior of the MR damper has been proposed by Spencer *et al*. (1997). Comparison between numerical simulations and experimental results were made to validate the efficiency of this model. The phenomenological Bouc-Wen model was further modified by Jiang *et al*. (2010) to better accommodate a time varying current. More recently, a hyperbolic tangent model has been presented by Bass *et al*. (2007) to model the behavior of MR dampers. This model describes the dynamics of the damper and the force output in a state space form, making this model suitable for a faster numerical analysis (Jiang *et al*. 2010).

Although numerous semi-active control algorithms have been proposed in the literature, it has been observed that the performances of MR dampers using currently available semi-active controllers are inferior to or is similar to those of MR dampers in PON modes. For example, Friedman *et al*. (2014) have carried out a detailed investigation on the performance of PON and COC controllers and have shown that the performance of PON is better or similar to COC. In this paper, the performances of two most competitive semi-active controllers for MR dampers have been compared with those of MR dampers in PON mode. Based on this investigation, a "Simple Passive Semi-Active Controller" (SPSAC) has been developed. Although this is semi-active controller, it can be implemented as a passive system (i.e., without requiring sensor and controller).

2. Performance of MR dampers in semi-active and PON modes

An extensive comparative investigation on performances of MR dampers in semi-active and PON modes have been carried out through numerical simulations on a 4-story evaluation model representing the moment resisting frame of a typical office building on stiff soil in Los Angeles, California. Detailed information on the property of this building and the development of the evaluation model can be found in Friedman *et al*. (2010). Fig. 1 shows the 13 degrees of freedom evaluation model consisting of eight horizontal DOFs and five vertical DOF (Zhang 2012). The first five natural frequencies for the structural model are 0.70, 1.82, 3.36, 5.22, 5.36 Hz.

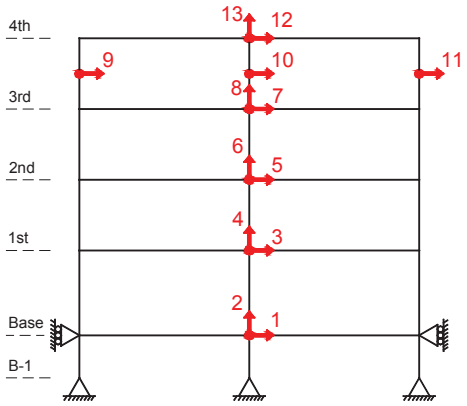

Fig. 1 Evaluation Model of the Moment Resisting Frame for Numerical Simulation

The model of MR damper in the numerical simulations is based on a 200 kN MR damper with a stroke of 584 mm. The phenomenological Bouc-Wen model for MR dampers discussed previously requires ten parameters as a function of current in the damper to fully characterize the dynamic behavior of the MR dampers. Polynomial functions for these parameters as a function of the current i are have been obtained by nonlinear optimization of model parameters using experimental data of MR dampers (Zhang 2012). Likewise, fourth order polynomial functions for parameters of the hyperbolic tangent model as functions of the current (i) have been derived by Jiang *et al*. (2010) through optimization using experimental data on MR dampers. Results by Jiang *et al*. (2010) show that, although both the Bouc-Wen and the hyperbolic-tangent models can predict the control force of the 200 kN MR damper very well, RMS errors (between experimental and theoretical responses related to dampers) are smaller in case of the hyperbolic-tangent model. They have shown that the hyperbolic-tangent model is 20% faster than the Bouc-Wen model. In this research, both Buoc-Wen and hyperbolic-tangent models has been used to model behavior of MR dampers.

The performance of large scale MR dampers in semi-active and passive-on modes has been evaluated by selecting two very competitive and widely investigated semi-active controllers: (i) Clipped-Optimal Controller (COC) (Jansen and Dyke 2000) and smooth boundary layer controller (SBLC) (He *et al*. 2003). The COC consists of two sub-controllers: a linear optimal controller and a secondary bang-bang controller. The force calculated by the linear optimal controller (the first sub-controller) can be generally expressed as

$$f_c = L^{-1}\left\{K_c(s)L\{\begin{bmatrix} y \\ f \end{bmatrix}\}\right\} \tag{1}$$

where y is the vector of measured structural response; f is the vector of measured force generated between MR dampers and the structure; $L\{\cdot\}$ and $L^{-1}\{\cdot\}$are the Laplace transform and inverse Laplace transforms, respectively; and $K_c(s)$ is a linear optimal controller designed to provide the desired control force based on the measured responses y and the measured force f. The term f_c is the optimal control force calculated by the linear optimal controller (or the first sub-controller of COC). It is noted that the linear optimal controller $K_c(s)$ can be obtained from a

variety of synthesis methods, e.g., LQG. In the COC, the rule based on which the control voltage is generated is stated as: (1) when the MR damper is providing the desired optimal force (i.e., $f = f_c$), the voltage applied to the damper should remain at the present level; (2) if the magnitude of the force produced by the damper is smaller than the magnitude of the desired optimal force, and the two forces have the same sign, the voltage applied to the current driver is increased to the maximum level so as to increase the force produced by the damper match the desired control force; (3) otherwise, the voltage applied to the current driver is set to zero. The algorithm for selecting the command signal can be expressed as

$$v = V_{max} H\{(f_c - f)f\} \tag{2}$$

where V_{max} is the voltage to the current driver associated with saturation of the magnetic field in the MR damper, and $H\{\cdot\}$ is the Heaviside step function.

The smooth boundary layer controller (SBLC) was developed by He *et al*. (2003) and has been modified for MR dampers as

$$u(t) = \beta \left| P\left[\dot{d}(t)\right] \right| tanh(\alpha d) \tag{3}$$

where u is the control voltage; term d is the displacement across the damper; α and β are the weighting parameters to be defined by the designers; $\left| P\left[\dot{d}(t)\right] \right|$ is the absolute value of the local peak displacement prior to the current time t. According to the control algorithm, the control voltage is determined by the velocity across the damper through a hyperbolic-tangent function. The hyperbolic-tangent function ensures that the control voltage will decrease to zero smoothly (the design parameter α controls how smooth this voltage-drop is) when the damper stops moving.Performance of this controller has been investigated extensively by He *et al*. (2003).

Nine evaluation criteria, similar to those used in several benchmark studies (Ohtori *et al*. 1998b, Agrawal *et al*. 2009), have been used to evaluate performance of MR dampers in semi-active and PON modes. However, among these 9 evaluation criteria, evaluation criteria J_1, J_2 and J_6 shown in Table 1 have been considered to be more important measures. The importance of these criteria lies in their definitions: J_1 (normalized displacement) and J_2 (normalized interstory drift) are related to the maximum damage caused to the structure, while J_6(normalized norm of drift) is related to cumulative seismic damage during the duration (t_f) of the earthquake. In these evaluation criteria, $x_i(t)$ is the horizontal displacement of i^{th} floor; x_{max} is the maximum displacement of the uncontrolled structure for a particular earthquake; $d_i(t)$ is the inter-story drift of the ith floor; h_i is the height of ith floor and $d_{n,max} = \max(d_i(t)/h_i)$ is the uncontrolled maximum inter-story drift ratio. Evaluation criteria J_6 corresponds to normed response quantities (e.g., $\|x_i(t)\| = \sqrt{\int_0^{t_f} x_i^2(t)dt}$).

Four recorded earthquakes, which have also been adopted in several benchmark structural control studies (Agrawal *et al*. 2009), have been selected for this study. These four historical ground motions are: (1) El Centro (N-S, 1940), (2) Hachinohe (N-S, 1968), (3) Kobe (N-S, 1995), (4) Northridge (N-S at Sylmar County Hospital parking lot, 1994). These earthquakes are denoted as ELC, HAC, KOB and NOR, respectively.

Two 200 kN MR dampers, one between Base and 1stfloor and another between 1st and 2nd floor, have been installed in the evaluation model in Fig. 1. As described previously, COC consists of two sub-controllers: a linear optimal controller in Eq. (1) and a secondary bang-bang controller in Eq. (2). A state-space linear quadratic Gaussian (LQG) regulator is chosen as the linear optimal

controller to calculate the optimal control force. The LQG controller has been designed by considering floor accelerations as measured responses, weighting matrix$Q = q[I]$) and control weighting matrix R = a $[4 \times 4]$ diagonal matrix with R(1,1) = R(2,2)= r, and R(3,3)= R(4,4) = 0 (Zhang 2012).Parameters for COC and SBLC controllers have been designed using El Centro earthquake such that (1) the normalized inter-story drift (J_2) is minimized, and (2) the force capacity (200 kN) of MR damper is fully utilized. Resulting design parameters of above two controllers are: $q = 1 \times 10^{10}$, $r = 1 \times 10^{-5}$ for COC, $\alpha = 20$, $\beta = 40$ for SBLC. In addition, a saturation voltage V_{max} = 2.5 volt is designated for all the controllers to avoid damage to MR damper coils. It should be noted that weighting matrices Q and R are the weights on the response reduction and control cost in a typical LQG controller (Friedman *et al*. 2014).

Simulation results have been analyzed for 4 earthquakes described previously. It has been observed from simulation results that while passive-off case is almost similar to the uncontrolled case, performances of other three controllers are quite similar. In fact, the performance of PON controller is better than two semi-active controllers during Northridge earthquake, which is the most severe among 4 earthquakes, although other earthquakes also yield similar results (Zhang 2012).

It has been observed from simulation results that the maximum peak control force during passive-off case is around 0.5% of the effective seismic weight. During semi-active modes, the peak control force is increased to 2% of the effective seismic weight, since there are two MR dampers of 200 kN capacity each. Hence the reduction of peak response quantities in semi-active case is more obvious as compared to the passive-off case. Such reduction in the structural responses can be further quantified by calculating the evaluation term "Gain/Loss of J", which is percentage response reduction. The Gain/Loss of J (shortened as GLJ) for a controller with respect to uncontrolled response can be calculated as

$$GLJ_{Uncontrolled,i}^{COC,EQ} = \left(1 - J_i^{COC,EQ}\right) \times 100\%; \quad GLJ_{Uncontrolled,i}^{SBLC,EQ} = \left(1 - J_i^{SBLC,EQ}\right) \times 100\% \quad (4)$$

where subscript i denotes evaluation criteria number, the label EQ (= ELC, HAC, KOB, NOR) is the ground motion under which the criteria J_i has been obtained. The calculated GLJ error directly reflects gain or loss in the performance of a specific control strategy with respect to uncontrolled response. When a control strategy fails to reduce the structural responses, the sign of the calculated error would be negative; and the magnitude of the absolute value of this negative error represents increase in response with respect to uncontrolled structure.

Table 1 Evaluation Criteria for the Performance Comparison

Peak Horizontal Disp.	Peak Interstory Disp.	Normed Interstory Disp.
$J_1 = max\left(\frac{max\lvert x_i(t)\rvert}{x_{max}}\right)$	$J_2 = max(\frac{max\lvert d_i(t)/h_i\rvert}{d_{n,max}})$	$J_6 = max(\frac{max\frac{\lVert x_i(t)\rVert}{h_i}}{\lVert d^{max}\rVert})$ Peak Absolute

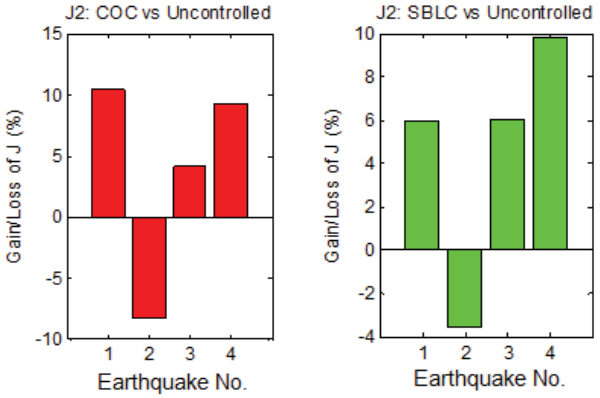

Fig. 2 Plots of Gain/Loss of J2for COC SBLC with Respect to Uncontrolled Responses

It has been observed from simulation results that the evaluation criteria $J_6$is generally more than 15% in cases of both COC and SBLC for all earthquakes and J_1 is positive for both controllers during all 4 earthquakes, although it is close to zero for COC during Hachinohe earthquake. In particular, the SBLC reduces the cumulative floor displacement (J_6) by more than 20% during Hachinohe, Kobe, and Northridge earthquakes, and 32% during the El Centro earthquake. Hence, bar plots only for the evaluation criteria J2 (interstory drift) are shown for two controllers in the Fig. 3 below. Evaluation criteria J_2 for the Hachinohe earthquake (earthquake 2) shows a loss in Fig. 3, whereas J_6 for this earthquake has been found to be a gain for both COC and SBLC controllers. This shows that the two controllers are more effective in reducing the overall interstory drift time-history of the building and not effective in reducing the peak interstory drift during the Hachinohe earthquake. However, overall the SBLC is more effective in reducing the peak drift than the COC.

Although the two semi-active controllers achieved a better performance than the passive -off mode, both controllers have been observed to achieve a performance similar to that of the passive-on mode (Zhang 2012). To better illustrate of the two controllers with respect to the PON case, a quantified comparison is made by calculating the GLJ for COC and SBLC cases with respect to PON during the four earthquakes. The GLJ is calculated with respect to passive-on case using the following equations,

$$GLJ_{PON,i}^{COC,EQ} = \left(J_i^{PON,EQ} - J_i^{COC,EQ}\right) \times 100\%;\ GLJ_{PON,i}^{SBLC,EQ} = \left(J_i^{PON,EQ} - J_i^{SBLC,EQ}\right) \times 100\% \quad (5)$$

where i represents subscript for evaluation criteria J_i, and label EQ (= ELC, HAC, KOB, NOR) indicates the ground motion. A positive GLJ calculated by Eq. (5) indicates that MR dampers in semi-active mode achieves a better performance than the passive-on case, while a negative GLJ implies an inferior performance of MR dampers in semi-active mode with respect to the passive-on case. Fig. 4 shows GLJ for COC and SBLC with respect to the PON case.

Out of the total twelve $GLJ_{PON,i}^{COC,EQ}$ shown in Fig. 5 for the COC case, only three values ($GLJ_{PON,1}^{COC,ELC}$, $GLJ_{PON,1}^{COC,HAC}$, $GLJ_{PON,2}^{COC,HAC}$) are found to be positive. On the other hand, 5 $GLJ_{PON,i}^{SBLC,EQ}$ values are positive for the SBLC case. In particular, among 8 GLJ values for the evaluation

criterion J_6 for COC and SBLC, only $GLJ_{PON,6}^{COC,KOB}$ shows an improvement of 1% over the PON case. Considering the fact that semi-active controllers utilize advanced control algorithms and sensors for achieving an optimized control of structural responses, their performance in Fig. 5 is not attractive for practical applications.

3. Energy dissipation pattern

The performance of the damper as well as the controller largely depends on the amount of the dissipated seismic energy and the way in which the energy is dissipated during the earthquake ground motion. The energy dissipation by the 200 kN MR damper occurs during each of the reciprocating piston strokes as the structure is subjected to external load. The total energy dissipated (E_D) by a MR damper during a displacement interval of $[x_1, x_2]$ can be calculated as (Chopra 2001)

$$E_D = \int f_D \cdot d(x_d) \,, \qquad x_d \in [x_1, x_2] \tag{6}$$

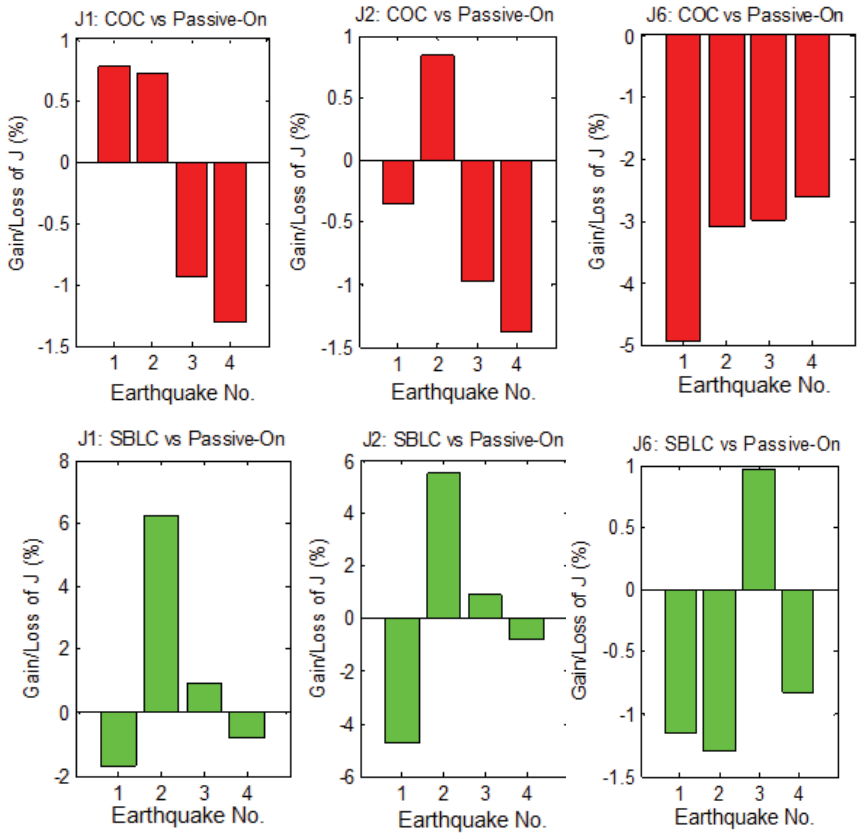

Fig. 3 Plots of Gain/Loss of J between COC and Passive-On Cases

In Eq. (6), f_D is the damper force, x_d is the damper piston movement (equivalent to inter-story displacement when damper is horizontally connected between two stories), x_1 and x_2 are the lower and upper limits of the displacement interval of interest.

In order to investigate energy dissipation pattern of MR dampers in semi-active and passive modes, numerical simulations have been carried out by installing two MR dampers in the building (one in base floor and one in 1st floor in Fig. 1) subjected to the El Centro earthquake. Both MR dampers have been controlled in passive-on (Constant voltages of 2.0 V for damper 1 on first floor and 1.0 V for damper 2 on second floor) and semi-active control (COC) modes. Energy dissipated by MR dampers has been calculated from numerical simulation results using Eq. (8).

Fig. 6 shows the plots of energy dissipated by the MR Damper 1 as a function of inter-story drift (or damper stroke) for the two control strategies (COC and passive-on). The bars in the figure represent the amount of cumulative dissipated energy within each damper stroke interval. The plots for MR Damper 2 and those during other earthquakes have been found to be similar to those in Fig. 6.

It is observed from Fig. 6 that the pattern of the dissipated energy distribution is nearly triangular, and most of the energy is dissipated around the zero interstory drift (or maximum interstory velocity during each vibration cycle). For example, total energy dissipated by MR Damper 1 in PON mode is 268.6 kN·m, the maximum interstory drift of that floor is 0.035 m, and 68% (183.1 kN·m) of the total dissipated energy occurs within ±0.01 m displacement around the zero position of the piston. For the case of COC in Figure 6, 64% (110.7 kN·m) of the total energy is dissipated within ±0.01 m displacement around the zero position of the piston. It is interesting to note that, although clipped-optimal controller utilizes sophisticated sensor-based feedback control logic, its dissipated energy distribution is very similar to that of the PON case. It has been observed from simulation results that the total energy dissipated by MR damper 1 in PON mode (268.6 kN·m) is 55% more than the amount dissipated (173.0 kN·m) in COC mode. Such significant difference in dissipated energy can explain why the performance of MR dampers in semi-active model is inferior to that in PON mode.

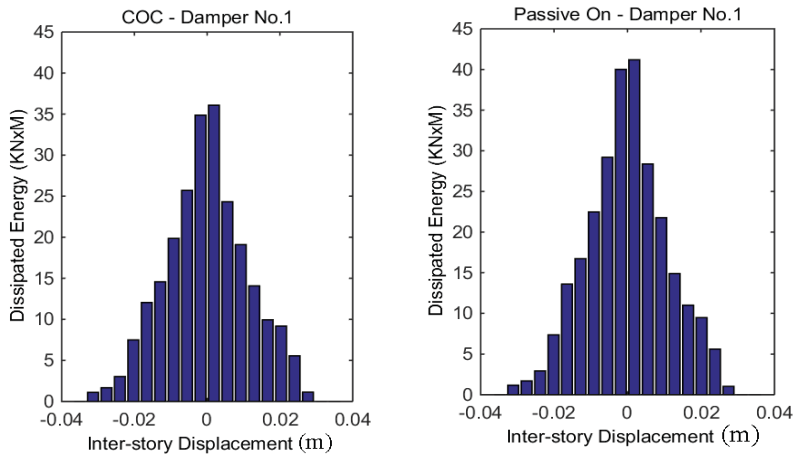

Fig. 6 Energy Dissipation Pattern by MR Damper in Semi-active and PON Modes

4. Development of an innovative simple passive controller

It has been observed from results presented above that the dissipated energy (E_D) is a function of the control force (f_D) and the damper piston displacement (x_D). For MR dampers, the magnitude of control force f_D is determined by the control voltage and the damper piston movement. Fig. 7 shows the force-displacement and force-velocity relationships obtained during the MR damper characterization testing. Green (light black in print paper) and black loops are the force-displacement loops of the 200 kN MR damper obtained using different testing facilities. Each loop in Fig. 7(a) is the force-displacement relationship under a different constant current. It is observed that when the control current increases from 0 A to 2.5 A, the magnitude of the peak damper force jumps from a minimum of ±15 kN to a maximum of ±200 kN. Maximum values of damper forces in both stroke directions in each loop are around x_D= 0 mm. It is also observed from Fig. 7(a) that the damper force drops to zero at the maximum strokes of ±25 mm. Essentially, the velocity is the maximum at zero stroke and decreases gradually as the stroke increases to its maximum value. Hence, no control force can be generated at the instant of the maximum stroke. It is observed from the force velocity loop in Fig. 7(b) that the peak value of damper force increases with an increase in the control current or voltage and maximum force appears at tip-ends of each "S" shape hysteretic loop. The full force capacity (200 kN) of the damper is utilized when both the voltage and the velocity reach their peak values.

Hence, a regulation of the control force magnitude cannot be achieved by merely changing the control voltage when the piston movement is slow. Likewise, decreasing the voltage at the moment when the piston velocity is large is not an "optimal" control option because larger amount of seismic energy could be dissipated if the voltage is kept high at the instant of high velocity. Based on these observations, a concept of simple-passive semi-active controller (SPSAC) is proposed as: input a high voltage to the MR damper to generate a relatively large control force when the floor with dampers or the damper piston vibrates across its zero position. Both the high input voltage and large input velocity will guarantee a large output force and lead to maximum energy dissipation. However, keeping the MR damper working under high voltage (e.g., 2.5 volt) for a long duration may result in a floor lock-up, thus increasing the absolute acceleration of the floors with dampers and drifts of floors without dampers (Jansen *et al*. 2000). The proposed SP controller to maximize the energy dissipation as well as to avoid the floor lock-up is described as

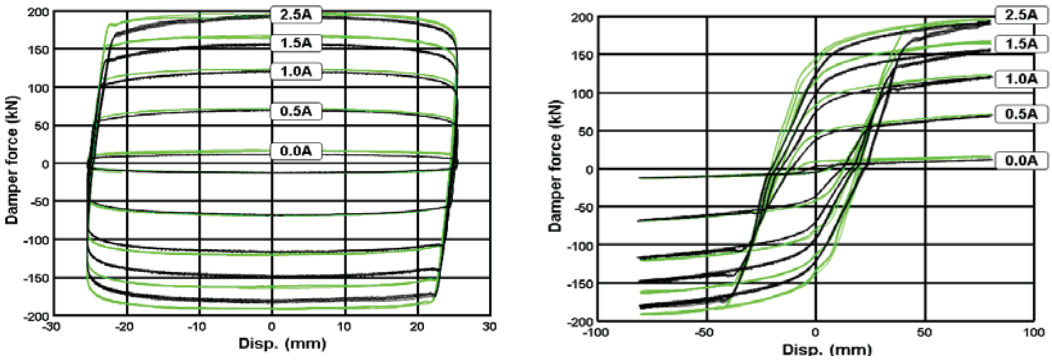

Fig. 7 Behavior of MR Dampers: (a) Force-Displacement Loops and (b) Force Velocity Loops

$$V = \begin{cases} V_1 & |X| < X_1 \\ V_2 & X_1 \le |X| < X_1 + X_2 \\ V_3 & X_1 + X_2 \le |X| < X_1 + X_2 + X_3 \\ 0 & X_1 + X_2 + X_3 \le |X| \end{cases} \tag{7}$$

where V is the control voltage; X (in m) is the damper piston movement or inter-story displacement of the floor on which the MR damper is horizontally installed;X_1, X_2,X_3 ,V_1, V_2, and $V_3$are the design parameters to be determined based on control objectives. The proposed SP control algorithm is represented graphically in Fig. 8 below.

According to the SPSAC algorithm in Eq. (7) and Fig. 8, a voltage of V_1will be input to the damper when the piston displacement or the inter-story drift is within the range of $\pm X_1$. When the floor swings away from its undeformed position beyondX_1, the control voltage drops to V_2 in order to avoid locking up of the floor. However, as the peak inter-story drift increases, voltage will be increased to V_3 after the threshold drift $X_1 + X_2$ so that the damper can act as a stiffness element to limit the peak inter-story drift. Note that the voltage is dropped from V_3 to zero for $|X| \geq X_1 + X_2 + X_3$, since the relatively high voltage V_3 can only be allowed to last for a short time period (usually 1 to 2 seconds) in order to avoid any permanent damage to the wired-coil in the piston. It should be noted that the controller parameters X_1, X_2, X_3, V_1, V_2, and V_3 can be identified through a multi-objective optimization for a particular structure subject to selected ground motions.

5. Emulation of SP controller using mechanical-electrical devices

All semi-active controllers require computational equipment (e.g., embedded microcontroller) inevitable for practical implementation of semi-active controllers. One of the innovative aspects of the proposed SPSAC is its emulation using mechatronics components, thereby eliminating the need for sensors, signal filters, computers/microcontrollers. This will not only enhance system stability and reliability, but will also make practical applications easier. Reliability of a semi-control system in a harsh environment is the biggest impediment in its implementation.

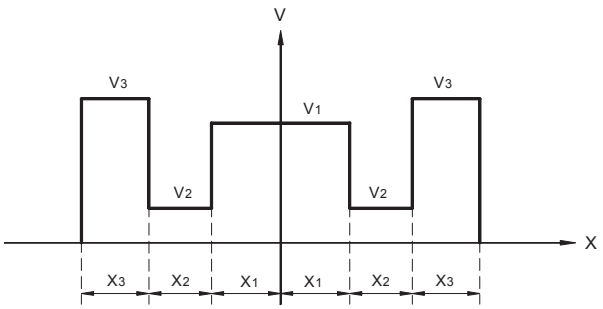

Fig. 8 Voltage Displacement Plot of Proposed Simple Passive Semi-Active Controller

The emulation of the SPSAC can be realized using a concept device called "electrical plate". Considering the control logic in Fig. 8 with voltages (V_1,V_2, and V_3) and linear section lengths (X_1, X_2 and X_3), an electrical plate can be manufactured as illustrated in Fig. 9. Essentially, the electrical plate consists of short metal pieces of lengths X_1, X_2 and X_3. Each of these metal pieces is supplied with voltagesV_1, V_2 or V_3 as per the logic in Fig. 9. Using a common battery power, all the metal pieces can be supplied by a desired voltage V_i for a length of X_i using a simple electrical circuit illustrated in Fig. 9. The operational voltage for most of the MR dampers is below 8 Volt, therefore the supplied voltages V_1, V_2 or V_3 can be easily modulated to the desired level using regular electrical resistances R_1, R_2 and R_3. In the case of tuning the voltages to a different level, these resistances can be easily replaced; adjustable resistances can also be used for tuning purposes.

Once the electrical plate and its peripheral circuits have been manufactured, the next step is to sample the voltage from the plate for commanding the MR damper. In a conventional way, such displacement feedback is achieved by sensor detection. For example, linear variable differential transducers (LVDT) or string pots can be used to detect the magnitude of the damper piston movement, and then the detected signal will be received by the microcontroller for calculating the output voltage. However, for the proposed control logic, the required input is simply the damper piston movement. Thus, a sampling pin can be rigidly attached to the damper piston which will swipe over the electrical plate with the movement of the piston. If the center of the electrical plate can be adjusted to align with the zero position of the piston, the displacement and control voltage relationship can be made to agree with the governing equation of the SPSAC logic in Eq. (7).

A rendering of hardware emulation of the SPSA Crule is illustrated in Fig. 10. The mechatronics device consists of two main parts: a sampling pin and an electrical plate. The pin is attached to the damper piston and the electrical plate is attached to the damper casing or to the fixture to which the damper is tied down. The pin is able to sample the voltage from the electrical plate depending on the piston displacement and input this voltage to the MR damper. The voltage distribution on the electrical plate is designed based on control logic in Eq. (7). It is observed from Fig. 8 that a voltage V_1, V_2, or V_3 may still be input to the damper after the motion stops, depending on the final displacement of the piston (permanent deformation in case of nonlinear structural behavior). In the hardware implementation of the control logic in Fig. 10, a motion detector switch can be installed in the damper to automatically shut down the power when MR damper piston stops moving or if the motion is below certain threshold.

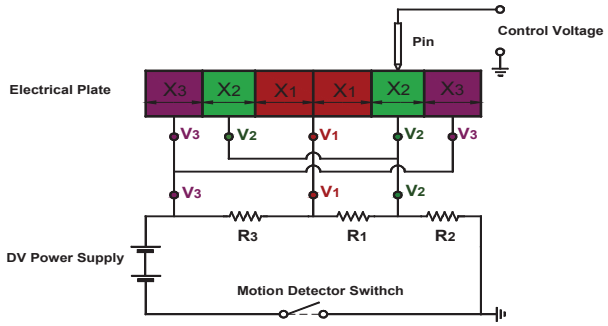

Fig. 9 Hardware Emulation of the Proposed SPSAC Algorithm

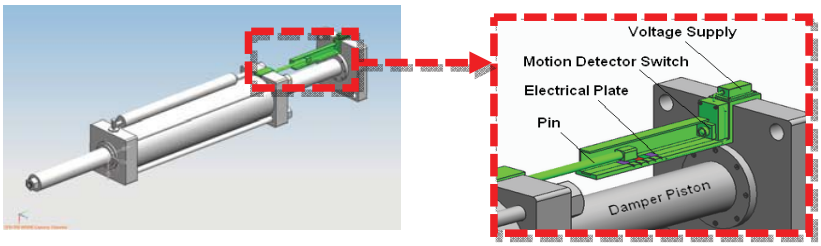

Fig. 10 Rendering of Hardware Emulation of the Proposed SPSAC Algorithm

A typical MR damper semi-active control system requires sensors and controller shown by shaded region in Fig. 11 below. Performance of the control system may be affected by undesired interference between the MR damper and these components. For example, electromagnetic interference to the adjacent circuits and devices may occur due to the presence of the massive wired coil embedded inside of the MR damper piston.

The typical MR damper control system can be simplified to the system shown in the green dashed block in Fig. 11 because of the elimination of sensors and controllers as separate components in the SPSAC mechanism. Hence, the proposed SPSAC mechanism is more reliable than a typical control system.

6. Performance of the simple passive semi-active controller

A three-story structure has been used to carry out detailed investigation on performance of the SPSAC algorithm. This building represents 60% scaled down frame of a building designed for stiff soil location in Los Angeles, CA, and was used for carrying out large scale testing of MR dampers (Jiang *et al*. 2010). Fig. 12 shows the evaluation model of the building. The first three modal frequencies of the reduced model are 1.13 Hz, 3.69 Hz, and 8.44 Hz. It is noted that only the DOFs in the horizontal direction are considered in the reduced model.

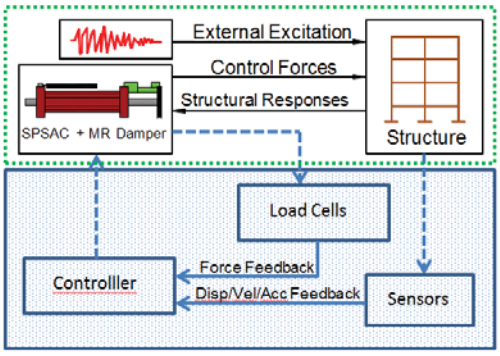

Fig. 11 Comparison between MR Damper Control Systems: (a) Conventional, (b) SPSAC Mechanism

Four DOFs are associated with the corresponding floors, while remaining DOFs No. 5, 6, and 7 are located at the Chevron braces joints. In this evaluation model, one 200 kN MR damper is assumed to be horizontally installed on each of the three above-ground floors, as shown in Figure 12. The positive control force generated by the MR dampers is applied at the Chevron brace joints (DOFs 5, 6, 7) and the negative damper forces are applied on the floors (DOFs 1, 2, 3). Bouc-Wen model has been used to model MR dampers in numerical simulations. Detailed information on the model in Fig. 12 can be found in Zhang (2012).

In addition to ground motions described previously, additional 60 recorded ground motions from the SAC project ground motion suites have been selected. These 60 ground motion records, which were used for the analysis of buildings located in Los Angeles, include records from historic earthquakes as well as artificially-generated time histories based on the modeling of the rupture process and wave propagation through the soil strata. Among these 60 ground motion records, 22 ground motions have peak accelerations smaller than 0.4 g, 20 ground motions have maximum accelerations varying between 0.4 g and 0.7 g and remaining 18 ground motions have peak accelerations larger than 0.7 g. Hence, numerical simulations have been carried out using 64 earthquakes. Performance of MR dampers with the proposed SPSAC has been compared with the performances of MR dampers with clipped-optimal controller (COC), smooth-boundary-layer controller (SBLC), and the passive-on (PON) controller. Parameters for designing these controllers are: $q = 5 \times 10^6$, $r = 1$ for COC, $\alpha = 1000$, $\beta = 120$ for SBLC and X_1=0.008, X_2=0.004, X_3 = 0.001, V_1=7.5V, V_2=0Vand V_3 = 7.5V for the SPSAC. The saturation voltage for all controllers is V_{max} = 7.5 V.

It has been observed from simulation results that the performance of SPSAC is the best among all controllers, including PON, during all 4 previously described earthquakes, although other controllers also have a performance similar to SPSAC during some earthquakes. For example, interstory drifts using different controllers during the Northridge earthquake show that the performances of SPSAC, PON and SBL controllers are quite close to each other and are significantly better than that of the COC.

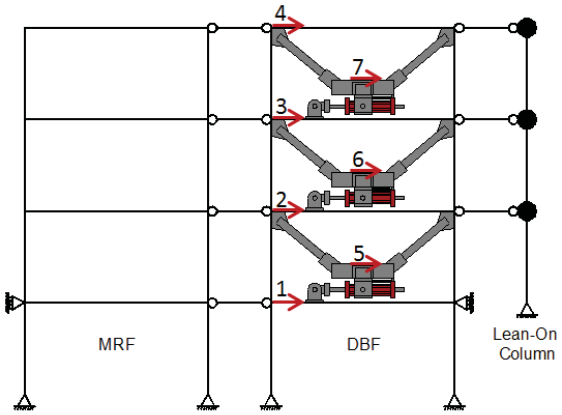

Fig. 12 Evaluation model of a 60% Scaled-Down Frame of a Prototype Building

Because of space limitations, only evaluation criteria J_1 andJ_2 in Table 1 have been calculated for MR dampers with all control strategies (PON, COC, SBLC, SPSAC, and SPB) under all 64 earthquakes. Since the objective is to compare performance of SPSAC with respect to other control strategies, we define "Gain/Loss Ratio of J" ($GLRJ$) for comparison as

$$GLRJ_{Control\ B,i}^{Control\ A,EQ} = \left[\left(J_i^{Control\ B,EQ} - J_i^{Control\ A,EQ}\right)/J_i^{Control\ B,EQ}\right] \times 100\% \tag{8}$$

In Eq. (8), $GLRJ_{Control\ B,i}^{Control\ A,EQ}$ calculates "the Gain/Loss ratio of control strategy A over control strategy B in terms of evaluation criteria J_i under earthquake EQ". We use $GLRJ$ instead of GLJ defined in Eq. (5), since $GLRJ$ is a more reasonable and fair evaluation quantity for large number of control scenarios. For instance, we consider performance of control strategies A and B during EQ1 and EQ2 as: (1) $J_i^{Control\ B,EQ1} = 0.2$, $J_i^{ControlA,EQ1} = 0.1$; (2) $J_i^{ControlB,EQ2} = 0.9$, $J_i^{ControlA,EQ2} = 0.8$. Then, based on the definition of GLJ in Eq. (5), $GLJ_{ControlB,i}^{ControlA,EQ1}$ and $GLJ_{ControlB,i}^{ControlA,EQ2}$ are both calculated as 10%. However, the reduction from 0.2 to 0.1 in the first case is more significant than the reduction from 0.9 to 0.8 in the second case, because the first case has a reduction of 50% whereas the second case has a reduction of mere 11.1%. During a moderate earthquake, some of the evaluation criteria can be smaller than 0.1. However, during a severe earthquake, these criteria can increase to more than 0.8, since the evaluation criteria in Table 1 are normalized using the maximum of peak uncontrolled response quantities for a particular earthquake. The performance measure $GLRJ$ addresses this issue.

Since the purpose of this study is to investigate the performance of the SPSAC, $GLRJ$ values have been calculated for SPSAC with respect to COC, SBLC, and PON cases for evaluation criteria J_2 (interstory drift) for all 64 earthquakes. Other criteria have not been presented because of space limitations. Figs. 13 shows plots of $GLRJ$ values for SPSAC with respect to COC, SBLC, and PON cases for J_2.

It is observed from Fig. 13 that all values of GLRJ for SPSAC with respect to COC are positive, implying that the SPSAC always performs better than COC in reducing the interstory drift. When compared with SBLC, there are only two negative $GLRJ$ values. In these cases also, performance of SPSAC is almost similar to SBLC. For SPSAC with respect to PON, there is only one negative value of GLRJ, which is close to zero. Hence, performance of SPSAC is generally better than those of COC, SDLC and PON.

Based on extensive simulation results, Table 2 shows average values of $GLRJ$ for SPSAC with respect to COC, SBLC, and PON cases for evaluation criteriaJ_1, J_2 and J_3. It is observed that the SPSAC case has a significantly superior performance over other two semi-active controllers (COC and SBLC) in reducing peak displacement, peak inter-story drift, and cumulative floor drift. However, it has only slightly better average performance than the PON case in reducing all three response quantities.

Table 2 Average GLRJ: SPSAC vs COC, SBLC, and PON

$GLRJ_{COC,1}^{SPC,Average}$	+72.95%	$GLRJ_{SBLC,1}^{SPC,Average}$	+43.65%	$GLRJ_{PON,1}^{SPC,Average}$	+4.41%
$GLRJ_{COC,2}^{SPC,Average}$	+69.54%	$GLRJ_{SBLC,2}^{SPC,Average}$	+36.63%	$GLRJ_{PON,2}^{SPC,Average}$	+4.21%
$GLRJ_{COC,6}^{SPC,Average}$	+71.65%	$GLRJ_{SBLC,6}^{SPC,Average}$	+40.70%	$GLRJ_{PON,6}^{SPC,Average}$	+3.63%

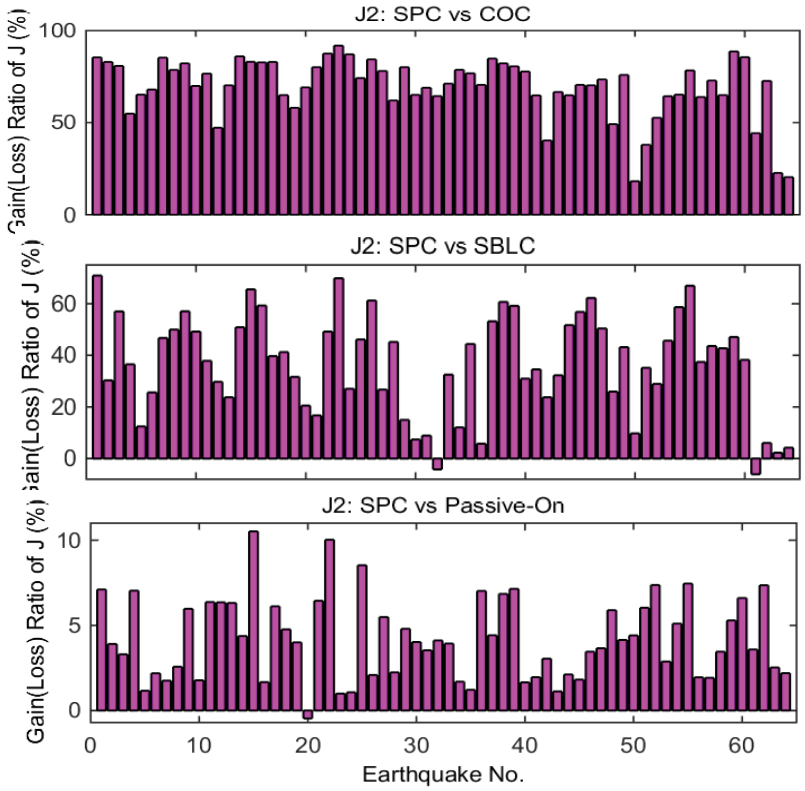

Fig. 13 Plots of Gain/Loss Ratio of J between SPC and COC, SPC and SBLC and SPC and PON

7. Conclusions

This paper presents an investigation on the performance of large-scale MR dampers controlled by semi-active and passive algorithms. Simulations models of MR dampers are based on testing data on 200 kN large scale MR dampers. It is observed that the energy dissipations of semi-active controllers are almost similar or even inferior to those of PON cases. Based on energy dissipation pattern by MR dampers in semi-active and PON modes, an innovative controller, termed as simple passive semi-active controller, is proposed for the control of MR dampers. The controller maximizes energy dissipation and can be emulated by hardware, thereby eliminating the need for sensors and controllers. It is observed that the SPSAC performs better than other semi-active controllers and the PON cases. Performance of the SPSAC algorithm has been verified through extensive numerical time-history analysis. It is mentioned that the performance of the SPSAC has also been verified through large scale real-time hybrid testing. The hardware emulation of the SPSAC has also been tested in the laboratory. Results on these tests will be presented in future publications.

Acknowledgements

This research is supported by the grant from the National Science Foundation (NSF) NEESR Grant No. CMMI-1011534. Any opinions, findings, and conclusions expressed in this paper are those of the authors and do not necessarily reflect the views of the sponsors.

References

Agrawal, A., Tan, P., Nagarajaiah, S. and Zhang, J. (2009), "Benchmark structural control problem for a seismically excited highway bridge—Part I: Phase I problem definition", *Struct. Control Health Monit.*, **16**(5), 509-529.

Bass, B.J. and Christenson, R.E. (2007), "System identification of a 200 kN magneto-rheological fluid damper for structural control in large-scale smart structures", *Proceedings of the 2007 American Control Conf.*, July 11-13, 2007, New York, NY.

Carlson, J.D. and Spencer Jr., B.F. (1996), "Magneto-rheological fluid dampers for semi-active seismic control", *Proceedings of the 3rd Int. Conf. on Motion and Vibr. Control* , Chiba, Japan.

Carlson, J.D., Catanzarite, D.M. and St. Clair, K.A. (1996), "Commercial magneto-rheological fluid devices", *I. J. Modern Physics B*, **10**, 2857-2865.

Chen, Z.Q., Wang, X.Y., Ko, J.M., Ni, Y.Q., Spencer Jr., B.F. and Yang, G. (2003), "MR damping system on Dongting Lake cable-stayed bridge", *In Smart Structures and Materials, International Society for Optics and Photonics*, 229-235.

Chopra, A.K. (2001), *Dynamics of Structures: Theory and Applications to Earthquake Engineering*, Prentice Hall, New Jersey.

Friedman, A., Dyke, S., Phillips, B., Ahn, R., Dong, B., Chae, Y., Castaneda, N., Jiang, Z., Zhang, J., Cha, Y., Ozdagli, A., Spencer, B., Ricles, J., Christenson, R., Agrawal, A. and Sause, R. (2014), "Large-scale real-time hybrid simulation for evaluation of advanced damping system performance", *J. Struct. Eng. - ASCE* ,10.1061/(ASCE)ST.1943-541X.0001093 , 04014150

He, W.L., Agrawal, A.K. and Yang, J.N. (2003), "Novel semiactive friction controller for linear structures against earthquakes", *J. Struct. Eng.- ASCE* , **129**(7), 941-950.

Jansen, L.M. and Dyke, S.J. (2000), "Semiactive control strategies for MR dampers: comparative study", *J. Eng. Mech. - ASCE*, **126**(8), 795-803.

Jiang, Z., Mantoni, D., Christenson, R., Chae, Y., Ricles, J., Friedman, A., Dyke, S., Phillips, B. and Spencer Jr., B.F. (2010), "Comparison of 200 KN MR damper models for use in real-time hybrid simulation", *Proceedings of the 5th World Conference on Structural Control and Monitoring,* 12-14 July 2010, Tokyo, Japan, Paper No. 5WCSCM- 10325.

Spencer Jr., B.F. and Nagarajaiah, S. (2003)"State of the art of structural control", *J. Struct. Eng. - ASCE*, **129**(7), 845-856.

Spencer Jr., B.F., Dyke, S.J., Sain, M.K. and Carlson, J. (1997), "Phenomenological model for magnetorheological dampers", *J. Eng. Mech. - ASCE*, **123**(3), 230-238.

Spencer Jr., B.F., Yang, G., Carlson, J.D. and Sain, M.K. (1998a), "Smart dampers for seismic protection of structures: a full-scale study", *Proceedings of the 2nd World Conf. Struct. Control*, Kyoto, Japan.

Ohtori, Y., Christenson, R., Spencer Jr., B.F. and Dyke, S. (2004), "Benchmark control problems for seismically excited nonlinear buildings", *J. Eng. Mech. - ASCE* , **130**, 366-385.

Taylor Devices (2012), "Structural applications of fluid viscous dampers", http://www.taylordevices.com/pdf/2011-StructuralApp.pdf.

Smart Structures and Systems, *Vol. 15, No. 3 (2015) 847-862*
DOI: http://dx.doi.org/10.12989/sss.2015.15.3.847

Efficient optimal design of passive structural control applied to isolator design

Mahmoud Kamalzare[1a], Erik A. Johnson[*1] and Steven F. Wojtkiewicz[2b]

[1]*Sonny Astani Department of Civil and Environmental Engineering, University of Southern California, 3620 S Vermont Ave, KAP 210, Los Angeles, CA 90089, USA*
[2]*Department of Civil and Environmental Engineering, Box 5710, Clarkson University, Potsdam, NY 13699-5710, USA*

(Received December 18, 2014, Revised January 20, 2015, Accepted January 27, 2015)

Abstract. Typical base isolated buildings are designed so that the superstructure remains elastic in design-level earthquakes, though the isolation layer is often quite nonlinear using, e.g., hysteretic elements such as lead-rubber bearings and friction pendulum bearings. Similarly, other well-performing structural control systems keep the structure within the linear range except during the most extreme of excitations. Design optimization of these isolators or other structural control systems requires computationally-expensive response simulations of the (mostly or fully) linear structural system with the nonlinear structural control devices. Standard nonlinear structural analysis algorithms ignore the localized nature of these nonlinearities when computing responses. This paper proposes an approach for the computationally-efficient optimal design of passive isolators by extending a methodology previously developed by the authors for accelerating the response calculation of mostly linear systems with local features (linear or nonlinear, deterministic or random). The methodology is explained and applied to a numerical example of a base isolated building with a hysteretic isolation layer. The computational efficiency of the proposed approach is shown to be significant for this simple problem, and is expected to be even more dramatic for more complex systems.

Keywords: computationally-efficient simulation; passive structural control; optimal design; lead-rubber bearings.

1. Introduction

Passive structural control strategies (Housner *et al.* 1997, Soong and Dargush 1997) — such as passive (linear or nonlinear) dampers, friction elements, yielding metal elements, isolation devices, and tuned-mass dampers — are some of the most commonly implemented forms of structural control. For linear structures with linear structural control elements, the simulation, design and optimization of such systems is relatively straightforward as linear response computation, driven by deterministic or stochastic excitation, is well-understood and can be performed with good efficiency. However, if the passive control element is nonlinear, or if there are nonlinearities in the structural system model, then the response computation, and any design optimization using the

*Corresponding author, Professor & Associate Chair, E-mail: JohnsonE@usc.edu
[a] Formerly, Graduate Research Assistant, E-mail: kamalzar@usc.edu
[b] Associate Professor, E-mail: swojtkie@clarkson.edu

http://www.techno-press.org/?journal=sss&subpage=8 ISSN: 1738-1584 (Print), 1738-1991 (Online)

responses, becomes more computationally challenging. The typical approach simulates these systems by employing a generic nonlinear solver, a general tool that can be used to simulate a wide variety of dynamical systems, but cannot exploit the localized nature of the passive control elements within the overall model.

This paper proposes a design optimization approach for linear structures with local passive structural control elements, enabled by a computationally-efficient simulation of the structural responses as well as their sensitivities to isolator design parameters. The authors' simulation methodology (Gaurav *et al.* 2011) can be considered an exact model reduction of a linear structure with local features, features that are linear or nonlinear, deterministic or random, to a low-order Volterra integral equation (VIE) in the forces generated by these features. When the number of local features is small relative to the system order, and the local forces depend on a low-rank subset of the system degrees of freedom, this VIE can be solved forward in time with significant reductions in computational requirements relative to those of a conventional nonlinear solver (Kamalzare *et al.* 2015). Further, the authors have shown (Wojtkiewicz and Johnson 2014, Johnson and Wojtkiewicz 2014) how response sensitivities, both gradients and Hessians, can be computed in a similar manner. This paper, then, proposes and implements this methodology for design optimization of passive structural control elements in a realistic structure.

While the approach proposed herein is general, the numerical example is an optimal parameter design of a hysteretic lead-rubber bearing in a base-isolated building. Base isolation (Kelly, 1986; Buckle and Mayes 1990, Skinner *et al.* 1993, Naeim and Kelly 1999) seeks to separate the superstructure from ground motion, insulating it, insofar as is possible, from the excitation. However, there are distinct trade offs between the displacement across the isolation layer and the motion of (and within) the superstructure. The numerical example considered herein is not intended to be an exhaustive study of the optimal isolation problem, but a demonstration of the computational advantages of the proposed simulation methodology for design optimization problems. One of the earliest studies of optimal base isolation parameters is by Bhatti *et al.* (1978). A series of papers by Constantinou and Tadjbakhsh (1983, 1984, 1985) examined optimal isolators with linear stiffness and damping alone (using a frequency domain analysis), and with friction and with hysteretic elements (using linearization), respectively. Park and Otsuka (1999) performed a parameter study, over a (small) grid of values for each key isolator parameter, of the responses of a bridge to scaled versions of the 1940 El Centro earthquake. Jangid studied linearization (Jangid 2000) and time-domain approaches (Jangid 2005, 2007) to find optimal isolation parameters, primarily the isolator yield force, for different isolator types/models. Fragiacomo *et al.* (2003) used energy measures to search for optimal isolator parameters. Others have used probabilistic / reliability approaches, such as Taflanidis and Beck (2008a, b, 2009, 2010), Bucher (2009), Jensen and Sepulveda (2012), and Roy *et al.* (2014).

The nonlinear nature of these systems makes computationally challenging the use of a complex superstructure model to perform a full parameter study or optimization without simplifications. Thus, most studies of optimal isolation design make simplifying assumptions, such as using statistical linearization of the nonlinear hysteresis, or using very simplified models of the superstructure, such as rigid or single-degree-of-freedom (SDOF) models. Conventional model reduction must necessarily make assumptions on the behavior of the nominal system without regard for whether the added localized nonlinearities may excite dynamics that are poorly approximated by the reduced model. Other approximate methods have been employed to study systems with local nonlinearities, including Guyan and static reduction, component mode synthesis, and dynamic condensation; the reader is referred to Gaurav *et al.* (2011), and the

references cited therein, for more details. Another class of approaches, including the fast nonlinear analysis method (Wilson 1999) and the work of Gordis and students (Gordis and Radwick 1999, Norton 2002), computes the response of the locally nonlinear system as the superposition of the response of a related linear system with the addition of a pseudo-force imparted on the nominal linear system by the local features; the authors' analysis method used herein (Gaurav *et al.* 2011) falls in this class as well but, unlike other methods in this class, fully exploits the locality of the nonlinear features and performs an exact model reduction.

The following sections first summarize the proposed formulation for exploiting the localized nature of the nonlinearities to rapidly perform design optimization. Then, a numerical example of an 11-story 2-bay superstructure on an isolation layer demonstrates the efficacy and computational advantages of the proposed method. A lead-rubber isolation bearing is modeled as a Bouc-Wen hysteresis in which the yield force, the pre-yield stiffness and the post-yield stiffness are optimized. The responses and their gradients to the three design variables are used to minimize a mean-square measure of the base drift and roof acceleration subject to physically-meaningful constraints. Finally, a robustness analysis of the optimal design to the sharpness of the hysteresis is conducted.

2. Methodology

The proposed approach is given in this section. First, the computationally-efficient simulation of responses is summarized for linear systems with localized features, using a trapezoidal integration of the convolution integrals to arrive at a VIE (Gaurav *et al.* 2011). Then, the derivation of the sensitivities of these responses to design parameters is summarized (Wojtkiewicz and Johnson 2014). Finally, an extension to a design optimization framework, a preliminary version of which the authors proposed in Johnson *et al.* (2013), is detailed.

2.1 Response calculation

Consider two state-space structural models: a nominal one that is linear in states $\mathbf{x}$, and a related model that is nonlinear in states $\mathbf{X}$, but with the same initial condition $\mathbf{x}_0$ and excitation $\mathbf{w}$

$$\begin{aligned} \dot{\mathbf{x}} &= \mathbf{A}\mathbf{x} + \mathbf{B}\mathbf{w} \\ \dot{\mathbf{X}} &= \mathbf{A}\mathbf{X} + \mathbf{B}\mathbf{w} + \mathbf{L}\mathbf{g}(\mathbf{G}\mathbf{X};\boldsymbol{\theta}) \end{aligned} \qquad \mathbf{X}(0) = \mathbf{x}(0) = \mathbf{x}_0 \tag{1}$$

where $\mathbf{x}$ and $\mathbf{X}$ are each n-element state vectors with state matrix $\mathbf{A}$ and excitation influence matrix $\mathbf{B}$, $\mathbf{g}(\mathbf{G}\mathbf{X};\boldsymbol{\theta})$ is a linear or nonlinear local feature vector function of a subset (or linear combination) $\overline{\mathbf{X}} = \mathbf{G}\mathbf{X}$ of the states and of design parameters $\boldsymbol{\theta}$ (time-invariant, though possibly random), with influence matrix $\mathbf{L}$. While the method is general, it is most efficient when both $\mathbf{G}$ and $\mathbf{L}$ have low rank; *i.e.*, only a few states enter into the nonlinearities, and there are a few local features.

If $\mathbf{p}(t) = \mathbf{g}(\overline{\mathbf{X}}(t);\boldsymbol{\theta})$ were known *a priori*, the principle of superposition dictates that the states $\mathbf{X}(t)$ and responses $\overline{\mathbf{X}}(t)$ of the nonlinear system can be written as the corresponding linear system responses $\mathbf{x}(t)$ and $\overline{\mathbf{x}}(t) = \mathbf{G}\mathbf{x}(t)$ plus convolution integrals involving $\mathbf{p}(t)$

$$\begin{aligned} \mathbf{X}(t) &= \mathbf{x}(t) + \int_0^t \mathbf{H}_{\mathrm{L}}(t-\tau)\mathbf{p}(\tau)\mathrm{d}\tau \\ \overline{\mathbf{X}}(t) &= \overline{\mathbf{x}}(t) + \int_0^t \overline{\mathbf{H}}_{\mathrm{L}}(t-\tau)\mathbf{p}(\tau)\mathrm{d}\tau \end{aligned} \tag{2}$$

where $\mathbf{H}_{\mathbf{L}}(t) = e^{\mathbf{A}t}\mathbf{L}$ is the state response to an impulse in the pattern of $\mathbf{L}$, and $\overline{\mathbf{H}}_{\mathbf{L}}(t) = \mathbf{G}\mathbf{H}_{\mathbf{L}}(t) = \mathbf{G}e^{\mathbf{A}t}\mathbf{L}$. The definition of $\mathbf{p}(t)$ then can be rewritten using Eq. (2)

$$\mathbf{p}(t) - \mathbf{g}\left(\bar{\mathbf{x}}(t) + \int_0^t \overline{\mathbf{H}}_{\mathbf{L}}(t-\tau)\mathbf{p}(\tau)\mathrm{d}\tau;\, \boldsymbol{\theta}\right) = \mathbf{0} \tag{3}$$

which is a system of Volterra integral equations (VIEs) in non-standard form. The authors previously showed (Gaurav *et al.*, 2011) how to solve a time-discretized Eq. (3) using second-order (trapezoidal) or fourth-order quadratures; the former is used herein as follows. Let subscript k denote a quantity at time $t_k = k\Delta t$; thus, $\mathbf{p}_k = \mathbf{p}(t_k)$, $\bar{\mathbf{x}}_k = \bar{\mathbf{x}}(t_k)$, $\overline{\mathbf{X}}_k = \overline{\mathbf{X}}(t_k)$ and $\overline{\mathbf{H}}_{\mathbf{L},k} = \overline{\mathbf{H}}_{\mathbf{L}}(t_k)$. Then, discretize the convolution, separating the portion known prior to time k

$$\overline{\mathbf{X}}_k \cong \boldsymbol{\alpha}_{k-1} + \tfrac{1}{2}\overline{\mathbf{H}}_{\mathbf{L},0}\mathbf{p}_k\Delta t \qquad \text{where} \quad \boldsymbol{\alpha}_{k-1} = \bar{\mathbf{x}}_k + \tfrac{1}{2}\overline{\mathbf{H}}_{\mathbf{L},k}\mathbf{p}_0\Delta t + \sum_{j=1}^{k-1}\overline{\mathbf{H}}_{\mathbf{L},k-j}\mathbf{p}_j\Delta t \tag{4}$$

Substituting the expression for $\overline{\mathbf{X}}_k$ in Eq. (4) back into a time-discretization of the VIE in Eq. (3), and using Newton's method to solve the resulting equation for $\mathbf{p}_k$, gives

$$\mathbf{p}_k^{j+1} = \mathbf{p}_k^{j} - \left[\mathbf{I} - \tfrac{1}{2}\left.\frac{\partial \mathbf{g}}{\partial \overline{\mathbf{X}}}\right|_{\overline{\mathbf{x}}_k,\mathbf{0}} \overline{\mathbf{H}}_{\mathbf{L},0}\Delta t\right]^{-1}\left[\mathbf{p}_k^{j} - \mathbf{g}\left(\boldsymbol{\alpha}_{k-1} + \tfrac{1}{2}\overline{\mathbf{H}}_{\mathbf{L},0}\mathbf{p}_k^{j}\Delta t;\boldsymbol{\theta}\right)\right] \tag{5}$$

where $\mathbf{p}_k^j$ denotes the j^{th} iteration on the value of $\mathbf{p}_k$, and the initial estimate $\mathbf{p}_k^0 = \mathbf{p}_{k-1}$ is the same as the previous time step. The iteration is terminated once the accuracy requirements are achieved (typical 2–3 iterations are sufficient). (Note: if $\overline{\mathbf{H}}_{\mathbf{L},0}$ were zero, which is the case for most structural systems when $\overline{\mathbf{X}}$ contains only displacements, then no iteration is required at all.) Once the sequence $\{\mathbf{p}_0, \mathbf{p}_1, \ldots\}$ has been determined, the time-discretized states $\mathbf{X}_k$ can be determined from convolution Eq. (2) using any standard approach (e.g., quadratures, FFT, etc.).

2.2 Sensitivity of responses

The sensitivity of $\mathbf{p}(t)$ to some parameter θ_i in $\mathbf{g}(\overline{\mathbf{X}};\boldsymbol{\theta})$ is given by

$$\mathbf{s}^i(t) = \frac{\partial \mathbf{p}(t)}{\partial \theta_i} = \frac{\partial \mathbf{g}}{\partial \theta_i} + \frac{\partial \mathbf{g}}{\partial \overline{\mathbf{X}}}\frac{\partial \overline{\mathbf{X}}}{\partial \theta_i} \tag{6}$$

The modified states depend on $\boldsymbol{\theta}$ only through $\mathbf{p}(t)$ so

$$\frac{\partial \mathbf{X}(t)}{\partial \theta_i} = \int_0^t \mathbf{H}_{\mathbf{L}}(t-\tau)\mathbf{s}^i(\tau)\mathrm{d}\tau \quad \text{and} \quad \frac{\partial \overline{\mathbf{X}}(t)}{\partial \theta_i} = \int_0^t \overline{\mathbf{H}}_{\mathbf{L}}(t-\tau)\mathbf{s}^i(\tau)\mathrm{d}\tau \tag{7}$$

$$\frac{\partial \overline{\mathbf{X}}_k}{\partial \theta_i} \cong \boldsymbol{\kappa}_{k-1} + \tfrac{1}{2}\overline{\mathbf{H}}_{\mathbf{L},0}\mathbf{s}_k^i\Delta t \quad \text{where} \quad \boldsymbol{\kappa}_{k-1} = \tfrac{1}{2}\overline{\mathbf{H}}_{\mathbf{L},k}\mathbf{s}_0^i\Delta t + \sum_{j=1}^{k-1}\overline{\mathbf{H}}_{\mathbf{L},k-j}\mathbf{s}_j^i\Delta t \tag{8}$$

where a trapezoidal integration is used to approximate the convolution. Substituting Eq. (8) into Eq. (6) evaluated at time t_k, and solving for sensitivity $\mathbf{s}_k^i$ gives straightforward matrix solution

$$\mathbf{s}_k^i = [\mathbf{I} - \tfrac{1}{2}\mathbf{E}_k \overline{\mathbf{H}}_{\mathbf{L},0}\Delta t]^{-1}[\mathbf{d}_k + \mathbf{E}_k \boldsymbol{\kappa}_{k-1}] \quad \text{where} \quad \mathbf{d}_k^i = \left.\frac{\partial \mathbf{g}}{\partial \theta_i}\right|_{\overline{\mathbf{X}}_k,\boldsymbol{\theta}} \quad \text{and} \quad \mathbf{E}_k = \left.\frac{\partial \mathbf{g}}{\partial \overline{\mathbf{X}}}\right|_{\overline{\mathbf{X}}_k,\boldsymbol{\theta}} \tag{9}$$

The full state sensitivity $\partial \mathbf{X}_k / \partial \theta_i$ can then be found from convolution Eq. (7) using any conventional method (e.g., quadratures, FFT, etc.). If needed by the optimization, second-order sensitivities (Hessians) can be found with a similar approach (Wojtkiewicz and Johnson 2014).

2.3 Optimization procedure

Consider a design optimization problem with cost functional $J(\tilde{\mathbf{X}}(t;\boldsymbol{\theta}))$, where $\tilde{\mathbf{X}} = \tilde{\mathbf{G}}\mathbf{X}$ is some linear combination of the states, and the "optimal" value of the design parameter(s) $\boldsymbol{\theta}$ is desired. To find the design point where J is minimized, one may employ non-gradient-based or gradient-based approaches. For the former, the proposed approach can be used to efficiently compute the response $\tilde{\mathbf{X}}(t;\boldsymbol{\theta})$, from which the cost functional J is determined. To implement a gradient-based optimization algorithm, the gradient $\partial J/\partial \boldsymbol{\theta}$ of the cost functional with respect to the design parameters may be approximated by numerical methods such as finite differences, or it can be provided using the response sensitivities in Eq. (9), requiring fewer function evaluations and, thus, more computationally efficient and, typically, more accurate. The cost functional derivatives with respect to the design parameters can be calculated using

$$\frac{\partial J(\tilde{\mathbf{X}}(t;\boldsymbol{\theta}))}{\partial \boldsymbol{\theta}} = \frac{\partial J(\tilde{\mathbf{X}}(t;\boldsymbol{\theta}))}{\partial \tilde{\mathbf{X}}} \frac{\partial \tilde{\mathbf{X}}}{\partial \boldsymbol{\theta}}, \qquad \frac{\partial \tilde{\mathbf{X}}}{\partial \theta_i} = \int_0^t \tilde{\mathbf{G}}\mathbf{H}_{\mathbf{L}}(t-\tau)\mathbf{s}^i(\tau)\mathrm{d}\tau \tag{10}$$

where $\partial \tilde{\mathbf{X}} / \partial \theta_i$ can be computed using the sensitivities $\mathbf{s}_k^i$ from Eq. (9) in any usual way. (Note that an additional term appears in Eq. (10) if J also has explicit dependence on $\boldsymbol{\theta}$.)

With this computationally-efficient approach for determining the cost functional J and its sensitivities in Eq. (10) to the design variables, a design optimization that requires many function evaluations can be performed in a manner that is much faster than if the response and sensitivity simulation utilizes conventional nonlinear solvers that cannot exploit the localized nature of the isolators or other structural control devices. The primary focus of this study is to propose the use of this VIE approach for design optimization of (nonlinear) passive structural control devices. The numerical example that follows is just one such application of this method.

3. Numerical example: Optimal design of isolation hysteresis for isolated building

This example demonstrates how the proposed method can be utilized for designing an optimal hysteretic isolator in the isolation layer of a 100-degree-of-freedom (DOF) frame structure. In this example, the proposed method calculates both the responses and sensitivities for use in a gradient-based optimization algorithm, which determines the optimal strategy in a very computationally efficient manner.

Consider the base isolated building in Fig. 1(a). The superstructure is 11 stories tall and 2 bays wide; the superstructure is treated as linear, with horizontal, vertical and rotational DOFs at each moment-bearing joint. The superstructure, if it were a fixed-base structure, would have a fundamental period of 1.05 s. As a fixed base structure, the equations of motion would be

$$\mathbf{M}_s\ddot{\mathbf{u}}_s + \mathbf{C}_s\dot{\mathbf{u}}_s + \mathbf{K}_s\mathbf{u}_s = -\mathbf{M}_s\mathbf{r}\ddot{u}_g \tag{11}$$

where $\mathbf{u}_s$ is a vector of generalized displacements of the structure relative to the ground, for a total of 99 DOFs, three at each of the 33 nodes; the superstructure consistent mass and stiffness matrices are denoted $\mathbf{M}_s$ and $\mathbf{K}_s$, respectively; the damping matrix $\mathbf{C}_s$ is computed using the Rayleigh method by assuming that the 1st and 10th modal damping ratios are each 3%; $\ddot{u}_g$ is the horizontal ground acceleration; and $\mathbf{r} = [1\ 0\ 0\ \ 1\ 0\ 0\ \ \ldots\ \ 1\ 0\ 0]^T$ (i.e., a 1 in each element corresponding to a horizontal displacement in $\mathbf{u}_s$, and zeros elsewhere) is the influence vector.

3.1 Hysteretic isolation: A lead-rubber bearing system

The structure sits on a base mass that is supported by an isolation layer composed of lead-rubber bearings (LRBs). The base drift is assumed sufficiently moderate that the low-damping rubber acts as a linear stiffness and viscous damping element. The lead plug is assumed to provide linear stiffness before yielding, and then a much lower (or zero) stiffness thereafter. Together, the rubber and the lead provide a hysteretic stiffness such as shown in Fig. 1b. While a bilinear model is commonly used for LRBs, it has been shown to result in computed accelerations that are larger than those observed (Skinner *et al.* 1993, Nagarajaiah and Sun 2000) as it overstates the sharpness of the lead transition from fully elastic to (partially) plastic; instead here, the computationally more tractable, smooth Bouc-Wen model (Bouc 1967, Wen 1976) is used. (The effect of elastic-to-partially-plastic transition sharpness is discussed in greater detail in §3.8.)

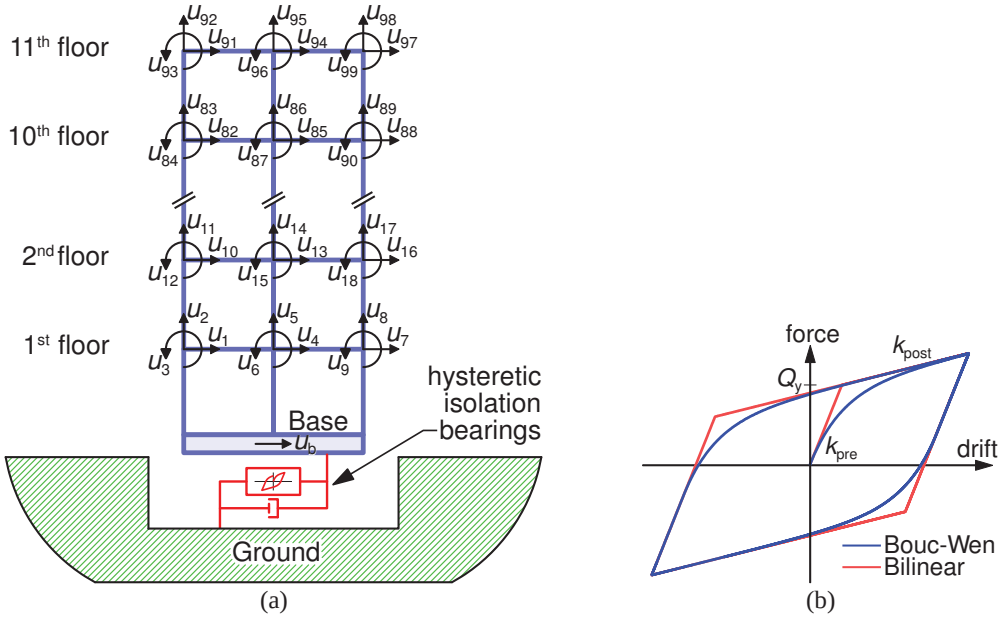

Fig. 1 (a) 100 DOF base-isolated structure and (b) bilinear and Bouc-Wen hysteresis loops

The nominal post-yield stiffness k_{post} and base mass m_b are chosen such that the fundamental mode of the isolated building, if the yield force Q_y were zero, would have a period of 2.76 s, which is in the typical expected range (Skinner *et al.* 1993); k_{pre} is the pre-yield stiffness; the isolation-layer viscous damping coefficient c_b, provided by the isolator (and/or supplemental passive viscous dampers), is chosen such that the isolation mode has a damping ratio of about 5.5%. The building weight (base plus superstructure) is $W = 1.28$ MN and its height from the base upwards is $h = 44$ m. The isolation layer is assumed to be constrained to move in the horizontal direction only, so multiple identical LRBs can be modeled as a single LRB. The result is a 100-DOF isolated structure model. The primary ground excitations used herein are the El Centro (N-S Imperial Valley Irrigation District substation record of the 1940 Imperial Valley earthquake; PGA 0.348 *g*) and Northridge (N-S Sylmar County Hospital parking lot record of the 1994 Northridge earthquake; PGA 0.843 *g*) ground motions sampled at 50 Hz (i.e., $\Delta t = 0.02$ s).

The Bouc-Wen model introduces an evolutionary variable *z* that is proportional to the base drift u_b for small motion, but asymptotically approaches ±1 for large motion as the lead shears (or a friction pendulum isolator surface slides). The equations of motion of the base mass are given by

$$m_b\ddot{u}_b + c_b\dot{u}_b + k_{post}u_b + \alpha z = -m_b\ddot{u}_g + \mathbf{r}^T\mathbf{C}_s(\dot{\mathbf{u}}_s - \mathbf{r}\dot{u}_b) + \mathbf{r}^T\mathbf{K}_s(\mathbf{u}_s - \mathbf{r}u_b) \tag{12a}$$

$$\dot{z} = A\dot{u}_b - \beta\dot{u}_b|z|^n - \gamma z|\dot{u}_b||z|^{n-1} \tag{12b}$$

where $\alpha = Q_y[1 - (k_{post}/k_{pre})]$ is the peak of the non-elastic force; $A = 2\beta = 2\gamma = k_{pre}/Q_y$ (which constrains $z \in [-1,1]$ and makes identical the loading and unloading stiffnesses); and the exponent *n* controls the sharpness of the hysteresis loop. The superstructure equations of motion, with displacements $\mathbf{u}_s$ relative to the ground, are given by

$$\mathbf{M}_s\ddot{\mathbf{u}}_s + \mathbf{C}_s(\dot{\mathbf{u}}_s - \mathbf{r}\dot{u}_b) + \mathbf{K}_s(\mathbf{u}_s - \mathbf{r}u_b) = -\mathbf{M}_s\mathbf{r}\ddot{u}_g \tag{13}$$

Combining the equations of motion in Eqs. (12 (a)) and (13) yields

$$\begin{aligned}
&\mathbf{M}\ddot{\mathbf{u}} + \mathbf{C}\dot{\mathbf{u}} + \mathbf{K}\mathbf{u} = -\mathbf{M}\tilde{\mathbf{r}}\ddot{u}_g - [1 \quad \mathbf{0}^T]^T[\alpha z + (k_{post} - k_b)u_b] \\
&\mathbf{M} = \begin{bmatrix} m_b & \mathbf{0}^T \\ \mathbf{0} & \mathbf{M}_s \end{bmatrix}, \quad \mathbf{C} = \begin{bmatrix} c_b + \mathbf{r}^T\mathbf{C}_s\mathbf{r} & -\mathbf{r}^T\mathbf{C}_s \\ -\mathbf{C}_s\mathbf{r} & \mathbf{C}_s \end{bmatrix}, \quad \mathbf{K} = \begin{bmatrix} k_b + \mathbf{r}^T\mathbf{K}_s\mathbf{r} & -\mathbf{r}^T\mathbf{K}_s \\ -\mathbf{K}_s\mathbf{r} & \mathbf{K}_s \end{bmatrix}
\end{aligned} \tag{14}$$

where $\mathbf{u}(t) = [u_b(t) \quad \mathbf{u}_s^T(t)]^T$ is the generalized displacement vector and $\tilde{\mathbf{r}} = [1 \quad \mathbf{r}^T]^T$. Note that, since $k_{post}u_b + \alpha z$ cannot be in the nominal system in Eq. (12(a)), as it depends on design parameters, $k_b u_b$ is added to both sides of the equation to preserve the stability of the nominal system, where $k_b = 750$ kN/m is the nominal post-yield stiffness that results in the 2.76 s isolation period. The equation of motion in Eq. (14) can be rewritten in the state space form of Eq. (1) with

$$\mathbf{X} = \begin{Bmatrix} \mathbf{u} \\ \dot{\mathbf{u}} \\ z \end{Bmatrix}, \quad \mathbf{A} = \begin{bmatrix} \mathbf{0} & \mathbf{I} & \mathbf{0} \\ -\mathbf{M}^{-1}\mathbf{K} & -\mathbf{M}^{-1}\mathbf{C} & \mathbf{0} \\ \mathbf{0}^T & \mathbf{0}^T & 0 \end{bmatrix}, \quad \mathbf{B} = \begin{Bmatrix} \mathbf{0} \\ -\tilde{\mathbf{r}} \\ 0 \end{Bmatrix}, \quad \mathbf{L} = \begin{bmatrix} \mathbf{0} & \mathbf{0} \\ -\mathbf{M}^{-1}[1 \quad \mathbf{0}^T]^T & \mathbf{0} \\ 0 & 1 \end{bmatrix} \tag{15}$$

and a modification $\mathbf{g}$ that is a 2×1 vector function

$$\mathbf{g}(\overline{\mathbf{X}};\boldsymbol{\theta}) = \begin{Bmatrix} \alpha z + (k_{post} - k_b)u_b \\ A\dot{u}_b - \beta\dot{u}_b|z|^n - \gamma z|\dot{u}_b||z|^{n-1} \end{Bmatrix} \tag{16}$$

where $\overline{\mathbf{X}}(t)=[u_\mathrm{b}\quad \dot{u}_\mathrm{b}\quad z]^\mathrm{T}$ and $\boldsymbol{\theta}=[Q_\mathrm{y}\quad k_\mathrm{pre}\quad k_\mathrm{post}]^\mathrm{T}$. While Q_y and k_pre do not appear explicitly in Eq. (16), α, A, β and γ are functions of them. Since g_1 is linear in the states, it would typically be included in the nominal system (in **A**); since g_1 depends on $\boldsymbol{\theta}$, it is excluded from the nominal system so that $\boldsymbol{\theta}$ can be varied as a modification to the nominal system. The exponent n is considered initially to be 1, which results in smooth hysteresis loops, but relaxed in §3.8.

3.2 Baseline LRB design

To provide a performance baseline, the same structure equipped with an LRB system, with the suggested (Skinner *et al.* 1993) yield force of 5% of the building weight for small to moderate earthquakes such as El Centro and 15% for strong earthquakes such as Northridge, and pre-yield to post-yield stiffness ratios of 6 and 10 for moderate and strong excitations, respectively (the values most commonly used in the literature). Thus, the two baseline designs are: (a) for El Centro, an LRB with a yield force $0.05W$, pre-yield stiffness $6k_\mathrm{b}$ and post-yield stiffness k_b; i.e., $\boldsymbol{\theta}^0_\mathrm{EC}=[0.05W\quad 6k_\mathrm{b}\quad k_\mathrm{b}]^\mathrm{T}$; and (b) for Northridge, an LRB with a yield force $0.15W$, pre-yield stiffness $10k_\mathrm{b}$ and post-yield stiffness k_b; *i.e.*, $\boldsymbol{\theta}^0_\mathrm{N}=[0.15W\quad 10k_\mathrm{b}\quad k_\mathrm{b}]^\mathrm{T}$. For a baseline LRB system, one may select either a smooth or bilinear hysteresis; the latter (using an $n=100$ Bouc-Wen model as an approximation) is adopted here due to its wide usage in the literature, with root mean square (RMS) base drift and roof acceleration of 1.84 cm and 77.40 cm/s^2, respectively, for El Centro, and 6.34 cm and 130.22 cm/s^2, respectively, for Northridge.

3.3 Sensitivity formulation

For this numerical example, the sensitivity to each design parameter is computed analytically. The required partial derivatives of $\mathbf{g}$ with respect to the parameters $\boldsymbol{\theta}$ and to the states $\overline{\mathbf{X}}$, are

$$\mathbf{d}^1_k=\left.\frac{\partial\mathbf{g}}{\partial\theta_1}\right|_k=\begin{Bmatrix}\partial g_1/\partial Q_\mathrm{y}\\ \partial g_2/\partial Q_\mathrm{y}\end{Bmatrix}_k=\begin{Bmatrix}z[1-(k_\mathrm{post}/k_\mathrm{pre})]\\ [\tfrac{1}{2}\dot{u}_\mathrm{b}|z|^n+\tfrac{1}{2}|\dot{u}_\mathrm{b}||z|^{n-1}-\dot{u}_\mathrm{b}]k_\mathrm{pre}/Q_\mathrm{y}^2\end{Bmatrix}_k \tag{17a}$$

$$\mathbf{d}^2_k=\left.\frac{\partial\mathbf{g}}{\partial\theta_2}\right|_k=\begin{Bmatrix}\partial g_1/\partial k_\mathrm{pre}\\ \partial g_2/\partial k_\mathrm{pre}\end{Bmatrix}_k=\begin{Bmatrix}zQ_\mathrm{y}k_\mathrm{post}/k_\mathrm{pre}^2\\ [\dot{u}_\mathrm{b}-\tfrac{1}{2}\dot{u}_\mathrm{b}|z|^n-\tfrac{1}{2}z|\dot{u}_\mathrm{b}||z|^{n-1}]/Q_\mathrm{y}\end{Bmatrix}_k \tag{17b}$$

$$\mathbf{d}^3_k=\left.\frac{\partial\mathbf{g}}{\partial\theta_3}\right|_k=\begin{Bmatrix}\partial g_1/\partial k_\mathrm{post}\\ \partial g_2/\partial k_\mathrm{post}\end{Bmatrix}_k=\begin{Bmatrix}u_\mathrm{b}-[zQ_\mathrm{y}/k_\mathrm{pre}]\\ 0\end{Bmatrix}_k \tag{17c}$$

$$\mathbf{E}_k=\left.\frac{\partial\mathbf{g}}{\partial\overline{\mathbf{X}}}\right|_k=\begin{bmatrix}\partial g_1/\partial u_\mathrm{b} & \partial g_2/\partial u_\mathrm{b}\\ \partial g_1/\partial \dot{u}_\mathrm{b} & \partial g_2/\partial \dot{u}_\mathrm{b}\\ \partial g_1/\partial z & \partial g_2/\partial z\end{bmatrix}^\mathrm{T}_k=\begin{bmatrix}k_\mathrm{post}-k_\mathrm{b} & 0\\ 0 & A-\beta|z|^n-\gamma z|z|^{n-1}\operatorname{sgn}\dot{u}_\mathrm{b}\\ \alpha & -\beta n\dot{u}_\mathrm{b}|z|^{n-1}\operatorname{sgn} z-\gamma n|\dot{u}_\mathrm{b}||z|^{n-1}\end{bmatrix}^\mathrm{T}_k \tag{18}$$

where the subscript k denotes evaluation at time $k\Delta t$. For example, the sensitivities of the base drift with respect to Q_y, k_pre and k_post (at the design point discussed subsequently) are shown in Fig. 2, along with those obtained by numerical integration of the analytical sensitivity equations, which were computed using `ode45` with relative and absolute tolerances both set to 10^{-10}; the expressions for the exact analytical sensitivity equations can be found in Kamalzare (2014).

3.4 Design of the optimal base isolation

To find the "best" choice of the design parameters, one may use a parameter study over a fine grid of design variable values or a conventional gradient-based optimization algorithm, with comparisons of some performance metric(s) to those of a baseline design. Studies in the literature have employed objectives such as minimizing the superstructure drift or absolute acceleration subject to a constraint on the base drift; others have used reliability measures. Here, a cost functional expressed in terms of mean square (MS) responses is used, defined as a weighted linear combination of the MS base drift $\sigma^2_{u_b}$ and the MS absolute roof acceleration $\sigma^2_{\ddot{u}_r^a}$, where $\ddot{u}_r^a = \ddot{u}_{94} + \ddot{u}_g$, as follows

$$J(\boldsymbol{\theta}) = [\sigma^2_{u_b}(\boldsymbol{\theta}) / \sigma^2_{u_b}(\boldsymbol{\theta}^0)] + [\sigma^2_{\ddot{u}_r^a}(\boldsymbol{\theta}) / \sigma^2_{\ddot{u}_r^a}(\boldsymbol{\theta}^0)] \tag{19}$$

where $\sigma^2_{(\cdot)}(\boldsymbol{\theta}^0)$ is a MS response of a baseline design. A MS response is approximated herein as

$$\sigma^2_{u_b} = \frac{1}{t_f}\int_0^{t_f} u_b^2(t)\mathrm{d}t \cong \frac{1}{N}\sum_{k=0}^{N} u_{b,k}^2 \tag{20}$$

where $t_f = N\Delta t$ is the simulation duration and $u_{b,k} = u_b(k\Delta t)$. The optimization is performed using a gradient-based active-set algorithm, the `fmincon` command in MATLAB™. The derivative of the cost functional with respect to the design parameters is given by

$$\frac{\partial J}{\partial \boldsymbol{\theta}} = \frac{2}{N}\sum_{k=0}^{N}\left[\frac{u_{b,k}}{\sigma^2_{u_b}(\boldsymbol{\theta}^0)}\frac{\partial u_{b,k}}{\partial \boldsymbol{\theta}} + \frac{\ddot{u}^a_{r,k}}{\sigma^2_{\ddot{u}^a_{r,k}}(\boldsymbol{\theta}^0)}\frac{\partial \ddot{u}^a_{r,k}}{\partial \boldsymbol{\theta}}\right] \tag{21}$$

`fmincon` is selected because it can exploit gradient information, which is available through Eq. (21), and can accommodate the constraints: (*i*) the yield force is always strictly positive, $Q_y > 0$; (*ii*) the pre-yield stiffness is greater than or equal the post-yield stiffness, $k_{pre} \geq k_{post}$; and (*iii*) the post-yield stiffness is always non-negative, $k_{post} \geq 0$.

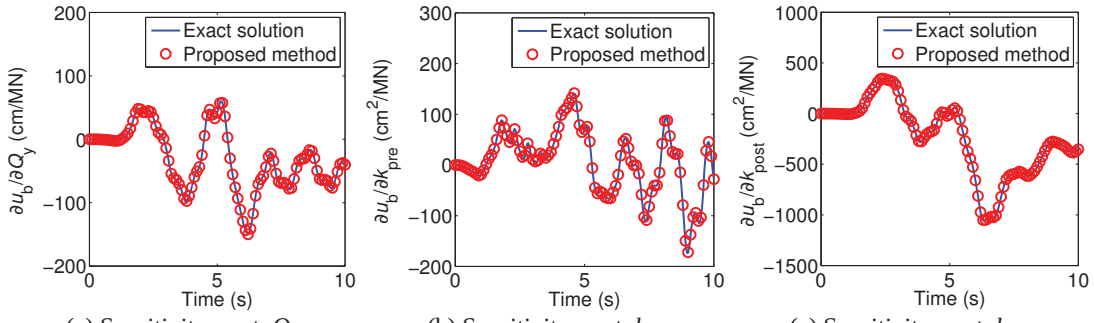

(a) Sensitivity w.r.t. Q_y (b) Sensitivity w.r.t. k_{pre} (c) Sensitivity w.r.t. k_{post}

Fig. 2 Base drift response sensitivity to the design parameters when subjected to the 1940 El Centro ground motion at the design point

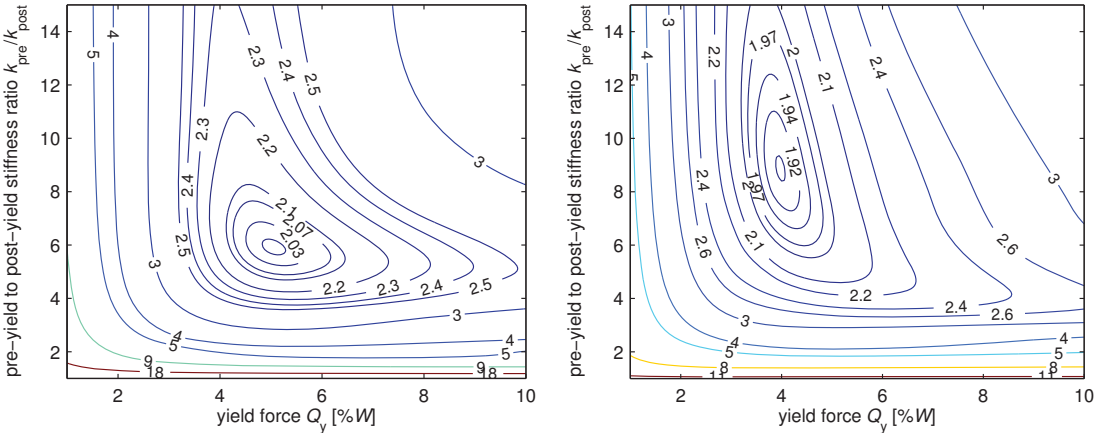

(a) 1940 El Centro (b) 1994 Northridge-Saticoy

Fig. 3 Cost contours as a function of two design parameters for two historical earthquakes

3.5 Preliminary Optimization over Q_y and k_{pre}

A preliminary study of this example in which only Q_y and k_{pre} are free design variables is useful as a first step since the response metrics can be computed over a fine grid of the two design variables to verify that the method is efficient and accurate. This simpler design optimization problem, discussed in greater detail in Johnson *et al.* (2013), uses the same model but fixes exponent $n = 1$ and post-yield stiffness $k_{post} = k_b$. Considering the cost functional Eq. (19), the design point for the El Centro earthquake is determined to be (0.0507W, 5.94k_b), which results (not surprisingly) in basically the same RMS base drift and roof acceleration performances as the baseline (0.05W, 6k_b). A record from the 1994 Northridge earthquake with a PGA similar to that of the El Centro record was also used for this 2-D optimization: the E-W motion of the Northridge earthquake recorded at the USC 90003 station at 17645 Saticoy St (PGA 0.368 g); using the same baseline (0.05W, 6k_b), the optimization converges to a different design point (0.0401W, 8.73k_b) for Northridge-Saticoy, which results in reductions of about 1% and 4% in RMS base drift and roof acceleration, respectively, relative to the baseline. To converge to the design point, these solutions required only 6 iterations, making a total of 19 function evaluations, for the El Centro earthquake, and 13 iterations (29 function evaluations) for Northridge-Saticoy; the quick convergence is facilitated by providing the gradient information. The proposed method was found to provide an optimization that is about an order of magnitude faster than with the conventional solver `ode45`. To verify that these optimizations converged to the correct results, a parameter study was performed over the two-dimensional design space as shown in Fig. 3, which confirms that the cost functionals are convex and well-behaved around the design points.

3.6 Optimization over Q_y, k_{pre} and k_{post}

The preliminary study in the previous section assumes a fixed post-yield stiffness $k_{post} = k_b$,

which likely limits the isolation performance and the optimal isolation design may be rather different if post-yield stiffness is included as a design variable. Thus, the full design space in this example includes the yield force Q_y, the pre-yield stiffness k_{pre} and the post-yield stiffness k_{post}; variations in these values are achievable in practice by changing the isolation device characteristics (*e.g.*, physical device size, proportion of lead plug to rubber/steel, ratio of steel-to-rubber, etc.). The initial guess to start the optimization is chosen to be the same as the baseline values: $(Q_y, k_{pre}, k_{post})_{initial} = (0.05W, 6k_b, k_b)$ and $(0.15W, 10k_b, k_b)$ for the El Centro and Northridge earthquakes, respectively.

The design point for the El Centro earthquake is determined to be $(0.0641W, 5.75k_b, 0.484k_b)$, which results in reductions of about 6% and 11% in RMS base drift and roof acceleration, respectively, relative to the baseline $(0.05W, 6k_b, k_b)$. When the Northridge (Sylmar) earthquake excitation is applied to the system, the optimization yields a different design point $(0.1371W, 12.45k_b, 0.61k_b)$, which results in reductions of about 4% and 8% in RMS base drift and roof acceleration, respectively, relative to the baseline $(0.15W, 10k_b, k_b)$. To converge to the design point, these solutions required only 12 iterations (26 function evaluations) for the El Centro earthquake, and 18 iterations (43 function evaluations) for Northridge; the quick convergence is again facilitated by providing the analytical gradient information from Eqs. (17) and (18).

To verify that these optimizations converged to the correct results, a small parameter study was performed. Fig. 4 shows contour line slices of the cost functional for the El Centro and Northridge (Sylmar) earthquake excitations. Clearly, each design point found by the optimization is in the region of the cost functional minimum, around which the cost functional is convex.

3.7 Timing and accuracy of the proposed approach

In this section, the computational cost of the proposed optimization method is compared with one employing a conventional nonlinear solver: the `ode45` command in MATLAB. The accuracy of both `ode45` and the proposed method can be tuned, the former by setting options for the absolute and relative tolerances, and the latter by choosing the integration time step. To ensure a fair comparison, preliminary studies showed that the accuracy of `ode45` with the default parameters (relative tolerance 10^{-3}, absolute tolerance 10^{-6}) and the proposed method using a second-order accurate trapezoidal integration with 2^{15} time steps of $\Delta t = 0.92$ ms duration each, both give relative response accuracy of order 10^{-3}. Fig. 5 shows the accuracy of the proposed method using graphs of base drift and absolute roof acceleration of the structure, respectively, at the design point for the El Centro excitation as calculated by the proposed method as well as a reference "exact" solution calculated by `ode45` with the relative and absolute tolerances both set to 10^{-10}. The computational cost of the proposed method includes one-time calculations and repeated ones that, in this example at the design point, take about 2.13 s and 5.81 s, respectively, on a computer with a 3.4 GHz Intel core i7-2600 processor and 8 GB of RAM, running MATLAB R2013a under Windows 7. The same calculation takes about 87.50 s if MATLAB's `ode45` (with default tolerances) is used as the solver. This leads to a computation speed-up of 11.0 for a single simulation but 14.8 in a typical optimization with 25 function evaluations performed.

Computing the sensitivities of the cost functional with respect to the three design parameters at each step doubles or triples the computation time, relative to computing the cost functional alone, of both MATLAB's `ode45` and the proposed method; however, as expected, including gradient information results in much faster convergence to the "optimal" design point: for El Centro,

MATLAB's `fminsearch` (a non-gradient based method) takes about 53 iterations (118 function evaluations), which is 4–5 times larger than for the gradient-based `fmincon`, so, at least for this example, there is a clear computational benefit provided by including the analytical gradients.

Note that the proposed method here uses a subdivision of the convolution space to compute portions of the integral in the Volterra integral equation using fast Fourier transforms (Gaurav *et al.* 2011); further, the accuracy and computational efficiency would be expected to be even more superior if the fourth-order integration previously discussed by the authors (Gaurav *et al.* 2011) were used instead of the second-order trapezoidal integration adopted in this study.

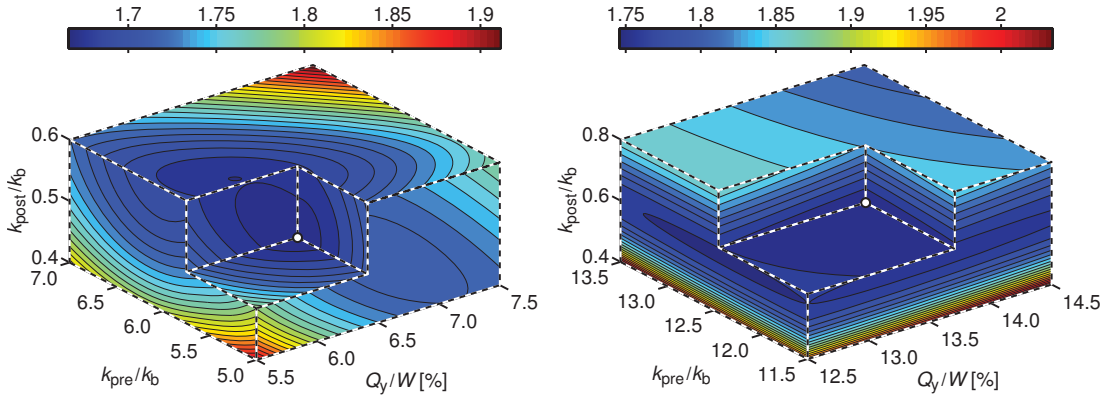

(a) 1940 El Centro earthquake (b) 1994 Northridge (Sylmar) earthquake

Fig. 4 Contour lines of the cost as a function of the design parameters for two earthquakes. The apex of the cutout shows the optimal design location

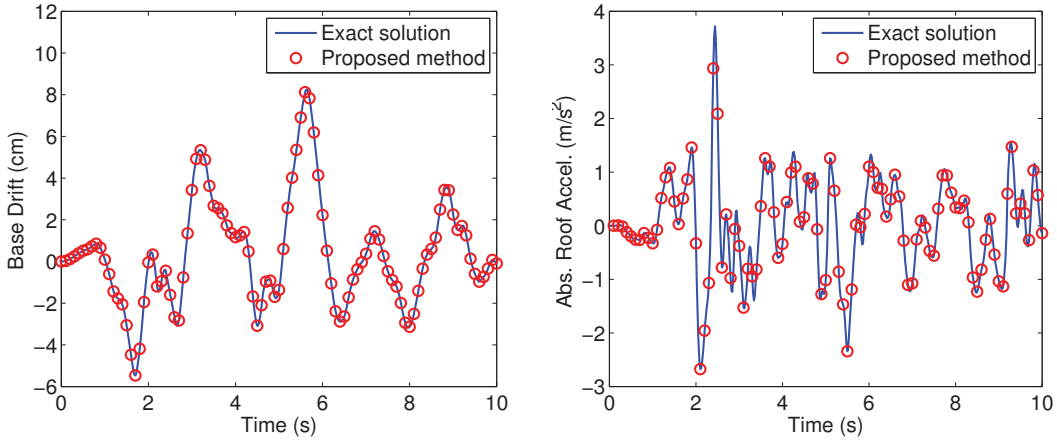

(a) Base drift response. (b) Absolute roof acceleration response.

Fig. 5 Structural responses to the El Centro earthquake using the design point isolation

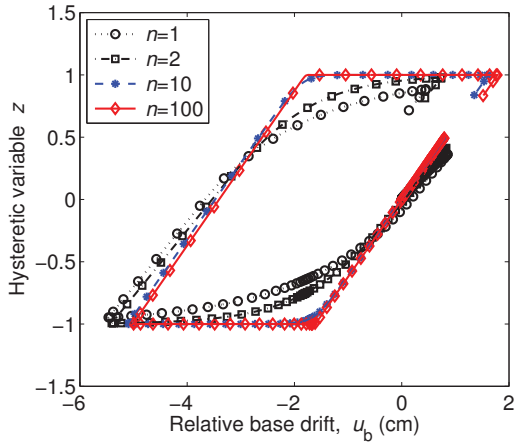

Fig. 6 Single hysteresis loop using the design point isolation calculated for different exponents n when subject to the El Centro earthquake

3.8 Investigation of the transitional region of the Bouc-Wen model

Traditionally, for the sake of simplicity, many researchers have used the bilinear behavior for the hysteretic loops. However, the Bouc-Wen model introduced in Eq. (12(a)) provides a formulation that allows modeling a smooth transition from the pre-yield to post-yield regions. This is mainly controlled by the exponent n, which is greater than or equal to 1. Using $n = 1$ results in a very smooth transition and $n \to \infty$ models the strict bilinear loops; the most common values used in the literature are $n = 1$, 2 and ∞. Among all parameters in this Bouc-Wen model (i.e., Q_y, k_{pre}, k_{post} and n), n is the one with the least tangible physical meaning; thus, this final section investigates the effect on the optimal isolator design of assuming different values for n.

As shown in Fig. 6, the shape of the hysteresis loops changes significantly for different values of n and, as expected, will result in a different "optimal" design point. Assuming the same baseline performance, the optimization is repeated for $n = 1$, 2, 10 and 100 and the design points and performance metrics (RMS base drift and roof acceleration) are shown in Table 1 for the El Centro earthquake. It is clear that the "optimal" Q_y and k_{post} are very sensitive to the value of n as they change by 21% and 130%, respectively, in this example as n changes from 1 to 100. In contrast, k_{pre} changes very slightly and appears relatively insensitive to exponent n.

It is also important to investigate the effect on response when the isolators are designed using an inaccurate value of n. (The effects of incorrect Q_y, k_{pre} and k_{post} are not studied herein because they can be experimentally determined fairly easily for a particular device whereas the exponent n is often neglected in curve-fitting from laboratory tests.) The response metrics for the system at the design points shown in Table 1 are evaluated for isolators with different n values and the percentage change in their performance metrics, compared to the original design point responses, are calculated and shown in Table 2. It is reported in the literature (Skinner *et al.* 1993, Nagarajaiah and Sun 2000) that assuming bilinear hysteresis overestimates the roof acceleration; this is confirmed by comparing the corresponding columns of Table 2. This study shows that

designing with a larger n always results in overestimating the actual RMS roof acceleration; but, no clear conclusions can be made about the RMS base drift. Further investigations (not included here for the sake of brevity) showed that the peak base drift and peak roof acceleration have similar variation trends as the corresponding RMS metrics, though the changes are less significant and mostly remain less than 4–5%.

4. Conclusions

To enable the optimal design of passive isolation systems, this paper proposes extending a computationally efficient approach previously developed by the authors for systems with local features (linear or nonlinear, deterministic or random) but are otherwise linear. This approach can provide highly efficient simulation of both responses and their sensitivities to the design parameters in the isolation element models. The methodology was briefly summarized and then applied to the optimal design of a base isolation system to find the optimal yield force and pre-yield and post-yield stiffnesses of a hysteretic isolation layer for an 11-story 2-bay isolated building. The isolator was modeled with Bouc-Wen hysteresis and (small) viscous damping. A baseline design, using a yield force that is 5% or 15% of the building weight and a pre-yield stiffness that is 6 or 10 times that of the post-yield stiffness, as suggested in the literature for a moderate and strong ground motions, respectively, are used for comparison. The optimal design for the El Centro earthquake results in about 6% and 11% reductions in RMS base drift and roof acceleration, respectively, relative to the baseline; for the Northridge earthquake, the corresponding reductions are 4% and 8%, respectively.

Table 1 Design points for different exponent n values for the El Centro earthquake

n	1	2	10	100
Q_y/W [%]	6.4142	5.8800	5.0892	5.0613
k_{pre}/k_b	5.7506	5.3100	5.3099	5.3527
k_{post}/k_b	0.4840	0.5490	1.0508	1.1144
σ_{u_b} [% change rel. to $\sigma^0_{u_b}$]	–6.42	–2.54	3.20	2.96
$\sigma_{\ddot{u}^a_r}$ [% change rel. to $\sigma^0_{\ddot{u}^a_r}$]	–10.81	–10.20	–6.44	–4.82
J	1.67	1.76	1.94	1.97

Table 2 RMS base drift and roof acceleration percent changes when the design points are evaluated at different exponent n values

	RMS base drift changes (%)				RMS roof acceleration changes (%)			
	Actual exponent n				Actual exponent n			
Design n	1	2	10	100	1	2	10	100
1	0	–1.57	8.27	10.93	0	9.98	20.62	22.31
2	3.51	0	6.24	9.25	–8.18	0	8.51	9.64
10	3.66	–0.72	0	0.58	–11.19	–5.87	0	0.86
100	3.94	–0.73	–0.47	0	–11.56	–6.48	–0.80	0

The proposed approach was able to perform the design optimization function evaluation simulations more than one order of magnitude faster; the computation speed-up was 14.8 for a typical parameter study or iterative optimization of this relatively small numerical example. However, since various types of passive structural control elements are being studied for large structures, such as high-rise buildings and long-span bridges, requiring far more complex models than the numerical considered herein, the gains in computational efficiency of the proposed optimization method are expected to be even more pronounced for such structural models.

Acknowledgments

The authors gratefully acknowledge support of this work by the National Science Foundation through awards CMMI 11-00528, 11-33023, and 13-44937. Any opinions, findings, and conclusions or recommendations expressed herein are those of the authors and do not necessarily reflect the views of the National Science Foundation. The first author also acknowledges the support of a Viterbi Doctoral Fellowship from the University of Southern California.

References

Bhatti, M.A., Pister, K.S. and Polak, E.L. (1978), *Optimal design of an earthquake isolation system*, Report No. UCB/EERC-78/22, Earthquake Engineering Research Center, University of California, Berkeley.

Bouc, R. (1967), "Forced vibration of mechanical systems with hysteresis", *Proceedings of the 4th Conference on Nonlinear Oscillation*, Prague, Czechoslovakia, 315.

Bucher, C. (2009), "Probability-based optimal design of friction-based seismic isolation devices", *Struct. Saf.*, **31**(6), 500-507.

Buckle, I.G. and Mayes, R.L. (1990), "Seismic isolation: History, application, and performance—a world view", *Earthq. Spectra*, **6**(2), 161-201.

Constantinou, M.C. and Tadjbakhsh, I.G. (1983), "Probabilistic optimum base isolation of structures", *J. Struct. Eng. - ASCE*, **109**(3), 676-689.

Constantinou, M.C. and Tadjbakhsh, I.G. (1984), "The optimum design of a base isolation system with frictional elements", *Earthq. Eng. Struct. D.*, **12**(2), 203-214.

Constantinou, M.C. and Tadjbakhsh, I.G. (1985), "Hysteretic dampers in base isolation: Random approach", *J. Struct. Eng. - ASCE*, **111**(4), 705-721.

Fragiacomo, M., Rajgelj, S. and Cimadom, F. (2003), "Design of bilinear hysteretic isolation systems", *Earthq. Eng. Struct. D.*, **32**(9), 1333-1352.

Gaurav, Wojtkiewicz, S.F. and Johnson, E.A. (2011), "Efficient uncertainty quantification of dynamical systems with local nonlinearities and uncertainties", *Probabilist. Eng. Mech.*, **26**(4), 561-569.

Gordis, J.H. and Radwick, J. (1999), "Efficient transient analysis for large locally nonlinear structures", *Shock Vib.*, **6**(1), 1-9.

Housner, G.W., Bergman, L.A., Caughey, T.K., Chassiakos, A.G., Claus, R.O., Masri, S.F., Skelton, R.E., Soong, T.T., Spencer, B.F. and Yao, J.T.P. (1997), "Structural control: Past, present, and future", *J. Eng. Mech. - ASCE*, **123**(9), 897-971.

Jangid, R. (2000), "Optimum frictional elements in sliding isolation systems", *Comput. Struct.*, **76**(5), 651-661.

Jangid, R. (2005), "Optimum friction pendulum system for near-fault motions", *Eng. Struct.*, **27**(3), 349-359.

Jangid, R. (2007), "Optimum lead-rubber isolation bearings for near-fault motions", *Eng. Struct.*, **29**(10), 2503-2513.

Jensen, H. and Sepulveda, J. (2012), "On the reliability-based design of structures including passive energy

dissipation systems", *Struct. Saf.*, **34**(1), 390-400.
Johnson, E.A., Kamalzare, M. and Wojtkiewicz, S.F. (2013), "Efficient optimal design of passive hysteretic base isolators by Volterra integral equations", *Proceedings of the 11th International Conference on Structural Safety & Reliability (ICOSSAR 2013)*, New York, NY, June 16-20.
Johnson, E.A. and Wojtkiewicz, S.F. (2014), "Efficient sensitivity analysis of structures with local modifications — Part II: Transfer functions and spectral densities", *J. Eng. Mech. - ASCE*, **140**(9), 04014068.
Kamalzare, M. (2014), *Computationally efficient design of optimal strategies for passive and semiactive damping devices in smart structures*, Ph.D. Dissertation, Univ. of Southern California, Los Angeles, CA.
Kamalzare, M., Johnson, E.A. and Wojtkiewicz, S.F. (2015), "Computationally efficient design of optimal strategies for controllable damping devices", *Struct. Control Health Monit.*, **22**(1), 1-18.
Kelly, J.M. (1986), "Aseismic base isolation: review and bibliography", *Soil Dyn. Earthq. Eng.*, **5**, 202-216.
Naeim, F. and Kelly, J.M. (1999), *Design of Seismic Isolated Structures: From Theory to Practice*, Wiley, Chichester, England.
Nagarajaiah, S. and Sun, X. (2000), "Response of base-isolated USC hospital building in Northridge earthquake", *J. Struct. Eng. - ASCE*, **126**(10), 1177-1186.
Norton, K.M. (2002), *Parameter optimization of seismic isolator models using recursive block-by-block nonlinear transient structural synthesis*, M.S. thesis, Naval Postgraduate School, Monterey, CA.
Park, J.G. and Otsuka, H. (1999), "Optimal yield level of bilinear seismic isolation devices", *Earthq. Eng. Struct. D.*, **28**(9), 941-955.
Roy, B.K., Chakraborty, S. and Mihsra, S.K. (2014), "Robust optimum design of base isolation system in seismic vibration control of structures under uncertain bounded system parameters", *J. Vib. Control*, **20**(5), 786-800.
Skinner, R.I., Robinson, W.H. and McVerry, G.H. (1993), *An Introduction to Seismic Isolation*, Wiley, Chichester, England.
Soong, T.T. and Dargush, G.F. (1997), *Passive Energy Dissipation Systems in Structural Engineering*. Wiley, Chichester, England.
Taflanidis, A.A. and Beck, J.L. (2008a), "An efficient framework for optimal robust stochastic system design using stochastic simulation", *Comput. Method. Appl. M.*, **198**(1), 88-101.
Taflanidis, A.A. and Beck, J.L. (2008b), "Stochastic subset optimization for optimal reliability problems", *Probabilist. Eng. Mech.*, **23**(2-3), 324-338.
Taflanidis, A.A. and Beck, J.L. (2009), "Stochastic subset optimization for reliability optimization and sensitivity analysis in system design", *Comput. Struct.*, **87**(5-6), 318-331.
Taflanidis, A.A. and Beck, J.L. (2010), "Reliability-based design using two-stage stochastic optimization with a treatment of model prediction errors", *J. Eng. Mech. - ASCE*, **136**(12), 1460-1473.
Wen, Y.K. (1976), "Method for random vibration of hysteretic systems", *J. Eng. Mech. Div.*, **102**(2), 259-263.
Wilson, E.L. (1999), *Three Dimensional Static and Dynamic Analysis of Structures: A Physical Approach with Emphasis on Earthquake Engineering*, Computers and Structures, 3rd Ed.
Wojtkiewicz, S.F. and Johnson, E.A. (2014), "Efficient sensitivity analysis of structures with local modifications — Part I: Time domain responses", *J. Eng. Mech. - ASCE*, **140**(9), 04014067.

Smart Structures and Systems, *Vol. 15, No. 3 (2015) 863-879*
DOI: http://dx.doi.org/10.12989/sss.2015.15.3.863

Experimental investigation of an active mass damper system with time delay control algorithm

Dong-Doo Jang[1], Jeongsu Park[2] and Hyung-Jo Jung[*2]

[1]*Korea Railroad Research Institute, Euiwang, Gyeonggi-do 437-757, Korea*
[2]*Department of Civil and Environmental Engineering, KAIST, Daejeon 305-701, Korea*

(Received November 27, 2014, Revised January 19, 2015, Accepted January 21, 2015)

Abstract. This paper experimentally investigates the effectiveness and applicability of the time delay control (TDC) algorithm, which is simple and robust to unknown system dynamics and disturbance, for an active mass damper (AMD) system to mitigate the excessive vibration of a building structure. To this end, the theoretical background including the mathematical formulation of the control system is first described; and then, a thorough experimental study using a shaking table system with a small-scale three-story building structural model is conducted. In the experimental tests, the performance of the proposed control system is examined by comparing its structural responses with those of the uncontrolled system in the free vibration and forced vibration cases. It is clearly verified from the test results that the TDC algorithm embedded AMD system can effectively reduce the structural response of the building structure.

Keywords: time delay control algorithm; unknown dynamics; vibration mitigation; active mass damper; shaking table test

1. Introduction

One of the widely used control strategies for mitigating excessive vibration of building structures having low inherent damping ratios is to introduce inertial control-type dampers (e.g., tuned mass damper (TMD), active mass damper (AMD), etc.) to the structures. Since the AMD system has several attractive features such as high control efficiency, good adaptability and relative insensitivity to site conditions compared to the TMD system, it can be considered as an effective means for response reduction of high-rise building structures subjected to dynamic loadings like earthquakes and winds, especially small-to-medium earthquakes and strong winds. The AMD system was first applied to a full-scale building structure 25 years ago (Kobori *et al*. 1991a, b). Since then, this type of the active control system has been implemented in more than 40 buildings (Nishitani and Inoue 2001, Spencer and Nagarajaiah 2003).

Successful operation of the AMD system is highly dependent upon an embedded control algorithm in the control system. For the AMD system, a lot of control algorithms (e.g., control algorithms based on linear optimal control theory such as LQG and H2, sliding mode control algorithm, adaptive control algorithm, intelligent control algorithms such as neural network-based

*Corresponding author, Associate Professor, E-mail: hjung@kaist.ac.kr

http://www.techno-press.org/?journal=sss&subpage=8 ISSN: 1738-1584 (Print), 1738-1991 (Online)

control and fuzzy logic-based control, etc.) have been studied (Datta 2001, Dyke *et al*. 1996, Pourzeynali *et al*. 2007). However, most of the algorithms have been originally developed in other engineering fields (e.g., electrical or mechanical engineering); so sometimes they might not fit very well with large-scale civil engineering structures such as bridges and buildings. For example, the most popular LQG and H2 algorithms require an exact mathematical model of a structure of interest, but it is too difficult to know a precise mathematical model of a large civil structure due to its complexity and uncertainty. Moreover, civil structures have slow dynamics; in other words, their dominant natural frequencies are relatively low compared to structural systems in mechanical or electrical engineering fields. Thus, a control algorithm which is appropriate to the structures having the abovementioned properties is needed for more effectively reducing the structural responses of the civil structures.

The time delay control (TDC) algorithm, which belongs to robust and adaptive control algorithms, might be one of the most suitable control algorithms for this purpose. It is not only simple and compact, but also very robust to unknown dynamics and disturbances. More than that, it is known that the TDC algorithm is especially powerful to a structure having slow dynamics. Even though it was first proposed in the field of mechanical engineering for motion control (Youcef-Toumi and Ito 1987a,b, 1988) and applied to robot manipulator, electrohydraulic servo system, DC servo motor system, and vibration isolation table (Hsia and Gao 1990, Chang *et al*. 1995, Chin *et al*. 1994, Chang and Lee 1994, Shin and Kim 2009, Sun and Kim 2012), the researches for vibration mitigation of large-scale structures such as buildings, bridges and towers using the TDC algorithm have not been done until Jang *et al*. (2014) numerically verified the feasibility of the TDC algorithm in the field of civil engineering. Still, its applicability to real structures is not guaranteed. Therefore, its applicability should be experimentally validated at least in a laboratory setting.

In this paper, the effectiveness and applicability of the TDC algorithm embedded AMD system is experimentally investigated. To this end, the theoretical background including the mathematical formulation of the control system is addressed first. And then, the performance of the proposed control system is thoroughly examined through a series of the experiments using a shaking table system with a small-scale three-story building structural model. After the experimental setup and the controller design, the free vibration and forced vibration tests are carried out, respectively. The test results of the proposed system are compared with those of the uncontrolled system in order to validate the effectiveness of the AMD system using the TDC algorithm.

2. Theoretical background

2.1 TDC algorithm

Let us consider a dynamic system in a general form, which can be either time invariant linear or time varying linear or nonlinear, described by

$$\dot{\mathbf{x}}(t) = \mathbf{f}(\mathbf{x}, t) + \mathbf{B}(\mathbf{x}, t)\mathbf{u}(t) + \mathbf{d}(t) \tag{1}$$

where $\mathbf{x}(t)$ is the plant state vector, $\mathbf{f}(\mathbf{x}, t)$ is the dynamics of the plant, $\mathbf{B}(\mathbf{x}, t)$ is the distribution matrix of the control input, and $\mathbf{d}(t)$ represents any kind of disturbance such as an external force. In Eq. (1), the plant dynamics, the distribution matrix of the control input and the

disturbance are assumed to be unknown. The objective of the TDC algorithm is to make the above system follow a reference model despite the presence of unknown dynamics and disturbances (Youcef-Toumi and Reddy 1992). A reference model with desirable dynamic characteristics is chosen as a stable time-invariant linear system as follows

$$\dot{\mathbf{x}}_{\mathbf{m}}(t) = \mathbf{A}_{\mathbf{m}}\,\mathbf{x}_{\mathbf{m}}(t) + \mathbf{B}_{\mathbf{m}}\,r(t) \tag{2}$$

where $\mathbf{x}_{\mathbf{m}}(t)$ is the state vector of the reference model, $\mathbf{A}_{\mathbf{m}}$ is the constant stable system matrix, $\mathbf{B}_{\mathbf{m}}$ is the constant command distribution matrix, and $r(t)$ is the command vector. The control input $\mathbf{u}(t)$ in Eq. (1) is determined such that the plant in Eq. (1) follows the reference model in Eq. (2); in other words, the difference between states of the plant and reference model (i.e., $\mathbf{e}(t) = \mathbf{x}_{\mathbf{m}}(t) - \mathbf{x}(t)$) to vanish according to the following error dynamic equation

$$\dot{\mathbf{e}}(t) = \mathbf{A}_{\mathbf{m}}\,\mathbf{e}(t) + \left[-\mathbf{f}(\mathbf{x},t) + \mathbf{A}_{\mathbf{m}}\,\mathbf{x}(t) + \mathbf{B}_{\mathbf{m}}\,r(t) - \mathbf{B}(\mathbf{x},t)\,\mathbf{u}(t) - \mathbf{d}(t)\right] = \mathbf{A}_{\mathbf{m}}\,\mathbf{e}(t) \tag{3}$$

Thus, the control input can be deduced from Eq. (3) as follows

$$\mathbf{u}(t) = \mathbf{B}^{+}\left[-\mathbf{f}(\mathbf{x},t) - \mathbf{d}(t) + \mathbf{A}_{\mathbf{m}}\,\mathbf{x}(t) + \mathbf{B}_{\mathbf{m}}\,r(t)\right] \tag{4}$$

where $\mathbf{B}^{+}\left(= (\mathbf{B}^{\mathrm{T}}\mathbf{B})^{-1}\mathbf{B}^{\mathrm{T}}\right)$ is the pseudo-inverse of the control input distribution matrix $\mathbf{B}(\mathbf{x}, t)$.

Because $\mathbf{B}(\mathbf{x}, t)$, $\mathbf{f}(\mathbf{x}, t)$ and $\mathbf{d}(t)$ in Eq. (4) are unknown, $\hat{\mathbf{B}}$ is used as an estimate of the $\mathbf{B}(\mathbf{x}, t)$ and it is assumed that $\mathbf{f}(\mathbf{x}, t)$ and $\mathbf{d}(t)$ have slow dynamic characteristics so that $\mathbf{f}(\mathbf{x},t) + \mathbf{d}(t)$ can be replaced approximately with $\mathbf{f}(\mathbf{x},t-\Delta t) + \mathbf{d}(t-\Delta t)$ for a small time delay Δt. Using Eq. (1), the estimate of $\mathbf{f}(\mathbf{x},t) + \mathbf{d}(t)$ can be given by

$$\mathbf{f}(\mathbf{x}, t) + \mathbf{d}(t) \cong \mathbf{f}(\mathbf{x}, t-\Delta t) + \mathbf{d}(t-\Delta t) \cong \dot{\mathbf{x}}(t-\Delta t) - \hat{\mathbf{B}}\,\mathbf{u}(t-\Delta t) \tag{5}$$

By substituting Eq. (5) into Eq. (4), the control input by the TDC algorithm is obtained as follows

$$\mathbf{u}(t) = \mathbf{u}(t-\Delta t) + \hat{\mathbf{B}}^{+}\left\{-\dot{\mathbf{x}}(t-\Delta t) + \mathbf{A}_{\mathbf{m}}\,\mathbf{x}(t) + \mathbf{B}_{\mathbf{m}}\,r(t)\right\} \tag{6}$$

As seen in Eq. (6), all states and their first derivatives should be available to apply the TDC algorithm.

2.2 Derivation of the state-space equation for a building structure

Let us consider an n-DOF building structure model as shown in Fig. 1. It is assumed that only one active control system is implemented at the top floor and the responses only at the top floor of the structure can be available in view of practical situation.

Because the information of all states and their derivatives has to be available in order to apply the TDC algorithm as stated previously, the dynamics equation for structure should be written so that all states are acquirable.

The equation of motion can be described in the modal coordinate by

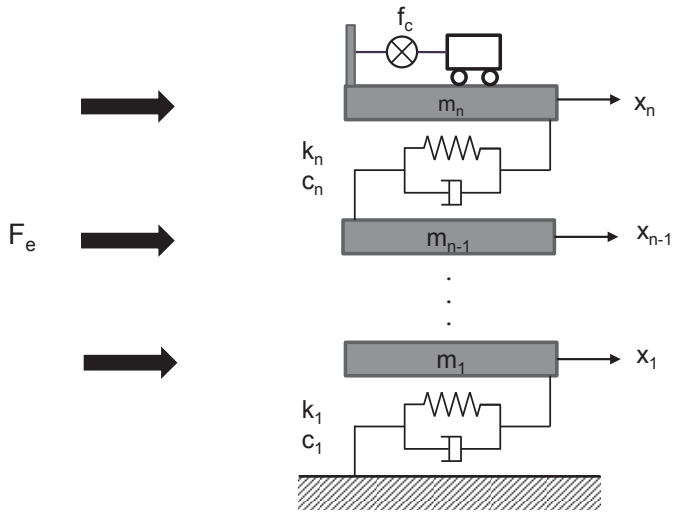

Fig. 1 n-DOF building structure

$$\overline{m}_j \ddot{q}_j + 2\xi_j \omega_j \dot{q}_j + \omega_j^2 q_j = f_c + \boldsymbol{\varphi}_j^T \mathbf{F_e}, \qquad j = 1 \sim n \tag{7}$$

where $\overline{m}_j = \boldsymbol{\varphi}_j^T \mathbf{M} \boldsymbol{\varphi}_j$ is the *j*th modal mass, ξ_j and ω_j are the *j*th damping ratio and natural frequency, respectively, f_c and $\mathbf{F_e}$ are the control force and the external force, respectively, and $\boldsymbol{\varphi}_j$ is the *j*th mode shape which is normalized so that $\boldsymbol{\varphi}_j(n) = 1$. Eq. (7) can be converted into the following state-space form

$$\begin{Bmatrix} \dot{q}_j(t) \\ \ddot{q}_j(t) \end{Bmatrix} = \begin{bmatrix} 0 & 1 \\ -\omega_j^2 & -2\xi_j\omega_j \end{bmatrix} \begin{Bmatrix} q_j(t) \\ \dot{q}_j(t) \end{Bmatrix} + \begin{bmatrix} 0 \\ 1/\overline{m}_j \end{bmatrix} f_c(t) + \begin{bmatrix} 0 \\ F_{ej} \left(= \dfrac{1}{\overline{m}_j} \boldsymbol{\varphi}_j^T \mathbf{F_e} \right) \end{bmatrix}, \quad j = 1 \sim n \tag{8}$$

By summing *n* equations of Eq. (8), we obtain

$$\begin{aligned} \sum_{j=1}^{n} \begin{Bmatrix} \dot{q}_j(t) \\ \ddot{q}_j(t) \end{Bmatrix} &= \sum_{j=1}^{n} \begin{bmatrix} 0 & 1 \\ -\omega_j^2 & -2\xi_j\omega_j \end{bmatrix} \begin{Bmatrix} q_j(t) \\ \dot{q}_j(t) \end{Bmatrix} + \sum_{j=1}^{n} \begin{bmatrix} 0 \\ 1/\overline{m}_j \end{bmatrix} f_c(t) + \sum_{j=1}^{n} \begin{bmatrix} 0 \\ F_{ej} \end{bmatrix} \\ &= \begin{bmatrix} \sum_{j=1}^{n} \dot{q}_j(t) \\ f\left(q_j(t), \dot{q}_j(t)\right) \end{bmatrix} + \begin{bmatrix} 0 \\ \sum_{j=1}^{n} 1/\overline{m}_j \end{bmatrix} f_c(t) + \begin{bmatrix} 0 \\ \sum_{j=1}^{n} F_{ej} \end{bmatrix} \end{aligned} \tag{9}$$

Since the mode shapes are normalized so that $\boldsymbol{\varphi}_j(n)=1$, the response at the top floor can be described by

$$x_n(t) = \sum_{j=1}^{n} \boldsymbol{\varphi}_j(n) q_j(t) = \sum_{j=1}^{n} q_j(t) \tag{10}$$

By substituting Eq. (10) into Eq. (9), we obtain the following state-space equation for a building structure in which the states and their derivatives are the responses at the top floor, which are assumed to be available

$$\begin{Bmatrix} \dot{x}_n(t) \\ \ddot{x}_n(t) \end{Bmatrix} = \begin{bmatrix} \dot{x}_n(t) \\ f\left(q_j(t), \dot{q}_j(t)\right) \end{bmatrix} + \begin{bmatrix} 0 \\ \sum_{j=1}^{n} 1/\overline{m}_j \end{bmatrix} f_c(t) + \begin{bmatrix} 0 \\ \sum_{j=1}^{n} F_{ej} \end{bmatrix} \tag{11}$$

2.3 Application of the TDC algorithm to structural control

As comparing Eq. (11) with Eq. (1), the control force $f_c(t)$ is obtained according to the TDC algorithm of Eq. (6) by

$$f_c(t) = f_c(t-\Delta t) + \hat{\mathbf{B}}^{+}\left[-\begin{Bmatrix} \dot{x}_n(t-\Delta t) \\ \ddot{x}_n(t-\Delta t) \end{Bmatrix} + \mathbf{A_m} \begin{Bmatrix} x_n(t) \\ \dot{x}_n(t) \end{Bmatrix} + \mathbf{B_m}\, r(t) \right] \tag{13}$$

where $\hat{\mathbf{B}} = \begin{bmatrix} 0 \\ \hat{b}_r \end{bmatrix}$ and $\hat{b}_r$ is the estimate of $\sum_{j=1}^{n} 1/\overline{m}_j$. The pseudo-inverse of $\hat{\mathbf{B}}$ is obtained by

$$\hat{\mathbf{B}}^{+} = \left(\begin{bmatrix} 0 & \hat{b}_r \end{bmatrix} \begin{bmatrix} 0 \\ \hat{b}_r \end{bmatrix} \right)^{-1} \begin{bmatrix} 0 & \hat{b}_r \end{bmatrix} = \begin{bmatrix} 0 & \dfrac{1}{\hat{b}_r} \end{bmatrix} \tag{14}$$

Because the control objective of structural control is to mitigate the vibration of a structure, the command term $r(t)$ is set to zero. And let us define the system matrix of the reference model $\mathbf{A_m}$ as follows

$$\mathbf{A_m} = \begin{bmatrix} 0 & 1 \\ -\omega_m^2 & -2\xi_m\omega_m \end{bmatrix} \tag{15}$$

where ω_m and ξ_m are the natural frequency and damping ratio of the reference model, respectively. By substituting Eqs. (14) and (15) into Eq. (13), it can be rewritten by

$$f_c(t) = f_c(t-\Delta t) + \frac{1}{\hat{b}_r}\left[-\ddot{x}_n(t-\Delta t) - \omega_m^2 x_n(t) - 2\xi_m \omega_m \dot{x}_n(t) \right] \tag{16}$$

As seen in Eq. (16), the design parameters are $\hat{b}_r$, the estimate of $\sum_{j=1}^{n} 1/\overline{m}_j$ and dynamic characteristics of reference model, ω_m and ξ_m. And all states and their first derivatives should be available to apply the TDC algorithm. Among the design parameters, $\hat{b}_r$ is related with the stability of the control system, and the inequality condition for guaranteeing the stability was derived as follows (Jang *et al*. 2014)

$$\hat{b}_r > \frac{1}{2} b_r \tag{17}$$

3. Experimental test results

3.1 Experimental setup

To investigate the feasibility and control performance of the TDC algorithm in mitigating the excessive vibration of a building a series of experimental tests were conducted by using a shaking table uniaxially driven by a servo-controlled hydraulic actuator in the Structural Control and Intelligent Systems Laboratory (SCaIS) at KAIST. The shaking table has a testing platform of 110 cm by 96 cm, a maximum payload of 600 kg, a maximum acceleration of ±0.4 g and a maximum velocity of 21 cm/s. The hydraulic actuator with the maximum dynamic force of 2 tons and the stroke length of ±5 cm can be controlled by a servo-hydraulic controller in a displacement or acceleration feedback mode. A schematic of the experimental setup is shown in Fig. 2.

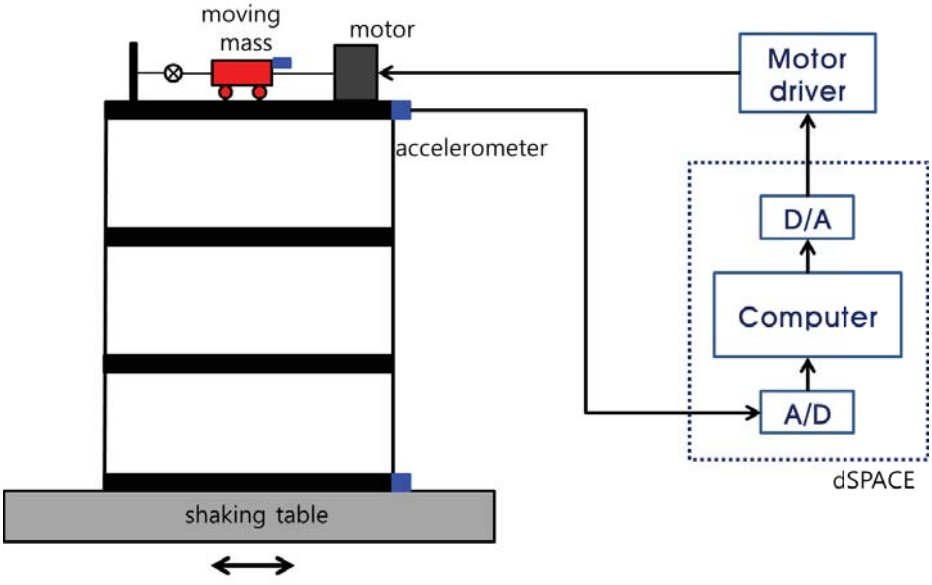

Fig. 2 Schematic of experimental setup

Fig. 3 Scaled 3-story shear building model

The test structure model used in the experiment is a scaled 3-story shear building model as shown in Fig. 3. The columns are constructed of aluminum and the total height is 1050 mm, and the floor masses are constructed of steel and the total weights are 48.27 kg, which is distributed evenly in each floor. The dynamic characteristics of the structure model were identified by a frequency-domain system identification technique. Fig. 4 shows representative magnitude and phase plots for the experimentally determined and analytically estimated frequency response functions (FRFs). The identified modal masses are 30, 43 and 160 kg, natural frequencies are 2.145, 6.595 and 10.531 Hz, and damping ratios are 0.26, 0.7 and 0.4%.

The AMD system shown in Fig. 5 which provides the control force to the structure consists of a moving mass, an LM guide rail, a ball screw, a timing belt and a servo motor (model: Mitsubishi HP-KP23 200W). The rotary motion of the servo motor delivered to the ball screw and it converts the rotary motion into rectilinear motion of the moving mass, which is driven on the LM guide rail. The motion of the moving mass generates the inertia force, and it is utilized as the control force for the structure. In order to induce the accurate inertia force by the moving mass, the dynamics of the AMD system should be considered. In the experiments, an inverse transfer function of the acceleration of the moving mass with respect to the command voltage into the servo motor driver is constructed and implemented in the control signal processing in order to compensate the dynamics of the AMD system. Fig. 6 presents the magnitude and phase plots for the experimentally determined and analytically estimated FRFs of the acceleration of the moving mass with respect to the command voltage of the AMD system, where the estimated FRF is determined using MATLAB/System Identification Toolbox in the discrete time-domain as follows

$$\hat{H}_{u\ddot{a}}(z) = \frac{1832.1\, z^{-1} - 1756.5\, z^{-2}}{1 - 1.6019\, z^{-1} + 0.71839\, z^{-2}} \tag{18}$$

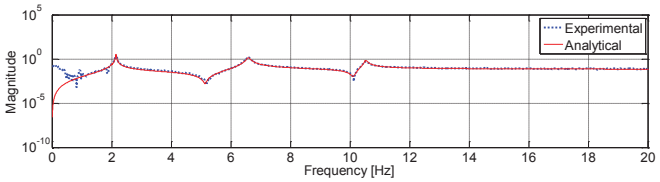

(a) Magnitude

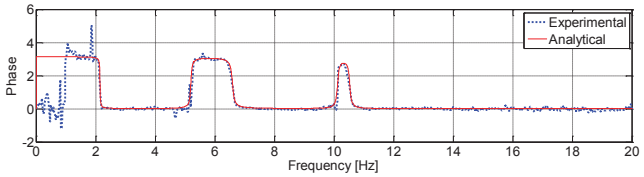

(b) Phase

Fig. 4 FRF from relative AMD acceleration to third floor acceleration

Fig. 5 Active mass damper system

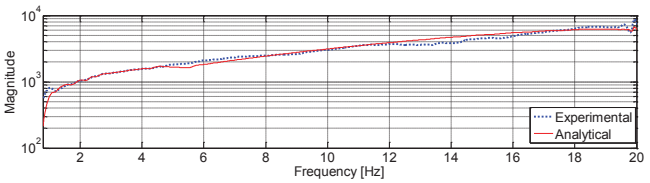

(a) Magnitude

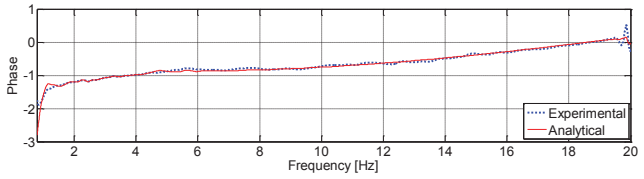

(b) Phase

Fig. 6 FRF from AMD command voltage to AMD acceleration

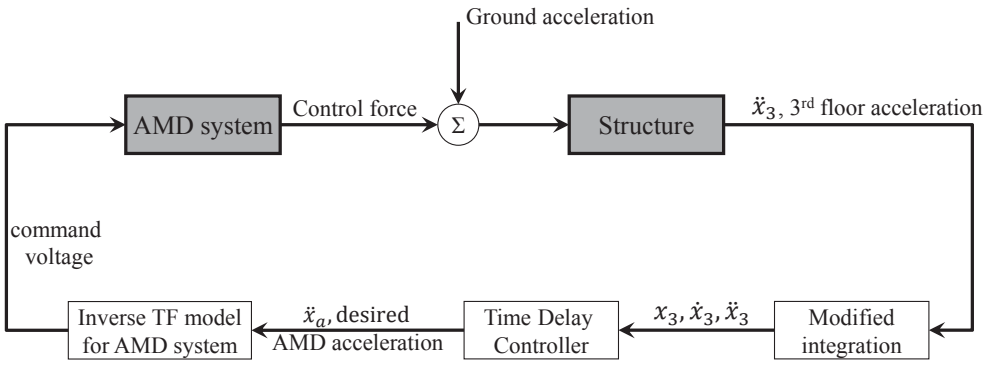

Fig. 7 Block diagram of the experiments for structural control using the TDC algorithm

The voltage into the servo motor of the AMD system was processed by dSPACE ControlDesk and Simulink of MatLab in a personal computer. The voltage calculated in the computer was supplied to the servo motor driver (model: Mitsubishi MR-J3-20A) by dSPACE Model ds1104 and the measured acceleration of the structure model is digitized also by the ds1104.

In the experiments, the acceleration at the third floor of the structure model was measured by an accelerometer (model: PCB 393B12) and it is used for calculating the required control force by the TDC algorithm. Besides, the accelerations of the shaking table platform and the moving mass of the AMD system were measured to check out the results. A block diagram for the whole closed-loop system is shown in Fig. 7, where the plant consists of the structure model and the AMD system.

As stated previously, all state variables and its first derivatives (i.e., displacement, velocity and acceleration of the structure model) should be available to apply the TDC algorithm. However, since only the acceleration is measured in practice, a numerical integrator or state estimator must be used to obtain the velocity and displacement. In this experiment, a numerical integration is used in order to avoid the difficulties in identifying the structure model, which is required to use the state estimator. However, the ideal integration method accumulates even a small DC-offset value measured acceleration; thus, a modified integration (Zhu 2004) is applied, which can remove the accumulation of the DC offset. The modified integrator is just a slight variation of the ideal integrator as follows

$$\frac{1}{s} : \text{ideal integrator} \quad \Rightarrow \quad \frac{1}{s+a} : \text{modified intgrator} \tag{19}$$

where s is Laplace operator. By using the modified integrator, the integration of the low frequency components converges to zero. The parameter a, which is referred as cut-off frequency of a first order system, affects distortion of the phase and magnitude of the signal. As a rule of thumb, the value of a is chosen as about 1/10 of the lowest frequency of interest. In this study, it is determined as 0.05 by considering the dynamic range of the accelerometer (> 0.5 Hz).

3.2 Controller design

The design parameters in the TDC algorithm are the dynamic characteristics of the reference model and the estimate of the input distribution matrix. The reference model, which is denoted by $\mathbf{A_m}$ in Eq. (15), is a target system which has to be achieved by the TDC algorithm; therefore, it should be selected as a stable system. In this experiment, the natural frequency and the damping ratio of the reference model were chosen as 0.1 Hz and the critical (i.e., $\xi_m = 1$), respectively.

The estimate of the input distribution matrix, which is denoted by $\hat{b}_r$ in Eq. (16), should be chosen by considering the inequality condition of Eq. (17) for guaranteeing the stability of the control system. As presented in Eq. (13), $b_r = \sum_{j=1}^{n} 1/\overline{m}_j$, where $\overline{m}_j = \boldsymbol{\varphi}_j^T \mathbf{M} \boldsymbol{\varphi}_j$ is the *j*-th modal mass. Because it is assumed that the exact values of the modal masses are unknown, the guideline for the determination of $\hat{b}_r$ is required. Because mode shapes are normalized such that $\boldsymbol{\varphi}_j(n) = 1$, the first modal mass, $\overline{\mathrm{m}}_1$, is the smallest among the modal masses. Therefore, the following inequality can be derived

$$b_r = \sum_{j=1}^{n} \frac{1}{\overline{m}_j} < \frac{n}{\overline{m}_1} < \frac{n}{m_n} \tag{20}$$

where m_n denotes the mass of the *n*-th floor. Thus, if we choose $\hat{b}_r$ larger than $\frac{n}{m_n}$, then the stability condition of Eq. (17) is satisfied obviously. The mass of the *n*-th floor, m_n, can be assumed easily, and it does not need to be exact.

At the test structure model, the number of floor is 3 and the mass of the 3rd floor is about 16 kg; thus the estimate $\hat{b}_r$ can be chosen larger than 0.2. In this experiment, $\hat{b}_r = 1.66$ is chosen by considering the maximum AMD stroke.

3.3 Free vibration test

At first, the free vibration test was performed to check an increase in the equivalent damping ratio of the structure model, because it is one of the simplest ways to verify the control performance. Fig. 8 shows the acceleration at the third floor of the structure model and the command voltage of the AMD system for the case of the excitation at the first natural frequency. The structure model was excited as a harmonic motion of the first mode by the AMD system, and then the AMD system was stopped in uncontrolled mode or operated by the TDC algorithm in the control mode.

As shown in Fig. 8, the free vibration response in the controlled case decays out much faster than in the uncontrolled case. It can be easily observed from the two shaded regions in the figure. The equivalent damping ratios can be calculated from the free vibration responses by using the logarithmic decrement method. The damping ratio in the uncontrolled case is 0.26%; on the other hand, the ratio in the controlled case is 6.0%. The damping ratio is increased over than 20 times. It is, therefore, said that the proposed control system can effectively mitigate the free vibration response of the building structure.

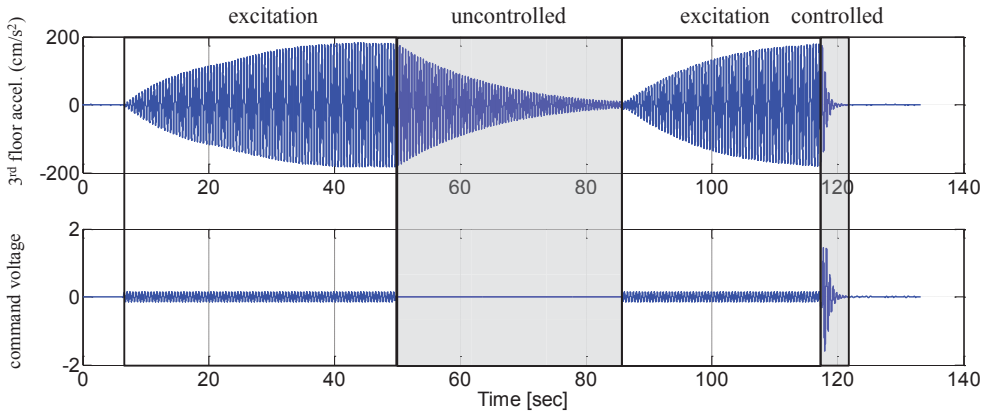

Fig. 8 Free vibration test result

3.4 Forced vibration test

As the inputs to the structure model, the band-limited white noise and two different historical earthquakes were used. The ground accelerations considered herein are

1) Artificially generated white noise ground acceleration which is uniformly distributed in the frequency range of 0-20 Hz;

2) El Centro earthquake (The N-S component recorded at the Imperial Valley Irrigation District substation in El Centro, California, during Imperial Valley, California earthquake, May 18, 1940) scaled to 10% amplitude and 2 times the recorded rate; and

3) Hachinohe earthquake (The N-S component recorded at Hachinohe City during the Tokachi-oki earthquake, May 16, 1968) scaled 15% amplitude and 2 times the recorded rate.

Fig. 9 shows the time histories of the third floor acceleration in the three different values of $\hat{b}_r$ under the 0-20Hz band-limited white noise. As seen from the figures, the acceleration response can be more effectively mitigated with a small value of $\hat{b}_r$. The results of the experiments are briefly summarized in Table 1. In the table, the values in the parentheses denote % reduction of the responses in the controlled case compared to those in the uncontrolled case. By contrast to the control performance, it is shown that a more control force, which is the inertia force of the AMD moving mass, is required as $\hat{b}_r$ being smaller.

Fig. 10 presents the experimental result under the band-limited white noise and $\hat{b}_r = 1.66$, in which (a) time history of the ground acceleration, (b) time history of the acceleration at the third floor, (c) the desired and measured AMD acceleration, and (d) FRF of the third floor acceleration. The overall maximum and RMS responses are reduced by 44.52% and 66.42%, respectively. It is demonstrated from the test results that the measured relative AMD acceleration agrees well with the desired one as presented in Fig. 10(c), which means the motion of the moving mass of the AMD follows the desired trajectory well, and consequently the proper control force is applied to the structure, resulting in the good control performance of the proposed control system.

Table 1 Experimental results under the band-limited white noise

Case	Uncontrolled	Controlled	
Maximum acceleration (cm/s^2)	30.75	$\hat{b}_r = 1.66$	17.06 (-44.52%)
		$\hat{b}_r = 3.32$	20.04 (-34.83%)
		$\hat{b}_r = 6.64$	21.99 (-28.48%)
RMS acceleration (cm/s^2)	8.88	$\hat{b}_r = 1.66$	2.98 (-66.42%)
		$\hat{b}_r = 3.32$	3.79 (-57.33%)
		$\hat{b}_r = 6.64$	4.76 (-46.42%)
Maximum control force (N)	-	$\hat{b}_r = 1.66$	1.90
		$\hat{b}_r = 3.32$	1.34
		$\hat{b}_r = 6.64$	0.86

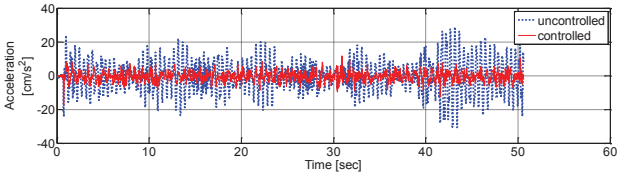

(a) $\hat{b}_r = 1.66$

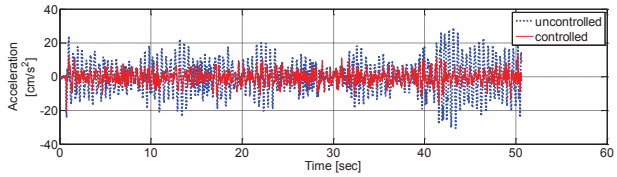

(b) $\hat{b}_r = 3.32$

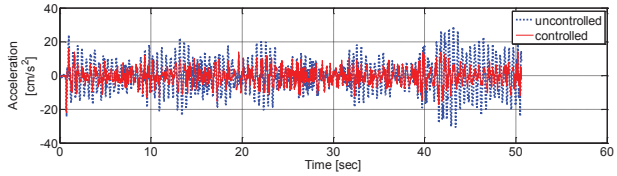

(c) $\hat{b}_r = 6.64$

Fig. 9 Acceleration responses at the third floor under the 0-20 Hz band-limited white noise with the different values of $\hat{b}_r$

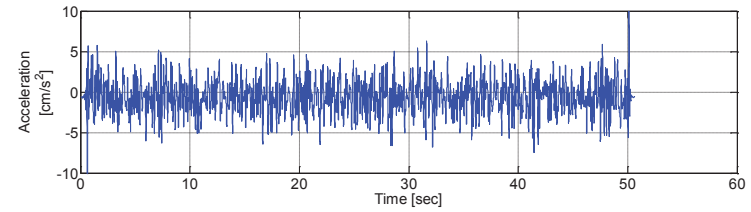

(a) Ground acceleration

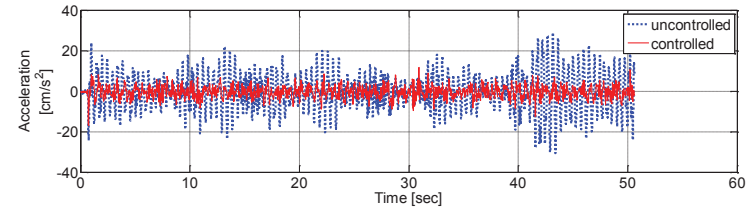

(b) Third floor acceleration

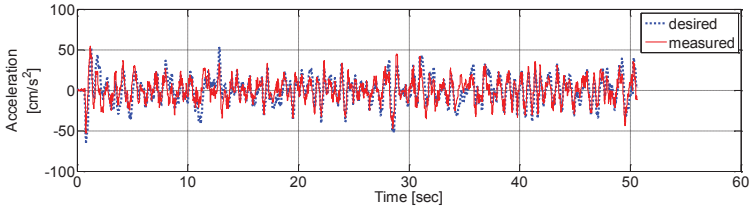

(c) Relative AMD acceleration

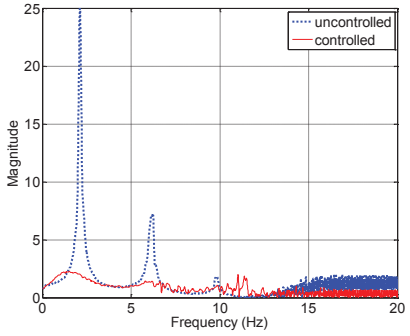

(d) FRF of the third floor acceleration

Fig. 10 Experimental results under the 0-20 Hz band-limited white noise

Figs. 11 and 12 present the experimental results under the scaled El Centro earthquake and Hachinohe earthquake, respectively, in which (a) time history of the ground acceleration, (b) time history of the acceleration at the third floor, (c) the desired and measured AMD acceleration, and (d) FRF of the third floor acceleration. As seen from Figs. 11(b), 11(d) and 12(b), 12(d), compared to the uncontrolled case, the third floor acceleration response is reduced significantly by the controlled system. The overall maximum and RMS of the third floor acceleration are reduced from 119.9 cm^2/sec (uncontrolled) to 89.3 cm^2/sec (controlled) and 44.7 cm^2/sec to 14.3 cm^2/sec under

the scaled El Centro earthquake, and from 201.5 cm^2/sec (uncontrolled) to 107.6 cm^2/sec (controlled) and 65.9 cm^2/sec to 19.3 cm^2/sec under the scaled Hachinohe earthquake. The motion of the moving mass of the AMD follows the trajectory well as shown in Figs. 11(c) and 12(c). In summary, it can be said that the proposed control system significantly reduces the structural response under the several different seismic loadings.

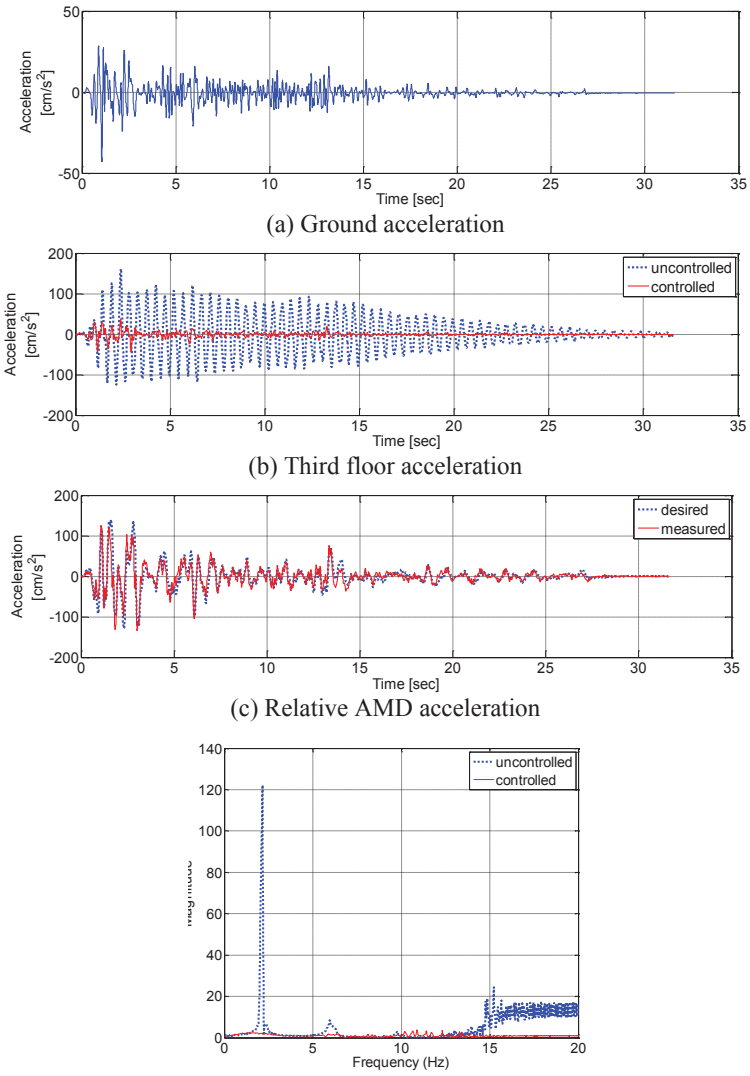

(a) Ground acceleration

(b) Third floor acceleration

(c) Relative AMD acceleration

(d) FRF of the third floor acceleration

Fig. 11 Experimental results under the scaled El Centro earthquake

Table 2 Experimental results under the scaled earthquakes (unit: cm/s^2)

Case		Uncontrolled	Controlled
The scaled El Centro earthquake	Max. acceleration	161.22	43.73 (-72.87%)
	RMS acceleration	45.28	5.82 (-87.14%)
The scaled Hachinohe earthquake	Max. acceleration	194.99	68.82 (-64.71%)
	RMS acceleration	57.83	6.50 (-88.76%)

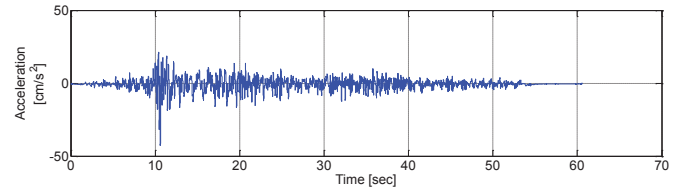

(a) Ground acceleration

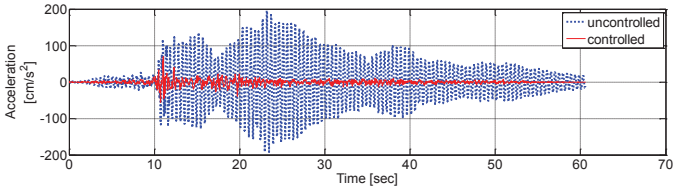

(b) Third floor acceleration

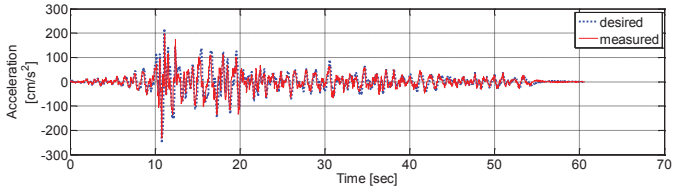

(c) Relative AMD acceleration

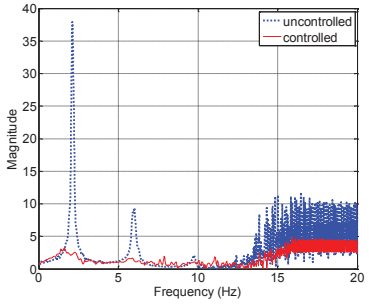

(d) FRF of the third floor acceleration

Fig. 12 Experimental results under the scaled Hachinohe earthquake

3.5 Discussion

As experimentally demonstrated in the preceding two sections, the proposed TDC algorithm could be effective to mitigate the excessive vibration of a building structure. At this section, a few issues related to the control performance and robustness of the TDC algorithm are discussed in more detail.

First, the control performance of the TDC algorithm is examined by comparing with the results of the experimental study conducted by other researchers. Dyke *et al*. (1996) developed the H_2/LQG control algorithm to reduce the vibration of the three-story building model equipped with the AMD system on the top floor subjected to the base excitation. This is exactly the same experimental setup as in this study. According their test results, the LQG control algorithm reduced the maximum acceleration at the third floor by 65% under the El Centro earthquake compared to the uncontrolled case. On the other hand, the proposed TDC algorithm has the 72% reduction under the same base excitation (see Table 2). Based on this comparison, it can be said that the control performance of the TDC algorithm is comparable to that of the LQG control algorithm.

During the design process of the TDC algorithm, decision of $\hat{b}_r$ in Eq. (16) is the most important step because it is related to the stability as well as the control performance of the control system. Eq. (17) means the inequality condition for guaranteeing the stability of the control system, and Eq. (20) shows the guideline to satisfy Eq. (17). The robustness of the control performance with respect to $\hat{b}_r$ was numerically examined in Jang *et al*. (2014). Also, according to Table 1 at Section 3.4, it is experimentally demonstrated that the TDC algorithm maintains the good control performance with the different values of $\hat{b}_r$. Moreover, it is well known that the TDC algorithm has the excellent robustness properties to unknown system dynamics and disturbances (Youcef-Toumi and Ito 1987a, b, 1988).

4. Conclusions

In this paper, the effectiveness and applicability of the time delay control (TDC) algorithm for an active mass damper (AMD) system to mitigate the excessive vibration of a building structure was experimentally investigated. First, the theoretical background including the mathematical formulation of the control system was described. And then, an experimental study using a shaking table system with a small-scale three-story building structural model was thoroughly carried out. In the experimental tests, the control performance of the proposed control system was examined by comparing its structural responses with those of the uncontrolled system in the cases of forced vibration as well as free vibration. The test results showed that the TDC algorithm embedded AMD system significantly reduced the structural response of the test model. Therefore, it is concluded that the proposed control system can be an effective means for mitigating the excessive vibration of a building structure.

Acknowledgements

This research was supported by a grant(14RTRP-B072484-02) from Railroad Technology Research Program funded by Ministry of Land, Infrastructure and Transport(MOLIT) of Korea government and Korea Agency for Infrastructure Technology Advancement (KAIA).

References

Chang, P.H. and Lee, J.W. (1994), "An observer design for time-delay control and its application to dc servo motor", *Control Eng. Pract.*, **2**(2), 263-270.

Chang, P.H., Kim, D.S. and Park K.C. (1995), "Robust force/position control of a robot manipulator using time-delay control", *Control Eng. Pract.*, **3**(9), 1255-1264.

Chin, S.M., Lee, C.O. and Chang, P.H. (1994), "An experimental study on the position control of an electrohydraulic servo system using time delay control", *Control Eng. Pract.*, **2**(1), 41-48.

Datta, T.K. (2001), "A state-of-the-art review on active control of structures", *J. Earthq. Technol. - ISET*, **40**(1), 1-17.

Dyke, S.J., Spencer, Jr., B.F., Quast, P., Kaspari, Jr. D.C. and Sain, M.K. (1996), "Implementation of an active mass driver using acceleration feedback control", *Microcomput. Civil Eng.*, **11**, 305-323.

Hsia, T.C. and Gao, L.S. (1990), "Robot manipulator control using decentralized linear time-invariant time-delayed controllers", *Proceedings of the IEEE International Conference on Robotics and Automation*, Cincinnati, OH, May.

Jang, D.D., Jung, H.J. and Moon, Y.J. (2014), "Active mass damper system using time delay control algorithm for building structure with unknown dynamics", *Smart Struct. Syst.*, **13**(2), 305-318.

Kobori, T., Koshika, N., Yamada, K. and Ikeda, Y. (1991a), "Seismic-response-controlled structure with active mass driver system. Part 1: Design", *Earthq. Eng. Struct. D.*, **20**(1), 133-149.

Kobori, T., Koshika, N., Yamada, K. and Ikeda, Y. (1991b), "Seismic-response-controlled structure with active mass driver system. Part 2: Verification", *Earthq. Eng. Struct. D.*, **20**(1), 151-166.

Nishitani, A. and Inoue, Y. (2001), "Overview of the application of active/semiactive control to building structures in Japan", *Earthq. Eng. Struct. D.*, **30**(11), 1565-1574.

Pourzeynali, S., Lavasani, H.H. and Modarayi, A.H. (2007), "Active control of high rise building structures using fuzzy logic and genetic algorithms", *Eng. Struct.*, **29**(3), 346-357.

Shin, Y.H. and Kim, K.J. (2009), "Performance enhancement of pneumatic vibration isolation tables in low frequency range by time delay control", *J. Sound Vib.*, **321**(3-5), 537-553.

Spencer, Jr., B.F. and Nagarajaiah, S. (2003), "State of the art of structural control", *J. Struct. Eng.* - ASCE, **129**(7), 845-856.

Sun, J.O. and Kim, K.J. (2012), "Six-degree of freedom active pneumatic table based on time delay control technique", *Proceedings of the Institution of Mechanical Engineers, Part 1; Journal of System and Control Engineering*, **226**(5), 638-650.

Youcef-Toumi, K. and Ito. O. (1987a), "Controller design for systems with unknown nonlinear dynamics", *Proceedings of the American Control Conference*, Minneapolis, MN, June, 836-845.

Youcef-Toumi, K. and Ito, O. (1987b), "Model reference control using time delay for nonlinear plants with unknown dynamics", *Proceedings of the 10th Triennial World Congress of International Federation of Automatic Control World Congress*, Munich, Germany, July.

Youcef-Toumi, K. and Ito. O. (1988), "A time delay controller for systems with unknown dynamics", *Proceedings of the American Control Conference*, Atlanta, GA, June.

Youcef-Toumi, K. and Reddy, S. (1992), "Analysis of linear time invariant systems with time delay", *J. Dynam. Syst. Measurement Control*, **114**(4), 544-555.

Zhu, W.H. (2004), "On active acceleration control of vibration isolation systems", *Proceedings of the 43rd IEEE Conference on Decision and Control*, Atlantis, Paradise Island, Bahamas.

Smart Structures and Systems, *Vol. 15, No. 3 (2015) 881-896*
DOI: http://dx.doi.org/10.12989/sss.2015.15.3.881

Drift displacement data based estimation of cumulative plastic deformation ratios for buildings

Akira Nishitani[*1], Chisa Matsui[2a], Yushiro Hara[1b], Ping Xiang[1c], Yoshihiro Nitta[3d], Tomohiko Hatada[4e], Ryota Katamura[4f], Iwao Matsuya[5g] and Takashi Tanii[1h]

[1]*Faculty of Science and Engineering, Waseda Univ., Shinjuku, Tokyo 169-8555 Japan*
[2]*Tokyo Metropolitan Government, Shinjuku, Tokyo 163-8001 Japan*
[3]*Department of Architecture, Ashikaga Institute of Technology, Tochigi 326-8558 Japan*
[4]*Kajima Technical Research Institute, Chofu, Tokyo 182-0036 Japan*
[5]*Department of Mechanical Engineering, Nagaoka Univ. of Technology, Nagaoka, Niigata 940-2188 Japan*

(Received November 17, 2014, Revised January 11, 2015, Accepted January 13, 2015)

Abstract. The authors' research group has developed a noncontact type of sensors which directly measure the inter-story drift displacements of a building during a seismic event. Soon after that event, such seismically-induced drift displacement data would provide structural engineers with useful information to judge how the stories have been damaged. This paper presents a scheme of estimating the story cumulative plastic deformation ratios based on such measured drift displacement information toward the building safety monitoring. The presented scheme requires the data of story drift displacements and the ground motion acceleration. The involved calculations are rather simple without any detailed information on structural elements required: the story hysteresis loops are first estimated and then the cumulative plastic deformation ratio of each story is evaluated from the estimated hysteresis. The effectiveness of the scheme is demonstrated by utilizing the data of full-scale building model experiment performed at E-defense and conducting numerical simulations.

Keywords: inter-story drift displacement; hysteresis; cumulative plastic deformation ratio; E-defense

1. Introduction

During these two decades many engineering fields have been drastically altering their conventional boundaries. That is also the case in the structural engineering field. The first active

∗Corresponding author, Professor, E-mail: anix@waseda.jp
[a] Former Research Associate at Waseda University
[b] Graduate Student
[c] Assistant Professor
[d] Associate Professor
[e] Ph.D. Research Engineer
[f] Research Engineer
[g] Assistant Professor
[h] Professor

http://www.techno-press.org/?journal=sss&subpage=8 ISSN: 1738-1584 (Print), 1738-1991 (Online)

control scheme implementation of a building structure in 1989 (Kobori *et al*. 1991) opened the door to smart structures technology integrating a variety of advanced techniques such as sensor, automatic control, information technologies, etc. This movement has been bringing a remarkable paradigm shift to the civil engineering field.

Based upon such a background, structural health monitoring has greatly appealed the attentions of structural engineers. For building structures, structural monitoring would be conducted based upon the daily and emergency vibration data sensing. These data records could provide useful information on how healthy or unhealthy, how safe or dangerous for continued use or stay the structure is. The significance of such health monitoring is demonstrated by recent accidents such as the ceiling board collapse at Sasago Tunnel (Kutsukake 2014) and the bridge fall-down in USA (www.ntsb.gov/investig ations/summary/har0803.htm). In addition to the preventing of these kinds of accidents mainly resulting from the time deterioration, it is also of great importance to establish the diagnosis scheme of building structures after a seismic event. With the establishment of such a scheme, it could be promptly judged which stories, or which structural elements if possible, are damaged. Such information would lead to the judgment of the appropriateness of continuous use or stay of building.

Most schemes for building health monitoring focusing on the diagnosis after a seismic event have been constructed with either accelerometers or velocity sensors. For instance, the schemes of Saito (1998), Nitta and Nishitani (2003) and Shinagawa and Mita (2013) were constructed based on the usage of accelerometers, and the scheme of Nakamura and Yasui (1999) was based on velocity sensor measurement. For the judgment of possibly-damaged building condition, however, inter-story drift displacement data could be more direct indices than acceleration and velocity response data. According to the Japanese Building Standard Law, most of the buildings in Japan are designed so as to satisfy the requirements of two levels of seismic excitations: Levels 1 and 2. Level 1 is such a medium level of earthquake input that the design base shear is 20% of total building weight for the typical situation; and Level 2 is such a large level of seismic input that induces the base shear equivalent of the total weight of building. During such Level 1 seismic event, all the stories of a building are required to remain in the elastic range and have the inter-story drift angles less than 1/200. These requirements indicate that if the drift angle is smaller than 1/200, the story would not deviate from the elastic range.

It would not be impossible to calculate the drift displacements from the acceleration or velocity data. However, the numerical integral calculations of displacements from acceleration or velocity data are not a trivial task. No numerical integral calculation technique is available which can manage to reach the accurate displacement results for any situation. For the case of shake table tests, the displacement responses of either a full- or small-scaled model building can be gauged with laser displacement sensors set up outside of the shaking table. For full-scaled or close-to-full-scaled model buildings, linear voltage transducer (LVT) type of sensors have been employed quite often. LVT is a typical displacement measurement sensor of contact type, and is set up so as to measure the relative displacement between two steel vertical elements: one hangs from the upper floor slab or beam and the other stands up from the lower. These two elements are needed to be close to perfectly-rigid as much as possible. However, this measurement system would occupy a large space and thus the sensor set-up is not practical at all for real buildings.

In this respect, the authors would say that non-contact type of direct measurement sensors for inter-story drift displacements were a long-wanted device. On such a background, the authors' research group has developed two kinds of non-contact type drift measurement sensors (Matsuya *et al*. 2010a, Matsuya *et al*. 2010b, Matsuya *et al*. 2011, Kanekawa *et al*. 2010), with which the

drift displacement time histories can be obtained. The sensors have been already recognized to have the measuring range and frequency resolution fitted to the vibration of a normal building structure. When excitation test experiments were conducted using a real building with an on/off switching mechanism of braces, the developed sensors successfully traced the resulting residual displacement from the forced on/off switching of the braces during the excitations, which is hardly traced via numerical integral calculations of acceleration or velocity data (Hatada *et al*. 2010).

The authors' group (Hatada *et al.* 2013) has presented a structural element based damage detection scheme integrating the three dimensional (3D) push-over analyses utilizing the measured drift displacement data. This damage detection scheme, however, needs the detailed information on structural elements of a building in question for performing the 3D analysis.

This paper proposes a simple scheme of estimating story cumulative plastic deformation ratios (CPDRs) utilizing the drift displacement data, which aims at providing useful information toward a prompt safety judgment or assessment soon after a seismic event. Mainly from the data of inter-story drift displacements, the story hysteresis loops are estimated and then the story CPDRs are evaluated. (In regard to the simple estimation of story hystereses, the authors' group (Matsui *et al*. 2012) has already presented the framework.) Other than the drift displacement data the presented scheme only needs the ground floor seismic acceleration data. It does not need any prior information or push-over analysis of a building. After showing how accurate story hysteresis loops are obtained using the data of experiments already conducted at E-defense, the validity of the scheme of obtaining CPDRs is demonstrated by numerical simulations. The values of CPDRs are significantly helpful in judging the story-based building damage state.

2. Inter-story drift displacement sensors

As mentioned in Introduction, the authors' group has developed two types of drift displacement sensors: one is referred to as PSD (position sensitive detector) sensor (Matsuya *et al*. 2010a, 2010b, 2011) and the other is PTr (photo-transistor) sensor (Kanekawa *et al*. 2010). The basic philosophy of measurement mechanism is quite similar to each other. The invented sensors are composed of two units: light source and light receiver units. In regard to PSD sensor, Fig. 1 schematically illustrates the sensor set-up. The configurations of the light source and receiver units for PSD sensor are briefly explained. The LED (Light Emitting Diode) light source is set beneath the upper floor slab and the light receiver unit is on the lower floor slab. The light receiver unit is composed of a collecting lens and PIN photodiode (consisting of Positive, Intrinsic and Negative semiconductors).

The measurement is conducted in the following way. The LED light going through the collecting lens reaches the PIN photodiode. Due to the photo-emissive effect the electrons in the photodiode start to move and then such movement of electrons induces electric current flows in the opposite direction of electrons in the photodiode. The photodiode, recognizing the difference of the induced electric current flows between the right- and left-hand sides, finds where the light source is located relative to the light receiver unit. The information of the light source location relative to the photodiode provides the time history data of inter-story drift displacements.

The developed sensors are mainly for a shear structure type of building. For a bending-deformation dominant type of building such as high-rise building, the measured data should be appropriately dealt with so as to take out the necessary information.

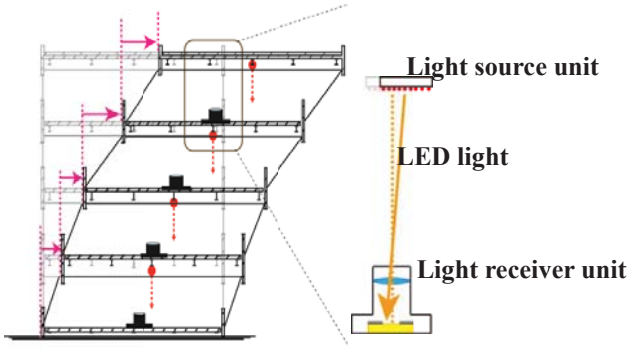

Fig. 1 Schematic illustration of drift displacement sensor

3. Estimation scheme of story hystereses and cumulative plastic deformation ratios

3.1 Estimate of story hystereses with inter-story drift displacement data

Compact for implementation, the developed drift displacement sensors do not occupy much space. Actually, the sensors were installed into a recently completed five-story building in Kajima Technical Research Institute and have started the measurement. In regard to the drift displacement data, even only the peak values could lead to a rough judgment of a building health condition. However, with the information on story hysteresis and cumulative plastic deformation ratio, more precise judgment on structural health can be conducted. In this subsection, it is presented how to estimate story hysteresis loops under the assumption that the sensors are implemented into every story of a building together with an accelerometer on the ground floor.

For hysteresis estimation, many identification-based methodologies have been proposed. Some of them are, for instance, Peng and Iwan (1997), Köylüoglu *et al.* (1997), Zhang *et al.* (2002) and Loh *et al.* (2011). In addition, Takewaki, Nakamura and Yoshitomi (2012) published a book of overviewing system identification techniques with the focus on structural health monitoring. Whereas these methodologies are rather for researchers, this paper aims at a "structural engineers-friendly" methodology for building health monitoring. For this reason, a presented scheme of estimating story hysteretic loops does not involve any identification process.

In a hysteresis loop, the vertical axis represents story shear force, while the horizontal axis presents drift displacement. The time histories of the drift displacements are directly measured with the PSD sensors. They provide the horizontal axis values and thus the information in regard to the story shear forces is needed for estimating the hysteresis. For the purpose of determining the vertical axis value based on the drift displacement data, the following steps are taken. Step (i): the double differential of the drift displacement data with respect to time is conducted to get the inter-story acceleration; Step (ii): accumulating those acceleration data from the first story to the

story in question leads to the relative acceleration to the ground; Step (iii): adding the ground floor acceleration data to the acceleration data obtained in Step (ii) provides the story absolute accelerations; and Step (iv): the story shear force is obtained by multiplying thus-obtained story absolute accelerations by the corresponding story mass value and summing up such values from the top to the story in question. The flowchart of the procedures is shown in Fig. 2.

Unlike the numerical integral calculations, the numerical derivative calculations of displacements need no particular technique. In addition, as discussed more specifically in Section 5, the accurate story mass information is not necessarily needed in the presented scheme for evaluating story-based cumulative plastic deformation ratios.

3.2 Estimate of cumulative plastic deformation ratios

With the story hystereses obtained from the drift displacement measurement data, cumulative plastic deformation ratios (CPDRs) are estimated. The information on the story CPDRs would provide the structural engineers with significant data in judging a building health condition. In this respect, CPDR based judgment is not only for researchers but also practicing engineers. Hence, the authors would say that the presented scheme is a "practicing engineers-friendly" framework.

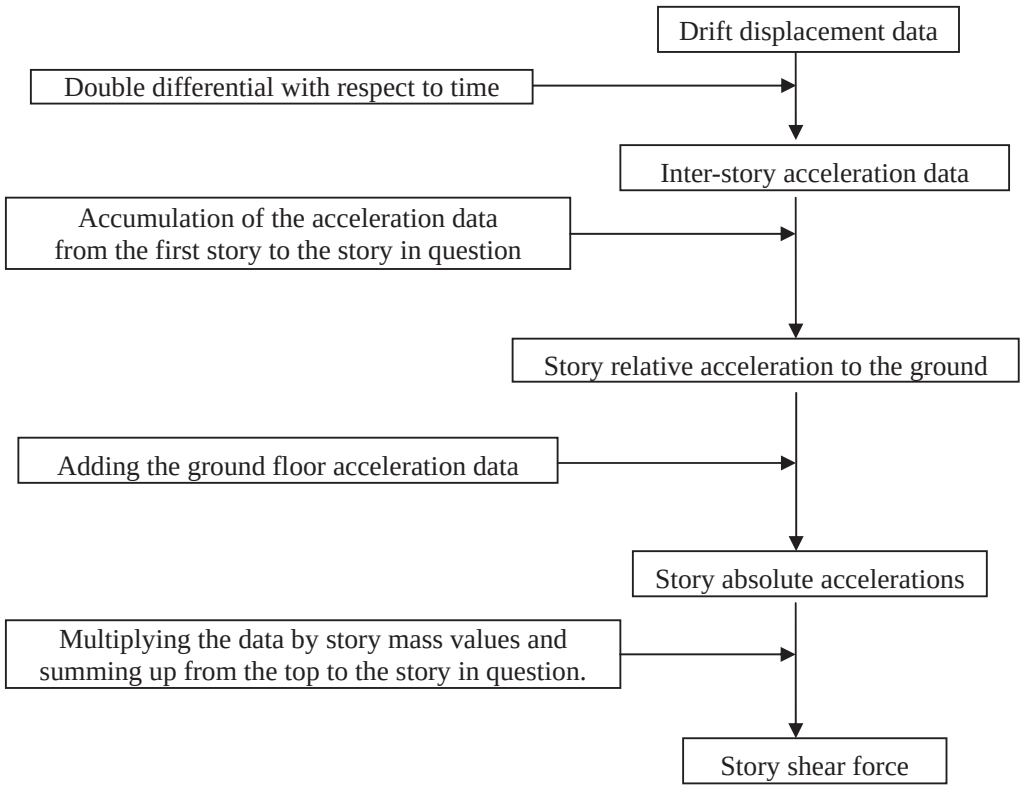

Fig. 2 Flowchart of estimation of story shear force from drift displacement data

The cumulative plastic deformations are the accumulation of the plastic deformations after exceeding the yield displacement. Then, CPDR would be directly calculated by dividing such accumulated plastic deformations by the yielding displacement.

Instead of the above direct calculation, herein, CPDR can be alternatively evaluated based on the area of hysteresis loops. By firstly accumulating the hysteretic areas and then dividing those accumulated areas by the product of the yield displacement and yielding force values, CPDR is obtained by

$$CPDR = \frac{\sum a_m}{\delta_y \cdot f_y} \tag{1}$$

where a_m: area of mth cycle hystersis loop; δ_y: yield displacement; and f_y: yield force. In conducting this calculation, the numerator does not include those hystersis loops of which the peak displacements do not reach the yield displacement .

For the case of idealistic hysteresis with a ductility factor of 1.2, for instance, as shown in Fig. 3, in which y and k, respectively, denote the yield displacement and initial stiffness coefficient. The area of the hysteresis loop in this case is $0.8\ k \cdot y^2$ and thus the division of $0.8\ k \cdot y^2$ by the product of y and ky leads to 0.8. This is identical to the value obtained directly by dividing the accumulated plastic deformation, $0.8y$, by y. This alternative way would be much simpler and more appropriate than the direct CPDR calculation, in particular, in the practical situations of dealing with complex hysteretic loops during a real seismic event. It would be a complicated task to apply the direct method to real, complex hysteretic loops.

As already mentioned, it is the purpose of the paper to simply estimate the CPDR of each story toward the safety assessment. However, it is beyond the purpose to judge the overall safety or damage condition of an entire building based upon those story CPDR data. This sort of discussion is the next step.

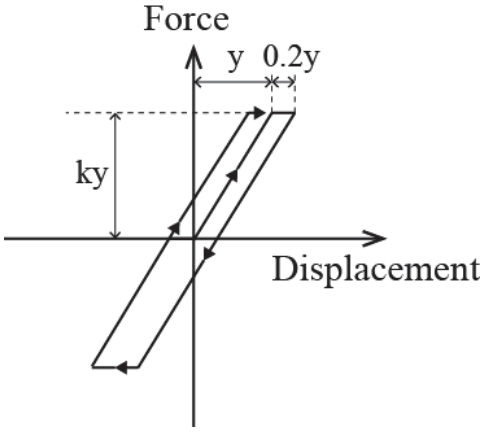

Fig. 3 Idealized hysteresis loop

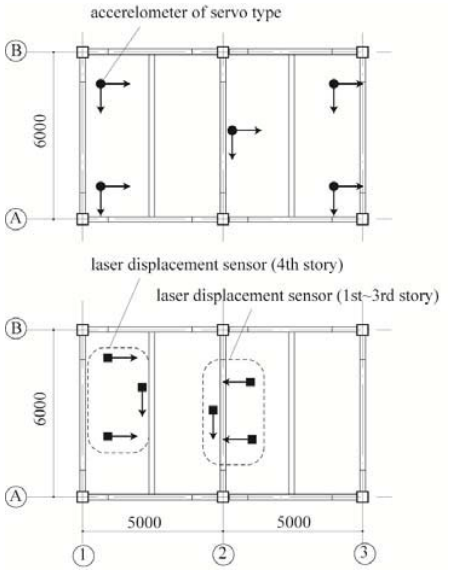

Fig. 4 Plan of model building with sensor locations

4. Validity of estimated story hystereses based on drift displacement data

Utilizing the experimental data available at the web-site of E-defense (https://www.edgrid.jp), the hystereses of a full-scaled four story steel building are, first of all, estimated with the above-presented scheme. The experimentally obtained data of "Full collapse experiments of steel building structure" performed in September 2007 is utilized, which are accessible via the web-site (https://www.edgrid.jp/lists/download_pubfile/0703). The full scale experimental model is a moment-resistant frame building with one-bay (6 m) frame in the shorter direction and two-bay frames (5 m for each) in the longer directions. The plan of this building is shown in Fig. 4. The further details are found at the above website. Fig. 4 also indicates the locations of implemented servo type accelerometers and laser displacement sensors. Although the displacement data in this experiment were not measured by the developed drift displacement sensors but the laser displacement sensors, they are herein utilized to demonstrate how effectively the presented scheme based on the drift displacement measurement works out to give quite accurate hysteresis loops. For comparison, those hystereses which are calculated with the directly measured acceleration data combined are also presented. In Figs. 5 and 6, respectively, the time histories of the directly measured accelerations and drift displacements are exhibited. The input excitation for this case was the JR Takatori earthquake observed during the 1995 Kobe earthquake with the peak value normalized as 60% of its original.

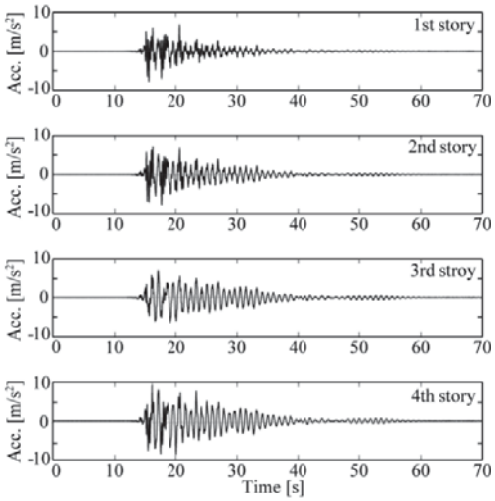

Fig. 5 Directly measured acceleration time histories

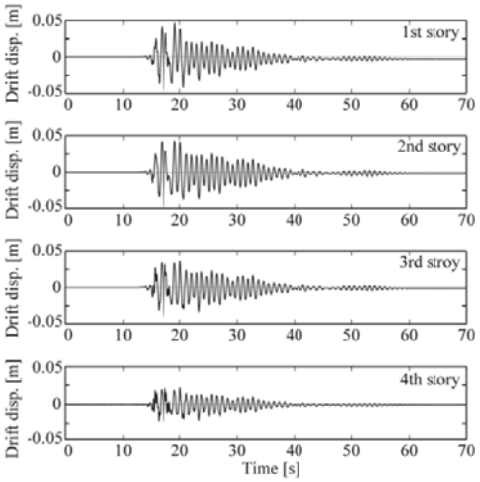

Fig. 6 Inter-story drift displacement time histories

The hysteresis loops estimated by the proposed scheme are shown in Fig. 7(a). In calculating the differentiated acceleration from the displacement data, a low-pass filter of cutting the frequency components over four times the natural frequency of the model building has been applied twice: it is applied firstly to the measured drift displacement data and secondly to the calculated acceleration data. The estimated hystereses, shown in Fig. 7(a), are found to agree fairly well with the ones obtained from the combined use of the directly measured acceleration and displacement data, which are presented in Fig. 7(b). This agreement demonstrates that the presented scheme based on the drift displacement information works well in estimating the hysteresis loops.

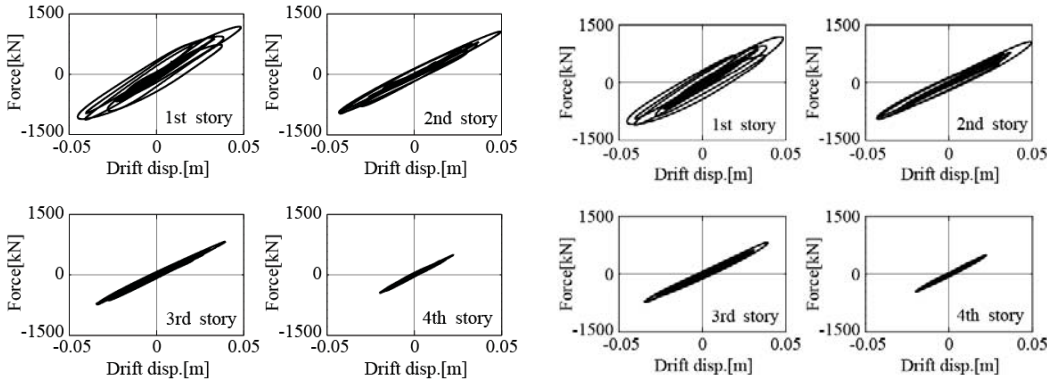

(a) Estimated hysteresis loops

(b) Hysteresis loops derived with measured acceleration data combined

Fig. 7 Comparison of story hysteresis loops

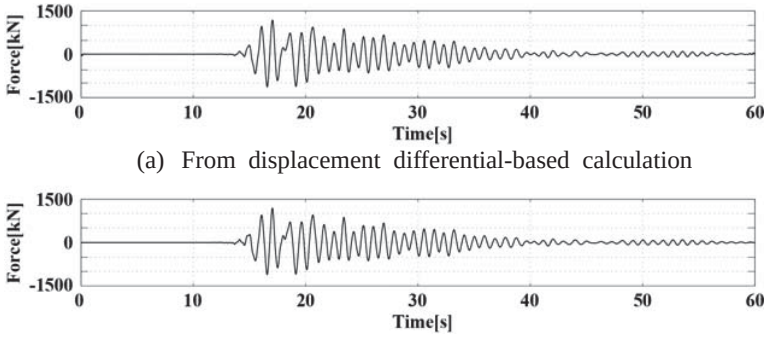

(a) From displacement differential-based calculation

(b) From measured acceleration data

Fig. 8 Comparison of shear force time histories

In addition to Fig. 7, Fig. 8 presents two kinds of time histories of the first story shear forces: (a) is obtained from the displacement differential-based calculation; and (b) is from the measured acceleration data. The two time histories are also in very good agreement, which indicates that the values corresponding to the hysteresis vertical axis is correctly estimated.

In the practical situation, unlike the full-scale model shake table test situation, even accurate story mass information is difficult to obtain. Most likely, there are some uncertainties involved in the mass information. The story mass contains live load values which are difficult to accurately evaluate in practice. In addition, it would not be a trivial work to obtain even the structural element mass values without any structural design documents available. Despite that, the estimating of story hysteresis loops herein is the step prior to estimating the story CPDRs. If accurate (or nearly

accurate) *shape* of the hysteresis is obtained, CPDRs should be satisfactorily evaluated by Eq. (1). The errors in the story mass information affect only the vertical axis values in drawing the hysteresis loop but do not necessarily deform the hysteresis itself. This fact is significantly related to the calculating processes of CPDRs and will be specifically discussed in Section 5 which will conduct the numerical simulations of eight-story building.

5. Numerical simulations for story cumulative plastic deformation ratios

This section discusses the proposed scheme of deriving the cumulative plastic deformation ratios (CPDRs) for the purpose of story-based damage assessment. Based on the obtained story hysteresis loops, CPDRs are estimated by the scheme specified in 3.2. The presented scheme presumes no structural design specification document available, because it aims at a prompt judgment of how close to the dangerous limit a story would be soon after a seismic event. All the calculation processes could be computer-programmed from the data measurement to the calculation of story CPDRs. The available data are, as repeatedly mentioned, the inter-story drift displacement of each story and the ground acceleration. The hystereses during a seismic event are not likely to be as idealized as the purely theoretical situation. For instance, even the yielding force values corresponding to the yield displacement are not always the same in the practical case. With such a case accounted for, story CPDRs are estimated utilizing the four-story building experimental data of E-defense and conducting the numerical simulations of an eight-story model building.

Firstly, CPDRs are estimated based on the hysteresis loops for the full-scale model building experiment of E-defense obtained in Section 4. As far as the accurate values of yield displacements are concerned, the estimated hysteresis loops would not provide any information, in particular without the structural design specification documents. For this reason, CPDRs are herein calculated assuming that the yield displacement of each story is 1/130 of the story height. Fig. 9 compares the two results: one is calculated based on the hystereses obtained by combining the measured acceleration and drift displacement data for each story (indicated as “w/ story accel. data” in the figure) and the other is by using only the drift displacement data for each story (indicated as “w/o story accel. data” in the figure). The two results of CPDRs provide the similar tendency of which story is likely to be more severely or earlier damaged than other stories, although the two kinds of CPDR results have differences of about 0.5 for all the stories. The yield force values corresponding to the yield displacement are not always the same in this case, and thus the average value of them is employed in estimating the estimating CPDRs.

In conducting numerical simulations, an eight-story steel model building represented by a lumped mass model is employed. The model parameters are given in Table 1. It is assumed that the story heights are 3.5 m, and the initial and second yield displacements are, respectively, 1/130 and 1/100 of the story height for all the stories. Nonlinear seismic response analyses are conducted utilizing this lumped mass model (8DOF model). The damping proportional to the stiffness matrix is employed with a damping ratio of 2%. The drift displacements obtained by the simulation are regarded as the measured data of the drift displacement PSD sensors. The employed seismic inputs are El Centro NS component, Taft EW component and Hachinohe EW component with two kinds of peak acceleration values, 4 and 7 m/s^2.

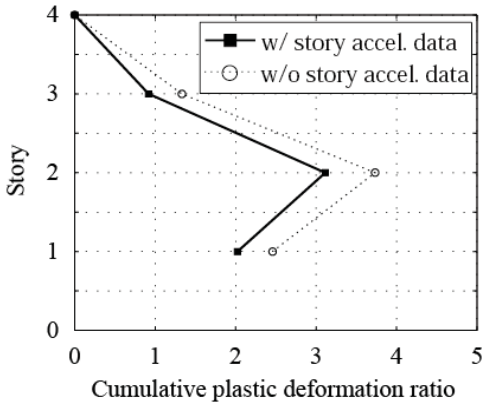

Fig. 9 Comparison between two CPDRs from actual and estimated hystereses

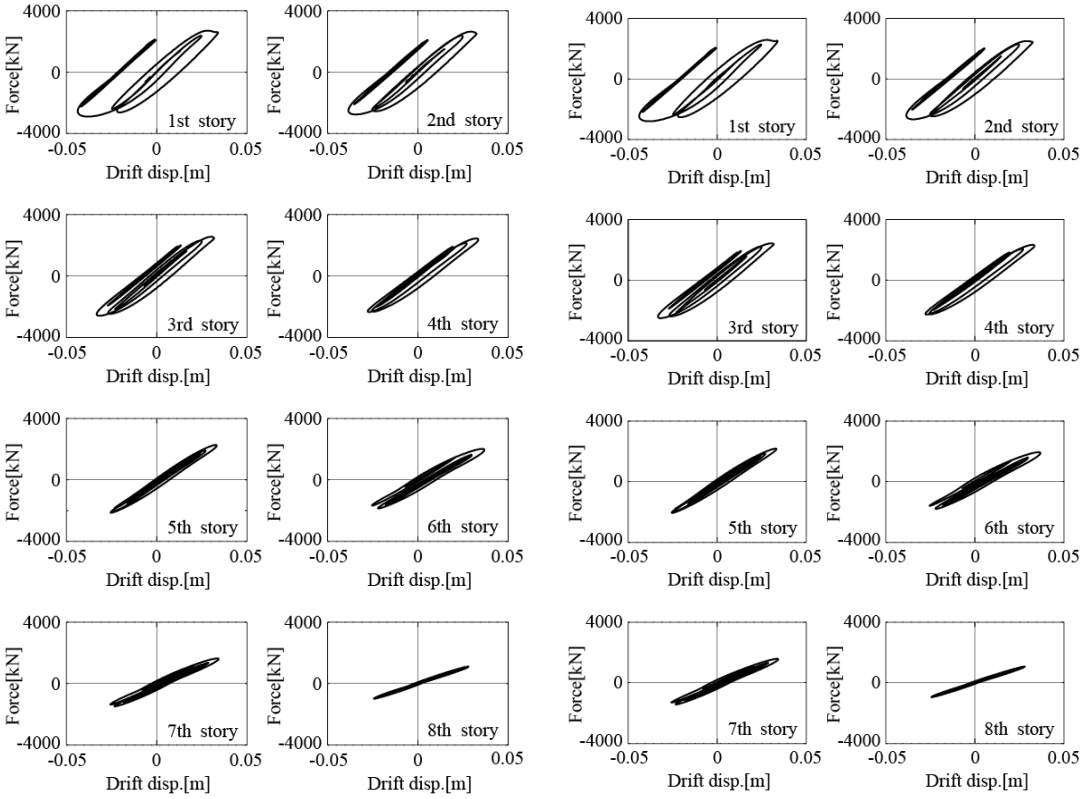

(a) Estimated hysteresis loops (b) Accurate hysteresis loops

Fig. 10 Comparison of story hysteresis loops for eight-story building (El Centro NS with peak acceleration of 7 m/s^2

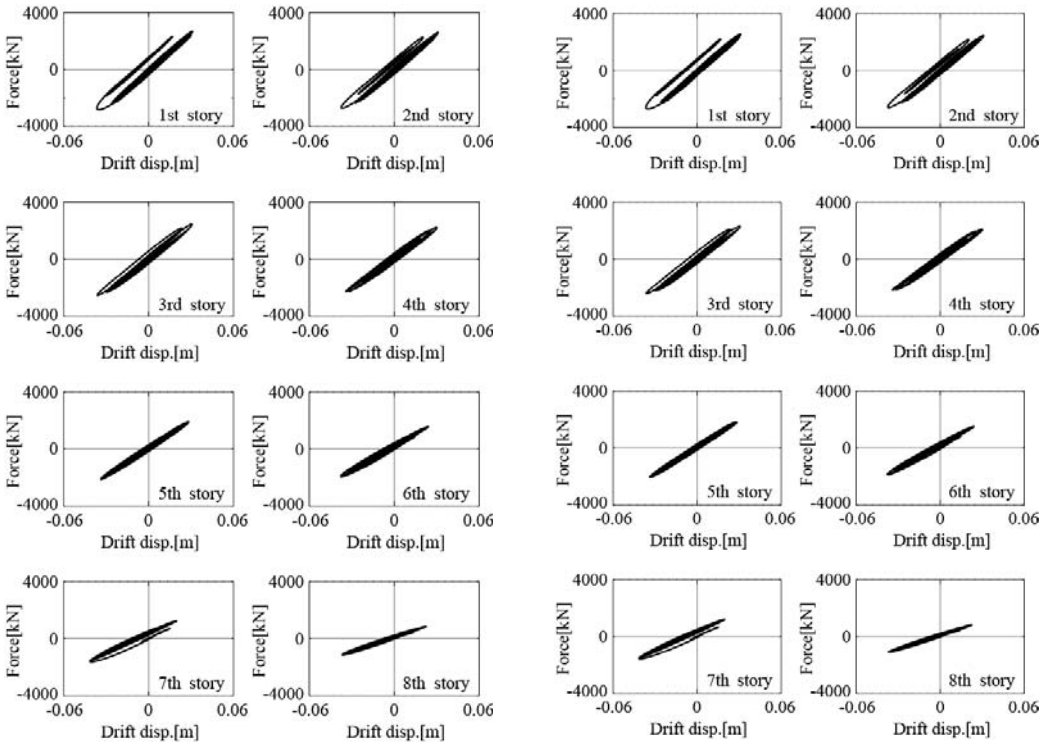

(a) Estimated hysteresis loops (b) Accurate hysteresis loops

Fig. 11 Comparison of story hysteresis loops for eight-story building (Taft EW with peak acceleration of 7 m/s^2

Figs. 10-12 compare the estimated and accurate hystereses for the case of three different seismic excitations with peak accelerations of 7m/s^2. The "accurate" loops are obtained using the simulated story shear forces and drift displacements. In calculating these estimated hysteresis loops, the measurement noises with S/N ratio of 26 dB have been added into the simulated drift displacement data. To those noise-added data, that low-pass filter explained in 3.1 has been applied.

In estimating the vertical axis values for hysteresis loops, the story absolute acceleration data multiplied by the corresponding mass value are accumulated for the stories above the story in question. However, there is no established way for obtaining or estimating accurate story mass values in the real situation. With such a situation reflected, the mass values for all the stories are assumed to have the identical values of 550 t. These assumed mass values could bring about more or less deviated values from the right ones in the vertical axis for the hysteretic loop. From the CPDR estimation point of view, even in such a case, the absolute values on the vertical axis are not expected to affect the estimate of CPDRs very much as long as CPDRs are calculated as the ratio of hysteresis area to the product of yielding displacement and force. In other words, CPDRs could be estimated fairly well unless the shape of an estimated hysteresis is deformed. As far as the

hysteresis shapes in Figs. 10-12 are concerned, the estimated hysteretic loops are in very good agreement with the accurate loops and even the vertical axis values for the estimated loops do not appear different from those for the accurate loops.

Figs. 13-15 compare the estimated and accurate CPDR values for the cases of El Centro, Taft and Hachinohe earthquakes, respectively, with peak accelerations of 4 m/s^2 in (a) and 7 m/s^2 in (b). These figures present two kinds of estimates for CPDRs based on Eq. (1): they set the yield displacements equal to 1/130 and 1/150 of the story height, respectively. The story shear forces corresponding to those displacements are regarded as the yielding forces in computing CPDRs with Eq. (1). The accurate data of yield displacements are not available in the practical situation, although the accurate results in Figs. 13-15 are obtained with them.

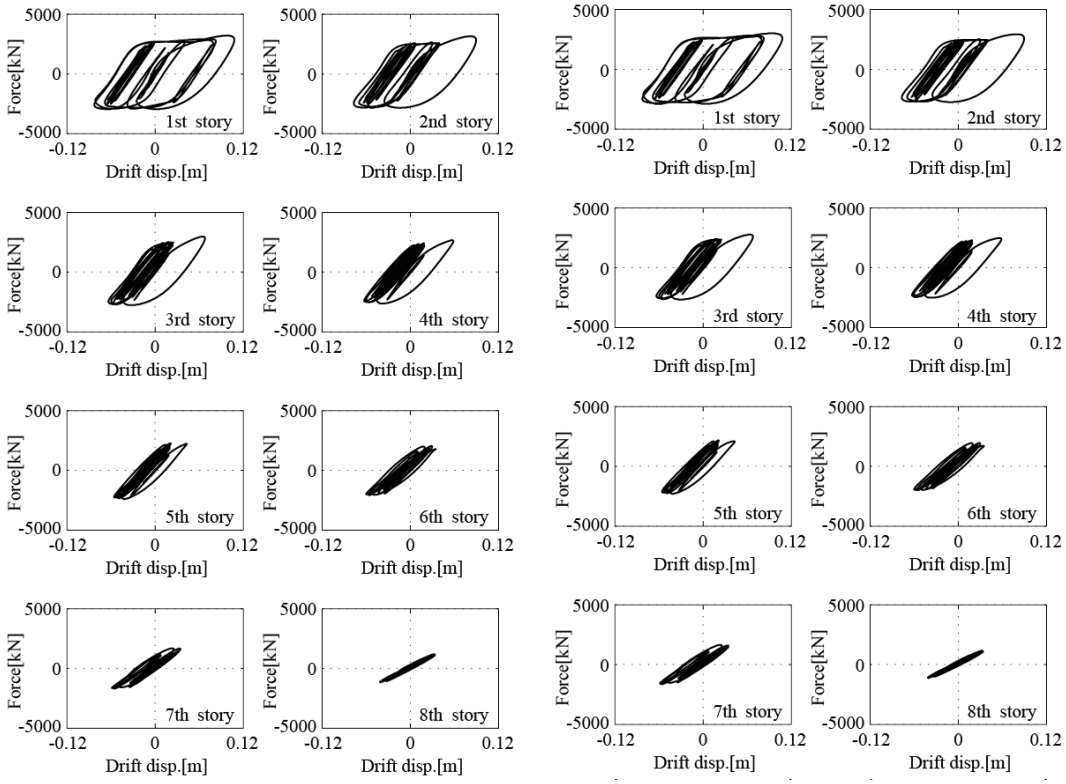

(a) Estimated hysteresis loops (b) Accurate hysteresis loops

Fig. 12 Comparison of story hysteresis loops for eight-story building (Hachinohe EW with peak acceleration of 7 m/s^2

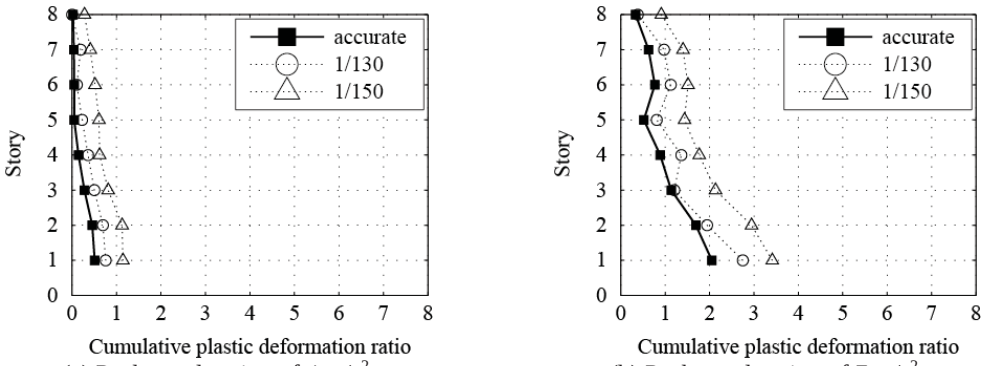

(a) Peak acceleration of 4 m/s^2 (b) Peak acceleration of 7 m/s^2

Fig. 13 Comparison of estimated and accurate CPDRs for El Centro excitations

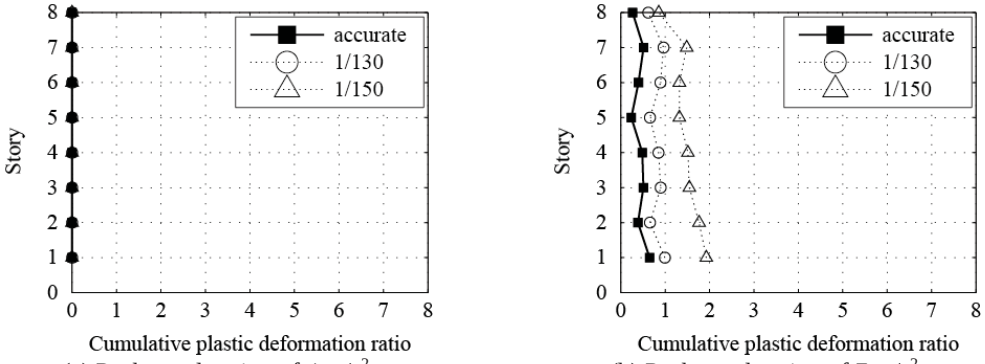

(a) Peak acceleration of 4 m/s^2 (b) Peak acceleration of 7 m/s^2

Fig. 14 Comparison of estimated and accurate CPDRs for Taft excitations

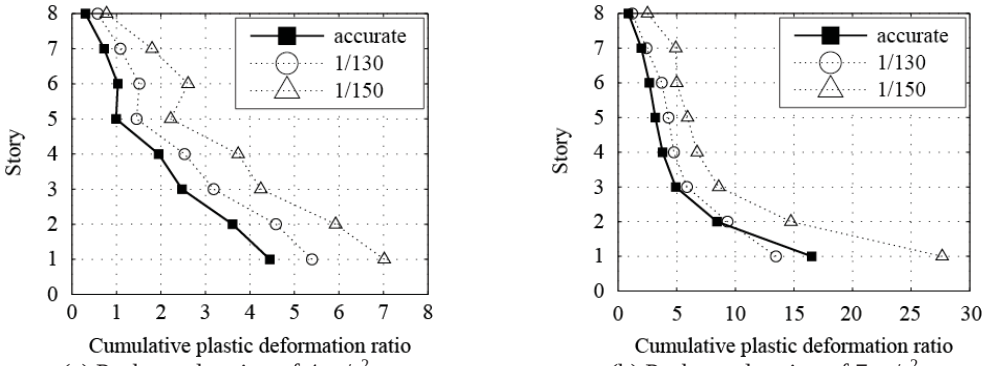

(a) Peak acceleration of 4 m/s^2 (b) Peak acceleration of 7 m/s^2

Fig. 15 Comparison of estimated and accurate CPDRs for Hachinohe excitations

Figs. 13-15 indicate how CPDR values depend on the characteristics and magnitudes of seismic excitations. Every estimate of CPDR demonstrates the same tendency as the accurate CPDR. The absolute values of estimated CPDRs depend on how the yield displacement values are assumed. The smaller the yield displacement is assumed, the larger CPDRs become. For this reason, the estimated CPDRs are different from the accurate values but the estimated CPDRs provide the information on which story is likely to be more severely damaged, earlier damaged or have smaller margin to the ultimate limit than the other stories. It is said that the engineers should be concerned about the severe damage if CPDR is close to around twenty in general, although this critical value of CPDR is varied from case to case.

6. Conclusions

The authors' research group has developed direct measurement sensors of inter-story drift displacements. With these sensors the time histories of drift displacements can be obtained for a building structure. The sensors are of non-contact type and could be installed into an actually used building without occupying much space. Presuming the employment of these drift displacement sensors, this paper presents a rather simple yet effective scheme of estimating the story cumulative plastic deformation ratios (CPDRs) toward safety assessment. The indices of story CPDRs provide structural engineers with quite helpful information in judging the damage condition or remaining earthquake resistance capacity of the story soon after a seismic event. In this respect, the presented scheme could construct a "practicing engineers-friendly" framework.

The validity of the scheme has been demonstrated using the data of full-scale building model experiments performed at E-defense and conducting numerical simulations. The direct sensing of drift displacements has a great potential for constructing a new diagnosis schemes of building structures and for bringing a new paradigm-shift in the building structural health monitoring field.

Acknowledgments

The research of this paper was partially supported by the Japan Society of Promotion of Sciences Grant-of-Aid (No. 26420564, PI: Akira Nishitani).

References

Hatada, T., Katamura, R., Hagiwara, H., Takahashi, M., Nitta, Y. and Nishitani, A. (2013), "Verification of damage evaluation method based on measurement of relative story displacements through shaking table test of full-scale building", *J. Struct. Cnstr. Eng*., **78**(686), 703-711.

Hatada, T., Takahashi, M., Suzuki, Y., Matsuya, I., Kanekawa, K., Nitta, Y. and Nishitani, A. (2010), "Measurement of relative story displacements by noncontact-type sensors on forced vibration test of an actual building", *J. Struct. Cnstr. Eng*., **75**(653), 1257-1264.

Kanekawa, K., Matsuya, I., Sato, M., Tomishi, R., Takahashi, M., Miura, S., Suzuki, Y., Hatada, T., Katamura, R., Nitta, Y., Tanii, T., Shoji, S., Nishitani, A. and Ohdomari, I. (2010), "An experimental study on relative displacement sensing using phototransistor array for building structures", *IEEJ T. Electrical Electonic Eng*., **5**(2), 251-255.

Kobori, T. *et al.* (1991), "Seismic-response-controlled structure with active mass driver system: (Part 1)

Design; (Part 2) Verification", *Earthq. Eng. Struct.D.*, **20**(2), 133-149, 151-166.
Köylüoglu, H.U., Nielsen, S.R.K., Çakmak, A.Ş. and Kirkegaard, P.H. (1997), "Prediction of global and localized damage and future reliability for RC structures subject to earthquakes", *Earthq. Eng. Struct. D.*, **26**(4), 463-475.
Kutsukake, T. *et al*. (2014), "Investigation of the tunnel ceiling collapse in the Central Expressway in Japan", *TRB 2014 Annual Meeting*, Washington D.C., USA, January, Paper Manuscript # 14-2559.
Loh, C.H., Mao, C.H., Huang J.R. and Pan, T.C. (2011), "System identification and damage evaluation of degrading hysteresis of reinforced concrete frames", *Earthq. Eng. Struct. D.*, **40**(6), 623-640.
Matsui, C., Nishitani, A. *et al*. (2012), "Structural monitoring scheme based on directly measured inter-story drift displacement response information", *Proceedings of the 15th World Conference on Earthquake Engineering*, Lisbon, Portugal, September.
Matsuya, I., Oshio, M., Tomishi, R., Sato, M., Kanekawa, K., Takahashi, M., Mimura, S., Suzuki, Y., Hatada, T., Katamura, R., Nitta, Y., Tanii, T., Shoji, S., Nishitani, A. and Ohdomari, I. (2010a), "Noncontact-type relative displacement monitoring system using position sensitive detector", *J. Techno. Des*., **16**(33), 469-472.
Matsuya, I., Katamura, R., Sato, M., Iba, M., Kondo, H., Kanekawa, K., Takahashi, M., Hatada, T., Nitta, Y., Tanii, T., Shoji, S., Nishitani, A. and Ohdomari, I. (2010b), "Measuring relative-story displacement and local inclination angle using multiple position-sensitive detectors", *Sensors*, **10**(11), 9687-9697.
Matsuya, I., Tomishi, R., Sato, M., Kanekawa, K., Nitta, Y., Takahashi, M., Miura, S., Suzuki, Y., Hatada, T., Katamura, R., Tanii, T., Shoji, S., Nishitani, A. and Ohdomari, I. (2011), "Development of lateral displacement sensor for real-time detection of structural damage", *IEEJ T. Electrical Electonic Eng*., **6**(3), 266-272.
Nakamura, M. and Yasui, Y. (1999), "Damage evaluation of a steel structure subjected to strong earthquake motion based on ambient vibration measurements", *J. Struct. Const. Eng.*, 517, 61-68.
Nitta, Y. and Nishitani, A. (2003), "Two stage based structural system identification utilizing absolute acceleration response information", *J. Struct. Const. Eng.*, **517**, 91-97.
Peng, C.Y. and Iwan, W.D. (1997), "An identification methodology for a class of hysteretic structures", *Earthq. Eng. Struct. D.*, **21**(8), 695-712.
Saito, T. (1998), "System identification of a high-rise building applying multi-input-multi-output ARX model of modal analysis", *J. Struct. Const. Eng.*, **508**, 47-54.
Shinagawa, Y., and Mita, A. (2013), "Estimation seismic response of seismic isolation layer using an accelerometer", *J. Technol. Des.*, **19**, (43), 861-864.
Takewaki, I., Nakamura, M. and Yoshitomi, S. (2012), *System Identification for Structural Health Monitoring*, WIT Press.
Website links, www.edgrid.jp/ (2013), Archives of Shakingtable Experimentation dataBase and Information (ASEBI) , National Institute for Earth Science and Disaster Prevention.
Website links, www.edgrid.jp/lists/download_pubfile/0703/ (2013), "Full collapse experiments of steel building structure (2007)", Archives of Shakingtable Experimentation dataBase and Information (ASEBI), National Institute for Earth Science and Disaster Prevention.
Website links, www.ntsb.gov/investigations/summary/har0803.htm (2007), "Highway Accident Report", National Transportation Safety Board.
Zhang, H., Foliente, G.C., Yang, Y. and Ma, F. (2002), "Parameter identification of inelastic structures under dynamic loads", *Earthq. Eng. Struct. D.*, **31**(5), 113-1130.

Smart Structures and Systems, *Vol. 15, No. 3 (2015) 897-911*
DOI: http://dx.doi.org/10.12989/sss.2015.15.3.897

Evolutionary computational approaches for data-driven modeling of multi-dimensional memory-dependent systems

Ali Bolourchi* and Sami F. Masri[a]

Viterbi School of Engineering, University of Southern California, 3620 South Vermont Avenue, KAP 210, Los Angeles, CA, 90089-2531 USA

(Received May 30, 2014, Revised August 20, 2014, Accepted August 30, 2014)

Abstract. This study presents a novel approach based on advancements in Evolutionary Computation for data-driven modeling of complex multi-dimensional memory-dependent systems. The investigated example is a benchmark coupled three-dimensional system that incorporates 6 Bouc-Wen elements, and is subjected to external excitations at three points. The proposed technique of this research adapts Genetic Programming for discovering the optimum structure of the differential equation of an auxiliary variable associated with every specific degree-of-freedom of this system that integrates the imposed effect of vibrations at all other degrees-of-freedom. After the termination of the first phase of the optimization process, a system of differential equations is formed that represent the multi-dimensional hysteretic system. Then, the parameters of this system of differential equations are optimized in the second phase using Genetic Algorithms to yield accurate response estimates globally, because the separately obtained differential equations are coupled essentially, and their true performance can be assessed only when the entire system of coupled differential equations is solved. The resultant model after the second phase of optimization is a low-order low-complexity surrogate computational model that represents the investigated three-dimensional memory-dependent system. Hence, this research presents a promising data-driven modeling technique for obtaining optimized representative models for multi-dimensional hysteretic systems that yield reasonably accurate results, and can be generalized to many problems, in various fields, ranging from engineering to economics as well as biology.

Keywords: computational intelligence; genetic algorithms; differential equations; hysteretic behavior; data-driven modeling; identification; multi-dimensional systems; genetic programming

1. Introduction

Modeling and analysis of complex multi-dimensional nonlinear memory-dependent systems is a broad research area with applications in many fields such as mechanics, economy, aeronautics, amongst others. Over the past several decades, nonlinear systems incorporating memory-dependent dissipative phenomena have been investigated in many studies, mainly through parametric or nonparametric modeling (Kerschen *et al.* 2006). Parametric modeling is a class of techniques used to characterize hysteretic systems by attributing a suitable model to the

*Corresponding author, Ph.D., E-mail: bolourch@gmail.com
[a] Professor, E-mail: masri@usc.edu

http://www.techno-press.org/?journal=sss&subpage=8 ISSN: 1738-1584 (Print), 1738-1991 (Online)

system, and identifying the model parameters or detecting their changes (Bouc 1967, Wen 1976 Smyth *et al.* 1999, Chatzi *et al.* 2010). However, the success of parametric modeling highly relies on the user providing an accurate representative model based on a clear understanding of the physical phenomena. Non-parametric modeling, on the other hand, carries out the identification automatically, without setting any major hypothesis about the system upfront. In this category, Neural Networks are powerful tools of modeling complex systems involving memory-dependent characteristics (Bani-Hani and Ghaboussi 1998, Pei and Smyth 2006a, b, Zhao and Tan 2008). Their data driven analysis is suitable when no additional information about the underlying systems is available. However, Neural Networks process data in a completely blind manner, that is not suitable for revealing the physics behind complex systems. Therefore, they leave no room for further investigation of the resultant models, and to provide physical insight into the systems under investigation. Polynomial-based approaches are another class of nonparametric techniques that are extensively employed for the modeling of nonlinear phenomena in dynamic environments (Masri and Caughey 1979, Masri *et al.* 2004, 2006a, b, Tasbihgoo *et al.* 2007). However, specifying the order of polynomials and the composition of basis functions requires insight into the dynamics of the problem. Moreover, polynomial approximations of systems exhibiting sharp corners in their response results in undesired Gibbs phenomena.

Consequently, there is currently a lack of intelligent data-driven computational techniques that provide robust physics-based computational models, that represent multi-dimensional dynamical systems with hysteresis effect. Evolutionary computational methodologies are inspired by natural phenomena to provide elegant solutions to complex real-world problems in various fields. In this class of problem-solving techniques, Genetic Programming (GP), is built on evolutionary algorithms, and offers a great potential for the identification of complex dynamical systems exhibiting non-conservative dissipative behavior. GP has proven to be successfully applicable to various classes of problems in different fields (Tackett 1993, Gruau 1994, Howard and Roberts 2002, Becker *et al.* 2007, Schmidt and Lipson 2009, Alavi *et al.* 2010, Silva *et al.* 2011, Gandomi and Alavi 2011). To our knowledge, GP has never been adapted to be employed for the modeling of multi-dimensional systems with hysteretic behavior. Therefore, this investigation explores the potential of evolutionary approaches to discover the system of differential equations that govern the behavior of complex nonlinear multi-dimensional hysteretic systems.

A general procedure concerning the modeling of complex one-dimensional systems associated with challenging type of nonlinearities was presented in Bolourchi (2014) and Bolourchi *et al.* (2015). That procedure is extended in this paper and is implemented for the modeling and analysis of non-linear multi-dimensional systems with memory-dependent dissipative characteristics. The eventual aim is to utilize GP as the main problem-solving engine for discovering the suitable "*structure*" of the differential equations that govern the behavior of multi-dimensional hysteretic systems. GP is also coupled with stochastic parameter optimization techniques, employing Genetic Algorithms, to optimize the "*parameters*" embedded in the differential equations based on the global performance of the integrated GP-found structures in the system of differential equations for estimating the response of the underlying multi-dimensional hysteretic system.

It is shown that the suggested identification methodology provides reduced-complexity systems of differential equations that govern the dynamics of complex nonlinear multi-dimensional systems with non-conservative dissipative traits. Several test cases are provided to assess the applicability, reliability, and validity of the methodology.

This paper is organized as follows: the formulation of the investigated system, the corresponding assumptions, and the details of the excitations and responses are provided in

Section 2; an introduction to GP within the scope of the investigation in this paper is presented in Section 3; the proposed evolutionary-based approach for the modeling of multi-dimensional hysteretic systems is presented in Section 4; the results of the introduced modeling procedure is presented in Section 5; in-depth interpretation of the findings are discussed in Section 6; advantages and challenges of the approach are described in Section 7; and the conclusion is provided in Section 8.

2. Multi-dimensional hysteretic systems

2.1 Investigated models

The identification method under discussion is implemented on a benchmark multi-degree-of-freedom (MDOF) system exhibiting non-conservative nonlinear behavior. This structure has been employed for testing the robustness of other identification schemes in the past (Masri *et al.* 1987, Smyth *et al.* 2002, Masri *et al.* 2005). This three degree-of-freedom system in Fig. 1 is composed of three unequal lumped masses that are linked by six arbitrary components to all other masses and to a fixed support.

In Fig. (1), x_i is the displacement, $f_i(t)$ is external excitation, and m_i is the mass at DOF i. The semi-physical Bouc-Wen model is well studied in the literature to represent non-conservative dissipative systems (Smyth *et al.* 2002). The interconnecting elements in the structure above, denoted as g_i, are governed by the Bouc-Wen model, and consequently, account for the hysteretic behavior of the MDOF system. The Bouc-Wen model for a single degree-of-freedom system is formulated as follows

$$f(t) = m\ddot{x} + r(x, \dot{x}) \tag{1}$$

$$r(x, \dot{x}) = \frac{1}{\eta}\left[A\dot{x} - \upsilon\left(\beta|\dot{x}||r(x, \dot{x})|^{n-1} r(x, \dot{x}) - \gamma\dot{x}|r(x, \dot{x})|^{n}\right)\right] \tag{2}$$

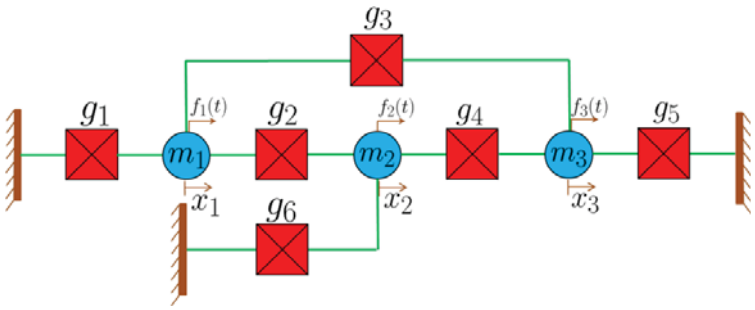

Fig. 1 The benchmark 3 degree-of-freedom system with hysteretic interconnecting links g_i s

where $f(t)$ is the external excitation, m is the lumped mass, $\ddot{x}$ is the acceleration, $r(x,\dot{x})$ is the restoring force, x is the displacement, and $\dot{x}$ is the velocity. The shape of the hysteretic loops is ruled by the parameters of the model: $\eta, \mathrm{A}, \nu, \beta, \gamma$ and n (Smyth *et al.* 2002). Therefore, the MDOF system of Fig. 1 under discussion is formulated as follows

$$\begin{cases} f_1(t) = m_1\ddot{x}_1 + g_1(u_1,\dot{u}_1) + g_2(u_2,\dot{u}_2) + g_3(u_3,\dot{u}_3) & 3(a) \\ f_2(t) = m_2\ddot{x}_2 + g_2(u_2,\dot{u}_2) + g_4(u_4,\dot{u}_4) + g_6(u_6,\dot{u}_6) & 3(b) \\ f_3(t) = m_3\ddot{x}_3 + g_3(u_3,\dot{u}_3) + g_4(u_4,\dot{u}_4) + g_5(u_5,\dot{u}_5) & 3(c) \\ \dot{g}_1(u_1,\dot{u}_1) = \dot{u}_1 - \left|\dot{u}_1\right| g_1(u_1,\dot{u}_1) + 0.5u_1\left|g_1(u_1,\dot{u}_1)\right| & 3(d) \\ \dot{g}_2(u_2,\dot{u}_2) = \dot{u}_2 - \left|\dot{u}_2\right| g_2(u_2,\dot{u}_2) + 0.5u_2\left|g_2(u_2,\dot{u}_2)\right| & 3(e) \\ \dot{g}_3(u_3,\dot{u}_3) = \dot{u}_3 - \left|\dot{u}_3\right| g_3(u_3,\dot{u}_3) + 0.5u_3\left|g_3(u_3,\dot{u}_3)\right| & 3(f) \\ \dot{g}_4(u_4,\dot{u}_4) = \dot{u}_4 - \left|\dot{u}_4\right| g_4(u_4,\dot{u}_4) + 0.5u_4\left|g_4(u_4,\dot{u}_4)\right| & 3(g) \\ \dot{g}_5(u_5,\dot{u}_5) = \dot{u}_5 - \left|\dot{u}_5\right| g_5(u_5,\dot{u}_5) + 0.5u_5\left|g_5(u_5,\dot{u}_5)\right| & 3(h) \\ \dot{g}_6(u_6,\dot{u}_6) = \dot{u}_6 - \left|\dot{u}_6\right| g_6(u_6,\dot{u}_6) + 0.5u_6\left|g_6(u_6,\dot{u}_6)\right| & 3(i) \end{cases}$$

where u_i and $\dot{u}_i$ are the relative displacement and the relative velocity of the two ends of the interconnecting link g_i. $\dot{u}_i$ is the derivative of u_i which is determined according to the topology of the system: $u_1 = x_1$, $u_2 = x_2 - x_1$, $u_3 = x_3 - x_1$, $u_4 = x_3 - x_2$, $u_5 = x_5$, $u_6 = x_6$.

For convenience, the parameters of the Bouc-Wen elements in all interconnecting components are identical, and presented in Table 1. Note that this system is more complex than regular MDOF systems, typically encountered in civil structures, in which characteristic matrices, such as stiffness and damping, are simplified because every mass is only connected to its adjacent masses. Thus, the non-parametric identification of this complex system to yield surrogate representative models is a challenging problem, and an ideal example to evaluate the capabilities of new modeling techniques. Lumped masses of the MDOF system under investigation are stimulated by dissimilar zero-mean stationary Gaussian white noise excitations. The applied training excitations at each degree-of-freedom (DOF) i have identical statistical properties, which are presented in Table 1, and are produced using different random numbers. The external excitations stimulate the system sufficiently strong to disclose the yielding region of the vibrating interconnecting components of the studied system. It is assumed that the external excitations, the lumped masses and their accelerations are known from measurements. Hence, the displacements and velocities can be obtained by careful integration of accelerations. As a result, all states x_i, $\dot{x}_i$ and $\ddot{x}_i$, $i = 1,2,3$, are assumed to be available from measurements.

The proposed non-parametric approach of this research aims to discover an equivalent system of differential equations that describes the three DOF system defined by Eq. (3). This approach benefits from an auxiliary variable that incorporates the effect of all restoring forces from other degrees-of-freedom on a certain mass m_i. Herein, this variable is named the compound restoring force, denoted as r_i at DOF i. Bolourchi (2014) and Bolourchi *et al.* (2015) showed that the presence of the derivative of the restoring force $\dot{r}_i$ in the system of differential equations of SDOF hysteretic systems plays a vital role in providing high-fidelity models for bilinear hysteretic systems. Thus, using the approach of this research, the differential equation associated with each

compound restoring force r_i is discovered and optimized. Thus, the target equivalent system of differential equation that is aimed to be discovered is as follows

$$\begin{cases} f_1(t) = m_1\ddot{x}_1 + r_1 & 4(a) \\ \dot{r}_1 = q_1(r_1, r_2, r_3, \dot{x}_1, \dot{x}_2, \dot{x}_3, x_1, x_2, x_3) & 4(b) \\ f_2(t) = m_2\ddot{x}_2 + r_2 & 4(c) \\ \dot{r}_2 = q_2(r_1, r_2, r_3, \dot{x}_1, \dot{x}_2, \dot{x}_3, x_1, x_2, x_3) & 4(d) \\ f_3(t) = m_3\ddot{x}_3 + r_3 & 4(e) \\ \dot{r}_3 = q_3(r_1, r_2, r_3, \dot{x}_1, \dot{x}_2, \dot{x}_3, x_1, x_2, x_3) & 4(f) \end{cases}$$

where x_i, $\dot{x}_i$ and $\ddot{x}_i$ are the displacement, velocity, and acceleration, respectively, $f_i(t)$ is external excitation, m_i is the mass, and r_i and $\dot{r}_i$ are the compound restoring force and its derivative at DOF i. While Eqs. (4(a)), (4(c)) and (4(e)) are known a priori, the discovered differential equations of the compound restoring forces $\dot{r}_i$ will be placed in Eqs. (4(b)), (4(d)) and (4(e)) to form the surrogate computational model that represent the system under discussion.

3. Introduction to genetic programming

3.1 Overview

Evolutionary Algorithms (EAs) are heuristic optimization methods that mimic the necessary processes for evolution in nature — selection, mutation and crossover — to evolve a population of candidate solutions. Genetic Programming, introduced and popularized by Koza (1992), is a branch of EAs that is capable of evolving any type of structures in the form of expression-trees with quantifiable performance in the domain. (Bolourchi 2014)

Table 1 Properties of the Bouc-Wen model and the applied excitations $f_i(t)$ for training and validation

Parameters of Excitations $f_i(t)$	Values	Bouc-Wen Links g_i	Values
Mean μ	0	n	1.00
Training Standard Deviation σ_t	1.00	A	1.00
Validation Standard Deviation σ_v	1.00	β	1.00
Sampling Frequency $\Delta t/T$	0.05	ν	1.00
Duration	80 Seconds	η	1.00
Masses : m_1, m_2, m_3	0.80, 2.00, 1.20	γ	-0.50

3.2 Population

In this study, the population of evolving candidate solutions are the differential equations of the compound restoring force at each DOF, that will eventually take part in the system of the differential equations of Eq. (4). In order to obtain distinct differential equations, a new population is formed for analyzing each degree-of-freedom. No additional information is assumed to be known about the topology of the system. Thus, the training data set is composed of all displacement and velocity states, $x_1, x_2, x_3, \dot{x}_1, \dot{x}_2, \dot{x}_3$ as well as the compound restoring forces r_1, r_2, r_3 at all degrees-of-freedom. Hence, they form a 9-dimensional function-space domain to estimate the derivative of the restoring force $\dot{r}_i$ at a specific DOF i in Eqs. (4(b)), (4(d)) and (4(e)). Therefore, the MDOF system under investigation has 3 degrees of freedom, but 9 introduced variables constitute 9 dimensions. Note that, due to the complexity of the system, all the available signals are considered as a variable, in the beginning, and consequently, add one dimension to the search domain. However, GP will intelligently remove unrelated variable that do not contribute to the target signal. As a result, dimensionality reduction is conducted automatically throughout the evolution.

In addition to the state variables, algebraic operations $(+,-,\times,/)$, as well as the abs and Heaviside $step$ functions are included in the library of essential building blocks, to construct the body of the evolving population. However, only appropriate elements will survive during the course of the evolution to form the most suitable structures, and subsequently, the most accurate differential equations. Then, evolutionary operators (mutation and crossover) are used to advance the evolution. The eventual goal is to discover optimized distinct differential equations for the compound restoring forces of the system to form a complete system of coupled differential equations that fully characterize the system under discussion.

3.3 Fitness criterion

Establishing a suitable fitness criterion is critical for guiding the evolution toward an admissible solution in a timely manner. The fitness error e in GP is calculated using the mean absolute error of the deviation of the model estimate from the target signal. $e = x - \hat{x}$, normalized by the mean absolute value of the reference signal x

$$\varepsilon = \frac{\frac{1}{n}\sum_{i=1}^{n}\left|\mathrm{x} - \hat{\mathrm{x}}\right|}{\frac{1}{n}\sum_{i=1}^{n}\left|\mathrm{x}\right|} = \frac{\sum_{i=1}^{n}\left|\mathrm{e}\right|}{\sum_{i=1}^{n}\left|\mathrm{x}\right|} \tag{5}$$

A different fitness criterion is implemented for advancing the parameter optimization by means of Genetic Algorithms. This criterion will be presented later in this paper.

4. Modeling multi-dimensional hysteretic systems: general procedure

The identification procedure consists of two major phases: training and validation.

Table 2 The parameters of Eureqa for obtaining the optimum structures using Genetic Programming

	Eureqa
Parameters	Values
Error Metric (Fitness)	Minimize the Absolute Error
Algebraic Operations	$+ - \times \div$
Basis Functions	*step, abs*
Terminals	Constants, Variables
Stop Criterion	48 hours
Number of Variables	9
Processing Unit	RAM: 16.0 GB; CPU: Intel quad core i7-3370 with hyper threading; CPU clock: 3.40 GHz

Note that due to the incorporation of non-differentiable basis functions, gradient-based methods are not suitable for the optimization process

4.1 Training

Step 1: Excitation

For training, first the synthetic training data set should be generated. Three different, but statistically similar, excitations stimulate the lumped masses at each degree-of-freedom. The properties of the excitations are in accordance with Table 1. They are stationary Gaussian white with zero mean and known standard deviation. The standard deviation controls the intensity of the external excitations. The produced excitations stimulate the lumped masses at all degrees-of-freedom.

Step 2: Response calculation

The reference response of the structure under investigation is calculated by solving the actual system of nonlinear differential equations, described by Eq. (3), using standard time-marching numerical techniques. Then, the compound restoring force at each degree-of-freedom is calculated using the general equation of motion $r_i = f_i(t) - m_i\ddot{x}_i$. The estimate of the derivative of the restoring force is also calculated using two-point finite-difference approximations as follows

$$\dot{r}_i^j = \frac{r_i^{j+1} - r_i^j}{\Delta t} \tag{6}$$

where $\dot{r}_i^j$ is the jth datum in the array of the estimate of the derivative of the restoring force r_i, and r_i^{j+1} and r_i^j are the $j+1$ th and j th data in the array of the restoring force r_i, and Δt is the time step.

Step 3: Training data preparation

The derivative of the restoring force $\dot{r}_i$ at DOF i, the restoring force at all degrees-of-freedom r_i, along with displacement and velocity of all degrees-of-freedom form the training data set.

Table 3 Properties of GA for parameter optimization

GA Parameters	Values
Method	**gaoptimset**
PopulationSize	200
Initial Population	From GP: $\boldsymbol{c}$
PopInitRange	[0.4c : 2.5c]
Bounds (**lb**, **ub**)	(0.4c,2.5c)
TolFun	0.01
StallGenLimit	50

Step 4: Genetic programming computation

Eureqa (Schmidt and Lipson 2009), which is a Genetic Programming toolbox that uses the principles of Genetic Programming to perform this task, was used for the analysis. The fitness is calculated using the absolute error defined earlier by Eq. (5). Algebraic operations and basis functions are the non-terminal building blocks that connect terminal building blocks of trees (ending leafs). Parameters of GP can be found in Table 2.

Step 5: Un-optimized model formation

At the end of three rounds of evolution, three distinct differential equations are obtained for the compound restoring forces at all degrees-of-freedom. Then, they are combined to form the system of differential equations of Eq. (4). However, while the fitness of the obtained models from GP is based on how every single discovered equation can estimate the derivative of the restoring force, the actual performance of the constructed system of coupled differential equations is measured based on their *global* performance. Therefore, since GP is not able to effectively optimize the parameters of the model based on the solution of the differential equation, Genetic Algorithms are employed next to optimize this system of differential equations to improve its global response estimates.

Step 6: Model's parameter optimization

Due to the dependency of the system response on all coupled differential equations combined together, the parameters are optimized using GAs, all together, to enhance the accuracy of the response estimates. Hence, the cost function is defined as the summation of equally-weighted errors between the displacement, velocity and acceleration of the model response and the reference response, at every degree-of-freedom, as follows

$$\varepsilon = \sum_{i=1}^{3} \frac{\left\| x_i - \hat{x}_i \right\|}{\left\| x_i \right\|} + \frac{\left\| \dot{x}_i - \hat{\dot{x}}_i \right\|}{\left\| \dot{x}_i \right\|} + \frac{\left\| \ddot{x}_i - \hat{\ddot{x}}_i \right\|}{\left\| \ddot{x}_i \right\|} \tag{7}$$

where x_i is the displacement, $\dot{x}_i$ is the velocity, and $\ddot{x}_i$ is the acceleration at DOF i and $\hat{x}_i$,

$\hat{\dot{x}}_i$ and $\hat{\ddot{x}}_i$ are their estimates, respectively. GA in Matlab is employed to optimize the parameters, and the assigned options are listed in Table 3. The **gaoptimset** method is used to conduct the evolution of parameters in Matlab. The size of the population is 200.

Step 7: Final optimized model completion

In the end, after the parameter optimization phase is completed, a system of differential equations is obtained whose parameters are also optimized, to accurately represent the MDOF system under investigation, and to yield the best estimates.

4.2 Validation and verification

The last phase of the modeling scheme involves validation and verification by predicting the accuracy of the discovered model when subjected to new excitations whose intensities are substantially different from the training excitations. This phase gages the generalizability of the discovered model, and its applicability in new dynamical environments.

5. Modeling multi-dimensional hysteretic systems: results

This section applies the introduced identification technique that incorporates GP and GA for the identification of a multi-dimensional non-linear hysteretic system with the Bouc-Wen formulation. The model shown in Fig. 1 is excited at all degrees-of-freedom by broad-band uncorrelated forces, described in Table 1, to undergo horizontal motion. The duration of the excitations is 80 seconds, and the time-history of the applied excitation to DOF 2 , as an example, is shown in the lower part of the time-history panels of Fig. 2. The response of the system is obtained by solving the system of coupled differential equations of Eq. (3). The inter-connecting links g_i undergo significant hysteretic deformation. Samples of this behavior for three inter-connecting elements g_i, i=1,2,3 are plotted against the relative displacement of their two ends in Fig. 3.

5.1 Discovering the optimized structure of differential equations by GP

The response of the stimulated 3-DOF system generates 3 batches of training data sets, and are fed to GP to obtain three differential equations associated with the compound restoring force at every degree-of-freedom. It is important to note that none of the information concerning the individual restoring forces g_i s, *i.e.,* neither the formulation of g_i, nor the measurements from a single g_i, is used in the modeling process.

The candidate GP-found differential equations that were obtained after the termination of the optimization for 3 different training datasets are combined to form the entire coupled system of differential equations in Eq. (8). Note that, according to Eq. (3), although 6 Bouc-Wen models are included in the MDOF system of Eq. (3), the estimate of the governing system of differential equations in Eq. (8) involves only three equations for the compound restoring forces. Thus, a fairly simple model is able to represent the investigated complex multi-dimensional system exhibiting nonlinear dissipative memory-dependent behavior.

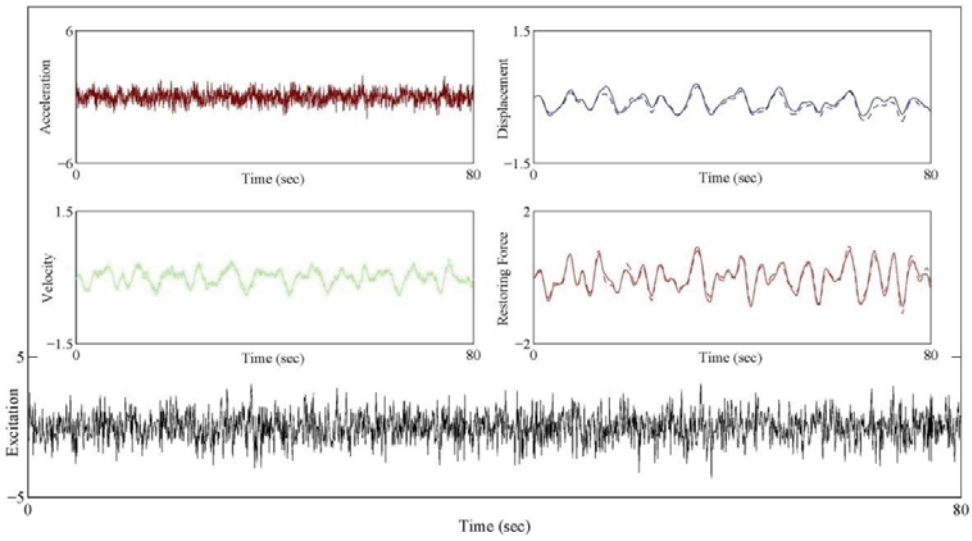

Fig. 2 Comparison of the reference and estimated response of the 3-DOF hysteretic system at DOF 2. The system is stimulated by 3 distinct external training excitations at all degrees-of-freedom. The graphs of the reference and identified response are plotted using solid and dotted lines, respectively

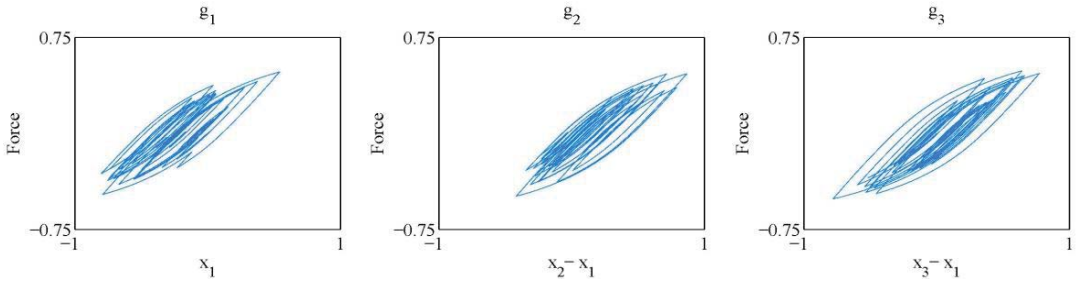

Fig. 3 Phase plots of the force at interconnecting elements of g_1 to g_3 vs. the relative displacement of the corresponding ends, when the 3-DOF hysteretic system is subjected to distinct training excitations with $\sigma_t = 1.0$ at all degrees-of-freedom

$$\begin{cases} \mathrm{f}_1(t) = m_1\ddot{\mathrm{x}}_1 + r_1 \\ \dot{r}_1 = 2.797\dot{\mathrm{x}}_1 - \dot{\mathrm{x}}_2 - \dot{\mathrm{x}}_3 - \mathrm{r}_1\mathrm{abs}(\dot{\mathrm{x}}_1) \\ \mathrm{f}_2(t) = m_2\ddot{\mathrm{x}}_2 + r_2 \\ \dot{r}_2 = 2.767\dot{\mathrm{x}}_2 - \dot{\mathrm{x}}_1 - \dot{\mathrm{x}}_3 - 0.217\mathrm{r}_2 \\ \mathrm{f}_3(t) = m_3\ddot{\mathrm{x}}_3 + r_3 \\ \dot{r}_3 = 2.798\dot{\mathrm{x}}_3 - \dot{\mathrm{x}}_1 - \dot{\mathrm{x}}_2 - \mathrm{r}_3\mathrm{abs}(\dot{\mathrm{x}}_3) \end{cases} \tag{8}$$

5.2 Optimizing the parameters of the system of differential equations by GA

Though the obtained expressions provide the best fit for the defined auxiliary variables $\dot{r}_i$s, which symbolize the compound restoring forces, the parameters of this system are not optimized by GP to yield accurate response estimates globally. Thus, the weight vector a is introduced to adjust the contribution of every single term in the system of differential equations in such a way that the least difference between the estimate and reference response is achieved. According to Eq. (9), the weight vector has 12 elements, and is optimized by Genetic Algorithms using the error measure defined by Eq. (7). Note that the fact that the weighting parameters are linearly dependent on $\dot{r}_i$ doesn't eliminate the need for a stochastic evolutionary-based optimizer because the cost function of Eq. (7) depends on the response of the *entire* system of a coupled differential equation, rather than the goodness of fit in Eqs. (4(b)), (4(d)) and (4(f)) separately.

$$\begin{cases} f_1(t) = m_1\ddot{x}_1 + r_1 \\ \dot{r}_1 = a(1)2.797\dot{x}_1 - a(2)\dot{x}_2 - a(3)\dot{x}_3 - a(4)r_1 abs(\dot{x}_1) \\ f_2(t) = m_2\ddot{x}_2 + r_2 \\ \dot{r}_2 = a(5)2.767\dot{x}_2 - a(6)\dot{x}_1 - a(7)\dot{x}_3 - a(8)\,0.217 r_2 \\ f_3(t) = m_3\ddot{x}_3 + r_3 \\ \dot{r}_3 = a(9)2.798\dot{x}_3 - a(10)\dot{x}_1 - a(11)\dot{x}_2 - a(12)r_3 abs(\dot{x}_3) \end{cases} \tag{9}$$

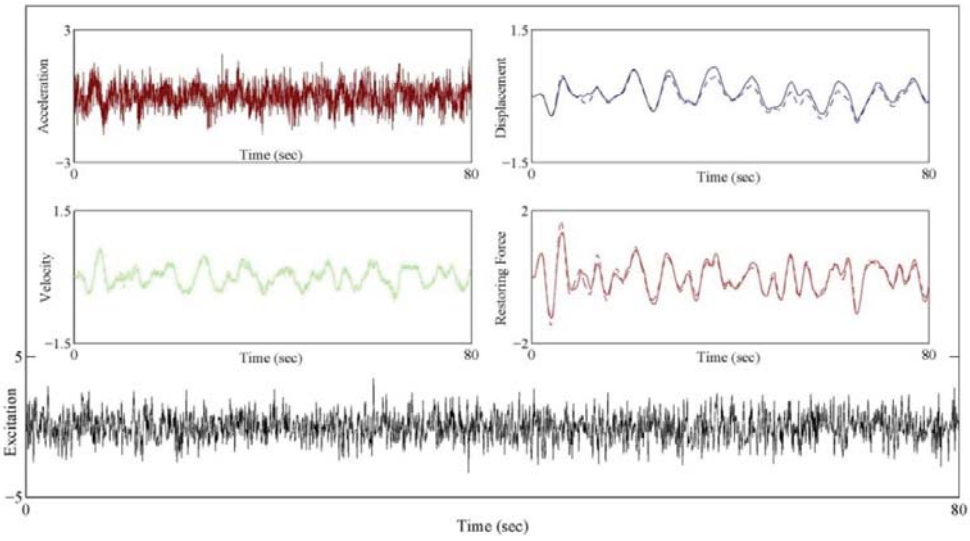

Fig. 4 Comparison of the reference and identified response of the 3-DOF hysteretic system at DOF 2. The system is stimulated by 3 distinct external validation excitations with $\sigma_v = 1.0$ at all degrees-of-freedom which have the same intensity as the training excitation with $\sigma_t = 1.0$. The graphs of the reference and estimated response are plotted using solid and dotted lines, respectively

The cost function associated with the original system of Eq. (9) before optimizing the weights, when $a_i = [111111111111]$, decreases from 266% to 175%, when the optimized weight vector is achieved: $a_f = [0.90, 1.14, 0.90, 0.97, 1.01, 1.12, 0.99, 0.81, 1.07, 0.94, 1.26, 0.90]$. Note that the cost function is defined by Eq. (7).

5.3 Validation of the model

At the end of the training phase, which consisted of both GP for optimizing structures and GA for optimizing parameters, the obtained system of differential equations is validated. The validation is conducted by applying a different random excitation which has the same standard deviation as that of the training, to the MDOF system. Solving the optimized coupled differential equation of Eq. (9) with a_f under the new validation excitation by means of standard numerical techniques provides the response estimate. The time histories of the estimated response and the reference response due to the training excitation are shown in the time history panels of Fig. 4 for DOF 2. Similar results are achieved for other degrees-of-freedom. The reasonable error associated with the estimates confirm that the proposed modeling technique yields reduced-order, reduced-complexity, optimized differential operators that effectively characterize the dynamics of the complex nonlinear MDOF system with hysteretic traits. It is also shown that the model performs well under new dynamical stimulations.

A more comprehensive validation process can be implemented by considering a variety of excitation levels, and conducting a statistical analysis on the outcomes.

6. Discussion

Based on Evolutionary Computational approaches presented herein for the identification of multi-dimensional hysteretic systems, it was shown that the obtained equivalent system of differential equations is fairly simple, and at the same time provides reliable estimates with reasonable error. Though the optimization starts off with 9 variables, the discovered equations at the end of the structure optimization by means of GP have only 4 variables, because only the variables will survive during the course of evolution that provide the best fit. It is seen that for the equation of the derivative of the compound restoring force $\dot{r}_i$ at DOF i only the compound restoring force at the same DOF i and the velocity measurements at all DOFs take part in that specific differential equation to attain the best fit for $\dot{r}_i$. The acceptability of the resultant model, despite its simplicity comparing to the complexity of the original system of differential equations, and the physical nature of the studied system, shows the effectiveness of the approach for discovering equivalent computational models for complex multi-dimensional phenomena.

Since only the vibration of lumped masses are measured, without measuring the forces at all interconnecting links associated with the Bouc-Wen elements, the measurements are not complete. Thus the exact original model of Eq. (3) cannot be reconstructed using these measurements by model-free approaches. However, the presented technique of this study is capable of discovering an accurate differential equation for an auxiliary variable that incorporates the vibrations from all other hysteretic links and masses. These differential equations are coupled and together construct the eventual representative model.

7. Advantages and challenges of the proposed technique

7.1 Advantages

In this study, no model was postulated up-front, and the modeling is merely carried out through processing of the provided input and output data. In real world problems, these data are obtained from sensor measurements. Therefore, this method doesn't require extensive prior information about the original underlying system, and as a result the discovered surrogate reduced-order reduced-complexity model can be significantly different from the original system of differential equations while resulting in accurate estimates. Achieving acceptable models through model-free approaches is a great advantage of this technique when dealing with memory-dependent systems. Because these systems do not only depend on the instantaneous values of the variables, their previous states should also be incorporated. Therefore, many conventional non-parametric modeling techniques, such as polynomial approximation, are not able to provide acceptable models for such systems.

Unlike many data-driven approaches, such as neural networks, that yield black-box models, without any insight into the physics of problem, the approach of this paper reveals the computational model of the studied system. On the other hand, if in addition to data, no information about the complex phenomena is available, the discovered model can provide insight into the constitutive properties behind the system associated with the data.

7.2 Challenges

The resultant models highly depend on the provided building blocks in GP, and the embedded basis functions, and not having appropriate basis functions in the pool of building blocks may cause poor results, including too many functions increases the computational cost. Moreover, adding more variables, and consequently more dimensions intensifies the computational cost. The nature of the external excitations also plays a vital role in the modeling process. While, slight perturbations cannot disclose the nature of the hysteretic phenomena to the extent that it is necessary for the modeling, very strong excitation may obscure the hysteretic properties and cause poor generalization capabilities when the system is subjected to less intense excitations.

8. Conclusions

The proposed technique of this paper benefits from advances in the field of Evolutionary Computation to provide high fidelity parsimonious computational models in the form of systems of differential equations that represent multi-dimensional memory-dependent systems, only based on input and output data. This approach employs Genetic Programming to optimize the structures of differential equations, and combines it with Genetic Algorithms to optimize the parameters of formerly discovered structures in a system of coupled differential equations, to result in accurate estimates globally. Thus, basis function and variable selection, dimensionality reduction, and parameter optimization are all preformed in the training phase. A benchmark example is used to assess the effectiveness of the proposed technique. After obtaining the equivalent model for this system based on training excitation, validation is carried out to verify the generalizability of the

achieved model in unseen dynamical environments. The validation results show that reasonably accurate responses are achieved though the discovered model is fairly simple compared to the exact formulation of the system, and verify the effectiveness of the presented approach for data-driven modeling of complex multi-dimensional hysteretic system.

References

Alavi, A.H., Gandomi, A.H., Sahab, M.G. and Gandomi, M. (2010), "Multi expression programming: a new approach to formulation of soil classification ", *Eng. Comput.*, **26**(2), 111-118.

Becker, Y., Fei, P. and Lester, A. (2007), "Stock selection: An innovative application of genetic programming methodology", (Eds., Riolo, R., Soule, T. and Worzel, B.), *Genetic Programming Theory and Practice IV, Genetic and Evolutionary Computation*, Springer, USA.

Bolourchi, A. (2014), *Studies into Computational Intelligence Approaches for the Identification of Complex Nonlinear Systems*, PhD Dissertation, University of Southern California, Los Angeles.

Bolourchi, A., Masri, S.F. and Aldraihem, O.J. (2015), "Development and application of computational intelligence approaches for the identification of complex nonlinear systems", *Nonlinear Dynam*., **79**(2), 765-786, Springer , Netherlands.

Bouc, R. (1967), "Forced vibration of mechanical systems with hysteresis", *Proceedings of the Fourth Conference on Non-linear Oscillation*, Prague, Czechoslovakia.

Chatzi, E.N., Smyth, A.W. and Masri, S.F. (2010), "Experimental application of on-line parametric identification for nonlinear hysteretic systems with model uncertainty", *Struct. Saf.*, **32**(5), 326–337.

Dracopoulos, D. and Effraimidis, D. (2012), *Genetic programming for generalised helicopter hovering control*, *In Genetic Programming, Volume 7244 of Lecture Notes in Computer Science*, Springer Berlin / Heidelberg, Germany.

Gandomi, A.H. and Alavi, A.H. (2011), "Multi-stage genetic programming: a new strategy to nonlinear system modeling", *Inform. Sciences*, **181**(23), 5227-5239.

Gruau, F. (1994), "Automatic definition of modular neural networks", *Adapt. Behav.*, **3**(2), 151-183.

Handley, S. (1995), *Predicting whether or not a nucleic acid sequence is an e. coli promoter region using genetic programming*, Intelligence in Neural and Biological Systems, Symposium on, Herndon, VA, USA.

Hornby, G.S., Lohn, J.D. and Linden, D.S. (2011), "Computer-automated evolution of an x-band antenna for nasa's space technology 5 mission", *Evol. Comput*., **19**(1), 1-23.

Howard, D. and Roberts, S. (2002), *The prediction of journey times on motorways using genetic programming*, Applications of Evolutionary Computing, Berlin, Germany.

Kerschen, G., Worden, K., Vakakis, A. and Golinval, J.C. (2006), "Past, present and future of nonlinear system identification in structural dynamics", *Mech. Syst. Signal. Pr*., **20**(3), 505-592.

Koza, J. (1992), *Genetic Programming: On the Programming of Computers by Means of Natural Selection*, MIT Press, Cambridge, MA.

Li, S., Yu, H. and Suzuki, Y. (2004), "Identification of non-linear hysteretic systems with slip", *Comput. Struct.*, **82**(2), 157-165.

Masri, S., Caffrey, J., Caughey, T., Smyth, A. and Chassiakos, A. (2004), "Identification of the state equation in complex non-linear systems", *Int. J. Nonlinear Mech.*, **39**(7), 1111-1127.

Masri, S., Caffrey, J., Caughey, T., Smyth, A. and Chassiakos, A. (2005), "A general data-based approach for developing reduced-order models of nonlinear mdof systems", *Nonlinear Dynam.*, **39**(1-2), 95-112.

Masri, S. and Caughey, T. (1979), "A nonparametric identification technique for nonlinear dynamic problems", *J. Appl. Mech. - T ASME*, **46**(2), 433-447.

Masri, S., Miller, R., Saud, A. and Caughey, T. (1987), "Identification of nonlinear vibrating structures. ii. applications", *J. Appl. Mech- T ASME.*, **54**(4), 923-950.

Masri, S., Tasbihgoo, F., Caffrey, J., Smyth, A. and Chassiakos, A. (2006a), "Data-based model-free

representation of complex hysteretic mdof systems", *Struct. Control Health.*, **13**(1), 365-387.
Masri, S. F., Ghanem, R., Arrate, F. and Caffrey, J. (2006b), "Stochastic nonparametric models of uncertain hysteretic oscillators", *AIAA J.*, **44**(10), 2319-2330.
Pei, J.S. and Smyth, A.W. (2006a), "New approach to designing multilayer feedforward neural network architecture for modeling nonlinear restoring forces. i: Formulation", *J. Eng. Mech. - ASCE*, **132**(12), 1290–1300.
Pei, J.S. and Smyth, A.W. (2006b), "New approach to designing multilayer feed-forward neural network architecture for modeling nonlinear restoring forces. ii: Applications", *J. Eng. Mech. - ASCE*, **132**(12),1301-1312.
Schmidt, M. and Lipson, H. (2009), "Distilling free-form natural laws from experimental data", *Science*, **324**(5923), 81-85.
Silva, S., Anunciac¸a˜o, O. and Lotz, M. (2011), *A comparison of machine learning methods for the prediction of breast cancer*, Evolutionary Computation, Machine Learning and Data Mining in Bioinformatics, Springer.
Smyth, A., Masri, S., Chassiakos, A. and Caughey, T. (1999), "On-line parametric identification of mdof nonlinear hysteretic systems", *J. Eng. Mech. - ASCE*, **125**(2), 133-142.
Spector, L. and Alpern, A. (1995), "Induction and recapitulation of deep musical structure", *Proceedings of the IJCAI-95 Workshop on Artificial Intelligence and Music*, Montreal, Quebec, Canada.
Tackett, W. (1993), "Genetic programming for feature discovery and image discrimination", *Proceedings of the 5th International Conference on Genetic Algorithms*, San Mateo, CA, USA.
Tasbihgoo, F., Caffrey, J.P. and Masri, S.F. (2007), "Development of data-based model-free representation of non-conservative dissipative systems", *Int. J. Nonlinear Mech.*, **42**(1), 99-117.
Wen, Y.K. (1976), "Method for random vibration of hysteretic systems", *J. Eng. Mech. - ASCE*, **102**(2), 249-263.
Wong, M.L., Leung, K.S. and Cheng, J. (2000), "Discovering knowledge from noisy databases using genetic programming", *J. Am. Soc. Inform. Sci.*, **51**(9), 870 -881.
Zhao, X. and Tan, Y. (2008), "Modeling hysteresis and its inverse model using neural networks based on expanded input space method", *IEEE T. Contr. Syst. T.*, **16**(3), 484-490.

Smart Structures and Systems, *Vol. 15, No. 3 (2015) 913-929*
DOI: http://dx.doi.org/10.12989/sss.2015.15.3.913

Enabling role of hybrid simulation across NEES in advancing earthquake engineering

Daniel Gomez[*1,2], Shirley J. Dyke[1a] and Amin Maghareh[1b]

[1]*Lyles School of Civil Engineering, Purdue University, West Lafayette, IN 47906, USA*
[2]*School of Civil Engineering and Geomatics, Universidad del Valle, Cali, Colombia*

(Received November 17, 2014, Revised February 15, 2015, Accepted February 17, 2015)

Abstract. Hybrid simulation is increasingly being recognized as a powerful technique for laboratory testing. It offers the opportunity for global system evaluation of civil infrastructure systems subject to extreme dynamic loading, often with a significant reduction in time and cost. In this approach, a reference structure/system is partitioned into two or more substructures. The portion of the structural system designated as 'physical' or 'experimental' is tested in the laboratory, while other portions are replaced with a computational model. Many researchers have quite effectively used hybrid simulation (HS) and real-time hybrid simulation (RTHS) methods for examination and verification of existing and new design concepts and proposed structural systems or devices. This paper provides a detailed perspective of the enabling role that HS and RTHS methods have played in advancing the practice of earthquake engineering. Herein, our focus is on investigations related to earthquake engineering, those with CURATED data available in their entirety in the NEES Data Repository.

Keywords: earthquake engineering; seismic experimentation; hybrid simulation; real-time hybrid simulation; design guidelines; building code

1. Introduction

Earthquakes area major source of catastrophic natural disasters, often leading to loss of human life, civil structures and infrastructures. Excessive disturbances produced by base excitation in civil structures can damage structural and non-structural elements and cause discomfort to occupants. To advance our understanding of seismic resilience to such impacts, establish performance-based seismic design methods, develop new mitigation technologies, and enhance lifeline systems, several classes of experimental methods are used to simulate and evaluate structural behavior under extreme dynamic loading. These including quasi-static testing, shake table testing, effective force testing, and hybrid simulation (HS) methods, and each has pros and cons. In quasi-static tests, displacements (or loads) are applied at a slow rate. Quasi-static testing can readily be implemented on large civil structures, although it has two drawbacks. A predefined displacement history is required, and the effects of acceleration-dependent inertial forces and

*Corresponding author, Associate Professor, Universidad del Valle, E-mail: dgomezp@purdue.edu
[a] Professor, E-mail: sdyke@purdue.edu
[b] Doctoral Candidate, E-mail: amaghare@purdue.edu

http://www.techno-press.org/?journal=sss&subpage=8 ISSN: 1738-1584 (Print), 1738-1991 (Online)

velocity-dependent damping forces are neglected. To by pass these issues, shake tables, or earthquake simulators, are widely available to evaluate the dynamic behavior of structures. Shake table testing is conducted in real time, typically enabling researchers to achieve quite realistic conditions. Researchers have used shake tables to evaluate critical issues such as collapse mechanisms, component failures, acceleration amplifications, residual displacements and post-earthquake capacities (Schellenberg and Mahin 2006). However, very few shake tables in the world are capable of full-scale testing of civil structures, and due to the scale of the specimen such experiments, may be prohibitively expensive. Thus, evaluating the dynamic behavior of structures using shake table is usually limited to proto types and often conducted for critical parts of a structure at the component level (Shing *et al.* 1996).

Advances in our ability to perform more complex computational simulations have also generated a need to validate the results, calibrating analytical models and developing new design guidelines. This need, and the desire to increase the size of our specimens for more realistic evaluations, increase the cost of testing, and sometimes exceed the capacity of our facilities. These objectives have driven the need to consider new methods of testing that combine physical experimentation with computational simulation, a class of experimentation known as hybrid simulation (HS). In HS, the experimental (or physical) portions of the structural system are tested in the laboratory, typically including the more complex components that are a focus of the investigation, while other portions of the structure are replaced with computational (or analytical) models which typically include the well-understood behaviors(see Fig. 1).

The concept of partitioning a reference system into numerical and experimental substructures originated in the field of aerospace and control engineering. Halbert *et al.* (1963) coupled digital and analog computers through a two-way data transfer system. In this study, adaptive path control of a two-dimensional maneuver under lunar attraction was simulated using HS. At each step, the digital computer performed a high-precision simulation of the rocket motion and sent its position and velocity to an analog computer. Then, the analog computer solved the corresponding boundary value problem and fed back the results to the digital computer (Halbert *et al.* 1963). Similarly, a HS of space vehicle guidance in a lunar landing was developed using a small digital computer tied to two fully-expanded analog computers (Heartz and Jones 1964). In another noteworthy study using HS, Witsenhausen (1964) solved the equation of a chemical tubular reactor under various input conditions when a controller was installed.

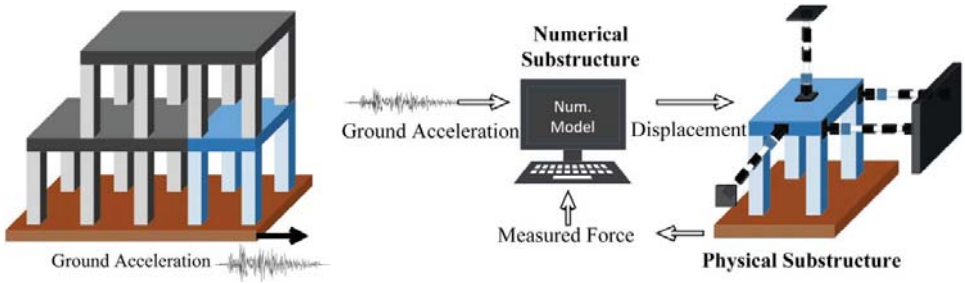

Fig. 1 Concept of hybrid simulation

Hybrid simulation found its way into structural engineering with Hakuno *et al.* (1969) who used HS to conduct a dynamic destructive test of a cantilever beam using an online system consisting of an analog computer and an electro-magnetic actuator. In this study, they developed an online computer-actuator system in an attempt to simulate earthquake responses of linear and nonlinear steel and concrete structures. To conduct HS, the floor displacement was computed using the numerical substructure (a nonlinear differential equation) and an actuator was used to apply the displacement to a one-story one-bay building frame (Takanashi *et al.*1975).

Structural engineers evolved this approach into a new cost-effective experimental technique to evaluate the dynamic performance of large civil structures. In the late 80s, researchers had shown that results of HS and shake table tests are comparable if experimental errors are effectively mitigated (Takanashi and Nakashima 1987, Mahin *et al.* 1989). When the structure under investigation (i.e., the reference structure) is divided into experimental and numerical substructures, coupling between the substructures is achieved by enforcing boundary conditions and equilibrium at the interface (Chen *et al.* 2012). One necessary assumption in HS is that the effect of loading rate on the interaction force of the numerical substructure is insignificant. Under certain conditions, this assumption has been validated for some structural materials, such as reinforced concrete and steel (Nakashima *et al.* 1992).The need to examine dynamic behavior and performance in rate-dependent structural components (e.g., rubber bearings, viscous dampers) combined with advances in embedded systems with hard real-time computing capabilities, have led researchers to conduct fast and real-time hybrid simulations (RTHS).

In recent years, HS and RTHS have played a noteworthy role in enabling new civil engineering concepts to be developed and validated under more realistic conditions, contributing to advance the practice of earthquake engineering around the world (Shao and Griffith 2013). A large number of the projects employing HS and RTHS are published in their entirety in the George E. Brown, Jr. Network for Earthquake Engineering Simulation (NEES) Data Repository (at nees.org), where these data are open and accessible for use by other researchers (Pejša *et al.* 2014). Over the last decade, more than 400 research projects (https://nees.org/retrospective) have benefitted from an initiative funded by the US National Science Foundation (NSF) to build, maintain, operate and use the equipment facilities, interconnected via cyber infrastructure, that comprise the George E. Brown, Jr. Network for Earthquake Engineering Simulation (NEES). This unique infrastructure was managed first by the NEES Consortium Inc. (CMMI-0402490)for the period 2004-2009. Subsequently, the NEEScomm center at Purdue University managed the network for the period of 2009-2014 (CMMI-0927178).The NEES network, a "Laboratory without Walls," includes fourteen geographically-distributed, experimental earthquake engineering facilities, linked together with a robust, user-driven cyber infrastructure which houses a curated, central data repository (Hacker, *et al.* 2013). The NEES laboratories are equipped with unique large-scale equipment, such as geotechnical centrifuge centrifuges, tsunami simulation facilities, field testing equipment, shake tables, hydraulic actuators and strong walls (Ramirez 2012). The cyber infrastructure integrates an open repository for experimental/simulation data with simulation tools, national high performance computing resources, documents and educational resources (known as NEES hub).

The arrival of the NEES hub has ushered in a new collaborative capability with vastly improved information technology resources for research and education in earthquake engineering (Hacker *et al.* 2013). Researchers have taken advantage of this shared-use network of facilities connected with a unique cyber infrastructure to accelerate progress in HS (Nakata *et al.* 2014, Christenson *et al.* 2014) and enable a new generation of testing to be performed. Capabilities, open-source software and algorithmic advances in HS and RTHS have developed in parallel with

the NEES facilities and research projects (Deierlein *et al*. 2011). To demonstrate the progress to date, and to explore the future potential, of HS and RTHS in developing new knowledge related to resilient infrastructure systems, relevant projects published in the NEES Data Repository are discussed herein. The public data repository (at nees.org) provides a wealth of information and open data from several HS and RTHS projects, and through these data and metadata the process for the contributions of these projects to civil engineering practice is reconstructed herein (Gomez *et al.* 2014).

2. Hybrid simulation in earthquake engineering

The power of HS and RTHS lies in its promise to accelerate the rate at which we can conduct research in earthquake engineering (Shao and Griffith 2013). In the last decade, an increasing number of researchers have used HS methods as an alternative to quasi-static or shake table testing. Its capability to induce local failure mode analysis under realistic loading and global response evaluation leads this type of test to be more flexible (various conditions, structures, loadings, are possible), without the limitations in size or shape that usually govern shake table tests. Within the NEES network, at least 29 projects have used HS/RTHS to investigate a variety of topics related to seismic engineering.

Recently, researchers have begun to rely on HS or RTHS to assess local and global responses and compare various aspects related with design guidelines, and specifically with design codes. For purposes of this discussion on the enabling roles, the NEES projects that have used HS or RTHS are categorized in two principal directions: (i) to review, support, oppose, or improve design guidelines in building codes requirements, and (ii) to develop and validate new structural systems or new devices to modify the structural response. A diagram summarizing the primary purpose of using HS for the projects is provided in Fig.2. In many cases HS was more economical than full scale shake table experiments, and perhaps even the only way to achieve the goals of the projects. Note that all images were provided through the NEES hub at nees.org in the respective projects.

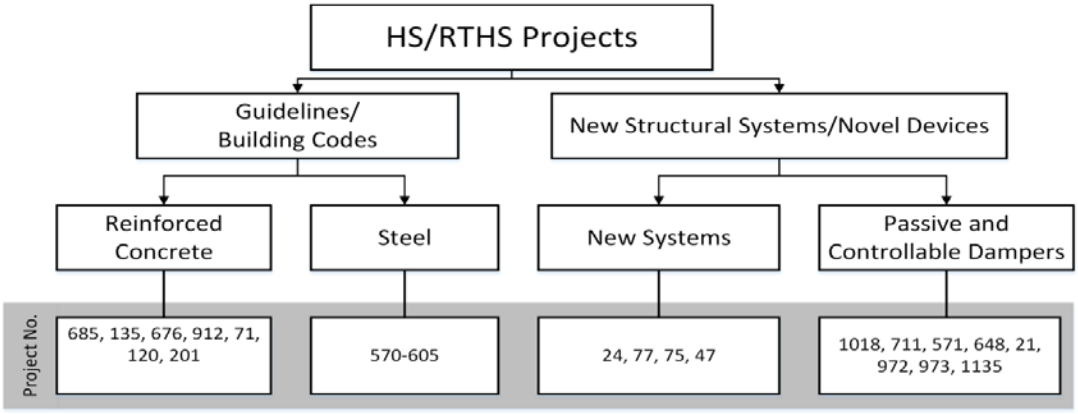

Fig. 2 Selected HS/RTHSprojects in earthquake engineering

2.1 Hybrid simulation for establishing and investigating guidelines and codes

In this section, we summarize the progress made using HS in the establishment of guidelines and codes toward the design of infrastructure systems to resist such hazards.

Framework for Development of Hybrid Simulation in an Earthquake Impact Assessment Context (Project 685). This project demonstrated that HS is an economical and efficient technique with many capabilities and applications. In this project, HS provided an innovative way to utilize field measurement data (free-field and structural sensor measurement), combined with system identification, model updating, probabilistic fragility analysis, and earthquake impact assessment packages to evaluate the impact of earthquakes on civil infrastructure in a robust framework. In the proposed framework, free-field measurements were used to define and characterize strong motion records. Structural sensors were used to update the bridge-foundation-soil model. Eight HS and one cyclic test were conducted using 1/25-scale reinforced concrete (RC) pier specimens (see Fig. 3). For the HS test, three tests with different hazard levels were conducted by using three synthetic ground motions with peak ground acceleration (PGA) values between 0.2 and 0.9 g. Simulation results indicated that the model calibrated with cyclic tests accurately predicts the response in the cases with lower PGA. However, that model underestimates the peak lateral drift response under large PGA, and HS is shown to provide an updated model that yields a more realistic failure probability in fragility functions in the range of high ground motion intensity (Lin *et al.* 2012).An important deliverable for this project was the development of a tool, NEES Integrated Risk Assessment Framework (NISRAF),that integrates the components of earthquake impact assessment such as structural damage, loss assessment, estimation of nonstructural damage, economic cost, retrofit cost, etc. (Lin *et al.* 2012). The clear advantage here in using HS is that it provided the capability to perform several inexpensive tests to reach the target structural response, thus creating a family of fragility curves.

Fig. 3 Small-scale RC pier experimental substructure
(NEES project 685, https://nees.org/warehouse/experiment/3322/project/685)

Fig. 4 Experimental substructure conformed by RC frame and URM infill in the middle (NEES project 135, https://nees.org/warehouse/experiment/205/project/135)

Hybrid Simulation and Shake-Table Tests on RC Buildings with Masonry Infill Walls (Project 135). One of the objectives of this project was to refine the modeling techniques of hysteretic response and stiffness degradation in elements of RC moment frames interacting with unreinforced masonry (URM) infill walls. The numerical substructure consisted of a 3/4 scale, five-story prototype moment-resisting frame structure designed with its exterior columns as the primary lateral load resisting system. The experimental substructure was the middle bays of the first story (see Fig. 4).

Hashemi and Mosalam (2006) concluded that URM infill walls should be included for the design and associated analysis of a structure. The experimental results show that the interaction between the RC frame and the infill wall made the test structure 3.8 times stiffer, reduced the initial natural period by 50%, and affected the structural behavior. Additionally, an increase in the structural damping depends upon the level of displacement. Finally, experimental results showed that the URM infill walls resulted in a 30% increase in the demand on the diaphragm, and directly affected the RC columns at the top and bottom of the infill wall (Hashemi and Mosalam 2006).Additionally, a novelty in this project was the comparison between HS and shake table (ST) testing results, which were conducted on a similar test structure with the same sequence of applied ground motions. This comparison revealed that both tests developed a similar cracking pattern and progressive stiffness degradation throughout the two experiments using HS and ST. However, differences between HS and ST experiments for test structure were obtained due to the variation in the damping with amplitude, and the lack of a numerical model able to capture that behavior (Elkhoraibi and Mosalam 2007).

Performance-based Design of Squat Concrete Walls of Conventional and Composite Construction (Project 676).Here researchers performed HS at the Berkeley facility to examine the behavior of squat reinforced concrete structural walls commonly used in nuclear energy plants as a seismic lateral force resisting system. Squat shear walls are those designed with an aspect ratio smaller than 0.5, and are quite thick to provide protection again stradiation and fire (Whyte and Stojadinovic 2012). The experimental substructures were 0.2 m thick, 3 m long and 1.65 m tall shear walls (aspect ratio 0.54, see Fig. 5). To simulate the excessive weight of a nuclear power

plant, the extra mass was modeled in the numerical substructure and it was adjusted to achieve a0.14 sec fundamental natural period, which is a realistic value. Various design code procedures were employed to predict the observed responses. In some cases, the recommended methods over predict the peak shear strength of squalls walls by almost a factor of 1.8. However more results would be needed to draw conclusions about the displacement capacities for thick walls. This project demonstrated an efficient use of HS in emulating the huge mass of a nuclear power plant, eliminating the need to use a high capacity shake table.

Collapse Simulation of Multi-Story Buildings Through Hybrid Testing (Project 912). In this project, a number of specific test were conducted to predict and evaluate structural collapse responses. A progressive collapse program was conducted to study structural failure using HS as an alternative to earthquake simulators due to the limited capacity of most facilities. Also, the adoption of HS eliminated or alleviated a number of safety concerns associated with a collapsing structure on a shake table. Particularly, a large-scale shake table test was conducted to study collapse in a 2D four-story steel structure (Lignos 2008). Using a similar frame, several HS were performed to compare the results with the shake table results where only critical components of the structure were tested experimentally with a small number of actuators at the interface of the experimental subassemblies (Hashemi and Mosqueda 2014a), demonstrating flexibility, cost-effectiveness and safety (see Fig. 6).

Seismic Simulation and Design of Bridge Columns under Combined Actions, and Implications on System Response (Project 71). To evaluate the impact of spatially-complex earthquake ground motions in bridge piers, an extensive test program was executed to understand the effects of combined demands (vertical and horizontal) that may result in large deformation, excessive structural damage, and structural performance degradation. Two hybrid simulations were performed at the Multi-Axial Full-Scale Sub-Structured Testing and Simulation (MUST-SIM) facility at the University of Illinois at Urbana Champaign. In these hybrid simulations, a pier was constructed as the experimental substructure, and the remainder of the bridge was modeled as the numerical substructure (see Fig. 7). In the first HS experiment, the bridge was subject to a horizontal ground motion. In the second HS experiment, the bridge was subject to combination of horizontal and vertical components ground motion (Kim *et al.* 2011). Because hybrid simulation allowed the research team to reproduce vertical and horizontal components of a ground motion at the same time in a single test, using a component as the specimen, it was unnecessary to perform more resource-intensive tests involving complete structural specimens and a shake table with multiple degrees of freedom.

The shear strength of the piers were evaluated and compared with ACI 318-08 (2008) and AASHTOLRFD Bridge Design Specifications (1995). In a first HS experiment, shear capacities calculated using the approximate and refined methods of ACI 318-08 (2008) were found to be7% and 4% higher than the shear demand, respectively. In contrast, the shear strength predicted by the AASHTO (1995) was 31% less than the shear demand (Kim *et al.* 2011). Furthermore, the measured shear demand of the specimen in the second HS experimentwas8% lower than the shear capacity estimated by ACI approach. Researchers concluded that guidelines predicted the shear capacity of the pier in the first experiment conservatively, but in the second experiment, the pier suffered significant damage producing a broadband range for shear capacities calculated with different methods. Combined, horizontal and vertical ground motion in the piers may yield a decrease in shear capacity. Furthermore, neglecting the vertical component of the ground motion in the design procedure can underestimate the consequences of an earthquake in the design of RC bridges.

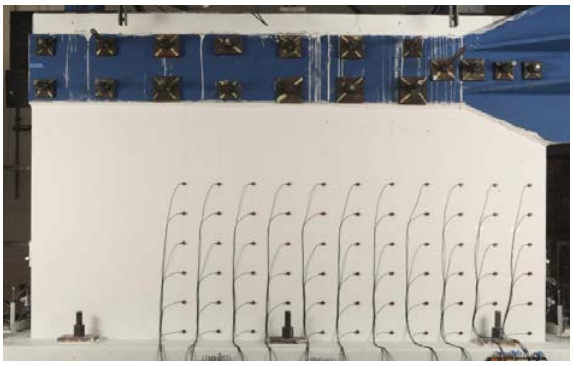

Fig. 5 RC experimental substructure compose by a thick wall specimen (NEES project 676, Whyte *et al.* 2013)

Fig. 6 Scheme for hybrid simulation used in collapse test (NEES project 912, Hashemi and Mosqueda2014b)

Fig. 7 Specimen in HS tests (NEES project 71, https://nees.org/warehouse/hybrid/4176/project/71)

International Hybrid Simulation of Tomorrow's Braced Frame Systems (Project 605). The objective of this project was to evaluate different bracing configurations and different design strategies intended to improve structural earthquake-resistant systems by increasing the ductility. A series of HS and cyclic tests were conducted using a three-story single-bay concentrically brace steel frames as the experimental substructure to obtain the response of the different buckling restrained brace frames (BRBF) and to investigate the brace-to-gusset connections. The numerical substructure consisted of two five-bay steel moment resisting frames and two one-bay concentrically brace frames in the longitudinal and transversal directions, respectively. As a result of these tests, the researchers recommend using a clearance of three times the thickness of the plate ($3t_p$), unlike the AISC (2010) suggestion of $2t_p$clearance, to provide an adequate space for welding and allowed enough rotations in the knife plate (Tsai *et al.* 2013). Also, Lin *et al.* (2012) proposed a design procedure for BRBF to avoid local failure produced for bulging of steel casing in the buckling restrained brace elements. In this project, HS and RTHS have been also used extensively to evaluate the capabilities of new materials, damping devices, and novel structural systems to improve the seismic response of building and bridges. The use of HS in this project was especially helpful to concentrate on realistic local behavior in the braces examined in a way that is consistent with the global response of the whole structure. Furthermore, flexibility and rapid deployment facilitated a wider variety of tests and configurations.

2.2 Hybrid simulation for developing novel structural systems and response modification devices

Next we discuss the achievements of several projects that adopted HS or RTHS to demonstrate and evaluate new structural systems and response modification devices at large scale.

Behavior of Braced Steel Frames with Innovative Bracing Schemes (Project 24).The system consisted of a bracing scheme using a suspended "zipper" frame. Conventional concentrically braced steel frames have the potential to lose stiffness and strength when buckling occurs in the brace, producing undesired vertical forces. In response, a new braced steel frame configuration was developed to meet the objective of providing efficient seismic response. Due to high nonlinearity of brace buckling, HS was conducted to capture the complex chevron brace buckling behavior. Although the zipper frame was not a new idea, the modification proposed here was intended to avoid undesirable deterioration of lateral strength in the frame and resist the potentially significant post-buckling force redistribution, resulting in very strong beams (Leon *et al.* 2005). In the new concept, the top story bracing members were designed to remain elastic when all the other compression braces buckled and the tension braces and zipper elements yielded.

In conducting HS, the experimental substructure, which is scaled to 1/3, represented the first-story braces and consisted of two braces along with the gusset plates connecting the braces to the beam at the top (see Fig. 8). The numerical substructure was a FEM model built in Open Sees (2006). This model used a flexibility-formulation nonlinear bean-column elements with fiber sections for the beams, columns, and zipper columns, and zero-length elements for the connections. A second-order displacement formulation was used to include the nonlinear buckling behavior (Yang *et al.* 2009). The results of the testing at the Colorado facility indicate that a suspended zipper column can successfully achieve the goal of redistributing the force along the frame height, although large inter-story drifts produced permanent deformation at the first floor. Here, HS was particularly useful in safely capturing the complex responses of the system subject to large deformation and buckling.

Fig. 8 Experimental substructure suspended-zipper braced frame
(NEES project 24, https://nees.org/warehouse/experiment/110/project/24)

Self-Centering Damage-Free Seismic-Resistant Steel Frame Systems (Project 77). In this project, an innovative structural system was developed to ensure that a moment-resisting frame would be able to survive the design basis earthquake (DBE) without any structural damage. In the design, post-tensioning strands would pre-compress the beams to the columns yielding a passive device with self-centering moment resisting frame (SC-MRF). The system was designed to return to its initial position while dissipating a significant amount energy under large seismic loads. Hybrid simulation was implemented to evaluate a 7-bay, 4-story SC-MRF building designed for a location in the Los Angeles area. The experimental substructure was a 2-bay, 4-story structure scaled to 60% and the remainder of the reference structure was the numerical substructure (Fig. 9).

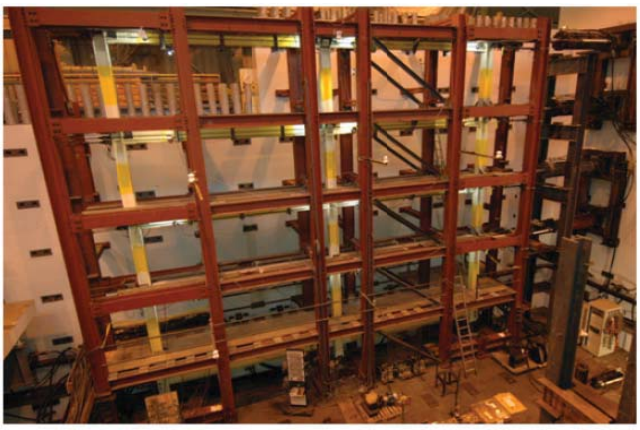

Fig. 9 SC-MRF 4-story test frame as experimental substructure
(NEES project 77, https://nees.org/warehouse/experiment/1151/project/77)

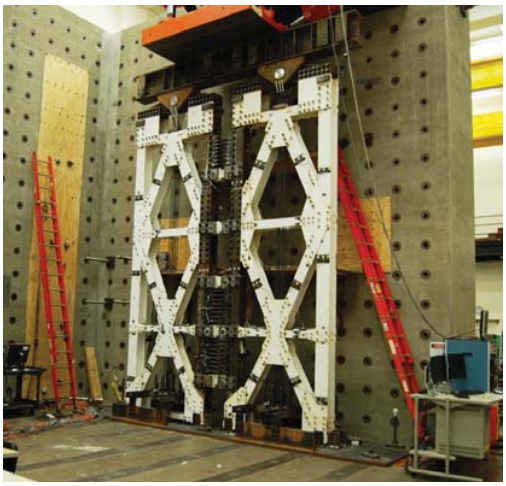

(a) Dual frame configuration specimen

(b) Steel shear plates removable fuse

Fig. 10 Self-centering rocking system (NEES project 75, https://nees.org/warehouse/experiments/75)

Using HS, the structure was subjected to four DBE level ground motions, and each lateral floor displacement returned to zero (thus, there were no residual drifts). These experiments demonstrated the system has sufficient performance for Immediate Occupancy (IO) of SC-MRF. Besides, the holes in the beam's web dissipate considerable energy under earthquake producing a structure 10% lighter than a traditional welded seismic moment resisting frame W-SMRF (Lin *et al.* 2013). The HS capabilities enabled a large number of evaluation tests to be performed rapidly and cost-effectively, and with fewer safety concerns.

Controlled Rocking of Steel-Framed Buildings (Project 75). A novel passive device was developed and designed to concentrate structural damage in a fuse element intended to be replaced after yielding. The structural system combines three components. The structural steel frames are designed to remain in the elastic range and are allowed to rock at the column base. Vertical post-tensioning strands provide self-centering forces. Fuse elements are used to dissipate energy while yielding. Nine large-scale quasi-static and HS tests were conducted at the University of Illinois at Urbana-Champaign to demonstrate the performance of the controlled rocking system (see Fig. 10(a)). Particularly, HS was used to demonstrate the robustness of the system to remain elastic when were subjected to ground motions, even when drift ratio was approximately 4% without any damage in the braced frame (Deierlein *et al.* 2005). Since the damage was located in the removable fuses (see Fig. 10(b)), a considerable amount of energy was dissipated (Eatherton *et al.* 2010). Here HS played an important role in capturing more realistic global responses of the structure, as well as incorporating its interaction with the fuse elements.

Tools to Facilitate Widespread Use of Isolation and Protective Systems (TIPS) (Project 571). This collaborative effort between researchers in the U.S and Japan (at E-Defense) focused on creating and promoting tools to facilitate adoption of isolation and protective systems. The existence of such tools was intended to simplify design procedures, disseminate knowledge regarding the use of seismic isolation technology, establish the linkage to building codes, and

confirm the impact of such isolators on seismic response of the buildings (Arendt *et al.* 2010, Ryan *et al.* 2013). A series of HS were performed using shake tables. A 2-story, 2-bay steel moment frame was the experimental substructure, representing the top two stories of a high rise building. The numerical substructure consisted of the lower portion of the building. The response of the numerical substructure was calculated and used as input to the upper stories (the experimental substructure) mounted on the shake table. The benefits of seismic isolation in such buildings were demonstrated. However, researchers concluded that changes in building codes and guidelines to simplify the use of seismic isolators are necessary. Moreover, these tests would not have been possible at this scale were it not for the HS method and its capacity to obtain specific responses from the experimental substructure to be used as feedback in the numerical analysis, which in this particular case, avoid the necessity of build a high-rise building for the test.

Innovative Applications of Damage Tolerant Fiber-Reinforced Cementitious Materials for New Earthquake-Resistant Structural Systems and Retrofit of Existing Structures (Project 47). In this project, to enhance the seismic performance of existing steel buildings, a retrofit system was developed and evaluated experimentally.A1980's steel building design in California was considered for the proposed retrofit. The proposed system consists of high-performance fiber-reinforced concrete (HPFRC) infill panels acting as energy dissipation elements that can be easily replaced after a major earthquake. The numerical substructure consisted of a 2-bay, 2-story SMRF building, and the experimental substructure consisted of a 2/3-scale model of 1-bay and 2-stories with 5 double infill panels per story. Hybrid simulation enabled realistic global assessment of the system, and showed that during a DBE the retrofit system reduces seismic demands by approximately 40% in terms of story and residual drift ratios compared with the un-retrofitted frame (Lignos *et al.* 2014).

Performance-Based Design for Cost-Effective Seismic Hazard Mitigation in New Buildings Using Supplemental Passive Damper Systems (Project 1018) and *Advanced Servo-Hydraulic Control and Real-Time Testing of Damped Structures* (Project 711).More than 170 RTHS were conducted at the Lehigh facility on 3-storysteel buildings and 2-storymoment resisting frame (MRF) buildings equipped with supplemental passive dampers. Both viscous fluid and elastomeric dampers were considered to assess their impact on the performance of the buildings, and to evaluate and validate the proposed design procedures (Dong *et al.* 2014). The experimental substructure was scaled to 60% with dampers. The numerical substructure was the remainder of the building. The results showed that when the elastomeric dampers were included in the MRF frame, the base shear was less than the design shear base specified by current specifications producing a structure lighter than a conventional SMRF (Mahvashmohammadi *et al.* 2013). The researchers concluded that advanced damping systems have strong potential for mitigating the impact of earthquakes on structures and meeting the objectives of performance-based design. However, additional realistic evaluations are a necessary step to increase awareness and encourage their adoption. Even so, the velocity dependent nature of the device and the need for including interactions between the device and frame necessitated the development of advances in RTHS as the test would not have been complete using only quasi-static testing.

Semiactive Control of Nonlinear Structures (Project 21), *Performance-Based Design and Real-Time Large-Scale Testing to Enable Implementation of Advanced Damping Systems* (Project 648),*Development of a Real-Time Multi-Site Hybrid Testing Tool for NEES* (Project 972), *Development and Validation of a Robust Framework for Real-time Hybrid Testing* (Project 1135), and *Real-Time Hybrid Simulation Test-Bed for Structural Systems with Smart Dampers* (Project 973).Each project produced an important contribution in different subjects. For instance, Project

21demonstrated the ability of semi-active control devices to improve the structural response subject to earthquake ground motion. Project 648conducted the first large-scale RTHS on a complex frame system using multiple actuators. Project 972 developed and demonstrated the capacity of NEES labs to conduct more complex RTHS by involving multiple laboratories and transferring information needed to conduct the test between those locations, which is known as geographically-distributed RTHS. Project 1135 concentrated on the evaluation of new hydraulic actuator control strategies to enable more representative RTHS. Project 973 worked to improve the performance of RTHS for evaluating structures controlled by semi-active devices.

This group of NEES projects were among the very first to successfully develop and validate RTHS methods to assess global structural response (Friedman *et al.* 2013).Initially, RTHS was conducted with a damper alone as the experimental substructure. Additional successes were achieved toward the development of geographically-distributed tests. After advances were made in the actuator controllers, more complex testing was performed using a damped steel MRF as the experimental substructure and RTHS was shown to be successful on a frame structure.

Once RTHS methods were developed and demonstrated, they were used to evaluate the global performance of the structures. Shared facilities capable of implementing large-scale RTHS were utilized to develop performance-based design methodologies for advanced damping systems and to develop high fidelity models for devices and improved control algorithms for model-based simulation study. New MR damper control strategies were developed and validated (Friedman *et al.*2014). The results indicated that large scale MR dampers could provide significant seismic response reduction even with the maximum credible earthquake (MCE). RTHS was essential to perform these tests as it provides an efficient and cost-effective tool for global evaluation of novel devices, such as MR damper controllers, that exhibit rate dependent behavior making real time execution necessary for accurate results (Phillips *et al.* 2010).

3. Conclusions

Developing resilient and sustainable communities will require an evolution in the ways that we conduct experiments and perform simulations. Infrastructure system design procedures must be supported by experiments that represent realistic conditions when those structures are in service. The availability of HS and RTHS have clearly expanded the types of testing that is possible to improve resilience and reduce earthquake risk in the built environment. The role of HS in enabling these tests has been exploited to evaluate the performance of new design concepts and structural systems and novel devices, as well as enabling code provisions to be examined with the most realistic loading conditions.

The projects revisited and reconstructed through the discussion herein encompass only those projects within the NEES network, providing a broad view albeit still a subset of what is possible using HS/RTHS. Among the projects considered are masonry, reinforced concrete, steel, dampers, bracing systems, and other novel concepts. Together these projects have demonstrated that HS and RTHS provide additional versatility, effectiveness, economy, safety and reliability for reproducing more realistic responses of complex structural and geotechnical systems. Because the numerical substructure can readily be replaced/modified, an unlimited number of structures and configurations can be examined with a single physical specimen. Furthermore, HS and RTHS enable testing of structural configurations that are too tall or too long to be adequately considered in a laboratory, such as long span bridges and high rise buildings. Several of these projects

concluded that such advantages were achieved with HS over traditional methods (quasi-static and shake table test). And when a test may be particularly costly or introduce certain safety concerns, HS and RTHS provides alternative approaches in enabling some new earthquake engineering concepts and research to be studied and performed.

Note that although HS has promising future, researchers such as those recognized herein are still working toward bringing this technology to the mainstream, and thus making them accessible to a broader set of researchers. A great deal is being learned about employing these methods in new situations to consider system behaviors. Each success leads HS and thus earthquake engineering toward achieving resilience through the examination and validation of novel systems under realistic situations. The possibility of conducting geographically distributed tests, as some of these projects have done, opens new doors to testing complex systems.

The capabilities of hybrid simulation continue to be explored in several more projects that are in progress. For updates and details, see: https://nees.org/wiki/RTHSwiki

Acknowledgments

Financial support was provided by the Colombia-Purdue Institute for Advanced Scientific Research (CPI), Universidad del Valle and Purdue University. The NEES hub (https://nees.org/) was established with funding from the US National Science Foundation under Award Number CMMI-0927178. The authors also acknowledge the dedication of NEES researchers who published their data via the Network for Earthquake Engineering Simulation Data Repository. Project data and images contained herein are available through the NEES hub, supported by the NSF Network for Earthquake Engineering Simulation Research (NEESR)Program under Award Numbers: CMMI-724172, CMMI-0116005, CMMI-0829978, CMMI-0936633, CMMI-0530737, CMMI-0324277, CMMI-0420974, CMMI- 0530756.

References

AASHTO (1995), *Standard specifications for highway bridges, division I-A: seismic design american association of state highway and transportation officials, Inc.*, 15th Ed., as amended by the Interim Specification - Bridges, Washington, DC.

ACI Committee, American Concrete Institute and International Organization for Standardization (2008), *Building code requirements for structural concrete and commentary (ACI 318-08)*, Farmington Hills, MI.

American Institute of Steel Construction AISC(2010),*Seismic provisions for structural steel buildings*, Chicago, IL.

Arendt, L.A., Earle, S. and Meyers, R. (2010), "Results of a cross-disciplinary survey on isolation systems decision making", *Proceedings of the 9th U.S. Natl. and 10th Canadian Conf. on Eq. Eng*, Toronto, Canada, July.

Chen, C., Ricles, J.M., Karavasilis, T.L., Chae, Y. and Sause, R. (2012), "Evaluation of a real-time hybrid simulation system for performance evaluation of structures with rate dependent devices subjected to seismic loading", *Eng. Struct.*, **35,** 71-82.

Christenson, R., Dyke, S.J., Zhang, J., Mosqueda, G., Chen, C., Nakata, N., Laplace, P., Song, W., Chae, Y., Marshall, G., Ou, G., Song, C. and Riascos, C.A. (2014), *Hybrid simulation: a discussion of current assessment measures*, https://nees.org/resources/12876.

Deierlein, G.G., Billington, S. and Hajjar, J.F. (2005), *Controlled rocking of steel-framed buildings*, April 24, 2014. https://nees.org/warehouse/project/75

Deierlein, G., Arduino, P., Assimaki, D., Caicedo, J.M., Dyke, S.J., Hachem, M.M., Irfanoglu, A., McKenna, F., Lynett P., Lowes, L.N., Mejia, L. Mazzoni, S., Mosqueda, G., Nakata, N., Zhang, J. and Rodgers, G.P. (2011), *NEES Vision Report on Computational and Hybrid Simulation*, NEEScomm Simulation Steering Committee,April 24, 2014. http://nees.org/resources/3834.

Dong, B., Sause, R., Ricles, J., Ahn, R., Chae, Y., Marullo, T. and Novak, G. (2014), "Real-time Hybrid Simulation of a large-scale steel structure with Viscous Dampers-Phase 2", Network for Earthquake Engineering Simulation (distributor), Dataset, DOI:10.4231/D3GH9B894

Elkhoraibi, T. and Mosalam, K.M. (2007), *Generalized hybrid simulation framework for structural systems subjected to seismic loading*, PEER report 101, University of California, Berkeley.

Eatherton, M., Hajjar, J.F., Deierlein, G.G., Ma, X. and Krawinkler, H. (2010), "Hybrid simulation testing of a controlled rocking steel braced frame system", *Proceedings of the 9th U.S. National and 10th Canadian Conf. on Earthquake Eng*, Toronto, Canada, July.

Friedman, A., Phillips, B., Ahn, R., Chae, Y., Zhang, J., Cha, Y., Dyke, S.J., Ricles, J., Spencer, B., Christenson, R. and Sause, R. (2013), "RTHS (Frame + Damper) - 3StoryPS - Single MR Damper (Floor 1)", Network for Earthquake Engineering Simulation (distributor), Dataset, DOI:10.4231/D3G15TB42

Friedman, A., Dyke, S.J., Phillips, B., Ahn, R., Dong, B., Chae, Y., Castaneda, N., Jiang, Z., Zhang, J., Cha, Y., Ozdagli, A.I., Spencer, B.F., Ricles, J., Christenson, R., Agrawal, A. and Sause, R. (2014), "Large-scale real-time hybrid simulation for evaluation of advanced damping system performance", *J. Struct. Eng*. - ASCE, 10.1061/(ASCE)ST.1943-541X.0001093 , 04014150.

Gomez, D., Dyke, S.J, and Maghareh, A. (2014), *Enabling role of hybrid simulation within the NEES network in advancing earthquake engineering practice and research*, Intelligent Infrastructure Systems Lab Technical Report IISL-008. Purdue University, August. https://nees.org/resources/13496

Hacker, T.J., Eignenmann, R., and Rathje, E. (2013), "Advancing earthquake engineering research through cyberinfrastructure", *J. Struct. Eng. - ASCE*, **139**(7), 1099-1111.

Hakuno, M., Shidawara, M. and Hara, T. (1969), "Dynamic destructive test of a cantilever beam controlled by an analog-computer", *T. Japan Soc. Civil Eng*., **171,** 1-9. (in Japanese).

Halbert, P.W., Landauer, J.P. and Witsenhausen, H.S. (1963), "Hybrid simulation of adapt path control", *Proceedings of the AIAA Simulation for Aerospace Flight Conference*, Columbus, Ohio, USA, August.

Hashemi, A. and Mosalam, K.M. (2006), "Shake-table experiment on reinforced concrete structure containing masonry infill wall", *Earthq. Eng. Struct. D.*, **35**(14), 1827-1852.

Hashemi, M.J. and Mosqueda, G. (2014a), "Innovative substructuring technique for hybrid simulation of multistory buildings through collapse", *Earthq. Eng. Struct. D.*, **43**(14), 2059-2074.

Hashemi, M.J. and Mosqueda, G. (2014b), "Hybrid simulation of 4 story frame to collapse using 1.5 story substructure", Network for Earthquake Engineering Simulation (distributor), Dataset, DOI:10.4231/D3F18SG1T

Heartz, R.A. and Jones, T.H. (1964), "Hybrid simulation of space vehicle guidance system", *Proceedings of the International Space Electronics Symposium*, Las Vegas, Nevada, USA, October.

Kim, S.J., Holub, C.J. and Elnashai, A.S. (2011), "Experimental investigation of the behavior of RC bridge piers subjected to horizontal and vertical earthquake motion", *Eng. Struct.*, **33**(7), 2221-2235.

Li, J., Spencer, B.F. and Elnashai, A.S. (2013), "Bayesian updating of fragility functions using hybrid simulation", *J. Struct. Eng. - ASCE*, **139**(7), 1160-1171.

Lignos, D. (2008), *Sidesway collapse of deteriorating structural systems under seismic excitations*, Ph.D. Dissertation, Stanford University, California.

Lignos, D., Moreno, D. and Billington, S. (2014), "Seismic retrofit of steel moment-resisting frames with high-performance fiber-reinforced concrete infill panels: large-scale hybrid simulation experiments", *J. Struct. Eng. - ASCE*, **140**(3), 04013072.

Lin, P.C., Tsai1, K.C., Wang, K.J., Yu, Y.J, Wei, C.Y., Wu, A.C., Tsai, C.Y., Lin, C.H., Chen, J.C., Schellenberg, A.H., Mahin, S.A. and Roeder, C.W. (2012), "Seismic design and hybrid tests of a full-scale three-story buckling-restrained braced frame using welded end connections and thin profile", *Earthq. Eng. Struct. D.*, **41**(5), 1001-1020.

Lin, S.L., Li, J., Elnashai, A.S. and Spencer, B.F. (2012), "NEES integrated seismic risk assessment

framework (NISRAF)", *Soil Dyn. Earthq. Eng.*, **42**, 219-228.
Lin, Y., Sause, R. and Ricles, J. (2013), "Seismic performance of steel self-centering, moment-resisting frame: hybrid simulations under design basis earthquake", *J. Struct. Eng. - ASCE*, **139**(11), 1823-1832.
Leon, R., Yang, C., DesRochers, R., Reinhorn, A., Schacter, M., Stojadinovic, B., Yang, T., Shing, B. and Wei, Z. (2005), "Results of early collaborative research on behavior of braced steel frames with innovative bracing schemes (Zipper Frames)", *Proceedings of the 1st International Conference on Advances in Experimental Structural Engineering*, AESE, Nagoya, Japan.
Mahin, S.A., Shing, P.B., Thewalt, C.R. and Hanson, R.D. (1989), "Pseudodynamic test method current status and future directions", *J. Struct. Eng. - ASCE*, **115**(8), 2113-2128.
Mahvashmohammadi, A., Sause, R., Ricles, J. and Marullo, T. (2013), *Real-time hybrid simulations on a large-scale steel MRF building with elastomeric dampers*, ATLSS Center, Department of Civil and Environmental Engineering, Lehigh University, Bethlehem, Pennsylvania. (Report)
Nakashima, M., Kato, H. and Takaoka, E. (1992), "Development of real-time pseudo dynamic testing", *Earthq. Eng. Struct. D.*, **21**(1), 79-92.
Nakata, N., Dyke, S.J., Zhang, J., Mosqueda, G., Shao, X., Mahmoud, H., Head, M.H., Bletzinger, M. Marshall, G.A., Ou, G. and Song, C. (2014), "Hybrid Simulation Primer and Dictionary", https://nees.org/resources/7702.
Open Sees (2006), "Open System for Earthquake Engineering Simulation", http://opensees.berkeley.edu
Pejša, S., Dyke, S.J. and Hacker, T. (2014), "Building infrastructure for preservation and publication of earthquake engineering research data", *Int. J. Data Curation*, **9**(2), 83-97.
Phillips, B M., Chae, Y., Jiang, Z., Spencer, B.F., Ricles, J.M., Christenson, R.E., Dyke, S.J, and Agrawal, A. (2010), "Real-time hybrid simulation benchmark study with a large-scale MR damper", *Proceedings of the 5th World Conference on Structural Control and Monitoring*, Shinjuku, Tokio, July.
Ramirez, J. (2012). "The George E. Brown Jr., Network for Earthquake Engineering Simulation (NEES): Reducing the Impact of EQs and Tsunamis", *Proceedings of the 15 World Conf. in Earthquake Engineering*, Lisbon, Portugal, September.
Ryan, K., Sato, E., Sasaki, T., Okazaki, T., Guzman, J., Dao, N., Soroushian, S. and Coria, C. (2013), "Full Scale 5-story Building with LRB/CLB Isolation System at E-Defense", Network for Earthquake Engineering Simulation (distributor), Dataset, DOI:10.4231/D3SB3WZ43
Schellenberg, A. and Mahin, S. (2006), "Integration of hybrid simulation within the general-purpose computational framework Open Sees", *Proceedings of the 100th Anniversary Earthquake Conference*, San Francisco, California, April.
Shao, X. and Griffith, C. (2013), "An overview of hybrid simulation implementations in NEES projects", *Eng. Struct.*, **56**, 1439-1451.
Shing, P.B., Nakashima, M. and Bursi, O.S. (1996), "Application of pseudo dynamic test method to structural research", *Earthq. Spectra*, **12**(1), 29-56.
Takanashi, K, and Nakashima, M. (1987), "Japanese activities on on-line Testing", *J. Eng. Mech. - ASCE*, **113**(7), 1014-1032.
Takanashi, K., Udagawa, K., Seki, M., Okada, T. and Tanaka, H. (1975), "Non-linear earthquake response analysis of structures by a computer-actuator on-line system", *Transactions of the Architectural Institute of Japan*, May.
Tsai, C.Y., Tsai, K.C., Lin, P.C., Ao, W.H., Roeder, C.W., Mahin, S.A., Lin, C.H., Yu, Y.J., Wang, K.J., Wu, A.C., Chen, J.C. and Lin, T.H. (2013), "Seismic design and hybrid tests of a full-scale three-story concentrically braced frame using in-plane buckling braces", *Earthq. Spectra*, **29**(3), 1043-1067.
Whyte, C.A, Barthes, C., Gunay, S., Park, S., Patterson, D., Takhirov, S. and Stojadinovic B. (2013), "Hybrid simulation of the seismic response of squat reinforced concrete walls - Wall 1 Test", Network for Earthquake Engineering Simulation (distributor), Dataset, DOI:10.4231/D34T6F32M
Whyte C.A. and Stojadinovic, B. (2012), "Hybrid simulation of the seismic response of squat reinforced concrete shear walls", *Proceedings of the 15 World Conf. in Earthquake Engineering*, Lisbon, Portugal, September.
Witsenhausen, H.S. (1964), "Development of a program for the hybrid simulation of a tubular reactor",

Annales de l'Association internacionale pour le calculana logique, **2**, 112-117.
Yang, T.Y., Stojadinovic, B. and Moehle, J. (2009), "Hybrid simulation of a zipper-braced steel frame under earthquake excitation", *Earthq. Eng. Struct. D.*, **38**, 95-113.

List of Recent NSEL Reports

No.	*Authors*	*Title*	*Date*
026	Hall, K., Eatherton, M.R., and Hajjar, J.F.	Nonlinear Behavior of Controlled Rocking Steel-Framed Building Systems with Replaceable Energy Dissipating Fuses	Oct. 2010
027	Yeo, D. and Jones, N.P.	Computational Study on 3-D Aerodynamic Characteristics of Flow around a Yawed, Inclined, Circular Cylinder	Mar. 2011
028	Phillips, B.M. and Spencer, B.F.	Model-Based Servo-Hydraulic Control for Real-Time Hybrid Simulation	June 2011
029	Linderman, L.E., Mechitov, K.A., and Spencer, B.F.	Real-Time Wireless Data Acquisition for Structural Health Monitoring and Control	June 2011
030	Chang, C.-M. and Spencer, B.F.	Multi-axial Active Isolation for Seismic Protection of Buildings	May 2012
031	Phillips, B.M. and Spencer, B.F.	Model-Based Framework for Real-Time Dynamic Structural Performance Evaluation	August 2012
032	Moreu, F. and LaFave, J.M.	Current Research Topics: Railroad Bridges and Structural Engineering	October 2012
033	Linderman, L.E., Spencer, B.F.	Smart Wireless Control of Civil Structures	January 2014
034	Denavit, M.D. and Hajjar, J.F.	Characterization of Behavior of Steel-Concrete Composite Members and Frames with Applications for Design	July 2014
035	Jang, S. and Spencer, B.F.	Structural Health Monitoring for Bridge Structures using Wireless Smart Sensors	May 2015
036	Jo, H. and Spencer, B.F.	Multi-scale Structural Health Monitoring using Wireless Smart Sensors	May 2015
037	Li, J. and Spencer, B.F.	Monitoring, Modeling, and Hybrid Simulation: An Integrated Bayesian-based Approach to High-fidelity Fragility Analysis	May 2015
038	Sim, S-H. and Spencer, B.F.	Decentralized Identification and Multimetric Monitoring of Civil Infrastructure using Smart Sensors	June 2015
039	Giles, R.K. and Spencer, B.F.	Development of a Long-term, Multimetric Structural Health Monitoring System for a Historic Steel Truss Swing Bridge	June 2015
040	Spencer, B.F., Moreu, F. and Kim, R.E.	Campaign Monitoring of Railroad Bridges in High-Speed Rail Shared Corridors using Wireless Smart Sensors	June 2015
041	Moreu, F. and Spencer, B.F.	Framework for Consequence-based Management and Safety of Railroad Bridge Infrastructure Using Wireless Smart Sensors (WSS)	June 2015
042	Spencer, B.F. and Gardoni, P. (Eds.)	Innovations and Advances in Structural Engineering: Honoring the Career of Yozo Fujino	June 2015

Appendix: Photo Album of Yozo FUJINO's Research Career with his Students, Friends, and Colleagues

Yozo FUJINO was born in September 27, 1949 in Tokyo.

With my father and mother, elder brother and elder sister

Researcher Parties No. 1
Bridge and Structure Laboratory, University of Tokyo

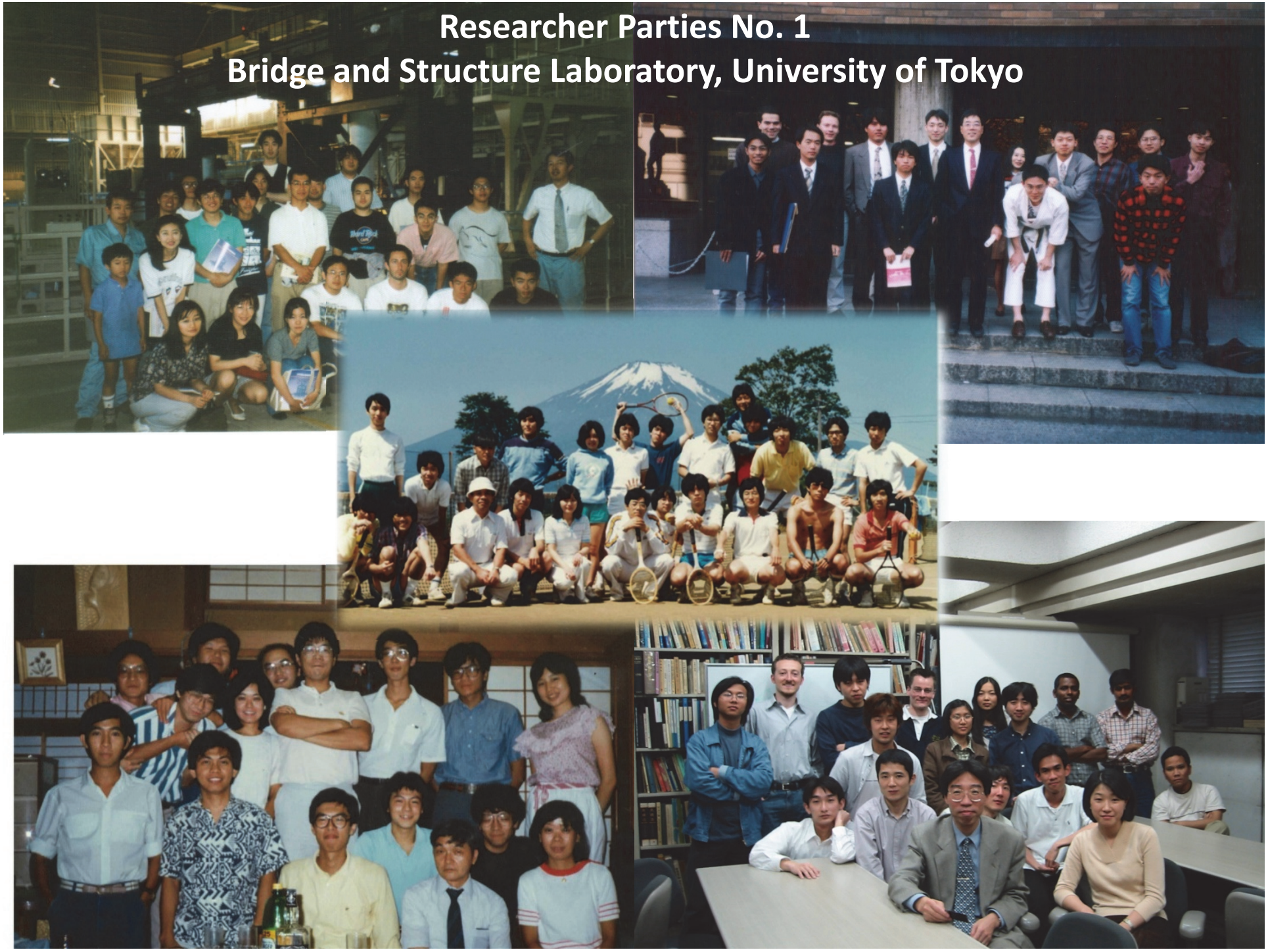


Researcher Parties No. 2

Bridge and Structure Laboratory, University of Tokyo


Field Trips
Bridge and Structure Laboratory
University of Tokyo

February 1990: Tennis trip of Bridge Lab of Todai, Prof. Fujino (1st row, 2nd from right); Limin Sun (3rd row, center)

At the top of a pylon of Rainbow Bridge, Tokyo, 2007.

Prof. Yamaguchi was an assistant professor of Bridge and Structures Laboratory just before I joined and is a very close friend of mine. He is now the president of Saitama University in Japan.

Mountain climbing with Prof. Hiroki Yamaguchi (left in the right photo and right in the right photo) in 1980's.

With Mr. Oguri (middle) (formerly research associate Bridge and Structure Lab) and Prof. H. Yamaguchi around 1980

Photo with Prof Yamaguchi (middle) in Stutgart, Germany after attending the First Cable Dynamics Conference in Belgium, 1995.

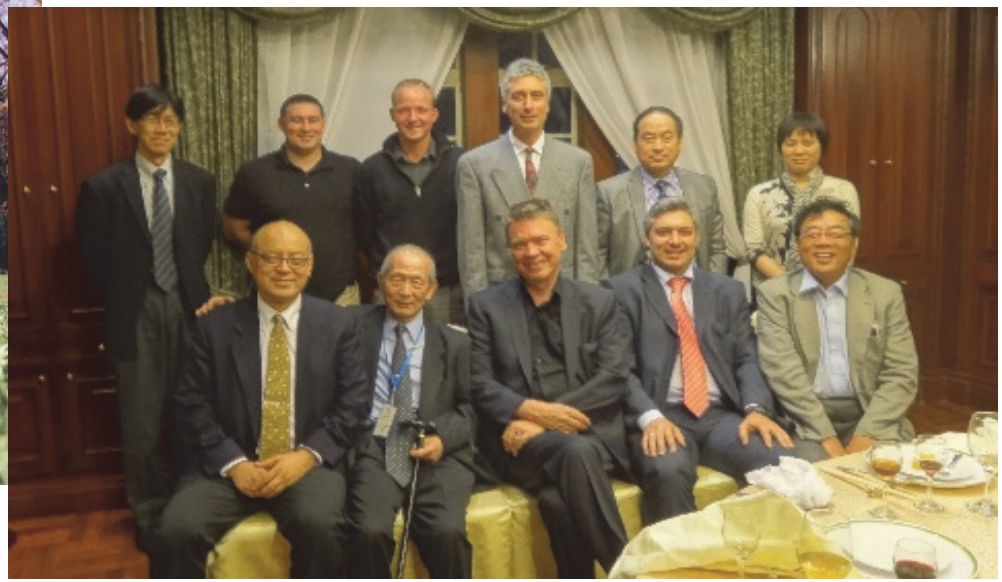

9th Cable Dynamics Conference in Shanghai, 2012.

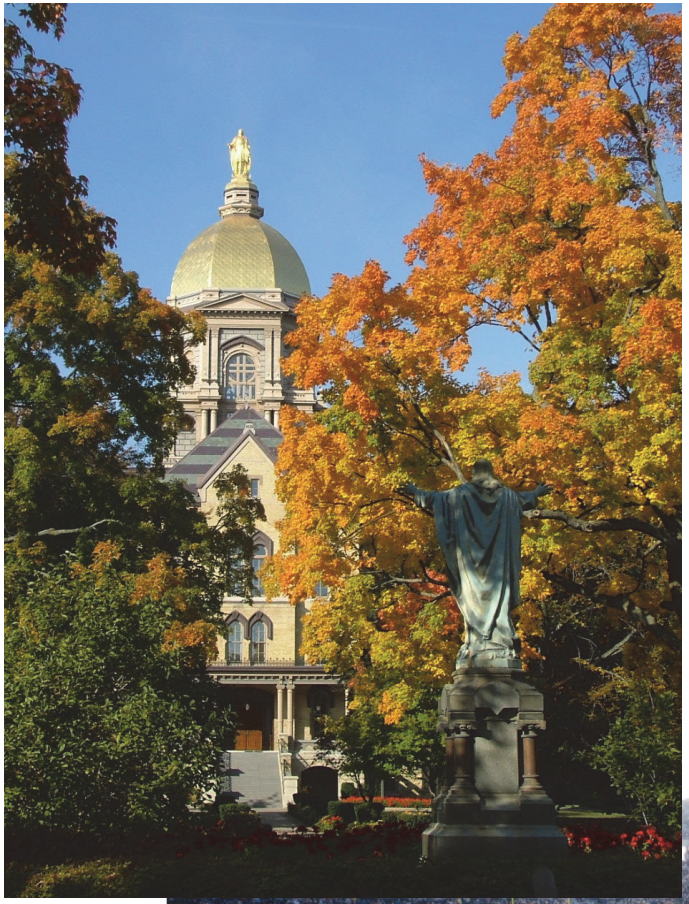

University of Notre Dame

Professor B.F. Spencer invited me to University of Notre Dame as a visiting professor in 1997. I spent about four months from August to December. I enjoyed this period with my family very much.

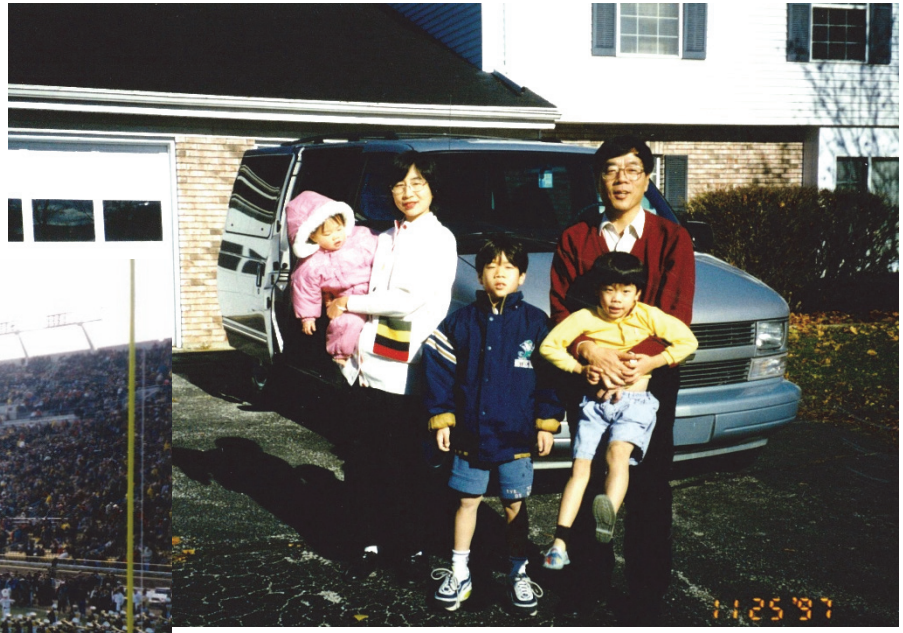

My residence in South Bend, Indiana

We enjoyed the American Football Games at Notre Dame Stadium

University of Notre Dame

Going away party at Spencer house
December 1997

Professor B.F. Spencer invited me to University of Notre Dame as a visiting professor in 1997. I spent about four months from August to December. I enjoyed this period with my family very much.

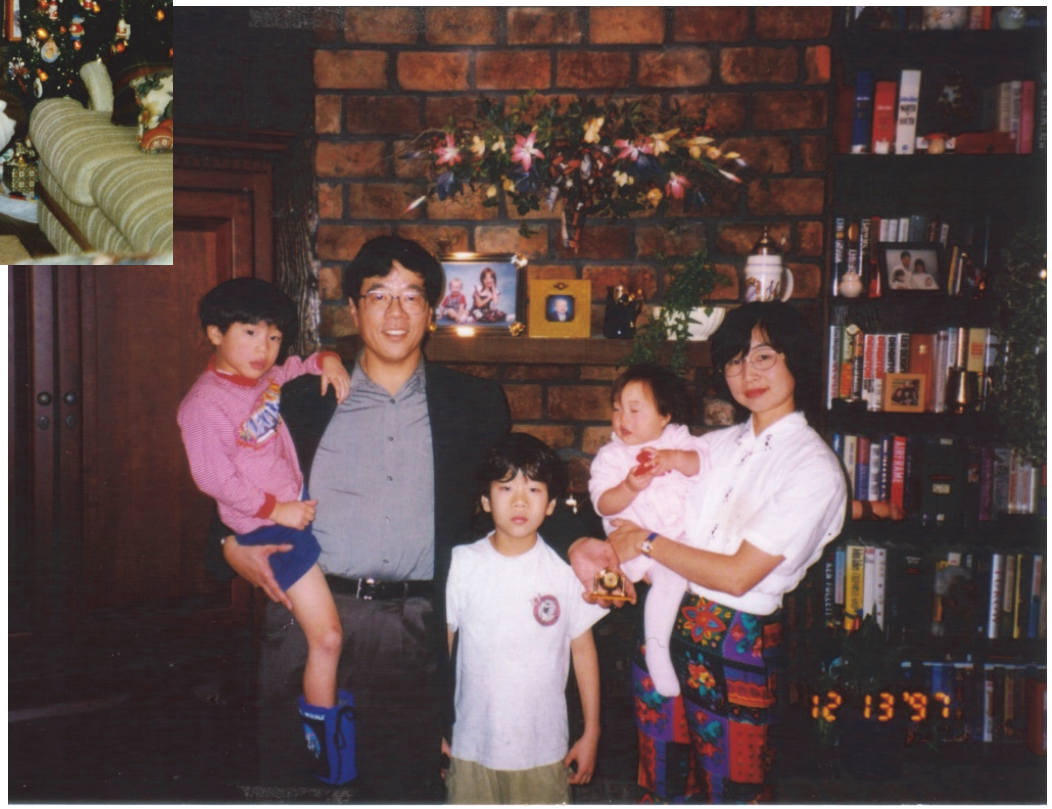

With my wife, Atsuko, and my three children:
Toru, Satoru and Kaoru

Our winter excursions (1997)

On the campus of University of Waterloo where I studied from 1973 to 1976 as a PhD student and later a Postdoc fellow

In Ottawa

At Orchard-Down Apartment of UIUC where we spent two months as a visiting fellow. Photo was taken in front of the apartment where we lived

Our winter excursions (1997)

We visited to Prof Robert W. Scanlan, Johns Hopkins University. Professor Scanlan is an expert in bridge aero-dynamics

Visit to to the home of David and Phyllis Billington, Princeton University. Professor Billington is an expert in structural form and elegance.

Dinner with my friends on a return visit to Notre Dame in 1998: Bill Spencer, David Kirkner, Ahsan Kareem, Gino Kurama, Rob Fleischman, and Erik Johnson

Prof. B.F. Spencer also often visited Japan and came to my residence too (February 2000)

Notre Dame Alumni Party in Tokyo, 2002

With Nishitani

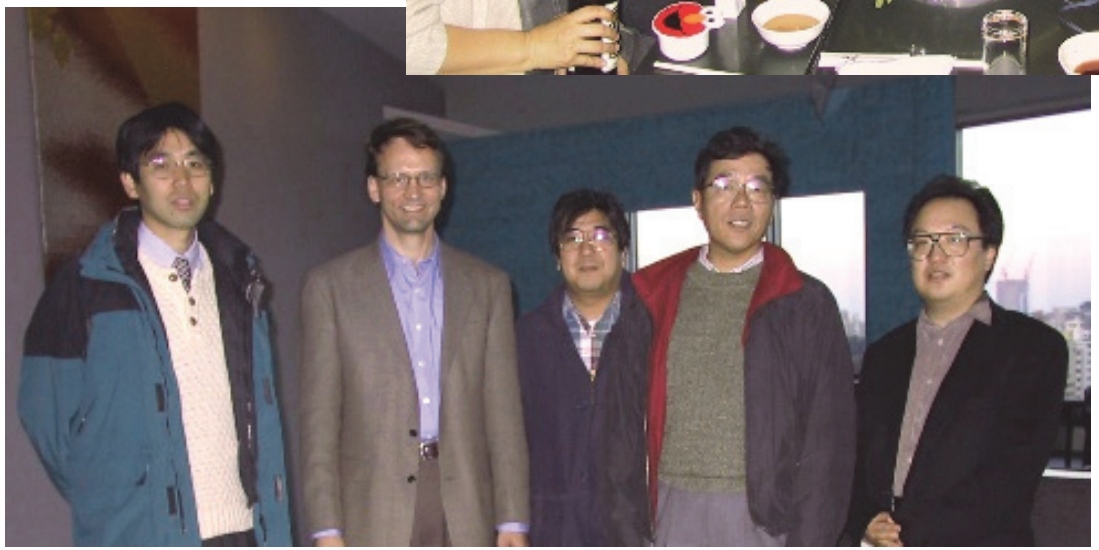

With Ohtori, Spencer, Ohdo, and Yoshioka

US-Japan Workshop on Structural Control in Hawaii, 1991 (photo by Yozo)
Prof. G. W. Housner, Prof. W. Hall, and Prof. S. Masri

George W. Housner visits Japan (1998)

Dr. Masato Abe and I interviewed Prof. Housner and asked his views on research and education.

Dr. Masato Abe worked with me for several years as a faculty at the University of Tokyo.

Prof G.W. Housner stayed at University of Tokyo in July 1998 for two weeks. I was very honored to serve as his host.

Prof. Housner and Prof. Kanai with me.

George W. Housner visits Japan (1998)

With many of friends at my residence, summer 1998

Shirley Dyke (front middle)
Akira's wife (front midle)
Atsuko and my three children
(Satoru, Kaoru and Toru)

Prof. Seto (middle from left)
Prof. Sami Masri
Prof. Larry Bergman
Prof. G.W. Housner
Dr. M. Abe
Dr. F. Sakai

George W. Housner visits Japan (1998)

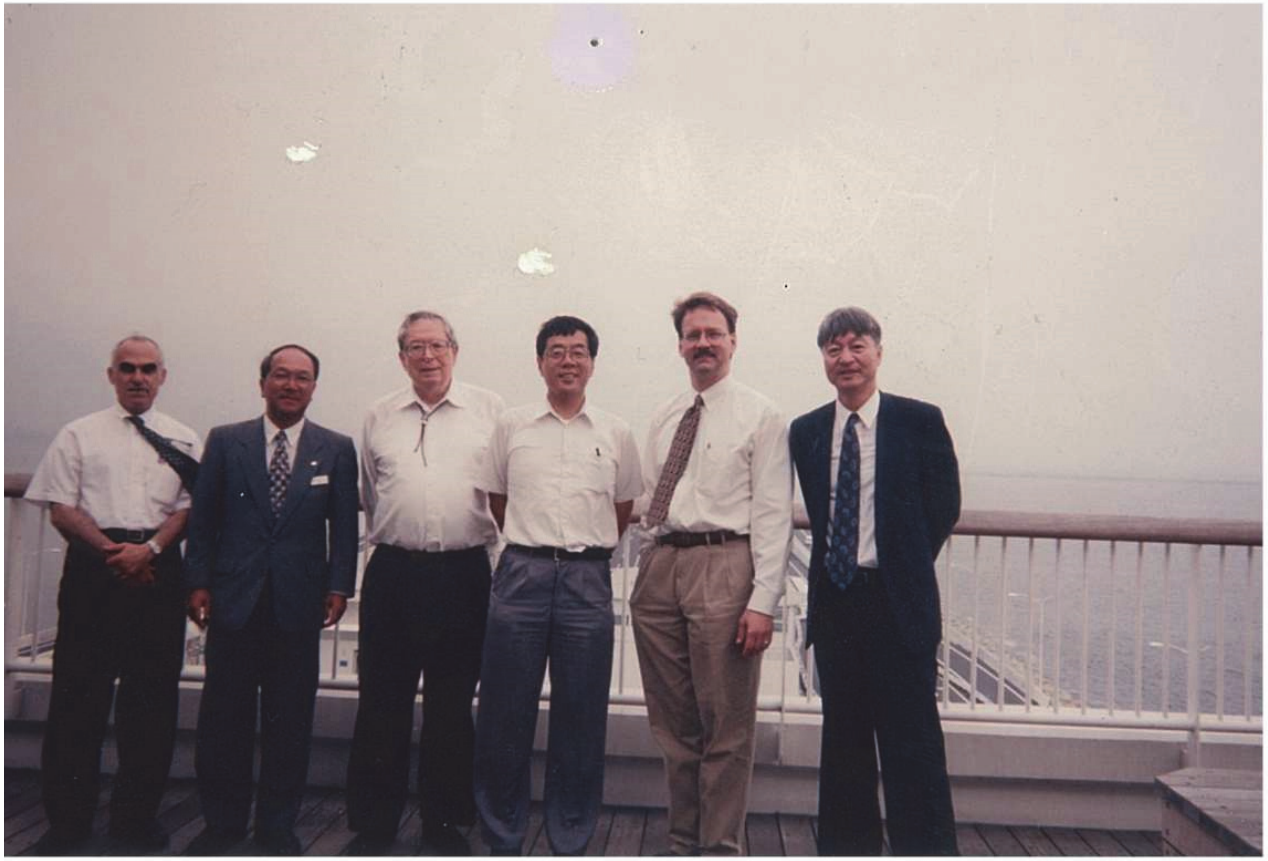

At the man-made island of Tokyo Bay Crossing (Tunnels and Bridges) in July 1998.

With Profs. Housner, Masri, and Spencer.

With Prof. Takuji Kobori at the International Worskshop on Structural Control, Paris, 2000.

At the Kobori Research Institute
November 2005

First US-Japan Summer Symposium for Young Researchers in Structural Engineering and Hazard Mitigation
University of Tokyo, July, 1998

Professor George W. Housner came to Japan to attend the 2nd WCSC in Kyoto and was staying at the University of Tokyo under the JSPS Fellowship program. We were very lucky he could join us.

Professor Spencer and I hosted this Symposium. Dr. Chi Liu at NSF has been a great supporter to this event. Some of participants in this Symposium became professors who are now very active in structural control and monitoring participated. You can find Profs. Lynch, Sun, Dyke, Watanabe, and Christensen in this photo.

NSF's Natural Hazard Mitigation in Japan Program

2nd Young Researchers Symposium at the University of Tokyo

NHMJ 2000. Yozo and Bill enjoying with the students.

3nd Young Researchers Symposium at the University of Tokyo, 2002

Field trip to the main campus of the University of Tokyo by participants of the 1st Asia-Pacific Workshop on Structural Health Monitoring, held at Keio University, December 2006.

US-Japan Workshop
University of Tokyo, 2007

5th World Conference on Structural Control and Monitoring, Tokyo, July 2010 (Chair: Yozo FUJINO)

5th World Conference on Structural Control and Monitoring, Tokyo, July 2010 (Chair: Yozo FUJINO)

Prof. C. Boller and his wife,
Yukari at the banquet of 5WCSCM

Retirement Celebration for Prof. J.M. Ko
of Hong Kong PolyU during 5WCSCM

With Profs. Shirley Dyke and Anil Agrawal

Board of Directors, International Association for Structural Control and Monitoring

At the 4th World Conference of Structural Control and Monitoring, San Diego, 2006

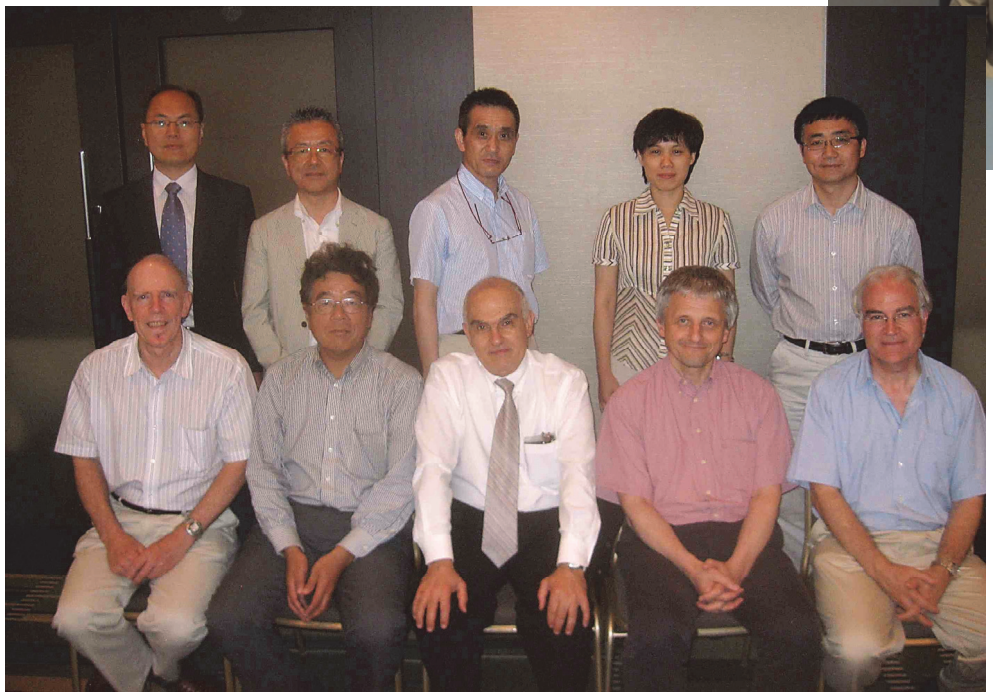

At the 5th World Conference of Structural Control and Monitoring, Tokyo, 2010

Asia-Pacific Summer School on Smart Structures Technology
University of Tokyo, July 2010

Opening Reception for APSS Students

Asia-Pacific Summer School on Smart Structures Technology
University of Tokyo, July 2010

Visit to Mt. Takao during 2010 APSS

Farewell party for APSS 2010 Students

Prof. Li-Min Sun of Tongji University studied for his Master and Ph. Degrees at University of Tokyo.
His research topic was modelling of TLD (Tuned Liquid Damper).

January 1989 – at Fujino's home party w/ Limin Sun (left)

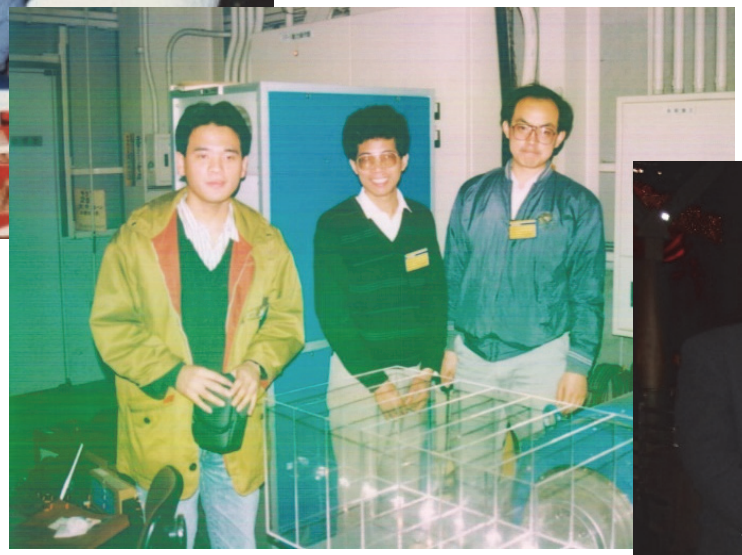

Limin Sun (right) in Shimizu Research Center in 1990.

After 20 years In 2012 at Shanghai with his family.

With my former students Profs. Piotr Omenzetter, Limin Sun, and Anil Agrawal at the 4th World Conference of Structural Control and Monitoring, San Diego, 2010.

Taken in Prof. Fujino's office on 29 June 2004, Dr. Xia's last day in Bridge and Structure Laboratory, the University of Tokyo (UT) after working with Prof. Fujino almost two years there as JSPS Fellow.

Field measurement at Jindo Bridge,
Korea in August , 2009

Collaboration project of KAIST, UIUC
and Univ. of Tokyo

Prof. Hyung-Jo Jung(left front)
Prof. Chung-Bang Yun(right, next to me)
Profs. Bill Spencer and Tomo Nagayama
can be found too.

ANCRiSST Workshop at UNIST, Korea on July 20, 2013.

Yozo's keynote lecture (Profs. Chung-Bang Yun, Prof. Bill Spencer and Prof. Hui Li (from right)

ANCRiSST Workshop Banquet at the Dalian Institute of Technology, Dalian, China, 2009

ANCRiSST Workshop 2012, Opening Session at the Indian Institute of Science, Bangalore, India

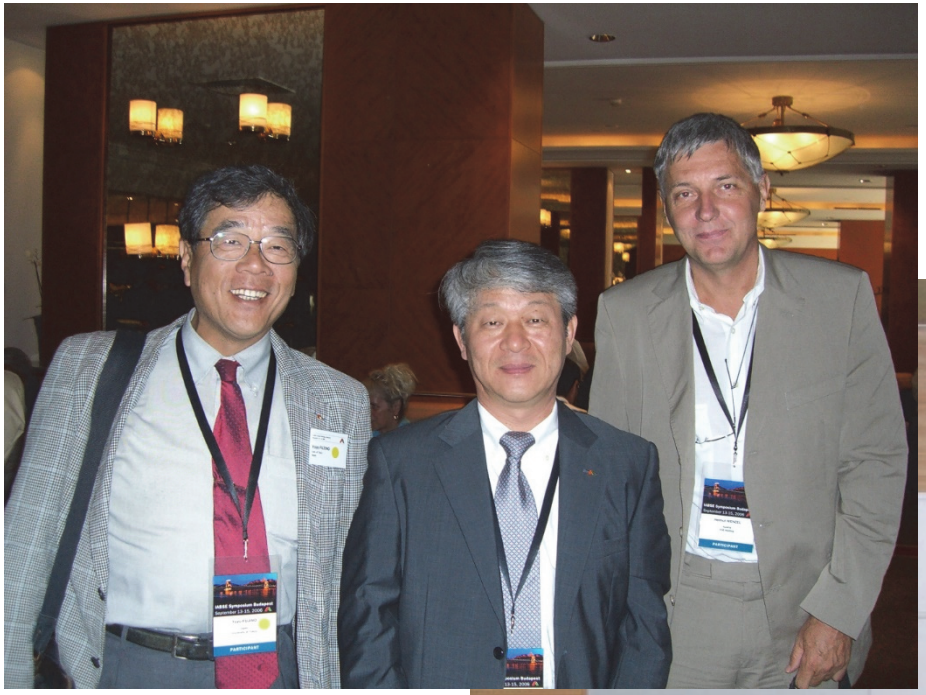

With Prof Myun-Moo Koh and Dr Helmut Wenzel
in IABSE Annual Conference at Budapest, Hungry,
In Sept., 2009

Visiting Prof. Koh with Prof K. Kawashima at Seoul National University in Nov., 2012

Prof. Fujino often visited the Hong Kong Polytechnic University since he has many friends there. The photo left after his seminar to students/staff of Department of Civil and Environmental Engineering in November 2006.

Prof. Fujino delivered a research seminar at Hong Kong Polytechnic University in 2009, chaired by Prof. Y.L. Xu.

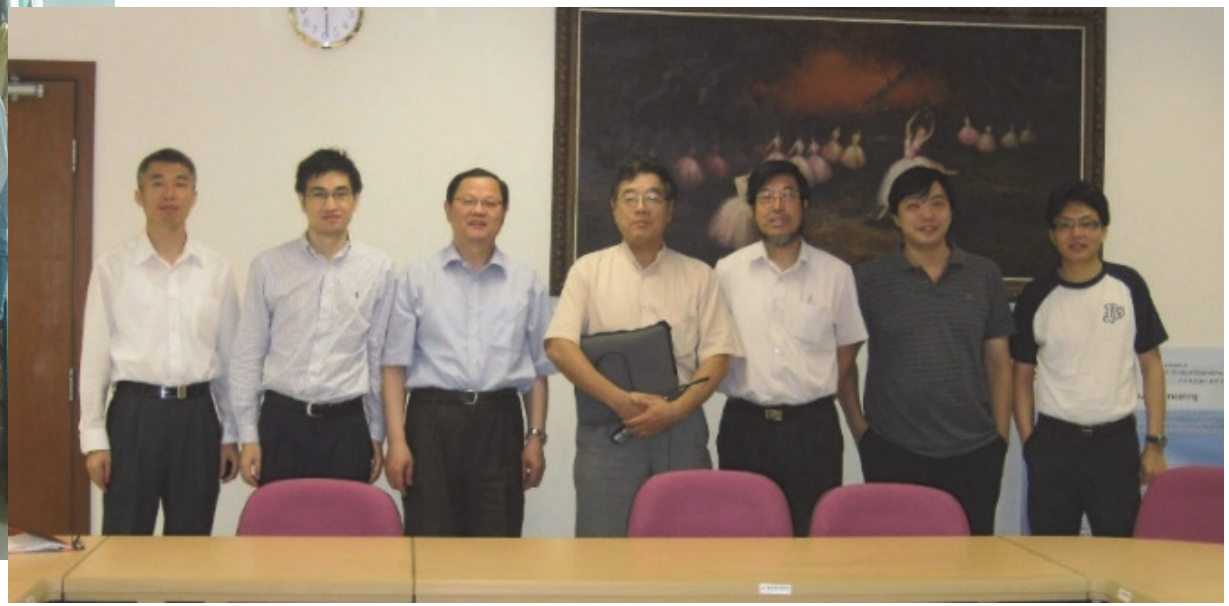

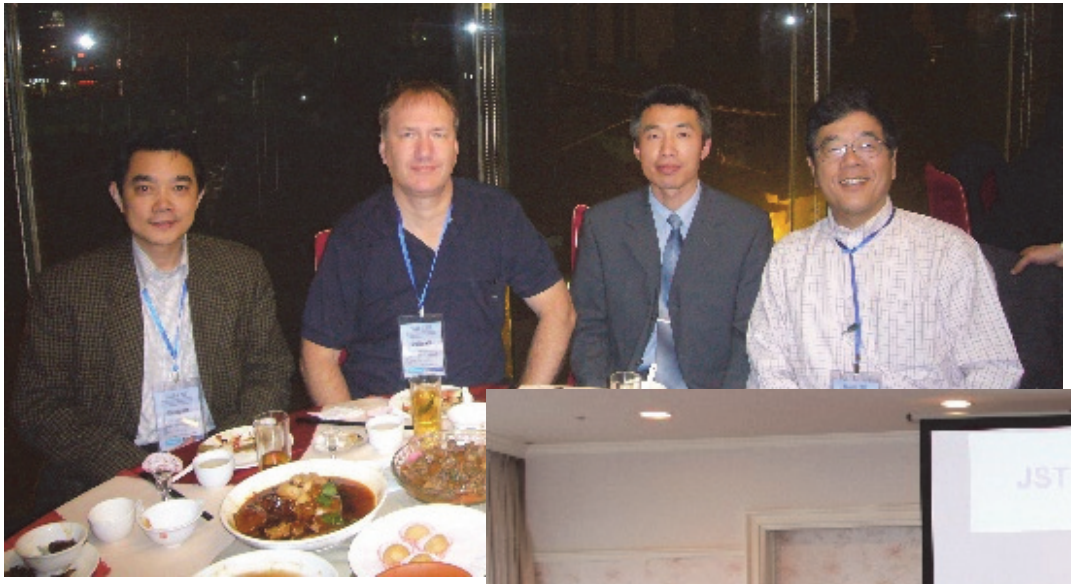

SHMII conference in Hong Kong, December 2013

JST-NSFC Joint Workshop
(Sapporo, June 10-11, 2009)

Lecture at Harbin Institute of Technology, April, 2011 (with Prof Li Hui)

With friends of Tongji University during the 100-year anniversary of the Department of Civil Engineering in November 2014.

With Profs. Ang, Frangopol, and Furuta at the IALCCE 2014 in Tokyo.

At Exeter University in March, 2014
with J.M.W. Brownjohn and
Prof. B. F. Spencer

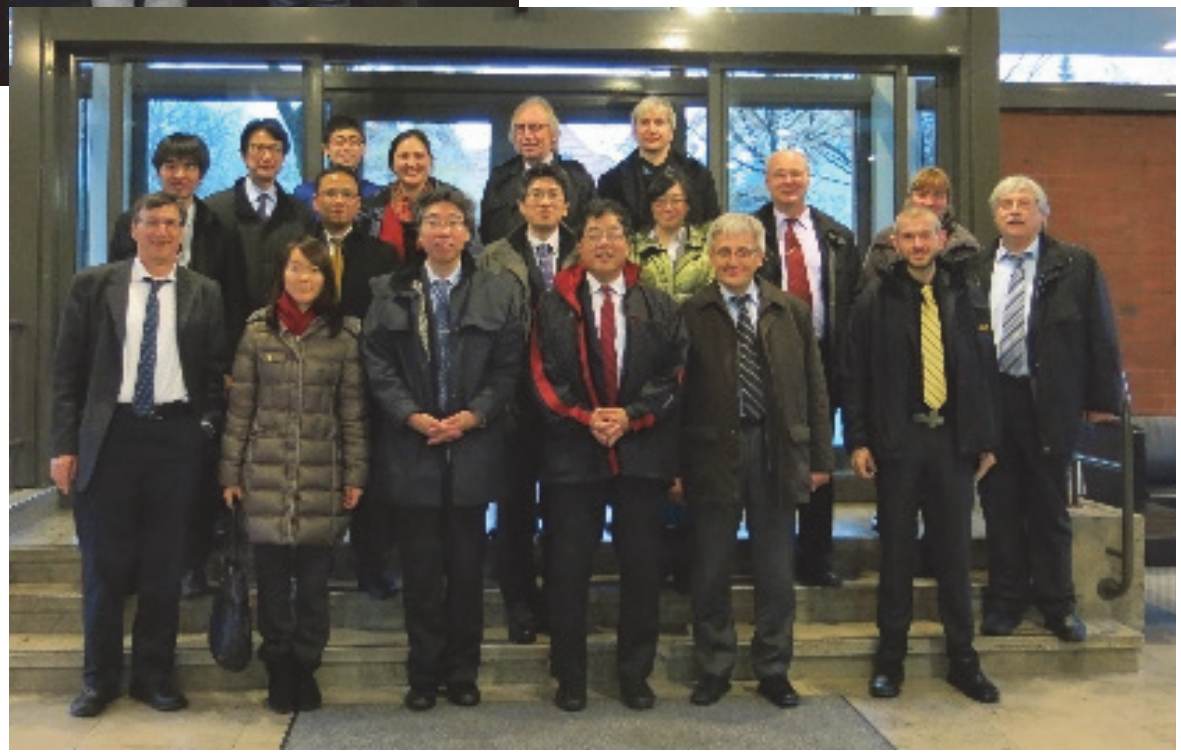

At BAM, Berlin, 2013
with Prof. Christian Boller
left in front line

Prof. Satish Nagarajaiah visited University of Tokyo in 2007.

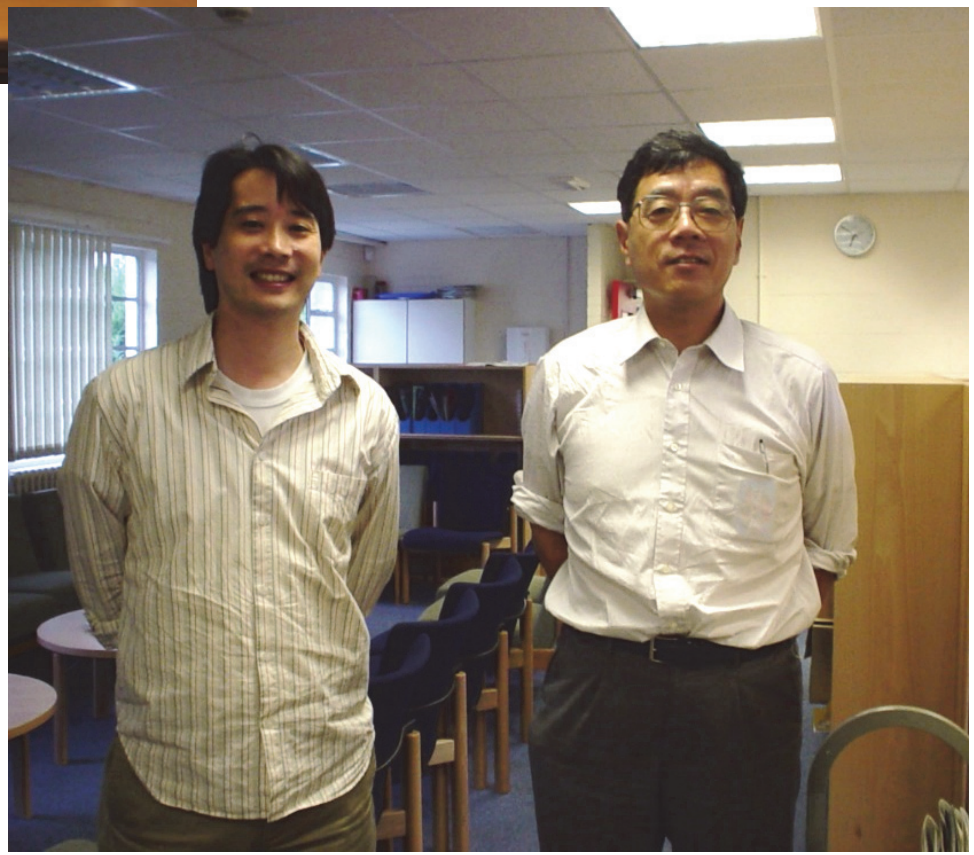

With Prof. K. Soga in July 2003 at Cambridge University.

Friends in New York City

Professor R. Betti and Dr. B. Yanev
at Columbia University, May, 2011
Cable corrosion experiment

Prof. Fujino leading a group of Japanese engineers on a visit to Dr. Bojidar's office at NYC DOT circa 1990s.

d Tokyo in 2009 to attend
bridge management
sion of his book was

At the Tokyo Gate Bridge in 2009

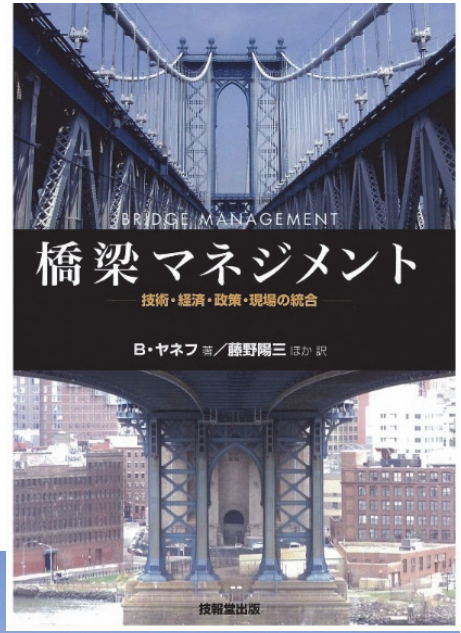

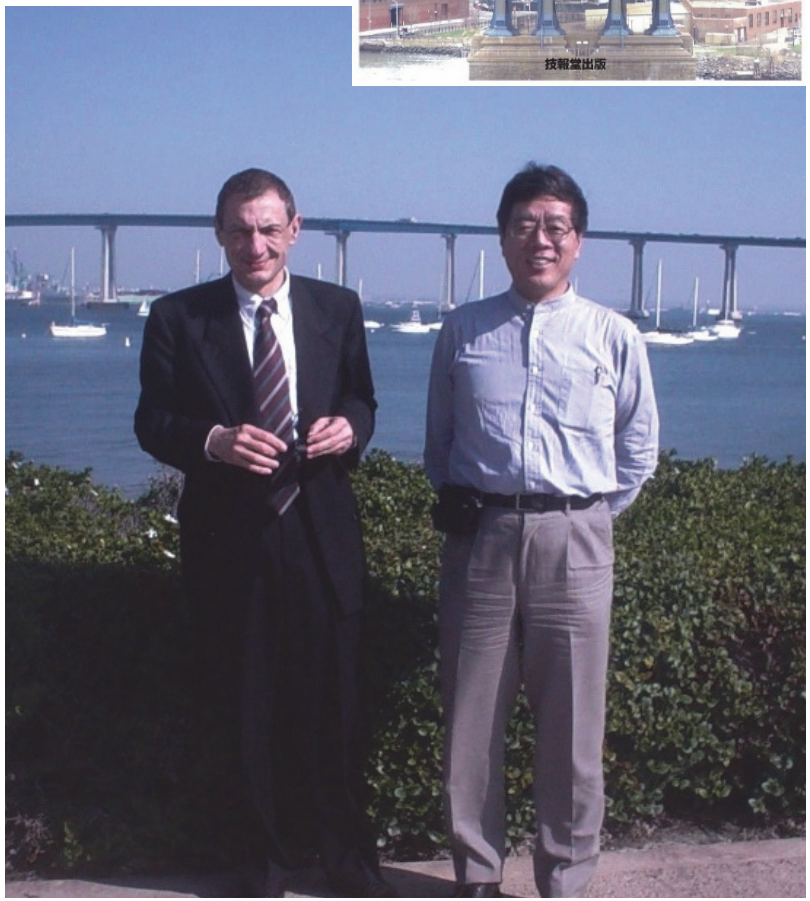

Dr. B. Yanev in San Diego.

Profs. Shirley Dyke and James Brownjohn with Yozo at the Cambridge Wireless Sensor Conference, June 2015.

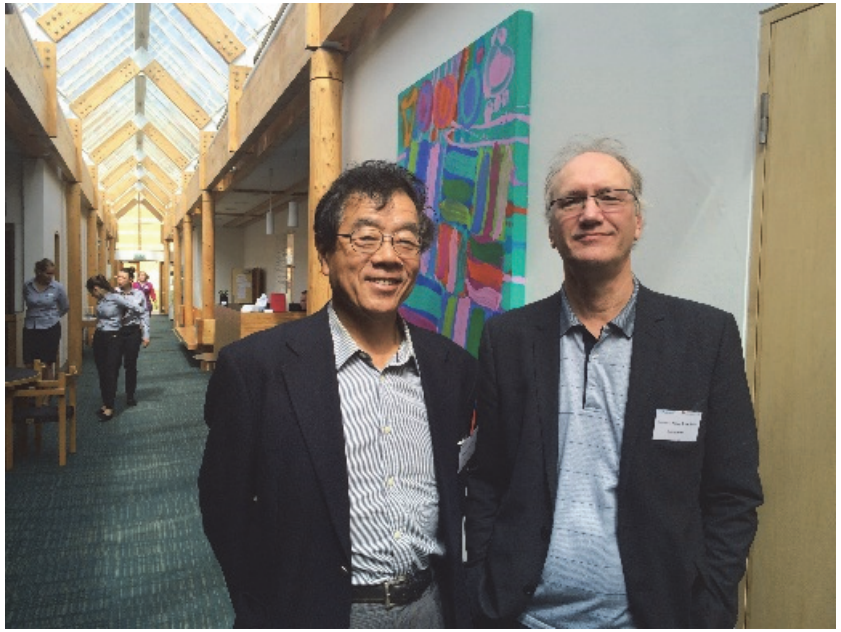

With Dr. Helmut Wenzel and Dr. Tomo Nagayama in NYC, 2010

Visiting Dr. Wenzel office and a bridge in Vienna, 2015

More than 20 Years of Bridge Paintings

① レインボーブリッジ

② 横浜ベイブリッジ

③岩淵水門

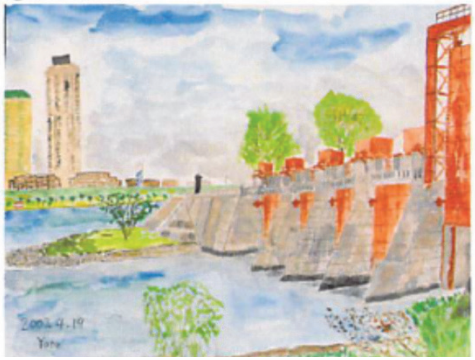

④紀伊国坂

⑤皇居前２連石積みアーチ

⑥勝鬨橋

⑦松住町架道橋

⑧聖橋

⑨打越橋（横浜）

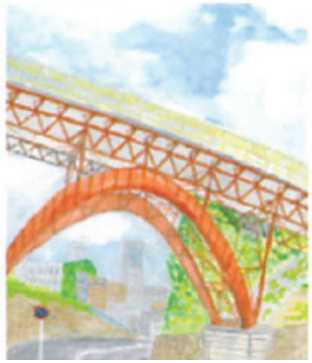

⑩東京駅

⑪南高橋

⑫日本橋

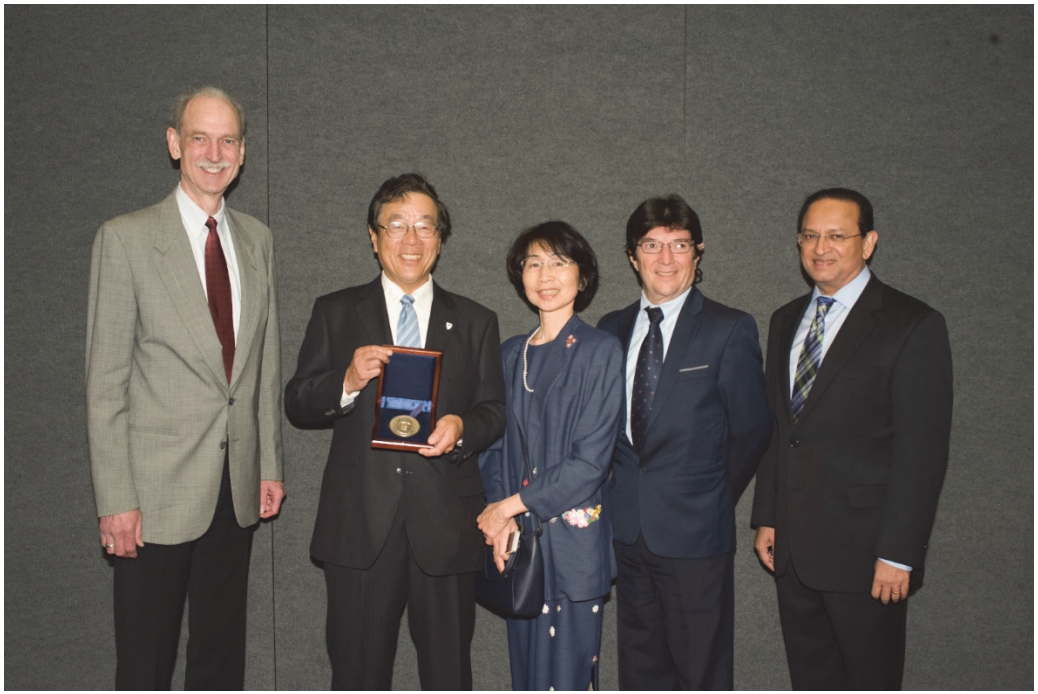

Receiving ASCE George Winter Medal
Award Ceremony in Portland, April 23, 2015
(with Prof. Satish Nagarajaiah on right)

Receiving Robert H. Scanlan Medal,
ASCE, 2011 (with Prof. Bill Iwan)

Receiving Raymond C. Reese Research Prize,
ASCE, 2007 (with Dr. T. Nagayama)

Final Lecture at University of Tokyo, March 1, 2013

Many of my former students came to celebrate my retirement. Prof. Paolo Gardoni, UIUC, was one of them. He is the coeditor with Prof. Bill Spencer for this special issue.

Yozo Fujino moved to Yokohama National University in April, 2014 and joined Institute of Advanced Sciences, in Oct., 2014 as a Distinguished YNU Professor.

Prof. B.F. Spencer and Prof K. Soga were appointed as
Distinguished Visiting Professor of IAS, YNU in June, 2015

Prof. Soga with President Y. Hasebe of YNU

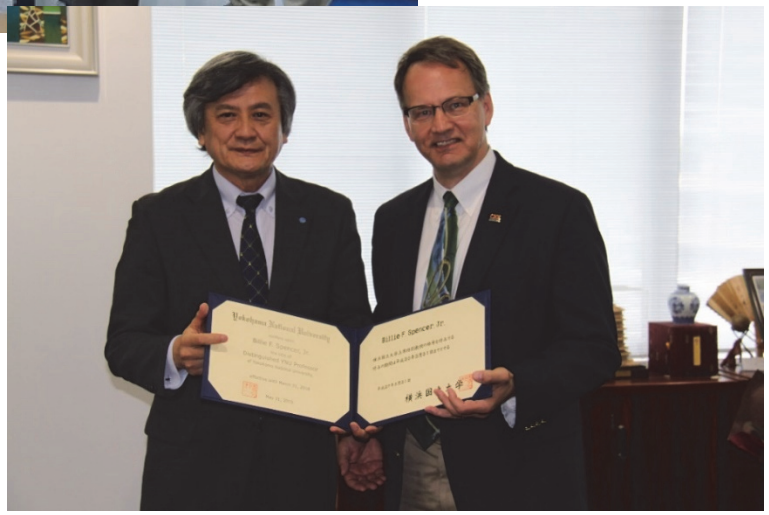

Photo of Prof. Spencer with President Y. Hasebe of YNU

Hoko Prize (SEIKO foundation)
Award ceremony on October 9th, 2015

Prof. H. Yamada, YNU, Mr. Yamawaki (one of my former students, director of Ministry of Education, Science, and Culture) Dr. Y. Mishima, President of Tokyo Inst. of Technology (friend for more than 60 years, my wife, Atsuko, Prof. Y. Fujino, Dr. Y. Hasebe, President of YNU and Dr. H. Yamaguchi, President of Saitama University (from left)